Cosmic ray background estimations in large liquid argon detectors for proton decay via $p \rightarrow K^{+}\overline{\nu}$ and ν_e appearance from ν_μ beams

Martin Richardson
Department of Physics and Astronomy
University of Sheffield

A thesis submitted for the degree of
Doctor of Philosophy

May 2016

Abstract

In recent years caverns deep underground at Sanford Underground Research Facility (SURF) near Lead, SD, have been proposed to house a large-scale liquid argon detector. This was once intended to be part of the "Deep Underground Science and Engineering Laboratory" (DUSEL) project to build extensive laboratory space for multidisciplinary scientific research, well-shielded from cosmic rays. The "Long Baseline Neutrino Experiment" (LBNE) later proposed such a detector at SURF and in 2015 LBNE evolved into the "Deep Underground Neutrino Experiment" (DUNE). All of these proposals have involved a detector suitable for the study of neutrino oscillation parameters, primarily using a ν_μ / $\overline{\nu}_\mu$ beam generated at Fermilab in Batavia, IL. The large target mass also enables a nucleon decay search, as well as the study of other phenomena. Cosmic-ray muons are capable of penetrating deep below the surface of the Earth and causing events that mimic rare signal events. Monte Carlo simulations of the cosmic muon-induced background for proton decay via the channel $p \to K^+ \, \overline{\nu}$ have been performed, where the signal is the observation of a single K^+ track. Cuts have been developed to reject the background $K^\pm$ observed, which has been estimated for a 10 kton (fiducial mass) LBNE/DUNE detector at a depth of 4850 ft and a 40 kton (fiducial mass) detector at 800 ft suitable for a DUSEL cavern. For the former the annual rate of background events for $p \to K^+ \, \overline{\nu}$ after cuts is $< 2.3 \times 10^{-3}$ kton^{-1} yr^{-1} (at 90% C.L.). For the latter this is < 0.026 kton^{-1} yr^{-1}. The cosmic ray-induced background for ν_e appearance from the ν_μ beam has also been estimated for a near-surface level detector (10 kton fiducial mass) once proposed for LBNE. The signal in this instance is an electromagnetic (EM) shower. After cuts the background has been estimated as 2.88 ± 0.25 yr^{-1} due to EM showers that start with $\gamma \to e^+ \, e^-$. The upper limits of the annual rates of EM showers starting with $K_L^0 \to \pi^\pm \, e^\mp \, \overline{\nu}_e/\nu_e$ in muon, proton and neutron-induced events are < 0.21 yr^{-1}, < 0.01 yr^{-1} and < 0.002 yr^{-1} (at 90% C.L.) after cuts. The upper limits of the annual rates of EM showers starting with $\pi^0 \to e^+ \, e^- \, \gamma$ in muon, proton and neutron-induced events are < 0.18 yr^{-1}, < 0.01 yr^{-1} and < 0.03 yr^{-1} (at 90% C.L.) after cuts.

Acknowledgements

The first and highest acknowledgement must go to Dr. Vitaly Kudryavtsev, an excellent Ph.D. supervisor from whom I could not have asked any more, and to whom I will always be indebted. Thank-you also to my viva examiners, Dr. Matthew Malek and Prof. Alex Murphy. Thanks also to Prof. Neil Spooner for offering me the Ph.D. position, and to Alan Auld Engineering for funding my stipend. I would also like to thank Dr. Matt Robinson, Dr. Paul Hodgson and Dr. Elena Korolkova for assisting me with my computational difficulties in the early days, and for their often-amusing and informative conversation, whether physics-related or otherwise. Many thanks also to fellow HEP group student Karl Warburton, for his valuable assistance regarding the surface-level detector simulations, and to the rest of the students in the group for all the laughs. Thanks also to Dr. Joel Klinger for his advice regarding the underground detector simulations. Thank-you also to the rest of the LBNE cosmogenics working group - Dr. Milind Diwan, Dr. Dongming Mei, Dr. Jeff de Jong, Dr. Chao Zhang and any others - for their invaluable input/feedback on the surface-level simulations and analysis. Extra thanks must also be given to Milind as my host during my stay at Brookhaven National Laboratory, to Dr. Brett Viren for being so helpful with any computational issues I had during my time on Long Island, and to all the staff there who made it such a welcoming place to work. A special mention here must also go to Leann and Hayven Thaw, for brightening up some long days. Thanks also to Dr. Eric Church and Dr. Tom Junk at Fermilab for their advice and assistance. I also want to thank all of the staff at the University of Sheffield Physics & Astronomy department (and elsewhere) who have ever taught me, or given up their time for the many questions I've bothered them with over the years.

Finally I must also give a massive thank-you to my parents and the rest of my family for their unwavering love, support and patience throughout all these years; I wouldn't be writing these words without it.

Contents

List of Figures

List of Tables

1 Foreword

This thesis reports primarily on simulations related to the proposed experiment formerly referred to as 'LBNE' (the Long Baseline Neutrino Experiment), which has recently evolved into 'DUNE' (the Deep Underground Neutrino Experiment). DUNE is very similar to LBNE in terms of primary goals, locations and collaborators but the two projects differ somewhat in terms of size and scope. Both programmes involved/involve generating a beam of $\nu_\mu/\overline{\nu}_\mu$ with a proton accelerator at Fermi National Accelerator Laboratory (Fermilab), IL, and directing it towards a detector at Sanford Underground Research Facility (SURF), SD. The simulations in this thesis involve estimating background rates for the detection of two phenomena in various versions of this detector - $\nu_e/\overline{\nu}_e$ appearance from the $\nu_\mu/\overline{\nu}_\mu$ beam (i.e. neutrino oscillation) and also the decay of the proton via the channel $p \to K^+\,\overline{\nu}$. This thesis is therefore divided into two main parts (ignoring the introductory chapter). Part of the thesis also relates to the formerly-proposed DUSEL (Deep Underground Science and Engineering Laboratory). This was to involve a similar detector at a different depth and with a different target mass to LBNE/DUNE; a background estimate for proton decay via $p \to K^+\,\overline{\nu}$ for that detector is also discussed in this thesis.

Both tasks (neutrino oscillation studies and the search for proton decay) are affected by the presence of cosmic rays. Particles of cosmic origin that strike the atmosphere can generate secondary particles. Some of these primary and secondary cosmic rays will reach a detector and mimic the signal events the detector is intended to look for. Since the signal events in both cases are rare events, it is necessary to know the size of this background and understand how it can be mitigated. The results stated in this thesis are the Monte Carlo 'truth' output of simulations made using the Geant4 toolkit; no consideration has been given to the detector response/track reconstruction downstream of this.

The set of simulations discussed first will involve estimating the cosmic ray muon-induced background for proton decay via the channel $p \to K^+\,\overline{\nu}$. The annual rate of background events in which a K^+ or K^- appears is estimated for a detector buried underground at a depth of 4850 ft (LBNE/DUNE) and at 800 ft (DUSEL), with a local geography appropriate for SURF. Various cuts are investigated with the aim of rejecting as many of these background events as possible, without eliminating genuine signal events in the process.

The second set of simulations discussed will involve estimating the cosmic ray muon, proton, neutron and photon-induced background for $\nu_e/\overline{\nu}_e$ appearance from the $\nu_\mu/\overline{\nu}_\mu$ beam. The signal for this is an electromagnetic (EM) shower; a cosmic ray-induced EM shower can mimic an EM shower that would constitute a $\nu_e/\overline{\nu}_e$ appearance event. The annual rate of background EM showers due to cosmic rays is estimated, for a detector design approximating an LBNE detector near the surface that preceded the DUNE design. Again a series of cuts are investigated in an attempt to efficiently identify and dismiss these unwanted background events.

The first chapter will discuss the theoretical and experimental justifications for the ongoing interest in these phenomena. This starts with a summary of the Standard Model (SM) to provide context for the discussion of its failures, and for the 'Grand Unified Theories' (GUTs) proposed to address these failures (which the construction of the SM acts as a template for). In the course of this discussion, proton decay emerges as one of the testable predictions of GUTs and is followed by a summary of experimental searches. This leads into a discussion of neutrino oscillation. After sections involving basic neutrino oscillation theory and experiments comes a description of the design and aims of LBNE/DUNE itself. Following this is a chapter relating to the design of the proton decay background simulations, which is itself followed by the a chapter detailing the results of these simulations. The next two chapters then cover the design and results of the simulations of the $\nu_e/\overline{\nu}_e$ appearance background, followed by a conclusion and appendices.

2 Introduction

2.1 The Standard Model

The "Standard Model" (SM) collectively refers to theories of the strong and the unified electromagnetic and weak interactions, which have been found to describe accurately (but incompletely) the behaviour of fundamental particles up to at least the TeV scale [1]. Its various components have been validated experimentally during the 20th and now 21st centuries by a variety of evidence, such as observations of the W [2,3], Z [4] and Higgs bosons [5,6], the gluon [7–10] the charm [11,12], bottom [13] and top quarks [14,15], and making such predictions as the relations between the W, Z masses and the electromagnetic and weak couplings [16], and the anomalous magnetic moment of the electron [17]. The SM is thus considered to be a great success, however, it is now clear that there are experimental and theoretical questions that the SM fails to address. Its basic features and some of these successes, difficulties and potential solutions will be briefly outlined in the following sections.

2.1.1 Electromagnetic interaction

Electromagnetism is dealt with by Quantum Electrodynamics (QED), a gauge-invariant quantum field theory of the interaction of light with electrically charged matter. QED is invariant [18,19] under local $U(1)$ group transformations, that is, the infinite group of spacetime-dependent phase transformations parameterized by $\alpha(x)$:

$$\psi(x) \to \psi'(x) = e^{i\alpha(x)}\psi(x), \qquad \overline{\psi}(x) \to \overline{\psi}'(x) = e^{-i\alpha(x)}\overline{\psi}(x). \tag{1}$$

For a fermion such as an electron described by a Dirac field $\psi(x)$, the Dirac Lagrangian (density) is

$$\mathcal{L}_{Dirac} = i\overline{\psi}\gamma^\mu\partial_\mu\psi - m\overline{\psi}\psi. \tag{2}$$

This Lagrangian structure can be recovered despite having made a transformation according to Eq. 1 if one replaces the ordinary partial derivate ∂_μ with a particular 'covariant' derivate D_μ that contains a 'gauge field' A_μ. These transform as follows:

$$\begin{gathered} D_\mu = \partial_\mu + ieA_\mu \qquad \text{where} \qquad A_\mu \to A'_\mu = A_\mu - \frac{1}{e}\partial_\mu\alpha(x) \\ \implies D_\mu\psi(x) \to D'_\mu\psi'(x) = e^{i\alpha(x)}D_\mu\psi(x), \end{gathered} \tag{3}$$

where the coupling e in the first line of Eq. 3 is the charge on the electron. The appropriately modified version of Eq. 2 is then found to be invariant under the transformations shown in Eq. 1 and the second line of Eq. 3:

$$i\overline{\psi}'\gamma^\mu D'_\mu\psi' - m\overline{\psi}'\psi' = ie^{-i\alpha(x)}\overline{\psi}\gamma^\mu e^{i\alpha(x)}D_\mu\psi - me^{-i\alpha(x)}\overline{\psi}e^{i\alpha(x)}\psi = i\overline{\psi}\gamma^\mu D_\mu\psi - m\overline{\psi}\psi \tag{4}$$

$$\to \mathcal{L}_{QED} = i\overline{\psi}\gamma^\mu\partial_\mu\psi + ie\overline{\psi}\gamma^\mu A_\mu\psi - m\overline{\psi}\psi - \tfrac{1}{4}F^{\mu\nu}F_{\mu\nu}. \tag{5}$$

The QED Lagrangian $\mathcal{L}_{QED}$ is completed by the inclusion of a kinetic term $-\frac{1}{4}F^{\mu\nu}F_{\mu\nu}$ (also $U(1)$ invariant) for the electromagnetic field (where $F^{\mu\nu} = \partial_\mu A_\nu - \partial_\nu A_\mu$). Expanding the $i\overline{\psi}\gamma^\mu D_\mu\psi$ term also yields the term $ie\overline{\psi}\gamma^\mu A_\mu\psi$, interpreted as the interaction of the gauge and fermion fields. Thus, requiring that the Lagrangian exhibits local $U(1)$ gauge symmetry requires/predicts the field A_μ. The necessarily massless [1], spin-1, neutral 'gauge boson' associated with this field is identified with the photon. Taking similar approaches involving other gauge groups has also produced important results for the weak and strong interactions. It also provides a template for other as-yet-unverified theories that are discussed in later sections and motivate the experiment to which this thesis relates.

2.1.2 Electroweak interaction

Unification of the electromagnetic and weak interactions is achieved in the 'GSW' model, proposed by Glashow, Weinberg and Salam in the 1960s [20–23]. The weak interaction only couples to left-handed/right-handed particles/anti-particles and groups pairs of particles into left-handed quark or lepton doublets according to their fermion generation. The doublet members are effectively treated as the same particle, being in one of two possible states of weak isospin (T) third component (T_3):

$$(\psi_{e,\mu,\tau,d,s,b})_L = \begin{pmatrix}\nu_e\\ e^-\end{pmatrix}_L, \begin{pmatrix}\nu_\mu\\ \mu^-\end{pmatrix}_L, \begin{pmatrix}\nu_\tau\\ \tau^-\end{pmatrix}_L, \begin{pmatrix}u\\ d\end{pmatrix}_L, \begin{pmatrix}c\\ s\end{pmatrix}_L, \begin{pmatrix}t\\ b\end{pmatrix}_L \qquad \begin{pmatrix}T_3=+\frac{1}{2}\\ T_3=-\frac{1}{2}\end{pmatrix} \tag{6}$$

In other words, the weak interaction has invariance under rotations in 'weak isospin' space (e.g. rotating ν_e into e^- or vice versa).

The $SU(2)$ group is the simplest group with doublet representations, the generators of this group being the 2×2 Pauli matrices τ_1, τ_2, τ_3 (Appendix 8.1). $SU(2)$ transformations can therefore be applied to these left-handed doublets but since the SM also contains right-handed fields, the SM Lagrangian cannot have a simple $SU(2)$ symmetry. However, it is invariant under transformations of the group $SU(2)_L \times U(1)_Y$[2]. One may denote the first lepton generation[3] as follows:

$$\psi_1(x) = \begin{pmatrix}\nu_e\\ e^-\end{pmatrix}_L, \qquad \psi_2(x) = \nu_{eR}, \qquad \psi_3(x) = e^-_R.$$

The free Lagrangian (analogous to the first term in Eq. 2) is $i\overline{\psi}_i(x)\gamma^\mu\partial_\mu\psi_i(x)$ $(i = 1,2,3)$. This is invariant under the following local $SU(2)_L \times U(1)_Y$ transformations of $\psi_{1,2,3}$, at the expense of introducing massless gauge fields B_μ and $W^{1,2,3}_\mu$ in the appropriate covariant derivatives D_μ :

$$\psi_1(x) \to \psi_1'(x) = e^{iY_1\beta(x)}U(x)\psi_1(x)\,, \qquad \psi_j(x) \to \psi_j'(x) = e^{iY_j\beta(x)}\psi_j(x) \qquad (j = 2,3)$$

$$D_\mu\psi_1(x) = \big[\partial_\mu - \tfrac{1}{2}igW_\mu(x) - ig'Y_1B_\mu(x)\big]\psi_1(x)\,, \quad D_\mu\psi_j(x) = \big[\partial_\mu - ig'Y_jB_\mu(x)\big]\psi_j(x) \tag{7}$$

where $U(x) = exp(\frac{1}{2}i\tau_i\alpha^i(x))$ and g, g' are the $SU(2)_L$ and $U(1)_Y$ couplings.

Here $\psi_{2,3}$ only undergo $U(1)$ transformations, which require a gauge field B_μ that transforms the same way as the photon field A_μ in QED (Eq. 3). The three other massless gauge fields for each of the three $SU(2)$ generators τ_i are defined as $W_\mu(x) \equiv W^i_\mu(x)\tau_i$:

$$W_\mu \equiv W^i_\mu\tau_i = \begin{pmatrix} W^3_\mu & W^1_\mu - iW^2_\mu \\ W^1_\mu + iW^2_\mu & -W^3_\mu \end{pmatrix} \qquad \to \qquad W^\pm \equiv W^1_\mu \mp iW^2_\mu. \tag{8}$$

---

[1] A mass term of the form $\frac{1}{2}m_\gamma A_\mu A^\mu$ would ruin the Lagrangian gauge invariance.

[2] The 'L' subscript refers to 'left-handed'. The 'Y' subscript refers to 'weak hypercharge', analogous to electric charge in the $U(1)_Q$ transformations in Section2.1.1 and will be discussed further in this section.

[3] This is equally valid for any quark or lepton generation; even though the SM has no right-handed neutrino due to its non-observation, it can still be included like this.

Symmetry under $SU(2)_L \times U(1)_Y$ transformations require B_μ and W_μ to transform as follows:

$$B_\mu(x) \to B'_\mu(x) = B_\mu(x) + \tfrac{1}{g'}\partial_\mu B_\mu(x)\ , \quad W_\mu(x) \to W'_\mu(x) = UW_\mu(x)U^\dagger - \tfrac{i}{g}\partial_\mu U U^\dagger.$$

With $W^\pm$ defined according to Eq. 8, this results in the following interaction terms when the free Lagrangian is computed:

$$\overline{\psi}_1\gamma^\mu D_\mu\psi_1 \qquad \to \qquad \tfrac{1}{\sqrt{2}}g\nu_{eL}\gamma^\mu W^+_\mu e^-_L, \quad \tfrac{1}{\sqrt{2}}g\overline{\nu}_{eR}\gamma^\mu W^-_\mu e^+_R. \tag{9}$$

The terms in Eq. 9 correspond to interaction vertices, shown in Figure 1 (i),(ii) respectively.

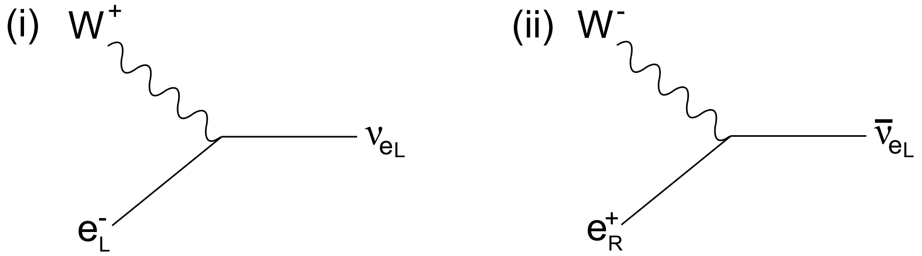

Figure 1: *The charged current (CC) weak interaction vertices associated with the Lagrangian terms in Eq. 9.*

Thus, the observable charged bosons W^+ and W^- are identified as combinations of the gauge fields $W^{1,2}$ and act as mediators of the weak interaction. This was confirmed when the $W^\pm$ bosons were discovered in 1983 through $\overline{p}p$ collisions, via the channel $\overline{p}p \to W \to l\,\overline{\nu}_l + X$ [2,3].

The W^3 and B_μ bosons are involved in mediating neutral current weak interactions. The $U(1)_Q$-invariant electromagnetic current J^{em}_μ (Eq. 5 ; $eA_\mu\sum_j\overline{\psi}_j\gamma^\mu Q\psi_j \equiv eA_\mu J^{em}_\mu$) may be expressed as

$$J^{em}_\mu = \overline{e}\gamma_\mu Qe = \overline{e}_L\gamma_\mu Qe_L + \overline{e}_R\gamma_\mu Qe_R, \tag{10}$$

where Q is the charge operator. This is not invariant under $SU(2)_L$ transformations since it involves the singlets $e_{L,R}$ rather than a doublet such as ψ_1. However, an $SU(2)$-invariant $U(1)$ current J^Y_μ can be introduced:

$$J^Y_\mu = \overline{\psi}_1\gamma_\mu Y_L\psi_1 + \overline{e}_R\gamma_\mu Y_R e_R.$$

The operators Y_L, Y_R are for ‘weak hypercharge’. Analogous terms for weak currents $J^i_\mu = \overline{\psi}_1\gamma^\mu\frac{1}{2}\tau_i\psi_1$ $(i = 1, 2, 3)$ can also be expressed as follows:

$$J^1_\mu = \tfrac{1}{2}(\overline{e}_L\gamma^\mu\nu_{eL} + \overline{\nu}_{eL}\gamma^\mu e_L), \quad J^2_\mu = \tfrac{i}{2}(\overline{e}_L\gamma^\mu\nu_{eL} - \overline{\nu}_{eL}\gamma^\mu e_L), \quad J^3_\mu = \tfrac{1}{2}(\overline{\nu}_{eL}\gamma_\mu\nu_{eL} - \overline{e}_L\gamma_\mu e_L).$$

$$\Longrightarrow \text{Defining also} \quad J^\pm_\mu \equiv J^1_\mu \pm iJ^2_\mu, \quad \text{then} \quad J^+_\mu = \overline{\nu}_{eL}\gamma^\mu e_L\ , \quad J^-_\mu = \overline{e}_L\gamma^\mu\nu_{eL}. \tag{11}$$

The EM current J^{em}_μ of Eq.10 can be split into two parts by combining J^Y_μ and J^3_μ:

$$J^{em}_\mu = J^3_\mu + \tfrac{1}{2}J^Y_\mu\ ,$$

$$\text{i.e.} \quad \overline{e}_L\gamma_\mu Qe_L + \overline{e}_R\gamma_\mu Qe_R = (\overline{\nu}_{eL}\gamma_\mu\tfrac{1}{2}\nu_{eL} - \overline{e}_L\gamma_\mu\tfrac{1}{2}e_L) + (\tfrac{1}{2}\overline{\psi}_L\gamma_\mu Y_L\psi_L + \tfrac{1}{2}\overline{e}_R\gamma_\mu Y_R e_R). \tag{12}$$

This contains the relationships $Y_R = 2Q$ and $Y_L = 2Q + 1$; the general relationship between hypercharge, charge and weak isospin is $Y = 2(Q - T_3)$. The interaction part of the electroweak Lagrangian $\mathcal{L}_{int}$ can thus be split up into the charged current (CC) part (featuring the W^+ and W^- of Eq. 9) and a neutral curent (NC) part involving the third weak isospin boson W^3_μ and the weak hypercharge boson B_μ:

$$\mathcal{L}_{int} = \mathcal{L}_{CC} + \mathcal{L}_{NC} = \tfrac{-1}{\sqrt{2}} g(J^+_\mu W^+_\mu + J^-_\mu W^-_\mu) + (-gJ^3_\mu W^3_\mu - \tfrac{1}{2} g' J^Y_\mu B^\mu),$$

where J^+, J^- were defined in Eq. 11.

The short range of the weak interaction implies that the gauge bosons involved are not massless, so the Higgs mechanism (Section 2.1.3) is invoked to generate mass terms for the weak bosons and break the $SU(2)_L \times U(1)_Y$ symmetry of the Lagrangian. When electroweak symmetry is broken (working in the 'unitary gauge', Section 2.1.3), the Lagrangian gains the following terms, some of which can be expressed in terms of a 4×4 mass matrix:

$$\mathcal{L}_{Higgs} = \tfrac{1}{2}\partial_\mu H \partial^\mu H - \tfrac{1}{2} 4\lambda v^2 H^2 + \sqrt{2}\lambda v H^3 + \tfrac{1}{4}\lambda H^4 \tag{13}$$

$$+ \tfrac{1}{4}\left(v + \tfrac{1}{\sqrt{2}} H\right)(W^1_\mu, W^2_\mu, W^3_\mu, B_\mu) \begin{pmatrix} g & 0 & 0 & 0 \\ 0 & g & 0 & 0 \\ 0 & 0 & g^2 & -gg' \\ 0 & 0 & -gg' & g'^2 \end{pmatrix} \begin{pmatrix} W^{\mu 1} \\ W^{\mu 2} \\ W^{\mu 3} \\ B^\mu \end{pmatrix} \tag{14}$$

where λ, v and H are defined in (Section 2.1.3). When this 4×4 matrix is diagonalised, two members of the corresponding eigenbasis may be expressed as combinations of W^3_μ and B_μ. One of the eigenvalues is zero, corresponding to a massless field; one combination can identified with the photon A_μ of QED (Section 2.1.1), highlighting a unifying link between the electromagnetic and weak interactions. Two of the other eigenvalues are g^2, which translate into masses for $W^\pm$. The last eigenvalue is $g^2 + g'^2$ and pertains to the mass of the other combination of W^3_μ and B_μ. This mixture is referred to as the Z boson and mediates the NC weak interactions:

$$\begin{pmatrix} Z_\mu \\ A_\mu \end{pmatrix} = \begin{pmatrix} cos\ \theta_W & -sin\ \theta_W \\ sin\ \theta_W & cos\ \theta_W \end{pmatrix} \begin{pmatrix} W^3_\mu \\ B_\mu \end{pmatrix} \quad \text{where } \cos\theta_W = \frac{g}{\sqrt{g^2 + g'^2}}, \quad \sin\theta_W = \frac{g'}{\sqrt{g^2 + g'^2}} . \tag{15}$$

The Z boson was discovered in 1983 via $\bar{p}p$ collisions and its subsequent decay to fermion-antifermion pairs [4]. The measurement of this weak mixing angle θ_W offers some supporting evidence [24]. It is related to the masses of the $W^\pm$ and Z bosons via $\frac{M_W}{M_Z} = cos\ \theta_W$ [25]. Measurements of $M_W = 80.385 \pm 0.015$ [26], $M_Z = 91.1876 \pm 0.0021$ [26] and $sin^2\ \theta_W = 0.23126 \pm 0.00022$ [27] are found to closely match this prediction.

2.1.3 Electroweak Symmetry Breaking

The fermions ψ and gauge bosons $W^{1,2,3}_\mu, B_\mu$ in the electroweak theory of Section 2.1.2 cannot have mass terms; such terms would mix left and right-handed fields, destroying the local $SU(2)_L \times U(1)_Y$ gauge symmetry of the Lagrangian. However, the fermions clearly do have masses and as already mentioned, the short range of the weak interaction implies that the physical bosons $W^\pm_\mu$ and Z_μ require masses also. Fortunately mass terms can arise downstream of the GSW model, through spontaneous breaking of electroweak gauge symmetry via the 'Higgs mechanism' [28–30] [4].

---

[4] More completely, the 'Englert-Brout-Higgs-Guralnik-Hagen-Kibble' mechanism.

One may start [25, 31] with the $SU(2)_L \times U(1)_Y$ covariant derivative of Eq. 7 as well as a doublet Φ of complex scalar Higgs fields with components ϕ^+, ϕ^0 :

$$\Phi = \begin{pmatrix} \phi^+ \\ \phi^0 \end{pmatrix}, \qquad \text{where} \quad \phi^+ = \frac{1}{\sqrt{2}}(\phi_1 + i\phi_2), \qquad \phi^0 = \frac{1}{\sqrt{2}}(\phi_3 + i\phi_4). \tag{16}$$

A contribution $\mathcal{L}_\Phi$ can be added to the electroweak Lagrangian by involving the $SU(2)_L \times U(1)_Y$-invariant, renormalizable scalar potential V:

$$\mathcal{L}_\Phi = T - V = (D_\mu\Phi)^\dagger(D_\mu\Phi) - \big(\mu^2(\Phi^\dagger\Phi) - \lambda(\Phi^\dagger\Phi)^2\big) \tag{17}$$

where T is kinetic energy. This Lagrangian is invariant under the following gauge transformation:

$$\Phi \rightarrow \Phi' = exp(-\tfrac{1}{2}ig\vec{\tau}.\vec{\Delta} - \tfrac{1}{2}ig'\Lambda)\Phi$$

where $\vec{\Delta}$ and Λ parametrize the SU(2) and U(1) transformations as α did in Eq. 1. The minimum of the potential $V = \mu^2(\Phi^\dagger\Phi) - \lambda(\Phi^\dagger\Phi)^2$ (Eq. 17) is given by

$$\frac{dV}{d(\Phi^\dagger\Phi)} = \mu^2 - 2\lambda(\Phi^\dagger\Phi) = 0 \qquad \Longrightarrow \qquad \Phi^\dagger\Phi|_{min} = \frac{\mu^2}{2\lambda}. \tag{18}$$

The $SU(2)_L \times U(1)_Y$ symmetry may be spontaneously broken in such a way that the 'Goldstone' fields $\phi_{1,2,4}$ of Eq. 16 are eliminated. This may be achieved by using the 'unitary gauge', i.e. choosing zero vacuum expectation values (VEVs) of these fields ($\langle 0|\phi_{1,2,4}|0\rangle^2 = 0$). A non-zero VEV of $v = \mu/\sqrt{2\lambda}$ (Eq. 18) is also chosen for ϕ_3 (where $\phi_3 \equiv v + H$ and the field H is the neutral scalar Higgs field.

The Higgs doublet (Eq. 16) is then $\Phi = \frac{1}{\sqrt{2}}(0, v + H)^T$ and using Eq. 7, the first term on the right hand side of Eq. 17 is as follows:

$$D_\mu\Phi = \begin{pmatrix} \frac{1}{\sqrt{2}}igW_\mu^+(v+H) \\ \big[\partial_\mu - \frac{1}{2}i(gcos(\theta_W) + g'sin(\theta_W)Z_\mu)\big](v+H) \end{pmatrix}, \tag{19}$$

$$(D_\mu\Phi)^\dagger = \begin{pmatrix} -\frac{1}{\sqrt{2}}igW_\mu^-(v+H) \\ \big[\partial_\mu + \frac{1}{2}i(gcos(\theta_W) + g'sin(\theta_W)Z_\mu)\big](v+H) \end{pmatrix}. \tag{20}$$

The contribution $\mathcal{L}_\Phi$ (Eq. 17) to the electroweak Lagrangian therefore becomes

$$\mathcal{L}_\Phi = \tfrac{1}{2}\partial_\mu H\partial^\mu H + \tfrac{1}{4}g^2(H^2 + 2vH + v^2)W_\mu^+W^{-\mu} \tag{21}$$

$$+ \tfrac{1}{8}(g^2 + g'^2)(H^2 + 2vH + v^2)Z_\mu Z^\mu - \mu^2H^2 - \tfrac{\lambda}{4}(H^4 + 4vH^3), \tag{22}$$

which is also Eq. 14 stated in terms of the physical bosons $W_\mu^\pm$, Z_μ. Thus at the expense of introducing a massive spin-0 scalar boson H, one finds mass terms $\frac{1}{4}g^2v^2W_\mu^+W^{-\mu}$ and $\frac{1}{8}v^2(g^2 + g'^2)Z_\mu Z^\mu$ for the previously massless $W^\pm$ and Z bosons, as required. They have masses of $M_W = \frac{1}{2}gv$ and $M_Z = \frac{1}{2}v\sqrt{(g^2 + g'^2)}$ [5] respectively whilst the photon A_μ remains massless [6].

A Higgs boson discovery was announced in 2012 by the ATLAS and CMS collaborations [5, 6] from pp collisions resulting in the decay channels $H \rightarrow WW, ZZ, \gamma\gamma, \tau\tau, b\bar{b}$, at

---

[5] These lead to the relation between M_W, M_Z and θ_W mentioned in Section 2.1.2 since $\frac{g'}{g} = tan\ \theta_W$.

[6] The Higgs itself also gets a mass due to the term $-\mu^2H^2$ in Eq. 22.

a mass of $126.0 \pm 0.4\,(\text{stat}) \pm 0.4\,(\text{sys})$ GeV (by ATLAS) and $125.3 \pm 0.4\,(\text{stat}) \pm 0.5\,(\text{syst})$ GeV (by CMS).

In addition to boson masses, the Higgs mechanism also allows for the fermions to have mass without spoiling the gauge invariance. A Dirac mass term of the form $-m\overline{\psi}\psi = -m(\overline{\psi}_R\psi_L + \overline{\psi}_R\psi_L)$ is not invariant under $SU(2)_L \times U(1)_Y$ since a left-handed doublet will transform differently to a right-handed singlet. However, the Higgs doublet Φ allows a term [25] that is a singlet under $SU(2)_L$ and $U(1)_Y$, of the form $-Y_f(\overline{\psi}_L\Phi\psi_R + \overline{\psi}_R\overline{\Phi}\psi_L)$ [7]. This yields mass terms and fermion-Higgs interaction terms, for example

$$-Y_e\frac{1}{\sqrt{2}}\left[(\nu_e, e)_L \begin{pmatrix} 0 \\ v+H \end{pmatrix} e_R + \overline{e}_R(0, v+H)\begin{pmatrix} \nu_e \\ e \end{pmatrix}_L\right] = \frac{-Y_e v}{\sqrt{2}}\overline{e}e + \frac{-Y_e}{\sqrt{2}}H\overline{e}e.$$

Generally a fermion mass m_f is related to the Higgs VEV v and Yukawa coupling Y_f via

$$m_f = \frac{Y_f v}{\sqrt{2}}. \tag{23}$$

Notably since the weak interaction does not appear to involve right-handed neutrinos, there is no right-handed neutrino field in the SM and hence no such mass terms for neutrinos. This is a problem for the SM, given that tiny but still non-zero masses for the neutrinos have now been established experimentally (Section 2.2.1). These masses can be understood in terms of a 'see-saw' mechanism (Section 2.4.5) if one treats the list of fields in the SM as incomplete and postulates the existence of right-handed neutrinos.

2.1.4 Strong interaction

The SM also includes a theory of strong interactions between quarks and the gauge bosons that mediate it, referred to as Quantum Chromodynamics (QCD). Quarks were theorized as fundamental participants in strong interactions by Gell-Mann and Zweig in 1964 [32, 33], with the gluons (and the asymptotic freedom[8] of the interaction) proposed by Politzer [34], Wilczek and Gross in 1973 [35]. The quarks were eventually identified with partons, the point-like constituents of the proton proposed by Feynman [36] and Bjorken [37] in 1969 to account for deep inelastic e^-p scattering experiments [38, 39].

It was proposed that the quark fields ψ_q possess a quantum number ('colour') to preserve the antisymmetry of certain baryon wavefunctions, which would otherwise be symmetric under interchange of their constituent quarks. Direct evidence of three quark colours first came from e^+e^- collisions, in which the ratio of cross-sections for hadron and $\mu^+\mu^-$ production were consistent with there being three quarks of each flavour [40].

In a manner analogous to the QED and Electroweak theories, gauge symmetry also led to a successful model in QCD. In this case the quark fields are organised into colour triplets $\psi_q^T \equiv (\psi_q^r, \psi_q^g, \psi_q^b)$ and so invariance of the Lagrangian under local gauge transformations of the $SU(3)$ group was postulated. Since the Special Unitary groups $SU(N)$ have $N^2 - 1$ generators [41], a total of eight massless, spin-1 gauge bosons (referred to as 'gluons') are required. The QCD Lagrangian is as follows [42]:

$$\mathcal{L}_{QCD} = \sum_q \overline{\psi}_{q,a}\big(i\gamma^\mu\partial_\mu\delta_{ab} - g_s\gamma^\mu\lambda^c_{ab}\mathcal{A}^c_\mu - m_q\delta_{ab}\big)\psi_{q,b} - \tfrac{1}{4}F^A_{\mu\nu}F^{A\mu\nu}$$

---

[7] This only applies to down-type fermions, but up-type fermions can be dealt with via $\Phi \to -i\tau_2\Phi^*$.

[8] The strength of the interaction becoming asymptotically weaker with increasing energy/decreasing length scales.

where the subscript q, a on the quark spinors ψ_{qa} denote quark flavour and colour respectively, g_s is the strong interaction coupling, λ^c_{ab} are the eight 3×3 generator matrices of the $SU(3)$ group ($c = 1, ..., 8$) (Appendix 8.2), and $\mathcal{A}^c_\mu$ are the gauge fields (a.k.a. gluons) required for the $SU(3)$ symmetry of $\mathcal{L}_{QCD}$ under the transformation $\psi(x) \to \psi'(x) = e^{it^c\alpha_c(x)}\psi(x)$.

The gluon was confirmed via e^+e^- collisions by the TASSO, PLUTO and JADE collaborations [7–10]. Two-jet events from $e^+e^- \to \bar{q}q$ were expected to have a leading correction from $e^+e^- \to \bar{q}qg$, which was indeed indicated by the observation of three-jet events.

Also a total of six quark fields $\psi_q = (u, d, c, s, t, b)$ are known to exist, with SM predictions leading to the discovery of the three heaviest. The fourth quark (charm) was predicted in 1970 by the Glashow-Iliopoulos-Maiani (GIM) mechanism, proposed to explain the suppression of flavour-changing neutral currents and $\Delta S = 2$ transitions in weak interactions [23]. Its discovery came in 1974 through the observation of the J/Ψ meson ($\bar{c}c$) through e^+e^- collisions [11, 12]. Kobayashi and Maskawa predicted the top and bottom quarks in 1973, realizing that four quarks could not account for CP violation in kaon decays [43] and extending the GIM mechanism to include a third weak isodoublet (Eq. 6). Confirmation of the bottom quark came in 1977 through the discovery of the Υ meson ($\bar{b}b$) in p-nucleus collisions [13]. The top quark discovery came in 1995 through $\bar{p}p$ collisions resulting in the decay $\bar{t}t \to WW\bar{b}b$ [14, 15]. However, the SM provides no indication of why there should be six quarks in a total of three generations; a way to account for this in terms of charge quantization is offered by theories that go beyond the SM (Section 2.2).

Thus QCD and the Electroweak model together form the SM, said to possess $SU(3)_C \times SU(2)_L \times U(1)_Y$ gauge symmetry and be spontaneously broken to $SU(3)_C \times U(1)_Y$ via the Higgs mechanism. Since the ATLAS and CMS discoveries of a Higgs-like particle in 2012, all the particles that are required by the SM have been accounted for. Table 1 shows a summary of the SM fermions, which has relevance for subsequent sections in this chapter. However, whilst no experimental result poses any compelling threat to its correctness, the SM is known to provide an incomplete description of the physics of fundamental particles (Section 2.2.1). Consequently many theories have been proposed, and many experiments have been proposed and performed, in attempts to answer questions that the SM leaves open.

Table 1: *A summary of the fermions that feature in the SM. The first row shows symbols frequently used throughout this chapter. The second row indicates in parentheses whether a field is a singlet, doublet or triplet under ($SU(3)_C$, $SU(2)_L$). The last three rows show the specific quark and lepton content for each generation of SM fermions.*

Multiplet symbol	Q	L	q^C	l^C
($SU(3)_C$, $SU(2)_L$)	$(3, 2)$	$(1, 2)$	$(3, 1)$	$(1, 1)$
Generation 1	$\begin{pmatrix} u_L^{r,g,b} \\ d_L^{r,g,b} \end{pmatrix}$	$\begin{pmatrix} \nu_L^e \\ e_L \end{pmatrix}$	$u_R^{r,g,b}, \quad d_R^{r,g,b}$	e_R
Generation 2	$\begin{pmatrix} c_L^{r,g,b} \\ s_L^{r,g,b} \end{pmatrix}$	$\begin{pmatrix} \nu_L^\mu \\ \mu_L \end{pmatrix}$	$c_R^{r,g,b}, \quad s_R^{r,g,b}$	μ_R
Generation 3	$\begin{pmatrix} t_L^{r,g,b} \\ b_L^{r,g,b} \end{pmatrix}$	$\begin{pmatrix} \nu_L^\tau \\ \tau_L \end{pmatrix}$	$t_R^{r,g,b}, \quad b_R^{r,g,b}$	τ_R

2.2 Beyond the Standard Model - GUTs and proton decay

2.2.1 Shortcomings of the Standard Model

As mentioned in Section 2.1.3, whilst greatly successful, the SM has some major shortcomings. For example, one issue is that it treats neutrinos as being massless. However, they must have non-zero masses to explain the well-established phenomenon of 'neutrino oscillation' (Section 2.4). The study of this phenomenon is a primary motivation for the experiment upon which part of this thesis is based (Sections 5, 6). There are also numerous other issues, such as the SM providing no viable candidate for non-baryonic dark matter [44]. Nor does the SM offer an explanation for the apparent extent of matter-antimatter asymmetry of the universe [45], the investigation of which (via neutrino oscillation analysis) was/is the ultimate goal of LBNE/DUNE. Also only three of the four known interactions are addressed in the SM since a theory of gravitation is completely absent. A further issue is the 'hierarchy problem', i.e. that the Higgs boson mass acquires quadratically divergent quantum corrections; for the SM to be valid many orders of magnitude above the electroweak scale, the theory parameters must undergo an unsatisfying 'fine-tuning' to keep the measurable Higgs mass at an acceptable level of $\mathcal{O}(10^2\text{ GeV})$ [46]. There are also as many as 19 free parameters in a supposedly fundamental theory (namely the three couplings g, g', g_s for the gauge group $SU(3)_C \times SU(2)_L \times U(1)_Y$, the Higgs mass and vacuum expectation value, nine Yukawa coefficients for the masses of the quarks and charged leptons, three mixing angles and one phase for the CKM matrix, and a phase for the QCD vacuum [47]) with no predictions for how they may be related [48]. Nor does the SM provide any insight as to why there are three families of quarks and leptons, or why there is a hierarchy of masses among them. Neither is there any explanation of why the strengths of the three gauge couplings differ so much at the energy scales so far investigated, or why charge should be quantized in fractions of that of the electron.

As discussed in Sections 2.1.1- 2.1.4, requiring that a Lagrangian exhibits local gauge symmetry under some transformation of the fields involved has proven a successful approach to model-building. The unification of the electromagnetic and weak interactions under the larger gauge group $SU(2) \times U(1)$ has also been fruitful. It has therefore been suspected that the $SU(3)_C \times SU(2)_L \times U(1)_Y$ gauge symmetry of the SM may be the result of breaking a larger gauge symmetry in the same manner that $SU(3)_C \times SU(2)_L \times U(1)_Y$ is broken to $SU(3)_C \times U(1)_Y$ (Section 2.1.3). Such a 'Grand Unified Theory' (GUT) in which the electroweak and strong interactions are found to belong to some overarching symmetry group has long been pursued. Many theories have been constructed based on this idea, which often give rise to elegant solutions for some of the above-mentioned problems that the SM leaves open.

Unfortunately most of the predictions made by such theories are at very high energy scales, far beyond present experimental capabilities. One major exception to this is that GUTs in general can predict (by virtue of accommodating quarks and leptons in the same multiplet) the extremely slow decay of protons - a particle that is fully stable in the SM and one that has never been observed to decay. This so-far-unobserved phenomenon has been the subject of decades-long searches and also partly motivates the experiment upon which some of this thesis is based (Sections 3, 4). The following sections discuss some frequently-encountered GUTs, their proton decay predictions and a few ways they can address the problems left open by the SM.

2.2.2 Grand unification via the SU(5) group

The first GUT was the Georgi-Glashow model [49,50] proposed in 1974. It is based on $SU(5)$, the smallest single gauge group to contain the SM (i.e. $SU(3)_C \times SU(2)_L \times U(1)_Y$) as a subgroup. It turns out to predict a proton decay lifetime that is now too short to agree with experiment, as well as making other inaccurate predictions. However, it is still a useful starting point to demonstrate features that are shared by other GUTs that have not yet been ruled out experimentally.

To begin with one may categorise the fermion fields by their Standard Model 'decomposition'. This is denoted by three numbers in parentheses that refer to how they transform under $SU(3)_C \times SU(2)_L \times U(1)_Y$ (as discussed in Appendix 8.3). For example, the quark fields $q \equiv u, d, c, s, t, b$ each form an $SU(3)$ colour triplet such as $(q_r, q_g, q_b)^T$, and the left-handed quarks in a given fermion generation form an $SU(2)$ weak isospin doublet such as $(u_L, d_L)^T$. Thus, if the fermion in question is a left-handed, up-type quark, then it will have a hypercharge of:

$$\tfrac{1}{2}Y = \tfrac{1}{2}(2(Q - T_3)) = \tfrac{1}{2}(2(\tfrac{2}{3} - \tfrac{1}{2})) = \tfrac{1}{6}.$$

The quarks u_{rL} ,u_{gL}, u_{bL} therefore have SM gauge quantum numbers that can be denoted as $(3, 2, \frac{1}{6})_L$. Similarly a down-type, right-handed quark has $T_3 = 0$, $Q = -\frac{1}{3} \implies \frac{1}{2}Y = -\frac{1}{3}$, so would be categorised as $(3, 1, -\frac{1}{3})_R$. This is summarised for the first generation of fermions in Table 2.

Table 2: *The assignment of SM gauge quantum numbers for the fifteen fermions of the first SM generation, where everything is stated in terms of left-handed fields. The upper row indicates the quantum numbers and the lower row indicates which fields they correspond to.*

$(3,\ 2,\ \frac{1}{6})$	$(3^*,\ 1,\ \frac{1}{3})$	$(3^*,\ 1,\ -\frac{2}{3})$	$(1,\ 2,\ -\frac{1}{2})$	$(1,\ 1,\ 1)$
$(u_{r,g,b})_L$, $(d_{r,g,b})_L$	$(d_{r,g,b})^c_L$	$(u_{r,g,b})^c_L$	e^-_L, ν_{eL}	$(e^-_L)^c$

Models based on the $SU(5)$ group utilise two irreducible representations that together neatly contain all fifteen fields of a given generation of SM fermions (Table 2). These multiplets are denoted **5** and **10** due to the number of fields they each contain. The construction of some important representations of $SU(5)$ and the SM group decompositions for each (in terms of the first row in Table 2) are discussed in Appendix 8.3 and 8.4. For instance, the **5** has the SM decomposition $(3, 1, -\frac{1}{3}) \oplus (1, 2, \frac{1}{2})$. Another important representation is the adjoint, constructed from the product of the fundamental representation with itself ($\overline{\mathbf{5}} \otimes \mathbf{5} = \mathbf{1} \oplus \mathbf{24}$); the $SU(5)$ gauge bosons and the Higgs bosons that relate to breaking $SU(5)$ to $SU(3)_C \times SU(2)_L \times U(1)_Y$ are placed in a **24** and $\mathbf{24}_H$.

Regardless of its colour, a quark will still have the same $SU(2)_L \times U(1)_Y$ charges. Unification under $SU(5)$ therefore demands that the $SU(3)_C$ and $SU(2)_L \times U(1)_Y$ groups must commute [51]. This requires that the $SU(2)_L \times U(1)_Y$ generators behave as unit or zero matrices with respect to the $SU(3)_C$ generators and vice versa. A way to achieve this is is to have the bottom-right 2×2 region of the first three 5×5 $SU(5)$ generators $T^{\alpha=1,2,3}$ occupied by the Pauli matrices $\tau^{1,2,3}$ of $SU(2)_L$ (Appendix 8.1) and the upper-left $3{\times}3$ area of $T^{\alpha=5,\ldots,12}$ occupied by the Gell-Mann matrices $\lambda^{a=1,\ldots,8}$ of $SU(3)$ (Appendix 8.2) [52,53]:

$$T^{1,2,3} = \begin{pmatrix} 0 & 0 & 0 & 0 & 0 \\ 0 & 0 & 0 & 0 & 0 \\ 0 & 0 & 0 & 0 & 0 \\ 0 & 0 & 0 & \multicolumn{2}{c}{\multirow{2}{*}{$\tau^{1,2,3}$}} \\ 0 & 0 & 0 & & \end{pmatrix} \qquad T^{\alpha=5,\ldots,12} = \begin{pmatrix} & & & 0 & 0 \\ & \lambda^{\alpha-4} & & 0 & 0 \\ & & & 0 & 0 \\ 0 & 0 & 0 & 0 & 0 \\ 0 & 0 & 0 & 0 & 0 \end{pmatrix}$$

$$\text{and also} \quad T^4 = diag(\tfrac{-1}{3}, \tfrac{-1}{3}, \tfrac{-1}{3}, \tfrac{1}{2}, \tfrac{1}{2}) \equiv \tfrac{1}{2}Y.$$

The structure of these generators determines the fermion content of the $SU(5)$ fundamental representation **5**. Based on the generators $T^{5,\ldots,12}$, the first three elements in **5** must be $SU(3)$ triplet (i.e. quark) fields; this corresponds to the $(3, 1, -\frac{1}{3})$ part of the SM decomposition of **5**. Since $(3, 1, -\frac{1}{3})$ indicates an $SU(2)$ singlet, the quark fields must be right-handed. Finally the hypercharge of T^4 determines the identity of the quark:

$$\tfrac{1}{2}Y = \tfrac{1}{2}(2(Q - T_3)) = \tfrac{1}{2}(2(Q - 0)) = -\tfrac{1}{3} \quad \rightarrow \quad Q = -\tfrac{1}{3}$$

so the first three elements of **5** are a right-handed down-type quark in red, green and blue. Similarly the generators $T^{1,2,3}$ determine that the last two elements in **5** are an $SU(2)$ doublet, $SU(3)$ singlet (which corresponds to the $(1, 2, \frac{1}{2})$ part of the SM decomposition of **5**). Since they must also have the same handedness as the first three elements, and require a hypercharge of $\frac{1}{2}Y = \frac{1}{2}$, the fourth and fifth components of **5** are the right-handed charged and neutral antileptons of the appropriate fermion generation. For the sake of consistently working with left-handed fields, the conjugate representation $\overline{\mathbf{5}}$ is often used. For example, the **5** multiplet for first fermion generation is filled as follows:

$$\mathbf{5} = \begin{pmatrix} d_r \\ d_g \\ d_b \\ e^+ \\ \overline{\nu}_e \end{pmatrix}_R \quad \rightarrow \quad \overline{\mathbf{5}} = \begin{pmatrix} \overline{d}_r \\ \overline{d}_g \\ \overline{d}_b \\ e^- \\ -\nu_e \end{pmatrix}_L \tag{24}$$

With $T_3 = diag(0, 0, 0, \frac{1}{2}, -\frac{1}{2})$, the charge operator $Q = T_3 + \frac{1}{2}Y$ is a linear combination of $SU(2)$ and $U(1)$ generators. Since the generators of any $SU(N)$ group must have zero trace, the sum of the eigenvalues of $Q = diag(-\frac{1}{3}, -\frac{1}{3}, -\frac{1}{3}, 1, 0)$ must be zero and so

$$Q(\overline{\mathbf{5}}) = 0 \quad \rightarrow \quad 3Q(d) + Q(\overline{\nu}_e) + Q(\overline{e}^+) = 0 \quad \rightarrow \quad Q(d) = -\tfrac{1}{3}.$$

Thus, having quarks of three colours provides a reason for charge quantization in fractions of the electron charge; a solution to one question left unanswered by the SM (Section 2.2.1) emerges from $SU(5)$ theory.

The remaining ten fermion fields may be placed into the (antisymmetric) **10** [54], which has the SM decomposition (Table 67) required to accommodate them: $(3, 2, \frac{1}{6}) \oplus (3^*, 1, -\frac{2}{3}) \oplus (1, 1, 1)$ (Table 2). This is built by taking the direct product $\mathbf{5} \otimes \mathbf{5}$ [9] via the use of Young's diagrams (Appendix 8.3) and is constructed for the first SM generation as

---

[9] The product $\mathbf{5} \otimes \mathbf{5} = \mathbf{10} \oplus \mathbf{15}$ but the **15** contains a colour sixtuplet (Table 67) which does not match any SM state and can therefore be dismissed.

follows:

$$\begin{array}{c|ccccc} & d_r & d_g & d_b & e^+ & \overline{\nu}_e \\ \hline d_r & 0 & \lambda_{12} & \lambda_{13} & \lambda_{14} & \lambda_{15} \\ d_g & -\lambda_{12} & 0 & \lambda_{23} & \lambda_{24} & \lambda_{25} \\ d_b & -\lambda_{13} & -\lambda_{23} & 0 & \lambda_{34} & \lambda_{35} \\ e^+ & -\lambda_{14} & -\lambda_{24} & -\lambda_{34} & 0 & \lambda_{45} \\ \overline{\nu}_e & -\lambda_{15} & -\lambda_{25} & -\lambda_{35} & -\lambda_{45} & 0 \end{array}_L \rightarrow \mathbf{10} = \frac{1}{\sqrt{2}} \begin{pmatrix} 0 & \overline{u}_b & -\overline{u}_g & u_r & d_r \\ -\overline{u}_b & 0 & \overline{u}_r & u_g & d_g \\ \overline{u}_g & -\overline{u}_r & 0 & u_b & d_b \\ -u_r & -u_g & -u_b & 0 & \overline{e} \\ -d_r & -d_g & -d_b & -\overline{e} & 0 \end{pmatrix}_L \tag{25}$$

where the fermion occupying element $\mathbf{10}_{ij}$ is given by summing the quantum numbers of Q, T_3 and colour from the i^{th} field on the left of the matrix λ and the j^{th} field above it. This organization of all fifteen fields of the first generation of SM fermions into $\mathbf{\overline{5}}$ and $\mathbf{10}$ can be repeated for the other two generations.

Since the $SU(5)$ group has 5^2-1 generators, this demands the introduction of a further twelve generators $T^{\alpha=13,...,24}$, none of which exist in the SM:

$$T^{\alpha=13,...,24} = \begin{pmatrix} 0 & 0 & 0 & & \\ 0 & 0 & 0 & \multicolumn{2}{c}{t^{13+k}} \\ 0 & 0 & 0 & & \\ \multicolumn{3}{c}{(t^{13+k})^\dagger} & 0 & 0 \\ & & & 0 & 0 \end{pmatrix} \qquad (k = 0, 1, ..., 11), \tag{26}$$

where t^{13+k} are the 3×2 matrices given in Appendix 8.5.

One may demand Lagrangian gauge invariance under $SU(5)$ in a manner analogous to that outlined for the SM (Sections 2.1.1- 2.1.4). In this instance a gauge transformation of ψ and the covariant derivative it requires to preserve the Lagrangian invariance are

$$\psi \rightarrow exp(-i\tfrac{1}{2}\eta^\alpha T^\alpha)\psi \qquad D_\mu = \partial_\mu - ig_5 T^\alpha V^\alpha_\mu \qquad (\alpha = 1, 2, ..., 24). \tag{27}$$

The gauge bosons are placed in the $SU(5)$ adjoint representation $\mathbf{24} \equiv \frac{1}{\sqrt{2}} T^\alpha V^\alpha_\mu$ which contains twenty-four gauge bosons V^α_μ [10] . Thus, in addition to the twelve SM gauge bosons [11], an $SU(5)$-based GUT predicts that there are also three X and three Y bosons, plus their antiparticles. These X and Y bosons are referred to as 'leptoquarks', since they allow vertices in which a quark can transmute into a lepton or vice versa.

As shown in Table 67 the **24** has a SM decomposition of

$$(8, 1, 0) \oplus (3, 2, -\tfrac{5}{6}) \oplus (3^*, 2, \tfrac{5}{6}) \oplus (1, 3, 0) \oplus (1, 1, 0),$$

where the SM gauge bosons fit into $(8, 1, 0)$ (for gluons), $(1, 3, 0)$ (for $W^\pm_\mu$, Z_μ) and $(1, 1, 0)$ (for A_μ) [53]. The weak-isodoublet and colour-triplet/anti-triplet $X/\overline{X}$ and $Y/\overline{Y}$ bosons are required by the $(3, 2, \frac{5}{6})$ / $(3^*, 2, -\frac{5}{6})$ part and X and Y must therefore have electric charges of $+\frac{4}{3}$ and $+\frac{1}{3}$ respectively. The gauge bosons are arranged in $\frac{1}{\sqrt{2}} T^\alpha V^\alpha_\mu$ as follows,

---

[10] Requiring zero trace removes one degree of freedom from the gluons g_{ij} in the top left 3×3 region.

[11] The photon, $W^\pm_\mu$, Z_μ and eight gluons are equivalent to $V^{1,2,...,12}$ in an $SU(5)$-based GUT.

where its construction is shown in Appendix 8.6:

$$\frac{1}{\sqrt{2}}T^{\alpha}V_{\mu}^{\alpha}=\begin{pmatrix} g_{11}-\frac{2B}{\sqrt{30}} & g_{12} & g_{13} & \overline{X}^{r} & \overline{Y}^{r} \\ g_{21} & g_{22}-\frac{2B}{\sqrt{30}} & g_{23} & \overline{X}^{g} & \overline{Y}^{g} \\ g_{31} & g_{32} & g_{33}-\frac{2B}{\sqrt{30}} & \overline{X}^{b} & \overline{Y}^{b} \\ X^{r} & X^{g} & X^{b} & \frac{W^3}{\sqrt{2}}+\frac{3B}{\sqrt{30}} & W^{+} \\ Y^{r} & Y^{g} & Y^{b} & W^{-} & -\frac{W^3}{\sqrt{2}}+\frac{3B}{\sqrt{30}} \end{pmatrix} (\equiv \mathbf{24}). \quad (28)$$

Since the $\overline{\mathbf{5}}$ and $\mathbf{10}$ representations each contain quarks and leptons, vertices involving their coupling to these new X and Y bosons allow for two quarks in a baryon to transform into an anti-quark and a lepton. This anti-quark and the spectator quark then join together as a meson and the original baryon ceases to exist. *In short, the $SU(5)$ model predicts that nucleons should decay.* This is a feature not just of $SU(5)$ but of GUTs in general. Figure 2 shows some X and Y-mediated decay modes for $SU(5)$.

Using Eq. 24, 25, 27 and 28, the main contribution to proton decay in minimal $SU(5)$ comes from the kinetic terms in the Lagrangian [55]:

$$i\overline{\mathbf{5}}\gamma^{\mu}D_{\mu}\mathbf{5} \quad \rightarrow \quad \tfrac{1}{2}g_5\left[\overline{d}^{\beta}\gamma^{\mu}(\overline{X}_{\mu})^{b}_{\beta}\epsilon_{ba}L^{a}+\overline{L}_{a}\epsilon^{ab}\gamma^{\mu}(X_{\mu})^{\beta}_{b}d_{\beta}\right],$$

$$i\overline{\mathbf{10}}\gamma^{\mu}D_{\mu}\mathbf{10}\rightarrow \tfrac{1}{2}g_5\left[\epsilon_{\alpha\beta\gamma}\overline{u}^{\alpha}\gamma^{\mu}Q^{\gamma b}+\overline{Q}_{\alpha\beta}\epsilon^{ab}\gamma^{\mu}e\right](X_{\mu})^{\beta}_{b}-\tfrac{1}{2}g_5\left[\epsilon^{\alpha\beta\gamma}\overline{Q}_{b\alpha}\gamma^{\mu}u_{\gamma}+\overline{e}\gamma^{\mu}\epsilon_{ba}Q^{\beta a}\right](\overline{X}_{\mu})^{b}_{\beta}$$

where Q_L, L_L are shown in Table 1, g_5 is the coupling at the GUT scale, $a, b = 1, 2$ are $SU(2)_L$ indices, $\alpha, \beta, \gamma = 1, 2, 3$ are $SU(3)_C$ indices, and ϵ is the Levi-Civita tensor. The superheavy $X_{\mu}, \overline{X}_{\mu}$ can be 'integrated out' of these expressions to obtain low-energy effective [56] 'dimension-6' [12] operators [57], which typically provide the greatest contribution to proton decay in non-supersymmetric theories (Section 2.2.3) [55, 58]:

$$\frac{g_5^2}{2M_{X,Y}^2}\epsilon_{\alpha\beta\gamma}\epsilon_{ab}\overline{u}^{C}_{\alpha iL}\gamma^{\mu}Q_{\beta aiL}\overline{e}^{C}_{jL}\gamma_{\mu}Q_{\gamma bjL}, \qquad \frac{g_5^2}{2M_{X,Y}^2}\epsilon_{\alpha\beta\gamma}\epsilon_{ab}\overline{u}^{C}_{\alpha iL}\gamma^{\mu}Q_{\beta aiL}\overline{d}^{C}_{\gamma jL}\gamma_{\mu}L_{bjL} \quad (29)$$

where i, j are fermion generation indices and $M_{X,Y}$ is $\mathcal{O}(10^{14-15})$ GeV.

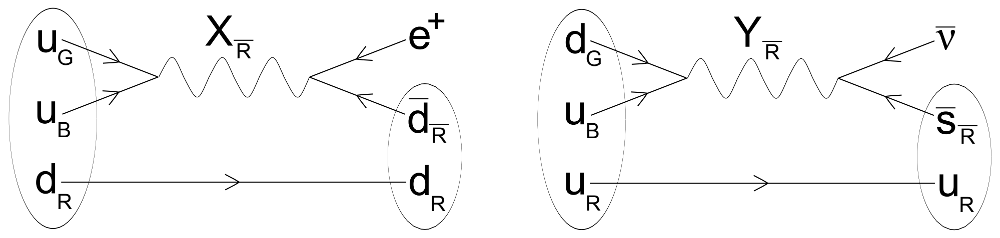

Figure 2: *Two examples of how a proton decay could proceed via $SU(5)$ leptoquarks (X and Y bosons). The left diagram shows a proton decaying in the channel $p \rightarrow \pi^0 e^+$ mediated by an X boson. The right diagram shows a proton decaying in the channel $p \rightarrow K^+\overline{\nu}$ mediated by a Y boson.*

The decay channel $p \rightarrow e^+\pi^0$ is typically the dominant one in non-supersymmetric theories. Based on the 'perturbative chiral Lagrangian' technique [59] used to translate

---

[12] 'Dimension' in this sense refers to the mass dimension, which for bosons is 1 and for fermions is $\frac{3}{2}$ → an operator with four fermions such as Eq. 29 has dimension $4 \times (\frac{3}{2}) = 6$.

operators at quark level (Eq. 29) to those at hadron level, the decay width for the decay channel $p \to e^+\pi^0$ due to these dimension-6 operators is calculated as follows [58, 60]:

$$\Gamma = \frac{m_p}{16\pi f_\pi^2} A_L^2 |\alpha|^2 (1 + D + F)^2 \frac{g_5^4}{4M_{X,Y}^4} \left(|V_1^{11} V_3^{\beta\alpha}|^2 + \left|V_1^{11} V_2^{\alpha\beta} + (V_1 V_{UD})^{1\beta} (V_2 V_{UD}^\dagger)^{\alpha 1}\right|^2 \right) \tag{30}$$

where m_p is the proton mass, f_π is the pion decay constant, α, D, F are parameters of the chiral Lagrangian, A_L takes into account renormalization from the electroweak scale M_Z to the proton decay scale of 1 GeV [61] [13] . Also $V_{1,2,3,UD}$ are mixing matrices where

$$V_1 = U_C^\dagger U, \qquad V_2 = E_C^\dagger D, \qquad V_3 = D_C^\dagger E, \qquad V_{UD} = U^\dagger D$$

and U,D,E define the diagonalizations of the Yukawa couplings $Y_{U,D,E}$ to up-type quarks, down-type quarks and charged leptons respectively (via $U_C^T Y_U U = Y_U^{diag}$ and so on).

From Eq. 30 lenient estimate of the proton decay rate $\Gamma_{p\to e^+\pi^0}$ may be calculated using [61–64]

$$m_p = 938.3\,MeV, \qquad D + F = 1.2670, \qquad f_\pi = 130\,MeV, \qquad \alpha = 0.003, \qquad A_L = 1.43,$$

$$|V_1^{11} V_3^{\beta\alpha}|^2 + |V_1^{11} V_2^{\alpha\beta} + (V_1 V_{UD})^{1\beta} (V_2 V_{UD}^\dagger)^{\alpha 1}|^2 = 1^2 + |1 + 1|^2 = 5,$$

which yields a decay lifetime $\tau_{p\to e^+\pi^0} = 1/\Gamma_{p\to e^+\pi^0} \approx 1.6 \times 10^{32}$ years. However, even this has now been experimentally ruled out as being too short (as will be discussed in later sections).

A further possible route to proton decay is provided by the various Higgs bosons in this model. The electroweak symmetry-breaking $SU(2)$ Higgs doublet Φ (Section 2.1.3) is placed in a Higgs multiplet denoted $\mathbf{5}_H$. Accompanying this doublet is a superheavy Higgs colour triplet T that is involved in breaking $SU(5) \to SU(3)_C \times SU(2)_L \times U(1)_Y$ at a much higher energy than the electroweak scale (>10^{11} GeV) and has a charge of $-\frac{1}{3}$ [65]:

$$\mathbf{5}_H = \big(\{T_r, T_g, T_b\}, \{\phi^+, \phi^0\}\big)^T \equiv (T, \Phi)^T. \tag{31}$$

where the superscript T in Eq. 31 indicates the transpose.

The exchange of members of this Higgs triplet T provides another way for proton decay to occur. In the simplest model only one $\mathbf{5}_H$ is needed. The Yukawa terms pertaining to these fermion-Higgs interactions are [55, 58]

$$\mathcal{L}_{Y_T} = \overline{T} L Y_{\mathbf{5}} Q - \overline{T} d^C Y_5 u^C - \tfrac{1}{2} Q Y_{\mathbf{10}} Q T - \tfrac{1}{2} u^C Y_{\mathbf{10}} e^C T,$$

where $Y_{5,10}$ represent Yukawa couplings. Integrating out the T, $\overline{T}$, these terms give rise to more dimension-6 effective operators:

$$O_T^I = \frac{1}{2}\frac{1}{M_T^2}(Q Y_{\mathbf{10}} Q)(Q Y_{\mathbf{5}}^T L), \qquad O_T^{II} = \frac{1}{M_T^2}(d^C Y_{\mathbf{5}} u^C)(u^C Y_{\mathbf{10}} e^C).$$

The Higgs triplet T must have a very large mass M_T to avoid predicting that protons should decay far more readily than they do[14]. In this instance a decay to the heaviest

---

[13] The subscript L on A_L refers to ‘Long distance’, since the gap in energy between M_Z and 1 GeV is relatively small compared to the gap for A_S ($S \equiv$ ‘Short distance’) appearing in Eq. 35.

[14] Having to make an ad-hoc choice of a very large mass for the colour triplet Higgs compared to the $SU(2)$ doublet Higgs mass is represents a new fine-tuning known as ‘doublet-triplet splitting’ problem.

possible particle is favoured due to larger Yukawa couplings with heavier quarks [66] so the leading decay mode is to a meson containing a strange quark. In other words, such proton decays favour the production of K^+ mesons. Figure 3 shows some Higgs triplet-mediated decay modes for $SU(5)$.

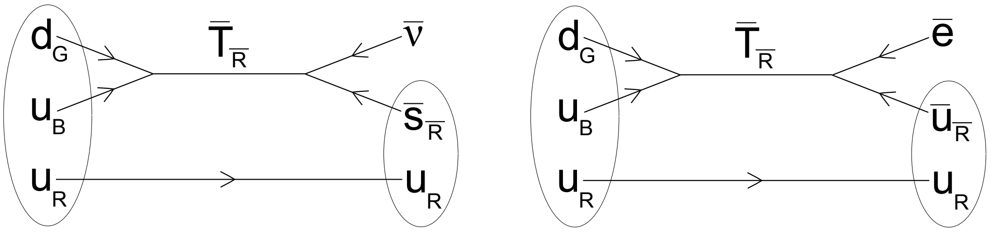

Figure 3: *Two examples of how a proton decay could proceed via the Higgs colour triplet. The left diagram shows a proton decaying in the channel* $p \to K^+\overline{\nu}$ *mediated by a member of the Higgs colour antitriplet. The right diagram shows a proton decaying in the channel* $p \to \pi^0 e^+$ *mediated also by a member of the Higgs colour antitriplet.*

The predicted rate of proton decays mediated by Higgs triplet is model dependent [58] and generally not as fast as those mediated by X and Y bosons, but Higgs-mediated decays take on more importance in supersymmetric models (Section 2.2.3).

Table 3: *The most recently available lower limits on a selection of proton decay channels at 90% C.L., measured by Super-Kamiokande [67–69].*

Decay channel	Partial lifetime ($\times 10^{33}$ years)
$p \to \overline{\nu} K^+$	> 5.9
$p \to e^+ \pi^0$	> 8.2
$p \to \mu^+ \pi^0$	> 6.6
$p \to e^+ \eta$	> 4.2
$p \to \mu^+ \eta$	> 1.3
$p \to e^+ \rho^0$	> 0.71
$p \to \mu^+ \rho^0$	> 0.16
$p \to e^+ \omega$	> 0.32
$p \to \mu^+ \omega$	> 0.78
$p \to \nu \pi^+$	> 0.32

Table 3 shows a summary of the lower limits on a number of decay channels formally announced by Super-Kamiokande. In proton decay experiments each channel has a different partial lifetime, owing to the efficiency of the detector at detecting each type of decay product, and also the different backgrounds that each channel suffers from. For example, the Super-Kamiokande lower limit on the partial lifetime for $p \to K^+\,\overline{\nu}$ is lower than that for $p \to e^+\,\pi^0$. Such kaons will travel slower than positrons so, assuming they can even exceed the Cerenkov threshold in the water, the resulting Cerenkov radiation cones detected by the PMTs are wider and less bright. Events complicated since the K^+ can decay to various particles (unlike the positron).

The lower limit on the lifetime of the dominant decay channel $p \to \pi^0 e^+$ measured by Super-Kamiokande at 90% confidence is 8.2×10^{33} years [67], and for $p \to K^+\overline{\nu}$ is 5.9×10^{33} years [68]. Minimal $SU(5)$ is therefore ruled out as the correct GUT, although there are possible extensions to the model that result in a decay lifetime long enough to survive the current lower limit. For example, one model which incorporates more Higgs bosons in a $\mathbf{15}_H$ multiplet predicts an upper limit of $\sim 10^{39}$ years [70]. Still, $SU(5)$ has other issues, such as predicting the following quark-lepton mass relations at the GUT scale [71]:

$$m_d = 3m_e, \qquad m_\mu = 3m_s, \qquad m_b = m_\tau. \tag{32}$$

The problematic predictions can be avoided if the model is extended to include Higgs bosons in a $\mathbf{45}_H$ multiplet [71] or higher-dimensional operators [72]. The lack of unification of all three couplings at the same energy scale is another drawback for minimal $SU(5)$, although making the theory supersymmetric is one way to correct this (Section 2.2.3). The non-zero mass of neutrinos is also left unaccounted for in minimal $SU(5)$, although extending it to include a $\mathbf{15}_H$ provides a solution [73, 74]. The doublet-triplet splitting (Footnote 14) of the $\mathbf{5}_H$ Higgs masses is also an undesirable feature, although a natural alternative to this fine tuning can emerge when a supersymmetric approach is taken [75].

2.2.3 Supersymmetry and supersymmetric SU(5)

Supersymmetry

The merging of the three SM couplings at very high energy suggests that some other GUT is still correct. If a coupling α is measured at some energy scale μ then the coupling can be calculated [76] for some momentum transfer q^2 via

$$\alpha(q^2) = \frac{\alpha(\mu^2)}{1 - \alpha(\mu^2)\beta_0\, ln(q^2/\mu^2)} \tag{33}$$

where β_0 is a model-dependent function of the number of fermions and bosons $n_{f,b}$ in the theory; $\beta_0 = (12\pi)^{-1}(4n_f - 11n_b)$ is appropriate for the SM. From this the strong, weak and electromagnetic gauge couplings can be extrapolated to high energies. The electromagnetic coupling is seen to increase with increasing energy whereas the weak and strong couplings decrease in strength. For the SM this fails to produce a point where all three couplings intersect with each other. This is also the case in the minimal $SU(5)$ model. However, this can be remedied in 'Supersymmetric' (SUSY) theories, which contain more particles and do in fact predict the three couplings unifying at $\sim 10^{16}$ GeV [77] (as shown in Figure 4).

Supersymmetric theories [79, 80] assume a symmetry between bosons and fermions where each boson or fermion has an identical 'superpartner' differing only by spin of $\frac{1}{2}\hbar$. The bosonic superpartners of the ordinary fermions are prefixed with an 's' (e.g. the 'sup squark' partners the up quark) and the fermionic superpartners of the ordinary bosons are suffixed with 'ino' (e.g. the 'Wino' partners the W boson) [15].

The most simple SUSY model is the Minimal Supersymmetric Standard Model (MSSM) [81], which just contains double the number of known SM fermions, gauge bosons and Higgs bosons. These additional fields contribute to the running of the gauge couplings (Eq. 33) and force the unification scale M_{GUT} to occur at a higher energy. This can significantly affect the proton decay lifetime. For example, the higher unification scale gained by making $SU(5)$ supersymmetric increases the $p \to e^+ \pi^0$ decay lifetime due to dimension-6 operators up to $\sim 10^{35\pm1}$ [82] [16]. Figure 4 compares the running of the gauge couplings in the SM and the MSSM.

---

[15] A significant benefit of SUSY is that quadratic divergences are no longer a problem, with loop diagrams of each superpartner automatically cancelling that of their 'ordinary' counterpart.

[16] However, dimension-5 operators in SUSY $SU(5)$ make decays via $p \to K^+ \overline{\nu}$ more rapid than $p \to e^+ \pi^0$ by a few orders of magnitude, as will be discussed later in this section.

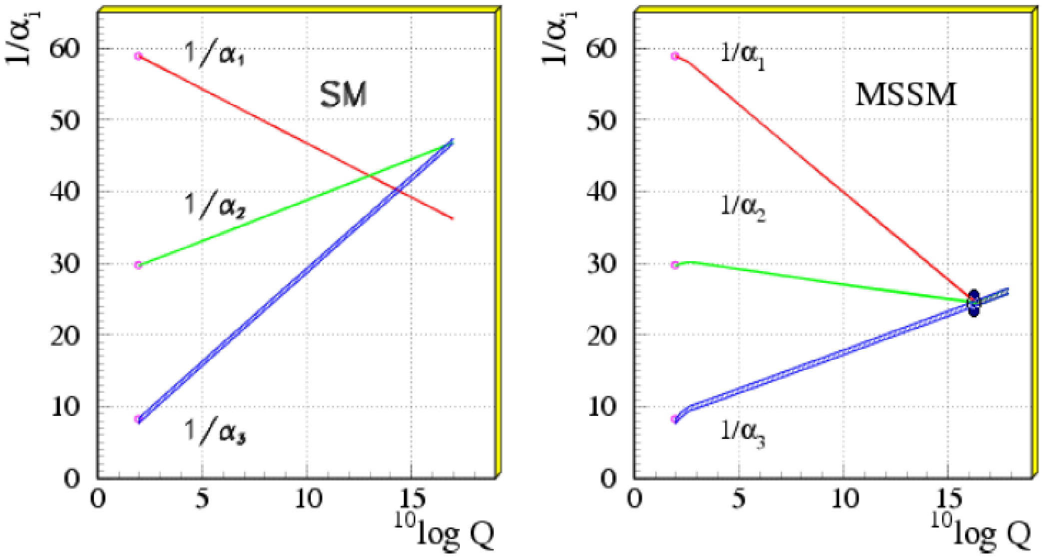

Figure 4: *A comparison of the energy dependence of the three gauge couplings for the SM and the Minimal Supersymmetric SM [78]. The dark region in the right-hand-side plot represents model-dependent corrections. The introduction of superpartners causes the high-energy extrapolation of all three couplings to cross in a much tighter region.*

However, there are also dimension-4 and dimension-5 baryon and lepton-number-violating operators that predict faster proton decays than these dimension-6 operators. The dimension-4 operators should provide very rapid decays (relative to both dimension-5, 6 operators and experimental bounds) but can be avoided (along with most dimension-5 operators) by postulating 'R-parity' [83].

Regarding R-parity, it is possible to construct certain gauge-invariant, renormalizable 'super'-potential terms that allow baryon number B and lepton number L to change in interactions [79], most generally:

$$O_{\Delta B=1} = \tfrac{1}{2}\lambda^{ijk}\overline{u}_i\overline{d}_j\overline{d}_k, \qquad O_{\Delta \mathrm{L}=1} = \tfrac{1}{2}(\lambda')^{ijk}L_iL_j\overline{e}_k + (\lambda'')^{ijk}L_iQ_j\overline{d}_k + \mu^iL_iH_u$$

If couplings λ, λ'' are not very small then these operators could allow proton decay lifetimes far shorter than one second, but no B- or L-violating processes have ever been observed. This is not a problem for the SM since no B- or L-violating terms are possible in the SM. However, such terms are possible in SUSY theories such as the MSSM, so their omission to preserve the conservation of B and L would merely be ad-hoc assumptions in the MSSM. Furthermore there are non-perturbative, high-energy electroweak effects that violate B and L [84], so this assumption is unwanted. To avoid this assumption, but still avoid any unwanted B- and L-violating terms, one could instead postulate R-parity; the conservation of a quantum number based on B, L and spin s:

$$P_R = (-1)^{3(\mathrm{B}-\mathrm{L})+2s}.$$

Thus each of the SM particles would have $P_R = +1$ and the SUSY sparticles would all have $P_R = -1$. If P_R is conserved in interactions then dimension-4 operators become forbidden and the lightest sparticle is stable. If this particle only interacts via the weak interaction (ignoring gravitation) then such SUSY threories provide candidates for dark matter particles (e.g. the lightest sneutrino or the lightest neutralino) - something else that the SM is unable to do (Section 2.2.1).

Supersymmetric SU(5)

The Yukawa interaction terms in minimal SUSY $SU(5)$ are as follows [85]:

$$W_Y = \tfrac{1}{4}Y_1^{ij}\mathbf{10}_i\mathbf{10}_j\mathbf{5}_H + \sqrt{2}Y_2^{ij}\mathbf{10}_i\overline{\mathbf{5}}_j\overline{\mathbf{5}}_H$$

where $\mathbf{5}_H, \overline{\mathbf{5}}_H$ are the Higgs 5-plets of Eq. 31 and its conjugate (analogous to the two Higgs doublets required in the MSSM) and the Yukawa coefficients $Y_{1,2}$ are

$$Y_1 = Y_u = Y_{qq} = Y_{ue}, \qquad\qquad Y_2 = Y_d = Y_e = Y_{ql} = Y_{ud}.$$

In terms of Higgs(ino) doublet/triplet and (s)fermion (super)fields, the Yukawa terms are:

$$\begin{aligned} W_Y^H &= Y_u^{ij}Q_iu_{jR}H + Y_d^{ij}Q_id_{jR}\overline{H} + Y_e^{ij}e_{iR}L_j\overline{H}, \\ W_Y^T &= \tfrac{1}{2}Y_{qq}^{ij}Q_iQ_jT + Y_{ql}^{ij}Q_iL_j\overline{T} + Y_{ue}^{ij}u_{iR}e_{jR}T + Y_{ud}^{ij}u_{iR}d_{jR}\overline{T}. \end{aligned}$$

Two effective dimension-5 operators are obtained from W_Y^T by integrating out the heavy T, $\overline{T}$, each of which can facilitate proton decay:

$$O_{LLLL} = \frac{1}{2M_T}Y_{qq}^{ij}Y_{ql}^{km}Q_iQ_jQ_kL_m \qquad O_{RRRR} = \frac{1}{M_T}Y_{ue}^{ij}Y_{ud}^{km}u_{iR}e_{jR}u_{iR}d_{jR} \tag{34}$$

where the subscripts $LLLL$ and $RRRR$ indicatethe involvement of left- and right-handed fields. Figure 5 illustrates some possible proton decays involving dimension-5 operators O_{LLLL} and O_{RRRR}.

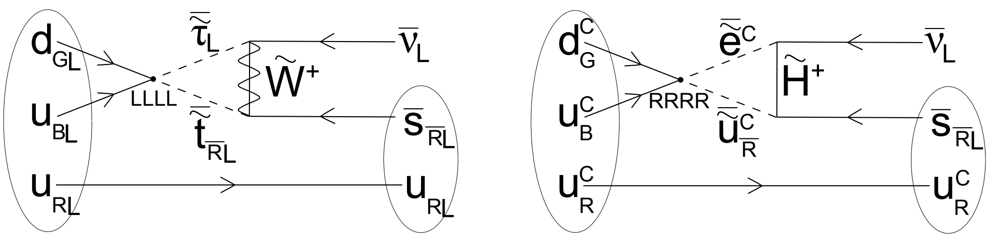

Figure 5: *Two examples of how a proton decay in the channel $p \to K^+\overline{\nu}$ could proceed via dimension-5 effective operators in SUSY $SU(5)$, whereby two fermions can interact with two bosonic superfields. The proton decay in the left diagram is then completed by 'dressing' it with a Wino. The right diagram is dressed by a charged Higgsino.*

The operators in Eq. 34 are only suppressed by one inverse power of M_T whereas the dimension-6 operators relating to X or Y boson-mediated proton decay (Eq. 29) are suppressed by two inverse powers of $M_{X,Y}$ (both are GUT scale masses). However, this does not necessarily mean the dimension-5 operators require a proton to decay too many orders of magnitude faster than the dimension-6 operators allow [86, 87], or experimental lower limits require. There are additional factors [88] which can affect the decay lifetime by a few orders of magnitude.

For instance, $SU(5)$ can be broken to $SU(3)_C \times SU(2)_L \times U(1)_Y$ via a 24-plet of Higgs which contains a colour octet, weak triplet in its SM decomposition (Table 67). The Higgs colour octet and weak triplet have sub-GUT-scale masses. This affects the running of the couplings, resulting in a higher GUT scale and a longer proton lifetime. Further suppression of dimension-5 decays comes from the proton containing only the lightest quarks, so the Yukawa couplings Y_{xy}^{ij} can be small. Furthermore, the minimal

$SU(5)$ predicts some inaccurate mass relations at the GUT scale (Eq. 32) and to correct this, higher dimensional Yukawa operators can be introduced; consequently the colour triplet couplings are affected, causing M_T to increase and the proton decay rate due to these operators to decrease. Uncertainty over sparticle masses and mixings also broadens the range of predicted decay lifetimes.

Bose-Einstein statistics demands antisymmetry in the colour indices of the scalar superfields appearing in the dimension-5 operators, requiring the operators to feature two families [89]. The strange quark will therefore be the quark most readily produced through this sort of operator (Eq. 34), meaning the decay channel $p \to K^+\overline{\nu}$ is generally the dominant one for SUSY GUTs (in models with discrete family reflection symmetry [17]). The decay rate can be calculated as follows [58]:

$$\Gamma_{p\to K^+\overline{\nu}} = \frac{\beta_p^2 m_p}{32\pi M_T f_\pi^2}\left(1-\frac{m_K^2}{m_p^2}\right)^2 |\mathcal{A}_{K\nu}|^2 A_L^2 (A_S^L)^2 \left|1+\frac{m_p(D+F)}{m_B}\right|^2 \tag{35}$$

where each symbol is described in Appendix 8.7. Calculating the decay rate here involves large uncertainties [90]. Primarily this is due to the ratio of the VEVs of the two neutral Higgses involved in MSSM symmetry breaking being a free parameter, i.e.

$$tan\,\beta = \frac{\langle H_2\rangle}{\langle H_1\rangle} \tag{36}$$

(which appears in $\mathcal{A}_{K\nu}$). Also there are uncertanties in the size of dressing loop functions (which also appear in $\mathcal{A}_{K\nu}$) due to the unknown masses of the supersymmetric particles involved, none of which have been discovered to date. The same also applies to the Higgsino triplet mass. Thus the prediction for the proton lifetime made by minimal SUSY $SU(5)$ ranges between $10^{28} - 10^{32}$ years [86, 91], decaying most rapidly via the channel $p \to K^+\,\overline{\nu}$.

The lower limit on the proton decay lifetime measured by Super-Kamiokande is 8.2×10^{33} years in the channel $p \to e^+\,\pi^0$ and 5.9×10^{33} years in the channel $p \to K^+\,\overline{\nu}$ (Table 3), which has excluded SUSY $SU(5)$ in its minimal form. However, there modifications/extensions[18] are possible that push the predicted proton lifetime beyond the current experimental lower limit. For example, one SUSY $SU(5)$ model [92] includes new matter fields in additional $\mathbf{5}+\overline{\mathbf{5}}$ multiplets, which raises the GUT scale and produces a decay lifetime of up to 4×10^{33} years, only slightly below the most recently published lower limit. Section 2.2.5.2 discusses a SUSY $SU(5)$ GUT that allows proton decay lifetimes significantly in excess of this limit. It is also possible to eliminate dimension-5 operators in SUSY $SU(5)$ GUTS [93] by the inclusion of an additional pair of $\mathbf{5}+\overline{\mathbf{5}}$ Higgs multiplets and specific couplings[19]. Assuming sfermion masses signficantly higher than the electroweak scale has also been shown [94] to allow decay lifetimes spanning the range $10^{33} - 10^{36}$ years, depending on the value of $\tan\beta$ (Eq. 36).

---

[17] 'Discrete family reflection symmetry' is a natural discrete symmetry defined by $\Phi^i_Q \to -\Phi^i_Q$, $\Phi^i_{\overline{u}} \to -\Phi^i_{\overline{u}}$, $\Phi^i_{\overline{d}} \to -\Phi^i_{\overline{d}}$, $\Phi^i_L \to -\Phi^i_L$, $\Phi^i_{e^+} \to -\Phi^i_{e^+}$ [89].

[18] Minimal supersymmetric SU(5) is not considered a realistic model anyway, since the relation between fermion masses it yields disagree with experiment [58].

[19] Some couplings can be zero if, say, one postulates discrete symmetry, R-parity, anomalous U(1), accidental symmetry.

2.2.4 Unification via SO(10)

Gauge groups other than $SU(5)$ have also been explored in an attempt to find the correct GUT. Models based on the $SO(10)$ group, which itself contains $SU(5)$ as a subgroup, are are highly-favoured. An attractive feature of $SO(10)$ [58, 95] is its ability to accommodate sixteen fields in one spinorial representation denoted $\mathbf{16}$, which has the $SU(5)$ decomposition $\mathbf{10}+\overline{\mathbf{5}}+\mathbf{1}$. It therefore contains the fifteen SM fermions (in a given generation) that in $SU(5)$ are split between the two representations $\overline{\mathbf{5}}$ and $\mathbf{10}$ (Section 2.2.2), but also a SM singlet; the right-handed neutrino. For example, the first generation is

$$\mathbf{16}_1 = (Q_1, u^C, d^C, L_1, e^C, \nu_e^C),$$

where the symbols used are the same as in Table 1. The inclusion of a right-handed neutrino is significant since they are required in the 'see-saw' mechanism (Section 2.4.5), which is commonly invoked to explain tiny yet finite mass of the left-handed neutrino. The SM contains no right-handed neutrino and also does not include a tiny left-handed neutrino mass.

At a minimum, breaking $SO(10)$ to $SU(3)_C \times SU(2)_L \times U(1)_Y$ requires [58] Higgs fields in $\mathbf{16}_H$, $\overline{\mathbf{16}}_H$ and $\mathbf{45}_H$ representations, with the two light Higgs doublets in a $\mathbf{10}_H$ then breaking electroweak symmetry. However, there are numerous ways to break $SO(10)$ all the way to $SU(3)_C \times U(1)_Y$ and many models have been built, differing in their choice of Higgs sector. $SO(10)$ models commonly employ Higgs multiplets of $\mathbf{10}_H$, $\mathbf{16}_H + \overline{\mathbf{16}}_H$, $\mathbf{45}_H$, $\mathbf{54}_H$, $\mathbf{120}_H$, $\mathbf{126}_H + \overline{\mathbf{126}}_H$, $\mathbf{144}_H + \overline{\mathbf{144}}_H$ and/or $\mathbf{210}_H$. This provides another appealing aspect of $SO(10)$ models - unification of all three SM gauge couplings can be achieved without requiring supersymmetry (Section 2.2.3). As the gauge group structure changes, so does the number of Higgs and gauge bosons and hence also the running of the couplings [96–100].

This is significant since SUSY theories can predict sparticles with masses at the TeV scale, which to date the LHC has failed to observe [101]. This non-observation of low-energy SUSY has motivated a recent re-examination of non-SUSY GUTs which had fallen out of favour. For example, one recently revisted [20] model [102] (Babu & Khan, 2015) claims to be the most minimal non-SUSY $SO(10)$ GUT that can predict a proton decay lifetime in excess of the current lower limit. The dominant decay modes in this model are $p \to \pi^0 e^+$ (47%) and $p \to \pi^+ \overline{\nu}$ (48%), with proton decay lifetimes in the range $\tau_p \approx 10^{34} - 10^{36}$ years (observable with the next generation of large-scale detectors (Section 2.3)).

This model belongs to a wider class of $SO(10)$ models that are broken to intermediate groups exhibiting 'left-right' symmetry. Such models involve making the weak interaction symmetric with regards to left and right-handed fermions, by introducting heavy mirror-like twins of the weak gauge bosons [103]. Thus, the intermediate groups involve $SU(2)_L \times SU(2)_R$. Table 4 shows some left-right symmetric, non-SUSY $SO(10)$ models that are capable of predicting proton decay lifetimes that survive the Super-Kamiokande lower limits.

---

[20] The model has been updated with new 'threshold corrections', i.e. the difference between the amplitude of a process calculated in a full theory and that calculated with a low-energy effective theory. Such a correction is sensitive to the masses and vacuum expectations values of the Higgs and gauge bosons involved in the model.

Table 4: *The partial lifetimes in the decay channel $p \to e^+\pi^0$ for a selection of minimal non-supersymmetric SO(10) models with left-right symmetry [104]. The D refers to 'D-parity' (a local discrete Z_2-subgroup of SO(10), which transforms a fermion into its charge conjugate [105]).*

Intermediate group	$p \to e^+\pi^0$ partial lifetime (years)
G_{224} $(SU(2)_L \times SU(2)_R \times SU(4)_C)$	$10^{30.7-39.6}$
G_{224D} $(SU(2)_L \times SU(2)_R \times SU(4)_C \times D)$	$10^{28.5-35.7}$
G_{2213} $(SU(2)_L \times SU(2)_R \times U(1)_{B-L} \times SU(3)_C)$	$10^{31.0-37.4}$
G_{2213D} $(SU(2)_L \times SU(2)_R \times U(1)_{B-L} \times SU(3)_C \times D)$	$10^{34.1-40.0}$

Another recent non-SUSY $SO(10)$ model [106] (Patra & Pritimita, 2014) with four intermediate stages in the symmetry-breaking chain before $SU(3)_C \times SU(2)_L \times U(1)_Y$ results in a decay lifetime via $p \to K^+\overline{\nu}$ of $\sim 2 \times 10^{34}$ years. As previously discussed this is often the dominant mode in SUSY models, and there are many based on the $SO(10)$ group. It has been shown [107–110] that SUSY $SO(10)$ models have a number of appealing features that the SM and $SU(5)$ lack - such as producing sensible values and relations for fermion masses/mixings and neutrino oscillation parameters, sufficiently slow proton decay and an acceptable degree of CKM charge-parity (CP) violation. These features are also common to the $SO(10)$ subgroup G_{224} mentioned in Table 4 and arise due to the combination of left-right symmetry and '$SU(4)$ colour'. These models utilise 8-plets to accommodate the sixteen fields in each fermion generation, for example:

$$F_L^{1st\,gen} = \begin{pmatrix} u_r & u_g & u_b & \nu_e \\ d_r & d_g & d_b & e^- \end{pmatrix}_L, \qquad F_R^{1st\,gen} = \begin{pmatrix} u_r & u_g & u_b & \nu_e \\ d_r & d_g & d_b & e^- \end{pmatrix}_R.$$

Here the $SU(2)_{L,R}$ symmetries treat each column of $F_{L,R}$ as a doublet and $SU(4)_C$ treats each row as a quartet (i.e. the neutral and charged leptons are treated as a fourth colour of the up-type and down-type quarks respectively). A right-handed neutrino is therefore a necessity in such models, which is useful due to its importance to the see-saw mechanism (Section 2.4.5) used to account for neutrino masses.

In SUSY models these right-handed neutrinos acquire heavy Majorana masses through extra Higgs colour-triplets [111]. Like the 'standard' colour triplets introduced in Eq. 31, the exchange of the superpartners of these new Higgs bosons also give rise to more dimension-5 effective operators. These also favour the $p \to K^+\overline{\nu}$ and $p \to \pi^+\overline{\nu}$ decay channels.

One SUSY $SO(10)$ model that produces an acceptable proton decay lifetime is the BPW (Babu-Pati-Wilczek) model [107]. Here $SO(10)$ is broken to the G_{224} subgroup (Table 4) as an intermediate stage by Higgses in $\mathbf{45}_H$, $\mathbf{16}_H$, $\overline{\mathbf{45}}_H$ multiplets (with a $\mathbf{10}_H$ for electroweak symmetry breaking). It reproduces several parameters accurately (to within $\sim 10\%$) as well as a $p \to K^+\overline{\nu}$ decay lifetime on the order of $\sim 10^{34}$ years.

Renormalizable minimal SUSY $SO(10)$ [110,112–115] also predicts viable proton decay lifetimes, employing Higgs multiplets of $\mathbf{10}_H$ and $\overline{\mathbf{126}}_H$ in the Yukawa couplings with matter fields. The proton decay lifetime calculation is dependent on a few free parameters but a numerical analysis [110] where these are varied yields decay lifetimes spanning a range of $10^{30} - 10^{35}$ years.

Also an 'extended supersymmetric SM' (ESSM) SUSY $SO(10)$ [116] uses an extra pair of vectorlike families in $\mathbf{16}$- and $\overline{\mathbf{16}}$-plets, raising the unification scale to $\sim 10^{17}$ GeV and predicting $\tau_{p \to K^+\overline{\nu}} \sim 10^{33-35}$ yr.

Table 5 shows a summary of the decay lifetimes from a review of SUSY $SO(10)$ models [109].

Table 5: *Upper limits on predicted proton decay lifetimes in the channel* $p \to K^+\overline{\nu}$ *according to a review of SUSY* $SO(10)$ *models [109]. The decays are due to either the 'standard' dimension-5 operators discussed in Section 2.2.3, or the 'new' dimension-5 operators discussed in this section. The models considered are in either a minimal (MSSM) or extended (ESSM) supersymmetric SM scheme (the latter incorporating two extra* $SO(10)$ $\boldsymbol{16}+\overline{\boldsymbol{16}}$*-plets containing extra vector-like fermions with TeV-scale masses [116]).*

Gauge group, particle content (operator responsible)	$p \to K^+\overline{\nu}$ partial lifetime
SUSY $SO(10)$, MSSM (standard $d = 5$)	$\lesssim 10^{33}$ years
SUSY $SO(10)$, ESSM (standard $d = 5$)	$\lesssim 10^{35}$ years
SUSY $SO(10)$ / G224, MSSM / ESSM (new $d = 5$)	$\lesssim 10^{34}$ years

2.2.5 Unification via other models

2.2.5.1 Flipped SU(5)

'Flipped' $SU(5)$-based models [58, 117–119] can predict a proton decay lifetime comfortably in excess of current experimental bounds. The gauge group in this instance is $SU(5) \times U(1)$, which unifies only two SM gauge couplings α_2 and α_3 at the scale $M_{23} \sim 5 \times 10^{15}$ GeV [120] (this group can be embedded in a higher group to achieve unification of all three couplings at a later stage). The fermions are arranged differently within the $SU(5)$ mutliplets $\overline{\mathbf{5}}$ and $\mathbf{10}$ compared to Section 2.2.2 and an $SU(5)$ singlet $\mathbf{1}$ also features (Appendix 8.8). In Flipped $SU(5)$ GUTs the proton decay lifetime due to dimension-6 operators is longer than in standard $SU(5)$, since these operators depend on M_{23} (a somewhat higher unification scale compared to $M_{X,Y}$ from Eq. 29). If the dimension-6 operators are retained, Flipped $SU(5)$ predicts proton decay lifetimes in the range $\sim 10^{34}$ - 10^{36} years [120, 121] with the dominant channels being $p \to e^+/\mu^+\pi^0$.

However, in Flipped $SU(5)$ the dimension-6 proton decay operators can be eliminated, causing the dimension-5 operators (which favour $p \to K^+\,\overline{\nu}$) to dominate. This is not possible in conventional $SU(5)$ GUTs [122, 123] since it requires constraints on the CKM matrix parameters that conflict with their measured values. These operators (Eq. 29) can be expressed in terms of coefficients $c(...)_{SU(5)}$; also shown here are the effective operators for decays to neutrinos:

$$\begin{aligned}
O(e^c_\alpha, d_\beta)_{SU(5)} &= c(e^c_\alpha, d_\beta)_{SU(5)} \quad\ \times \epsilon_{ijk}\overline{u}^c_i\gamma^\mu u_j \overline{e}^c_\alpha\gamma_\mu d_{k\beta},\\
O(e_\alpha, d^c_\beta)_{SU(5)} &= c(e_\alpha, d^c_\beta)_{SU(5)} \quad\ \times \epsilon_{ijk}\overline{u}^c_i\gamma^\mu u_j \overline{d}^c_{k\beta}\gamma_\mu e_\alpha,\\
O(\nu_l, d_\alpha, d^c_\beta)_{SU(5)} &= c(\nu_l, d_\alpha, d^c_\beta)_{SU(5)} \times \epsilon_{ijk}\overline{u}^c_i\gamma^\mu d_{j\alpha} \overline{d}^c_{k\beta}\gamma_\mu \nu_l,\\
O(\nu^c_l, d_\alpha, d^c_\beta)_{SU(5)} &= c(\nu^c_l, d_\alpha, d^c_\beta)_{SU(5)} \times \epsilon_{ijk}\overline{d}^c_{i\beta}\gamma^\mu u_j \overline{\nu}^c_l\gamma_\mu d_{k\alpha}.
\end{aligned} \tag{37}$$

The corresponding operators in Flipped $SU(5)$ have the same form as those shown in Eq. 37 but the factors $c(...)_{SU(5)}$ are replaced by $c(...)_{Flipped\,SU(5)}$:

$$c(e^c_\alpha, d_\beta)_{Flipped\,SU(5)} = 0, \qquad c(e_\alpha, d^c_\beta)_{Flipped\,SU(5)} = k_2^2 (V_4 V^\dagger_{UD})^{\beta 1}(V_1 V_{UD} V^\dagger_4 V_3)^{1\alpha},$$

$$c(\nu_l, d_\alpha, d^c_\beta)_{Flipped\,SU(5)} = k_2^2 V_4^{\beta\alpha}(V_1 V_{UD} V^\dagger_4 V_3 V_{EN})^{1l} \qquad (\alpha = 1 \textit{ or } \beta = 1),$$

$$c(\nu^c_l, d_\alpha, d^c_\beta)_{Flipped\,SU(5)} = k_2^2 \big[(V_4 V^\dagger_{UD})^{\beta 1}(U^\dagger_{EN} V_2)^{l\alpha} + V_4^{\beta\alpha}(U^\dagger_{EN} V_2 V^\dagger_{UD})^{l1}\big] \ (\alpha = 1 \textit{ or } \beta = 1),$$

where matrices $V_{1,2,3,UD,EN}$ are defined the same way as stated after Eq. 30 and also $V_{UD} = K_1 V_{CKM} K_2$ (with $K_{1,2}$ being matrices containing CP-violating phases), $k_2 =$

$g_5^{Flipped}/M_{23}^{Flipped}$ (where $g_5^{Flipped}$ is the coupling at which α_2 and α_3 unify), $V_4 = D_c^\dagger D$ and $U_{EN} = E_c^\dagger N_c$.

Here the operator containing $c(\nu_l, d_\alpha, d_\beta^c)_{Flipped\,SU(5)}$ can be eliminated since $V_4^{\beta\alpha} = 0$ is allowed. Then $c(e_\alpha, d_\beta^c)_{Flipped\,SU(5)}$ can be eliminated without conflict with the measured V_{CKM} parameters by setting $(V_1 V_{UD} V_4^\dagger V_3)^{1\alpha} = 0$, and since in Flipped $SU(5)$ the neutrino is a Majorana particle, $c(\nu_l^c, d_\alpha, d_\beta^c)_{Flipped\,SU(5)}$ is automatically removed too.

Proton decay via dimension-5 operators would then dominate but can also be suppressed. This is possible via the 'missing partners' mechanism [119, 124] which avoids decays resulting from Higgsino triplet exchange (if the model is supersymmetric), or by the inclusion of extra Higgs bosons in $\mathbf{5}+\overline{\mathbf{5}}$ or $\mathbf{10}+\overline{\mathbf{10}}$ multiplets [93]. It is worth noting that although $SU(5) \times U(1)$ on its own does not unify all three gauge couplings, it can still be embedded in $SO(10)$ [125]. However, the missing partners mechanism is destroyed by this, as well as a natural solution to doublet-triplet splitting (Footnote 14) - unless the $SO(10)$ model is in five or more spacetime dimensions [124] (Section 2.2.5.3). If the missing partners mechanism is not invoked then dimension-5 Higgsino-mediated proton decay is no longer negligible, and $p \to K^+\,\overline{\nu}$ could be expected to occur at rates similar to those stated at the end of Section 2.2.3.

2.2.5.2 SUSY SU(5) with U(1) flavour symmetry

The proton decay lifetime can be extended quite significantly in SUSY $SU(5)$ by the inclusion of a $U(1)_f$ flavour symmetry. This suppression is a result of the use of the 'Froggatt-Nielsen' mechanism [126, 127] as an attempt to explain mass and mixing hierarchies without using very different Yukawa couplings. This involves assigning a model-dependent $U(1)_f$ flavour charge to the superfields Q. A scalar Standard Model singlet S (the 'flavon' field) is also introduced and gets a charge of -1. When S acquires a VEV $\langle S\rangle$ it breaks the $U(1)_f$ symmetry and a parameter ϵ may be defined as $\epsilon = \langle S\rangle/M_*$ (the fermion masses can be expressed as powers of this ϵ), where M_* is a Planck-scale mass.

As in Eq. 34 the proton decay LLLL and RRRR dimension-5 effective operators [128] are of the form

$$O_{LLLL} = \frac{1}{2M} C_L^{ijkl} Q_i Q_j Q_k L_m, \qquad O_{RRRR} = \frac{1}{M} C_R^{ijkl} E_i^c U_j^c U_k^c D_l^c. \tag{38}$$

However, in this instance the factors $C_{L,R}$ (and hence the rate of proton decay) are dependent on the Froggatt-Nielsen parameter ϵ and the choice of $U(1)_f$ flavour charge assignments, which appear here as the exponents of ϵ:

$$C_L^{ijkl} \sim \epsilon^{q_i+q_j+q_k+l_l}\big(\sim Y_U^{ij} Y_D^{kl} \epsilon^{-h_u-h_d} \epsilon^{q_j-u_j^c+l_l-d_l^c}\big)$$

$$C_R^{ijkl} \sim \epsilon^{e_i^c+u_j^c+u_k^c+d_l^c}\big(\sim Y_U^{ij} Y_D^{kl} \epsilon^{-h_u-h_d} \epsilon^{e_i^c-q_i+u_k^c-q_k}\big)$$

where constants have been omitted before each ϵ.

For example, in the SUSY $SU(5)$ scheme with the fermions in three copies of $\overline{\mathbf{5}}$ and $\mathbf{10}$ multiplets and Higgs superfields in $\mathbf{5}_H$ and $\mathbf{5}_{\overline{H}}$, the following $U(1)_f$ charge assignments produce useful results [129]:

$$Q_{10_1} = 3, \quad Q_{10_2} = 2, \quad Q_{10_3} = 0, \quad Q_{\overline{5}_1} = 2+n, \quad Q_{\overline{5}_2} = Q_{\overline{5}_3} = n, \quad Q_H = Q_{\overline{H}} = 0,$$

where $n = 0, 1, 2$, and determines $tan\beta$ (Eq. 36) via $tan\beta \sim \epsilon^n \frac{m_t}{m_b}$. Through this the dimension-5 proton decay operators are suppressed and one can obtain a proton decay lifetime of $\tau_{p\rightarrow K^+\overline{\nu}} \sim 10^{32-35}$ years, which still survives the current experimental lower limit and is within the reach of the next generation of experiments (Section 2.3). This approach also predicts sensible ratios for the Yukawa couplings of charged fermions and also the magnitudes of the elements of V_{CKM}.

2.2.5.3 Higher dimensional GUTs

Grand unification has also been pursued through models that involve extra dimensions. So-called 'orbifold' GUTs invoke more dimensions than conventional 4D spacetime, curled up or 'compactified' into some tiny topology. Higher-dimensional GUTs can also utilise notions of a 'bulk' and a 'brane' [130], where the bulk is the overall higher-dimensional spacetime, and a brane is a subspace embedded in the bulk, such as the brane the familiar 3+1 spacetime dimensions are assumed in such models to exist on. Figure 6 illustrates this for one 5-D SUSY $SU(5)$ model.

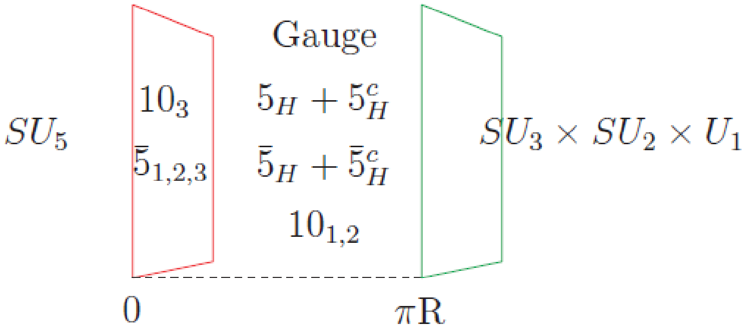

Figure 6: *An illustration [131] [132] of two branes located at* 0 *and* πR *on the fifth-dimension axis from a 5-D SUSY* $SU(5)$ *GUT. The fifth dimension is an orbifold with* $SU(5)$ *symmetry on the brane at* 0 *as well as in the bulk between the two branes. The brane at* πR *has Standard Model symmetry. The* $SU(5)$ *fermion, gauge and Higgs multiplets are distributed between the bulk and the* 0 *brane.*

Unification can then be realised in some higher dimension in ways that avoid certain problems that other GUTs run into (such as the fine-tuning involved in Higgs doublet-triplet splitting (Footnote 14)). The proton decay lifetime is also different in these extra-dimensional $SU(5)$ models (e.g. [131, 133, 134]) for a number of reasons. In some models decays via dimension-5 operators are absent. Also in an equation analogous to Eq. 30 for decay due to dimension 6 operators, the decay lifetime is proportional to the fourth power of the compactification scale M_c (which ranges between $\sim 10^{14-16}$ GeV and has large theoretical uncertainty according to the analysis performed in [135]) rather than M_{XY}. Also the treatment of fermions in these models as brane fields or bulk fields affects their coupling to the gauge bosons X, which mediate the proton decay via these operators. The analysis in [135] for some 5D $SU(5)$ models shows that this can decide which is the dominant decay mode and predict decay lifetimes spanning many (>10) orders of magnitude due to the uncertainties involved. For example, one set of field bulk-brane choices (option II in [135]) have $p \rightarrow K^+\overline{\nu}$ the dominant channel and predict a lifetime potentially within the reach of the next generation of detectors: $\tau_{p\rightarrow K^+\overline{\nu}} \sim 10^{34-40}$ years.

Another 5D model based on $SO(10)$ has been shown to predict a proton decay lifetime in the range $7 \times 10^{33\pm2}$ years with $p \to e^+\pi^0$ the dominant channel [136]. Six-dimensional SUSY $SO(10)$ has also been shown to be within reach of the next generation of experiments with a predicted decay lifetime in the channel $p \to e^+\pi^0$ (rather than $p \to K^+\overline{\nu}$ due to enhanced dimension-6 decay operators, with dimension-5 decays forbidden) of $\sim 10^{35}$ years [137].

2.3 Experiments searching for proton decay events

It is clear from the short overview of GUTs given in Sections 2.2.2- 2.2.5 that they often offer solutions to problems left open by the SM. Although many GUTs have been ruled out, many of them still predict proton decay with lifetimes that have not yet been ruled out by past/current experiments, and that are within the reach of the next generation of detectors. This is particularly true of decays via the channels $p \to e^+\ \pi^0$ and $p \to K^+\ \overline{\nu}$, the latter channel motivating the simulations in this thesis (Sections 3, 4). At this point it is appropriate to review the main experiments of the past, present and future aimed at detecting this elusive event.

Major experimental searches for proton decay have been performed since the 1980s and have so far failed to observe any such events. Instead they have been restricted to setting lower limits on what the decay lifetime of the proton could be, ruling out some GUTs in the process. The most recent partial limits set by Super-Kamiokande can be found in Table 3. Since these lifetimes are extremely long, the basic approach is to use very large numbers of protons to see if any decay; if the decay lifetime of the proton is in fact 10^{34} years, then observing 10^{34} protons for one year offers a good chance of observing it. Fortunately, large detectors with high target masses built for other purposes (such as neutrino physics) may also be used to perform a proton decay search.

One early experiment was NUSEX (Nucleon Stability Experiment) [138], which was located under Mont Blanc, France, and so shielded by a 5000 m rock overburden. This detector was a tracking calorimeter consisting of 134 sheets of iron, each 1 cm thick. These layers were interleaved with 9 mm thick planes of streamer tubes filled with gas (Ar-CO_2-n-pentane(1+2+1)) for particle detection via ionization. The detector had a total mass of 0.15 kton. NUSEX became operational in 1982 and in 1983 reported observing no definite proton decay candidates. By the time NUSEX ended it indicated a lower limit on the decay lifetime of $\tau_{p \to e^+\ \pi^0} > 1.5 \times 10^{31}$ years and $\tau_{p \to K^+\ \overline{\nu}} > 2.0 \times 10^{30}$ years [139] with lifetimes for other channels falling within that range.

The FREJUS experiment [140] also involved a tracking calorimeter and started taking data in Fréjus, France, in 1985. Buried under a rock overburden of 1800 m, the detector had a mass of 0.9 kton and was constructed from 912 layers of iron (3 mm thick) sandwiched between layers of plastic flash tubes (each containing a Ne-He gas mixture). The planes were oriented in various directions to allow particle tracking. Every eighth plane of flash tubes contained Geiger tubes (cross-section 15×15 mm^2) used for triggering. In 1991 FREJUS reported lower limits on proton decay partial lifetimes ranging from 5×10^{30} to 1×10^{32} years [141].

The Soudan I and Soudan II experiments [142–144] were located in the Soudan mine, MN. Soudan I became operational in 1981 as a 30 ton tracking calorimeter, shielded by a rock overburden of 590 m and acted as a prototype for the larger Soudan II detector. Its successor Soudan II was operational between 1989 and 2001. It consisted of 224 modules and had a total mass of 0.96 kton. The modules were boxes filled with Ar-CO_2 mixture and contained corrugated steel plates arranged in a honeycomb structure (allowing very isotropic detection in comparison to other detectors), with readout enabled by plastic drift tubes. Soudan I determined a lower limit on the proton decay lifetime of 1.6×10^{30} years. In 1999 Soudan II extended this to $\tau_{p \to e^+ \pi^0} > 3.8 \times 10^{31}$ years and $\tau_{p \to K^+ \overline{\nu}} > 4.3 \times 10^{31}$ years.

The IMB (Irvine-Michigan-Brookhaven) experiment [145] used a water Cerenkov detector to search for a proton decay from 1981. Located near Lake Erie, OH, with a rock overburden of 670 m, the detector contained a cuboidal volume of water of mass 6.8 kton, lined with PMTs. After ten years of operation and no proton decay events observed, the lower limit on the $p \to e^+ \pi^0$ set by IMB, and its upgrades IMB-2 and IMB-3 was 5.5×10^{32} years [146].

The Kamiokande (Kamioka Nucleon Decay Experiment) [147] and Super-Kamiokande experiments [148] have also been involved in the search for proton decay, with the latter setting the current best limit on the proton decay lifetime. Kamiokande (located at the Kamioka Observatory, Japan) became operational in 1983 and consisted of a cylindrical container holding 3 kton of pure water, surrounded by ~1000 inward-facing photomultiplier tubes (PMTs). It had a rock overburden of 1000 m. Unlike the tracking calorimeters mentioned in the previous paragraphs, this experiment relied on the PMTs detecting rings of Cerenkov radiation emitted by particles travelling faster than the phase velocity of light in water. Kamiokande failed to observe any proton decay events, as has its successor Super-Kamiokande, which became operational in 1996. This is a larger version of its predecessor, containing 50 kton of water (22.5 kton fiducial mass) and ~11,200 PMTs, as well as having an outer-detector muon veto system. As of June 2012 the Super-Kamiokande limit on the proton decay lifetime via the channel $p \to e^+ \pi^0$ was 8.2×10^{33} years [67]. As of August 2014 the limit on decay lifetime via the channel $p \to K^+ \overline{\nu}$ was 5.9×10^{33} years [68]. The successor to Super-Kamiokande will be Hyper-Kamiokande [149], expected to become operational in 2025. It will be a water Cerenkov detector like its predecessors but will contain one megaton of water, allowing it to probe proton decay lifetimes far in excess of the current lower limits. Assuming no proton decay event is observed, after ten years of operation Hyper-Kamiokande will set a 3 σ limit of 5.2×10^{34} years for $p \to e^+ \pi^0$ and 1.2×10^{34} years for $p \to K^+ \overline{\nu}$.

To summarise this section, many GUTs have been proposed over the past four decades and their discussion in this chapter has been far from exhaustive. They often provide solutions to problems discussed in Section 2.2.1 which cannot be solved within the framework of the SM. The instability of the proton is one of the only testable predictions common to GUTs and its detection would provide powerful evidence in their favour - but no experimental searches to date have detected it. The predicted decay lifetime differs widely among specific GUTs (Figure 7 [150] shows the range of proton decay lifetimes spanned by various models, as well as the lower bounds set by experiments). The current lower limit has been set by Super-Kamiokande and has already ruled out many proposed models. However, there are still many GUTs which predict proton lifetimes in excess of this limit. The continued search for such events (particularly in the channels $p \to e^+ \pi^0$ and $p \to K^+ \overline{\nu}$) is therefore well-motivated. The lifetime ranges predicted by numerous GUTs will be testable by the next generation of large-scale detectors. LBNE/DUNE (Section 2.6) is one such experiment, capable of detecting decaying protons, should they indeed have a lifetime in the range $\sim 10^{34}$-10^{35} years.

However, a proton decay search is not the sole or primary aim of this experiment; LBNE/DUNE primarily aims to detect neutrinos from multiple sources. The remainder of this chapter will focus on another 'beyond-the-SM' phenomenon that provides the main motivation for LBNE/DUNE - specifically that of ‘neutrino oscillation’.

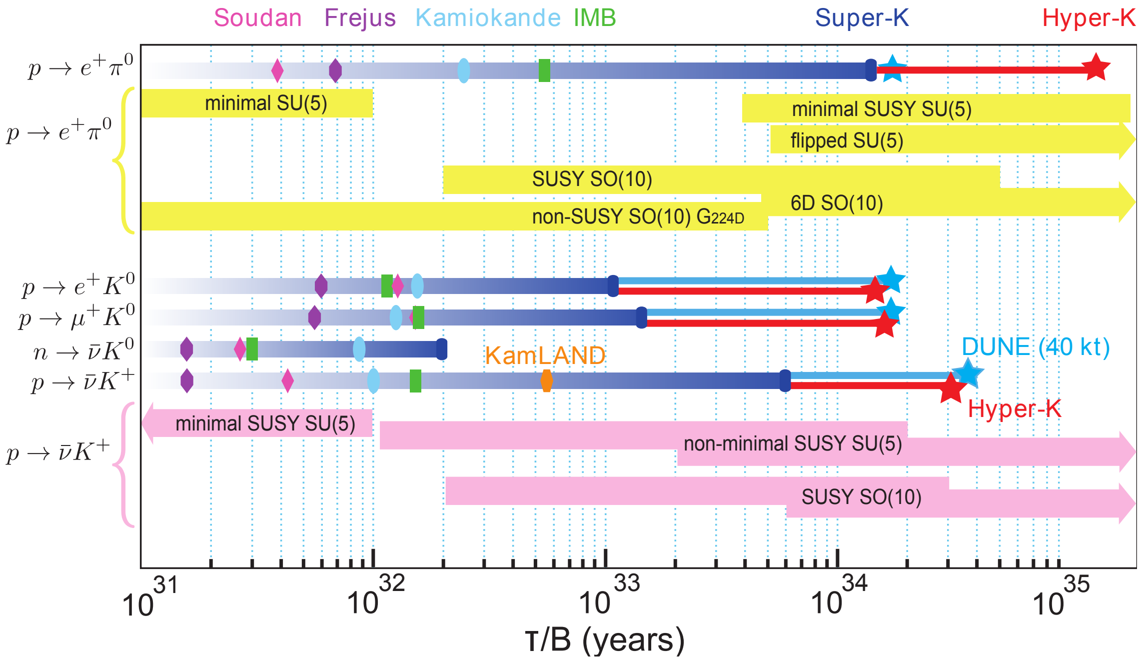

Figure 7: *The ranges of proton decay lifetime predicted by a selection of common models, broken down by the specific channel [42, 67, 150]. The upper region deals with* $p \to e^+\pi^0$*, the dominant channel in non-SUSY models. The lower region deals with channels that dominate SUSY models, most importantly* $p \to K^+\overline{\nu}$*. Also shown are the published lower limits on decay lifetime measured by various experiments.*

2.4 Neutrino oscillation

In the SM the three flavours of neutrino ν_e, ν_μ, ν_τ are treated as massless leptons and thought of as three distinct entities. However, there is now much evidence that neutrinos switch flavours as they propagate [151]. This has come to be interpreted in terms of 'neutrino oscillation', a theory (first proposed in 1958 by Bruno Pontecorvo [152–154]) that requires neutrinos have non-zero, non-degenerate masses that, as already mentioned, are unaccounted for within the SM.

Neutrino oscillation theory stems from each of the weak 'flavour' / 'interaction' eigenstates not corresponding directly to one of the mass eigenstates. The SM fermions ψ can be decomposed [155] [156] into left and right-handed chiral states ($\psi = \psi_L + \psi_R$), so from the Dirac Lagrangian $\overline{\psi}(i\gamma^\mu\partial_\mu - m_D)\psi$ the mass terms are of the form

$$m_D\overline{\psi}\psi = m_D(\overline{\psi}_L+\overline{\psi}_R)(\psi_L+\psi_R) = m_D(\overline{\psi}_L\psi_L+\overline{\psi}_L\psi_R+\overline{\psi}_R\psi_L+\overline{\psi}_R\psi_R) = m_D(\overline{\psi}_L\psi_R+\overline{\psi}_R\psi_L)$$

(since $\overline{\psi}_L\psi_L = \overline{\psi}_R\psi_R = 0$). The SM includes no right-handed neutrino field, meaning no such Dirac mass term for the neutrino (which was for decades assumed to be massless). However, as this section will discuss, a tiny but non-zero neutrino mass is now well-established. This could mean a right-handed neutrino does exist but has avoided discovery due to not participating in weak interactions, or that another type of mass term can be allowed.

Neutrino mass terms can be obtained that involve solely left or right-handed fields, which can be related via $\psi_R = C\overline{\psi}_L^T$ (where $C = i\gamma^2\gamma^0$ is the charge conjugation operator). Defining also $\psi_L^C = C\overline{\psi}_L^T$ ($= \psi_R$) one finds that $\psi = \psi_L + \psi_L^C$ and therefore $\psi^C = \psi$ (i.e. ψ and its antiparticle are identical).

For neutrinos[21] this means a Majorana mass term of the form $-\frac{1}{2}m_L\overline{\nu}_L^C\nu_L$ can be written[22]. If one allows for the existence of a right-handed neutrino field then the Lagrangian also gains a term of the form $-m\overline{\nu}_L\nu_R$ and $-\frac{1}{2}m_R\overline{\nu}_R^C\nu_R$, so the full complement of mass terms would then be

$$m_D\overline{\nu}_R\nu_L + m_D\overline{\nu}_L^C\nu_R^C + m_L\overline{\nu}_L^C\nu_L + m_R\overline{\nu}_R^C\nu_R \quad + \quad \text{H.c.}$$

which can instead be expressed in terms of a mass matrix:

$$\mathcal{L}_{\text{mass terms}} = -\frac{1}{2}(\overline{\nu}_L^C\overline{\nu}_R)\begin{pmatrix} m_L & m_D \\ m_D & m_R \end{pmatrix}\begin{pmatrix} \nu_L \\ \nu_R^C \end{pmatrix} \quad + \quad \text{H.c.}$$

Since this mass matrix would not be diagonal, these interaction/flavour states $\nu_{L,R}$ are not eigenstates of definite mass that correspond to physical particles. To obtain mass eigenstates one may diagonalise the mass matrix; the eigenbasis in which this matrix is diagonal is then a superposition of the interaction states.

A neutrino may thus emerge from an interaction in a state of definite flavour ν_e, ν_μ, ν_τ, but with an indeterminate mass (a superposition of the mass eigenstates ν_1, ν_2, ν_3). As the neutrino travels the relative amplitudes of the mass eigenstates evolve, until their amplitudes correspond to a flavour other than the neutrino originally possessed. The

---

[21] Clearly this can only work for fields with zero charge, which in terms of the SM fermions means this applies only to the neutrinos.

[22] Such a left-handed neutrino term is actually not allowed in the SM due to conflict with the weak isospin and hypercharge quantum numbers of the Higgs field H. This can be removed by setting $m_L = 0$ but the term can still be considered in this discussion.

probability of observing this flavour change for a given neutrino varies sinusoidally (i.e. 'oscillates') with time elapsed/distance travelled. Furthermore the probability of flavour change for a neutrino may differ from that of an antineutrino. This presents an opportunity to study weak charge-parity (CP) violation - something significant in its own right but also something that can potentially account for the apparent imbalance of matter over anti-matter in the universe.

This section will outline basic theoretical aspects of neutrino oscillation and CP-violation in the neutrino sector, the current state of experimental evidence for each, and the parameters relating to each that LBNE/DUNE seeks to measure.

2.4.1 Neutrino oscillation in two flavours

For simplicity only two lepton generations (e and μ) are required to demonstrate the basic features of neutrino oscillation, although it will be extended to three generations in Section 2.4.3. One may start [157] [156] by assuming that there are a set of orthogonal flavour eigenstates $|\nu_\alpha\rangle$ ($\alpha = e, \mu$) which are each some linear combination of orthogonal mass eigenstates $|\nu_i\rangle$ ($i = 1, 2$), related by the matrix U:

$$|\nu_\alpha\rangle = \sum_{i=1}^{2} U_{\alpha i}|\nu_i\rangle. \tag{39}$$

The matrix U may be parameterized in terms of a mixing angle θ; the flavour eigenstates may be rotated into the mass eigenstates as follows:

$$\begin{pmatrix} \nu_e \\ \nu_\mu \end{pmatrix} = \begin{pmatrix} \cos\theta & \sin\theta \\ -\sin\theta & \cos\theta \end{pmatrix} \begin{pmatrix} \nu_1 \\ \nu_2 \end{pmatrix}. \tag{40}$$

The Schrödinger equation $i\partial_t\Psi = \hat{H}\Psi$ is satisfied by a plane-wave solution for the mass eigenstates:

$$|\nu_i(t)\rangle = e^{i(\vec{p_i}\cdot\vec{x})-E_i t}|\nu_i(0)\rangle. \tag{41}$$

Immediately after a neutrino has been created in some interaction it will be in a pure flavour state and therefore in its own particular superposition of mass eigenstates. If this flavour state is $|\nu_e\rangle$ then Eq. 40 yields

$$|\nu_e(x=0, t=0)\rangle = \cos\theta|\nu_1(0,0)\rangle + \sin\theta|\nu_2(0,0)\rangle \equiv \cos\theta|\nu_1\rangle + \sin\theta|\nu_2\rangle.$$

This will evolve over time according to Eq. 41. After reaching some time $t = T$, distance $x = L$ away from its initial location the wavefunction will be a different superposition of the mass states $|\nu_i\rangle$. Defining phases $\phi_i \equiv E_i T - \vec{p_i}\cdot\vec{L}$, the neutrino state may be expressed as

$$\begin{aligned} |\psi(L,T)\rangle &= \cos\theta|\nu_1\rangle e^{i(\vec{p_1}\cdot\vec{L}-E_1T)} + \sin\theta|\nu_2\rangle e^{i(\vec{p_2}\cdot\vec{L}-E_2T)} \\ &\equiv \cos\theta|\nu_1\rangle e^{-i\phi_1} + \sin\theta|\nu_2\rangle e^{-i\phi_2}. \end{aligned} \tag{42}$$

Using the unitarity of the mixing matrix in Eq. 40, the mass states may be expressed in terms of the flavour basis:

$$|\nu_1\rangle = \cos\theta|\nu_e\rangle - \sin\theta|\nu_\mu\rangle, \qquad |\nu_2\rangle = \sin\theta|\nu_e\rangle + \cos\theta|\nu_\mu\rangle$$

and so in the flavour basis, Eq. 42 becomes

$$\begin{aligned}|\psi(L,T)\rangle &= \cos\theta\big(\cos\theta|\nu_e\rangle - \sin\theta|\nu_\mu\rangle\big)e^{-i\phi_1} + \sin\theta\big(\sin\theta|\nu_e\rangle + \cos\theta|\nu_\mu\rangle\big)e^{-i\phi_2} \\ &= (\cos^2\theta e^{-i\phi_1} + \sin^2\theta e^{-i\phi_2})|\nu_e\rangle \quad + \sin\theta\cos\theta(-e^{-i\phi_1} + e^{-i\phi_2})|\nu_\mu\rangle.\end{aligned} \tag{43}$$

The phases ϕ_1, ϕ_2 are only different if the masses they correspond to are different. If $\phi_1 = \phi_2$ then the mass eigenstates $|\nu_1\rangle$ and $|\nu_2\rangle$ would stay in phase and their relative amplitudes would never evolve. The state would obey $|\psi(L,T)\rangle = |\psi(0,0)\rangle$ and the neutrino would therefore have to interact in the same flavour state as it was produced. However, a difference between mass eigenstates $|\nu_1\rangle$ and $|\nu_2\rangle$ implies some non-zero probability that the neutrino created in the flavour eigenstate $|\nu_e\rangle$ may interact in the detector as a $|\nu_\mu\rangle$. This can be calculated from Eq. 40 and 42 as follows:

$$\begin{aligned}P_{\nu_e\to\nu_\mu} = |\langle\nu_\mu|\psi\rangle|^2 \quad &= \quad \Big|\big(\langle\nu_2|\cos\theta - \langle\nu_1|\sin\theta\big)\,\big(\cos\theta|\nu_1\rangle e^{-i\phi_1} + \sin\theta|\nu_2\rangle e^{-i\phi_2}\big)\Big|^2 \\ = \big|\cos\theta\sin\theta(e^{-i\phi_1} - e^{-i\phi_2})\big|^2 \quad &= \quad \cos^2\theta\,\sin^2\theta\big(2 - 2\cos(\phi_1-\phi_2)\big) \\ = \sin^2(2\theta)\big(\tfrac{1}{2} - \tfrac{1}{2}\cos(\phi_1-\phi_2)\big) \quad &= \quad \sin^2(2\theta)\sin^2\big(\tfrac{1}{2}\Delta\phi_{12}\big),\end{aligned} \tag{44}$$

where $\Delta\phi_{12} = |\phi_1 - \phi_2|$. Thus, as the neutrino propagates the probability of the flavour change $|\nu_e\rangle \to |\nu_\mu\rangle$ varies sinusoidally, with an amplitude given by $\sin^2(2\theta)$. One may then make the simplifying assumption that each mass eigenstate has equal momentum ($\vec{p}_1 = \vec{p}_2 \equiv \vec{p}$) and so $\Delta\phi_{12}$ approximates to:

$$\begin{aligned}\Delta\phi_{12} = (E_1T - |\vec{p}_1|L) - (E_2T - |\vec{p}_2|L) \;\approx\; (E_1 - E_2)T \;&=\; \left(\sqrt{|\vec{p}|^2 + m_1^2} - \sqrt{|\vec{p}|^2 + m_2^2}\right)T \\ \approx \left[\left(|\vec{p}| + \frac{m_1^2}{2|\vec{p}|}\right) - \left(|\vec{p}| + \frac{m_2^2}{2|\vec{p}|}\right)\right]L \;&=\; \frac{m_1^2 - m_2^2}{2|\vec{p}|}L \;\approx\; \frac{\Delta m_{12}^2}{2E}L\end{aligned} \tag{45}$$

where $L/T \approx c = 1$ has been used and the mass-splitting $m_1^2 - m_2^2$ is denoted by Δm_{12}^2. Finally, the factor $\frac{1}{4}$ that would appear by substituting Eq. 45 into Eq. 44 is replaced by 1.27 when converting $\hbar, c$ to their proper units [23] . The probabilities for the two-flavour disappearance and survival are then

$$P_{\nu_e\to\nu_\mu} = \sin^2(2\theta)\sin^2\left(\frac{1.27\,\Delta m_{12}^2 L}{E}\right), \qquad\qquad P_{\nu_e\to\nu_e} = 1 - P_{\nu_e\to\nu_\mu}. \tag{46}$$

Figure 8 shows an example plot of two-flavour oscillation analogous to Eq. 46 with a realistic choice of mixing angle and mass-splitting.

To measure these probabilities, instead of considering a single neutrino one may examine a source of many neutrinos and count how many change or maintain their initial flavour. The mixing angle θ can be determined from the amplitude of the oscillation curve $\sin^2(2\theta)$, and the mass splitting Δm_{12}^2 can be calculated from the oscillation wavelength. The probability of observing flavour change is maximised when $1.27\Delta m_{12}^2\frac{L}{E} = \frac{\pi}{2}$, so when designing an experiment one may tune L, E or both to the optimum values for investigating a given mass splitting.

This section has dealt with oscillations between neutrinos of only two flavours, but in fact it must be extended to include the three known flavours of lepton. Without this there would be a conflict between the results of experiments involving atmospheric neutrinos

---

[23] Conventionally the distance L has units of km, Δm^2 of eV^2 and E of GeV.

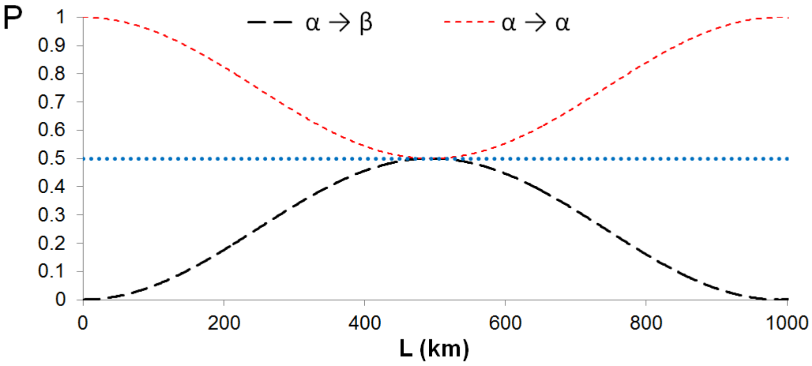

Figure 8: *An example of the dependence of flavour change probabilities* $P_{\nu_\alpha \to \nu_\beta}$ *and* $P_{\nu_\alpha \to \nu_\alpha}$ *on distance* L *from the initial position of the neutrino, in a two-flavour scheme (Eq. 72). The parameters used are* $\Delta m^2 = 2.5 \times 10^{-3}\ eV^2$, $E = 1\ GeV$ *and* $sin^2(2\theta) = 0.5$, *with the latter indicated by the horizontal line.*

and those involving solar neutrinos. The values of Δm^2 measured using these sources are not in agreement, implying that there are oscillations involving at least three flavour eigenstates (Section 2.4.3).

2.4.2 Neutrino oscillation within matter - the MSW effect

In Section 2.4.1 only oscillations for neutrinos propagating in the vacuum have been considered. However, there are situations where matter effects become significant. Flavour change between neutrino flavour states occurs due to a difference in the phase between the mass eigenstates [24] (Eq. 44). When neutrinos are propagating through matter, the phase difference is modified to take account of an interaction potential V associated with the medium and the phase difference then depends on the total energy $E+V$. This affects the character of the oscillations and is referred to as the MSW (Mikheyev-Smirnov-Wolfenstein) effect [155, 158, 159].

In the vacuum the time evolution of the mass eigenstates obey Schrödinger‘s equation:

$$i\partial_t \begin{pmatrix} \nu_1 \\ \nu_2 \end{pmatrix} = H \begin{pmatrix} \nu_1 \\ \nu_2 \end{pmatrix} \quad \text{where} \quad H = \begin{pmatrix} E_1 & 0 \\ 0 & E_2 \end{pmatrix} \approx \begin{pmatrix} \frac{m_1^2}{2|\vec{p}|} & 0 \\ 0 & \frac{m_2^2}{2|\vec{p}|} \end{pmatrix} + |\vec{p}| \begin{pmatrix} 1 & 0 \\ 0 & 1 \end{pmatrix}. \tag{47}$$

where the Taylor expansion $E = \sqrt{|\vec{p}|^2 + m^2} \approx |\vec{p}| + \frac{m^2}{2|\vec{p}|}$ has been used and $p_1 = p_2 \equiv p$ as before. The time evolution can also be expressed in terms of the flavour states:

$$\begin{pmatrix} \nu_\alpha \\ \nu_\beta \end{pmatrix} = U \begin{pmatrix} \nu_1 \\ \nu_2 \end{pmatrix} \qquad \rightarrow \qquad i\partial_t \begin{pmatrix} \nu_1 \\ \nu_2 \end{pmatrix} = i\partial_t U^\dagger \begin{pmatrix} \nu_\alpha \\ \nu_\beta \end{pmatrix} = HU^\dagger \begin{pmatrix} \nu_\alpha \\ \nu_\beta \end{pmatrix} \tag{48}$$

$$\Longrightarrow \; i\partial_t \begin{pmatrix} \nu_\alpha \\ \nu_\beta \end{pmatrix} = UHU^\dagger \begin{pmatrix} \nu_\alpha \\ \nu_\beta \end{pmatrix} \equiv H' \begin{pmatrix} \nu_\alpha \\ \nu_\beta \end{pmatrix} \tag{49}$$

where the unitary rotation matrix U is shown explicitly in Eq. 40. One may then compute $H' = UHU^\dagger$ to find the Hamiltonian transformed into the flavour basis:

$$H' = \frac{m_1^2 + m_2^2}{4E} \begin{pmatrix} 1 & 0 \\ 0 & 1 \end{pmatrix} + \frac{\Delta m_{12}^2}{4E} \begin{pmatrix} -\cos\,2\theta & \sin\,2\theta \\ \sin\,2\theta & \sin\,2\theta \end{pmatrix}. + |\vec{p}| \begin{pmatrix} 1 & 0 \\ 0 & 1 \end{pmatrix} \tag{50}$$

---

[24] A non-zero probability of flavour change is due to a difference in phase $\Delta\phi_{12}$, but more specifically, that the probability sinusoisally oscillates in time/distance is due to this phase difference having time-dependence.

where $E^2 = p^2 + m_i^2$ i.e. $E \approx p$. In vacuum the time-evolution for the flavour states obeys Eq. 49 but to incorporate the matter interaction potential V, the Hamiltonian must be modified:

$$i\partial_t \begin{pmatrix} \nu_\alpha \\ \nu_\beta \end{pmatrix} = (H' + V) \begin{pmatrix} \nu_\alpha \\ \nu_\beta \end{pmatrix} \qquad \text{where} \qquad V = \begin{pmatrix} V_\alpha & 0 \\ 0 & V_\beta \end{pmatrix}. \tag{51}$$

Here two different interaction potentials V_α and V_β are required since the two flavours $|\nu_\alpha\rangle$ and $|\nu_\beta\rangle$ can have different interactions with the medium. This is necessary since, in a medium such as rock (which is rich in electrons), $|\nu_e\rangle$ may undergo charged-current (CC) and neutral-current (NC) interactions whereas the other flavours are limited to just the latter.

In Eq. 50 the last term can be omitted, since it ends up introducing a constant phase factor that has no bearing on the calculation of the effective mass-splitting or mixing angle [155]. With the first term on the right-hand-side of Eq. 50 abbreviated as H_0, from Eq. 50, 51 the time-evolution of flavour states propagating in matter is

$$i\partial_t \begin{pmatrix} \nu_\alpha \\ \nu_\beta \end{pmatrix} = \left[H_0 + \frac{\Delta m_{12}^2}{4E} \begin{pmatrix} -\cos\, 2\theta + V_\alpha & \sin\, 2\theta \\ \sin\, 2\theta & \sin\, 2\theta + V_\beta \end{pmatrix} \right] \begin{pmatrix} \nu_\alpha \\ \nu_\beta \end{pmatrix}. \tag{52}$$

Adding a constant to this leaves the result unaffected since it corresponds to a constant phase in an exponential; when the probability of observing a given state is calculated, the constant phase vanishes. Adding a term proportional to $-V_\beta$ to Eq. 52 can produce

$$i\partial_t \begin{pmatrix} \nu_\alpha \\ \nu_\beta \end{pmatrix} = \left[H_0 + \frac{\Delta m_{12}^2}{4E} \begin{pmatrix} -\cos\, 2\theta + V_\alpha - V_\beta & \sin\, 2\theta \\ \sin\, 2\theta & \sin\, 2\theta \end{pmatrix} \right] \begin{pmatrix} \nu_\alpha \\ \nu_\beta \end{pmatrix} \equiv H_M \begin{pmatrix} \nu_\alpha \\ \nu_\beta \end{pmatrix}. \tag{53}$$

The interaction with the medium results in a different effective neutrino mass. To calculate this the time-evolution can then be transformed into the vacuum mass basis:

$$i\partial_t \begin{pmatrix} \nu_1 \\ \nu_2 \end{pmatrix} = U^\dagger i\partial_t \begin{pmatrix} \nu_\alpha \\ \nu_\beta \end{pmatrix} = U^\dagger \left[H_0 + \frac{\Delta m_{12}^2}{4E} \begin{pmatrix} -\cos\, 2\theta + V_\alpha - V_\beta & \sin\, 2\theta \\ \sin\, 2\theta & \sin\, 2\theta \end{pmatrix} \right] \begin{pmatrix} \nu_\alpha \\ \nu_\beta \end{pmatrix} \tag{54}$$

$$= \left(U^\dagger \left[H_0 + \frac{\Delta m_{12}^2}{4E} \begin{pmatrix} -\cos\, 2\theta & \sin\, 2\theta \\ \sin\, 2\theta & \sin\, 2\theta \end{pmatrix} \right] U + U^\dagger \begin{pmatrix} V_\alpha - V_\beta & 0 \\ 0 & 0 \end{pmatrix} U \right) \begin{pmatrix} \nu_1 \\ \nu_2 \end{pmatrix} \tag{55}$$

$$= \frac{1}{2E} \begin{pmatrix} m_1^2 + \Delta V\, \cos^2\, \theta & \Delta V\, \cos\, \theta \sin\, \theta \\ \Delta V\, \cos\, \theta \sin\, \theta & m_2^2 + \Delta V \sin^2\, \theta \end{pmatrix} \begin{pmatrix} \nu_1 \\ \nu_2 \end{pmatrix} \tag{56}$$

where $\Delta V \equiv V_\alpha - V_\beta$. The vacuum mass eigenstates are not eigenstates of H_M but mass eigenvalues for propagation within matter m_1^M, m_2^M can be obtained by diagonalizing this mass matrix. This yields

$$m_{1,2}^M = \left(\tfrac{1}{2}(m_1^2 + m_2^2 + \Delta V) \pm \tfrac{1}{2}\sqrt{(\Delta m_{12}^2 \cos\, 2\theta - \Delta V)^2 + (\Delta m_{12}^2)^2 \sin^2\, 2\theta} \right)^{\frac{1}{2}} \tag{57}$$

and so the effective mass-splitting in matter is

$$\Delta(m_{12}^M)^2 \;=\; (m_1^M)^2 - (m_2^M)^2 \;=\; \Delta m_{12}^2 \sqrt{\left(\cos\, 2\theta - \frac{\Delta V}{\Delta m_{12}^2}\right)^2 + \sin^2\, 2\theta} \;\equiv\; \Delta m_{12}^2 f_M. \tag{58}$$

The flavour probabilities may be calculated analogous to Eq. 46 with:

$$\Delta m_{12}^2 \to \Delta(m_{12}^M)^2 = \Delta m_{12}^2 f_M, \qquad \sin^2\, 2\theta \to \sin^2\, 2\theta^M = \sin^2\, 2\theta / f_M. \tag{59}$$

2.4.3 Neutrino oscillation in three flavours

2.4.3.1 General three-flavour theory

The two-neutrino theory of Sections 2.4.1, 2.4.2 can be extended to include all three known flavours of neutrino [156, 157]. In this case the oscillation parameters are three mixing angles θ_{12}, θ_{13}, θ_{23} and three mass-splittings Δm^2_{12}, Δm^2_{13}, Δm^2_{23} (Figure 9). The mixing matrix analogous to Eq. 39 is 3×3 and is referred to as the Pontecorvo-Maki-Nakagawa-Sakata (PMNS) matrix [160]:

$$\begin{pmatrix} \nu_e \\ \nu_\mu \\ \nu_\tau \end{pmatrix} = \begin{pmatrix} U_{e1} & U_{e2} & U_{e3} \\ U_{\mu 1} & U_{\mu 2} & U_{\mu 3} \\ U_{\tau 1} & U_{\tau 2} & U_{\tau 3} \end{pmatrix} \begin{pmatrix} \nu_1 \\ \nu_2 \\ \nu_3 \end{pmatrix} \approx \begin{pmatrix} 0.82 & 0.54 & 0.15 \\ 0.35 & 0.70 & 0.62 \\ 0.44 & 0.45 & 0.77 \end{pmatrix} \begin{pmatrix} \nu_1 \\ \nu_2 \\ \nu_3 \end{pmatrix}. \tag{60}$$

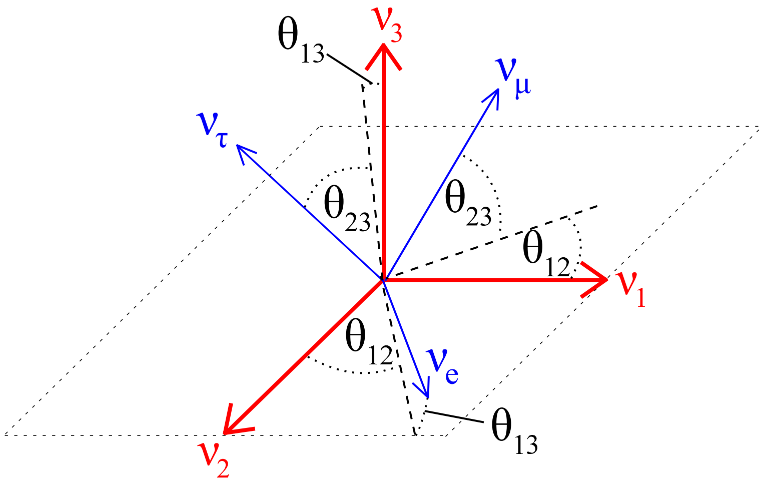

Figure 9: *An illustration of the mixing of the three neutrino mass and flavour states, showing the approximate sizes of the mixing angles* $\theta_{12} \sim 34°$, $\theta_{13} \sim 9°$ *and* $\theta_{23} \sim 41°$ *[42].*

The time-evolution of the flavour states in the mass eigenbasis is given by

$$|\nu_\alpha(t)\rangle = \sum_{i=1}^{3} U_{\alpha i} e^{-i(E_i t - \vec{p}\cdot\vec{x})} |\nu_i\rangle \quad \text{where} \quad |\nu_{\beta,i}\rangle \equiv |\nu_{\beta,i}(t=0)\rangle. \tag{61}$$

When Eq. 61 is written explicitly (with $\phi_i \approx |\vec{p}| + \frac{m_i^2}{2|\vec{p}|}$ as in Eq. 45) this is

$$|\nu_\alpha(t)\rangle = U_{\alpha 1}|\nu_1\rangle e^{-i\phi_1} + U_{\alpha 2}|\nu_2\rangle e^{-i\phi_2} + U_{\alpha 3}|\nu_1\rangle e^{-i\phi_3} \tag{62}$$

which can be rewritten in the flavour eigenbasis as

$$\begin{aligned} |\nu_\alpha(t)\rangle \;=\; & U_{\alpha 1}\left[U^*_{e1}|\nu_e\rangle + U^*_{\mu 1}|\nu_\mu\rangle + U^*_{\tau 1}|\nu_\tau\rangle\right] e^{-i\phi_1} \\ & + U_{\alpha 2}\left[U^*_{e2}|\nu_e\rangle + U^*_{\mu 2}|\nu_\mu\rangle + U^*_{\tau 2}|\nu_\tau\rangle\right] e^{-i\phi_2} \\ & + U_{\alpha 3}\left[U^*_{e3}|\nu_e\rangle + U^*_{\mu 3}|\nu_\mu\rangle + U^*_{\tau 3}|\nu_\tau\rangle\right] e^{-i\phi_3} \\ =\; & (U_{\alpha 1}U^*_{e1}e^{-i\phi_1} + U_{\alpha 2}U^*_{e2}e^{-i\phi_2} + U_{\alpha 3}U^*_{e3}e^{-i\phi_3})|\nu_e\rangle \\ & + (U_{\alpha 1}U^*_{\mu 1}e^{-i\phi_1} + U_{\alpha 2}U^*_{\mu 2}e^{-i\phi_2} + U_{\alpha 3}U^*_{\mu 3}e^{-i\phi_3})|\nu_\mu\rangle \\ & + (U_{\alpha 1}U^*_{\tau 1}e^{-i\phi_1} + U_{\alpha 2}U^*_{\tau 2}e^{-i\phi_2} + U_{\alpha 3}U^*_{\tau 3}e^{-i\phi_3})|\nu_\tau\rangle \end{aligned} \tag{63}$$

Noting the orthogonality of the flavour eigenstates ($\langle \nu_\alpha | \nu_\beta \rangle = \delta_{\alpha\beta}$), the probability of flavour change can then be calculated via

$$P_{\nu_\alpha \to \nu_\beta} = \left| \langle \nu_\alpha | \nu_\alpha \rangle \right|^2 = \left(U_{\alpha 1} U^*_{\beta 1} e^{-i\phi_1} + U_{\alpha 2} U^*_{\beta 2} e^{-i\phi_2} + U_{\alpha 3} U^*_{\beta 3} e^{-i\phi_3} \right)^2. \tag{64}$$

Finally the following complex number identity [161] can be used to separate this into real and imaginary parts (which has significance for investigating CP-violation):

$$|z_1 + z_2 + z_3|^2 = |z_1|^2 + |z_2|^2 + |z_3|^2 + 2Re(z_1 z_2^* + z_1 z_3^* + z_2 z_3^*) \tag{65}$$

$$\begin{aligned} \implies P_{\nu_\alpha \to \nu_\beta} = \delta_{\alpha\beta} &- 4 \sum_{i>j} Re(U^*_{\alpha i} U_{\beta i} U_{\alpha j} U^*_{\beta j}) \sin^2 \left(\frac{1.27 \Delta m^2_{ij} L}{E} \right) \\ &+ 2 \sum_{i>j} Im(U^*_{\alpha i} U_{\beta i} U_{\alpha j} U^*_{\beta j}) \sin^2 \left(2 \times \frac{1.27 \Delta m^2_{ij} L}{E} \right). \end{aligned} \tag{66}$$

where $\delta_{\alpha\beta} = 1$ if $\alpha = \beta$ or 0 if $\alpha \neq \beta$.

The PMNS matrix is commonly parametrized [162] in terms of three mixing angles θ_{12}, θ_{13} and θ_{23} (Figure 9) and an extra parameter δ that quantifies CP-violation if any is observed (Section 2.4.6). Defining $\cos\,\theta_{ij} \equiv c_{ij}$ and $\sin\,\theta_{ij} \equiv s_{ij}$ the matrix U is constructed as follows:

$$\begin{aligned} U = &\begin{pmatrix} 1 & 0 & 0 \\ 0 & c_{23} & s_{23} \\ 0 & -s_{23} & c_{23} \end{pmatrix} \times \begin{pmatrix} e^{-i\delta/2} & 0 & 0 \\ 0 & 1 & 0 \\ 0 & 0 & e^{i\delta/2} \end{pmatrix} \times \begin{pmatrix} c_{13} & 0 & s_{13} \\ 0 & 1 & 0 \\ -s_{13} & 0 & c_{13} \end{pmatrix} \\ &\times \begin{pmatrix} e^{i\delta/2} & 0 & 0 \\ 0 & 1 & 0 \\ 0 & 0 & e^{-i\delta/2} \end{pmatrix} \times \begin{pmatrix} c_{12} & s_{12} & 0 \\ -s_{12} & c_{12} & 0 \\ 0 & 0 & 1 \end{pmatrix} \\ = &\begin{pmatrix} c_{12} c_{13} & s_{12} c_{13} & s_{13} e^{-i\delta} \\ -s_{12} c_{23} - c_{12} s_{23} s_{13} e^{i\delta} & c_{12} c_{23} - s_{12} s_{13} s_{23} e^{i\delta} & c_{13} s_{23} \\ s_{12} s_{23} - c_{12} s_{13} c_{23} e^{i\delta} & -c_{12} s_{23} - s_{12} s_{13} c_{23} e^{i\delta} & c_{13} c_{23} \end{pmatrix}. \end{aligned} \tag{67}$$

2.4.3.2 Specific oscillation probability approximations

If one assumes $\delta = 0$ (i.e. no CP-violation) and also approximates $\Delta m^2_{13} \approx \Delta m^2_{23}$ then Eq. 66 yields simplified results when considering small and large L/E. For small L/E the term containing Δm^2_{12} becomes irrelevant and so

$$\text{Small } L/E: \qquad P_{\nu_e \to \nu_\mu} \approx \sin^2(2\theta_{13}) \sin^2(\theta_{23}) \sin^2 \left(\frac{1.27 \Delta m^2_{23} L}{E} \right), \tag{68}$$

$$\text{Small } L/E: \qquad P_{\nu_e \to \nu_\tau} \approx \sin^2(2\theta_{13}) \cos^2(\theta_{23}) \sin^2 \left(\frac{1.27 \Delta m^2_{23} L}{E} \right), \tag{69}$$

$$\text{Small } L/E: \qquad P_{\nu_\mu \to \nu_\tau} \approx \cos(\theta_{13}) \sin^2(2\theta_{23}) \sin^2 \left(\frac{1.27 \Delta m^2_{23} L}{E} \right). \tag{70}$$

Assuming invariance under a time-reversal transformation, these equations for $P_{\nu_\alpha \to \nu_\beta}$ also hold for $P_{\nu_\beta \to \nu_\alpha}$.

Alternatively for large values of L/E, the sin() term involving Δm^2_{23} oscillates rapidly and averages to $\frac{1}{2}$, so Eq. 66 leads to

$$\text{Large } L/E: \qquad P_{\nu_e \to \nu_{\mu,\tau}} \approx \cos^2(\theta_{13}) \sin^2(2\theta_{12}) \sin^2\left(\frac{1.27\Delta m^2_{12} L}{E}\right) + \tfrac{1}{2}\sin^2(2\theta_{13}). \quad (71)$$

One may also make the approximation that $sin^2(2\theta_{13}) \approx 0$ (although a non-zero value has actually been measured (Sections 2.5.3, 2.5.4)) to find the following two-flavour approximations:

$$\text{Small } L/E: \qquad (i)\ P_{\nu_e \to \nu_\mu, \nu_\tau} \approx 0, \quad (ii)\ P_{\nu_\mu \to \nu_\tau} \approx \sin^2(2\theta_{23}) \sin^2\left(\frac{1.27\Delta m^2_{23} L}{E}\right), \quad (72)$$

$$\text{Large } L/E: \qquad P_{\nu_e \to \nu_{\mu,\tau}} \approx \sin^2(2\theta_{12}) \sin^2\left(\frac{1.27\Delta m^2_{12} L}{E}\right). \quad (73)$$

Thus, experiments with small L/E have been used to probe the values of θ_{23} and Δm^2_{23} by measuring the amount of ν_τ appearance from a flux of ν_μ.

Also analysis of the amount of ν_e disappearance can allow investigation of θ_{12}, θ_{13}, Δm^2_{12} and Δm^2_{13}, depending on the choice of L/E. A survival probability in which θ_{13} is the only mixing angle involved (still using $\Delta m^2_{13} \approx \Delta m^2_{23}$) can be found from Eq. 66 since

$$P_{\nu_e \to \nu_e} = 1 - \cos^4(\theta_{13}) \sin^2(2\theta_{12}) \sin^2\left(\frac{1.27\Delta m^2_{12} L}{E}\right) - \sin^2(\theta_{13}) \sin^2\left(\frac{1.27\Delta m^2_{13} L}{E}\right). \quad (74)$$

The second and third terms oscillate with significantly different wavelengths, so with an appropriate choice of L/E this reduces to

$$\text{Small } L/E: \qquad P_{\nu_e \to \nu_e} \approx 1 - \sin^2(\theta_{13}) \sin^2\left(\frac{1.27\Delta m^2_{23} L}{E}\right), \quad (75)$$

$$\text{Large } L/E: \qquad P_{\nu_e \to \nu_e} \approx 1 - c^4_{13} \sin^2(2\theta_{12}) \sin^2\left(\frac{1.27\Delta m^2_{12} L}{E}\right) - \tfrac{1}{2}\sin^2(2\theta_{13}). \quad (76)$$

This expression for large L/E has also been used to investigate θ_{12} since the small θ_{13} allows the following approximation of Eq. 76:

$$P_{\nu_e \to \nu_e} \approx c^4_{13} \left[1 - \sin^2(2\theta_{12}) \sin^2\left(\frac{1.27\Delta m^2_{12} L}{E}\right)\right]. \quad (77)$$

The choice of neutrino source and detector location dictates which of these probability equations is appropriate to use and which of the oscillation parameters θ_{ij}, Δm^2_{ij} can be studied in a given experiment. A discussion of neutrino oscillation experiments is given in Section 2.5.

2.4.3.3 Neutrino mass hierarchy and the octant of θ_{23}

In three flavours, a certain mass hierarchy exists such that two of the squared masses (m_1^2 and m_2^2) are close to each other but quite different from the third. However, it is not known whether the absolute value of m_3^2 is much greater or smaller than the other two. There are therefore two possible hierarchies of neutrino mass (Figure 10). The 'normal hierarchy' is $m_1 < m_2 << m_3$ and the 'inverted hierarchy' is $m_3 << m_1 < m_2$. Thus, one of the remaining unanswered questions concerning neutrino physics is that of the sign of Δm_{23}^2.

It is clear from Eq. 58, 59 that if one switches $\Delta m_{ij}^2 \rightarrow -\Delta m_{ij}^2$, the effective mixing angle within matter is affected. This offers a way of determining the sign of the mass splitting that is unavailable to vacuum oscillations.

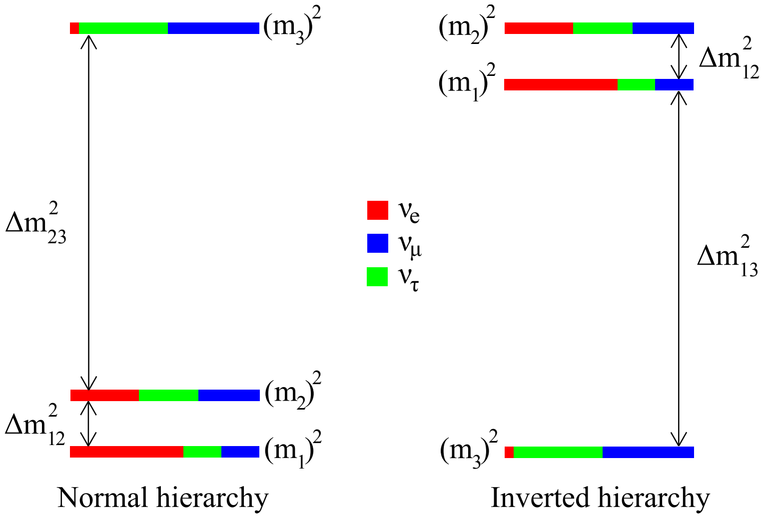

Figure 10: *An illustration of the two possible hierarchies of neutrino masses [163] . The normal hierarchy is* $m_1 < m_2 << m_3$ *and the inverted hierarchy is* $m_3 << m_1 < m_2$ *. The approximate flavour composition of each mass eigenstate is indicated by their relative amounts of red, green and blue, corresponding to* ν_e*,* ν_μ *and* ν_τ *respectively.*

Another ambiguity in the results of neutrino oscillation experiments to date involves the measurement of θ_{23}. Studies of atmospheric neutrinos (Section 2.5) have determined that $sin^2(2\theta_{23}) > 0.95$ at 90% C.L., which means an approximate range of $38.5° < \theta_{23} < 51.5°$. More precision measurement is therefore necessary to determine if θ_{23} lies in the upper (i.e. $> 45°$) or lower (i.e. $< 45°$) octant. This is of interest to the current/next generation of experiments, particularly since a value of $\theta_{23} = 45°$ would mean ν_μ and ν_τ have equal amounts of ν_3 - a potential hint towards some as-yet-undiscovered symmetry pertaining to theories of quark-lepton complementarity [164–169].

2.4.4 CP-violation in neutrino oscillation

CP-violation is considered necessary to account for the apparent dominance of matter over antimatter in the universe and has been observed in other situations such as neutral kaon decay [170]. The C refers to the charge conjugation operation, which causes the charge of the particles involved to be reversed; C replaces particles with their antiparticles ($\nu_\alpha \rightarrow \overline{\nu}_\alpha$). The P refers to the parity operation, which reverses spatial coordinates to create a mirror image of the original interaction; P transforms a left-handed particle into a right-handed particle ($\nu_L \to \nu_R$). Since only left-handed neutrinos and right-handed antineutrinos participate in the $SU(2)_L$ weak interaction, the weak interaction is not symmetric under either a C or P transformation alone. However, since the combined action of C and P causes $\nu_L \leftrightarrow \overline{\nu}_R$, the natural assumption may be that weak interactions are invariant under CP transformation. In terms of neutrino oscillation, invariance under CP transformation would require $P_{\nu_\alpha \to \nu_\beta} = P_{\overline{\nu}_\alpha \to \overline{\nu}_\beta}$. Comparing the rate of neutrino and antineutrino oscillation can therefore test whether this symmetry holds.

The PMNS matrix (Eq. 67) contains a parameter δ to quantify any CP-violation that might occur in neutrino oscillation. The equations in the latter part of Section 2.4.3 assume $\delta = 0$, meaning the imaginary part of Eq. 66 disappears. However, with non-zero δ, the terms in the PMNS matrix proportional to $e^{\pm i\delta}$ can be split into a real and imaginary part. The probability equations for $P_{\overline{\nu}_\alpha \to \overline{\nu}_\beta}$ involve the complex conjugate of the PMNS matrix, resulting in the sign of the imaginary terms being opposite to that of $P_{\nu_\alpha \to \nu_\beta}$. The result from Eq. 66 is that

$$\begin{aligned} P_{\nu_\alpha \to \nu_\beta} - P_{\overline{\nu}_\alpha \to \overline{\nu}_\beta} &= 4\sum_{i>j} Im(U^*_{\alpha i} U_{\beta i} U_{\alpha j} U^*_{\beta j}) \sin^2\left(2 \times \frac{1.27\Delta m^2_{ij} L}{E}\right) && (78) \\ &\equiv 4J_{\alpha\beta}\big(\sin(2\Delta_{12}) + \sin(2\Delta_{13}) + \sin(2\Delta_{23})\big) \quad \text{where} \quad \Delta_{ij} = \frac{1.27\Delta m^2_{ij} L}{E}. && (79) \end{aligned}$$

Here the CP-violation is given in terms of the parameterization-independent 'Jarlskog invariant' [171–174] $J_{\alpha\beta}$ according to

$$J_{\alpha\beta} = Im(U_{\alpha 1} U_{\beta 2} U^*_{\alpha 2} U^*_{\beta 1}) = \pm J_{CP} \qquad \rightarrow \qquad J_{CP} = c_{12} c^2_{13} c_{23} s_{12} s_{13} s_{23} \sin\delta. \tag{80}$$

This makes it clear that if any of the parameters θ_{12}, θ_{13}, θ_{23} or δ are zero then $J_{CP} = 0$ and consequently no CP-violation will be observed. However, recent experiments have established non-zero values for all three mixing angles, meaning a potential discovery of CP-violation now rests on the measurement of δ.

Many neutrino oscillation experiments involve sending a beam of neutrinos through the Earth. Even if $\delta = 0$ the interaction with matter (Section 2.4.2) causes an effect that can mimic CP-violation given a long enough baseline. This is important for current/future long-baseline experiments with accelerator-generated neutrinos that will study $\nu_\mu \to \nu_e$ and $\overline{\nu}_\mu \to \overline{\nu}_e$ oscillations. The probability for this transition in vacuum is given by [175]:

$$\begin{aligned} P_{\nu_\mu \to \nu_e} &= \left|U_{e1} U^*_{\mu 1} e^{-im_1^2 L/2E} + U_{e2} U^*_{\mu 2} e^{-im_2^2 L/2E} + U_{e3} U^*_{\mu 3} e^{-im_3^2 L/2E}\right|^2 \\ &= \left|2U_{e2} U^*_{\mu 2} \sin\Delta^2_{12} + 2U_{e3} U^*_{\mu 3}\ \sin\Delta_{13} e^{-i\Delta_{23}}\right|^2 \\ &\approx \left|\sqrt{P_{12}} + \sqrt{P_{13}}\ e^{-i(\Delta_{23}+\delta)}\right|^2 \\ &= \sqrt{P_{12}} + \sqrt{P_{13}} + 2\sqrt{P_{12}}\sqrt{P_{13}}\ \cos(\Delta_{23} + \delta). \end{aligned} \tag{81}$$

Here the amplitudes $\sqrt{P_{12}}$ and $\sqrt{P_{13}}$ depend only on Δm^2_{12} and Δm^2_{13} respectively [25] :

$$\begin{aligned} P_{12} &= c_{23} c_{13} \sin(2\theta_{12}) \sin\Delta_{21} \approx c_{23} c_{13} \sin(2\theta_{12}) \Delta_{12}, \\ P_{13} &= s_{23} \sin(2\theta_{13}) \sin\Delta_{13}. \end{aligned} \tag{82}$$

---

[25] Also the unitarity of the PMNS matrix leads to $U_{e1}U^*_{\mu 1} + U_{e2}U^*_{\mu 2} + U_{e3}U^*_{\mu 3} = 0$, which allows the term containing U_{e1}, $U_{\mu 1}$ in the first line of Eq. 81 to be removed.

In matter these are modified according to Eq. 57, 58, in which the potential may be expressed as $V = 2\sqrt{2}G_F N_e$ (where N_e is the electron density in the matter and G_F is the Fermi constant). Defining $\lambda = G_F N_e/\sqrt{2}$, the modified amplitudes in matter are

$$\begin{aligned} P_{12} \to P_{12}^M &= c_{23}\sin(2\theta_{12})\frac{\sin \lambda L}{\lambda L}\Delta_{12}, \\ P_{13} \to P_{13}^M &= s_{23}\sin(2\theta_{13})\frac{\sin(\Delta_{13} - \lambda L)}{\Delta_{13} - \lambda L}\Delta_{13}. \end{aligned} \tag{83}$$

The antineutrino equivalent of Eq. 81 involves the changes $\delta \to -\delta$ and $\lambda \to -\lambda$, so even if $\delta = 0$ the medium can still cause an effect that mimics CP violation (Figure 11). Any experiment examining $\nu_\mu/\overline{\nu}_\mu$ beams for CP-violation must therefore take this into account; LBNE/DUNE is configured such that a large matter effect will occur (Section 2.6.2). Having a long enough baseline to ensure that the matter effect exceeds the maximum possible CP-violating effect (i.e. when $\delta = \pm 90°$) means that the two effects can be distinguished (if indeed $\delta \neq 0$).

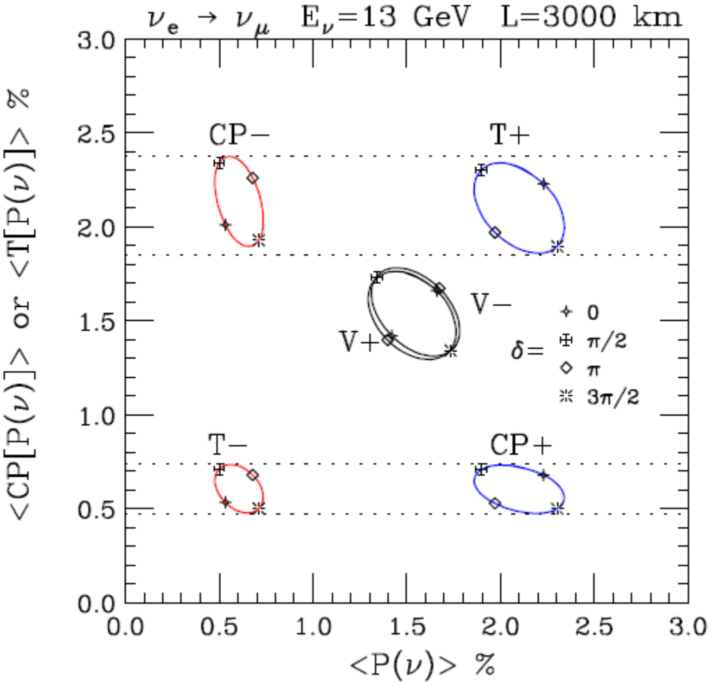

Figure 11: $P_{\nu_\mu\to\nu_e}$ *vs.* $P_{\overline{\nu}_\mu\to\overline{\nu}_e}$ *(CP transformation) and also* $P_{\nu_\mu\to\nu_e}$ *vs.*$P_{\nu_e\to\nu_\mu}$ *(Time-reversal transformation) in matter [175]. The horizontal axis shows the probability of the* $\nu_\mu \to \nu_e$ *transition. The vertical axis shows the probability of the CP- or T-transformed counterpart of that transition (i.e.* $P_{\overline{\nu}_\mu\to\overline{\nu}_e}$ *or* $P_{\nu_e\to\nu_\mu}$ *respectively). The ± sign indicates normal or inverted neutrino mass hierarchy. Each ellipse consists of points plotted for* $0 \leq \delta \leq 2\pi$*. The central (overlapping) ellipses are for the vacuum case of* $P_{\nu_\mu\to\nu_e}$*. The parameters used are* $sin^2(\theta_{12}) = 0.31$*,* $sin^2(2\theta_{13}) = 0.05$*,* $\Delta m^2_{12} = 8.0 \times 10^{-5}\ eV^2$*,* $\Delta m^2_{13} = 2.5 \times 10^{-3}\ eV^2$*. This shows that the matter effect can causes a significant difference in rates of* $P_{\nu_\mu\to\nu_e}$ *vs.* $P_{\overline{\nu}_\mu\to\overline{\nu}_e}$ *even when the CP-violation parameter* $\delta = 0$*.*

2.4.5 Neutrino mass via the see-saw mechanism

As discussed at the start of Section 2.4, mass terms for neutrinos could be of the Dirac and/or Majorana type and each involve fields of right and left-handed chirality [155]:

$$\begin{aligned} \text{Dirac:} \quad & - m_D(\overline{\nu}_L \nu_R + \overline{\nu}_R \nu_L) \\ \text{Majorana:} \quad & - \tfrac{1}{2} m_M^L (\overline{\nu}_L \nu_L^C + \overline{\nu}_L^C \nu_L) - \tfrac{1}{2} m_M^R (\overline{\nu}_R \nu_R^C + \overline{\nu}_R^C \nu_R) \end{aligned} \tag{84}$$

These expressions may be written in terms of a mass matrix M containing Dirac and Majorana masses m_D, $m_M^{L,R}$:

$$-\tfrac{1}{2}(\overline{\nu}_L \, \overline{\nu}_R^C) M \begin{pmatrix} \nu_L^C \\ \nu_R \end{pmatrix} + \text{Hermitian conjugate} \qquad \text{where} \qquad M = \begin{pmatrix} m_M^L & m_D \\ m_D & m_M^R \end{pmatrix} \tag{85}$$

and $m_M^{L,R}$ denote left- and right-handed Majorana masses. If symmetry-breaking happens in such a manner that the neutrino-Higgs coupling gave only Majorana mass terms for the neutrino, then the matrix would be the diagonal M_d instead of M. A similar expression involving M_d and the eigenstates of definite mass ν, N could then be written:

$$-\tfrac{1}{2}(\overline{\nu} \, \overline{N}) M_d \begin{pmatrix} \nu \\ N \end{pmatrix} + \text{Hermitian conjugate} \qquad \text{where} \qquad M_d = \begin{pmatrix} m_\nu & 0 \\ 0 & m_N \end{pmatrix}. \tag{86}$$

The eigenvalues $\lambda_{+,-}$ of the matrix M are found from the characteristic equation:

$$(m_M^L - \lambda)(m_M^R - \lambda) - m_D^2 = 0 \tag{87}$$

$$\Longrightarrow \qquad \lambda_{+,-} = \tfrac{1}{2}(m_M^L + m_M^R) \pm \tfrac{1}{2}\sqrt{(m_M^L + m_M^R)^2 - 4(m_M^L m_M^R - m_D^2)}. \tag{88}$$

In the SM there are left-handed, massless neutrinos, so setting $m_D^2 = m_M^L m_M^R$ will give $\lambda_- = 0 = m_\nu$. This also gives $\lambda_+ = m_M^L + m_M^R = m_N$, so substituting λ_+ in the eigenvalue equation ($(M - \lambda\mathcal{I})\psi = 0$) for Eq. 85 yields

$$\big(m_M^L - (m_M^L + m_M^R)\big)\nu_L^C + m_D \nu_R = 0 \qquad \Longrightarrow \qquad \nu_L^C = \frac{m_D}{m_M^R}\nu_R. \tag{89}$$

Including also the so-far-neglected Hermitian conjugate part of Eq. 85, one finds

$$N = (\nu_R + \nu_R^C) + \frac{m_D}{m_M^R}(\nu_L + \nu_L^C), \qquad \nu = (\nu_L + \nu_L^C) - \frac{m_D}{m_M^R}(\nu_R + \nu_R^C). \tag{90}$$

One may also treat $m_D << m_M^R$ since (with $m_\nu = 0$) the matrix M_d used here is of the form $A = \left(\begin{smallmatrix} 0 & 0 \\ 0 & a \end{smallmatrix}\right)$, which yields such a disparity when a small rotation $A \to A' = R^\dagger A R$ (analogous to rotating mass states N, ν into weak interaction states ν_L, ν_R) is applied:

$$A' = \begin{pmatrix} A'_{11} & A'_{12} \\ A'_{21} & A'_{22} \end{pmatrix} = \begin{pmatrix} \cos\phi & \sin\phi \\ -\sin\phi & \cos\phi \end{pmatrix} \begin{pmatrix} 0 & 0 \\ 0 & a \end{pmatrix} \begin{pmatrix} cos\phi & -\sin\phi \\ \sin\phi & \cos\phi \end{pmatrix} \tag{91}$$

$$= \begin{pmatrix} a \cdot \sin^2\phi & a \cdot \cos\phi \sin\phi \\ -a \cdot \cos\phi \sin\phi & a \cdot \cos^2\phi \end{pmatrix} \quad \Longrightarrow \quad A'_{11} < A'_{12} << A'_{22} \text{ for small } \phi. \tag{92}$$

Thus, assuming such a rotation applies between neutrino mass and neutrino flavour eigenstates yields $m_D << m_M^R$. Having $m_D/m_M^R << 1$ makes m_M^L small since ν_L is almost completely composed of the massless ν (Eq. 90). The relationship $m_M^L m_M^R = m_D^2$ therefore requires a correspondingly large m_M^R to compensate for m_M^L, hence this is termed the (type-1) 'see-saw mechanism' [176–179].

The introduction of very heavy right-handed neutrinos (an automatic feature of $SO(10)$-based GUTs (Section 2.2.4)) therefore allows the tiny non-zero left-handed neutrino mass to be accounted for with no fine tuning. A very high ν_R mass could explain its non-observation at currently-explored energies and the conceptually-awkward tiny ν_L mass would be accounted for by a mass eigenstate ν having no Higgs coupling whatsoever (something more theoretically-appealing).

2.4.6 CP-violation, leptogenesis and matter-antimatter asymmetry

The universe has an apparant asymmetry of matter over antimatter, the amount of which may partially be accounted for depending on the size of the CP-violating PMNS matrix parameter δ (Section 2.4.4) [175]. It is hypothesised that a 'leptogenesis' process [180, 181] created an imbalance of leptons over antileptons, which were then converted into an excess of baryons via a sphaleron[26] process [183].

Leptogenesis in three SM families involves the heavy states $N_{1,2,3}$ that are part of the see-saw mechanism (Section 2.4.5) and have Yukawa couplings $\mathcal{L} = Y_{\alpha i}\overline{L}_\alpha \overline{H} N_i$ ($\alpha = e, \mu, \tau$). They are thought to decay via

$$N_i \to L_\alpha\, H, \quad N_i \to \overline{L}_\alpha\, \overline{H} \quad \to \quad \epsilon_i = \frac{\Gamma(N_i \to L_\alpha\, H) - \Gamma(N_i \to \overline{L}_\alpha\, \overline{H})}{\Gamma(N_i \to L_\alpha\, H) + \Gamma(N_i \to \overline{L}_\alpha\, \overline{H})} \tag{93}$$

where ϵ_i quantifies the asymmetry in the decay rate to leptons $\Gamma(N_i \to L_\alpha\, H)$ compared to antileptons $\Gamma(N_i \to \overline{L}_\alpha\, \overline{H})$. A non-zero ϵ_i could arise if the Yukawa couplings $Y_{\alpha i}$ are complex, since the Yukawa couplings are related to the decay rates as follows [184]:

$$\Gamma(N_i \to L_\alpha\, H) \propto |Y_{\alpha 1} + A Y_{\alpha 1}^* Y_{\alpha 2,3}^2|^2, \qquad \Gamma(N_i \to \overline{L}_\alpha\, \overline{H}) \propto |Y_{\alpha 1}^* + A Y_{\alpha 1} Y_{\alpha 2,3}^{*2}|^2.$$

The asymmetry for a given lepton flavour α can also be expressed in terms of the PMNS matrix U [185]:

$$\epsilon_\alpha = \frac{-3M_1}{16\pi v^2} \frac{Im(\sum_{\beta\rho} m_\beta^{1/2} m_\rho^{3/2} U_{\alpha\beta}^* U_{\alpha\rho} U_{1\beta} U_{1\rho})}{\sum_\beta m_\beta |R_{1\beta}|^2} \tag{94}$$

where M_1 is the mass of the lightest right-handed neutrino (with the light and heavy neutrino masses contained in $m_L = \text{diag}(m_1, m_2, m_3)$ and $M_R = \text{diag}(M_1, M_2, M_3)$), the orthogonal complex matrix $R = vM_R^{-1/2} Y U m_L^{-1/2}$ and v is the Higgs vacuum expectation value. This lepton asymmetry may then be translated into a baryon asymmetry via a sphaleron process [183], thus accounting for matter remaining to dominate the universe, rather than having completely annihilated with antimatter. It is also possible to extend the PMNS matrix to include 'Majorana' phases α_{21}, α_{31} (as opposed to the 'Dirac' phase δ) via multiplication with $\text{diag}(1, e^{i\alpha_{21}/2}, e^{i\alpha_{31}/2})$ [186, 187]. These new phases pertain to CP-violation at energies out of reach of neutrino oscillation experiments. However, low-energy CP-violation may depend on δ only, to which the baryon asymmetry Y_B can be

---

[26] 'Sphaleron' [182] refers to a saddle point of energy of the gauge & Higgs fields. Transitions between different vacua over this potential barrier are possible at temperatures in excess of about 100 GeV, allowing violation of B and L number.

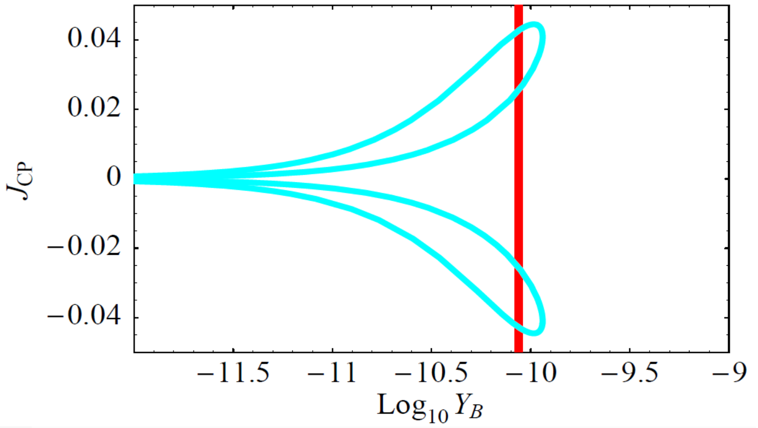

Figure 12: *The relationship between the Jarlskog parameter (Eq. 80) and the baryon asymmetry paramter Y_B. This is plotted in the range $0 \leq \delta \leq 2\pi$ [185] with $s_{13} = 0.2$, $R_{12} = 0.86$, $R_{13} = 0.5$, $M_1 = 5 \times 10^{11}$ GeV and $\alpha_{32} = \alpha_{31} - \alpha_{21} = 0$.*

related [188, 189] as follows:

$$Y_B = \frac{n_B - n_{\overline{B}}}{s} = \kappa c_s \frac{\epsilon_1}{g_*} \quad \text{where} \quad |Y_B| \cong 2.8 \times 10^{-13} \left| \sin\,\delta \right| \left(\frac{s_{13}}{0.2} \right) \left(\frac{M_1}{10^9 \mathrm{GeV}} \right)$$

where $n_{B,\overline{B}}$ are baryon and antibaryon number densities, s is the entropy density, κ parametrises the effect of CP-violation due to the matrix R in the asymmetry ϵ_α, c_s is the conversion factor from lepton to baryon asymmetry through the sphaleron process, $g_* \sim 100$ is the number of degrees of freedom in the early universe and ϵ_1 is the CP asymmetry in the decay of the lightest heavy neutrino N_1 over all flavour indices. Thus, the measurement of J_{CP} in neutrino oscillation experiments will allow the baryon asymmetry to be assessed (Figure 12). Investigating this is one of the primary aims of DUNE.

2.5 Experimental status of neutrino oscillation

Experiments determine the different parameters of the PMNS matrix and the mass splittings by measuring the probability of flavour changes. Analysis of neutrino 'appearance' looks for a greater flux of neutrinos of a given flavour than should otherwise be observed without oscillations occuring, whereas analysis of 'disappearance' seeks to observe a smaller flux of the initial flavour than there should otherwise be. The oscillation probability equations can involve many parameters but can be simplified; a judicious choice of baseline L and/or neutrino energy E can tune an experiment towards oscillations dominated by a certain θ_{ij}, Δm^2_{ij} (Section 2.4.3.2). Detectors may be placed at oscillation maxima/minima to emphasise the effect as much as possible.

Only a few types of neutrino source exist to base experiments upon, but those that are available produce fluxes diverse enough in L, E and initial flavour for experimenters to have already determined a great deal. Neutrinos originating in the Sun (solar neutrinos) are well suited to measuring θ_{12}, Δm^2_{12}. Cosmic rays also strike the atmosphere, providing a flux of atmospheric neutrinos which have been used to measure θ_{23}, Δm^2_{23}. Beams of neutrinos may also be generated at particle accelerators to study θ_{23}, Δm^2_{23} and more recently θ_{13}, Δm^2_{13}, depending on the choice of L and E. Finally, antineutrinos are also produced as a by-product of fission in nuclear reactors. Experiments where the detector is sited far from the reactor (so-called 'long-baseline' reactor experiments) have investigated θ_{12}, Δm^2_{12}. Short-baseline experiments have investigated θ_{13}, Δm^2_{13}.

The remainder of this section will provide a short overview of neutrino oscillation experiments.

2.5.0.1 Solar neutrino experiments

In the 'Standard Solar Model' [190] nuclear fusion within the Sun proceeds via a sequence of steps, some of which provide the flux of solar neutrinos. Their energies are dependent on which step in the chain they originate from (Figure 13). The model of the fusion reactions in the sun only involve creating neutrinos in the ν_e state.

The first experiment to hint at neutrino oscillation was the Homestake experiment [191], employing a radiochemical detector with the purpose of measuring the solar neutrino flux. Incoming neutrinos entered a volume of tetrachloroethylene and interacted via $\nu_e + {}^{37}\text{Cl} \rightarrow {}^{37}\text{Ar}^* + e^-$, which was sensitive to the '^{8}B' step in the Sun's fusion chain (Figure 13). This radioactive argon was periodically collected and the decay rate measured between 1970-1994, providing a measurement of the ν_e flux. However, the number of solar neutrinos detected was only around one third of the expected number ($(2.56 \pm 0.16) \times 10^{-36}$ target atom^{-1} s^{-1} and $(9.3 \pm 1.3) \times 10^{-36}$ target atom^{-1} s^{-1} respectively). This result became known as the solar neutrino anomaly.

Similar radiochemical experiments sensitive to the much-more-abundant ν_e from the '*pp*' step of the solar fusion chain via $\nu_e + {}^{71}\text{Ga} \rightarrow {}^{71}\text{Ge}^* + e^-$ (namely GALLEX (1991-1996) [192], its successor GNO (1998-2003) [193] and SAGE (1990-2006) [194]) also observed a deficit; approximately half of the expected flux was missing [195] .

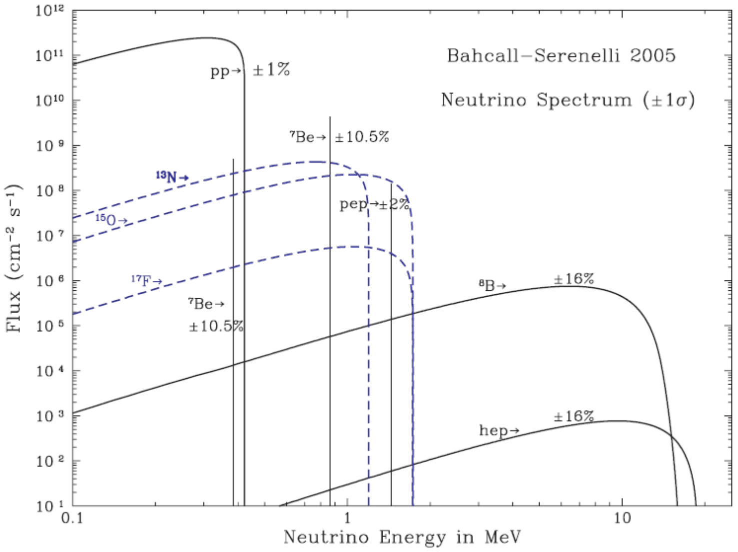

Figure 13: *The energy spectra of neutrinos produced in various stages of the fusion reactions occurring in the Sun [190].*

Further evidence was provided via the experiments Kamiokande [147, 196] and its successor Super-Kamiokande. Kamiokande was a cylindrical detector containing 3 kton of pure water, surrounded by inward-facing PMTs. ^{8}B solar neutrinos were detected by rings of Cerenkov radiation emitted from electrons scattered via $\nu_e + e^- \rightarrow \nu_e + e^-$. Kamiokande was operational from 1983 and was eventually replaced by Super-Kamiokande, a scaled-up version which used a 50 kton of water and has been operational since 1996 [148]. Kamiokande and Super-Kamiokande confirmed that the neutrinos involved in the deficit observed by the aforementioned radiochemical experiments were coming from the Sun, since the direction of incoming neutrinos could be determined. The measured ν_e deficit was $\sim$ 47%. As of August 2011, the Super-Kamiokande solar neutrino best-fit results including MSW effect were $sin^2(2\theta_{12}) = 0.30^{+0.02}_{-0.01}$ and $\Delta m^2_{12} = 6.2^{+1.1}_{-1.9} \times 10^{-5}$ eV^2 [197].

Confirmation that neutrino oscillation was the cause of the solar neutrino anomaly came in 2001 at the Sudbury Neutrino Observatory (SNO) (1999-2006) [198]. This experiment also relied partly on detecting Cerenkov radiation, the detection medium consisting of a spherical vessel containing 1 kton of heavy water, itself within a barrel-shaped container filled with standard water and lined with PMTs. The energy threshold of SNO made it essentially only sensitive to ^8B via:

$$\begin{array}{ll} \text{nucleon interaction (NC) :} & \nu_\alpha + d \;\; \rightarrow \nu_\alpha + n + p \\ \text{nucleon interaction (CC) :} & \nu_e + d \;\; \rightarrow e^- + 2p \\ \text{electron scattering :} & \nu_\alpha + e^- \rightarrow \nu_\alpha + e^- \end{array}$$

Solar neutrinos lack the energy (Figure 13) required to create μ or τ leptons, meaning only ν_e may participate in the CC interaction. The NC interaction would split the deuteron but does not involve creating a heavy lepton, so all three neutrino flavours could undergo this interaction (with a flavour-independent cross-section). The free neutron could then be captured by another deuteron, causing emission of detectable photons.

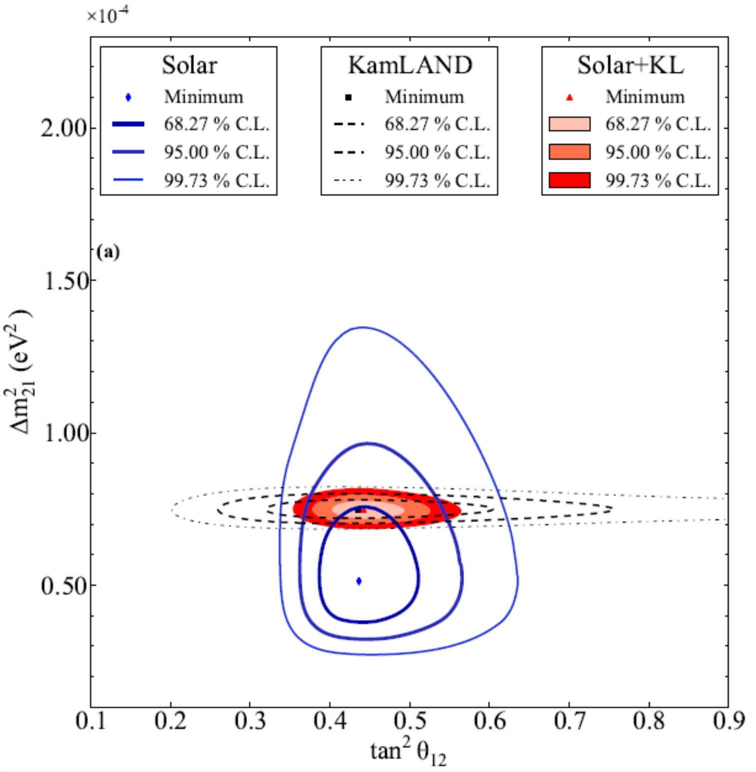

Figure 14: *The parameter space to which tan*$^2\theta_{12}$ *and* Δm^2_{12} *have been confined by SNO and all other solar neutrino experiments [199] (blue lines) at* 68%, 95% *and* 99% *C.L.. The result from the KamLAND reactor antineutrino experiment (Section 2.5.3) is shown in black dashed lines. Also shown is all of these results combined.*

Incoming neutrinos could also undergo elastic scattering with atomic electrons. This could involve any of the three neutrino flavours, with the cross-section for ν_e being greater.

SNO observed a ν_e flux of $(1.8 \pm 0.1) \times 10^{-6}$ cm^{-2} s^{-1} and a ν_μ, ν_τ flux of $(3.4 \pm 0.6) \times 10^{-6}$ cm^{-2} s^{-1}. This compares to a predicted overall neutrino flux of $\sim (5.9 \pm 0.1) \times 10^{-6}$ cm^{-2} s^{-1}, providing strong evidence that solar neutrinos undergo oscillation; the total flux from the Sun was consistent with solar models, and the ν_e deficit was compensated by an increase in $\nu_{\mu,\tau}$.

The final SNO results released in 2013, when combined with all other solar neutrino experiments and the KamLAND reactor neutrino experiment (Section2.5.3), are [199] $\tan^2 \theta_{12} = 0.466^{+0.030}_{-0.029}$ and $\Delta m^2_{12} = (7.41^{+0.2}_{-0.19}) \times 10^{-5}$ eV^2. Figure 14 shows the allowed region to which these parameters have been confined.

Figure 15 [200]shows a comparison of the results of solar neutrino experiments to the theoretically expected neutrino flux in the absence of neutrino oscillation.

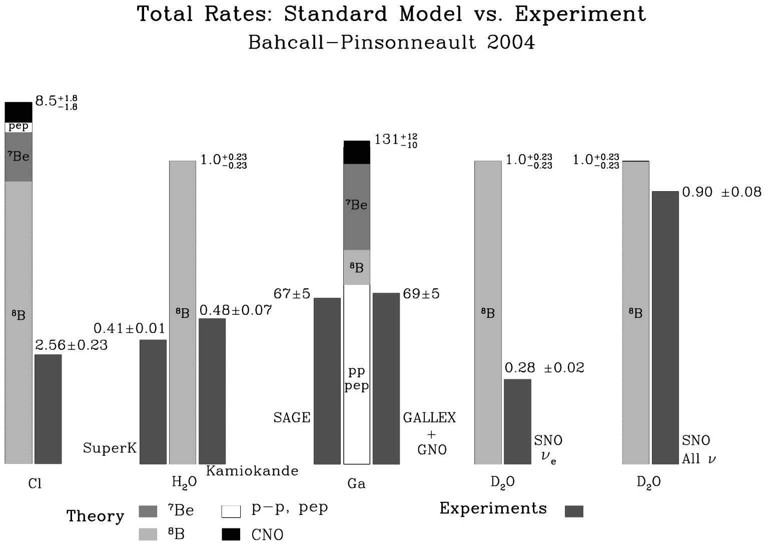

Figure 15: *A* 2004 *comparison [200] of the theoretical predictions of the solar neutrino flux based on the Standard Solar Model (see Figure 13) and experimental findings of solar neutrino experiments.*

2.5.0.2 Atmospheric neutrino experiments

Further evidence of neutrino oscillation has been provided by the study of neutrinos resulting from cosmic rays. These provided a source of neutrinos of a significantly different range of L/E to that of solar neutrinos, with energies ranging from $\sim 10^6$ - 10^{20} eV [201]. Primary cosmic rays, composed mainly of protons as well as some heavier nuclei and electrons, strike Earth′s atmosphere and initiate hadronic showers which predominantly produce pions. The pions then decay via $\pi^- \rightarrow \mu^- \, \overline{\nu}_\mu$ $(\pi^+ \rightarrow \mu^+ \, \nu_\mu)$, and the resulting muons can also decay via $\mu^- \rightarrow e^- \, \nu_\mu \, \overline{\nu}_e$ $(\mu^+ \rightarrow e^+ \, \overline{\nu}_\mu \, \nu_e)$. Each pion will generate two ν_μ and one ν_e. Assuming all the muons decay before they reach Earth′s surface, one would expect to observe an approximate 2:1 ratio of $\nu_\mu : \nu_e$, although above $\sim$ 1 GeV muons begin to reach the surface before decaying, increasing this ratio [202].

Early experiments searching for proton decay (IMB, Kamiokande) had a background due to atmospheric neutrinos but observed fewer ν_μ than expected [203, 204]. Neutrinos could enter the detector from all directions, meaning a variation in L of $\sim$ 15 km for those travelling down from directly above the detector to $\sim 13,000$ km for those travelling in the opposite direction. The ν_e, ν_μ CC interaction rates were therefore measured for a range of L/E. A zenith-angle-dependent deficit of upward-going, multi-GeV ν_μ was observed, which came to be known as the atmospheric neutrino anomaly.

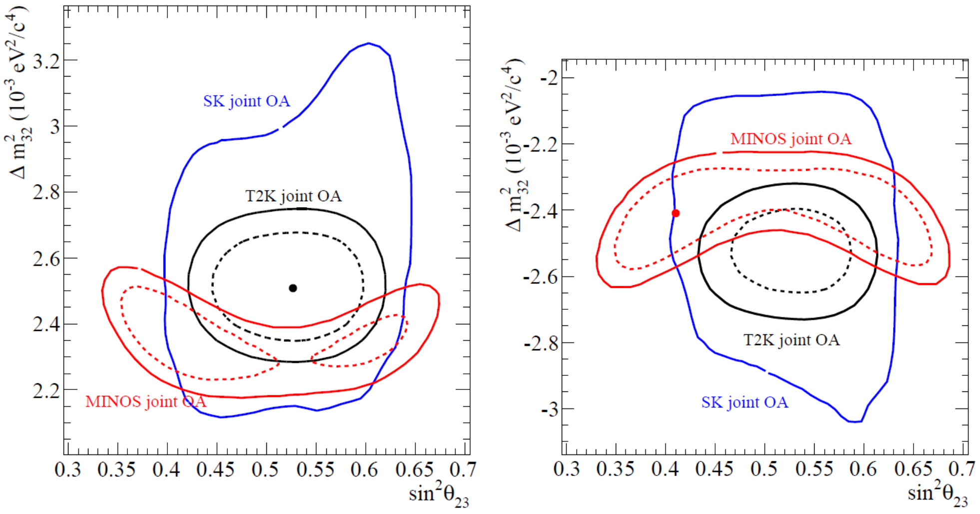

Figure 16: *The parameter space to which* $sin^2\theta_{23}$ *and* Δm^2_{23} *have been confined by T2K [205] (black), MINOS [206] (red) and Super-Kamiokande [207] (blue) combined with the results of reactor neutrino experiments (Section 2.5.3) at* 68% *(dashed) and* 90% *(solid) C.L. [199]. The plot on the left/right is made using the normal/inverted neutrino mass hierarchy. "Joint OA" refers to joint appearance and disappearance oscillation analysis.*

Explaining atmospheric neutrino anomaly in terms of neutrino oscillation requires $\Delta m^2 \sim 10^{-3}$ eV^2, whereas the solar neutrino anomaly requires $\Delta m^2 \sim 10^{-5}$ eV^2 (and the MSW effect). Both anomalies could therefore not be explained using $\nu_e \rightarrow \nu_\mu$ oscillations, implying the existence of at least a third neutrino mass and flavour eigenstate. Evidence of ν_τ appearance from atmospheric ν_μ has also been reported by Super-Kamiokande [208].

Super-Kamiokande and experiments involving reactor- and accelerator-generated neutrinos (Sections 2.5.3, 2.5.4) have been instrumental in measuring the oscillation parameters associated with the atmospheric neutrino anomaly. As of March 2015 the T2K collaboration places the atmospheric oscillation parameters at [205] $sin^2(2\theta_{23}) = 0.514^{+0.055}_{-0.056}$, $\Delta m^2_{23} = (2.51 \pm 0.10) \times 10^{-3}$ eV^2 (normal hierarchy) and $sin^2(2\theta_{23}) = 0.511 \pm 0.055$, $\Delta m^2_{23} = (2.48 \pm 0.10) \times 10^{-3}$ eV^2 (inverted hierarchy). Figure 16 shows the parameter space to which Δm^2_{23} and $sin^2(2\theta_{23})$ have been confined by the T2K, MINOS, Super-Kamiokande experiments combined with results from reactor neutrino experiments.

2.5.0.3 Reactor neutrino experiments

The fission of heavy nuclei in nuclear reactors produces unstable fragments which undergo β-decay ($n \rightarrow p\, e^-\, \overline{\nu}_e$), resulting in a copious flux of low-energy $\overline{\nu}_e$. Detection typically relies on inverse β-decay ($p + \overline{\nu}_e \rightarrow e^+\, n$), which has a 1.8 MeV threshold. Like solar neutrinos, their energies are on the scale of $\sim 1 - 10$ MeV. Unlike solar neutrinos, the baselines involved are far shorter and matter effects (Section 2.4.2) are unimportant. As the $\overline{\nu}_e$ energy is too low for a CC interaction to produce leptons heavier than a positron, reactor neutrino experiments focus on $\overline{\nu}_e$ disappearance rather than the appearance of other flavours. The three-flavour ν_e survival probability is given by Eq. 74. The choice of baseline decides whether the second or third term dominates; a reactor-based experiment can be tuned to oscillations dominated by Δm^2_{12}, θ_{12} or Δm^2_{13}, θ_{13}.

The CHOOZ experiment [209] (1997-1998) was situated 1.05 km from the Chooz nuclear power plant, France, and was one of the first reactor-based neutrino oscillation experiments. The detector consisted of a 5 ton cylindrical volume of Gd-doped liquid scintillator (GdLS), held within 17 tons of updoped liquid scintillator (LS) surrounded PMTs, itself shielded by 90 tons of LS. It was designed to investigate parameter ranges corresponding to the atmospheric neutrino anomaly ($\Delta m^2 \sim 10^{-3}$ eV^2, $sin^2(2\theta) \sim 0.1$) (Section 2.5.2). In the atmospheric neutrino anomaly the possibilities (assuming only three flavours of neutrino) were either that $\nu_\mu \rightarrow \nu_e$ or $\nu_\mu \rightarrow \nu_\tau$ was being observed. The CHOOZ detector observed no deficit in the $\overline{\nu}_e$ flux attributable to disappearance due to oscillation, implying that the atmospheric neutrino anomaly was due to $\nu_\mu \rightarrow \nu_\tau$. A similar experiment was was performed at the Palo Verde nuclear power plant between 1998-2000 [210], where the $\overline{\nu}_e$ rate was measured at 0.75 km and 0.89 km. Like CHOOZ, this experiment also failed to observe $\overline{\nu}_e$ disappearance.

KamLAND [211] is another reactor neutrino experiment which began taking data in 2002. It is located at the Kamioka observatory, Japan, surrounded by 53 nuclear reactors at a much longer mean baseline of ~180 km. This makes KamLAND sensitive to a smaller Δm^2 than CHOOZ of $\sim 10^{-5}$ eV^2 (appropriate for the solar neutrino anomaly). The detector is comprised of a spherical container 18 m in diameter and lined with PMTs, which houses a spherical nylon container 13 m in diameter and filled with 1 kton of LS. This apparatus is all contained within a cylindrical water Cerenkov detector which allows muons to be vetoed. The appropriate $\overline{\nu}_e$ survival probability is Eq. 77. KamLAND has further constrained the solar neutrino parameters, with measurements of $tan^2(\theta_{12}) = 0.452^{+0.035}_{-0.033}$ and $\Delta m^2_{12} = 7.50^{+0.19}_{-0.20} \times 10^{-5}$ eV^2 [212] reported in 2011. The combined KamLAND and solar neutrino results are stated in Section 2.5.1.

With the values of the solar and atmospheric oscillation parameters established using solar neutrinos, atmospheric and reactor neutrinos, attention has since turned to making more accurate measurements of θ_{13} and δ. These have been the focus of more recent and planned experiments, as well as the question of determining the correct mass hierarchy. KamLAND has also made θ_{13} measurement of $sin^2(\theta_{13}) = 0.009^{+0.013}_{-0.007}$ at 79% C.L. [212] reported in 2011.

The current generation of reactor neutrino experiments have different baselines and have been able to make more accurate measurements of θ_{13}. The successor to the CHOOZ experiment is Double-CHOOZ, which started taking data in 2011. Double-CHOOZ uses the original CHOOZ site as its far detector at ~ 1 km, and an identical one located 0.4 km from the reactor [213]. This near detector allows measurement of the beam content pre-oscillation; having a design identical to the far detector minimises systematic errors. The detection principle is the same and the identical detectors are a similar design, but use larger target volumes. In December 2014 Double-CHOOZ reported $\overline{\nu}_e$ disappearance pointing to $sin^2(2\theta_{13}) = 0.090^{+0.032}_{-0.029}$.

RENO is a South Korean reactor experiment (operational since 2010 at the Hanbit Nuclear Power Plant) designed to measure θ_{13}. It is a short-baseline experiment, employing two identical detectors at 290 m and 1380 m from the reactors. The cylindrical innermost part of each detector contains 16 tons of GdLS, contained within a 60 cm jacket of LS, which is itself inside a cylindrical container lined with PMTs and filled with 65 tons of mineral oil [214]. At the EPS 2015 conference in Vienna, June 2015, a measurement of $sin^2(2\theta_{13}) = 0.087 \pm 0.008$ (stat.) ± 0.008 (syst.) [215] was presented.

The Daya Bay experiment (operational since 2011 at the Daya Bay nuclear power plant, China) has provided the most precise measurement of θ_{13} and $|\Delta m^2_{23}|$ to date. It involves six identical detectors (each containing 20 ton of GdLS) at baselines of 364 m, 500 m, 1540 m and 1912 m from the reactors, making it a short-baseline experiment. In May 2015 Daya Bay has reported $sin^2(2\theta_{13}) = 0.084 \pm 0.005$ and $|\Delta m^2_{23}| = 2.39^{+0.10}_{-0.11} \times 10^{-3}$ eV^2 (normal hierarchy), $|\Delta m^2_{23}| = 2.49^{+0.10}_{-0.11} \times 10^{-3}$ eV^2 (inverted hierarchy) [216].

2.5.0.4 Accelerator neutrino experiments

Neutrino oscillations have also been studied using particle accelerators to generate high-intensity beams of neutrinos. Neutrino beams are traditionally generated by first directing a proton beam at a nuclear target, which produces secondaries (e.g. predominantly pions, some kaons). These may be focussed using magnetic fields to produce an intense beam of ν_μ or $\overline{\nu}_\mu$ when these secondaries decay, e.g.

$$\begin{aligned} \pi^+ &\to \mu^+\ \nu_\mu, & \pi^- &\to \mu^-\ \overline{\nu}_\mu, \\ K^+ &\to \mu^+\ \nu_\mu, & K^- &\to \mu^-\ \overline{\nu}_\mu, \\ K^0_L &\to \pi^+\ \mu^-\ \overline{\nu}_\mu, & K^0_L &\to \pi^-\ \mu^+\ \nu_\mu. \end{aligned}$$

Accelerator-based experiments compare the initial flux and energy spectrum of neutrinos seen at the near detector with those arriving at the far detector. It is possible to enhance the ν_μ or $\overline{\nu}_\mu$ content of the beam through the use of a magnetic horn, which typically consists of two axially symmetric conductors, one situated inside of the other. Passing current down one conductor and up the other generates a toroidal magnetic field between the two conductors, causing forces that focus charged secondaries of one sign and defocus those of the opposite sign (before they decay). This provides an effective way to study CP violation (Section 2.4.4) since a beam can be operated in neutrino or antineutrino mode.

The first long-baseline experiment was K2K [217] (1999-2004), built primarily to investigate the atmospheric oscillation parameters. A 12 GeV proton beam produced at the KEK laboratory, Japan, was used to direct ν_μ with energies of ~1.0-1.5 GeV at the Super-Kamiokande detector located 250 km away. This L/E made the experiment sensitive to $\Delta m^2 \sim 10^{-3}$ eV^2. The near detector was a 1 kton water Cerenkov in front of a fine-grain detector consisting of scintillating fibre, situated 0.3 km from the source. At energies of a few GeV the dominant oscillation was expected to be $\nu_\mu \to \nu_\tau$ so a two-flavour treatment was used to examine ν_μ disappearance. The appropriate survival probability equation for examining $\Delta m^2_{23}, \theta_{23}$ is given by Eq. 72 (ii). A deficit of ν_μ at the far detector was observed at 4.3 σ, with a measurement of 1.9×10^{-3} eV^2 $< \Delta m^2_{23} < 3.5 \times 10^{-3}$ eV^2 assuming $sin^2(2\theta_{23}) = 1$, at 90% C.L., with a best-fit value of $\Delta m^2_{23} = 2.8 \times 10^{-3}$ eV^2. This was in good agreement with the Super-Kamiokande atmospheric neutrino results.

The MINOS experiment (2005-present (as MINOS+)) is another that uses accelerator neutrinos primarily to study the atmospheric oscillation parameters Δm^2_{23}, $sin^2(2\theta_{23})$. Neutrinos are generated from a 120 GeV proton beam (the NuMI accelerator) at Fermilab, IL, to produce a ν_μ beam in the 1-3 GeV energy range. Like K2K, the experiment was built primarily to study the disappearance of ν_μ. The near and far detectors are positioned 1.04 km and 725 km (the latter at the Soudan mine, MN) from the source. Both detectors are magnetized tracking calorimeters of consisting of alternating layers of iron and strips of scintillator. In June 2015 MINOS together with its upgraded successor MINOS+ [218] (operational since 2013) reported results of a three-flavour disappearance and appearance analysis of $\Delta m^2_{23} = 2.37^{+0.11}_{-0.07} \times 10^{-3}$ eV^2 and $sin^2(2\theta_{23}) = 0.43^{+0.19}_{-0.05}$ at 90% C.L. [219].

In addition to this, MINOS also searches for the small amount of ν_e appearance from the ν_μ beam at the far detector. The probability of this is given by Eq. 68, which demands a non-zero θ_{13} for observation of $\nu_\mu \rightarrow \nu_e$. This has been observed, and in March 2013 MINOS reported a non-zero θ_{13} at 90% C.L. consistent with reactor experiments: $2sin^2(2\theta_{13})sin^2(2\theta_{23}) = 0.051^{+0.038}_{-0.030}$ (normal mass hierarchy) and $2sin^2(2\theta_{13})sin^2(2\theta_{23}) = 0.093^{+0.054}_{-0.049}$ (inverted mass hierarchy), assuming $\delta = 0$ [220].

The successor to the K2K experiment is T2K, which started in 2010 and directs a beam from the J-PARC facility in Tokai, Japan, to Super-Kamiokande. With a baseline of 295 km and using a few-degrees-off-axis far detector, the neutrino beam has a peak energy of 0.6 GeV. The near detector set-up consists of an on-axis iron-scintillator 'sandwich' to measure the beam direction and profile, and an off-axis detector to measure the ν_μ content and the ν_e contamination of the beam in the direction of Super-Kamiokande. In November 2013 T2K announced $\nu_\mu \rightarrow \nu_e$ appearance implying $sin^2(2\theta_{13}) = 0.140^{+0.038}_{-0.032}$ (normal hierarchy) or $sin^2(2\theta_{13}) = 0.170^{+0.045}_{-0.037}$ (inverted hierarchy) at 7.3 σ. The latest T2K measurements for θ_{23}, Δm^2_{23} can be found in Section 2.5.2.

The accelerator experiments mentioned so far lack the energy to produce the τ lepton required in such a CC interaction and are therefore limited to ν_μ disappearance and ν_e appearance analyses. The OPERA experiment (730 km baseline, ~17 GeV neutrino beam energy, located at Gran Sasso, operational from 2008-2014) uses the CNGS beam in an attempt to observe ν_τ appearance from the ν_μ beam. The detector uses bricks of fine-grained emulsion and planes of scintillator strips. As of July 2015 OPERA has observed five ν_τ appearance events at 4.2 σ, only one of which is attributed to atmospheric neutrinos [221].

Using neutrinos from reactors and accelerators it is now apparent that θ_{13} has a significantly non-zero value. More accurate measurements of θ_{13} will allow the CP-violating phase δ to be measured to a meaningful accuracy (Eq. 80). A number of current and planned experiments have these parameters in mind and so are designed for increased sensitivity to $\nu_\mu \rightarrow \nu_e$ appearance.

NoVA [222] (2014-present) is one such experiment, using the Fermilab NuMI beamline to send neutrinos 810 km to Ash River, MN. with the 14 kton liquid scintillator far detector positioned off-axis to observe neutrinos of energy $\sim$ 2.3 GeV. In addition to improving current θ_{13}, θ_{23} and Δm^2_{23} measurements, NoVA also seeks to measure δ and determine the mass hierarchy. The significant increase in baseline compared to T2K means matter effects become apparent, allowing the sign of Δm^2_{23} to be investigated. In August 2015 it was announced that NoVA had already observed six ν_e appearances, as well as only 33 ν_μ compared to the 201 ν_μ expected assuming no oscillations [223, 224].

The LAGUNA/LBNO project [225] was a proposal involving the CNGS beam with three possible detectors, although all apart from LENA have joined DUNE (Section 2.6) and will not be going ahead. One proposal was the MEMPHIS detector (two 330 kton water Cerenkov detectors) located in Frejus, France, 130 km away from CERN. The short baseline would eliminate the matter effect and so enable a less ambiguous measurement of δ. The GLACIER detector was a proposed 100 kton liquid argon TPC sited 2,300 km away at Pyhasalmi, Finland, with the very long baseline able to exaggerate the matter effect for determination of the neutrino mass hierarchy. GLACIER could have instead been placed in Caso, Italy, at a baseline of 660 km for the CNGS beam and 2,300 km from a possible beam originating in Protvino, Russia. LENA was the third possible detector (50 kton liquid scintillator) and could have been located at either of the first two possible locations.

Hyper-Kamiokande [149] is the proposed successor to Super-Kamiokande and is scheduled to become operational in 2025. Hyper-Kamiokande will also be a water Cerenkov detector, but will have a far larger total mass of 1000 kton compared to the 50 kton of Super-Kamiokande. This very large mass will allow a search for proton decay with decay lifetimes in excess of 10^{35} years. Hyper-Kamiokande will also allow precision measurements of solar and atmospheric neutrino oscillation parameters, the mass hierarchy and neutrino CP violation, and will act as an upgrade to T2K and a supernova neutrino telescope.

DUNE is another proposed experiment and the subject of this thesis. It is discussed in Section 2.6.

2.6 The Long Baseline Neutrino Experiment (LBNE) & Deep Underground Neutrino Experiment (DUNE)

The Deep Underground Neutrino Experiment (DUNE) [226–228] (a progression from the previously-proposed Long Baseline Neutrino Experiment (LBNE) [150]) is currently in development and aims to broaden understanding of topics discussed in Sections 2.2.1, 2.4. With the first of four detector units scheduled to be operational by 2023, DUNE will use a neutrino beam generated by protons from the Main Injector accelerator at Fermilab in Batavia IL, with a near detector at Fermilab and a far detector at Sanford Underground Research Facility (SURF) in Lead, SD. Simulations relating to the far detector are reported in this thesis. However, they have been performed for slightly different far detector configurations that until recently were proposed for LBNE[27].

2.6.1 The LBNE / DUNE far detector

The far detector [228] will rely on Liquid Argon Time Projection Chamber (LAr TPC) technology [230–239]. Whether under the LBNE or DUNE version of this experiment, the plan has been to take a multi-phased approach to the project. The current proposal is to use four 10 kton (fiducial mass) detectors each becoming operational in consecutive years (Figure 17) to eventually make an effective 40 kton detector. Two possibilities are currently proposed for the far detector design [228]. One is a dual-phased TPC, where ionization charge is extracted, amplified and detected in gaseous argon above the liquid surface. The other (based largely on the LBNE design) is single-phase; the charge generation, drift and collection all occurs within the LAr. Here each detector houses cryostats containing large volumes of ultra-pure LAr at 88 K. Submerged within the LAr will be rows and columns of identical TPC cells. Each TPC cell will consist of an anode plane and a cathode plane oriented parallel to each other, generating a uniform electric field in the intervening region. A field cage will surround the open sides of the alternating anode and cathode plane assemblies (APAs and CPAs), providing the boundary conditions necessary for the uniformity of the field.

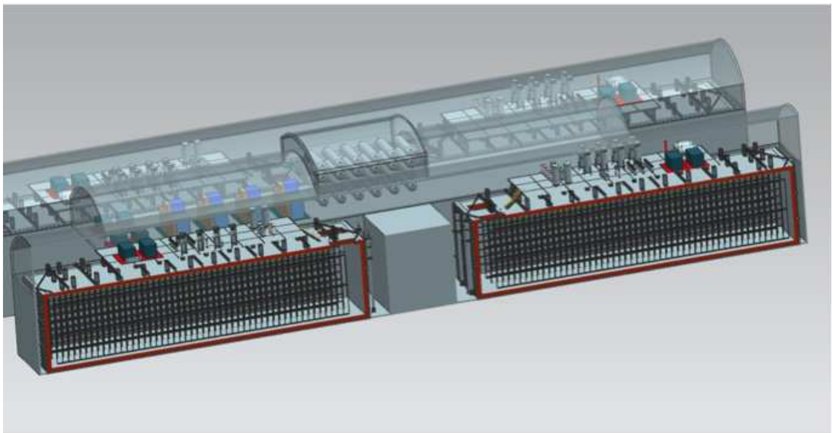

Figure 17: *An illustration of the* 10 *kton (fiducial mass) constituents of the currently-proposed (single-phase) far detector, showing cryostats (in red) each containing rows and columns of TPC cells [228]. Only two of the four cryostats are visible.*

---

[27] As well as for the quite different design proposed for the now-cancelled Deep Underground Science and Engineering Laboratory (DUSEL) [229]).

The beam axis points parallel to the plane in which the APAs and CPAs lie (i.e. along the long side of the cryostat). Defining this direction as the x-axis and the vertical as the z-axis, then each cryostat contains $25 \times 4 \times 2$ TPC cells. The ionization tracks left by particles interacting with the LAr inside a TPC cell will be slowly drifted along the y-axis towards the APA under the influence of the field, retaining their track shape. This drifting charge will induce a signal upon reaching readout wires wrapped around the APA frame, providing accurate measurement of energy deposition and enabling track reconstruction in two dimensions (with the third dimension given by timing the arrival of the charge). These features will allow different types of particle to be efficiently distinguished, with a vertex position resolution better than 1 cm anticipated (readout wires are assumed to be separated by 3-6 mm). Whether a single-phase or dual-phase TPC design is used, the detector will be supplemented by a photon detection system to rapidly detect scintillation photons. The reference design consists of light-guides fitted to the outside of the anode plane assemblies that will absorb rapidly emitted 128 nm scintillation photons ($\mathcal{O}(10^4)$ photons produced per MeV deposited [150]) on their wavelength-shifter coating, then channel re-emitted 430 nm photons towards silicon photomultipliers at the end of the light-guides. This will provide accurate event timing, eliminating background events that occur between beam spills ($\sim 10^{-5}$ s in duration). Strong shielding from cosmic rays will be provided by positioning the detector underground at a depth of 4850 ft.

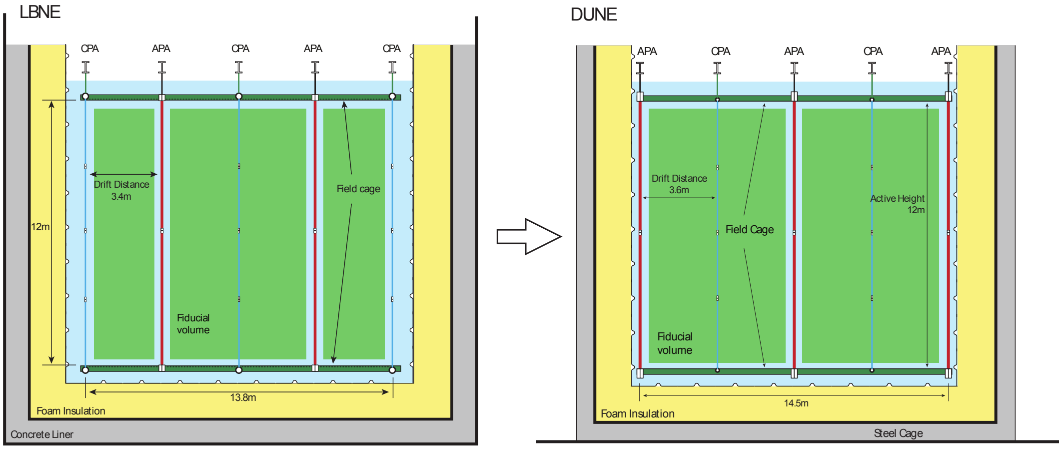

Figure 18: *End-view sketches [228] of the cryostats containing the (single-phase) TPC cells, for the past* 5 *kton-cryostat LBNE design (left) and the current* 10 *kton cryostat DUNE design (right). The DUNE design has a different arrangement of APA (red lines) and CPA (blue lines) planes and a slightly higher fiducial volume (green) than LBNE for an identical cryostat volume, as well as slightly larger drift distance between CPA and APA planes (*3.6 *m vs.* 3.4 *m). The beam axis direction points- into the page.*

Most of the simulations in this thesis are based on 10 kton (LAr fiducial mass) detectors from two past LBNE designs, which were very similar to the current single-phase DUNE option. Figure 18 shows an illustration of a detector cross-section for each. In 2012 the LBNE collaboration was considering a 10 kton detector buried close to the surface. Simulations discussed in Sections 5, 6 relate to this detector. By late 2013 this had evolved into a combined 34 kton detector separated into a 10 kton + 24 kton configuration and buried deep underground. Simulations discussed in Sections 3, 4 relate to the 10 kton component of this detector.

2.6.2 Aims of LBNE/DUNE

The experiment has a number of primary aims, the most important of which involve studying oscillations involving $\nu_\mu \rightarrow \nu_e$ and $\overline{\nu}_\mu \rightarrow \overline{\nu}_e$ (an appearance analysis) to make precise measurements of the CP-violating phase δ (Section 2.4.4), the θ_{13} mixing angle (Section 2.4.3) and the mass-splitting $\Delta m_{13}^2 = m_1^2 - m_3^2$ to determine the neutrino mass hierarchy (Section 2.4.3).

For neutrinos propagating in matter of uniform density, the probability of flavour change $\nu_\mu \rightarrow \nu_e$ or $\nu_e \rightarrow \nu_\mu$ is given (in the three-flavour scheme, to second order in $\sin^2(\theta_{13})$ and in $\alpha = |\Delta m_{12}^2|/|\Delta m_{13}^2|$) by [42, 240]:

$$\begin{aligned} P_{\nu_{\mu,e}\rightarrow\nu_{e,\mu}} \cong {} & \sin^2\theta_{23}\left[\frac{\sin^2(2\theta_{13})}{(A-1)^2}\right]\sin^2\big((A-1)\Delta\big) \\ & + \alpha\left[\frac{8J_{CP}}{A(1-A)}\right]\sin\Delta\ \sin(A\Delta)\ \sin\big((1-A)\Delta\big) \\ & + \alpha\left[\frac{8J_{CP}\ \cot\delta}{A(1-A)}\right]\cos\Delta\ \sin(A\Delta)\ \sin\big((1-A)\Delta\big) \\ & + \alpha^2\cos^2\theta_{23}\left[\frac{\sin^2(2\theta_{12})}{A^2}\right]\sin^2(A\Delta), \end{aligned} \tag{95}$$

where $\Delta = \Delta m_{13}^2 L/4E$, $A = 2\sqrt{3}G_F N_e E/\Delta m_{13}^2$ and J_{CP} is the Jarlskog parameter of Eq. 80. The first term on the right-hand side of Eq. 95 will allow measurement of θ_{13}. The second term switches sign when comparing neutrinos to antineutrinos and thus allows measurement of δ (Section 2.4.4). Neglecting any matter effects (Section 2.4.2), the lepton/antilepton production asymmetry in leptogenesis (Eq. 93, 94) approximates

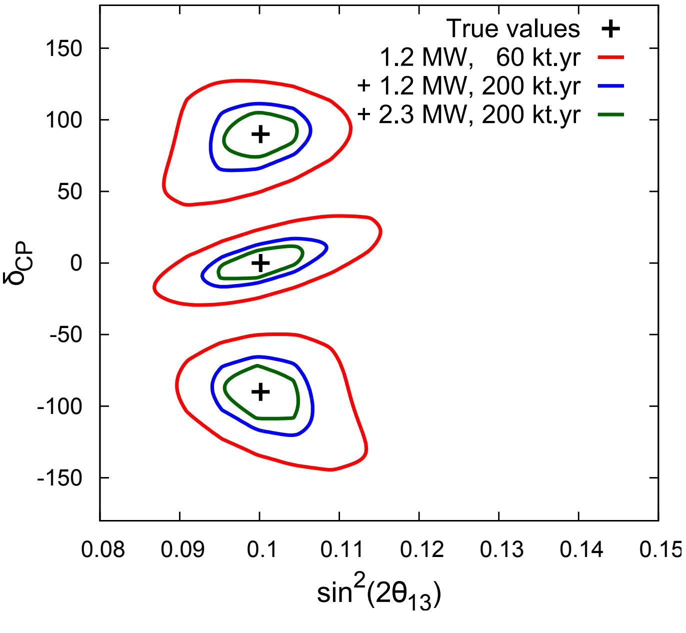

Figure 19: *The parameter space to which DUNE alone will constrain* δ *and* $\sin^2(2\theta_{13})$ *at* 1 σ*, for different proton beam power and detector exposures [150]. A normal neutrino mass hierarchy has been assumed for this plot. Three* δ *values are examined here* $(0°, \pm 90°)$ *and for each is shown three contours corresponding to different beam powers and detector exposures.*

(to first order in Δm^2_{12}) as [241]:

$$\epsilon \sim \frac{\cos\,\theta_{23}\ \sin(2\theta_{12})\ \cos\,\delta}{\sin\,\theta_{13}\ \sin\,\theta_{23}} \left(\frac{\Delta m^2_{12} L}{4E}\right).$$

Figure 19 shows the constraints DUNE will be capable of placing on δ and $sin^2(2\theta_{13})$ simultanously, ignoring the constraints set by any other experiments.

Also the terms proportional to Δm^2_{13} in Eq. 95 are dependent on the choice of normal or inverted neutrino mass hierarchy. The 1300 km baseline will exaggerate the matter effect beyond the maximum possible effect due to CP-violation, making them distinguishable from each other. Due to the matter effect the neutrino mode will be enhanced and the antineutrino mode suppressed if the normal hierarchy is correct, with the opposite indicating the inverted hierarchy. Figure 20 shows the dependence of $P_{\nu_\mu \to \nu_e}$ and $P_{\overline{\nu}_\mu \to \overline{\nu}_e}$ on neutrino energy E_ν.

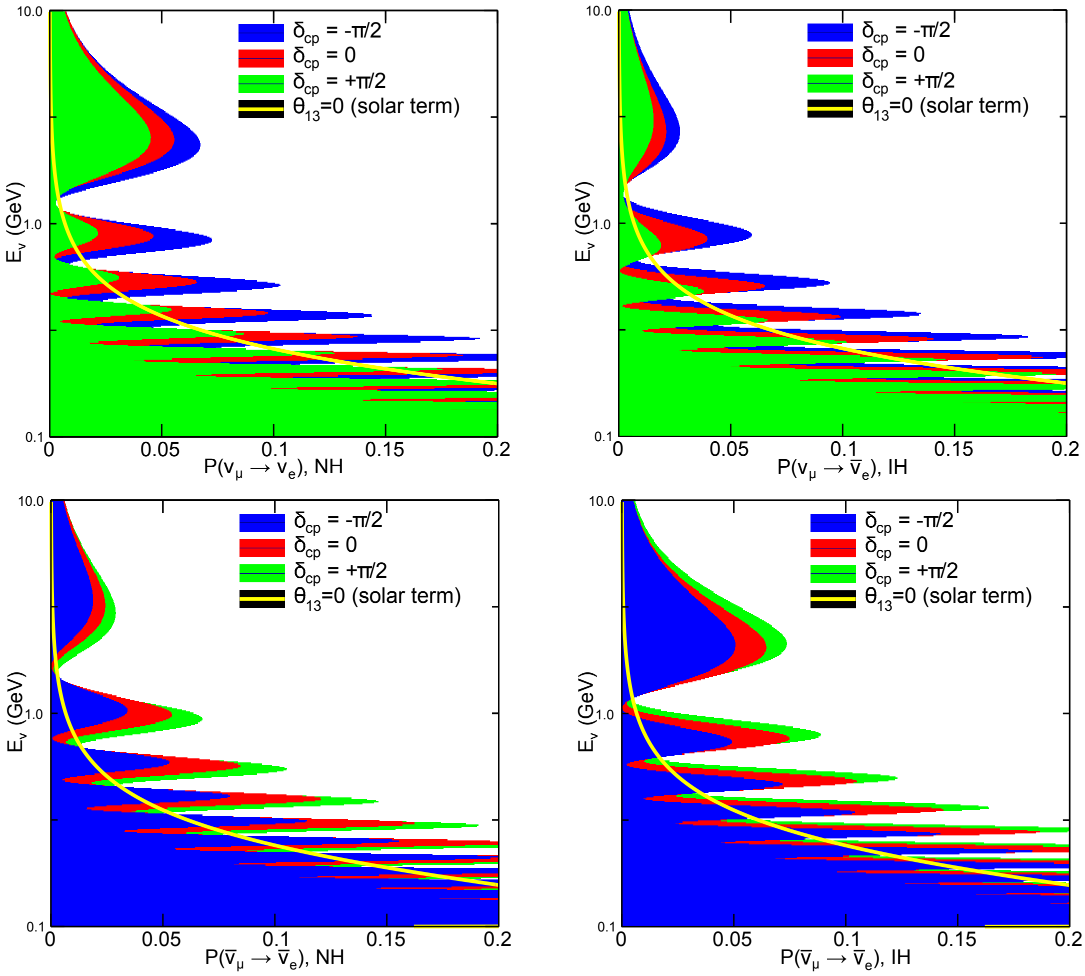

Figure 20: *The dependence of the* $\nu_\mu \to \nu_e$ *and* $\overline{\nu}_\mu \to \overline{\nu}_e$ *flavour change probability on neutrino (upper plots) and antineutrino energy (lower) using the normal (left) and inverted (right) mass hierarchy [150]. Each plot shows an oscillation pattern for* $\delta = 0$, $\pi/2$ *and* $-\pi/2$. *The yellow line shows the oscillation pattern with* $\theta_{13} = 0$.

A 1300 km baseline means the first and second oscillation maxima due to Δm^2_{13} occur at energies of ~2.55 GeV and ~0.85 GeV. This is well-matched to the neutrino/antineutrino beam, with an expected energy of ~0.5 - 5.0 GeV, broadly peaking at ~2.5 GeV (Figure 21). For this baseline, the dependence of the oscillation probability on the neutrino/antineutrino energy is shown in Figure 20 for $\delta = 0, \pm\frac{\pi}{2}$, where the choice of mass hierarchy can be compared. The difference between normal and inverted hierarchies is most pronounced at the first oscillation maximum regardless of whether CP symmetry holds, and switching between hierarchies also shifts the oscillation curve by ~ 100 MeV. However, the second oscillation maximum can have a much more pronounced CP asymmetry than the first maximum and therefore offer sensitivity to smaller values of δ. Adjusting the wide-band beam will allow focussing on either the first or second maximum, so DUNE is well-poised to determine the neutrino mass hierarchy and measure δ.

Figure 22 shows the ability of DUNE to resolve δ, Δm^2_{13}, $\sin^2(2\theta_{13})$ and $\sin^2\theta_{23}$ as a function of exposure based on the reference design used in the August 2015 DUNE Conceptual Design Report (CDR) [242]. An exposure goal of 300 MW·kton·year should allow $\mathcal{O}(10^3)$ appearances of $\nu_e/\overline{\nu}_e$ to be observed. With systematic uncertainties of a few percent this will allow a 5 σ measurement of δ to ±10° if δ is near maximum (±90°), and determination of the mass hierarchy regardless of the value of δ. However, there are options other than the CDR reference design available for the proton beam target and magnetic horn, so depending on the beam design, an exposure of 850 - 1320 MW·kton·year could allow 3 σ sensitivity to 75% of all possible δ values.

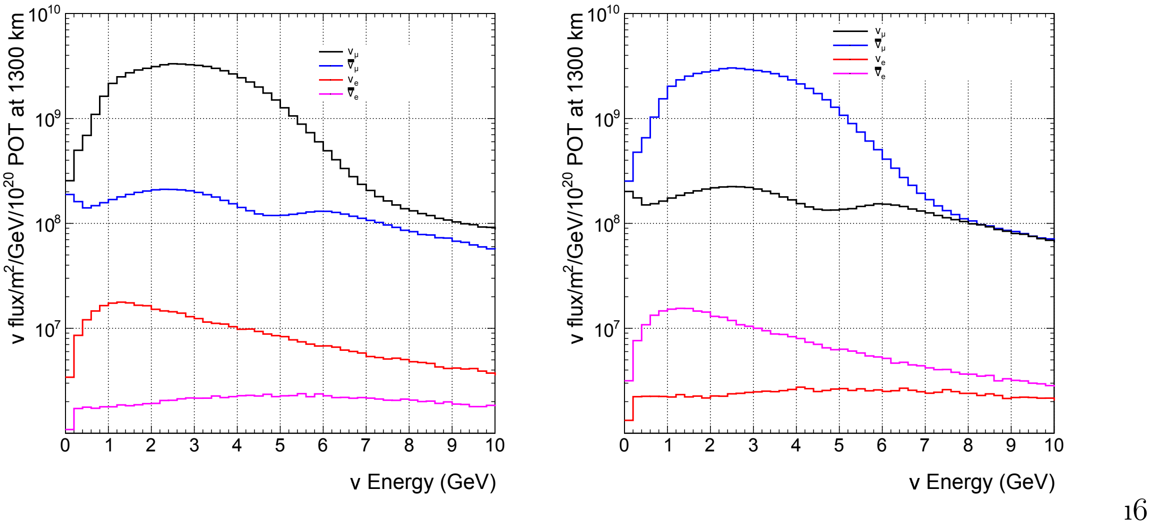

Figure 21: *The predicted energy spectra of* ν_μ, $\overline{\nu}_\mu$ *produced by the beam and the* ν_e, $\overline{\nu}_e$ *that the* ν_μ, $\overline{\nu}_\mu$ *oscillate into (shown in black, blue, red and magenta respectively) at the far detector with the beam running in neutrino (left) and antineutrino (right) mode [242]. These plots are based on parameters of* $\theta_{12} \sim (34\pm1)°$, $\theta_{23} \sim (38\pm1)°$, $\theta_{13} \sim (8.9\pm0.5)°$, $\Delta m^2_{12} = (7.54 \pm 0.22) \times 10^{-5}\ eV^2$, $|\Delta m^2_{23}| = (2.43^{+0.10}_{-0.06}) \times 10^{-3}\ eV^2$.

Another of the primary aims of DUNE is making a precision measurement of $\sin^2(2\theta_{23})$ by analysing the disappearance of ν_μ from the beam (Eq. 70). Analysing ν_e appearance from the beam (Eq. 95) allows sensitivity to $\sin^2\theta_{23}$ (shown as a function of exposure in Figure 22). A combined examination of the appearance and disappearance of beam neutrinos/antineutrinos will be sufficient for determination of the octant in which θ_{23} lies (Section 2.4.3.3), as well as measuring $|\Delta m^2_{23}| = |m^2_2 - m^2_3|$.

The observation of ν_e and $\overline{\nu}_e$ appearance is therefore fundamental to the main goals

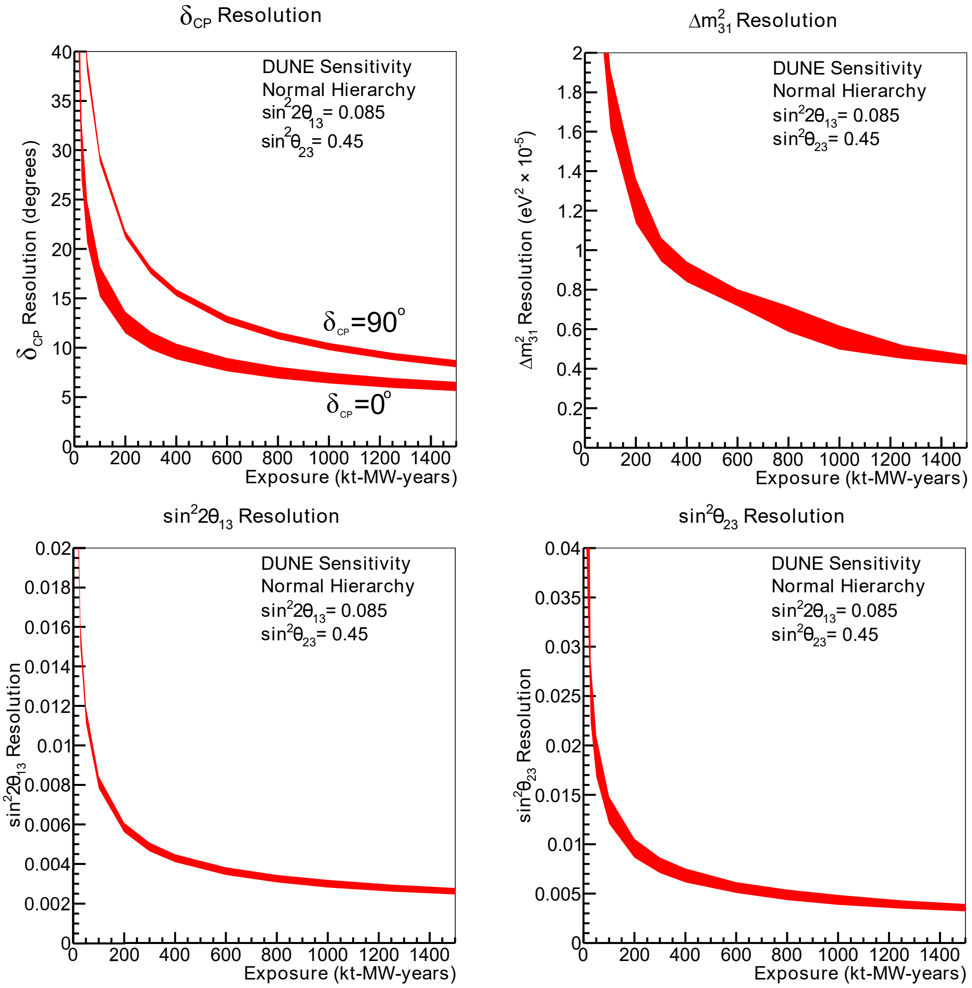

Figure 22: *The resolution as a function of exposure achievable by DUNE for oscillation parameters* δ, Δm^2_{13}, $\sin^2(2\theta_{13})$ *and* $\sin^2\theta_{23}$, *based on the current global fits for the latter three parameters, and* 0° *or* 90° *for* δ *[242].*

of DUNE. Part of this thesis is devoted to estimating the irreducible[28] background to these appearance events caused by cosmic rays, albeit for a previously-proposed 10 kton detector at shallow depth (Section 5).

Extending the search for proton decay up to presently-unexplored decay lifetimes is another important aim of DUNE. As discussed in Sections 2.2.2-2.2.5, the most likely proton decay modes that could be observed are $p \to e^+\,\pi^0$ and $p \to K^+\,\overline{\nu}$ for non-SUSY and SUSY GUTs respectively. The larger nuclei in LAr compared to those in water means that intra-nuclear effects are more problematic for $p \to e^+\pi^0$ in a LAr TPC, even though the detection efficiency ($\sim$ 45% [243]) is still slightly higher than the $\sim$ 40% of Super-Kamiokande [244]. However, this is less of a problem for the heavier, longer-lived kaon, which can also ionize more heavily than other potential decay products when stopping, improving its identification [245]. A LAr TPC thus offers a 97% detection efficiency for the $p \to K^+\overline{\nu}$ decay channel, compared to just 10% for a water Cerenkov [244] (the kaon is below the Cerenkov threshold in water). The LAr TPC also offers a superior cosmic ray and ν-induced background event rate, with 1 Mton^{-1} yr^{-1} estimated at a shallow depth [243] compared to 4 Mton^{-1} yr^{-1} for Super-Kamiokande [244].

---

[28] "Irreducible" being used to describe any background events that survive all attempts at identifying it as such and rejecting it.

The increased efficiency of the LAr TPC means DUNE will be able to explore decay lifetimes an order of magnitude above the Super-Kamiokande $p \rightarrow K^{+}\overline{\nu}$ limit, using a smaller detector than would be required for a water Cerenkov detector to achieve the same [29]. The DUNE far detector will also slightly out-perform the much larger Hyper Kamiokande detector in searching for this decay mode (Figure 7), allowing the $p \rightarrow K^{+}\,\overline{\nu}$ decay lifetime in the $\sim 10^{34} - 10^{35}$ year range to be investigated (Figure 23). This has the potential to rule out or constrain many GUTs, should no proton decay be observed (Figure 7). Due to the very high resolution and accurate identification of particles, just a single candidate event may already be considered as evidence of proton decay.

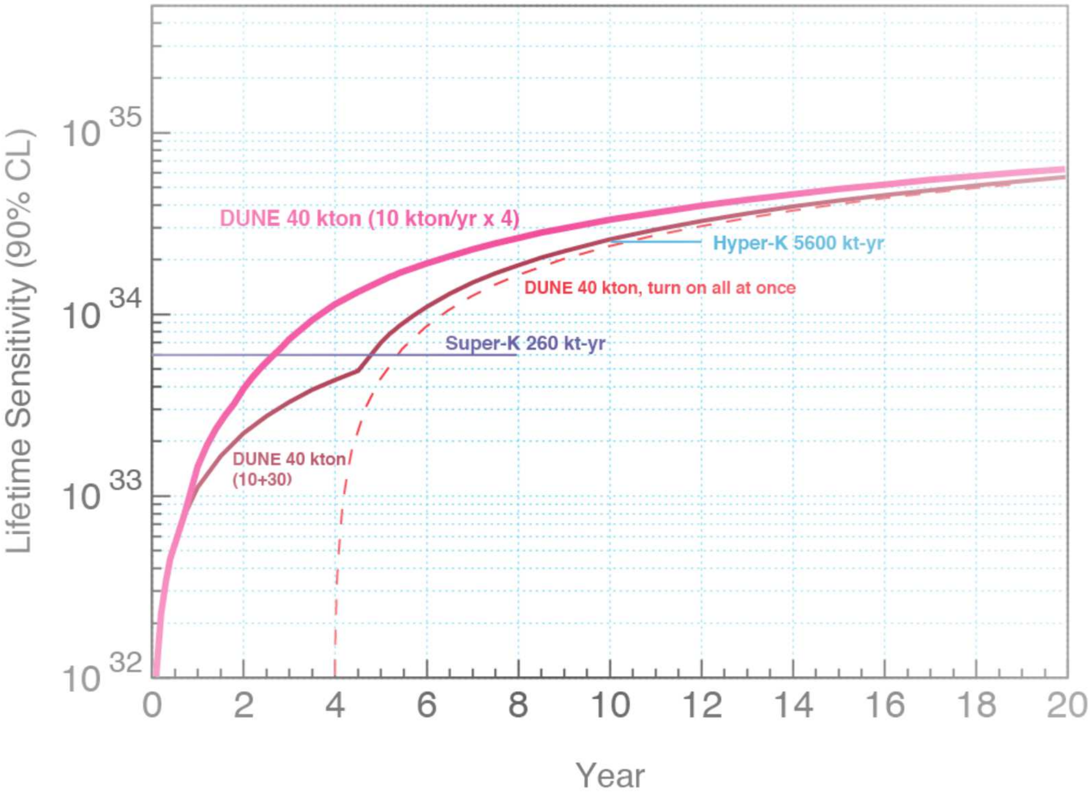

Figure 23: *The proton decay lifetime in the channel $p \rightarrow K^{+}\overline{\nu}$ that DUNE will be sensitive to as a function of time at 90% C.L. Three cases are plotted: the four 10 kton detectors starting in consecutive years (thickest curve), one initial 10 kton detector followed by a 30 kton after 4 years (medium curve), or starting with all four 10 kton detectors. Also shown are the current and projected lower limits for Super and Hyper Kamiokande.*

If protons can decay, DUNE stands a chance of detecting very few (if any) such events during 30 years of operation. It is crucial to efficiently identify and reject background events to stand any chance of observing this phenomenon. Part of this thesis involves estimating the cosmic ray-induced background rate to the $p \rightarrow K^{+}\overline{\nu}$ decay channel for a detector similar to a single 10 kton fiducial volume detector, and also for a 40 kton detector at a shallower depth (Section 3).

---

[29] The proposed Hyper Kamiokande experiment [149] is a 1000 kton water Cerenkov detector (successor to the 50 kton Super-Kamiokande) and is not expected to be operational until 2025. Hyper Kamiokande will perform much better for a $p \rightarrow e^{+}\,\pi^{0}$ search.

DUNE has other goals not relevant to this thesis, such as potentially measuring the neutrino flux from a core-collapse supernova, if such an event occurs within the Milky Way. As secondary aims the facility will also allow the study of the oscillation of atmospheric neutrinos (Section 2.5.2) and also of astrophysical phenomena using medium-energy neutrinos, as well as being sensitive to other possible effects of beyond-Standard-Model physics through the oscillation of beam neutrinos. Upgrades to the detector may also allow the study of solar neutrinos to investigate their oscillation and other solar physics, as well as the diffuse supernova neutrino flux and that of low-energy astrophysical and geophysical neutrinos.

3 Cosmic muon-induced background to $p \to K^+ \overline{\nu}$ events in deep underground detectors

3.1 Background events for $p \to K^+\overline{\nu}$

If proton decay is possible, such events are so rare that they require large-scale detectors operating for long periods to stand any chance of being observed. For instance, if the proton decay lifetime is actually 10^{34} years, a single proton decay event should be observable in one year with a detector containing 10^{34} protons. Observation is made more difficult by cosmic rays, which can cause events that mimic a proton decay signal. Detectors must therefore be located deep below Earth's surface, where a thick layer of rock can provide shielding from problematic incoming particles. However, muons produced in the atmosphere are capable of penetrating deep below the surface and causing events that could be mistaken for a decaying proton.

For the decay $p \to K^+\overline{\nu}$ the signal is a lone K^+ track since neither the neutrino nor the recoiling nucleus are detectable in a practical sense. The nuclear interaction of an incoming muon and subsequent hadronic cascade can result in neutral particles. In particular the problem is caused by K_L^0 that can then undergo a charge-exchange interaction with nuclei (Figure 24) to produce a $K^\pm$. Events featuring a K^- also pose a risk since K^- tracks cannot be efficiently distinguished from those of K^+.

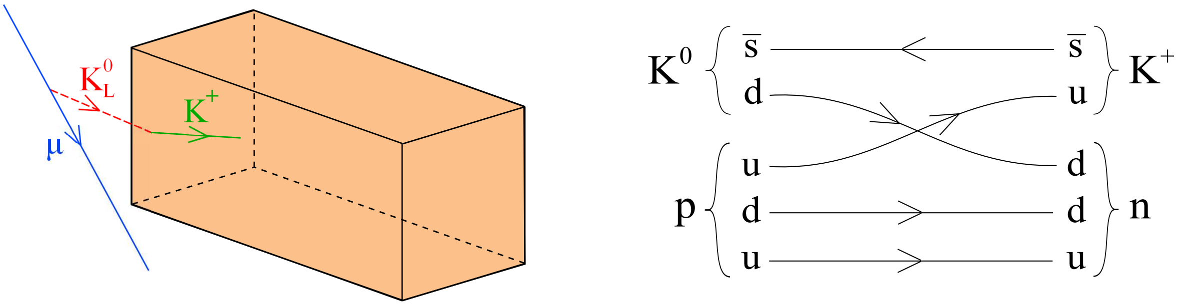

Figure 24: *(i) A background event in which a cosmic ray muon passes close to a detector and produces a neutral particle such as a K_L^0, which crosses inside the detector without leaving a track before creating a $K^\pm$. (ii) A generalized depiction of a charge-exchange process through which K^0 Ar $\to$ K^+ Cl (the main contributor to the background rate, Section 4.1.1) can occur.*

The detection of a muon or other charged particle in the vicinity of a $K^\pm$ would identify the $K^\pm$ as background rather than signal, so events where a $K^\pm$ appears in the detector without a muon track are the main concern. A muon could pass close to (or through an uninstrumented region of) the detector and create a neutral particle. This could then cross into an active region of the detector undetected before creating a $K^\pm$ which appears unconnected to any track. This chapter is concerned with estimating the annual rate of these $K^\pm$ background events for different detector configurations and also investigating how many of these can be distinguished from a genuine $p \to K^+\overline{\nu}$ signal event.

3.2 Kinematics of $p \to K^+\overline{\nu}$

One way to determine that a $K^\pm$ has not been produced in a genuine proton decay event is by considering the energy deposited by the $K^\pm$ and by any secondary, tertiary etc. particles that can be traced back to it. For a free proton decaying in its own rest frame, the total energy of the resulting K^+ and $\overline{\nu}$ is equal to the proton mass ($E_K + E_\nu = m_p$ using $c = 1$), therefore:

$$\begin{aligned} p_K^2 &= E_K^2 - m_K^2 \\ &= (m_p - E_\nu)^2 - m_K^2 \\ &= m_p^2 + E_\nu^2 - 2m_pE_\nu - m_K^2 \\ &\approx m_p^2 + p_\nu^2 - 2m_pp_\nu - m_K^2 \quad \text{where} \quad m_\nu \approx 0 \therefore\ E_\nu \approx p_\nu \\ &= m_p^2 + p_K^2 - 2m_pp_K - m_K^2 \quad \text{where} \quad \vec{p}_K = -\vec{p}_\nu \\ \implies 0 &= m_p^2 - 2m_pp_K - m_K^2 \\ \implies p_K &= \frac{m_p^2 - m_K^2}{2m_p}. \end{aligned} \tag{96}$$

Since $m_p = 938.272$ MeV, $m_K = 493.667$ MeV, the K^+ has momentum $p_K = 339.266$ MeV and therefore a total energy $E_K = \sqrt{p_K^2 + m_K^2} = 599.006$ MeV. The K^+ produced by a free proton decaying has a kinetic energy of $T_K = 599.006$ MeV - 493.667 MeV = 105.339 MeV in the proton rest frame.

However, in reality the protons will be bound within argon nuclei and thus have energy associated with their Fermi motion within the nucleus. The nuclear binding energy of the proton and the possibility of the kaon re-scattering as it exits the nucleus must also be considered [246]. Figure 25 compares model-dependent momentum distributions of K^+ from simulations of protons decaying within argon nuclei.

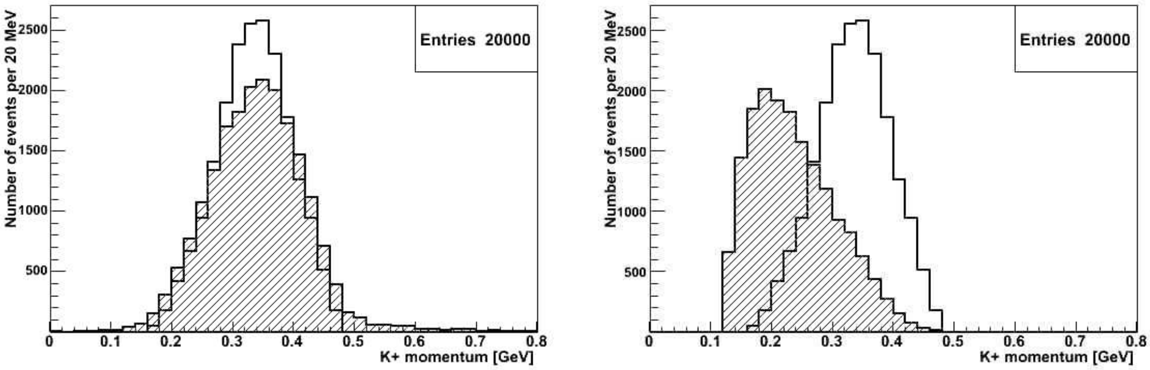

Figure 25: *The momentum distribution of K^+ from protons decaying within argon nuclei generated according to different models [246], notably peaking around* 340 *MeV as per Eq. 96. This $p \to K^+\,\overline{\nu}$ is a two-body decay; it is the Fermi motion and nuclear binding energy of the nucleons, as well as the K^+ rescattering within the nucleus, that cause the peaks to have non-zero width. The left plot compares the 'spectral function' of argon [247] (taking into account nuclear shell structure and nucleon short-range correlations) (shaded) to the 'local Fermi gas' model [248, 249] from GEANT4 without an intranuclear cascade to deal with K^+ rescattering. The right plot compares the latter with (shaded) and without the intranuclear (Bertini [250]) cascade.*

From Figure 25 a bound proton should produce kaons with momenta ranging between ∼100-500 MeV, corresponding to kinetic energy ∼10-210 MeV. The imperfect energy resolution of the K^+ track must also be considered; the electromagnetic energy resolution of the ICARUS T600 detector is $\sigma(E)/E = 0.03/\sqrt{E(GeV)} \pm 0.01$ [251], so for a K^+ with a kinetic energy of ∼210 MeV the resolution would be ∼12-16 MeV. The upper limit of this energy range could therefore be ∼226 MeV.

Using this one can distinguish a background $K^\pm$ from a signal K^+, since any $K^\pm$ that deposits more energy than this upper limit cannot be a product of proton decay. Even if the energy deposition of the $K^\pm$ itself does not exceed this limit, the energy deposited by any particles that branch off the $K^\pm$ track before the $K^\pm$ decays (referred to as the "non-decay descendents" in later sections) must also not exceed this limit. However, the above calculation applies to energy deposited by a single track, but the uncertainty in the measured energy deposition increases if the true energy available is divided between multiple tracks and deposited separately by each. A conservative upper limit on this energy deposition, above which a $K^\pm$ is no longer counted as part of the background, is therefore taken to be 250 MeV. Various thresholds are tested in Section 4.1.1.

If the $K^\pm$ does decay then the decay products and any secondaries they create (the "decay descendents") share the additional 493.667 MeV associated with the $K^\pm$ rest mass. For an energy resolution given by $\sigma(E)/E = 0.03/\sqrt{E(GeV)} \pm 0.01$ then an energy deposition equal to this mass, if deposited entirely by one track, could be measured as up to 520 MeV. If the maximum measured energy deposition by a K^+ and its non-decay descendents is taken as 250 MeV then adding these together gives a total of 770 MeV. However, in reality there would be multiple tracks resulting from a K^+ decay, each depositing a fraction of this kaon rest mass-energy, meaning that the overall uncertainty in the energy deposition would increased. A conservative upper limit of 1 GeV is therefore used for the energy deposition by a background $K^\pm$, its non-decay descendents and its decay descendents, although various upper limits are tested in Section 4.1.1

Simulations of muon-induced events have been performed for two different detectors at separate locations using Geant4 version 9.4 [252]. The first simulation is for a detector with a total LAr mass of 52.975 kton (appropriate for an intended 40 kton fiducial mass) located 800 ft below the surface that approximates a design for the once-proposed DUSEL project [229]. With a rock density of 2.72 g cm^{-3}, an 800 ft rock overburden corresponds to 0.3074 ft m$^{-1}\times$ 800 ft $\times 2.72 \approx$ 663 metres of water equivalent (m.w.e.). The second is for a detector with a total LAr mass of 16.748 kton (appropriate for an intended 10 kton fiducial mass) at an approximate vertical depth of 4850 ft (or 4021 m.w.e.) that approximates a recently proposed LBNE/DUNE design.

3.3 Physics processes enabled

The particle interaction models used in these simulations are specified in a Geant4.9.4 'reference physics list' known as "Shielding" [253]. The interactions enabled for significant particles at relevant energies are as follows.

For photons, Shielding includes the ability to undergo photoelectric absorption, Compton scattering, electron/positron pair-production and also inelastic scattering with nuclei and nucleons. Shielding includes standard EM processes for all charged particles including leptons, mesons, baryons and generic ions (namely ionization, Bremsstrahlung radiation, multiple elastic scattering, nuclear inelastic scattering). Electron-positron annihilation is also enabled. Muons may also participate in direct electron/positron pair production.

Neutrons may undergo elastic and inelastic scattering with nuclei (as may protons), as well as being captured by nuclei and initiating fission. Specific interaction models for each significant type of particle and the energies to which they apply are as follows.

For photons, Shielding includes the ability to undergo Compton scattering, electron/positron pair-production via the Bethe-Heitler model [254], up to 100 GeV, the photoelectric effect (using the photon absorption cross-section according to Biggs et al. [255], atomic shell data for the energy of the ejected electron [256] and its angular distribution according to Sauter-Gavrila [257]) and also inelastic scattering with nuclei and nucleons. The latter uses the Chiral Invariant Phase Space (CHIPS) model [258–260] for the fragmentation of hadronic systems for energies 0.0-3.5 GeV and the Quark-Gluon String [261] with Precompound [262] (QGSP) model for energies 3.0 GeV - 100 TeV.

Electrons and positrons are able to cause ionization (Moller scattering for e^-e^- [263], Bhabha scattering for e^+e^-) [264], emit Bremsstrahlung photons according to the Seltzer-Berger model [265], undergo nuclear inelastic scattering via CHIPS and undergo multiple elastic scattering based on Lewis theory [266]. Positrons may also annihilate with atomic electrons according to the Heitler formula [267].

Muons and anti-muons are able to cause ionization, emit Bremsstrahlung photons, cause direct electron/positron pair-production, undergo multiple scattering and nuclear inelastic scattering. For the latter, muons produce virtual photons which are converted to real photons below 10 GeV or neutral pions above 10 GeV If photons are produced, the interaction proceeds via Bertini cascade [268]. Alternatively if neutral pions ar produced, they interact with nucleons via the FRITIOF [269] Precompound (FTFP) model.

Charged pions may cause hadron ionization according to Bethe-Bloch formula [270] (as may other heavy hadrons), undergo multiple scattering, undergo inelastic scattering with nuclei via the Bertini cascade at energies 0.0-5.0 GeV or via FTFP between 4.0 GeV - 100 TeV, scatter elastically with nuclei based on the Glauber model [271]. Negative pions may also undergo hadron capture by nuclei via the CHIPS model.

The same applies for charged kaons as for charged pions. For long- and short-lived neutral kaons, Shielding enables elastic scattering with nuclei and inelastic scattering with nuclei as stated for charged pions.

Protons are able to undergo multiple scattering, cause ionization, undergo inelastic scattering with nuclei as stated for charged pions.

Neutrons may scatter elastically with nuclei via CHIPS for energies of 19.5 MeV-100 TeV and inelastically via Bertini (19.9 MeV-5.0 GeV) and FTFP (4.0 GeV-100 TeV). They may also be captured by nuclei and initiate fission according to the GEISHA model [272].

A general ion may undergo multiple scattering, undergo radioactive decay, cause ionization, and scatter inelastically with a Geant4 Binary Cascade [273] for energies of 0-110 MeV and a quantum-molecular-dynamics-based model [274] for energies of 100 MeV-10 GeV.

3.4 Detector Geometry

Each detector (Section 2.6.1) is surrounded by rock with the elemental composition [275] found in Table 6. The density is set to 2720 kg m^{-3} for all underground detector simulations (Sections 3, 4).

Individual TPC cells with gaps in between are neglected here and instead two large, continuous blocks of LAr are used. Information about particle interactions occurring anywhere within these LAr volumes is recorded.

Table 6: *The elemental composition of the rock used in the simulations. The density used for the underground simulations is 2720 kg* m^{-3}*. This is also used for surface-level detector simulations described in Sections 5, 6, for which the density is 2700 kg* m^{-3}*.*

Element	**Composition (%)**
Si	20.43
O	48.37
Ti	0.73
Al	7.20
Fe	9.87
Mn	0.10
Mg	4.22
Ca	5.65
Na	2.13
K	0.17
P	0.03
H	1.20

The outermost layer of the 800 ft detector (Figure 26, [229]) is created from a box filled with concrete measuring 159.0×19.0×19.0 m^3. This contains an insulation region; a polyurethane box oriented such that a 1 m layer of concrete covers each face. This polyurethane box is divided into two even sections by a 4.99 m thick concrete septum. Both sections each contain a cryostat represented by a steel box with 0.24 cm thick walls, positioned such that each face is covered by a ∼1 m thick polyurethane layer. Both cryostats are then filled with LAr. For a LAr density of 1392.8 kg m^{-3}, each steel container houses 26.385 kton of LAr.

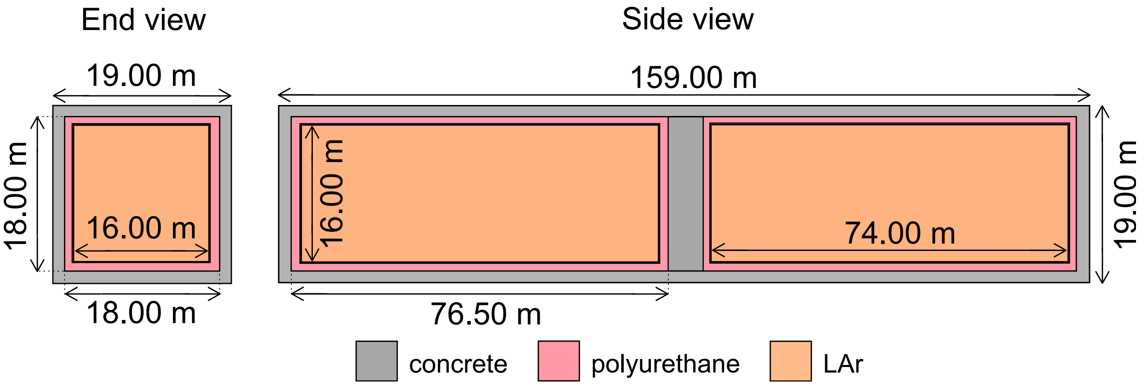

Figure 26: *The* 800 *ft detector seen from the end and from the side.*

The 4850 ft detector [276] (Figure 27) is structured similarly to the 800 ft detector. However, it is smaller, with the concrete enclosure measuring 78.4×18.2×18.6 m^3. In this case the concrete is 0.500 m thick above the polyurethane volumes, 1.285 m thick at their sides and 0.680 m thick at their outward-facing ends. The polyurethane surrounding the steel containers forms a layer 0.8 m thick on all sides. The LAr volumes do not completely fill the steel containers, but rather have a 0.99 m gap filled with air above them. The septum in this case is made from rock rather than concrete and is 12 m thick. Also included is an excavated upper region filled with air intended for access to the detector, 144.3 m long and with a curved ceiling 10 m high at its highest point. For a LAr density of 1398.2 kg m^{-3}, each steel container houses 8.374 kton of LAr.

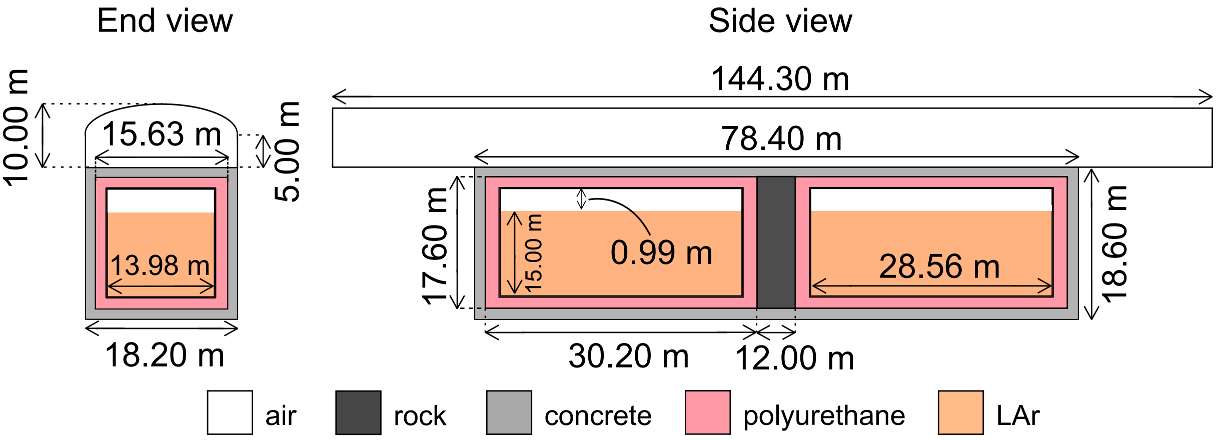

Figure 27: *The* 4850 *ft detector seen from the end and from the side. All detector components are indicated by the key aside from the steel that contains the LAr, indicated by their heavy outline.*

3.5 Primary muon flux

3.5.1 Cosmic rays

Background events can be caused by cosmic rays produced in astrophysical processes, both in the solar system and interstellar space. They may be categorised as 'primary' or 'secondary' cosmic rays depending on their origin. A primary cosmic ray [277, 278] is defined as all stable[30] charged particles and nuclei arriving at the top of Earth's atmosphere, which is mainly protons ($\sim$ 90%) and helium nuclei ($\sim$ 9%), with small numbers of heavier nuclei and electrons. They are thought to originate predominantly in the local galaxy [279], produced in large numbers by supernovae (and other sources) and accelerated by shockwaves from expanding supernova remnants [280]. The sources of all but the most energetic primary cosmic rays are obscured by the time they reach the solar system; galactic magnetic fields in the interstellar medium (mostly atomic and molecular hydrogen with 10% He and heavier nuclei) randomize the direction of the charged particles, resulting in an essentially isotropic flux at most energies. The peak energy of primary cosmic rays is in the range of 0.1-1.0 GeV, although their energy can be many orders of magnitude higher. The overall cosmic ray nucleon intensity obeys the following:

$$I(E) \approx 1.8 \times 10^4 (E/1\text{ GeV})^{-\alpha} \frac{\text{nucleons}}{\text{m}^2\text{ s sr GeV}} \qquad (\alpha \equiv 1+\gamma, \quad \gamma = 1.7), \qquad (97)$$

where α is the differential spectral index of the cosmic ray flux and γ is the integral spectral index. Figure 28(i) shows the energy dependence of the fluxes of specific primary cosmic ray nuclei.

Secondary cosmic rays are particles produced when primary cosmic rays interact either with the interstellar medium or the atmosphere. Copious amounts of mesons are produced through their interaction with atmospheric nuclei and in the ensuing hadronic cascades. Primarily these are pions, which decay rapidly to produce muons via $\pi^\pm \to \mu^\pm\, \nu_\mu(\overline{\nu}_\mu)$

---

[30] Particles/nuclei with rest-frame half-lives of 10^6 years or longer.

($>$ 99.98% of decays) and also kaons, which decay via $K^{\pm} \rightarrow \mu^{\pm}\,\nu_{\mu}(\overline{\nu}_{\mu})$ (63.56% of decays). Muons are therefore a major component of the secondary cosmic ray flux and since muons penetrate matter much more easily than other charged particles, they are the dominant cosmic ray at sea level and below ground, with neutrinos also surviving in large numbers. This is demonstrated in Figure 28(ii), which plots predictions and measurements of the altitude dependence of the main components of the vertical flux of secondary cosmic rays, at energies where those particles are most abundant.

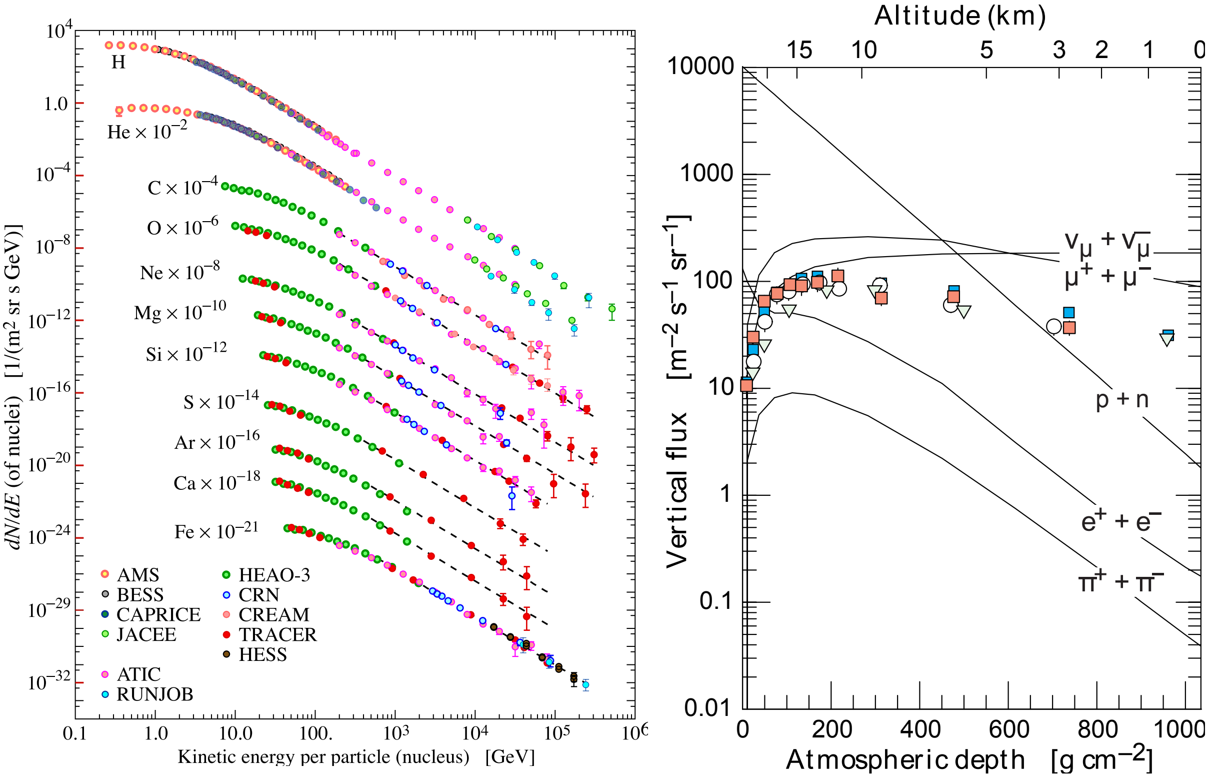

Figure 28: *(i) The flux (in particles per energy-per-nucleus) of primary cosmic ray nuclei as a function of energy per nucleus [277]. Protons are by far the dominant primary cosmic ray at all energies. (ii) The altitude dependence of the composition of the vertical flux of secondary cosmic rays ($E > 1$ GeV) [277]. The curves represent predictions and the points are measurements of the μ^- flux (not $\mu^+ + \mu^-$, hence the points not aligning with the $\mu^+ + \mu^-$ curve) ($E_\mu > 1$ GeV). Muons and neutrinos dominate down to sea level.*

When travelling vertically the muons typically have around 15 km of atmosphere to traverse before reaching the surface. As they propagate they generally lose around 2 GeV by ionizing the atmosphere. The muon flux at sea level has a zenith angle (θ) dependence corresponding to the thickness of atmosphere that a muon must traverse. The mean muon lifetime in its own frame of reference is 2.2×10^{-6} s, giving it a range of ~660 m at close to light speed, but special-relativistic time dilation extends the range of the muon[31]. Assuming the muons have sufficient energy (i.e. $E_\mu > 100/\cos\theta$ GeV) to reach the ground

---

[31] Energy losses in the atmosphere do slow the muon, lessening the time dilation and shortening its range somewhat.

before they decay, the differential muon flux at sea level is [277, 278]

$$\frac{dN_\mu}{dE_\mu d\Omega} \approx \frac{0.14E_\mu^{-2.7}}{cm^2\ s\ sr\ GeV}\left(\frac{1}{1+\dfrac{1.1E_\mu cos\theta}{115\,GeV}} + \frac{0.054}{1+\dfrac{1.1E_\mu cos\theta}{850\,GeV}}\right). \tag{98}$$

where the two terms in brackets are the contribution from $\pi^\pm$ and $K^\pm$ decays respectively. This is valid for zenith angles of $\theta < 60° - 70°$ (i.e. when the curvature of the earth can be neglected), although this can be accommodated (Section 3.5.2).

Muons are the only charged particle capable of penetrating large distances of rock and are the only cosmic ray (other than neutrinos) that can cause a problem for detectors buried deep underground. The energy loss per distance X travelled can be expressed in terms of ionization losses a and fractional radiative losses b, both of which vary slowly with energy:

$$-\frac{dE_\mu}{dX} = a + bE_\mu. \tag{99}$$

At some critical energy a/b (a few hundreds of GeV in rock-like media; the) radiative losses via Bremsstrahlung, photonuclear interactions and direct production of $e^+\ e^-$ outweigh ionization losses. The muons used in these simulations range between 1 and $\sim 10^5$ GeV. Based on a metre-water-equivalent depth calculated using a rock density of 2.65 g cm^{-3} in [281], the rock density of 2.72 g cm^{-3} used in these simulations means a muon of energy $\sim$ 2200 GeV can reach the detector depth of $\sim$ 4850 ft used in Section 4.1. Also a muon of energy $\sim$ 240 GeV can reach the detector depth of $\sim$ 800 ft used in Section 4.2. Figure 29(i) shows the vertical differential muon intensity at sea level, indicating that signficant numbers of muons are able to penetrate to these detector depths. Figure 29(ii) shows how the muon intensity decreases as the thickness of the rock they traverse increases.

3.5.2 MUSIC and MUSUN

The primary muons passed to Geant4 are generated using MUSIC (Muon Simulation Code) and MUSUN (Muon Simulations Underground) [284, 285]. MUSIC first propagates a set of muons through a medium with user-specified properties (e.g. density, elemental composition), given initial parameters of energy, position and direction cosines. It takes muons of energy ranging between 10^2-10^7 GeV and stores their energy distributions at distances of 100-15,000 m w.e. MUSUN then generates a muon energy spectrum and angular distribution appropriate for an underground location, by using the results of MUSIC, as well as details of the local surface profile (Section 3.5.3). The differential muon intensity at the underground location is given by:

$$\frac{dI_\mu}{dE_\mu d\Omega}(E_\mu, \theta) = \int_0^\infty P(E_\mu, X, E_\mu^0)\,\frac{dI_\mu^0(E_\mu^0, \theta^*)}{dE_\mu^0}\,dE_\mu^0 \tag{100}$$

where θ is the zenith angle underground, θ^* is the zenith angle at the surface and $P(E_\mu, X, E_\mu^0)$ is the probability that a muon of energy E_μ^0 at the surface has energy E_μ at slant depth X. Eq. 100 also depends on the differential muon intensity at sea level, which employs Gaisser's parameterization [278] (modified from Eq. 98 for large zenith angles [286], the fraction of prompt muons and the probability of muon decay) for the

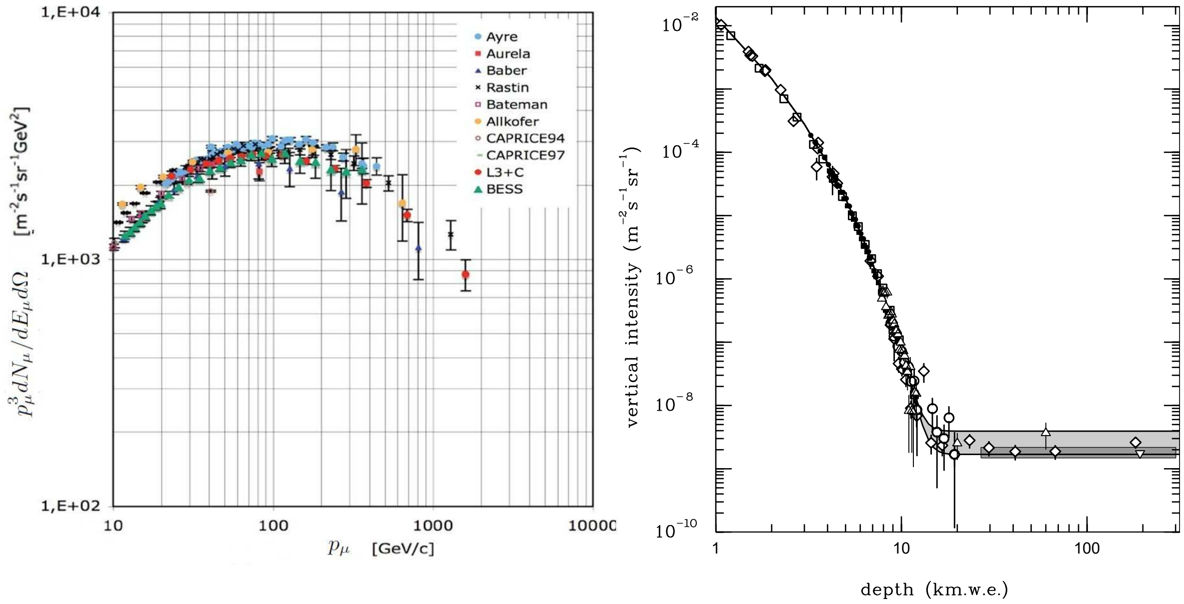

Figure 29: *(i) The momentum dependence of the vertical absolute differential muon intensity $p_\mu^3 dN_\mu/dE_\mu d\Omega$ at sea level measured by ten experiments, where $p_\mu \approx E_\mu$ [282]. (ii) A Particle Data Group compilation of various measurements of the underground depth dependence of the muon intensity [283]. The experimental data are from SNO, LVD, MACRO, and FREJUS experiments and points are also shown for compilations of Crouch and Baksan. The shaded region is for ν-induced muons ($E_\mu > 2$ GeV) (horizontal ones indicated by the upper line, with the lower line representing vertically upward muons. The darker shaded region is for the flux measured by Super-Kamiokande). The DUNE far detector will be at a depth of approximately 4 km.w.e.*

differential flux of atmospheric muons at sea level:

$$\frac{dI_\mu^0(E_\mu^0,\theta^*)}{dE_\mu^0} = \frac{0.14\,(E_\mu^0+\Delta E_\mu^0)^\gamma A\, p_d(\theta^{**})}{cm^2\cdot s\cdot sr\cdot GeV} \times \tag{101}$$

$$\left(\frac{1}{1+\dfrac{1.1\big(E_\mu^0+\Delta E_\mu^0(\theta^{**})\big)\,cos\,\theta^{**}}{115\,GeV}} + \frac{0.054}{1+\dfrac{1.1\big(E_\mu^0+\Delta E_\mu^0(\theta^{**})\big)\,cos\,\theta^{**}}{850\,GeV}} + R_C \right). \tag{102}$$

Here ΔE_μ^0 is the energy loss of the muon from its production point in the atmosphere to the surface, θ^{**} is the zenith angle at the production point ($cos\,\theta^{**} = \sqrt{1-0.99(1-cos^2\theta^*)}$), A is an additional normalization factor needed if the spectral index γ (Eq. 97) is different from that already proposed by Gaisser [278], p_d is the probability that a muon does not decay as it propagates down to the surface and R_C is the ratio of prompt muons to pions. Of the primary muons used to generate events, $\sim 57\%$ are μ^- and $\sim 43\%$ are μ^+.

3.5.3 Local geography

The muon flux used for each simulation has been tailored to the appropriate location for each detector site. The 800 ft detector was assumed to be at 44° 21' 5" N, 103°44' 54" W and the 4850 ft detector at 44° 20' 45.21" N, 103° 45' 16.13" W. Using a satellite-generated map detailing the surface contours of a 20×20 km^2 region near the detector sites (Figures 30, 31 show a 4 × 4 km^2 region of the map centred on the 4850 ft cavern sites), rays have been drawn out from the coordinates occupied by the centre of the detector. The length r of each ray is increased in steps of 1 m and at each step the Cartesian z-coordinate is compared to the elevation of the corresponding 5×5 m^2 cell of the surface map. Once z_{ray} becomes larger than z_{map}, the ray is stepped no further and the r at which the ray reaches the surface is recorded. This detector-surface distance calculation is done for integer values of θ, ϕ (using spherical polar coordinate system (r, θ, ϕ)). Figure 32 shows the coordinate at which each ray intersects the surface for the 4850 ft detector. Figure 33 shows the azimuth angle distribution of the muons used to generate events from the perspective of both the 4850 ft and 800 ft detectors. Figure 34 shows the same for the cosine of the zenith angle.

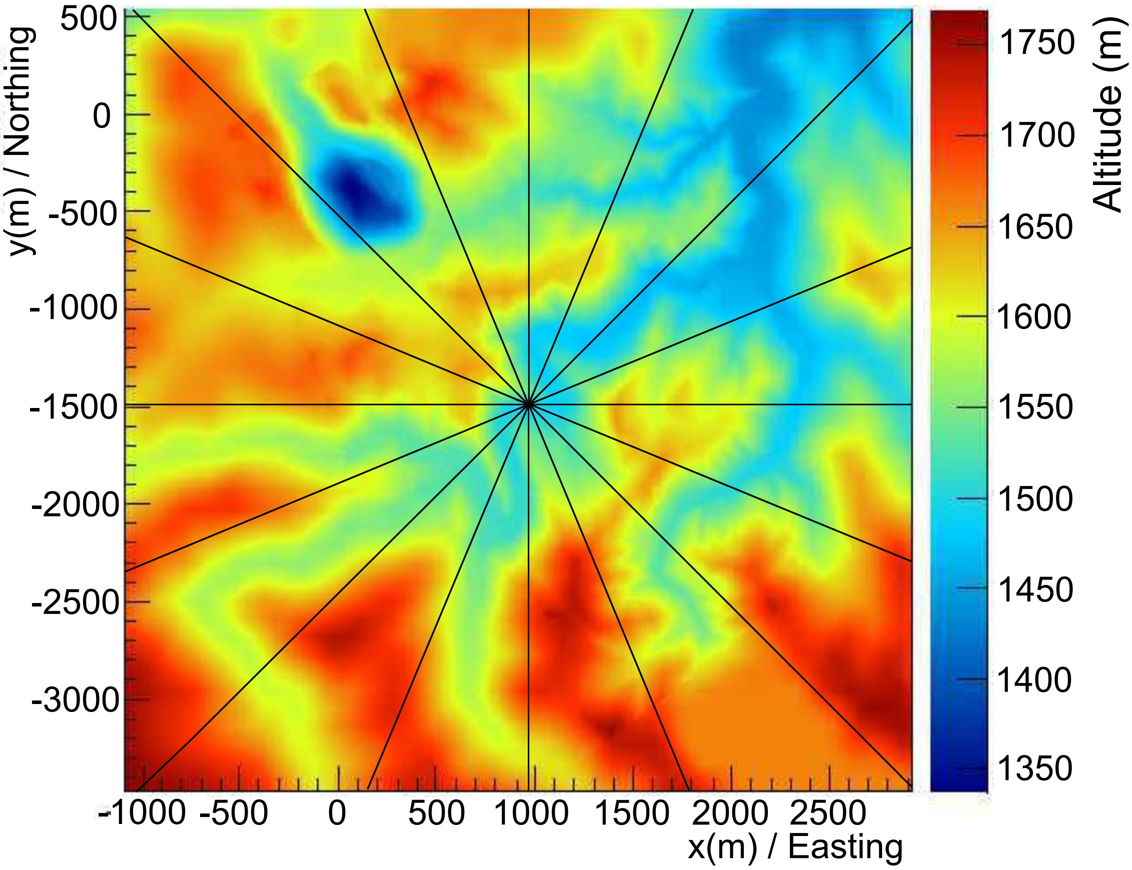

Figure 30: *A bird's eye view of a* 4×4 *km*^{2} *region on the map of the surface, where red/blue indicates high/low surface elevation. The centre of the image is directly above the* 4850 *ft detector site. The origin corresponds to global coordinates* 44° 20' 45.21" *N,* 103° 45' 16.13" *W. The lines emerging from this point are drawn at* 22.5° *intervals for comparison to Figure 33, which shows the azimuth angle distribution for the primary muons used to generate events. The* 800 *ft detector site is at coordinates* $(1175.90, -655.09)$.

This slant depth information is then passed to MUSUN (Section 3.5.2) which samples muons on the surface of a box. The centre of this box coincides with the centre of the detector enclosure, as illustrated in Figure 35 for the 800 ft and Figure 36 for the 4850 ft detector. Geant4 events are generated by injecting primary muons sampled from the surface of this box, meaning they start off close to the detector but still travel through a few metres of rock before reaching it.

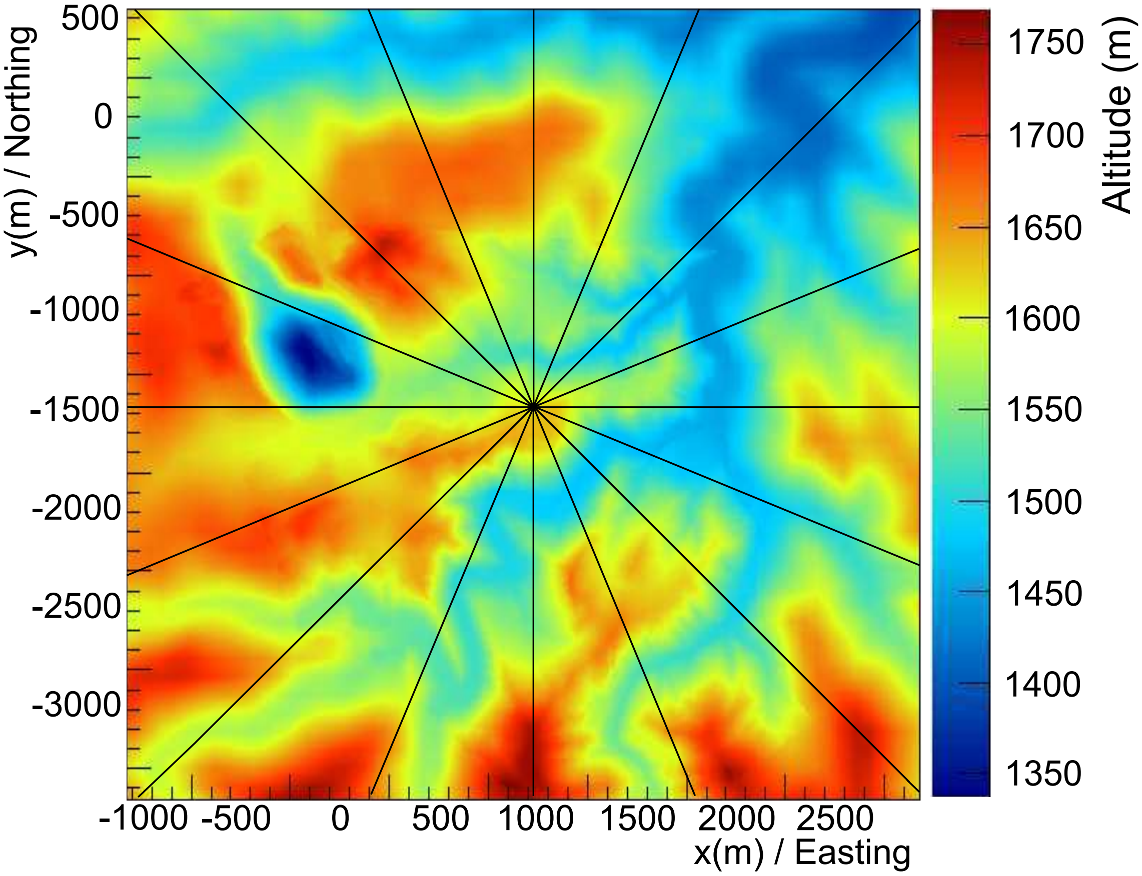

Figure 31: *As in Figure 30 but for the* 800 *ft detector. The proposed* 800 *ft and* 4850 *ft detector sites are close to each other in latitude and longitude but due to their difference in depth their respective muon fluxes differ significantly in azimuth and zenith angle distributions (Figures 33, 34). The origin corresponds to global coordinates* 44° 21' 5" *N,* 103° 44' 54" *W.*

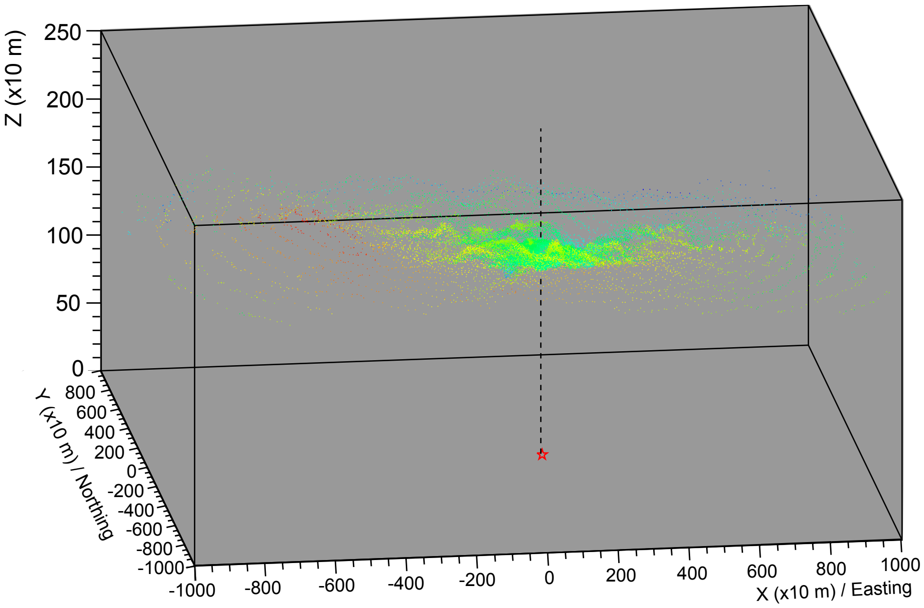

Figure 32: *The surface points at integer values of spherical coordinates θ, ϕ used to calculate the distance through rock crossed by muons. The red star indicates the* 4850 *ft detector location.*

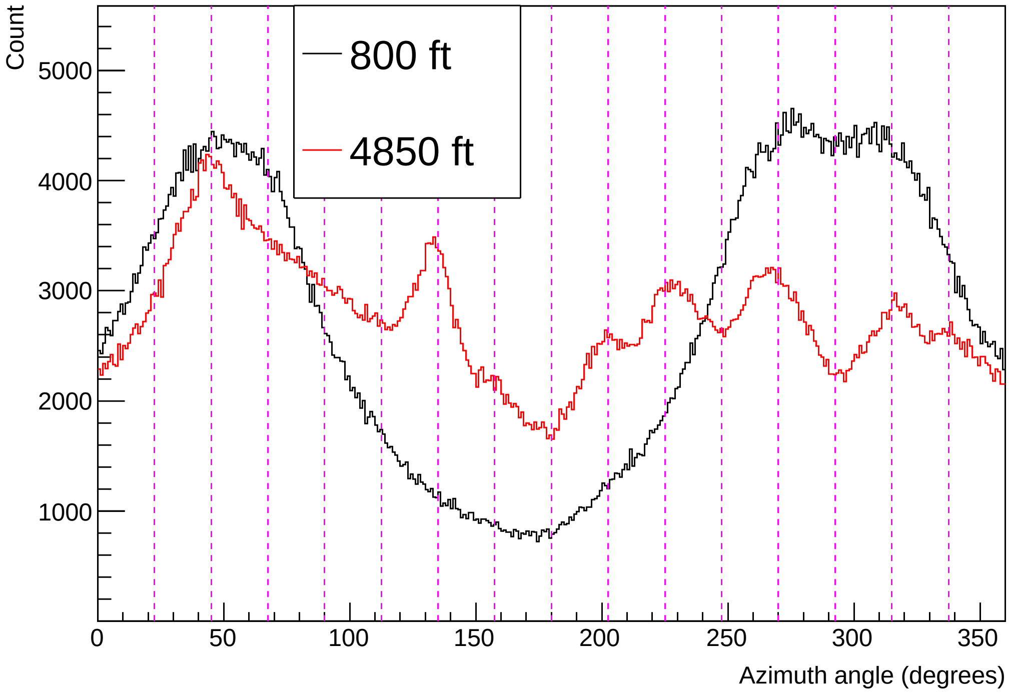

Figure 33: *The azimuth angle distributions of* 10^7 *primary muons used to generate events for the* 800 *ft (black line) and* 4850 *ft (red line) simulations.* 0°/90° *degrees corresponds to the easting/northing direction. The points at which the dashed vertical lines drawn at* 22.5° *intervals intersect the curves may be compared to the radial lines drawn on Figures 30, 31. A line intersecting more red region in those figures corresponds to a lower count at the same angle in this plot.*

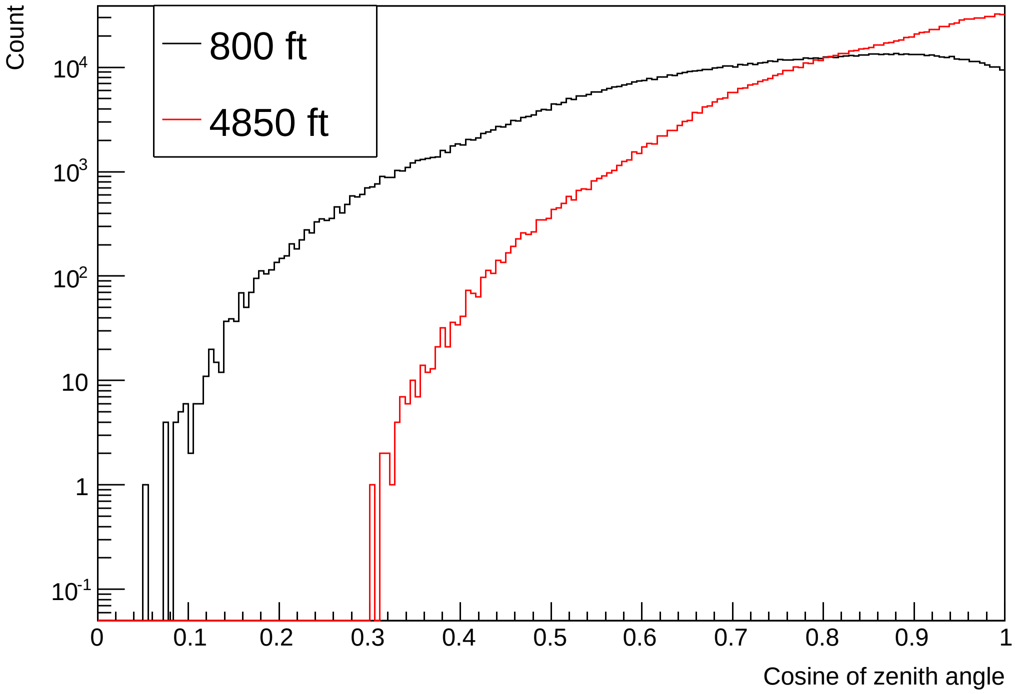

Figure 34: *The cosine of zenith angle distributions of* 10^6 *of the primary muons used to generate events for the* 800 *ft (black line) and* 4850 *ft (red line) simulations.*

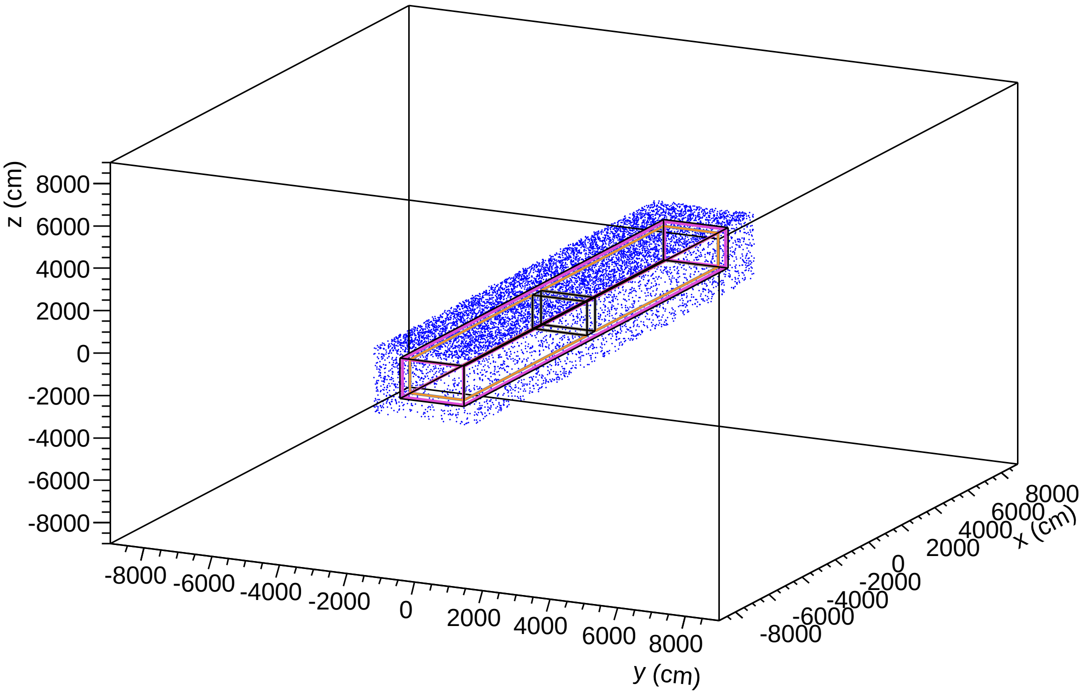

Figure 35: *The blue points indicate the initial positions of* 10^4 *of the muons used to generate events for the* 800 *ft detector. A total of* $2{\times}10^9$ *muons are sampled on the surface of this box around the detector.*

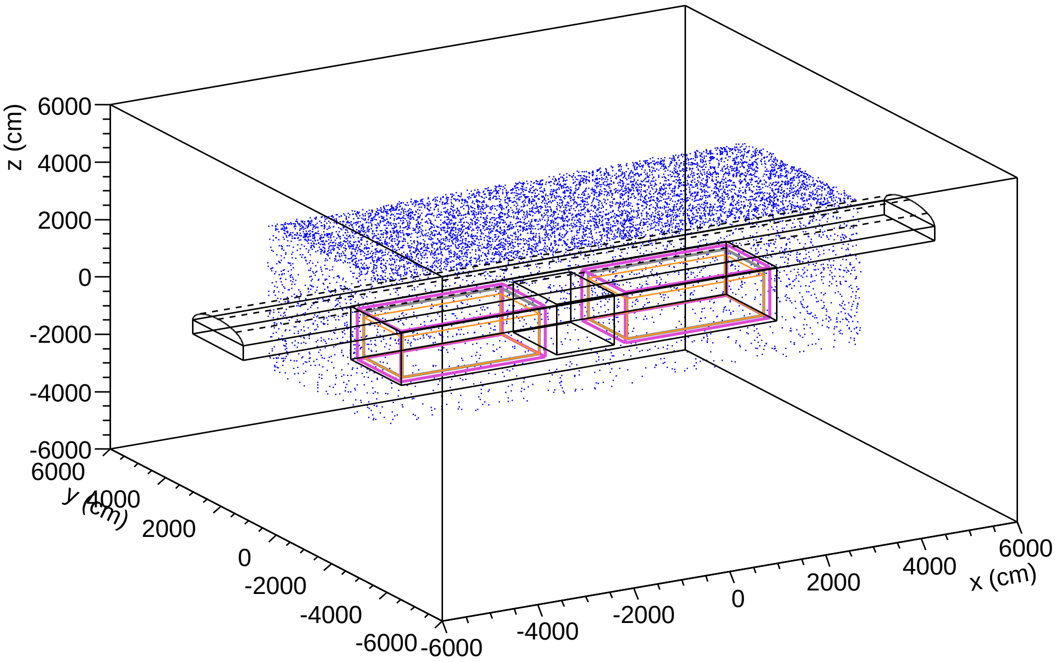

Figure 36: *The blue points indicate the initial positions of* 10^4 *of the muons used to generate events for the* 4850 *ft detector. A total of* 10^8 *are sampled on the surface of this box around the detector.*

3.5.4 Muon flux information

For the 800 ft detector, the total flux into the box from which the muons are sampled is 981.4 s^{-1}, with a mean energy of 89.2 GeV (Figure 37), a mean azimuth angle of 186.5° from the easting direction (Figure 33), a mean zenith angle of 38.8° from the upward vertical direction (Figure 34) and a mean slant depth of 648 m w.e.. This is normalized to a single point on the ceiling of the cavern[32], i.e. it includes no minor correction for different points on the cavern. For a detector enclosure height of 18 m this is equivalent to $\sim$ 48 m w.e. overburden, which is $\sim$ 7.5% of the mean slant depth. Also the vertical depth at various points in the detector can differ due to having an uneven surface profile, causing a maximum variation of $\sim 10 - 15$ m w.e.. Variations in the flux throughout the detector are estimated to be up to 50%. The muons are sampled from the top, ends and sides of a box measuring $169\times29\times31$ m^3 (Figure 35), over a surface area of 17177 m^2, and passed to Geant4. To generate one year of statistics, the required number of muons is 981.4 $\mathrm{s}^{-1} \times 31536000$ s $\approx 3.095\times10^{10}$.

For the 4850 ft detector, the total flux into the box from which the muons are sampled is 0.3074 s^{-1}, with a mean energy of 284.4 GeV (Figure 37), a mean azimuth angle of 172.6° from the easting direction , a mean zenith angle of 26.0° from the upward vertical direction (Figure 34) and a mean slant depth of 4531.7 m w. e.. The flux is once again normalized to the ceiling of the detector, which in this case also contains regions of air.

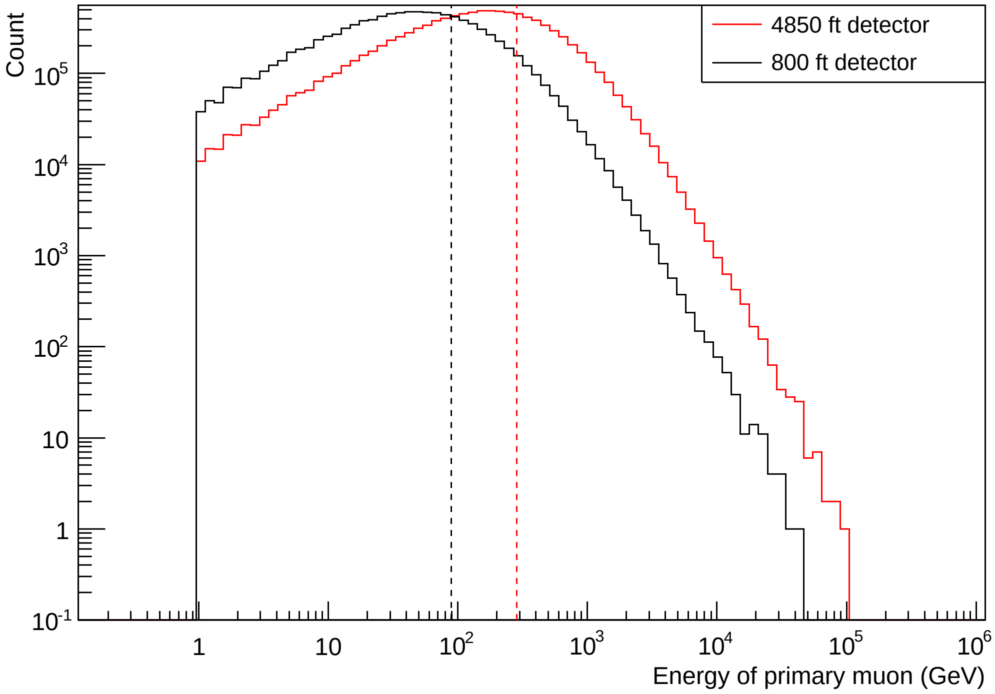

Figure 37: *The energy spectra of* 10^7 *of the primary muons used to generate events for the* 4850 *ft detector (black) and* 800 *ft detector (red). The dashed vertical lines indicate mean energies of* 284.4 *GeV and* 89.2 *GeV for all muons generated. This may be compared to the muon fluxes measured at sea level in Figure 29; at greater depths, fewer muons of low energy survive.*

---

[32] Since the muon flux decreases with increasing depth, normalizing the flux throughout the detector to a point on the ceiling rather than lower down in the detector allows the most conservative estimate of the background rate.

An 18.6 m tall detector enclosure is $\mathcal{O}(1\%)$ of the 4850 ft overburden, so the difference in flux between the ceiling and floor of the detector is negligible. The variation in flux throughout the detector is estimated at $\sim 10\%$ in this instance. The muons are sampled from the top, ends and sides of a box measuring $100\times40\times50$ m^3 (Figure 36), over a surface area of 18000 m^2. To generate one year of statistics, the required number of muons is 0.3074 s^{-1} $\times$ 31536000 s $\approx 9.694\times10^6$.

3.6 Additional details of the simulations

Measures have been taken to reduce the computation time and storage space required without compromising the validity of the results. This section provides context for comparing the results shown in Sections 4.1.1, 4.1.2, 4.2.

3.6.1 Energy and primary muon track limits

If a $K^\pm$ track is detected and it is accompanied by a muon track, it could be assumed that the $K^\pm$ is related to the muon and therefore not a K^+ from a proton decay. It is assumed that a track longer than 0.2 m left by a muon crossing into the detector can easily be identified as such. For the results shown in Sections 4.1.2,4.2, events in which a muon enters either LAr volume and reaches a track length of 0.2 m are not considered anymore and are excluded from further analysis. Furthermore, Eq. 96 indicates that a K^+ produced by a free proton decaying would have a total energy of 599.006 MeV. Since the protons are bound within argon nuclei their nuclear binding energy and Fermi motion must also be considered (Section 3.2). Thus, if a $K^\pm$ is observed in an event in which the total energy deposited significantly exceeds this amount, such a $K^\pm$ would be dismissed.

For the results shown in Sections 4.1.2,4.2, events are stopped and not recorded if the total energy deposited in either LAr volume reaches 2 GeV. This is comfortably in excess of the 1 GeV upper limit on energy deposition allowed for a background $K^\pm$ and any decay descendents it might have (Section 3.2). Figure 38 shows the distribution of the total energy depositions during 2725 events in which a K^+ appears in the 4850 ft detector (based on the 1.341 years of initial results discussed in Section 4.1.1), where this limit has not been applied.

3.6.2 Cut volume

Some primary muons are also skipped before the event even starts, based on their initial position, energy and direction cosines. Figure 39 shows the simulated energy loss of 10^6 muons injected into a large volume of rock. For a few tens of metres / low energies, the maximum muon energy loss is proportional to the distance travelled. Since the muons require only at most a few tens of metres to pass through the detector, their initial energy E_μ is used to calculate their maximum range d:

$$d(cm) = \frac{E_\mu(GeV)}{f_c\rho} \tag{103}$$

where ρ is the rock density of 2.7 g cm^{-3} and f_c=0.002 GeV cm^2 g^{-1} is a conversion factor for the approximate mean muon energy loss due to ionization of 2 MeV cm^2 g^{-1}.

At the start of each event, the initial trajectory of the muon track is extrapolated forwards (Figure 40) and if this ray intersects the detector, the coordinates at which it crosses into and out of the detector are stored. The muon is skipped whenever the

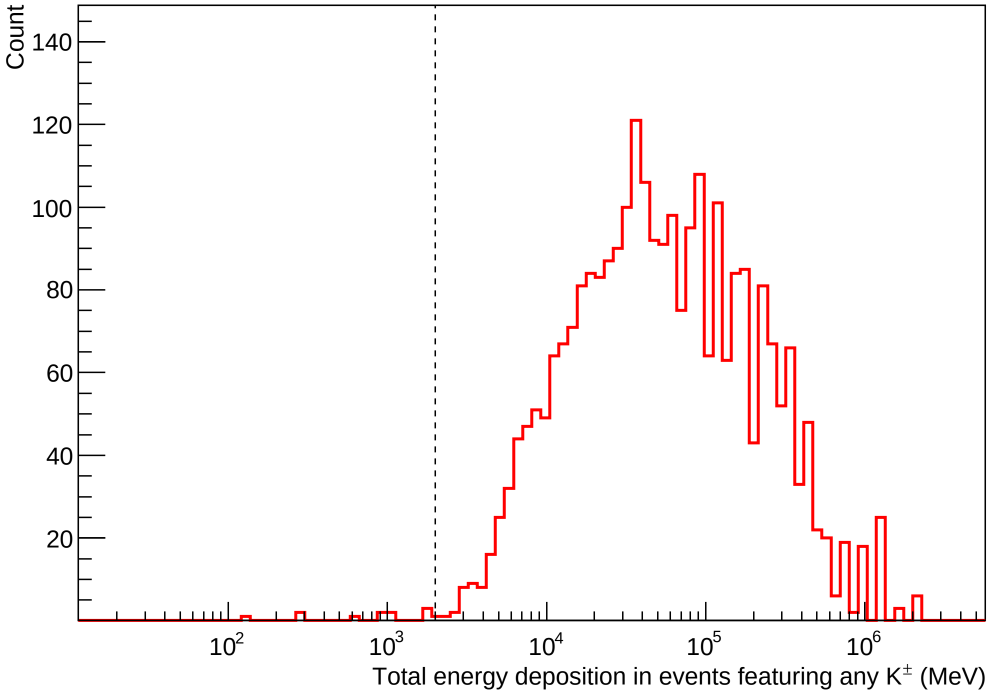

Figure 38: *The distribution of total energy depositions for* 2725 *events in which a* $K^\pm$ *appears in the* 4850 *ft detector. This is based on* 1.341 *years of statistics for which only 'weak' production cuts were used (Section 3.6.3). For later results in Sections 4.1.2, 4.2, events are terminated once the total energy deposition exceeds* 2 *GeV, indicated by the vertical line.*

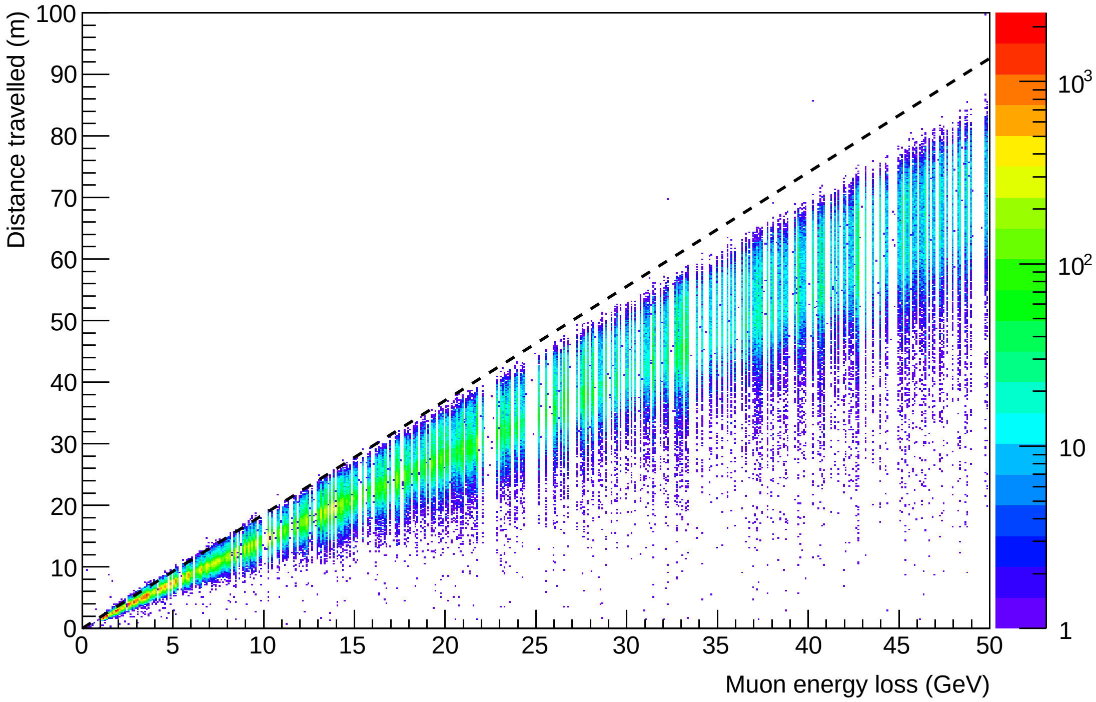

Figure 39: *The relationship between energy lost and distance travelled by* 10^6 *of the primary muons used for the* 800 *ft detector when injected into a large volume of rock. This corresponds to the value of the constant* f_c *in Eq. 103, which is indicated by the dashed line.*

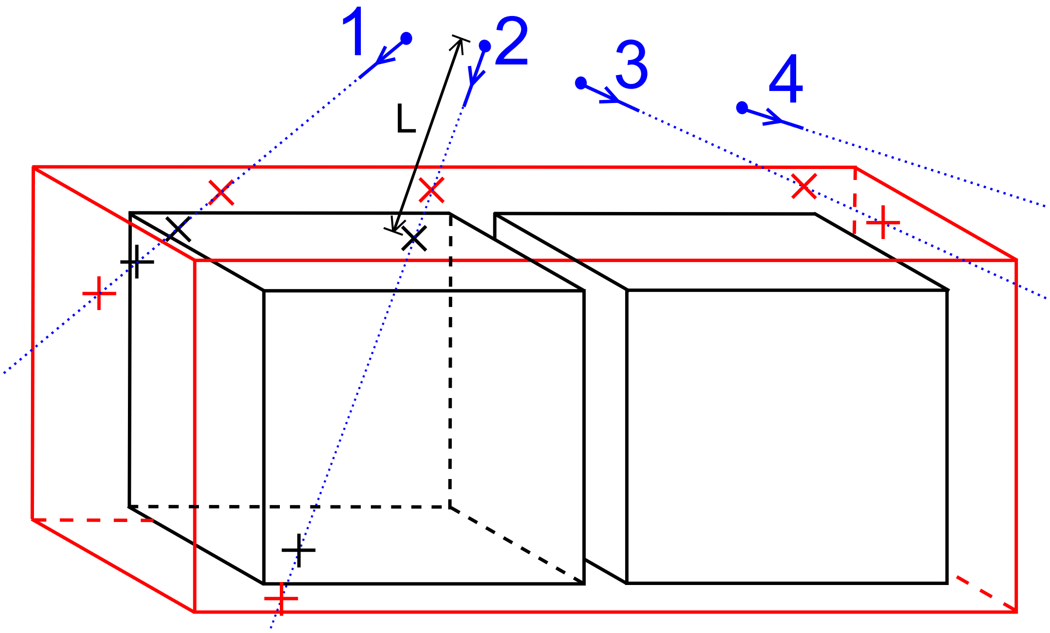

Figure 40: *An illustration of how the cut region used to skip unnecessary primary muons works. Two LAr volumes are shown in black. The cut region is shown in red, which actually surrounds the entire detector enclosure (not shown). Before an event begins, the initial direction of the primary muon is extrapolated forward (any scattering is neglected). The '×' and '+' points indicate the extrapolated muon track entering and exiting a volume respectively, with the colour indicating the relevant volume. The extrapolated trajectory of the muon in case* 1 *enters through the back side face of the LAr and exits a short distance away through the left end face. The entry and exit points in such cases may be less than* 20 *cm apart and if so, the muon would not be skipped. However, in case* 2 *the extrapolated entry and exit points on the LAr volume are further than* 20 *cm apart. If the distance L is under* 50 *m and is also under* 90% *of the maximum distance that the muon could potentially travel (based on its energy, Eq. 103) then the muon is skipped. In case* 3 *the extrapolated track intersects the cut region but not the LAr. This event would be allowed to continue. In case* 4 *the extrapolated trajectory misses the cut region, so this muon would be skipped. A cut volume of* $164 \times 24 \times 24$ m^3 *is used for the* 800 *ft detector, and one of* $83.40 \times 23.20 \times 23.60$ m^3 *for the* 4850 *ft detector. In both cases this leaves* 2.5 *m of rock between each face of the cut volume and corresponding face of the detector enclosure, with roughly a further* 2.5 *m of concrete, polyurethane and steel before reaching the LAr volumes.*

distance between the entry and exit points of the extrapolated ray are more than 0.2 m apart - provided that the distance L between the muon initial position and its detector entry point is less than 90% of the distance the muon could potentially travel (based on Eq. 103), and provided that that L is under 50 m (since muons at wide zenith angles projected to travel a long way close to the long top face of the detector could scatter into it). Figure 41 shows the distribution of these entry-exit distances for $3{\times}10^6$ primary muons.

Muons that miss the LAr volumes by too great a margin to be of any concern are also unnecessary to simulate. Based on measuring the distance from the final position of many K^0_L to a primary muon track (Figure 42), a cuboidal volume can be defined as the region around the detector enclosure that the extrapolated initial trajectory of a primary muon must intersect for the event to avoid being automatically terminated. Since the 800 ft detector enclosure measures $159.0{\times}19.0{\times}19.0$ m^3, a cut volume measuring $164{\times}24{\times}24$

m^3 surrounds it. This means the extrapolated initial trajectory of a muon must not miss the LAr volumes by more than ~5 m (of which 2.5 m is rock surrounding the detector enclosure) to be further considered in the analysis. For the 4850 ft detector with a detector enclosure of 78.4×18.2×18.6 m^3, a cut volume of 83.40×23.20×23.60 m^3 is used. This cut volume has been for all 800 ft results (Section 4.2) and 65.524 years of the total 66.865 years of statistics for the 4850 ft detector (Section 4.1.2). For the latter, the detector enclosure is a curved roof section filled with air (Figure 27). The lower 2.5 m of this air is enclosed by the cut volume. This is a problem for case 3 in Figure 40 since particles created in the air above the cut volume would not be shielded by rock. However, this is not a major problem since the vast majority of the muons stored on the box around the detector (Figure 36) start on a trajectory that does pass through the detector, and in any case the results turn out to be similar to a related study discussed in (Section 4.1.4).

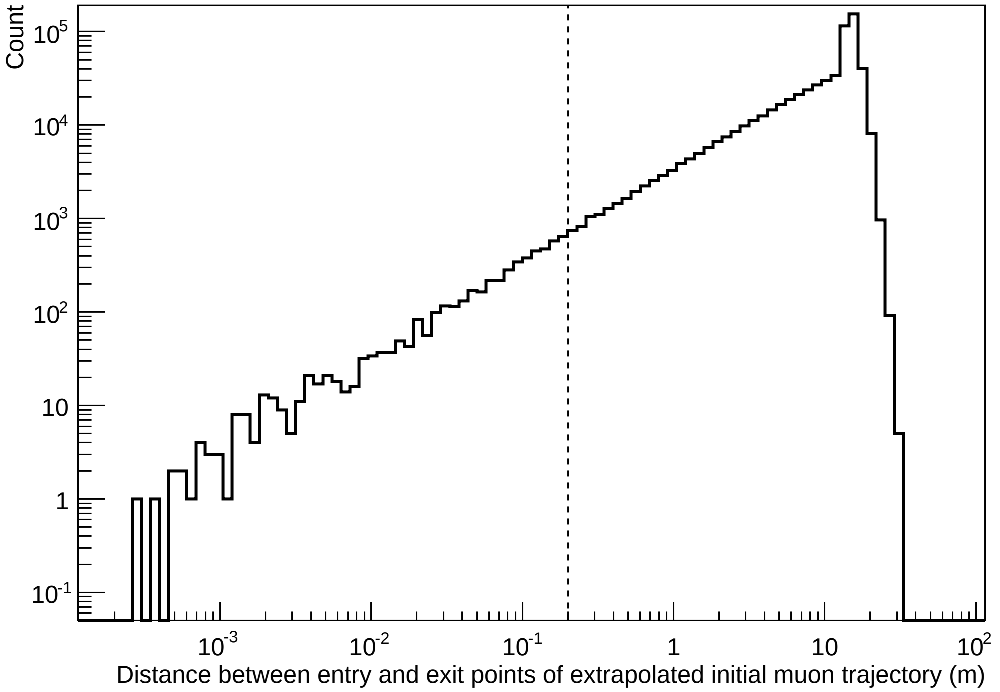

Figure 41: *The distribution of distances between the entry and exit points of the initial muon trajectory when it is extrapolated through the detector. Muons travelling* > 20 *cm (vertical line) are assumed to be detectable and be identifiable as an incoming muon. If the energy of the muon is sufficient to allow it to follow this extrapolated trajectory into and back out of the LAr (neglecting any scattering), then it is not used to generate an event.*

Further potential constraints on muons have been considered, including comparing the energy of any $K^{\pm}$ observed with that of the primary muon responsible (Figure 43) and also comparing the primary muon energy with the distance from the muon track at which the K^{+} first appear (Figure 44). However, since no correlation is observed in either case, they could not form the basis of any further cuts.

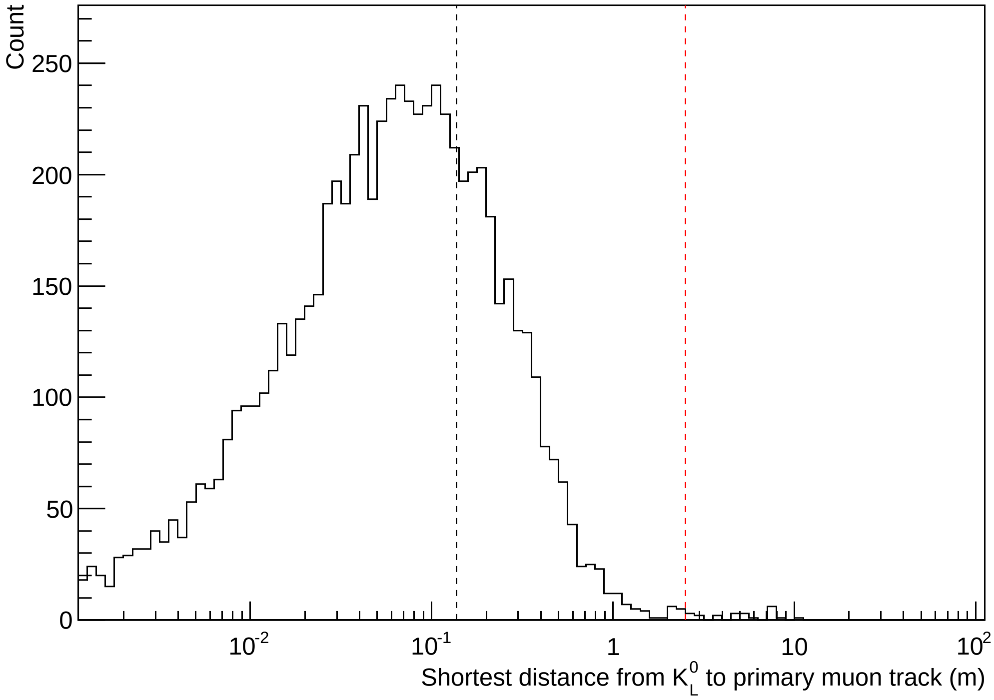

Figure 42: *The radial distance from the final position of* 7117 K_L^0 *(i.e. the point at which they could create a* K^+*) to the track of* 10^6 *muons injected into a large volume of rock. This is used to define the size of the region around the detector that primary muons must be expected to pass through to be deemed worth simulating - any muons missing the detector enclosure by more than* 2.5 *m are not simulated. The red vertical line indicates the* 2.5 *m cut-off and black vertical line indicates a mean of* 0.137 *m.*

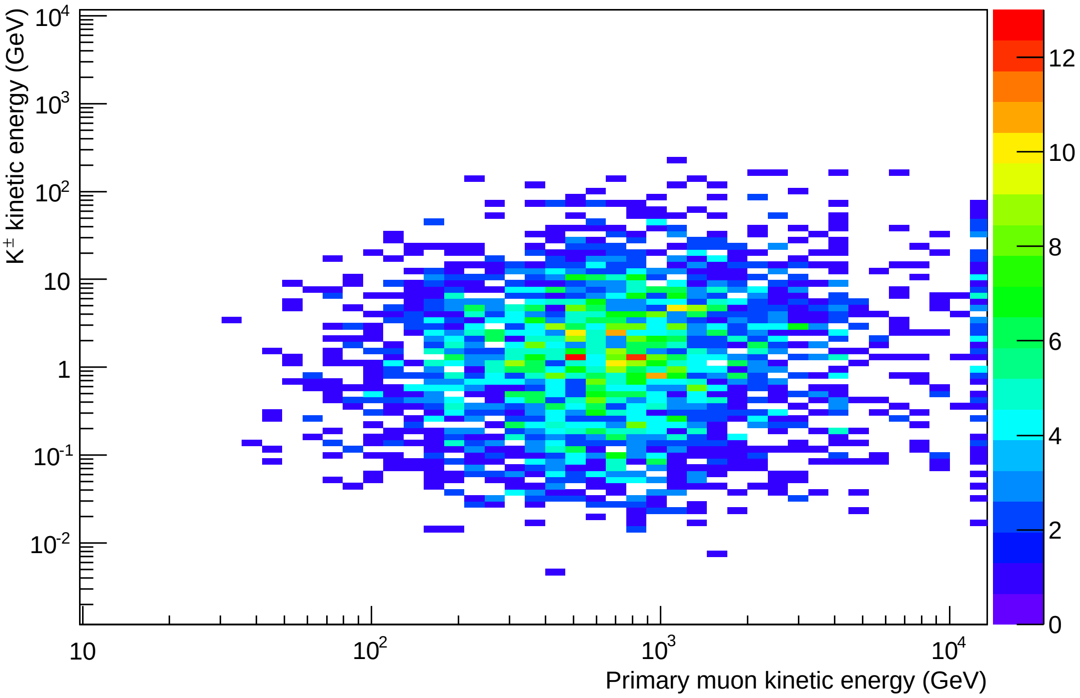

Figure 43: *Primary muon kinetic energy versus* $K^{\pm}$ *kinetic energy for the* 1.341 *years of initial results discussed in Section 4.1.1. The lack of a correlation between these energies means no further energy cut could be imposed on which primary muons to use.*

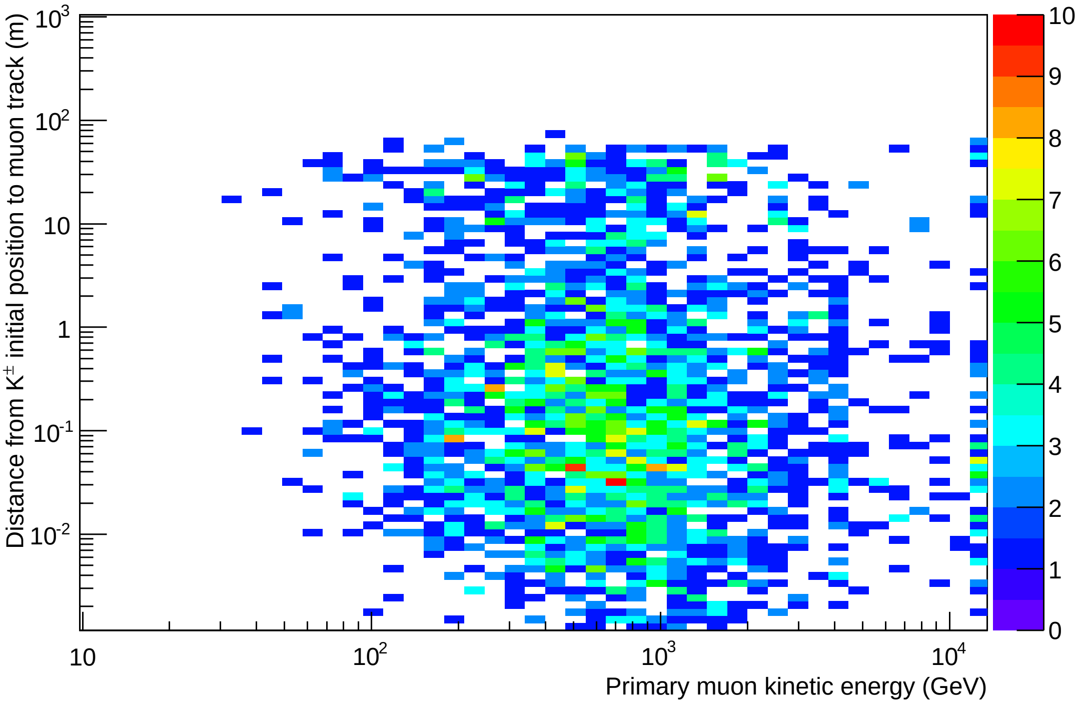

Figure 44: *The distance from the initial position of* 2725 $K^{\pm}$ *to primary muon track vs. the initial energy of the primary muon, in* 1.341 *years of initial results for the* 4850 ft *detector (Section 4.1.1). This was checked in case it could suggest an energy limit on which primary muons to use and thus reduce computation time. Since no correlation is observed, this has not been possible.*

3.6.3 Production cuts

Production cuts have been applied to tracks of photons, electrons and positrons within different parts of each detector to reduce computation time and disk space. Only electrons, positrons and photons capable of travelling a specified distance in a given material are simulated, otherwise the tracks are killed and their energy is deposited at this point.

For the 4850 ft detector, simulated data (Section 4.1.1) corresponding to 1.341 years of detector operation is recorded using the 'weak' production cuts shown in Table 7. A further 65.524 years of simulated data (Section 4.1.2) is recorded using the 'strong' production cuts shown in Table 8. All simulated data gathered for the 800 ft detector (Section 4.2) also has these production cuts imposed.

Table 7: *The 'weak' production cuts applied to the various geometric components of the 4850 ft detector simulation for the first 1.341 years of statistics.*

Detector Component	**Production cuts by particle**		
	γ	e^-	e^+
Rock	700 μm / 0.006 MeV	700 μm / 0.499 MeV	700 μm / 0.476 MeV
Concrete enclosure	700 μm / 0.006 MeV	700 μm / 0.433 MeV	700 μm / 0.419 MeV
Polyurethane insulation	700 μm / 0.001 MeV	700 μm / 0.082 MeV	700 μm / 0.081 MeV
Steel container	700 μm / 0.017 MeV	700 μm / 0.997 MeV	700 μm / 0.926 MeV
LAr detection volume	700 μm / 0.005 MeV	700 μm / 0.272 MeV	700 μm / 0.267 MeV
Air above LAr	700 μm / 0.001 MeV	700 μm / 0.001 MeV	700 μm / 0.001 MeV

Table 8: *The 'strong' production cuts applied to the various geometric components of the 800 ft detector simulation and for 65.524 of the 66.865 years of statistics for the 4850 ft detector.*

Detector Component	**Production cuts by particle**		
	γ	e^-	e^+
Rock	10 cm / 0.088 MeV	10 cm / 59.719 MeV	10 cm / 56.594 MeV
Concrete enclosure	5 mm / 0.016 MeV	5 mm / 2.13 MeV	5 mm / 1.992 MeV
Polyurethane insulation	5 mm / 0.002 MeV	5 mm / 0.269 MeV	5 mm / 0.262 MeV
Steel container	5 mm / 0.048 MeV	5 mm / 6.245 MeV	5 mm / 5.839 MeV
LAr detection volume	5 mm / 0.014 MeV	5 mm / 1.164 MeV	5 mm / 1.103 MeV
Air above LAr (4850 ft only)	5 mm / 0.001 MeV	5 mm / 0.006 MeV	5 mm / 0.006 MeV

3.6.4 Primary muon energy threshold

In the initial 1.341 years of simulated data recorded for the 4850 ft detector, >95% of the 2725 $K^{\pm}$ observed are due to primary muons with energies greater than 135 GeV, as shown in Figure 45. However, these muons account for $\sim$ 50% of the total flux (Figure 37). The additional 65.524 years of simulated data have therefore been gathered using primary muons with energies greater than 135 GeV and the annual rate of background $K^{\pm}$ events is scaled up to account for the missing $\sim$4% of $K^{\pm}$. Despite resulting from lower energy muons, these $K^{\pm}$ that are missed by not simulating muons under 135 GeV are not less energetic than the rest, as can be seen by comparison of Figures 46, 47(and also Figure 43]), so using this economization does not invalidate the results.

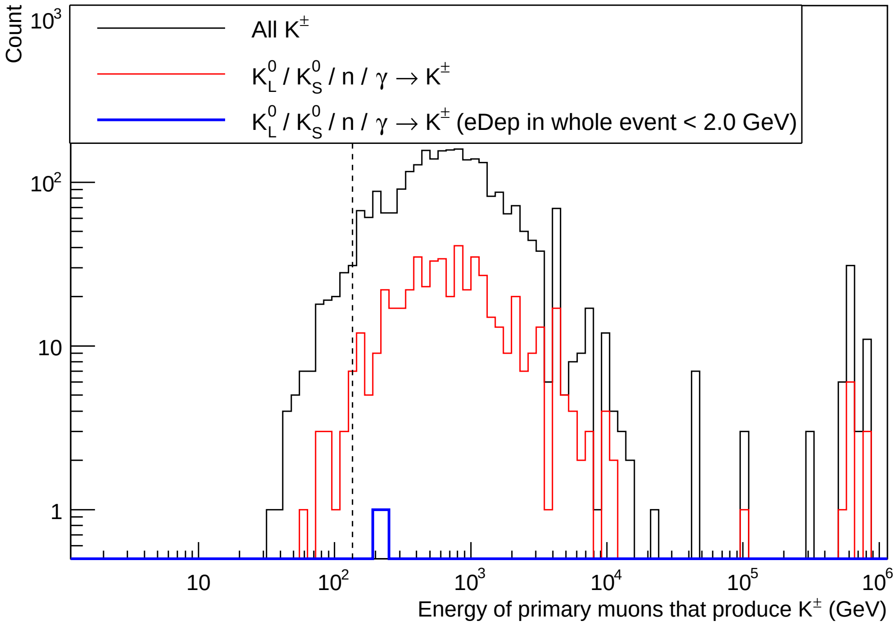

Figure 45: *The energy spectrum of the primary muons responsible for events in which at least one $K^{\pm}$ appeared, based on 1.341 years of initial results for the 4850 ft detector (Section 4.1.1), without the use of the cut volume (Section 3.6.2) and without interrupting any event in which the energy deposition exceeds 2 GeV or the primary muon track exceeds 20 cm. The black histogram includes all $K^{\pm}$-containing events observed. The red histogram includes only events which yielded $K^{\pm}$ that have a neutral parent particle (those that can be connected to the track left by a charged parent particle are rejected). The blue histogram includes the same $K^{\pm}$ as the second series but also requires that the energy deposition in the whole event does not exceed 2 GeV. The vertical line indicates the 135 GeV threshold.*

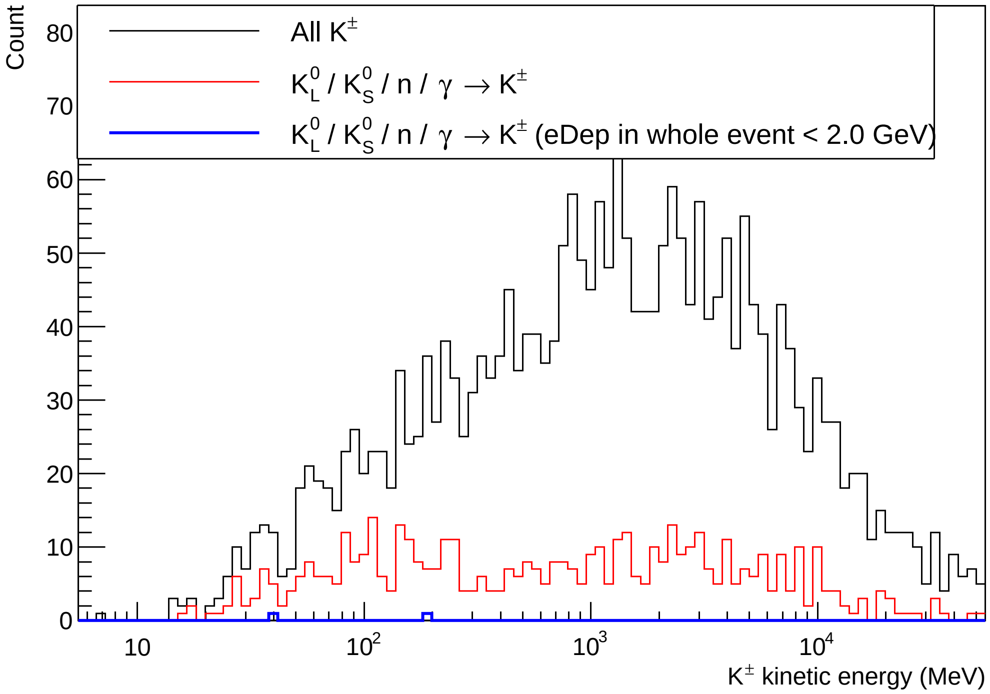

Figure 46: *The energy spectrum of the* $K^{\pm}$ *observed in* 1.341 *years of initial results for the* 4850 *ft detector, only including those* $K^{\pm}$ *that resulted from primary muons with energy higher than* 135 *GeV. The mean energy is* ~ 3.81 *GeV.*

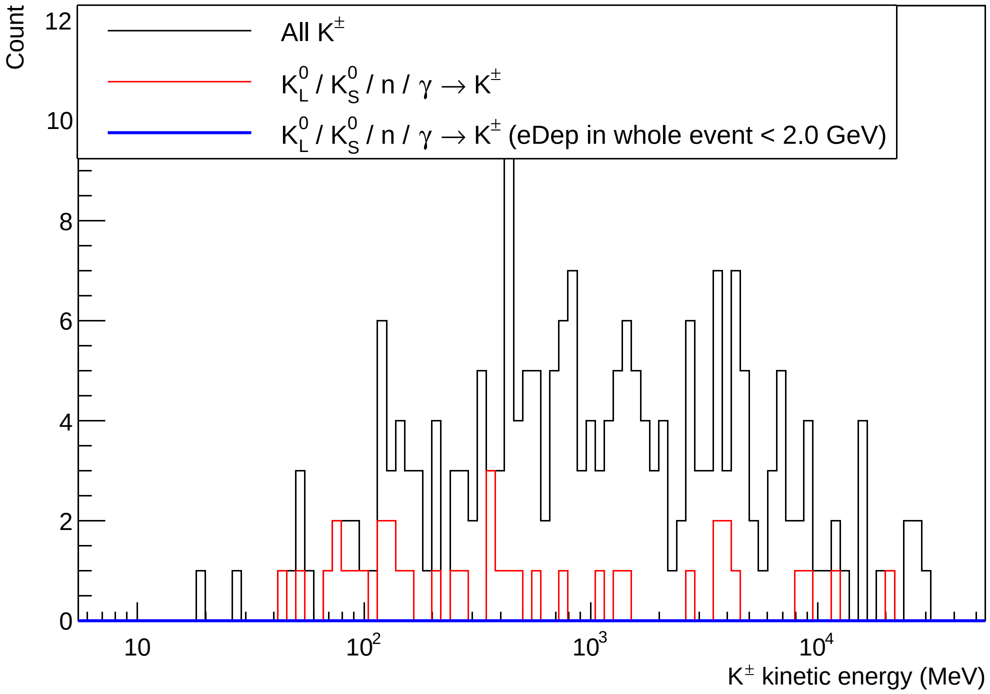

Figure 47: *The energy spectrum of the* $K^{\pm}$ *observed in* 1.341 *years of initial results for the* 4850 *ft detector, only including those* $K^{\pm}$ *that resulted from primary muons with energy lower than* 135 *GeV. The mean energy here is* ~ 3.09 *GeV. It is clear by comparison with Figure 46 that placing this lower limit on the primary muon energy does not affect the energies of the* $K^{\pm}$ *observed.*

4 Results for $p \rightarrow K^{+}\overline{\nu}$ background simulations

Simulated data totalling 66.865 years of statistics has been generated for the 4850 ft detector, which will be discussed in two parts.

The first part involves 1.341 years of statistics for which the minimum production cuts were applied to electrons, positrons and photons (Section 3.6.3). The detector will not be able to efficiently distinguish between K^{+} and K^{-} tracks so K^{-} are also counted. The pre-emptive dismissal of muons using the cut volume around the detector (Section 3.6.2) does not apply to this simulated data, nor were events terminated if the total energy deposition in an LAr volume exceeded 2 GeV, or if the muon track length exceeded 20 cm in the LAr (Section 3.6.1). Consequently a high number of $K^{\pm}$ are observed, the vast majority of which would not have otherwise been. This has been done to provide a more complete picture of what the detector could be expected to observe and also to keep a large number of $K^{\pm}$ available to assess the effect of the cuts.

The second set of results for the 4850 ft detector is an additional 65.524 years using the more stringent production cuts (Section 3.6.3). Only primary muons with energies in excess of 135 GeV have been used to generate events (Section 3.6.4). Also for this set of results, further events have been terminated if the total energy deposition in the LAr exceeds 2 GeV, or the primary muon track exceed 20 cm (Section 3.6.1). This means the $K^{\pm}$ count before any cuts are applied is far less for this set of results than for the initial 1.341 years discussed in the preceding paragraph.

The two sets of results are then compared and combined by first subtracting any $K^{\pm}$ from the initial 1.341 years of simulated data for which the energy deposition, or muon track length, exceeded the event termination limits.

All results are corrected for a feature of Geant4 that allows a $K^{\pm}$ to scatter and then have the same $K^{\pm}$ register as a different $K^{\pm}$ track. Instances of $K^{\pm}$ tracks deemed to have come from a $K^{\pm}$ 'parent' track are therefore subtracted from the total $K^{\pm}$ count, and the parent $K^{\pm}$ track is updated with the various energy depositions and decay information relating to the daughter $K^{\pm}$ track. This avoids overestimating the number of $K^{\pm}$ observed.

4.1 4850 ft Detector

4.1.1 Initial results using 'weak' production cuts

Simulated data totalling 1.341 years of statistics has been recorded for the 4850 ft detector with the least stringent electron/positron/photon production cuts (Section 3.6.3). Primary muons of energy 1 GeV and above are used (Figure 37). From 1.30×10^{7} muon-induced events, a total of 1874 K^{+} and 851 K^{-} are produced (corresponding to an annual rate of 2032 $K^{\pm}$ yr^{-1}). Tables 9, 10 show the number of $K^{\pm}$ observed as various cuts are imposed on which $K^{\pm}$ may be considered as background candidates. Table 9 shows the effect of applying each of these cuts individually, and Table 10 shows the effect of applying each cut in succession. The cuts will be described in more detail and their thresholds varied later in this section, but for now are simply stated and numbered as follows:

(1) No $K^{\pm}$ with charged parent.
(2) No $K^{\pm}$ which start from outside LAr regions where particle information is recorded.
(3) No $K^{\pm}$ with K^{0}_{S} parent if parent of K^{0}_{S} is charged.
(4) No $K^{\pm}$ which appear in same event as any other $K^{\pm}$.
(5) No $K^{\pm}$ with decay chain that lacks a $\mu^{\pm} \rightarrow e^{\pm}\,X$ decay or $K^{\pm} \rightarrow e^{\pm}\,Y$.

(6) No $K^{\pm}$ which appear in same event as muon track longer than 20 cm.
(7) No $K^{\pm}$ where any charged particle in the event fails a 10 cm fiducial cut.
(8) No $K^{\pm}$ where energy deposition by $K^{\pm}$ and any particles branching off from $K^{\pm}$ track before it decays exceeds 250 MeV.
(9) No $K^{\pm}$ where energy deposition by $K^{\pm}$ and all particles branching off from $K^{\pm}$ track exceeds 1000 MeV.
(10) No $K^{\pm}$ where energy deposition in rest of event exceeds 50 MeV.

Table 9: *The total number of $K^{\pm}$ seen in* 1.341 *years of simulated data generated for the* 4850 *ft detector using 'weak' production cuts (Section 3.6.3). The subtotal of K^{-} are shown in brackets. This table shows the number of background candidates that survive as cuts (1) - (5) are imposed separately (rather than successive cuts as in Table 10). Quantitative cuts based on muon track length, track position and energy deposition are dealt with in later tables.*

Total $K^{\pm}$ seen	No $x^{\pm} \to K^{\pm}$	No Ext $\to K^{\pm}$	No $x^{\pm} \to K^0_S \to K^{\pm}$	Only 1 $K^{\pm}$ in event	Decay chain
2725 (851)	734 (285)	2541 (791)	2672 (841)	1350 (478)	2634 (798)

Table 10: *As in Table 9 but as successive cuts (rather than stand-alone cuts) are imposed.*

Total $K^{\pm}$ seen	No $x^{\pm} \to K^{\pm}$	No Ext $\to K^{\pm}$	No $x^{\pm} \to K^0_S \to K^{\pm}$	Only 1 $K^{\pm}$ in event	Decay chain
2725 (851)	743 (287)	550 (225)	502 (215)	422 (180)	404 (171)

Cut (1): Any $K^{\pm}$ track connected to the track of a charged particle cannot mimic a proton decay, so only those $K^{\pm}$ produced by a neutral parent particle are a concern. Imposing this cut alone reduces the total background by 73% by removing any $K^{\pm}$ with charged parent particles (predominantly $\mu^{\pm}$ and $\pi^{\pm}$). Table 12 shows a summary of the parent particles responsible for all the $K^{\pm}$ observed. Figure 48 shows the distribution of track lengths of all the charged parents particles of the $K^{\pm}$, indicating that a TPC with a spatial resolution of better than 1 cm[33] will be able to successfully reject approximately 95% of these $K^{\pm}$.

Cut (2): Any $K^{\pm}$ created outside of the LAr that then cross inside can also be disregarded. On its own this cut provides a 7% total background reduction, leaving only those with charged and neutral parent particles (which are mostly K^0_L as well as some K^0_S, n, γ). When applied after dismissing those $K^{\pm}$ with charged parents, this succession of cuts reject 80% of the initial overall $K^{\pm}$ background.

Cut (3): Due to the short range of the K^0_S, any $K^{\pm}$ with a K^0_S parent and a charged grandparent are also treated as having a charged parent and therefore rejected. This cut when applied on its own causes a reduction in the total $K^{\pm}$ background of 2%. When applied after the previous two cuts the overall reduction in background is 82%.

Cut (4): The background is reduced further by rejecting any $K^{\pm}$ if they are not the only $K^{\pm}$ in that event. This cut removes 41% of the total background when applied on its own. When applied in succession with the previous cuts, the overall reduction in background is 85%. Figure 49 shows the relationship between the number of kaons in the event and the energy of the primary muon responsible. Tracks that are too close to each other become more difficult to separate, so with this in mind, Figure 50 shows

---

[33] The TPC readout wires are anticipated to be 3-6 mm apart.

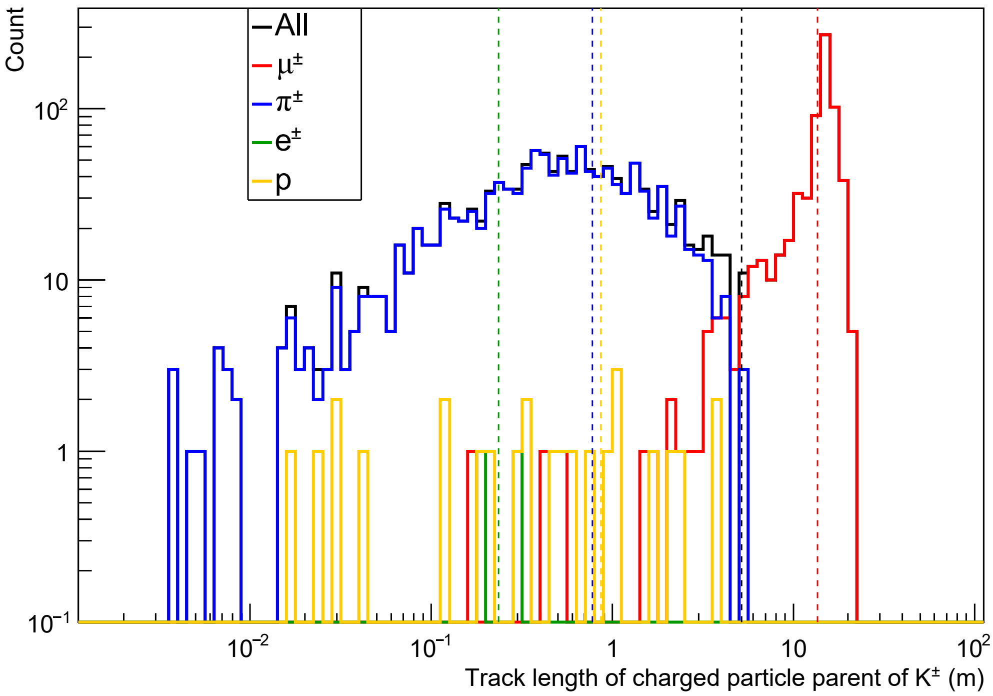

Figure 48: *The distribution of the track lengths of the various charged parent particles of the $K^{\pm}$ observed. Cut (1) rejects $K^{\pm}$ with charged parent particles; 97% of these charged parent particles are $\pi^{\pm}$ (63%) or $\mu^{\pm}$ (34%)(Table 12). 100% of these $\mu^{\pm}$ have track lengths in excess of 10 cm, and 96% / 94% of the $\pi^{\pm}$ have tracks exceeding 2 cm / 5 cm. Thus, for a detector with a spatial resolution of < 1 cm this will be able to reject ~ 95% of $K^{\pm}$ with charged parents.*

the distance between the initial positions of $K^{\pm}$ in these multiple-$K^{\pm}$ events. The angle between the tracks is also important, since only tracks with small angles between them are difficult to separate. Figure 50 therefore is also plotted with maximum angles of 45°, 22.5° and 10° imposed. Table 11 summarises the efficiency of this cut for a selection of minimum track separations and maximum angles between tracks. Assuming the TPC has 10° angular resolution, this cut efficiency is $97-99$% depending on the minimum allowed initial distance between the kaons (the spatial resolution of the TPC is assumed < 1 cm due to the anticipated wire spacing being 3-6 mm and also the $K^{\pm}$ track identification efficiency is assumed to be 100%).

Table 11: *Cut(4) involves rejecting events featuring >1 $K^{\pm}$, but tracks that are too close together would become more difficult to separate; the detector is assumed to have better than 1 cm spatial resolution due to the $3-6$ mm wire spacing. The distance between the starting coordinates of the $K^{\pm}$ tracks in such events is shown in Figure 50. Even if the tracks start close together, if the $K^{\pm}$ travel at wide enough angles to each other they are still easily distinguishable, so a selection of minimum angles below which this cut is assumed inapplicable have been tested.*

	1 cm	2 cm	3 cm	4 cm	5 cm
$\theta < 10.0°$	99.19%	98.53%	98.10%	97.58%	96.92%
$\theta < 22.5°$	98.89%	98.00%	97.12%	96.41%	95.50%
$\theta < 45.0°$	98.84%	97.73%	96.61%	95.81%	94.75%

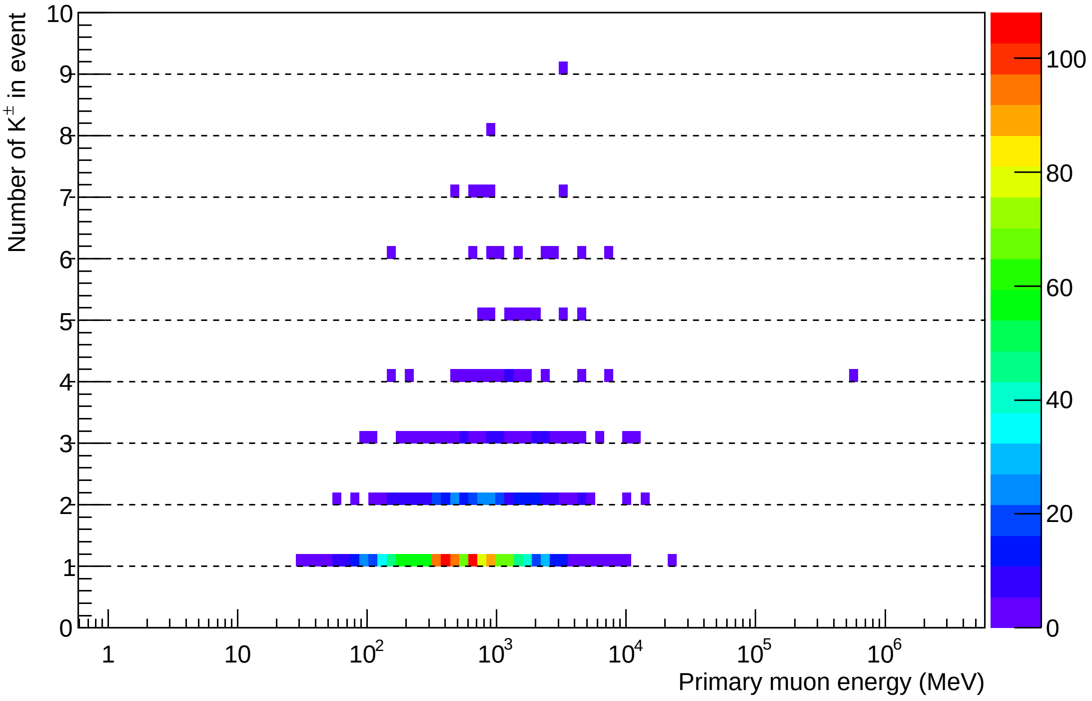

Figure 49: *The relationship between the number of $K^{\pm}$ observed in the LAr in a given event and the energy of the primary muon that started the event, for the initial* 1.341 *years of results for the* 4850 *ft detector. Cut (4) involves dismissing any events featuring more than* 1 *$K^{\pm}$.*

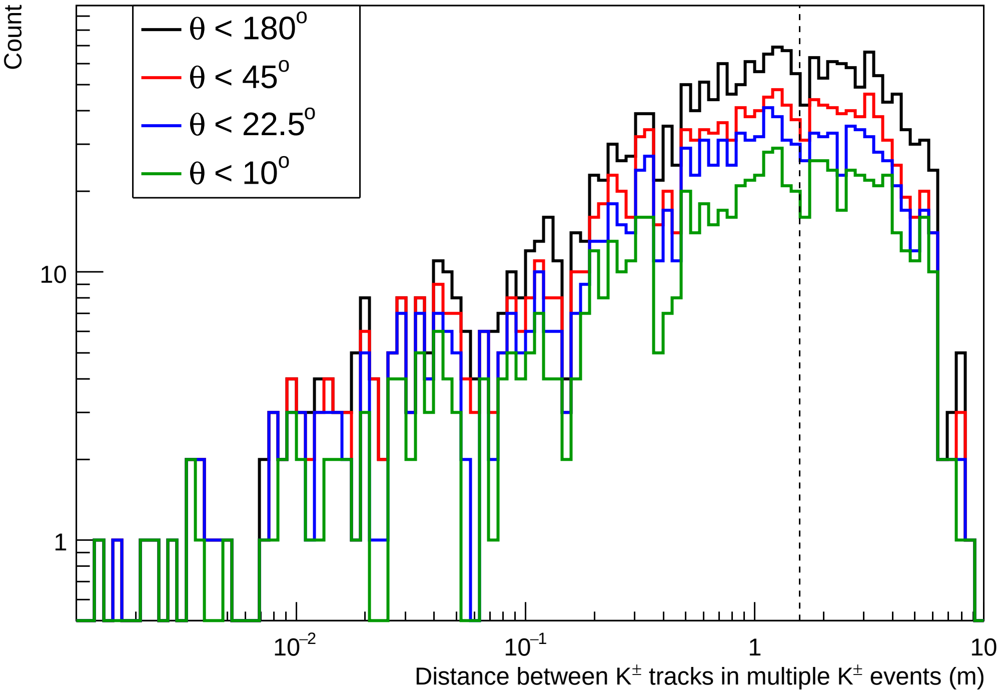

Figure 50: *The distribution of distances between the initial position of $K^{\pm}$ tracks in events that feature at least two $K^{\pm}$ tracks. The dashed vertical line indicates a mean separation of* 1.57 *m. Also only tracks that start close together and travel close to parallel with each other would be difficult to distinguish so this plot shows instances where the angle between $K^{\pm}$ tracks of $\theta < 45°, < 22.5°$ and $< 10°$. Table 11 summarises the percentage of tracks starting at least* 1, 2, 3, 4 *and* 5 *cm apart for each of these angles.*

Cut (5): Although the K^+ and K^- tracks cannot be distinguished directly in an unmagnetized TPC, it is still possible to distinguish them based on their decay chain. Approximately 67% of $K^\pm$ decays produce a $\mu^\pm$ [287]. Also 28% of $K^\pm$ decays produce a $\pi^\pm$, which will also produce a $\mu^\pm$ in >99% of their decays [287]. Therefore if a $K^\pm$ decays in a vacuum, there is a 95% probability of a $\mu^\pm$ being in the chain of particles that descend from the decaying $K^\pm$ (as either a 'daughter' or 'grand-daughter' of the $K^\pm$, assuming these charged pions all decay[34]). When muons decay it is essentially always via $\mu^- \to e^- \, \overline{\nu}_e \, \nu_\mu$ ($\mu^+ \to e^+ \, \nu_e \, \overline{\nu}_\mu$), however, unlike the μ^+ or π^+ that descend from a decaying K^+, the μ^- and π^- from a K^- can be captured by argon nuclei. This makes it unlikely (see below) that a μ^- will get to decay to an e^-. Thus, the observation of the decay chain $K \to \mu \to e$ or $K \to \pi \to \mu \to e$[35] would indicate that a K^+ was in fact probably being observed. Conversely a decaying K that is not followed by a decay chain featuring a $\mu \to e$ decay would indicate the presence of a K^-.

Table 12: *The types and amounts of parent particles from which the $K^\pm$ observed were created. The first number/percentage in a given cell is for the parents of all $K^\pm$, whereas the number/percentage in parentheses is the subtotal for parents of K^- only. Cut (1) involves rejecting any $K^\pm$ with a charged parent. Cut (2) involves rejecting $K^\pm$ that start outside the LAr and cross inside (labelled 'External' in this table).*

$K^\pm$ parent	Count	Percentage
π^+	632 (130)	23.19% (15.28%)
π^-	619 (172)	22.72% (20.01%)
μ^-	393 (147)	14.42% (17.27%)
K^0_L	355 (183)	13.03% (21.50%)
μ^+	280 (98)	10.28% (11.52%)
K^0_S	73 (14)	2.68% (1.65%)
n	63 (10)	2.31% (1.18%)
γ	58 (18)	2.13% (2.12%)
p	28 (6)	1.03% (0.71%)
K^-	17 (0)	0.62% (0%)
K^+	11 (11)	0.40% (1.29%)
e^-	2 (0)	0.07% (0%)
External	194 (62)	7.12% (7.29%)
Total	2725 (851)	100% (100%)

Muon decays occur with a mean lifetime of ~2.2 μs [287], whereas the muon capture (via a CC weak interaction of $\mu^- \, p \to n \, \nu_\mu$) lifetime in LAr is ~537 ns [288] (i.e. 24% of the decay lifetime). Upon being stopped a muon will be captured by nuclei 76% of the time [289] or decay the remaining 24% of the time. So, if one requires a background kaon to have $\mu \to e$ in its decay chain, then every K^- that decays to π^- within LAr will be eliminated from the background count (thereby rejecting 28% of all decaying K^-) as well as 76% of K^- that decay directly to μ^- ($0.76 \times 67\% \approx 51\%$ of all decaying K^-). This suggests a combined total of $51\% + 28\% = 79\%$ rejection of all K^- that decay[36].

Similarly, since K^+ and K^- tracks cannot be directly distinguished, this cut also rejects any K^+ that decays without the observation of either a e^+ track produced by its own decay, or a $\mu^+ \to e^+$ decay further down the decay chain. This is the case for a small

---

[34] The remaining 5% of $K^\pm$ decays involve $K^\pm \to e^\pm \, X$ (where X denotes any other products); any $K^\pm$ decaying this way is still counted as background.

[35] Here irrelevant decay products at each stage have been omitted and the +/− sign of each particle cannot be directly determined.

[36] Rather than the original 95% estimate in the previous paragraph that assumed all π^- and μ^- would be absorbed (as in vacuum).

number of K^+ decays; this cut rejects $\sim 1.7\%$ of K^+ (both background and signal) in addition to eliminating the majority of K^- that decay.

Tables 13, 14, 15 give a summary of the $K^\pm$ decays observed. Applying this cut on its own gives a total background reduction of 3% (1.7% and 6% of the initial K^+ and K^- observed) (Table 9). This is a small reduction owing to the fact that few K^- are found to decay.

Table 13: *The number of charged kaons that decay via specific channels in the entire Geant4 "world" volume (rather than just the LAr volumes) out of the* 2725 *that were observed for the initial* 1.341 *years of initial results with the* 4850 *ft detector. Each cell in the first row shows the total decay count observed for* $K^\pm$*, as well as the* K^- *subtotal in parentheses. The second row shows the percentage of* K^+ *decays each channel accounts for, with the corresponding percentage for* K^- *in parentheses. The third row shows the percentage expected for each channel according to the Particle Data Group [287], which are in agreement with the percentages observed. Of the total* 2725 $K^\pm$ *observed,* 51% *are found to decay, with the remainder of* $K^\pm$ *tracks coming to an end with new particles being produced via an inelastic scattering process. Although* 31% *of all recorded charged kaon tracks are* K^-*,* 95% *of the tracks that end in decay are* K^+*. The* 1397 $K^\pm$ *(of which* 72 *are* K^-*) that decay do so via the following channels:*

$K^\pm \to e^\pm\ X$	$K^\pm \to \mu^\pm\ \nu_\mu/\overline{\nu}_\mu$	$K^\pm \to \mu^\pm\ \nu_\mu/\overline{\nu}_\mu\ \pi^0$	$K^\pm \to \pi^\pm\ \pi^0$	$K^\pm \to \pi^\pm\ \pi^0\ \pi^0$	$K^\pm \to \pi^\pm\ \pi^\pm\ \pi^\mp$
85 (12)	885 (45)	46 (6)	315 (9)	0 (0)	67 (0)
5.4% (16.7%)	63.4% (62.5%)	3.0% (8.3%)	23.1% (12.5%)	0% (0%)	5.1% (0%)
5.1%	63.6%	3.4%	20.1%	1.8%	5.6%

Table 14: *The same as Table 13 but with some decay channels combined together. The second column corresponds to the first column in Table 13, the third column corresponds to columns* 2 *and* 3 *in Table 13, and the fourth column corresponds to the remaining columns in Table 13. The subtotal of* K^- *are shown in brackets. As anticipated, the* $K^\pm$ *decays produce a* $\mu^\pm$ *or* $\pi^\pm$ *in* 94% *of cases with the remaining* 6% *accounted for by decays in which* $e^\pm$ *are produced.*

Total	$K^\pm \to e^\pm$	$K^\pm \to \mu^\pm$	$K^\pm \to \pi^\pm$
1397 (72)	85 (12)	931 (51)	382 (9)
-	5.4% (16.7%)	66.4% (70.8%)	28.1% (12.5%)

Table 15: *As in Table 14 but only including instances where the decay chain includes* $\mu^\pm \to e^\pm$ *or the* $K^\pm$ *decaying directly to* $e^\pm$*. Although* 51% *of all* $K^\pm$ *are observed to decay (Table 13), only* 94% *of these decays have these decay chains (owing to the nuclear capture of the muon or the pion before either are able to decay) and only* 85% *have these decay chains and have them fully contained within the LAr volumes.*

	Total	$K^\pm \to e^\pm$	$K^\pm \to \mu^\pm \to e^\pm$	$K^\pm \to \pi^\pm \to \mu^\pm \to e^\pm$
Overall	1322 (12)	85 (12)	881 (0)	368 (0)
Within LAr	1192 (9)	63 (9)	784 (0)	345 (0)

The cumulative effect of these cuts ((1)-(5)) is to remove ~85% of the total background. The remaining $K^\pm$ background can then be eliminated by quantitative cuts based on the track length of the primary (or other) muon, the proximity of charged particle tracks to the sides of the LAr volumes and also the various classes of energy deposition. These cuts are actually far more effective and easier to implement than those already discussed. However, the cuts have been introduced in this order so the weaker cuts could be applied to greater numbers of background events and thus more clearly demonstrate the effect that the weaker cuts have. An alternative cut sequence in which the muon track length and fiducial cuts are the first cuts applied is discussed in Section 4.1.3 (for the main set of results totalling 66.865 years).

Table 16: *The number of* $K^{\pm}$ *passing the cuts shown in Table 10 as further cuts are applied. This is for* 1.341 *years of statistics gathered using the weak production cuts on electrons, positrons and photons (Section 3.6.3), no pre-emptive dismissal of any muons (Section 3.6.2) and no event termination for energy deposition exceeding* 2 *GeV, or primary muon track length exceeding* 20 cm*, in the LAr (Section 3.6.1). The subtotal of* K^{-} *are shown in brackets. This may be compared to Table 17, for which the two latter cuts have been imposed. Columns* 3-4 *show the number of surviving* $K^{\pm}$ *as successive cuts are applied. Columns* 5 *and* 6 *show columns* 2 *and* 4 *normalized to an annual rate, with the final column containing only the total* $K^{\pm}$ *rate at* 90% *C.L..*

				Annual rate	
Parent of $K^{\pm}$	$K^{\pm}$ before cuts	μ track <20 cm	<10 cm to LAr edge	Before cuts	After cuts
Total	404 (171)	1 (0)	0 (0)	301 (127)	0-1.82
K_L^0	286 (145)	0 (0)	0 (0)	213 (108)	-
K_S^0	23 (4)	1 (0)	0 (0)	17 (3)	-
n	41 (7)	0 (0)	0 (0)	31 (5)	-
γ	54 (15)	0 (0)	0 (0)	40 (11)	-

Table 16 contains only the $K^{\pm}$ that satisfy the cuts imposed in Table 10 and shows the number that survive as successive cuts on muon track length and track location are applied.

Cut (6): The third column in Table 16 shows the number of $K^{\pm}$ for which the primary muon travelled no more than 20 cm in the LAr. A threshold of 20 cm is chosen to ensure the track is correctly identifiied as a muon track. Figure 51 shows the distribution of muon track lengths within either LAr volume. This is a highly efficient cut that rejects >99% of background candidates since most primary muons strike an LAr volume directly rather than just passing in and out close to the edge (Figure 41), or missing entirely, and only 2.6% of muons that entered the LAr were stopped within it.

Although a threshold of 20 cm has been used for this cut, this may be unnecessarily conservative and could potentially be reduced. A selection of other thresholds have therefore been tested. The effect they have on the annual rate of background $K^{\pm}$ is shown in Figure 52. With the cut threshold at 20 cm, approximately 5.2 $K^{\pm}$ yr^{-1} out of the initial 2032 $K^{\pm}$ yr^{-1} survive; for thresholds of 10 cm and 5 cm this 3.0 $K^{\pm}$ yr^{-1} and 2.2 $K^{\pm}$ yr^{-1}. Making the threshold shorter therefore only allows a very minor improvement in background rejection. However, short track could potentially be misidentified so a conservative 20 cm threshold is used.

To estimate the amount of signal events this cut would mean losing, each of the $K^{\pm}$ observed have been used to generate a new event (using their initial position, energy and direction of travel). This has been done to be certain of a 'clean' event, free of any possible

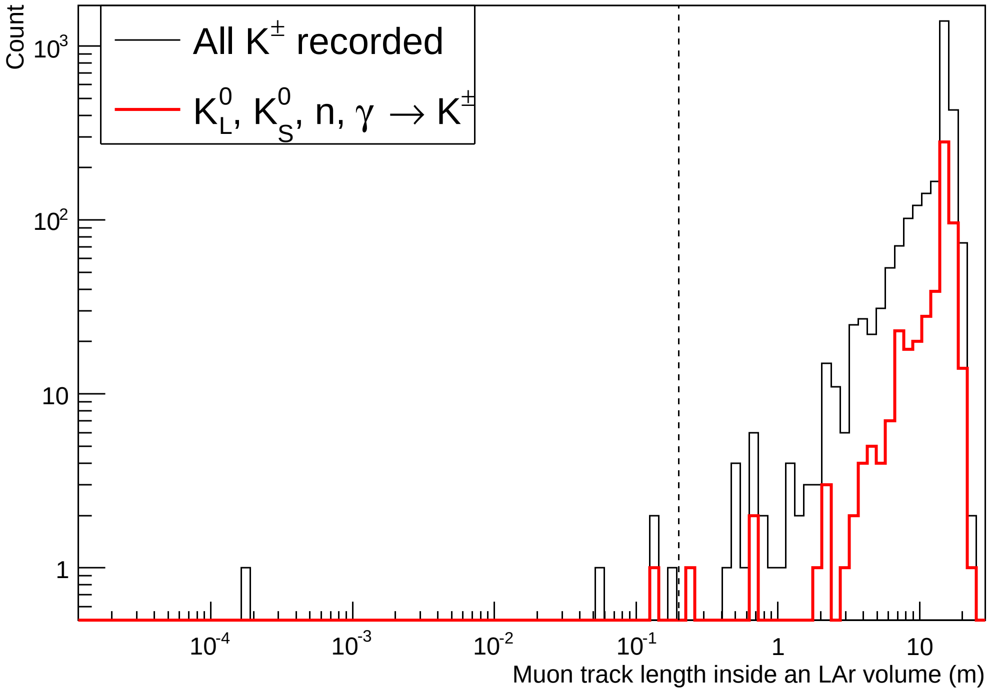

Figure 51: *The distribution of muon track lengths in* $K^{\pm}$ *events in either LAr volume for* 1.341 *years of initial results with the* 4850 *ft detector. The limit above which a* $K^{\pm}$ *would be rejected (cut* (6)*) is placed at an (already conservative)* 20 *cm but this could be adjusted significantly with negligible effect on the number of* $K^{\pm}$ *dismissed (Figure 52).*

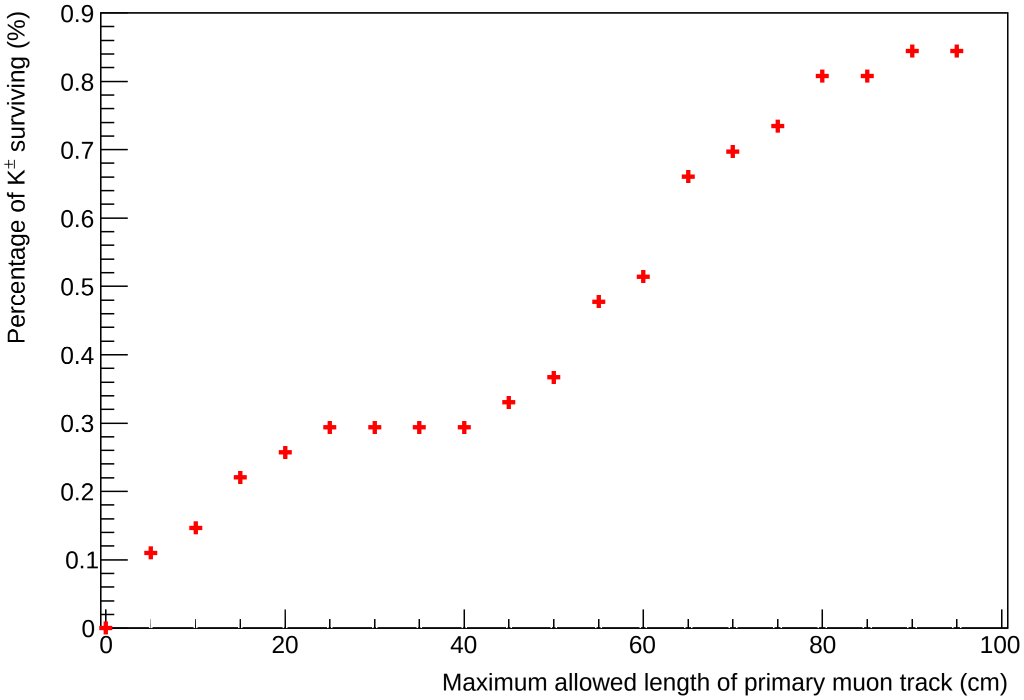

Figure 52: *The relationship between the maximum allowed muon track length before an event is rejected and the percentage of* $K^{\pm}$ *that survive this cut, for* 1.341 *years of initial results with the* 4850 *ft detector. A cut threshold of* 20 *cm eliminates* 99.7% *of background events (i.e.* ~ 5.2 $K^{\pm}$ yr^{-1} *survive), but this rises to* 99.9% *(i.e.* ~ 2.2 $K^{\pm}$ yr^{-1} *survive) if the threshold is* 5 *cm.*

complications from a cosmic muon. The distribution of the track lengths of all muons observed in these events is shown in Figure 53. The vast majority of muons observed have come from the decay of either the primary kaon or a charged pion, so although many of these muons have track lengths in excess of 20 cm, they would be associated with a K^+ produced by a decaying proton. However, muons produced by neutral parent particles can appear to the detector to not be a descendent of the primary kaon; there are four such muon tracks observed (all produced by K^0_L decays), of which three extend further than 20 cm in the LAr. Since 2725 of these kaon-initiated events have been generated, a 20 cm threshold for this cut therefore suggests a signal loss of 0.1%.

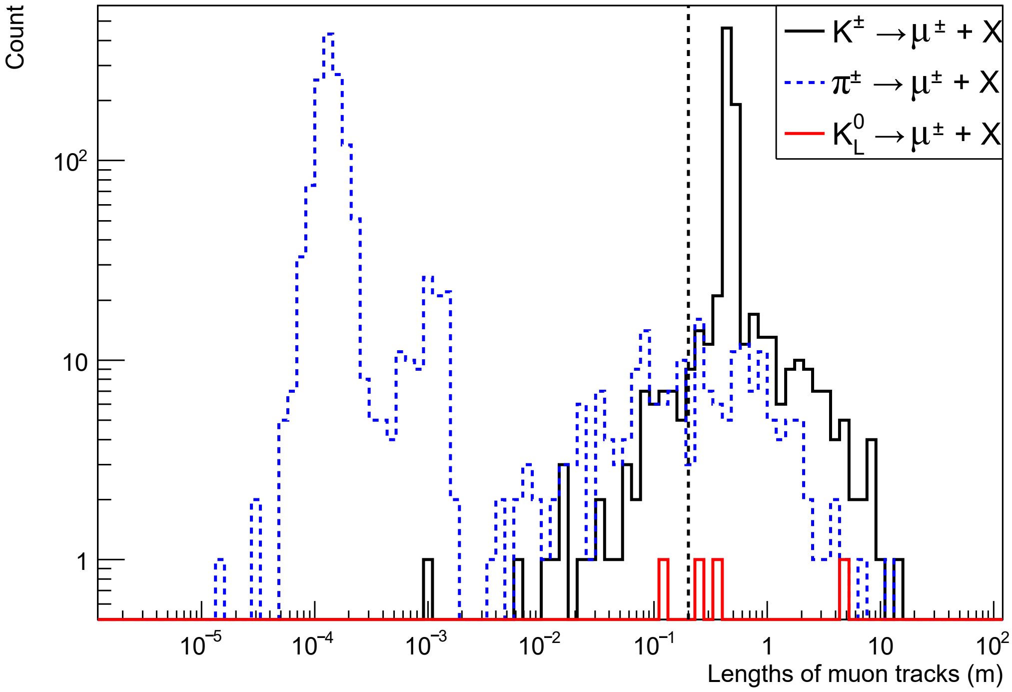

Figure 53: *The distribution of muon track lengths in additional events generated using the already-observed* $K^\pm$ *as the primary particle to start the event. Three sources of muon production have been observed, namely the decays of charged kaons and pions, and that of long-lived neutral kaons. The two peaks correspond to the signficant difference in kaon and pion mass, although the part of the* $\pi^\pm \to \mu^\pm + X$ *histogram above* 10^{-2} *m matches that of* $K^\pm \to \mu^\pm$ *since a* $\pi^\pm$ *is also one of the common products of a kaon decay. These pions can then decay to muons that have additional energy from the kaon rest mass, and the corresponding track length. Muon tracks connected to the original* $K^\pm$ *track are not problematic, but those apparently disconnected from it (due to being created by neutral particles) could result in such signal events being erroneously rejected. The third histogram shows the track lengths of muons produced by* K^0_L *decays; there are four such tracks, of which three are rejected by a* 20 *cm threshold for cut (*6*). Since there have been* 2725 *of these additional kaon-induced events simulated and three fail to survive this cut, the signal loss due to this cut is estimated at* 0.1*%.*

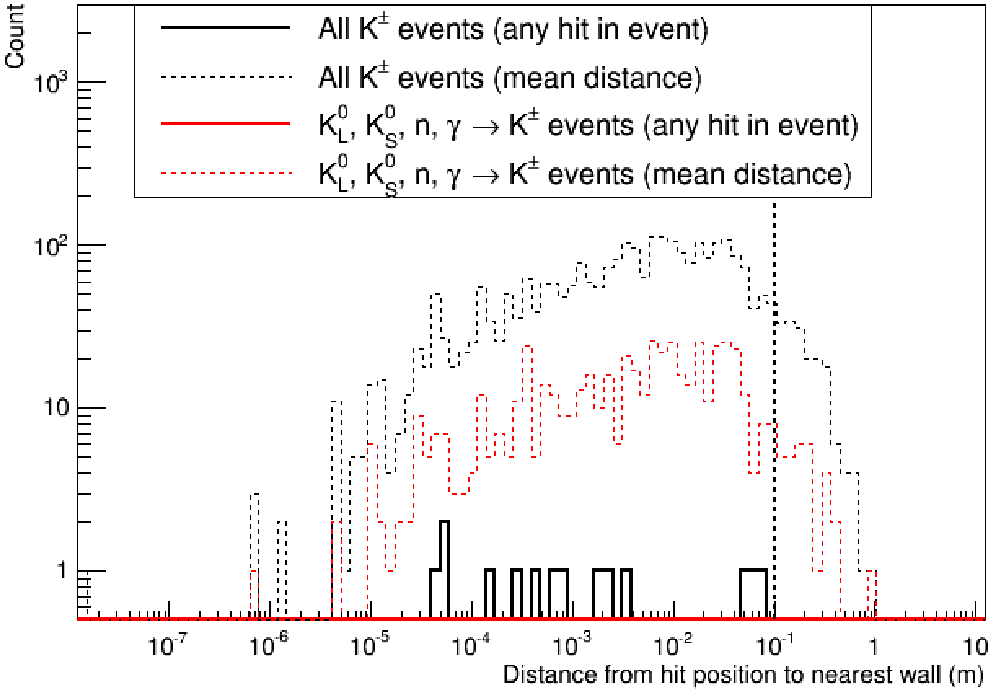

Figure 54: *The distribution of the shortest distance (in each event that features a* $K^\pm$*) between a charged particle track and the nearest face of the LAr volume they appear in (cut (7)), for the* 1.341 *years of initial simulated data in the* 4850 *ft detector. No other cuts are applied. Since each of these volumes measures* $28.56 \times 13.98 \times 14.00$ m^3*, this distance can be no more than* 6.98 *m. The vertical line indicates the fiducial cut of* 10 *cm, so any* $K^\pm$ *to the left of this line are dismissed. The solid red and black lines are the series to which this cut applies, but also shown for comparison are dashed lines which indicate the mean distance to the nearest face rather than the shortest distance. This cut removes all* $K^\pm$ *observed; even if the threshold was lowered from* 10 *cm to* 1 *cm only* 3 $K^\pm$ *(i.e.* 2.2 yr^{-1}*) would survive. The vast majority of* $K^\pm$ *are accompanied by charged particles originating outside of the detector that cross inside and register a hit just inside (in particular, the primary muon used to start the event), causing this distance to be small.*

Cut (7): The fourth column in Table 16 is a fiducial cut, requiring that no $K^\pm$ or other tracks be within some distance of the nearest face of whichever active LAr volume the tracks appear in; partially contained events will be disregarded. Figure 54 shows the distribution of these distances. With no other cuts applied, a 10 cm threshold is enough to reject 100% of the $K^\pm$ observed. Figure 55 shows the distribution of track lengths that start within 10 cm of an LAr volume face. This cut especially complements the previous cut on muon track length, which itself leaves only events for which muon tracks occur close to, or outside of, the edges of the LAr volumes. Even if this cut threshold was lowered from 10 cm to 1 cm, only 3 $K^\pm$ (2.2 $K^\pm$ yr^{-1}) would survive the cut. A 10 cm threshold is a suitable choice however, since according to Figure 42, the radial distance from a muon track to the point where a K^0_L stops and potentially creates a $K^\pm$ peaks at just under 10 cm, and most instances where a muon missing the detector creates a K^0_L, the muon will be some additional distance away from the LAr edge also. A $K^\pm$ due to a cosmic muon that narrowly misses the active LAr volume is thus unlikely to survive a 10 cm cut even if no other tracks accompany it. Figure 56 shows how the fiducial cut threshold affects the volume of LAr still available to detect signal events; with a 10 cm fiducial cut, there is still 97.3% of the total LAr volume available.

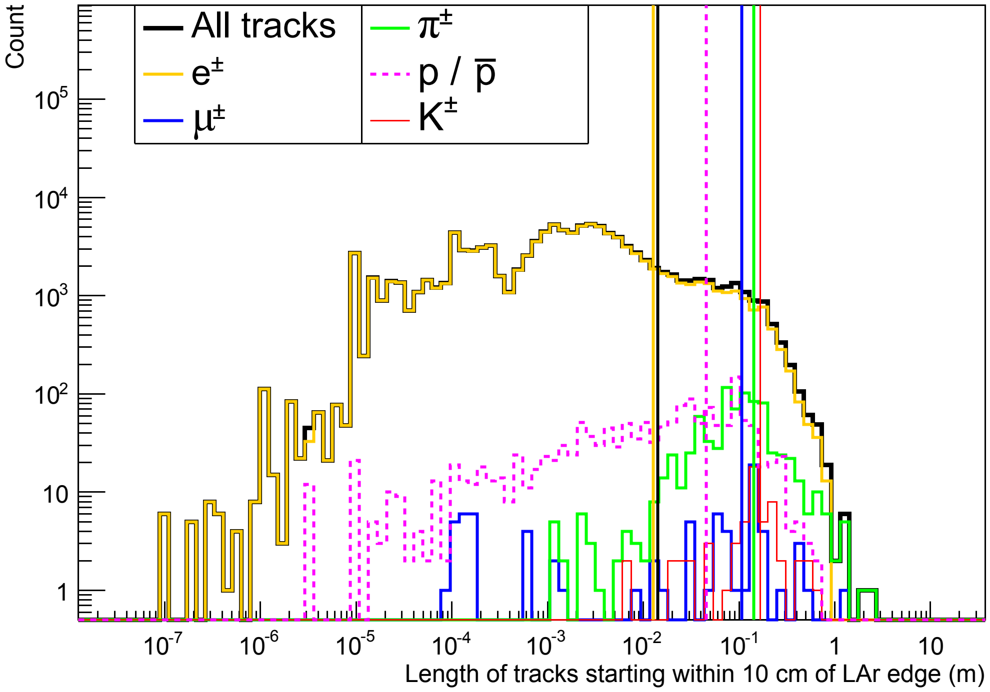

Figure 55: *The distribution of track lengths (primary muon track not included) for those tracks that start up to* 10 *cm inside the LAr volumes for all* 2725 $K^{\pm}$ *events. Vertical lines indicate mean lengths of* 10.6 *cm,* 1.3 *cm,* 14.3 *cm,* 16.7 *cm and* 4.5 *cm for* $\mu^{\pm}$, $e^{\pm}$, $\pi^{\pm}$, $K^{\pm}$ *and* $p/\overline{p}$ *tracks respectively. The fiducial cut (cut (7)) is based on calculating the distance from all hits registered by charged particles to the top, side and end faces of the LAr volumes, but this assumes the hit belongs to a track that is long enough to be detected. Even without the primary muon track (which is used in this cut) this plot still indicates an abundance of tracks that would be long enough. Above a threshold length of* 2 *cm,* 3 *cm,* 5 *cm,* 10 *cm,* 15 *cm or* 20 *cm there is a mean of* 5.4, 4.3, 3.1, 1.6, 0.9 *or* 0.5 *tracks per event respectively that start with* 10 *cm of the edge of an LAr volume.*

Since there are no $K^{\pm}$ surviving the fiducial cut there are no further columns included in Table 16 for the energy deposition cuts. However, these cuts are employed for some results discussed in later sections.

Cut (8): The first energy deposition cut involves the $K^{\pm}$ and any secondary particles that descend from the $K^{\pm}$ before it decays (a.k.a. “non-decay descendents”). A K^{+} from a decaying free proton has a kinetic energy of 105.339 MeV but uncertainty arises due to protons bound within nuclei having Fermi motion, as well as the K^{+} scattering on the nucleons as it emerges, and the energy resolution of the detector (Section 3.2). A background $K^{\pm}$ and its non-decay descendents can therefore deposit more than 105.339 MeV and still potentially mimic a real proton decay event (Section 3.1). Figure 57 shows the distribution of these energy depositions with and without the prior cuts applied. With no other cuts applied, a conservative maximum energy deposition of 250 MeV would retain >99% of signal events and remove 64% of the background. Calculations shown in Section 3.2 indicate this maximum could possibly be reduced closer to 226 MeV with negligible loss of signal (at which point a further $\sim$ 2% of the background (i.e. $\sim$40 background events per year) would be eliminated). Figure 58 shows the percentage of $K^{\pm}$ that would survive if different cut thresholds are used. Figure 59 compares the energy deposited by the $K^{\pm}$ and any particles descended from it before it decays, to the energy deposited by particles not descended from the $K^{\pm}$ (cut (10)).

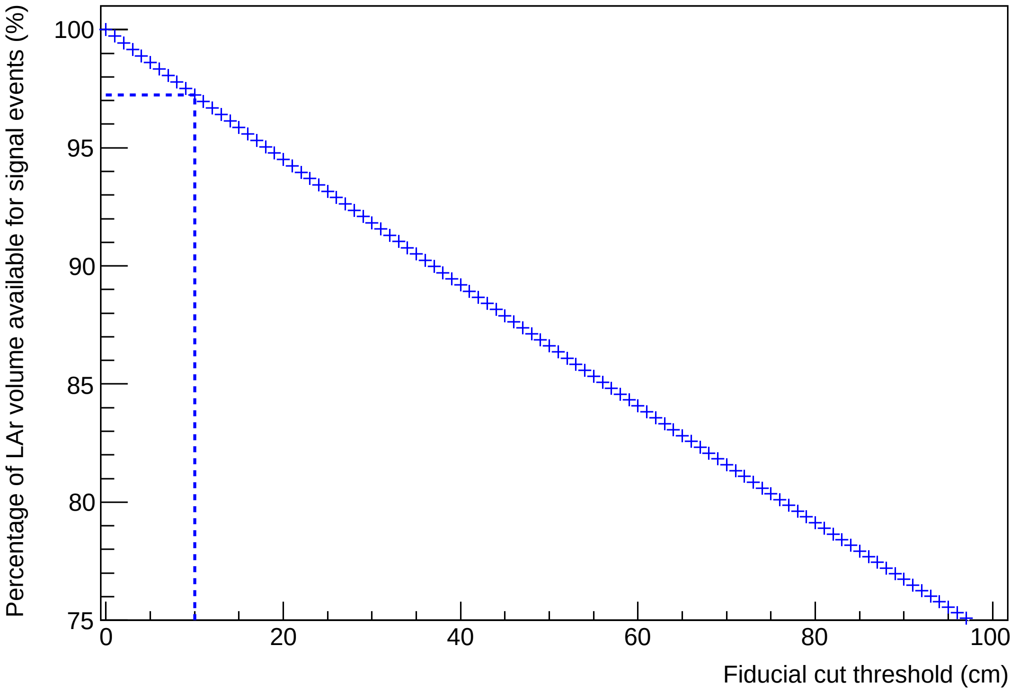

Figure 56: *The percentage of the* 4850 *ft detector LAr active volumes still left available for signal event detection for a given fiducial cut threshold (cut (7)). The vertical and horizontal dashed lines indicate the* 10 *cm threshold used in the results.*

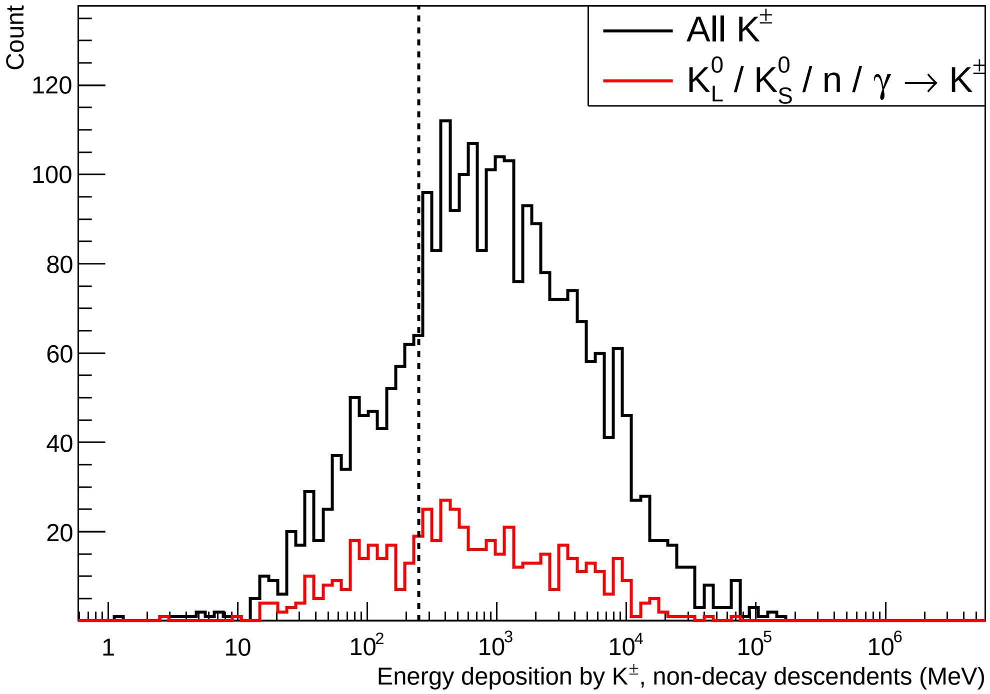

Figure 57: *The distribution of the energy depositions by a* $K^{\pm}$ *and any particles that descend from it before it decays, before any cuts are applied (cut(8)). This energy deposition due to all* $K^{\pm}$ *observed is shown in black, and that shown in red is due to only those* $K^{\pm}$ *with a neutral parent particle. The vertical line indicates the cut threshold at* 250 *MeV, with a* $K^{\pm}$ *being rejected if the energy deposited by itself and its 'non-decay descendents' exceeds this limit.*

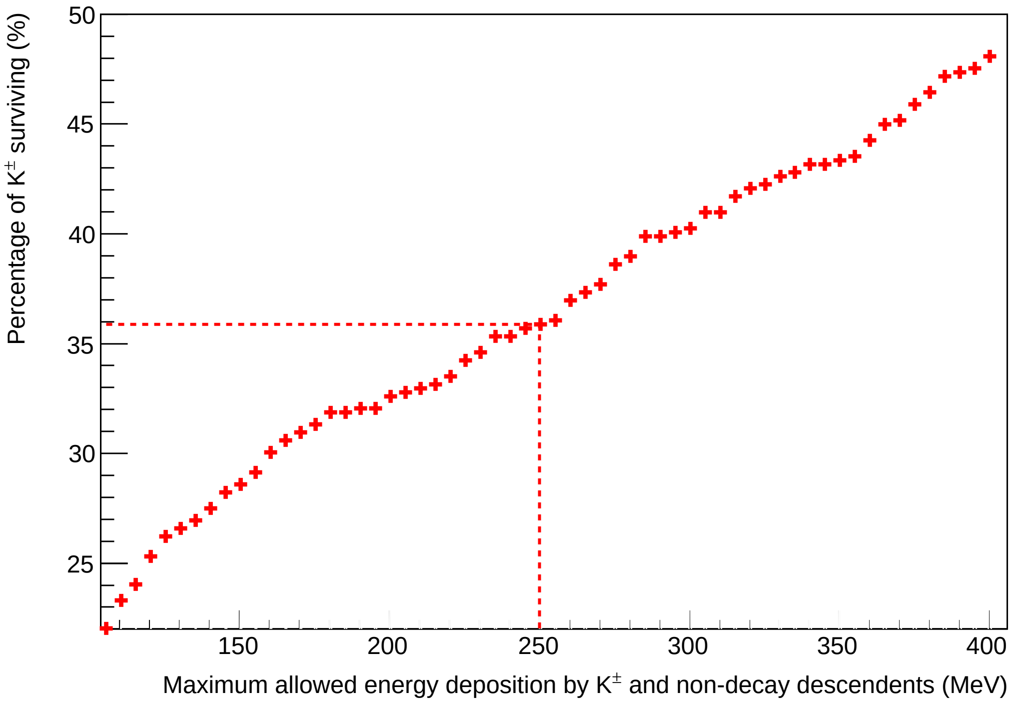

Figure 58: *A decaying free proton would produce a K^{+} with a kinetic energy of* 105.339 *MeV (Section 3.2). However, one must also consider the Fermi motion of the nucleons, the scattering of the K^{+} on the nucleons and the imperfect energy resolution of the detector. A $K^{\pm}$ and any particles descended from it before it decays could therefore deposit an energy greater than* 105.339 *MeV and still mimic a genuine signal event. This plot shows the percentage of all $K^{\pm}$ observed that survive a given threshold for cut (8).*

Cut (9): The second energy deposition cut involves the $K^{\pm}$ and any secondary particles that descend from the $K^{\pm}$, this time including decay products and their descendents. The upper limit on this energy deposition is taken as a conservative 1 GeV, based on the calculations discussed in Section 3.2. Figure 60 shows the distribution of these energy depositions. With no other cuts applied this cut would remove 50% of the background whilst retaining >99% of signal events.

However, a 1 GeV threshold for this cut may be unnecessarily conservative. In this instance a rest mass of 493.667 MeV is available for the $K^{\pm}$ decay products and any secondaries that descend from them to deposit. A K^{+} from a decaying free proton has a kinetic energy of 105.339 MeV, and thus a total energy of 599.006 MeV. However, as discussed in Section 3.2, a sensible upper limit on energy deposition for the K^{+} and any non-decay descendents (cut (8)) is 250 MeV (Section 3.2). Also, a 493.667 MeV energy deposition could be reconstructed as being up to 520 MeV, so adding this to 250 MeV suggests a less conservative cut threshold closer to ~770 MeV could possibly be used without significant loss of signal. This would improve the background rejection from 50% to 57%. Figure 61 shows the percentage of $K^{\pm}$ that would survive for a given cut threshold.

Figure 62 compares the energy deposited by the $K^{\pm}$ and all particles descended from it (including descendents produced in decays), to the energy deposited by particles not descended from the $K^{\pm}$ (cut (10)).

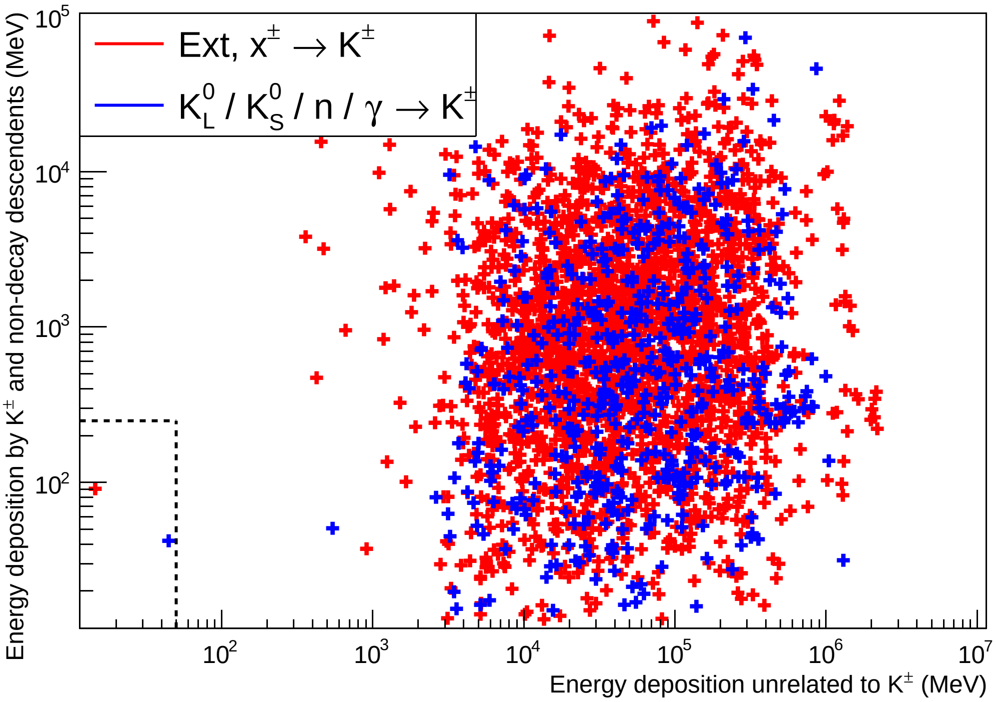

Figure 59: *The energy deposition in the LAr volumes by the $K^{\pm}$ and any particles descended from it before it decays (cut (8), mean energy 3.2×10^3 MeV) compared to the energy deposition in the rest of the event (cut (10)), mean energy 1.2×10^5 MeV), by particles unrelated to the $K^{\pm}$. The two points enclosed within the dashed lines survive cuts on both categories of energy deposition, but one is rejected by cut (2) and both are rejected by cut (7).*

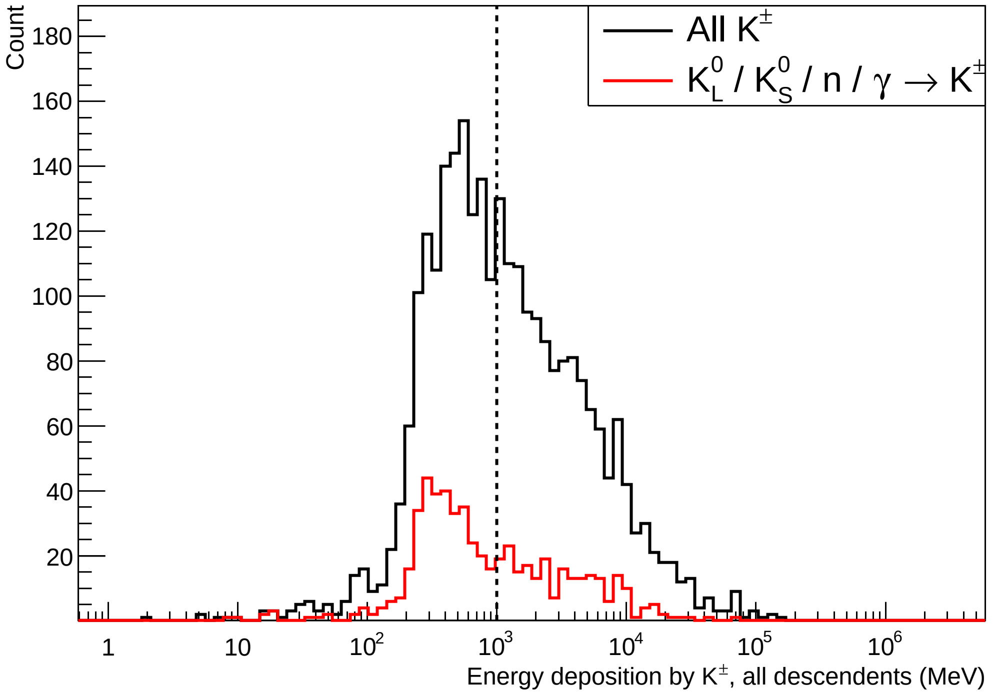

Figure 60: *The distribution of the energy depositions by a $K^{\pm}$ and any particles that descend from it before any cuts are applied, in this instance including any decay products and their descendents (unlike Figure 57) (cut (9)). The black line is for all $K^{\pm}$ observed, and the red line for only those $K^{\pm}$ with a neutral parent particle. The vertical line indicates the cut threshold at 1000 MeV, with a $K^{\pm}$ being rejected if the energy deposited by itself and any particles descended from it exceeds this limit.*

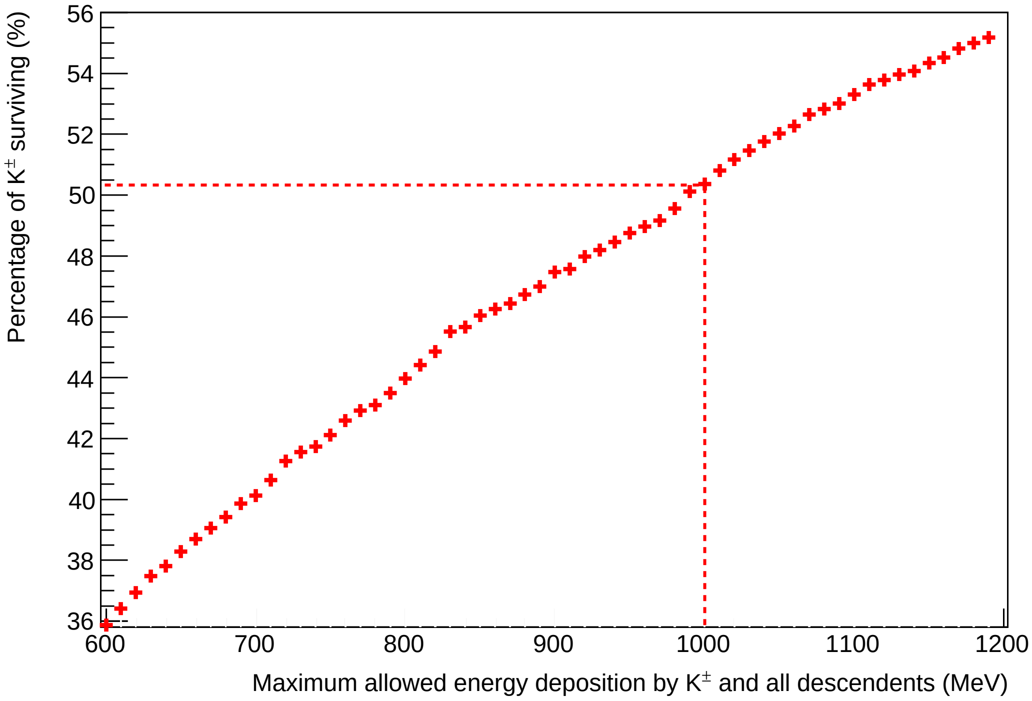

Figure 61: *The relationship between the survival rate of the* $K^{\pm}$ *and the upper limit of energy depositions allowed by a* $K^{\pm}$ *and all particles descended from it. The dashed line at* 1 *GeV indicates the threshold used in these results.*

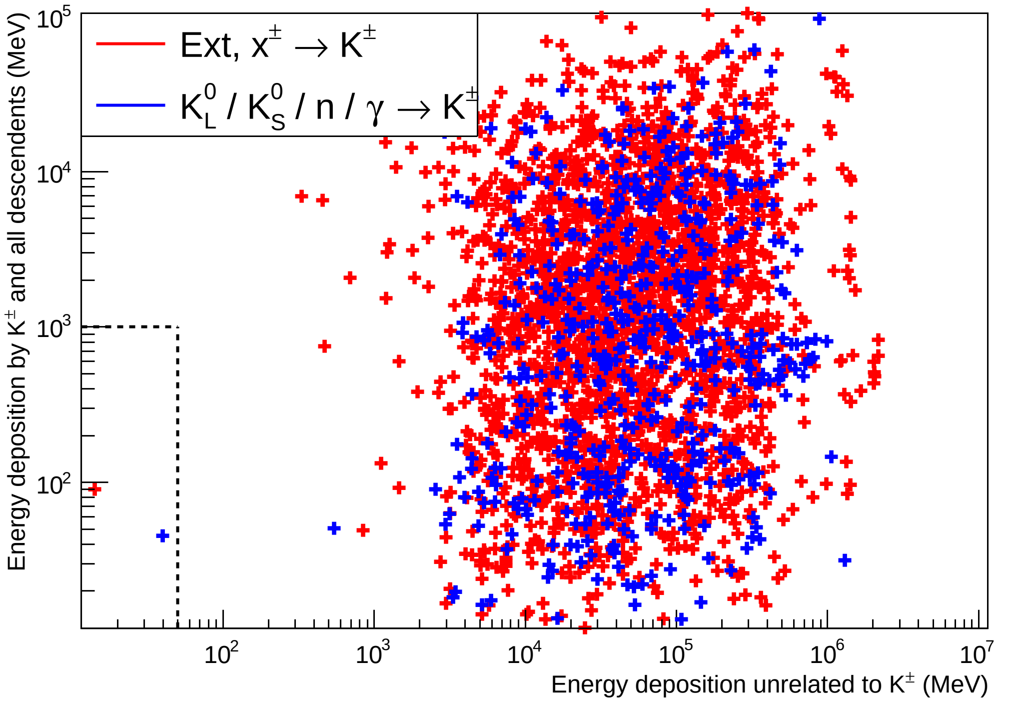

Figure 62: *The energy deposition in the LAr volumes by the* $K^{\pm}$ *and all particles descended from it (including decay products and their descendents) (cut (9), mean energy* 6.1×10^3 *MeV) compared to the energy deposition in the rest of the event (cut (10)), by particles unrelated to the* $K^{\pm}$*. The points shown in this figure that appear in the same position in Figure 59 are for those* $K^{\pm}$ *tracks that have not ended with the* $K^{\pm}$ *decaying.*

Cut (10): The third energy deposition cut is applied to energy depositions by particles other than the $K^{\pm}$ or any particles descended from it. Here a cut threshold of 50 MeV is used since it assumed that any energy deposition greater than this would be easily visible. Figure 63 shows the distribution of these energy depositions with and without the prior cuts applied, which corresponds to the x-axis on Figures 59, 62. With no other cuts applied this cut would remove >99% of the background. Figure 64 shows how the percentage of surviving background $K^{\pm}$ depends on the cut threshold; increasing the threshold to 500 MeV would only reject 0.25% less of the background. The 50 MeV cut threshold could be raised by an order of magnitude or more before significant numbers of background $K^{\pm}$ start to survive this cut, and the signal loss with either threshold is assumed to negligible.

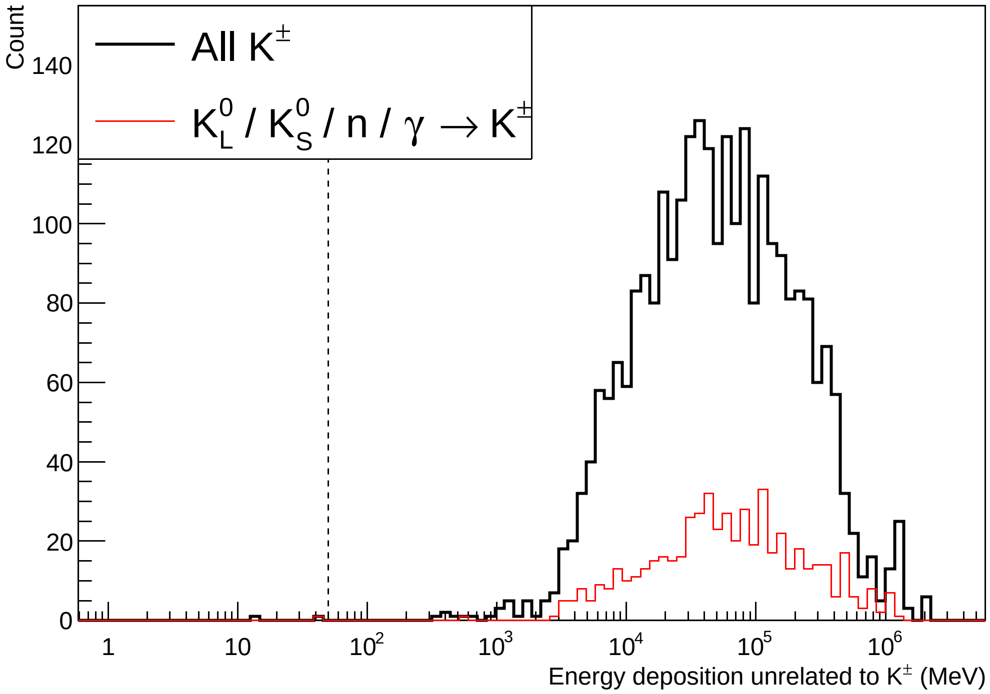

Figure 63: *The distribution of the energy depositions not by a $K^{\pm}$ or any particles that descend from it, including any decay products and their descendents (cut (10)). No other cuts are applied. The black line is for all $K^{\pm}$ observed, the red line is for only those $K^{\pm}$ surviving cuts (1) and (2) (i.e. no charged parent or originating outside the LAr). The vertical line indicates a cut threshold of 50 MeV. One of the two $K^{\pm}$ surviving this cut is rejected by cut (1), both are rejected by cut (7) (i.e. the fiducial cut).*

Finally the last 2 columns of Table 16 show the annual rate of background $K^{\pm}$ events before and after the cuts in Table 16 are applied. The second-last column is calculated by dividing the second column by 1.341 years. No background events survive the cuts and the last column provides an upper limit at 90% confidence [290] (Appendix 8.9) of 1.82 events per year. Since the total LAr mass is 16.748 kilotonnes, the upper limit based on these preliminary results can also be stated as 0.081 kton^{-1} yr^{-1}.

Table 17 shows how Table 16 would have looked if events had been terminated upon the total energy deposition reaching 2 GeV or the muon travelling more than 20 cm in the LAr. Table 17 can be compared with Tables 20, 26 in Sections 4.1.2, 4.2.

To summarise, based on this initial 1.341 years of statistics, the 4850 ft 10 kton detector should observe 0.00-1.82 background events per calendar year. This upper limit is reduced significantly in the main results of Section 4.1.2 that feature higher statistics. All cuts applied are efficient with only minor signal rejection, and just the 10 cm fiducial cut alone was sufficient to eliminate all background $K^{\pm}$ observed.

Table 17: *The same as table 16 but without any* $K^{\pm}$ *from events in which the total energy deposition or primary muon track length exceeds* 2 *GeV or* 20 *cm respectively. The subtotal of* K^{-} *are shown in brackets.*

				Annual rate	
Parent of $K^{\pm}$	$K^{\pm}$ before cuts	μ track <20 cm	<10 cm to LAr edge	Before cuts	After cuts
Total	1 (0)	0 (0)	0 (0)	1 (0)	0-1.82
K^0_L	1 (0)	0 (0)	0 (0)	1 (0)	-
K^0_S	0 (0)	0 (0)	0 (0)	0 (0)	-
n	0 (0)	0 (0)	0 (0)	0 (0)	-
γ	0 (0)	0 (0)	0 (0)	0 (0)	-

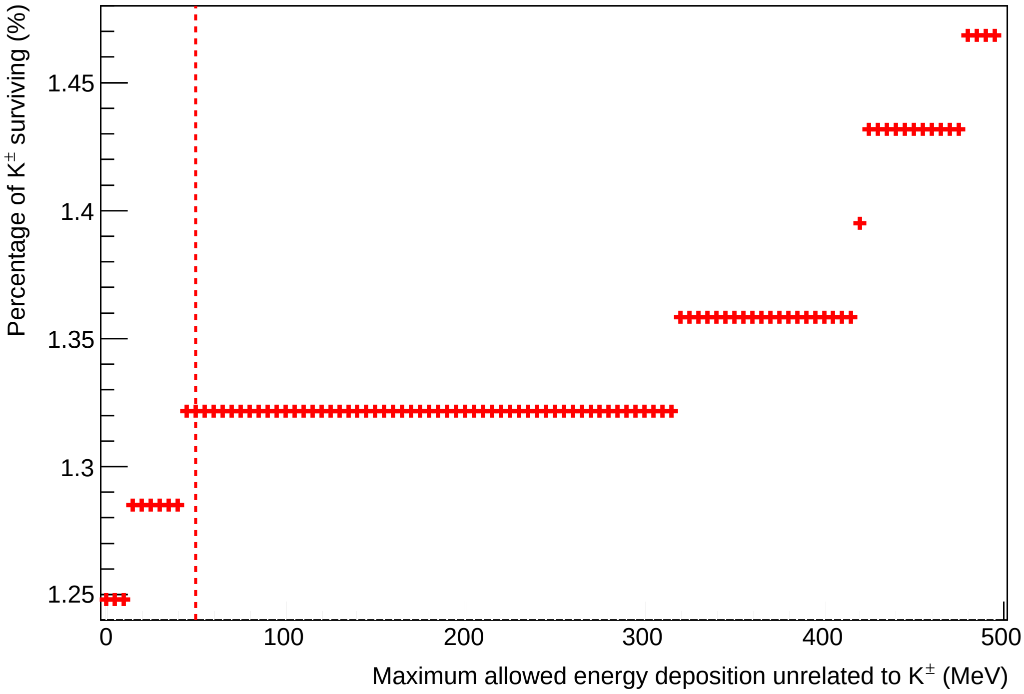

Figure 64: *The percentage of* $K^{\pm}$ *that survive cut* (10) *as the cut threshold is varied. The dashed vertical line indicates a* 50 *MeV threshold but making the cut threshold less stringent by a full order of magnitude to* 500 *MeV only increases the survival percentage by* $\sim 0.25\%$.

4.1.2 Stronger production cuts

A further 65.524 years of statistics has been generated using the more stringent production cuts on electrons, positrons and photons described in Section 3.6.3. Of these 65.524 years, events corresponding to 61.667 years are also pre-emptively terminated via the use of the cut volume (Section 3.6.2). The $K^{\pm}$ counts here are significantly lower than for the 1.341 years of simulated data shown in Tables 9, 10 and 16 since events are interrupted if the energy deposition exceeds 2 GeV in the LAr volume, or the primary muon track exceeds more than 20 cm in the LAr (Section 3.6.1). Also for 61.685 of these 65.524 years, the events were generated using primary muons with a minimum energy of 135 GeV (Section 3.6.4).

Table 18: *The number of $K^{\pm}$ observed in 66.865 years of statistics for the 4850 ft detector as successive cuts are applied. Of these 66.865 years, 65.524 years are gathered using the stronger production cuts on electrons, positrons and photons, as well as pre-event dismissal of unnecessary primary muons and termination mid-event whenever energy deposition exceeds 2 GeV, or primary muon track length exceeds 20 cm, in the LAr. The additional 1.341 years come from adding Table 17, which is valid since that table has the same cuts of muon track length < 20 cm and total energy < 2 GeV applied. Like Table 9, this table shows the effect of applying each qualitative cut separately.*

Total $K^{\pm}$ seen	No $x^{\pm} \to K^{\pm}$	No Ext $\to K^{\pm}$	No $x^{\pm} \to K^0_S \to K^{\pm}$	Only 1 $K^{\pm}$ in event	Decay chain
124 (28)	116 (28)	29 (7)	124 (28)	124 (28)	105 (27)

Table 19: *As in Table 18 but as consecutive (rather than individual) cuts are imposed.*

Total $K^{\pm}$ seen	No $x^{\pm} \to K^{\pm}$	No Ext $\to K^{\pm}$	No $x^{\pm} \to K^0_S \to K^{\pm}$	Only 1 $K^{\pm}$ in event	Decay chain
124 (28)	116 (28)	21 (7)	21 (7)	21 (7)	19 (7)

Table 20: *The number of $K^{\pm}$ observed in 66.865 years of statistics for the 4850 ft detector as cut (7) (the fiducial cut) is applied following on from Table 19. The subtotal of K^- are shown in brackets. Of these 66.865 years, 65.524 years are gathered using the stronger production cuts on electrons, positrons and photons (Section 3.6.3), as well as pre-emptive dismissal of any muons (Section 3.6.2) and termination mid-event whenever energy deposition exceeds 2 GeV, or primary muon track length exceeds 20 cm, in the LAr (Section 3.6.1). The additional 1.341 years come from Table 17.*

			Annual rate	
Parent of $K^{\pm}$	$K^{\pm}$ before cuts	<10 cm to LAr edge	Before cuts	After cuts
Total	19 (7)	0 (0)	0.28 (0.10)	0-0.038
K^0_L	19 (7)	0 (0)	0.28 (0.10)	-
K^0_S	0 (0)	0 (0)	0 (0)	-
n	0 (0)	0 (0)	0 (0)	-
γ	0 (0)	0 (0)	0 (0)	-

Table 18 shows the number of $K^{\pm}$ that survive the cuts (1) to (5) applied separately, and Table 19 shows the number of $K^{\pm}$ that survive these cuts when applied in succession.

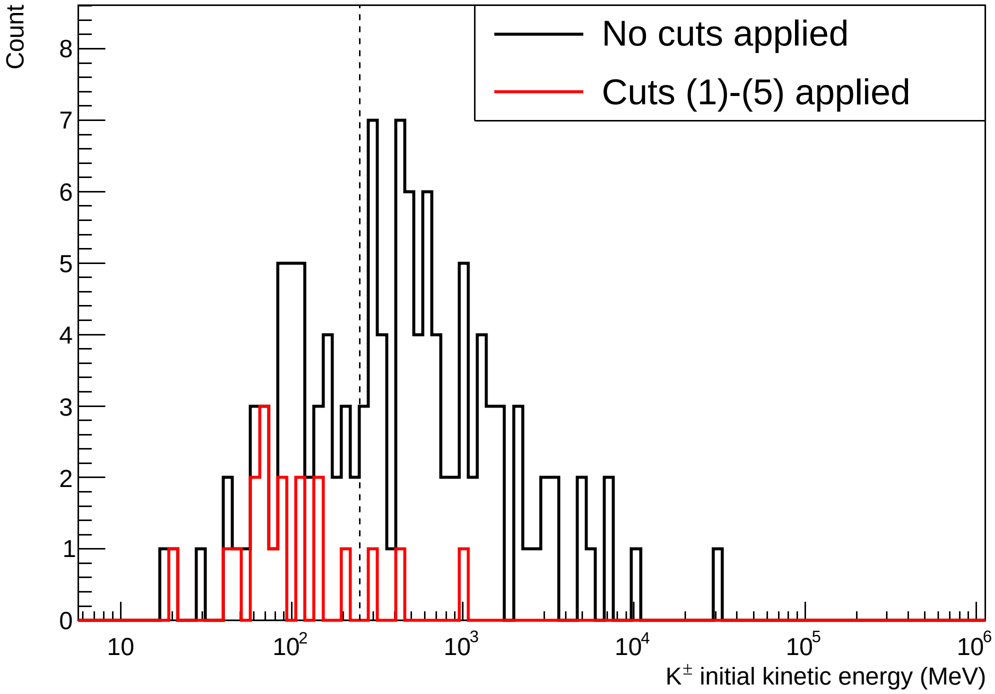

Figure 65: *The distribution of initial kinetic energies of the* $K^{\pm}$ *observed in* 66.685 *years of statistics for the* 4850 *ft detector. The black histogram shows the* $K^{\pm}$ *with no cuts applied, and the red histogram shows the* $K^{\pm}$ *with cuts* (1)*-*(5) *applied (i.e. requiring the* $K^{\pm}$ *do not have a charged parent or grandparent if the parent is* K^0_S*, do not originate outside the LAr, do not appear with other* $K^{\pm}$ *in the same event and have a decay chain featuring* $\mu^{\pm} \rightarrow e^{\pm}/K^{\pm} \rightarrow e^{\pm}$ *if they decay). Cut* (6) *(requiring the muon track length not exceed* 20 *cm) has already been enacted during event simulation, and cut (7) (the* 10 *cm fiducial cut) is enough to elimate the remaining* $K^{\pm}$*. Those* $K^{\pm}$ *to the right of the vertical line at* 250 MeV *are too energetic to mimic a proton decay, assuming all their energy is deposited (Figures 66, 67).*

Table 20 shows the number of $K^{\pm}$ as a further cut (7) is applied, where this 65.524 years has been added to the 1.341 years shown in Table 17 for a total of 66.865 years.

For the full 66.865 years there are 19 background candidates before cut (7) (the fiducial cut) is applied and none afterward. This compares to 1 event in the 1.341 years of initial simulated data (Table 17). For this set of results the application of the muon track length would remove none of the $K^{\pm}$ in the second column since events were already interrupted upon this track length being reached (Section 3.6.1). However, every $K^{\pm}$ is eliminated by the requirement that there be no tracks within 10 cm of the edge of the LAr volume in which a $K^{\pm}$ appears. Figure 68 shows the initial positions of the 124 $K^{\pm}$ observed; most of them fail this cut having originated outside of the LAr. Figure 65 shows the initial kinetic energy of each $K^{\pm}$ in Table 20. Figures 66, 67 show the energy deposition of these $K^{\pm}$ and the particles descended from them (cuts (8), (10) and (9),(10) respectively). With the increased statistics this places the annual background rate of less than 0.038 per calendar year at 90% confidence. For the total LAr mass (after correcting for the fiducial cut by neglecting the 10 cm of LAr closest to the top, side and end faces of the LAr volumes) of 16.220 kton this corresponds to a background rate upper limit of 2.3×10^{-3} kton^{-1} yr^{-1}.

Figures 66 shows the energy depostion by each $K^{\pm}$ and any particles that descend from it before it decays, plotted against the energy deposition in the event not due to the $K^{\pm}$ or their descendents. Figure 67 includes energy deposition by particles resulting from the decay of the $K^{\pm}$.

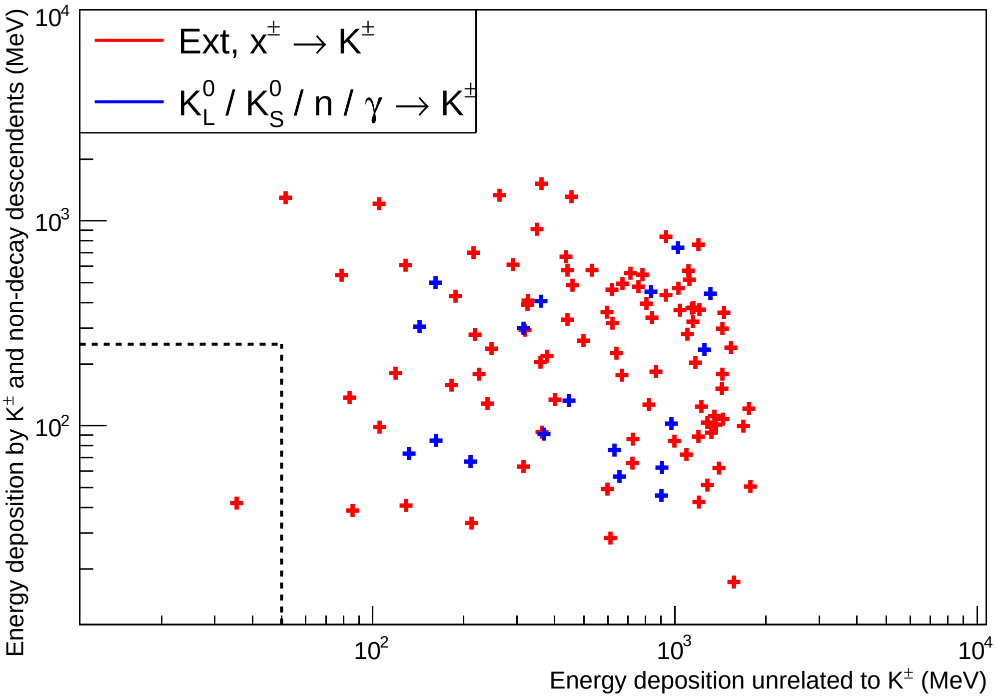

Figure 66: *The energy deposition in the LAr volumes by the $K^{\pm}$ and any particles descended from it before it decays (cut (8), mean deposition* 888 *MeV), compared to the energy deposition in the rest of the event (cut (10), mean deposition* 1075 *MeV), by particles unrelated to the $K^{\pm}$. Red points are for $K^{\pm}$ originating outside the LAr volumes or having been created by a charged parent particle. Blue points are $K^{\pm}$ with neutral parent particles. Energy depositions outside the box limited by dashed lines are too high, so the event will be rejected as a background event. The point inside the box is dismissed by cuts (2) and (7) (i.e. the* 10 *cm fiducial cut and requiring that $K^{\pm}$ tracks start within the active LAr).*

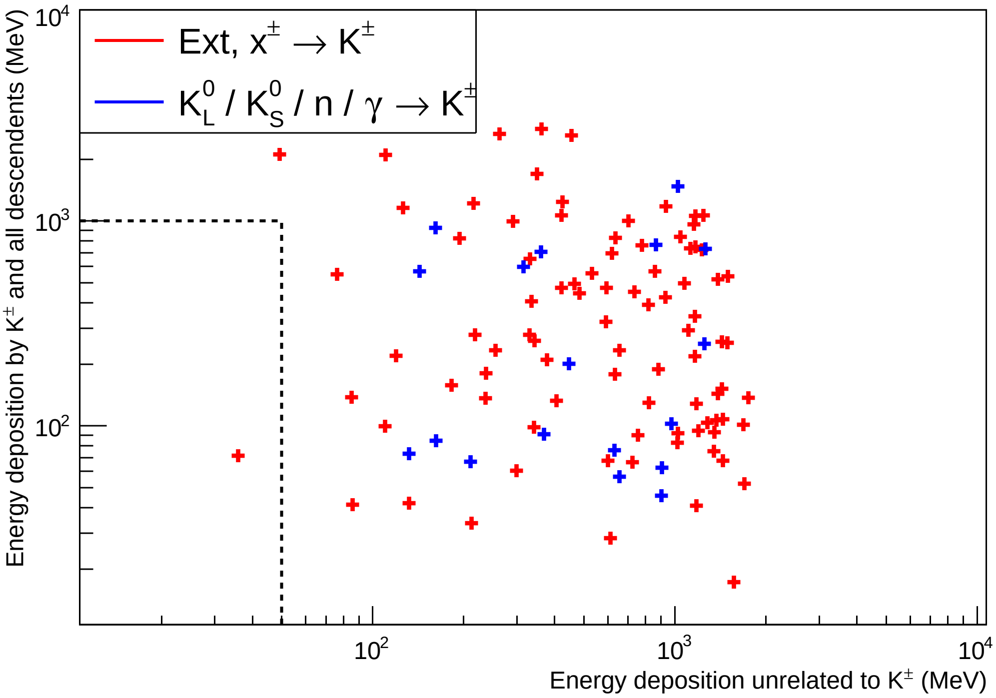

Figure 67: *As in Figure 66 but for the energy deposited in the LAr volumes by the $K^{\pm}$ and all particles descended from it, including decay products and their descendents (cut (9), mean deposition* 1468 *MeV).*

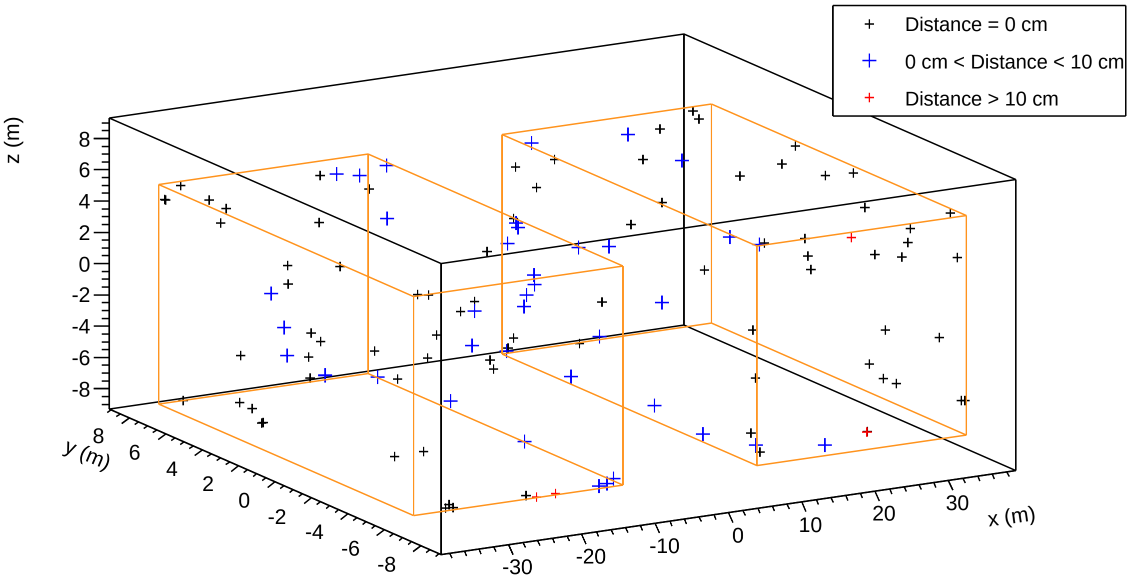

Figure 68: *The initial positions of the* 124 *background* $K^{\pm}$ *observed with the main set of results for the* 4850 *ft detector. Most of the time the distance from this position to the nearest LAr volume (orange boxes) face is zero (black crosses). The events are due to muons that miss the detector so most of the* $K^{\pm}$ *tracks start outside of the detector; this is reflected in their smaller energy depositions compared to those in the initial set of results. Most of the other points show the* $K^{\pm}$ *starting within* 10 *cm of a LAr volume face (blue crosses). The remaining* 4 $K^{\pm}$ *(red crosses) will survive the fiducial cut assuming no other tracks are present with them close to the edge of the LAr.*

4.1.3 Alternative cut sequences

The background count can also be reduced to zero using only quantitative cuts, specifically cuts (7),(9) and (10) listed in Section 4.1.1 (10 cm fiducial cut, energy deposition by $K^{\pm}$ and all particles descended from it <1000 GeV, and energy deposition in the rest of the event <50 MeV). Cut (6) (requiring muon track length <20 cm) has already been applied during the simulation of the events. Table 21 shows the effect of applying these cuts in that order. The first energy deposition cut (9) causes no reduction after the fiducial cut is applied. However, the energy deposition cut (10) is able to remove all remaining $K^{\pm}$ on its own.

4.1.4 Comparison to other studies

4.1.4.1 Overall background rate comparison

The results stated in Section 4.1.2 can be compared to those from a related 2015 study [291] appropriate for the LAGUNA/LBNO experiment (Section 2.5.4), which has been performed for a cylindrical (height 20 m, diameter 30 m) LAr detector with a mass of ∼20 kton, at a similar depth of 4 km.w.e.. This study has found an upper limit on the annual background rate of 1.2×10^{-3} kton^{-1} yr^{-1} at 90% C.L., with no $K^{\pm}$ surviving the cuts applied to simulated data representing 100 calendar years of detector operation. This is consistent with the annual background rate of less than 2.3×10^{-3} kton^{-1} yr^{-1} from the 66.865 years of statistics stated in Section 4.1.2.

These results may also be compared to those from a 2007 study [243] which too involved

Table 21: *The $K^{\pm}$ that survive as a different sequence of cuts are applied. The subtotal of K^{-} are shown in brackets. In this instance the cuts are applied to the $K^{\pm}$ shown in the first column of Tables 19, 18. The sequence of cuts applied (numbered according to the list in Section 4.1.1) is (7),(9),(10), with cut (6) already applied as the events were being simulated and therefore omitted from this table.*

			Energy deposition		Annual rate	
Parent of $K^{\pm}$	$K^{\pm}$ before cuts	<10 cm to LAr edge	<1000 MeV ($K^{\pm}$, all descendents)	<50 MeV (rest of event)	Before cuts	After cuts
Total	124 (28)	4 (0)	4 (0)	0 (0)	1.85 (0.42)	0-0.038
K^0_L	21 (7)	0 (0)	0 (0)	0 (0)	0 (0)	-
K^0_S	0 (0)	0 (0)	0 (0)	0 (0)	0 (0)	-
n	0 (0)	0 (0)	0 (0)	0 (0)	0 (0)	-
γ	0 (0)	0 (0)	0 (0)	0 (0)	0 (0)	-
Ext	95 (21)	4 (0)	4 (0)	0 (0)	1.42 (0.31)	-
π^+	5 (0)	0 (0)	0 (0)	0 (0)	0 (0)	-
π^-	1 (0)	0 (0)	0 (0)	0 (0)	0 (0)	-
μ^+	1 (0)	0 (0)	0 (0)	0 (0)	0 (0)	-
μ^-	1 (0)	0 (0)	0 (0)	0 (0)	0 (0)	-

a cylindrical LAr volume, but in this instance with a LAr mass of 100 kton with 1 year of exposure. Various rock overburdens were used, specifically 0.5, 1.0 and 3.0 km.w.e., as well as a conical ‘hill’ of height 200 m and diameter 800 m. In each of these four configurations, the upper limit on the background rate for the $p \to K^+ \overline{\nu}$ proton decay channel was estimated at 2×10^{-3} kton^{-1} yr^{-1} at 90% C.L., consistent with the results stated here.

4.1.4.2 Cut comparison

The LAGUNA/LBNO paper [291] employs most of the same cuts applied in Sections 4.1.1 4.1.2 but they are applied in a different order. This is shown in Figure 69. The cuts applied are (2), (4), (6), (7), (8), (9) and (10). The result of applying this sequence of cuts used in [291] to the $K^{\pm}$ in the first column of Tables 18, 19 is shown in Table 22.

Figure 69: *The $K^{\pm}$ that survive as successive cuts are applied in the LAGUNA/LBNO study [291].*

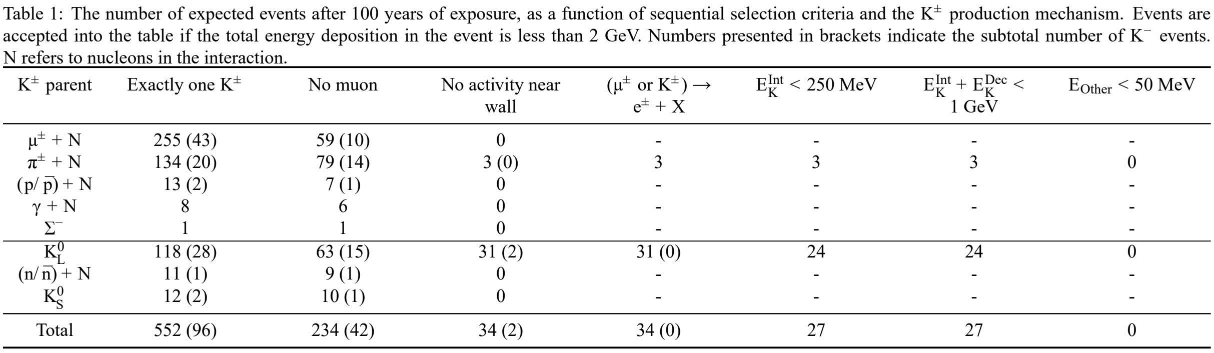

Table 1: The number of expected events after 100 years of exposure, as a function of sequential selection criteria and the $K^{\pm}$ production mechanism. Events are accepted into the table if the total energy deposition in the event is less than 2 GeV. Numbers presented in brackets indicate the subtotal number of K^{-} events. N refers to nucleons in the interaction.

$K^{\pm}$ parent	Exactly one $K^{\pm}$	No muon	No activity near wall	($\mu^{\pm}$ or $K^{\pm}$) $\to$ $e^{\pm}$ + X	$E_K^{Int} < 250$ MeV	$E_K^{Int} + E_K^{Dec} <$ 1 GeV	$E_{Other} < 50$ MeV
$\mu^{\pm}$ + N	255 (43)	59 (10)	0	-	-	-	-
$\pi^{\pm}$ + N	134 (20)	79 (14)	3 (0)	3	3	3	0
(p/ $\overline{p}$) + N	13 (2)	7 (1)	0	-	-	-	-
γ + N	8	6	0	-	-	-	-
Σ^-	1	1	0	-	-	-	-
K^0_L	118 (28)	63 (15)	31 (2)	31 (0)	24	24	0
(n/ $\overline{n}$) + N	11 (1)	9 (1)	0	-	-	-	-
K^0_S	12 (2)	10 (1)	0	-	-	-	-
Total	552 (96)	234 (42)	34 (2)	34 (0)	27	27	0

Table 22: *The effects of applying the cuts in the same sequence((2), (4), (6), (7), (8), (9), (10)) as the LAGUNA/LBNO paper [291] (Figure 69) to the* $K^{\pm}$ *in the first column of Tables 18, 19 . The muon track cut shows no effect here since it was already used in pre-event selection and mid-event termination. These were not used in the LAGUNA/LBNO study, so the first comparable column between these two tables is the third column. Comparing* $K^{\pm}$ *from the dominant neutral parent (and only parentage surviving to this stage in the cuts in both studies) (63 vs. 21* $K^{\pm}$ *from a* K_L^0 *parent), when corrected for the difference in statistics (100 years vs. 66.865 years) differ by a factor of 2. This difference could possibly be partially accounted for by differences the geometry and mass of the detector.*

					Energy deposition		
Parent of $K^{\pm}$	Only 1 $K^{\pm}$ in event	μ track <20 cm	<10 cm to LAr edge	Decay chain	<250 MeV (K^{+}, non-decay desc.)	<1000 MeV (K^{+}, all desc.)	<50 MeV (rest of event)
total	29 (7)	29 (7)	0 (0)	0 (0)	0 (0)	0 (0)	0 (0)
K_L^0	21 (7)	21 (7)	0 (0)	0 (0)	0 (0)	0 (0)	0 (0)
K_S^0	0 (0)	0 (0)	0 (0)	0 (0)	0 (0)	0 (0)	0 (0)
n	0 (0)	0 (0)	0 (0)	0 (0)	0 (0)	0 (0)	0 (0)
γ	0 (0)	0 (0)	0 (0)	0 (0)	0 (0)	0 (0)	0 (0)
π^+	5 (0)	5 (0)	0 (0)	0 (0)	0 (0)	0 (0)	0 (0)
π^-	1 (0)	1 (0)	0 (0)	0 (0)	0 (0)	0 (0)	0 (0)
μ^+	1 (0)	1 (0)	0 (0)	0 (0)	0 (0)	0 (0)	0 (0)
μ^-	1 (0)	1 (0)	0 (0)	0 (0)	0 (0)	0 (0)	0 (0)
p	0 (0)	0 (0)	0 (0)	0 (0)	0 (0)	0 (0)	0 (0)

4.2 800 ft detector

Statistics equivalent to 1.473 years of live time has been simulated for a LAr detector at 800 ft level described in Section 3.4. Since one year of simulated data at this depth requires vastly more computation time and storage space than for the 4850 ft detector, these events have been generated using the cut volume described in Section 3.6.2 to pre-emptively skip events. Also like the results for 4850 ft detector described in Section 4.1.2, events are halted and disregarded if total energy deposition exceeds 2 GeV in the LAr or the primary muon track exceeds 20 cm in the LAr (Section 3.6.1). The stronger production cuts on electron, positron and photon tracks have been applied according to Section 3.6.3.[37]

Table 23: *The total number of $K^\pm$ seen in* 1.473 *years of simulated data generated for the* 800 *ft detector using strong production cuts (Section 3.6.3), the cut volume (Section 3.6.2) and with events halted and disregarded if total energy deposition or muon track limits are exceeded (Section 3.6.1). The subtotal of K^- are shown in brackets. This table shows the number of background candidates that survive as individual cuts (1) to (5) are imposed (rather than successive cuts as in Table 24). Quantitative cuts based on muon track length, track position and energy deposition are dealt with in later tables.*

Total $K^\pm$ seen	No $x^\pm \to K^\pm$	No Ext $\to K^\pm$	No $x^\pm \to K^0_S \to K^\pm$	Only 1 $K^\pm$ in event	Decay chain
3331 (782)	3172 (764)	627 (215)	3331 (782)	3054 (733)	3207 (708)

Table 24: *As in Table 23 but as successive cuts (rather than individual cuts) are imposed.*

Total $K^\pm$ seen	No $x^\pm \to K^\pm$	No Ext $\to K^\pm$	No $x^\pm \to K^0_S \to K^\pm$	Only 1 $K^\pm$ in event	Decay chain
3331 (782)	3172 (764)	468 (197)	468 (197)	441 (189)	409 (168)

The number of background $K^\pm$ surviving the same qualitative cuts as in Tables 9, 10 for the 4850 ft detector is shown in Tables 23, 24. In this instance cut (1) and cut (2) behave differently compared to Section 4.1.1. This is due to use of the cut volume mentioned in the previous paragraph - in the majority of the events allowed to progress to completion, the primary muon misses the LAr volumes and so many more $K^\pm$ originate outside these volumes. The cut applied to these $K^\pm$ is therefore much more effective (dismissing $\sim$ 81% of $K^\pm$ on its own), whereas only requiring the $K^\pm$ not have a charged parent particle produces just a ~5% reduction here. Table 25 shows the amounts of each type of $K^\pm$ parent observed. Cut (3) that rejects $K^\pm$ with a K^0_S parent and a charged grandparent has no effect here; only three $K^\pm$ and their K^0_S parent are recorded in the LAr. Due to the use of the cut volume, much of the activity occurs near the corners/edges of the detector so fewer events which see multiple $K^\pm$ are fully contained within the LAr, and also events were halted if the energy deposition in the LAr exceeded 2 GeV. Consequently, requiring that each $K^\pm$ appear with no other K^+ or K^- (cut(4)) causes only an ~8% reduction here, compared to ~41% seen in Section 4.1.1. When applied sequentially this

---

[37] To avoid confusion, this paragraph states reasons why the 3331 $K^\pm$ in the first columns of Tables 23, 24 cannot be directly compared with the 2725 $K^\pm$ shown in the corresponding Tables 9, 10 for the detector at 4850 ft.

cut reduces the remaining background by ~6 %. Figure 70 compares the number of $K^{\pm}$ in a given event to the energy of the primary muon responsible for the event. The decay chain cut (cut (5)) causes a ~2% reduction in the number of K^{+} and ~10% reduction in the number of K^{-} when applied on its own, similar to the initial results in Section 4.1.1. However, when applied in sequence rejects ~4% and ~11% of the remaining K^{+} and K^{-} respectively.

Table 25: *The types and amounts of parent particles from which the $K^{\pm}$ observed were created for the* 800 *ft detector. The first number/percentage in a given cell is for the parents of all $K^{\pm}$, whereas the number/percentage in parentheses is the subtotal for parents of K^{-} only.*

$K^{\pm}$ parent	Count	Percentage
K^0_L	451 (195)	13.54% (24.94%)
π^+	87 (3)	2.61% (0.38%)
π^-	55 (7)	1.65% (0.90%)
μ^+	9 (3)	0.27% (0.38%)
n	8 (0)	0.24% (0.00%)
μ^-	6 (5)	0.18% (0.64%)
K^0_S	3 (0)	0.09% (0.00%)
$\overline{n}$	3 (2)	0.09% (0.26%)
γ	3 (0)	0.03% (0.00%)
p	1 (0)	0.03% (0.00%)
K^-	1 (0)	0.03% (0.00%)
External	2704 (567)	81.18% (72.15%)
Total	3331 (782)	100% (100%)

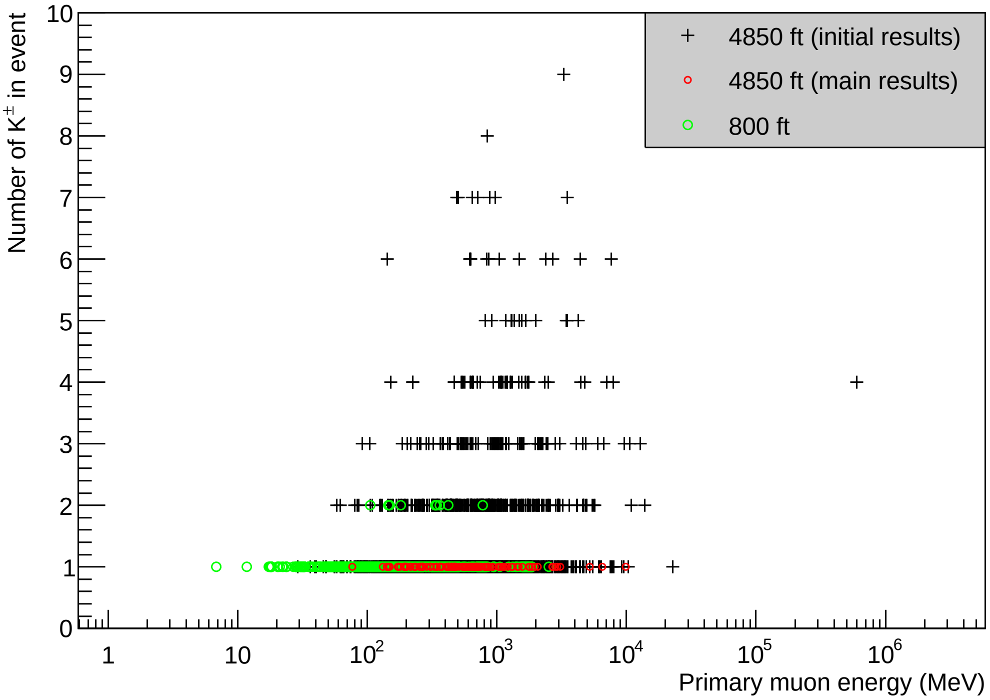

Figure 70: *The relationship between the number of $K^{\pm}$ observed in the LAr in a given event and the energy of the primary muon that started the event. Small red circles are for the* 2725 *$K^{\pm}$ observed in the initial results for the* 4850 *ft detector (Section 4.1.1). Large green circles are for the* 124 *$K^{\pm}$ observed in the main results for the* 4850 *ft detector. Red circles are for the* 3331 *$K^{\pm}$ observed for the* 800 *ft detector.*

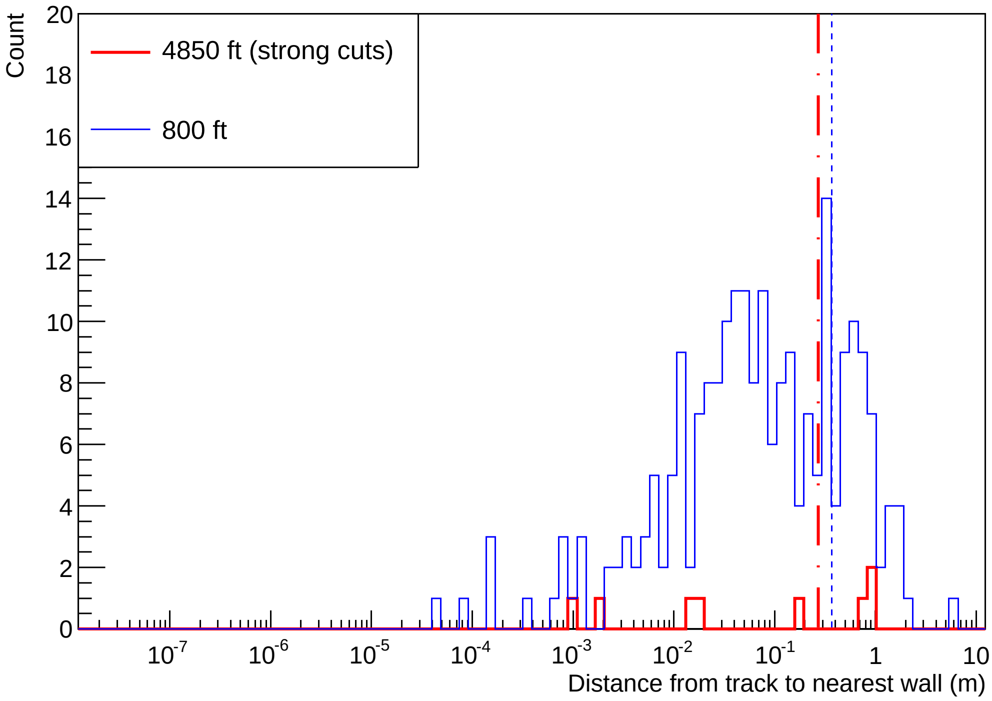

Figure 71: *The distribution of the shortest distance in each background event in the* 800 *ft detector (blue line) and* 4850 *ft detector (main results) (red line) between a charged particle track and the nearest face of the LAr volume they appear in (cut (7)). The vertical lines indicate mean distances of* 0.37 *m and* 0.25 *m for the* $K^{\pm}$ *that appear in the plot, keeping in mind that this distance is zero or very close to zero in* 3232 *of the* 3331 *events for the* 800 *ft detector and* 116 *of the* 124 *events for the* 4850 *ft detector.*

Table 26: *The number of* $K^{\pm}$ *observed in* 1.473 *years of statistics for the* 800 *ft detector, gathered using the strong production cuts on electrons, positrons and photons (Section 3.6.3), as well as pre-emptive dismissal of any muons (Section 3.6.2) and mid-event termination whenever energy deposition exceeds* 2 *GeV, or primary muon track length exceeds* 20 *cm, in the LAr (Section 3.6.1). The subtotal of* K^{-} *are shown in brackets. This can be compared with Table 20 for the* 4850 *ft detector.*

			Energy deposition			Annual rate	
Parent of $K^{\pm}$	$K^{\pm}$ before cuts	<10 cm to LAr edge	<250 MeV (K^{+}, non-decay descendents)	<1000 MeV (K^{+}, all descendents)	<50 MeV (rest of event)	Before cuts	After cuts
Total	409 (168)	3 (0)	3 (0)	3 (0)	0 (0)	277 (114)	0-1.66
K_L^0	394 (166)	3 (0)	3 (0)	3 (0)	0 (0)	267 (113)	-
K_S^0	3 (0)	0 (0)	0 (0)	0 (0)	0 (0)	2 (0)	-
n	10 (2)	3 (0)	2 (0)	2 (0)	0 (0)	7 (1)	-
γ	2 (0)	0 (0)	0 (0)	0 (0)	0 (0)	1 (0)	-

The consecutive application of the quantitative cuts is then shown in Table 26. Cut (6), the requirement that no muon track exceed 20 cm in an LAr volume, is already applied in during event simulation. The third column shows the effect of the fiducial cut (cut (7)), which removes 97% of the background when applied on its own, or reduces the remaining background by $> 99.9\%$ when applied sequentially. For previous results shown in Sections 4.1.1, 4.1.2, all possible background has been eliminated by these cuts. Figure 71 compares the fiducial cut for the 4850 ft and 800 ft detectors.

Since some background still remains here, the three cuts on energy deposition are applied. First of all an upper limit of 250 MeV is imposed on the energy deposition by a $K^{\pm}$ and any particles descending from it before it decays (cut (8)). This removes ∼59% when applied separately but no more of the remaining background when applied in sequence. Figure 72 plots these energy depositions against that unrelated to the $K^{\pm}$. The next cut applied is (8), an upper limit of 1 GeV on the energy deposition by the $K^{\pm}$ and all particles descended from it. This causes a reduction of ∼7% as a stand-alone cut but when applied sequentially it causes no reduction of the remaining background. This cut is significantly less effective than the 50% of background it rejects when applied in the initial results; this is due to most of the $K^{\pm}$ tracks starting outside of the LAr due to coming mostly from muons that miss the detector, so they deposit some energy on their way to the detector and thus are less susceptible to rejection by this cut. Figure 73 plots these energy depositions against that unrelated to the $K^{\pm}$. Finally cut (10), the requirement that the energy deposition unrelated to the $K^{\pm}$ be less than 50 MeV, eliminates ∼87% of $K^{\pm}$ on its own and rejects any $K^{\pm}$ that still remain when applied in sequence.

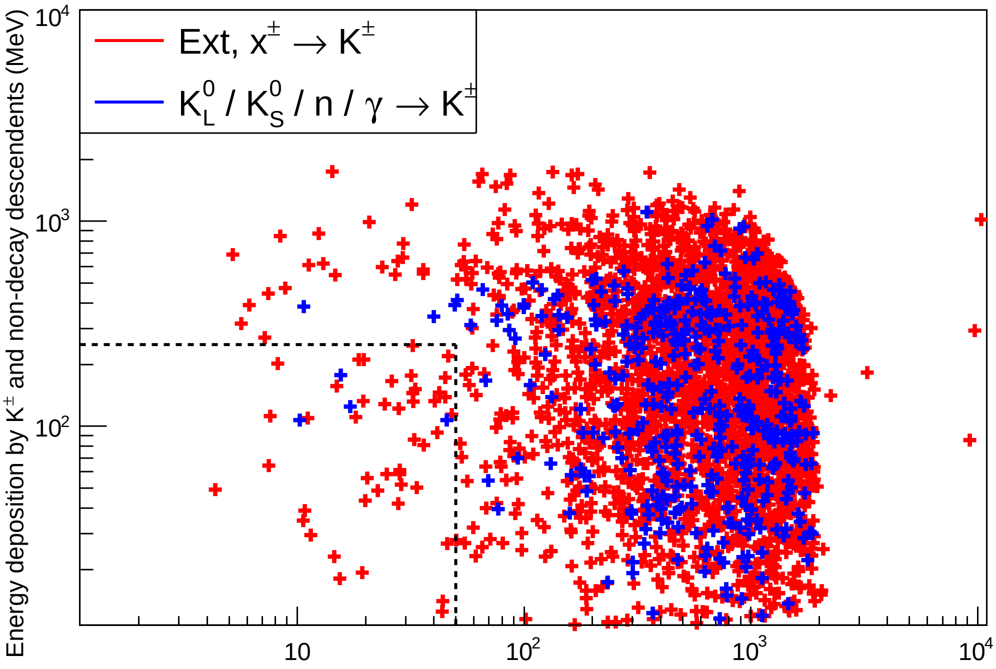

Figure 72: *The energy depositions in the LAr volumes of the* 800 *ft detector by the* $K^{\pm}$ *and any particles descended from it before it decays (cut (*8*), mean deposition* 615 *MeV), compared to the energy deposition in the rest of the event (i.e. by particles unrelated to the* $K^{\pm}$*) (cut(*10*)). Red points are for* $K^{\pm}$ *originating outside the LAr volumes or having been created by a charged parent particle (and therefore rejected). Blue points are* $K^{\pm}$ *with neutral parent particles. Events outside the box shown by the dashed lines will be rejected as having either too great an energy deposition from a kaon or too great and energy deposition from other particles not linked to the kaon, or both. The blue points surviving this cut are rejected by the fiducial cut (cut (*7*)) in Section 4.1.1. Comparing this to Figure 59, the significantly lower maximum energy depositions observed here (*$\sim 10^3$ *MeV) are due to activity being mostly at the corners / edges of the detector rather than fully-contained events since the events are due mainly to muons that miss the LAr volumes.*

The combined effect of all qualitative cuts ((1)-(5)) means the background is reduced by 88% overall. The application of the quantitative cuts ((6)-(10)) then dismisses all of the remaining background. This 1.473 years of statistics gathered for this detector corresponds to an upper limit of 1.66 background events per year (0.028 kton^{-1} yr^{-1}) at 90% confidence.

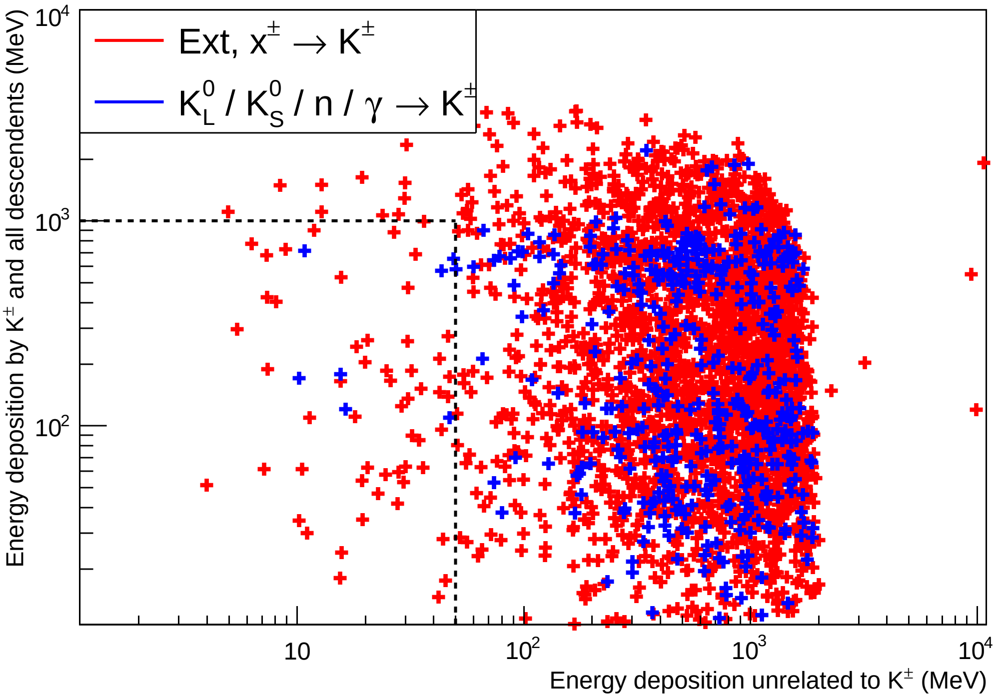

Figure 73: *As in Figure 72 but this time for the energy deposited by the* $K^{\pm}$ *and all particles descended from it, including those resulting from the decay of the* $K^{\pm}$ *(cut (9), mean deposition* 978 *MeV).*

Comparison of the results for the 4850 ft and 800 ft detectors can be made using the first column in Table 18 and Table 23. The total LAr volume mass for the 4850 ft detector is 16.748 ktonnes and with no cuts applied, 124 $K^{\pm}$ were observed for 66.865 years of statistics, corresponding to 0.11 $K^{\pm}$ kton^{-1} yr^{-1}. The total LAr volume mass for the 800 ft detector is 52.975 ktonnes and before cuts, 3331 $K^{\pm}$ were observed for 1.473 years of statistics, corresponding to 42.69 $K^{\pm}$ kton^{-1} yr^{-1}. The $K^{\pm}$ event rate in the 800 ft detector is therefore greater by a factor of $R_{event} \approx 385$. However, the muon rate through the box surrounding the detector from which muons were sampled is 0.3074 s^{-1} for the 4850 ft detector and 981.4 s^{-1} for the 800 ft detector. The box for the 4850 ft detector measures 100×40×50 m^3 so the surface area of the top, end faces and side faces is 18,000 m^2. The box for the 800 ft detector measures 169×29×31 m^3 so the surface area of the top, end faces and side faces is 17,177 m^2. If the flux for each detector is calculated as F_{det} = (muon rate) / (box surface area) then $F_{4850} = 0.3074$ s$^{-1}/18,000$ m$^2 = 1.7 \times 10^{-5}$ m^{-2} s^{-1} and $F_{800} = 981.4/17,177 = 0.057$ m^{-2} s^{-1}. The ratio of muon fluxes in each detector is therefore $R_{flux} = F_{800}/F_{4850} \approx 3345$. Then the muon flux rate may be compared to the event rate: $R_{flux}/R_{event} = 3345/385 \approx 8.68$.

For R_{flux}/R_{event} to approach 1 would require a higher $K^{\pm}$ count in the 800 ft detector, or lower in the 4850 ft detector. That $R_{flux}/R_{event} \neq 1$ may be attributed to the harder muon energy spectrum at the 4850 ft detector than at the 800 ft detector (Figure 74), allowing more particles to be produced (Figure 70). The 4850 ft detector also has a somewhat higher surface area (ignoring the bottom face of the LAr volumes which muons don't enter through) to volume ratio than the 800 ft detector (0.356 and 0.280 respectively), which is significant since the $K^{\pm}$ background is due to muons that narrowly miss the detector.

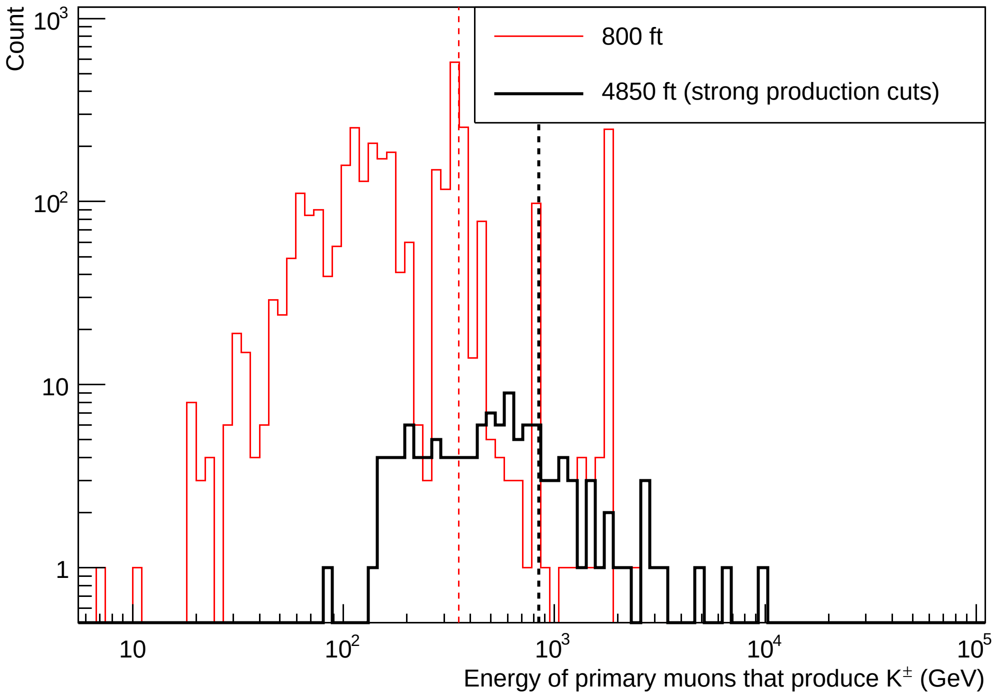

Figure 74: *The initial energy distribution of the primary muons responsible for producing the* $K^{\pm}$ *found in Tables 18, 23. The mean energy of these muons is* 843.2 *GeV for the* 4850 *ft level (black) and* 346.7 *GeV for the* 800 *ft level (red) .*

5 Cosmic-ray background estimation for $\nu_e/\overline{\nu}_e$ appearance in a shallow-depth detector

5.1 Background events for $\nu_e/\overline{\nu}_e$ appearance

The LBNE/DUNE experiment (Section 2.6) will generate beams of muon neutrinos and antineutrinos at Fermilab, IL, and analyse their oscillations with a far-detector located 1300 km away at the Sanford Underground research Facility, SD, USA. Although the currently-favoured DUNE far detector configuration is a 40 kton [38] (combined fiducial mass) detector at a depth of 4850 ft, one earlier design proposed for LBNE was a 10 kton detector buried approximately 3 m below the surface [292]. This detector enclosure was expected to house two cryostats each containing 5 kton (active volume) of liquid argon (LAr). Each cryostat contains rows and columns of adjacent time projection chambers (TPCs) (Section 2.6.1).

The rarity of neutrino interaction events means that, for a detector positioned close to Earth's surface, their signal is completely obscured by incoming cosmic-rays. A ν_e appearing at the far detector may undergo elastic scattering with an electron or a nucleon, which will be signalled by an electromagnetic (EM) shower that develops from the resulting electron track. This track may be also accompanied by hadronic debris. Cosmic rays can pass through or close to the detector and cause EM showers that mimic the signal.

These problematic EM showers have a variety of sources. They may start with a single electron track, an electron-positron pair, or a photon which then produces an electron-positron pair. Knock-on electrons produced by muons originating in the atmosphere are responsible for the majority of these background EM showers. These muons can also cause electron-positron pair production as well as generating Bremsstrahlung photons. Neutral hadrons are also an issue, most notably neutral pions, which can decay to photons that then go on to develop into full cascades. Other sources of potential concern are neutral pions decaying in another way ($\pi^0 \to e^+ \, e^- \, \gamma$) and the decays of neutral kaons ($\mathrm{K}^0_L \to \pi^\pm \, e^\mp \, \nu_e/\overline{\nu}_e$). EM showers which start in the surrounding rock or in uninstrumented regions of the detector but then overlap with an active region are also an issue.

It should be noted that in the case of ν_μ charged current (CC) interactions, the resulting muon track will be obscured by that of many cosmic-ray muons. However, since these background muons cross into the detector from outside, they are easily rejected by a fiducial cut.

Except for the background due to $K^0_L \to \pi^\pm \, e^\mp \, \nu_e/\overline{\nu}_e$ and $\pi^0 \to e^+ \, e^- \, \gamma$, EM showers are counted by just counting the first gamma in the shower (i.e. the gamma which is the parent of the first $\mathrm{e}^\pm$ pair in the shower, henceforth referred to as the 'first-generation gamma'). This avoids needing to record the entire cascade (if one is interested only in estimates of the event numbers). Only first-generation gammas with energies within the range 0.25 GeV - 5.00 GeV are of concern; 0.50 GeV - 5.00 GeV is the energy range of interest for neutrinos in the beam (shown in Figure 21) but the neutrino undergoing the CC interaction need not give up all of its energy to the resulting electron. Signal EM showers with energy lower than 0.50 GeV are therefore possible. Background EM showers beginning with a single electron track produced via Compton scattering are neglected, since pair production dominates in this energy range (Figure 75).

The goals of this study are therefore to assess the annual rate of these cosmic-ray-

---

[38] 40 kton is the combined fiducial mass of four separate 10 kton cryostats (Section 2.6.1).

induced EM showers causing the background for ν_e appearance at the far detector, and to suggest cuts for identifying and rejecting as much of this background as possible without throwing away signal events. However, this study has not involved any track reconstruction.

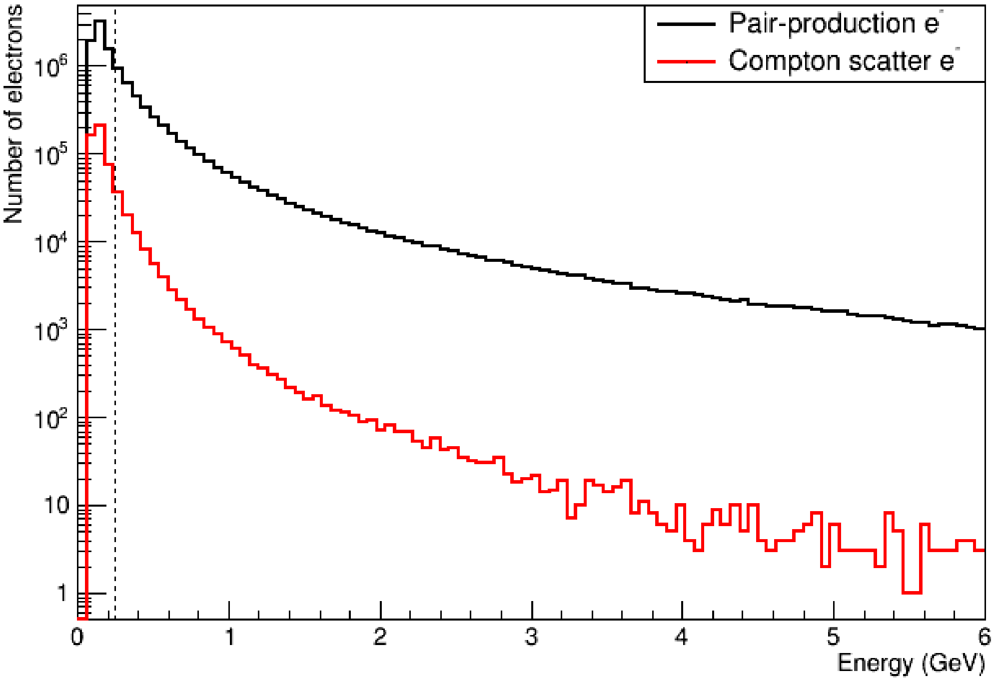

Figure 75: *Energy spectra of a total of* 1.15×10^7 *electrons generated by* 2×10^7 *cosmic-ray-muon-induced events. The black line indicates those resulting from pair production and the red line indicates those from Compton scattering. Compton electrons are neglected in further study since in the energy range appropriate for potential background to the neutrino beam (*$0.25\ GeV$ *-* $5.00\ GeV$*), pair production is the dominant source of electrons. The number of Compton electrons at* $100\ MeV$ *starts off as* $\sim 8\%$ *of the number of pair production electrons. This drops to* $\sim 4\%$ *at* $\sim 0.25\ GeV$ *(indicated by dashed vertical line) and becomes less than* 1% *by* $\sim 1.15\ GeV$*.*

5.2 Physics processes included in the simulation

This simulation has been built using Geant4 version 9.4 [293] [294]. The particle interaction models used in these simulations are specified in a Geant4 'reference physics list' known as "Shielding" [253]. The interactions enabled for significant particles at relevant energies are as follows.

For photons, Shielding includes the ability to undergo Compton scattering, electron/positron pair-production and also inelastic scattering with nuclei and nucleons. Shielding includes standard EM processes for all charged particles including leptons, mesons, baryons and generic ions (namely ionization, Bremsstrahlung radiation, multiple elastic scattering, nuclear inelastic scattering). Electron-positron annihilation is also enabled. Muons may also participate in direct electron/positron pair production. Neutrons may undergo elastic and inelastic scattering with nuclei (as may protons), as well as being captured by nuclei and initiating fission. Specific interaction models for each significant type of particle and the energies to which they apply can be found in Section 3.3.

5.3 Detector geometry

5.3.1 Simple detector geometry

For the first set of results, a simple detector geometry is implemented in Geant4 (Figure 76). It is contained within a flat layer of rock which measures 22 m in the vertical (i.e. z) direction and extends $5{\times}10^3$ m in the $\pm x$ and $\pm y$ directions (parallel and perpendicular to beam direction respectively). The detector is approximated by a cuboid of LAr measuring $30.0{\times}15.0{\times}16.0$ m^3. This LAr volume is an 'active' / 'sensitive' volume, meaning that Geant4 is instructed to record information about particle interactions occurring within it (with certain restrictions which will be discussed in later sections). The LAr volume is positioned such that its centre coincides with the centre of the rock volume, creating a layer of rock 3 m thick directly above the top of the detector.

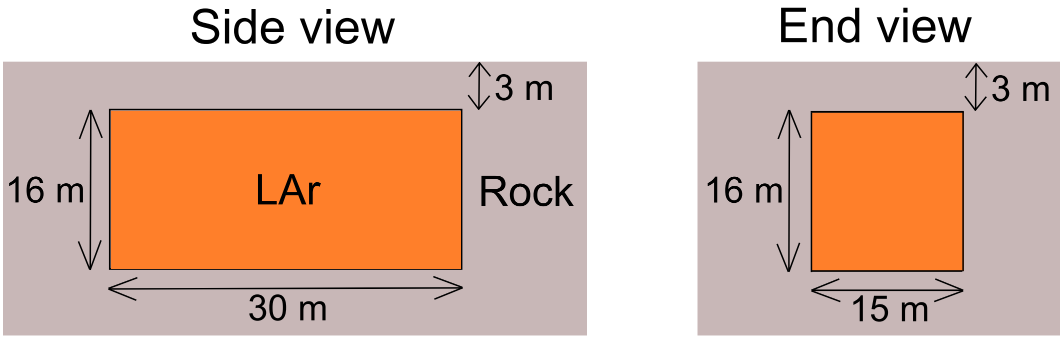

Figure 76: *The simple detector geometry implemented in Geant4. This is one continuous volume of LAr (*10.07 *kton) measuring* $30 \times 15 \times 16$ *m*^{3}*, placed* 3 *m below the flat surface of rock.*

5.3.2 Detailed detector geometry

The second set of results is for a more detailed detector geometry [295] (Figure 77) which approximates a once-proposed design for a surface-level far detector for LBNE. The detector is contained within a cuboidal concrete enclosure measuring $30.813 \times 33.551 \times 15.525$ m^3. Within this concrete volume are two fibreglass boxes measuring $29.813 \times 15.575 \times 15.025$ m^3 separated by 4.6 m and positioned such that 0.5 m of concrete surrounds the sides and top of the fibreglass. Within each fibreglass box is a steel box measuring $28.213{\times}13.975{\times}15.025$ m^3, positioned such that there are 0.8 m of fibreglass surrounding the steel on all sides. Each steel cuboid contains a volume of LAr measuring $28.20{\times}13.95{\times}15.0$ m^3. These LAr volumes each contain 120 LAr sub-volumes measuring $2.520{\times}2.280{\times}7.000$ m^3 which define the boundaries of the TPC cells. Each TPC cells contains a TPC active volume, also made from LAr but this time measuring $2.268 \times 2.245 \times 6.300$ m^3. Finally there is a steel grid (density 0.1796 g cm^{-3}) that approximates the cathode plane within each TPC cell measuring $2.520 \times 0.010 \times 7.000$ m^3, positioned such that it lies flat against one side of each row of TPC cells.

The rock density used is 2700.0 kg m^{-3} and its elemental composition is given in Table 6. The LAr density is set to 1392.8 kg m^{-3}, giving a total LAr mass of 10.03 kton for the simplified geometry and 10.70 kton mass (combined active volumes, each surrounded and separated by more LAr) for the detailed geometry. The LAr temperature is set to 87.25 K. Finally the region above the rock through which the primary particles approach the detector is vacuum rather than air.

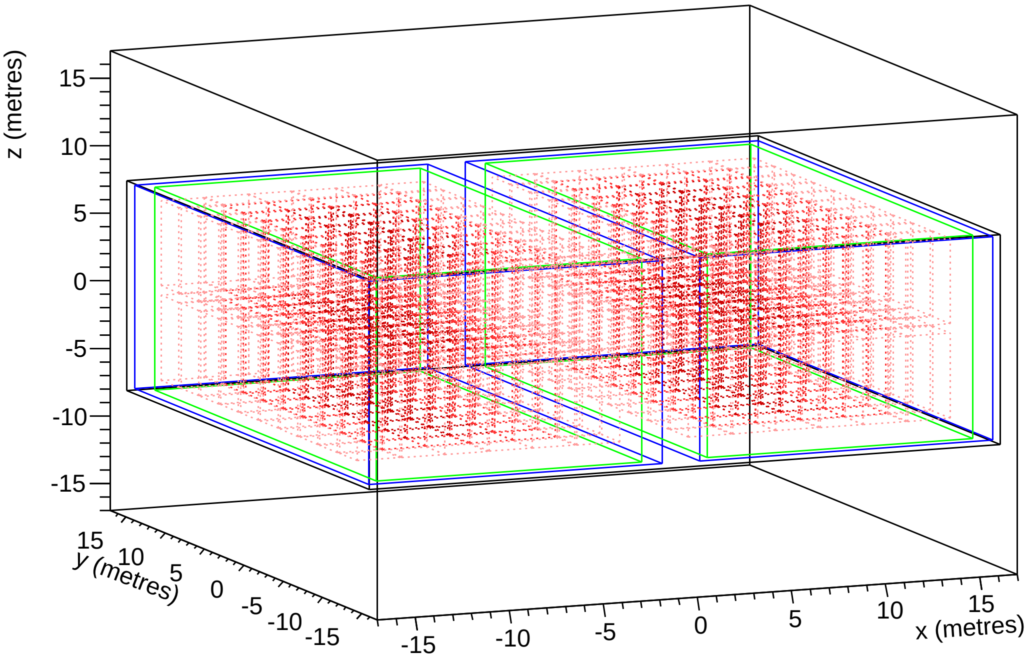

Figure 77: *The detailed detector geometry implemented in Geant4. The TPC cells are shown in red and are stacked* $(9 \times 6 \times 2)$ *in each cryostat. The steel walls of the cryostats are green. The outer edges of the polyurethane insulation are shown in blue and the outer edges of the concrete enclosure is coloured black. The cathode planes are omitted from this diagram. These cryostats are in the 'side-by-side' configuration (beam axis is almost to parallel to y-axis) rather than the other possible configuration, 'end-to-end'.*

5.4 Primary particles and normalization of the background rates

The energy spectra of the muons, neutrons, protons and photons used to initiate events (henceforth referred to as 'primary' particles) are shown in Figure 78. This section contains details about normalization of the simulated events to the annual background rates.

The muon flux has been generated using Gaisser's parametrization [278] (modified for large zenith angles [296] and muon decay) (discussed in Section 3.5.2) and the fluxes of protons, neutrons and photons were generated using Cosmic-ray Shower Library (CRY) [297], [298]. CRY is based on modelling the atmosphere as 42 flat layers of each of constant density that changes by 10% with each layer. This atmosphere is implemented using the simulation codes Geant4, MCNPX, and FLUKA (all giving results consistents with each other) which inject protons at the top of of the atmosphere (at an altitude of ~ 31 km) and transport them down to sea level, 2100 m or 11,300 m. The fluxes of the resulting secondary particles (protons, neutrons, photons, pions and muons) at these altitudes are stored. CRY reads from these pre-determined 'libraries' and returns details of the particles crossing through a square plane given a user-specified particle type, latitude, calendar date and choice of plane side length (1, 3, 10, 30, 100 or 300 m). Figures 79, 80 compare the MCNPX-generated proton and neutron fluxes with experimental data.

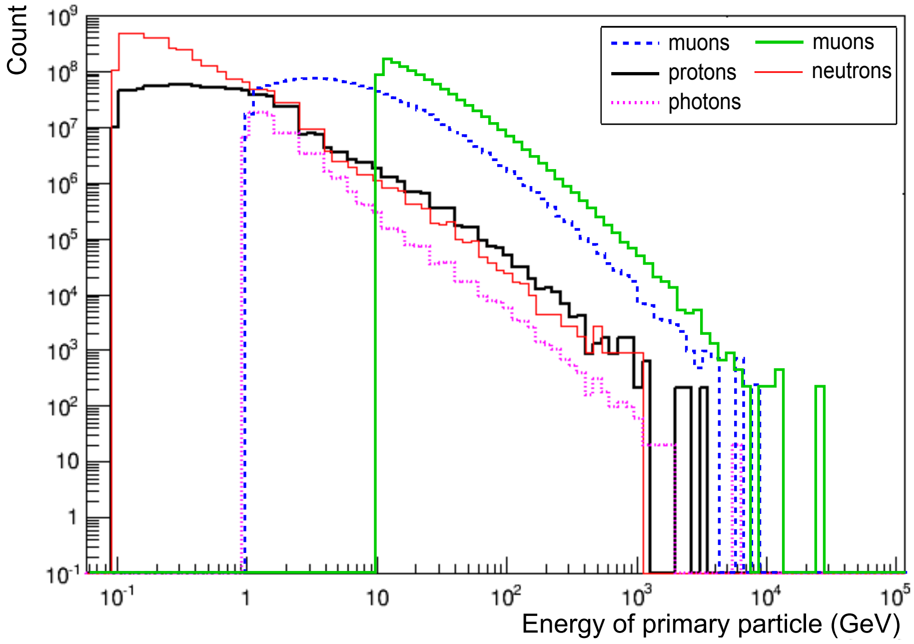

Figure 78: *Energy spectra of particles at the surface. The muons were generated using a modified Gaisser parametrization and the protons, neutrons and photons were all generated using CRY. The effective amount of live detector time simulated can be increased according to Eq. 108, since most EM showers observed are caused by primaries at higher energies. Muons with* $E_\mu > 10$ *GeV have been selected from those represented by the dashed blue line for use in Sections 6.3.1, 6.3.2, and 6.5, since they are* 19.6% *of the total but cause* 92.3% *of the EM showers (over* 100 *MeV) observed. The adjustment to the normalization this necessitates is given by Eq. 108. Another set of muons with the* 10 *GeV lower limit already imposed as they were being generated is shown by the green line. These are used in all other sections involving muon-induced events. Protons with* $E_p > 10$ *GeV have been selected for the results shown in Section 6.4.4, since* 92.7% *of EM showers are due to the* 0.76% *of protons above this threshold. Neutrons with* $E_n > 1$ *GeV have been selected for all sets of results for neutron-induced events (*95.6% *of showers come from* 6.5% *of the neutrons initially generated). Corrections for the small percentage of showers missed due to neglecting low-energy primary particles are shown in Eq. 109.*

The particle fluxes generated by CRY were done so on a plane positioned at an altitude of 2100 m above sea level. However, the detector itself is centred at an altitude of around 1504.90 m (where the flux is lower than at 2100 m) so the normalization includes a scaling factor c_a. The equation [302] used to calculate this scaling factor is as follows:

$$I_1 = I_2 e^{\frac{A_2 - A_1}{L}} \qquad \rightarrow \qquad c_a = \frac{I_2}{I_1} \tag{104}$$

where $I_{1,2}$ are the fluxes at 1504.9 m and 2100 m, $A_{1,2}(h_{1,2}) = 1033 - 0.03648 h_{1,2} + 4.26 \times 10^{-7} h_{1,2}^2$ ($h_{1,2}$ are the altitudes in feet above sea-level) and the value of L used for each type of primary particle is

$$L_\mu = 261\ g\ cm^{-2}, \qquad L_p = 110\ g\ cm^{-2}, \qquad L_n = 136\ g\ cm^{-2}, \qquad L_\gamma = 100\ g\ cm^{-2}.$$

Since the protons, neutrons and photons were generated for an altitude of 2100 m, and the muon fluxes were taken for sea level (which is defined as zero altitude), the fluxes

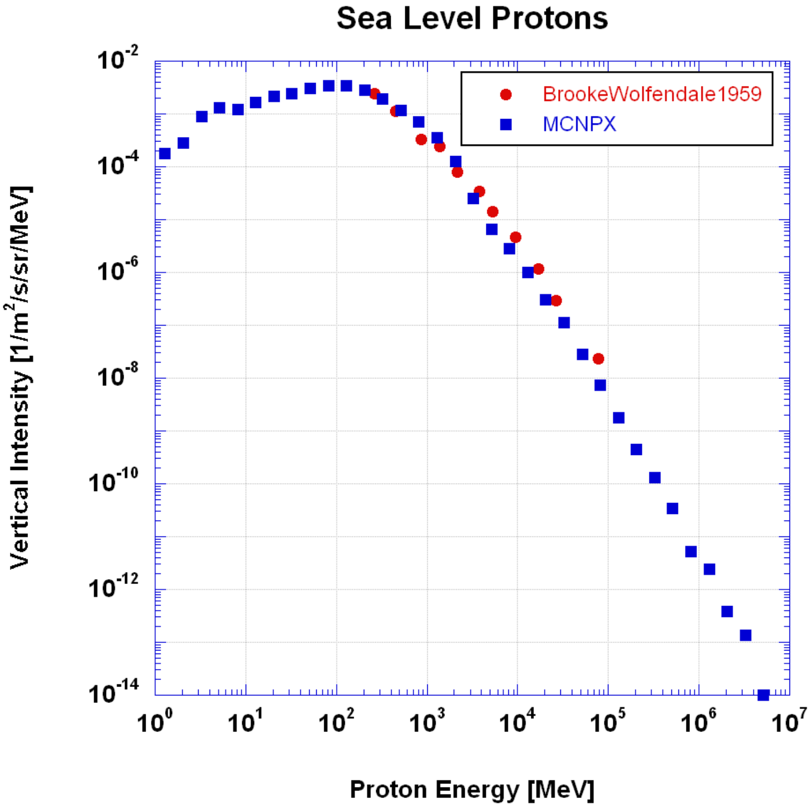

Figure 79: *A comparison [298] of the proton energy spectrum in the library generated by the particle transport and detector simulation code MCNPX [299] (which is used by CRY) to experimental data [300].*

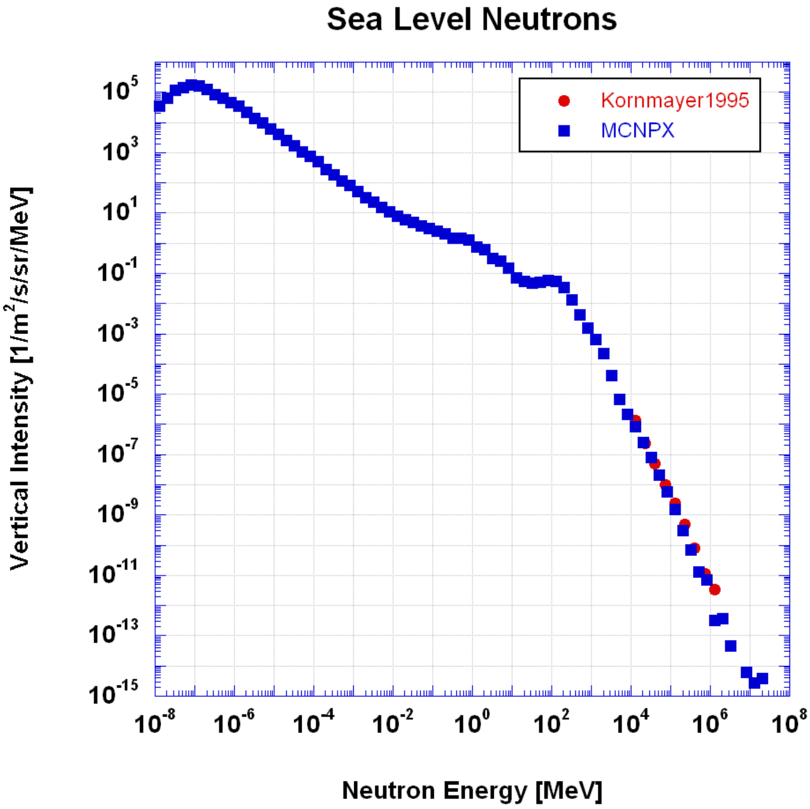

Figure 80: *A comparison [298] of the neutron energy spectrum in the library generated by the particle transport and detector simulation code MCNPX [299] (which is used by CRY) to experimental data [301].*

have been scaled by the following factors c_a:

$$c_a^p = 0.5784, \qquad c_a^n = 0.6418, \qquad c_a^\gamma = 0.5476, \qquad c_a^\mu = 1.4. \tag{105}$$

A further correction for the CRY-generated particle fluxes must be made since CRY calculates fluxes caused by primary cosmic-ray protons but not the heavier particles that also strike earth's atmosphere. This causes CRY to underestimate the flux by 70% [303] (although the energy dependence of this is not known), so any background count must be scaled up by a factor of 1.7. This factor may have an energy dependence but it has not been determined since there is no easy way of getting another calculation of proton fluxes (CORSIKA [304] code could be used but would require a lot of additional work, very large computation time and disk usage).

Another correction relating to the area over which the primary particles generated by CRY are sampled. To simulate neutron, proton and photon-induced events, their initial parameters (position, direction cosines, energy) were sampled on a plane measuring 100×100 m^2. For results in the simple detector geometry (Section 6.3), the area over which the primary neutrons are injected is 38×22 m^2 (Figure 82) and 100×100 m^2 for protons and photons. For the detailed detector geometry (Section 6.4), neutrons, protons and photons were all injected over a 50×50 m^2 area. If the area is reduced from the initial 100×100 m^2, the normalization is adjusted as follows:

$$t_f = t_i \frac{A_i}{A_f} \tag{106}$$

where $A_{i,f}$ refer to the area and before it has been reduced and $t_{i,f}$ are amount of the live time simulated.

The computation time is also greatly reduced by restricting the energy of the primary particle in question, since the vast majority of the background EM showers originate from relatively few primary particles at higher energies (Figure 81). For simulations where the primary particle is a muon, 92.3% of background EM showers result from muons with energies exceeding 10 GeV, yet muons above this threshold comprise only 19.6% of the flux. Similarly, in simulations where events are initiated a proton, 92.7% of the background showers descend from primary protons whose energy exceeds 10 GeV, yet these protons comprise just 0.76% of the CRY-generated flux. Also, for neutron primaries, 95.6%/78.9% of background showers come from neutrons whose energy exceeds 1 GeV/10 GeV, which comprise 6.5%/0.11% of the flux. For some sets of results the lower energy threshold imposed on muon, proton and neutron primaries have hence been chosen as E_μ >10 GeV, E_p >10 GeV and E_n >1 GeV respectively. The adjustment to the normalization required by this is described as follows.

As the flux of primary particles ($E > 0.1$ GeV and $E > 1$ GeV respectively) through a surface is generated, the time at which each particle crosses it is specified. The i^{th} primary particle would cross after time t_i so the mean time simulated per primary particle t_{mean} is:

$$t_{mean} = \frac{t_i}{i-1}. \tag{107}$$

For the 100×100 m^2 plane through which CRY generates the proton, neutron and photon fluxes, the reciprocal of the average rate of each type of particle t_{mean} is shown in Table 27.

Table 27: *The mean time per primary particle* t_{mean} *as generated via Gaisser's parametrization (for muons) and CRY (for protons, neutrons and photons [303]), where* $t_{mean} = (\textit{number of particles generated / time elapsed})^{-1}$ *(i.e. eqiuvalent to Eq. 107). The second column shows the minimum energy of the primary particle as generated by CRY or MUSIC. The third column shows which detector geometry the particles are stored on a surface appropriate for - the muons are on a box surrounding the detector enclosure and the protons, neutrons and photons are on a* 100×100 m^2 *plane that far-exceeds the boundaries of the top face of the detector enclosures. The fourth column shows the number of primary particles generated. The fifth column is the real time would be required to observe that number of particles arriving at the surface upon which they are stored. The sixth column shows* t_{mean}*, the ratio of the fourth and fifth columns.*

Primary particle	Minimum energy (GeV)	Detector	Number of particles generated	Time elapsed (s)	t_{mean} (s)
μ	1.0	simple	100,000,000	375.0	3.75×10^{-6}
μ	10.0	detailed	100,000,000	948.0	9.48×10^{-6}
p	0.1	both	7,639,676	758.6	9.93×10^{-5}
n	0.1	both	60,896,984	143.5	2.36×10^{-6}
γ	1.0	both	72,723,162	7761	1.07×10^{-4}

To impose a higher minimum energy thresholds than those shown in Table 27, the quantities t_{mean} are adjusted as follows:

$$t_{mean}^{eff} = t_{mean}\frac{N_{total}}{N_{threshold}}, \tag{108}$$

where t_{mean}^{eff} refers to the effective mean time simulated per primary particle, N_{total} is the number of primary particles generated and $N_{threshold}$ is the number of particles above the chosen energy threshold. For protons with energy greater than 10 GeV, $\frac{N_{total}}{N_{threshold}} = 131.579$. For neutrons with energy greater than 1 GeV, $\frac{N_{total}}{N_{threshold}} = 15.403$. No energy threshold is applied to the photons. Muons used with the simple detector geometry were generated with a minimum energy of 1 GeV and only using those of at least 10 GeV to generate events corresponds to $\frac{N_{total}}{N_{threshold}} = 5.102$. Muons used with the detailed detector geometry were generated with a minimum energy of 10 GeV, meaning all of these muons are used and so $\frac{N_{total}}{N_{threshold}} = 1$.

These $\frac{N_{total}}{N_{threshold}}$ values given for muons are appropriate for simulations with the flat surface profile but a further increase to $\frac{N_{total}}{N_{threshold}}$ is made depending on the choice of surface profile used. This is because of the process of preparing the muons to be suitable for an irregular surface causes some muons to be discarded, as discussed in Section 5.6. For the simple detector geometry the inclusion of the approximate surface profile (Section 6.5) causes $\frac{N_{total}}{N_{threshold}}$ to increase from 5.102 to 6.395, and for the detailed detector geometry the inclusion of the accurate surface profile causes $\frac{N_{total}}{N_{threshold}}$ to increase of $1 \rightarrow 1.122$.

The background rates are scaled up by a factor c_m to correct for the 7.7%, 7.3% and 4.4% of showers that are missed due to these low-energy primary muons, protons and neutrons not being simulated. This factor for each type of primary particle is as follows:

$$c_m^{\mu} = 1.077, \qquad c_m^{p} = 1.073, \qquad c_m^{n} = 1.044, \qquad c_m^{\gamma} = 1. \tag{109}$$

The amount of real detector time simulated t_{sim} is calculated from the corrected mean time per event (i.e. per primary particle) t_{mean}^{corr}, where t_{mean}^{corr} is t_{mean} after applying the corrections of Eq. 106 and Eq. 108 :

$$t_{sim} = n_{sim}\frac{A_i}{A_f} \cdot \frac{N_{total}}{N_{threshold}} \cdot t_{mean} \equiv n_{sim}t_{mean}^{corr} \tag{110}$$

where n_{sim} is the total number of events simulated with Geant4.

The number of background EM showers n_{sh} is converted into the annual rate using

$$f_y = \frac{t_{sim}}{t_w}, \tag{111}$$

where f_y is the fraction of one calendar year and t_w is the time window in a calendar year during which background events can pose a problem to beam measurements. The neutrino beam is expected to be operational for $2{\times}10^7$ s yr^{-1} [305]. Each beam spill is repeated every 1.33 s. The maximum time required to drift a track across a TPC cell is assumed to be 1.4 ms. The overall annual time window t_w for background EM showers to appear in the detector is therefore:

$$t_w = \frac{2 \times 10^7 \; s\; yr^{-1}}{1.33 \; s} \times 1.4 \times 10^{-3} s = 21052.62 \; s\; yr^{-1}. \tag{112}$$

Also each beam spill will last 10 μs so if the photon detection system (Section 6.2.6) is taken into consideration, the annual window for background to be considered decreases to:

$$t_w = \frac{2 \times 10^7 \; s\; yr^{-1}}{1.33 \; s} \times 10^{-5} s = 150.34 \; s\; yr^{-1} \tag{113}$$

This produces a reduction factor of 1/140 that is not included in the normalization calculation, but is eventually applied to the background rates to include the effect of the photon detection system. A 100% efficient photon detector is assumed, and will be able to locate EM showers in time and space.

The normalized annual rate of background EM showers R is therefore calculated as follows:

$$R = n_{sh} \times \frac{c_a c_c c_m}{f_y} \tag{114}$$

where n_{sh} is the number of EM showers/first-generation gamma counted. This is stated more explicitly in Eq. 115.

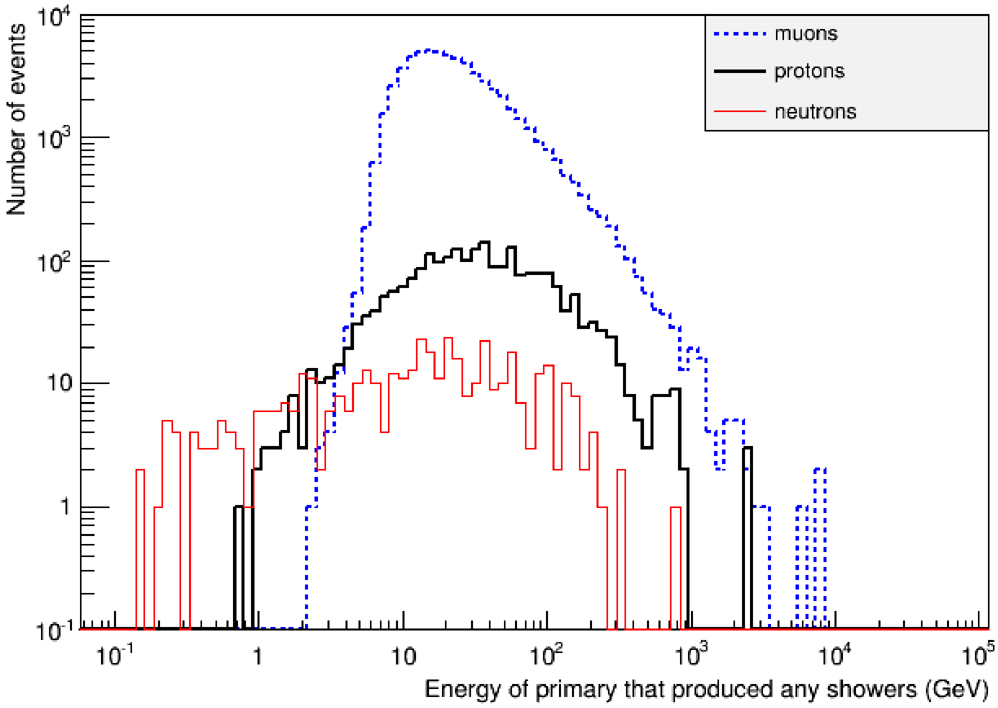

Figure 81: *Energy spectra of primary particles causing at least 1 EM shower* ($E > 100$ *MeV) in the active volume of the simple detector, after simulating* 2×10^7 *events for each type of primary particle. This justifies the minimum energy threshold (Eq. 108) for primary particles (thus reducing computation time). Primary photons have not been plotted here since only a small fraction of atmospheric photons can reach the detector.*

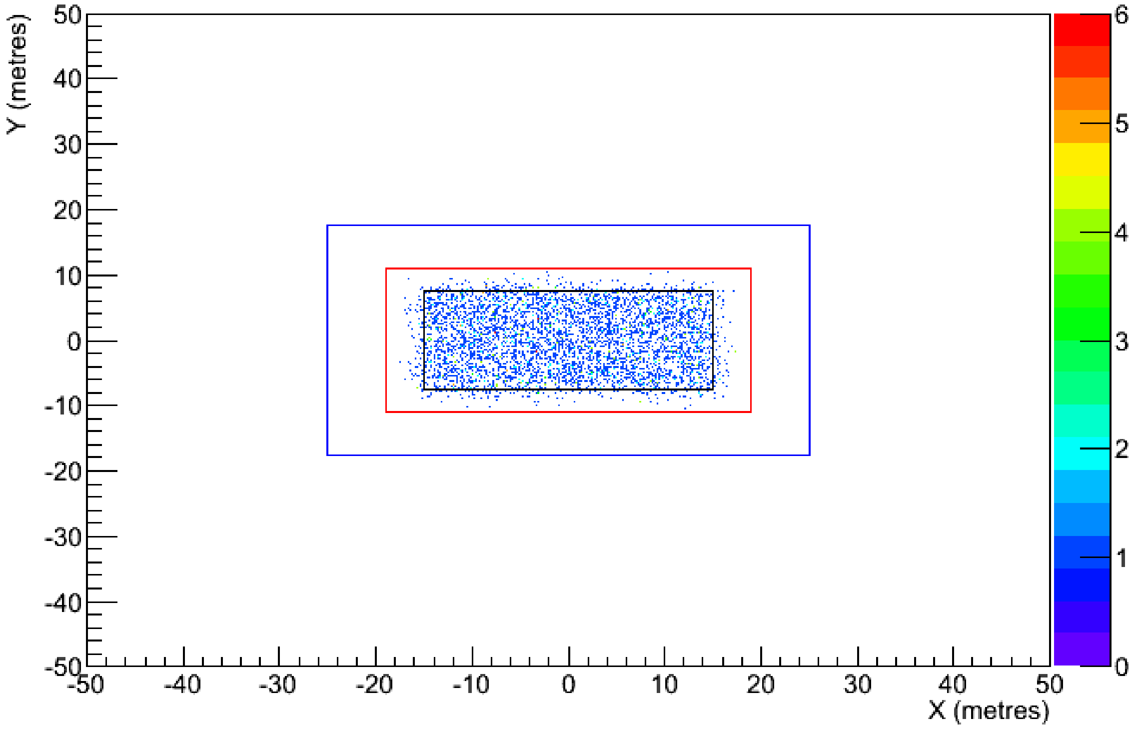

Figure 82: *The initial (x,y) positions of primary neutrons causing at least one EM shower* ($E > 100$ *MeV) to happen inside the LAr for the simple detector geometry, seen from a bird's eye view. To reduce computation time, the area of* 100×100 m^2 *for which CRY generated the neutron flux was scaled down to a* 38×22 m^2 *region (red box). Primary protons (not shown) were injected over the* 50×35 m^2 *area (blue box). Also (not shown) the injection area when using the detailed detector geometry was* 50×50 m^2 *for both neutrons and protons.*

Summary of the normalization calculation

Injecting a given number of primary particles n_{sim} into the simulation corresponds to some (mean) amount of detector operation time. The fraction of a year simulated (and hence the annual rate) is based on the detector being operational during beam spills for a total of 21053 seconds per calendar year. This yearly window for the detector to observe background events is based on a beam spill of 10 μs, a maximum of 1.4 ms to drift an electron across a TPC cell (shorter depending on where in the cell the electron track appears), the beam being operational for 2×10^7 seconds per calendar year and each beam cycle lasting 1.33 s. The normalized annual rate R of background EM showers is calculated as follows:

$$R = n_{sh} \times \left(\frac{c_a c_c c_m t_w}{n_{sim} \cdot \dfrac{A_i}{A_f} \cdot \dfrac{N_{total}}{N_{threshold}} \cdot t_{mean}} \right) \tag{115}$$

where:

- t_{mean} is the mean amount of time that each primary particle generated by CRY or Gaisser's parameterization corresponds to (Eq. 107, Table 27).
- N_{total} is the total number of these primary particles stored in an file that is used by Geant4 as the input to initiate simulate events.
- $N_{threshold}$ is the number of these primary particles above any energy threshold that may be imposed after the generation of the primary particle input files.
- n_{sim} is the number of events simulated via Geant4, each event being started by injecting a primary particle into the simulation.
- n_{sh} is the number of background EM showers/first-generation gammas counted.
- A_i (= 100×100 m^2) is the area of the plane upon which CRY is instructed to generate the proton, neutron and photon fluxes appropriate for an altitude of 2100 m.
- A_f is the area of the rectangle above the detector (i.e. near the rock surface within the Geant4 simulation) over which the primary neutrons, protons or photons are injected (muons are not injected over a plane, rather they are stored on the surface of a 3D box).
- c_a corrects for altitude of the detector being different to the altitudes for which the primary particle fluxes have been generated (shown in Eq. 105).
- c_m corrects for the small amount of background missed due to not using primary particles under a given energy threshold (shown in Eq. 109).
- c_c corrects for CRY's 70% underestimate of the flux intensity ($c_c = 1$ for muon-initiated events since CRY is not used to generate the muons).
- t_w is the total time per calendar year during which background events can occur (21053 s).

Table 28 shows a summary of all the parameters used to calculate the overall scaling factor applied to the number of EM showers observed, for each set of results.

Table 28: *A summary of the values used in the normalization calculation for each set of results. The final column shows the overall scaling factor applied to the number of EM showers observed to convert to an annual rate. This scaling factor is expression enclosed within parentheses in Eq. 115. The first and second row are both for muon-induced events, the former with the simple detector geometry and the latter with the detailed geometry. The muons used with the simple geometry were initially generated with energies greater than* 1 *GeV. From these muons only those over* 10 *GeV were used to produce the results presented in this thesis, causing* $\frac{N_{total}}{N_{threshold}} = 5.102$ *according to Eq 108. For the detailed geometry, a different set of muons were generated since the detector enclosure is a different shape and size. However, in this instance the* 10 *GeV lower limit was imposed on the muons as they were being generated, so none of them were discarded and* $\frac{N_{total}}{N_{threshold}} = 1$. *This is also the reason that* t_{mean} *is different for the two detector geometries. Also the first and third row are both for muon-induced events with the simple detector geometry, the former using the flat surface and the latter using the approximate surface. For the latter,* $\frac{N_{total}}{N_{threshold}}$ *is slightly greater. This is because the muons used for the third row are those used for the first row that have had their trajectory extrapolated from high altitude the detector altitude, and their energy loss is calculated based on the distance of rock the ray intersects. They are then stored on a surface much closer to the detector to be sampled by Geant4, as explained in Section 5.3.2. Due to their trajectory taking them too far from the detector to be necessary, or energy losses, some muons are deemed unnecessary and discarded, causing the ratio* $\frac{N_{total}}{N_{threshold}}$ *to increase. The same applies to the second and fourth rows, which are both for muon-induced events with the detailed detector geometry; the former is the flat surface and the latter is the accurate surface. For muon-induced events,* $c_c = \frac{A_i}{A_f} = 1$ *since CRY is not used to generate the primary muons.*

Primary particle	Section	E_{min} (GeV)	$\frac{A_i}{A_f}$	$\frac{N_{tot}}{N_{thr}}$	c_a	c_c	c_m	t_{mean} ($\times 10^{-6}$ s)	n_{sim} ($\times 10^{8}$)	Overall factor
μ	6.3.1, 6.3.2	10	1	5.102	1.4	1	1.077	3.491	2.8	6.36555
μ	6.4.1, 6.4.2	10	1	1	1.4	1	1	9.480	0.8	38.86366
μ	6.5	10	1	6.395	1.4	1	1.077	3.491	0.8	17.77490
μ	6.6.1, 6.6.2	10	1	1.122	1.4	1	1	9.480	2.0	13.85514
p	6.3.4	0.1	6.925	1	0.578	1.7	1.073	99.3	1.0	3.64831
p	6.4.4	10	4	131.579	0.578	1.7	1.073	99.3	0.1	0.42711
n	6.3.3	1	11.962	15.403	0.642	1.7	1.044	2.36	0.106	5.19435
n	6.4.3	1	4	15.403	0.642	1.7	1.044	2.36	1.1	1.50706
γ	6.3.5	0.1	5.714	1	0.548	1.7	1	107.0	0.8	0.40126

5.5 Energy, position and angular smearing

Smearing algorithms have been applied to the energy, position and direction cosines at each step of a particle's trajectory. The x, y and z components of each particle position recorded by Geant4 are smeared by choosing a random position from a Gaussian distribution with a width of 5 mm (since the wire separation of the anode plane assembly in the detector is assumed to be around 5 mm) centred on what Geant4 deems the 'true' position. Similarly each particle's energy is smeared by choosing a random energy from a Gaussian distribution centred on the 'true' energy E, where the Gaussian width depends on the energy of the particle in accordance with the LBNE 'Fast MC' simulations [306]:

$$0.15 \times \frac{1}{\sqrt{E(\text{MeV})}}.$$

Table 29: *The parameters used to smear the direction of each type of particle. These values are the same as those used in the LBNE 'Fast MC' simulations [306].*

particle	**bias (^{o})**	**spread (^{o})**
$\mu^{\pm}$	0.0	1.0
$e^{\pm}$	0.0	1.0
$\pi^{\pm}$	0.0	1.0
π^{0}	0.0	3.0
γ	0.0	1.0
p	0.0	5.0
n	0.0	5.0
other	0.0	5.0

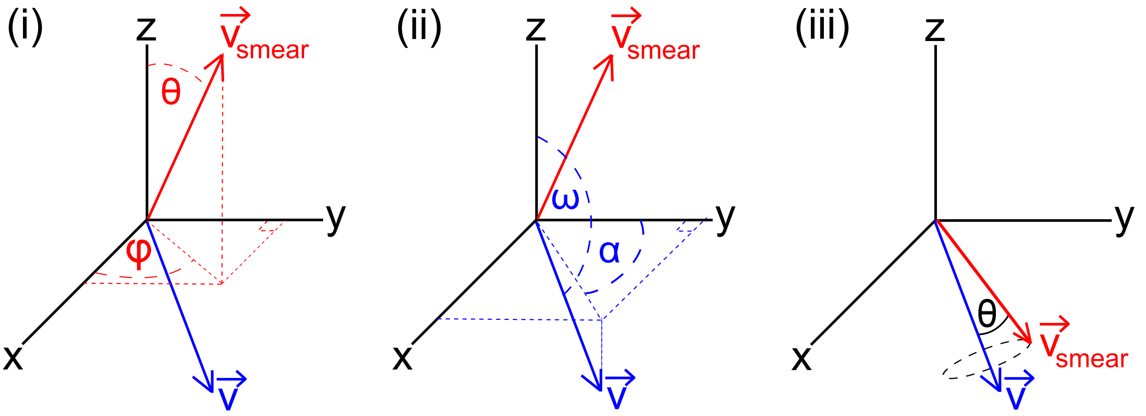

Figure 83: *Examples of the vectors and angles involved in the smearing of the direction of each segment along a particle's trajectory.*

Angular smearing is applied to a vector **v** that points along the particle's track (segment), where the Gaussian width depends on the type of particle involved. A table showing the smearing used for each particle is shown in Table 29.. First a random angle θ is chosen from a Gaussian distribution centred at 0° and with a width specific to the type of particle involved (Table 29). Using spherical polar coordinates (r, θ, ϕ) the Cartesian unit vector **z** = (0,0,1) is deflected away from the z-axis by this randomised zenith angle, θ. Then the azimuth angle ϕ is selected at random from a uniform distribution between 0 and 360^o, thus creating an initial smeared vector $\mathbf{v}_{smear}$ = (1, θ, ϕ) (an example of these angles is shown in diagram (i) of Figure 83). Then $\mathbf{v}_{smear}$ undergoes two rotations about the origin. First of all, $\mathbf{v}_{smear}$ is rotated about the x-axis by the angle ω that separates **v** from the +ve z-axis. Then **v** is projected onto the (x, y) plane, where this projection forms an angle α with the +ve y-axis (diagram (ii) of Figure 83). To complete the smearing process, $\mathbf{v}_{smear}$ is rotated about the z-axis by the angle α, making an angle θ with **v** (diagram (iii) of Figure 83). Figure 84 shows the result of smearing 10^4 vectors for two commonly used Gaussian widths.

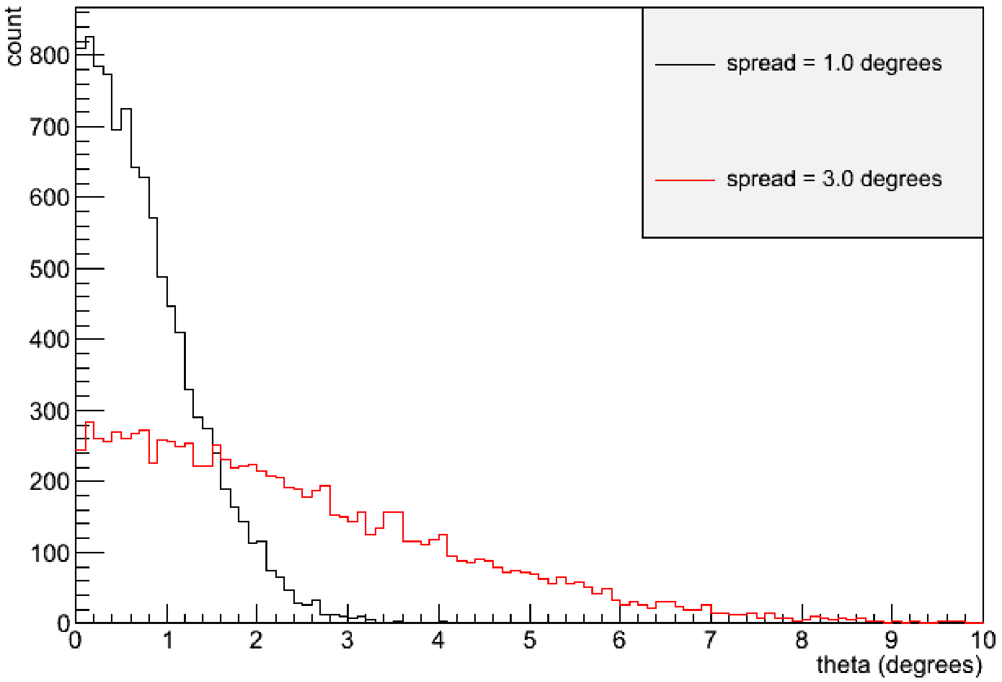

Figure 84: *Smearing has been performed using Gaussian widths appropriate for specific particles (see Table 29). Shown here are the angles formed between* 10^4 *initial vectors and their smeared counterparts for two example widths of* $1°$ *and* $3°$*.*

5.6 Accurate surface profile

For the detailed detector geometry described in Section 5.3.2, two sets of simulations have been performed. One set is for the flat surface, for direct comparison with the simple detector geometry. The other set is for an accurate surface profile. The surface coordinates of the detector site are 44^o 20' 41" N, 103^o 45' 5" W, as well as an elevation of 1534 m, which correspond to a once-proposed site for the 10 kton LBNE detector at the surface.

To reduce computation time, muons that initially occupied a plane 600 m above the detector have been gradually stepped along their trajectory before being stored in a region close to the detector enclosure. A satellite-generated map [307] of the surface profile in a $20{\times}20$ km^2 area around the detector site has been used to determine whether a muon is above or below ground at a given step along its journey towards the detector (Figure 85). The distance that a muon travels through rock is calculated and the muon is transported through this distance with Geant4 until it reaches the surface of a cuboid measuring $80{\times}80{\times}36$ m^3. This cuboid encompasses the detector and a few metres of rock around it; muons with an initial trajectory that does not pass through or close to the detector are discarded.

At this point the muons' parameters are stored on the disk. As a result the muons are transported through rock modelled with an accurate surface profile, close enough to the detector to save time when running repeated jobs, yet far enough away to avoid missing out on any particles that might enter the detector's active volumes after being created in interactions outside these volumes. During the process of preparing muons in this way,

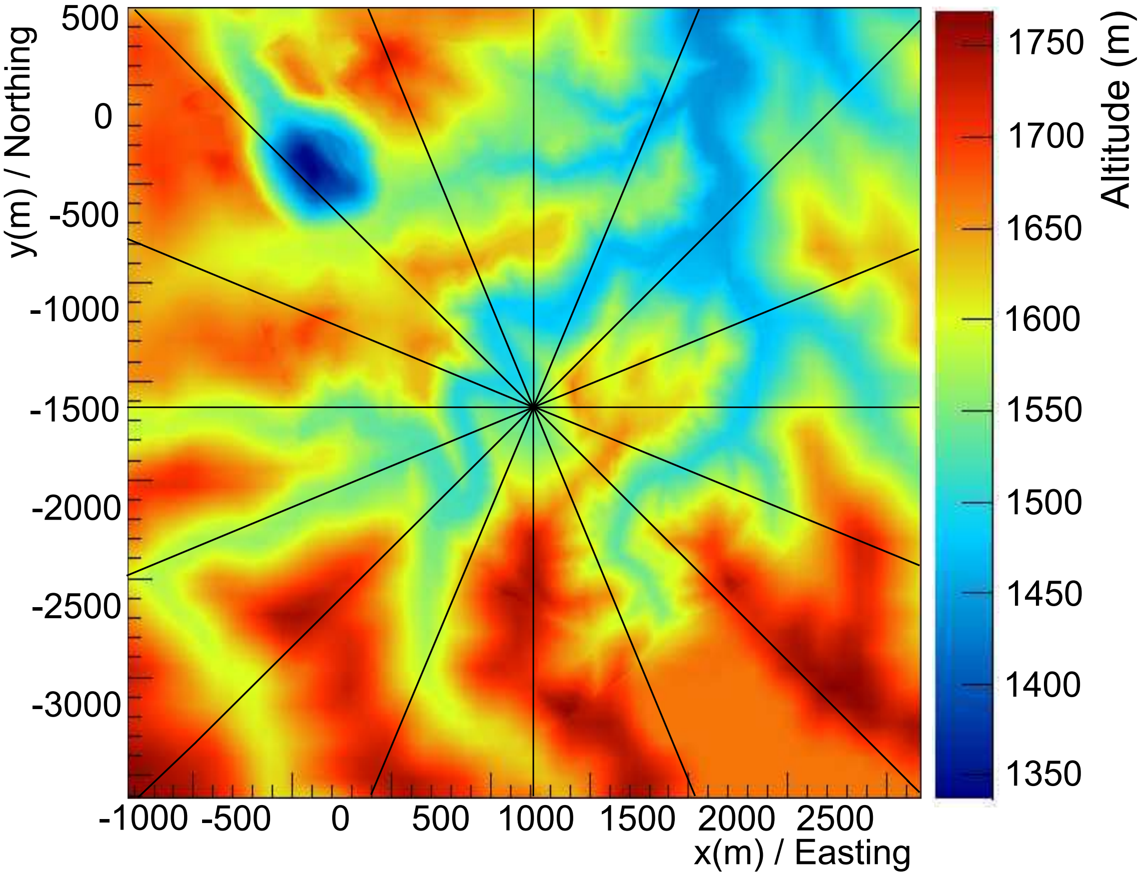

Figure 85: *A bird's eye view of the surface profile surrounding the detector site* 44° 20' 41" *N,* 103° 45' 5" *W, which is indicated by the dot at the centre of the image. The colour scheme shown in the right column denotes the altitude (in metres) above sea level. The beam approaches from a south-east direction, forming a* 7° *angle with east (the x-axis). The map used to generate this plot extends* 10^4 *m in the +/- x, y directions, and has* 5×5 *m^2 binning, although only a smaller area is shown here.*

some are discarded due to energy losses or their trajectory taking them too far from the detector to be worth simulating. This impacts the $\frac{N_{total}}{N_{threshold}}$ parameter in the normalization calculation (Table 28). The surface map has been modified to include a flattened area measuring 100×100 m^2 above the detector site, since it has been assumed that the detector would be placed beneath ground that would need to be flat to accommodate buildings/facilities. Since this is the same area as the plane over which the protons and neutrons were generated by CRY, and significantly larger than the top face area of both the simple and detailed detector enclosures, the same protons and neutrons can be used for both detector geometries.

5.7 Further details

5.7.1 Hit information

In each event a series of 'hits' is recorded, where each particle being stepped along its trajectory has possible certain kinematic variables associated with the particle at that moment written to file (as well as some other useful information). The information stored at each hit is the event ID number, the ID number of the parent particle from which the track in question was born, the ID number of the particle track itself, the name of the particle, the energy deposited during the previous step, the energy the particle now possesses, the process through which this particle was created, Cartesian coordinates of the current location of the particle, direction cosines, time elapsed since the start of the event, the ID number of the primary muon responsible for starting the event, its energy and its initial coordinates.

5.7.2 Production cuts

The computation time and amount of recorded information have been minimised without compromising the validity of the results. Geant4 provides the option of setting a threshold on the range that a given type of particle must be capable of travelling, below which no secondary particles will be generated. The chosen range is converted to an energy threshold specific to a given medium. Since the focus is on electrons, positrons and gammas with energy in excess of 250 MeV, to reduce computation, time the LAr volume has a production cut of 34.0 cm for electrons and 35.5 cm for positrons. This corresponds to an energy threshold of 100.869 MeV for each. The production cut for gammas is set to 1.495 m or 12.393 MeV, the maximum value permitted by Geant4. The amount of information recorded is reduced by only recording the interactions of particles with energies in excess of 100 MeV. To generate less simulated data, no electrons or positrons are recorded if their parent particle is a gamma (unless otherwise stated) since these are just a sub-branch of an EM shower.

6 Results for $\nu_e/\overline{\nu}_e$ appearance background simulations

When discussing EM showers in the following sections, the 'ancestry' of each shower is often mentioned. The term refers to the parent and sometimes also the grandparent particle of a 'first-generation gamma' (i.e. the first photon to produce an $e^+ e^-$ pair and initiate an EM shower) and is spoken of in terms of 'grandparent' $\rightarrow$ 'parent' $\rightarrow \gamma$ (for example, $\pi^\pm \rightarrow \pi^0 \rightarrow \gamma$). However, this is only concerned with the chain of particles preceding the first-generation gamma and should not be interpreted as indicating any specific process. For example, the ancestry $\pi^0 \rightarrow \gamma$ could refer to a photon produced through $\pi^0 \rightarrow 2\gamma$ or $\pi^0 \rightarrow e^+e^-\gamma$. Also each first-generation gamma is treated as the start of separate EM showers so, for example, in a single instance of π^0 decay via $\pi^0 \rightarrow 2\gamma$, both gammas (and therefore two distinct showers) would be counted.

The vast majority of potential background comes from EM showers that begin with $\gamma \rightarrow e^+e^-$ (Sections 6.3-6.7). However, a small number of background showers also start with e^+/e^- that produced from the decays $\pi^0 \rightarrow e^+e^-\gamma$ and $K_L^0 \rightarrow \pi^\pm e^\mp \overline{\nu_e}/\nu_e$, so discussion of this minor background is left until afterwards (Sections 6.9, 6.10).

All figures showing a number of EM showers are normalized to the annual rate unless otherwise stated. Table 28 shows the parameters used in the calculation of the normalization factor, which is given by Eq. 115. All tables show the annual rate of EM showers but the captions include the overall normalization factor, from which the raw number of EM showers counted from the simulated data can be determined. Table 28 shows a summary of the parameters involved in calculating each overall scaling factor applied to the number of showers observed.

6.1 Results before cuts

The counts of background EM showers due to each type of cosmic particle are shown in Table 30 for the simple detector geometry and flat surface profile.

Table 30: *The annual rate of first-generation gammas* ($E_\gamma > 100$ *MeV*) *resulting from each type of primary particle for the simple detector geometry. The second column indicates the years of live detector time that have been simulated. The last column contains the number of EM showers normalized to one calendar year of detector operation.*

primary particle	**years simulated**	**EM showers (annual rate)**
μ	0.237	$(5.059 \pm 0.001)\times10^8$
p	0.270	$(2.745 \pm 0.010)\times10^5$
n	0.424	$(1.798 \pm 0.009)\times10^5$
γ	2.317	53 ± 7

At $\mathcal{O}(10^8)$ yr^{-1}, the rate of background EM showers greatly exceeds the expected annual rate of ν_e interactions from the beam, which is $\mathcal{O}(10^2)$ yr^{-1}. A variety of cuts have therefore been investigated to identify and eliminate as many background EM showers as possible. Table 31 contains further details of the events simulated in the various subsections sometimes later referred to as the "Main results", which use a specific set of cut thresholds and have the best statistics. However, the justification for these thresholds and the effect of varying the thresholds for each cut are discussed in Section 6.3.7.

Table 31: *For each type of primary particle, detector and surface configuration (apart from muon-induced events with the simple detector geometry and approximate surface profile) investigated in Sections 6.3.1, 6.3.2, 6.3.3, 6.3.4, 6.3.5, 6.4.1, 6.4.2, 6.4.3, 6.4.4, 6.5, 6.6.1, and 6.6.2, the percentage of the events simulated for which some particle activity is recorded in an LAr volume is shown in the fourth column. The percentage of these events in which the primary particle itself appears in the LAr is shown in the fifth column. The number of primary particles passing through the LAr per second is shown in the sixth column and per* 10 μs *beam spill in the seventh column.*

Primary particle	Detector geometry	Surface profile	Events with activity in LAr (%)	Primary reaches LAr in these events (%)	Primaries in LAr per second	Primaries in LAr per spill
μ	simple	flat	38.19	>99.99	2.14×10^6	21.43
μ	detailed	flat	28.12	99.97	2.97×10^6	29.67
μ	detailed	accurate	30.85	99.97	2.92×10^6	29.21
p	simple	flat	0.12	0	0	0
p	detailed	flat	1.95	0.008	2.99×10^{-2}	2.99×10^{-7}
n	simple	flat	0.50	0.42	4.85	4.85×10^{-5}
n	detailed	flat	0.08	0.09	0.58	5.76×10^{-6}
γ	simple	flat	0.0003	0	0	0

6.2 Description of cuts and thresholds used for main results

6.2.1 Energy cut

The vast majority of neutrinos in the DUNE beam are assumed to be within an energy range of 0.5 - 5.0 GeV. Since the ν_e need not impart its full energy to the electron resulting from its CC interaction, any EM showers with total energy not within the range 0.25 - 5.00 GeV are dismissed as non-signal events (other energy ranges are tested in Section 6.3.7.2). For most of the results (Sections 6.3-6.7) one needs only to consider the first gamma in the shower (the ‘first-generation’ gamma) since it carries the energy of the whole shower. The cut has therefore been applied to this first-generation gamma energy, even though the gamma itself will not be observed by the detector.

6.2.2 Point of closest approach (PoCA)

Charged particles will leave a track in the detector. The trajectory of a gamma is also recorded by Geant4 (although invisible to the detector, the direction of the first-generation gamma can be reconstructed from the EM shower). This direction and the track of some other charged particle may be extrapolated (the extrapolated tracks may extend outside of the LAr). The minimum separation of these extrapolated lines is then calculated (Figure 86). Since the charged particle undergoes scattering, PoCA is calculated between the ‘true’ gamma direction and each segment of the path that the charged particle took[39].

---

[39] It should be noted that the PoCA cut efficiency is affected by the number of track segments there are to calculate PoCA with respect to, which in turn depends on user-specified thresholds for Geant4...

If the smallest PoCA out of all of the segments is below a certain threshold then the EM shower can be associated with the charged particle, and therefore be discounted as part of the background.

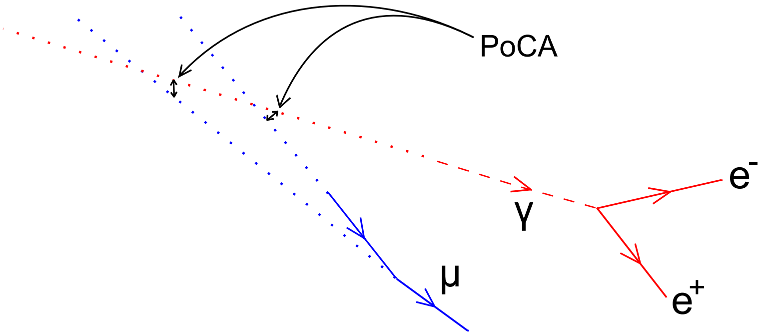

Figure 86: *The extrapolations of two segments of a muon track, for the PoCA calculation. This is a 2-D diagram of a 3-D calculation, so the closest approach of the gamma with respect to each extrapolated muon track segment has not been drawn where the lines intersect.*

When calculating the PoCA with respect to the muon track, a 30 cm cut is the main cut used, although the effect of a 10 cm cut is also briefly discussed in Section 6.3 as well as a wider range of thresholds in Section 6.3.7.3. PoCA is also calculated with respect to all other charged tracks in the event with a 10 cm cut threshold (other thresholds are tested in Section 6.3.7.4), to avoid rejecting the sought ν_e-induced showers. A lower threshold than that set for the primary muon is used because a genuine ν_e interaction could have hadrons and an electron coming from the same vertex, such as the situation shown in Figure 87. In such cases, the PoCA with respect to these hadron tracks would be small. The cut threshold should therefore be correspondingly small, to minimize the risk of mistakenly identifying signal EM showers as background showers in which the initial $\gamma \rightarrow e^+e^-$ vertex is very close to the creation vertex of a charged hadron.

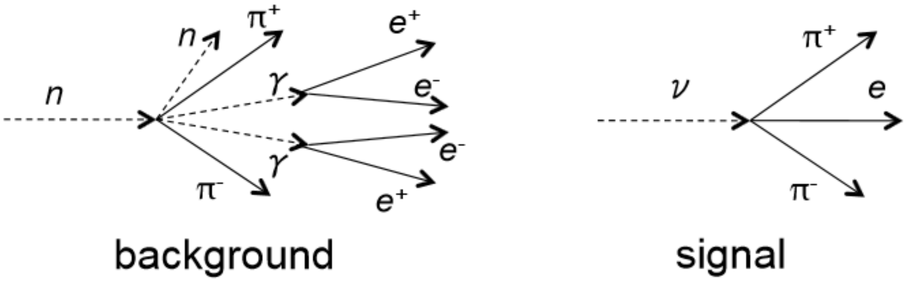

Figure 87: *Diagrams of a possible background shower and a ν_e interaction. This background EM shower may be indistinguishable from the ν_e interaction provided that the $\gamma \rightarrow e^+e^-$ vertex occurs close enough to the gamma creation vertex. For this reason the cut on PoCA with respect to all tracks (except for the primary muon track) in the event (including the primary and other muons) is only applied when this distance (see Figure 88) exceeds 2 cm, to avoid rejecting signal events.*

Specifically this is a concern since much of the background is due to EM showers where the ancestry is $p/\pi^+/\pi^- \rightarrow \pi^0 \rightarrow \gamma$. The π^0 will decay rapidly and produce the gamma

---

...to output information, as will be discussed later in this section.

close to the charged hadron vertex. If one of the gammas also rapidly produces an electron/positron pair, there will be no visible separation between the gamma creation vertex and $\gamma \rightarrow e^+e^-$ vertex. Only if the distance the gamma travels before causing $e^+ - e^-$ pair-production is large enough can the PoCA cut be safely applied with respect to these charged hadron tracks. Figure 88 shows the distribution of these distances. The TPC readout wires are separated by 0.5 cm so a conservative threshold distance of 2 cm is required before this PoCA cut is applied.

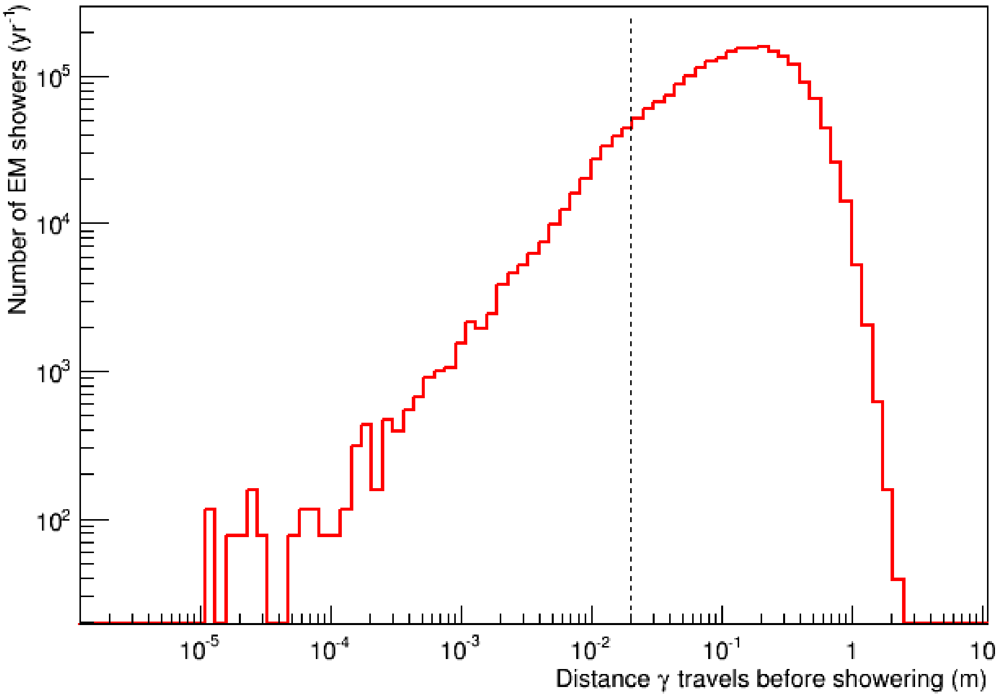

Figure 88: *The distribution of the distance between the* $\pi^0 \rightarrow \gamma\gamma$ *vertex and subsequent* $\gamma \rightarrow e^+e^-$ *vertices (each of these gammas is treated as the first-generation gamma of a distinct EM shower, so both have their PoCA calculated with respect to any charged parent that the* π^0 *may have). Much of the background is due to EM showers whose ancestry is* $p/\pi^+/\pi^- \rightarrow \pi^0 \rightarrow \gamma$*. The rapid decay of the* π^0 *places the gamma production vertex very close to the* π^0 *production vertex. If the* $\gamma \rightarrow e^+e^-$ *vertex happens too short a distance away from this for the detector to resolve a separation, this looks like a genuine* ν_e *interaction where tracks from an electron and charged hadrons appear at the same point, as illustrated in Figure 87. A PoCA cut could not be safely applied in such a situation.*

It should be noted that, as mentioned in footnote 39, the efficiency of the PoCA cut is significantly affected by the choice of production cuts discussed in Section 5.4. Only electrons and positrons with energies exceeding 100 MeV are recorded, otherwise they are not transported and their energy is deposited at a single point of their production in the detector. As a muon crosses the LAr it causes ionization (as well as stochastic energy losses) but will only have a hit recorded when the energy of the resulting electron or gamma exceeds this threshold. Lowering the threshold for electron production therefore means recording more hits by the ionizing muon, resulting in more, shorter, track segments to calculate PoCA with respect to. Figure 89 shows the distribution of primary muon track segment lengths after simulating 10^4 primary muons (10 GeV and above) for a range of electron/positron production cuts. Most results in this paper use production cuts of 340 mm and 355 mm (i.e. 100 MeV) for electrons and positrons respectively. With this choice of production cuts, only a few hits from muons are recorded, and typically this distance between hits is around 2.8 m in the sensitive volume. Figure 89 shows this spike at 2.8 m for large productions cuts.

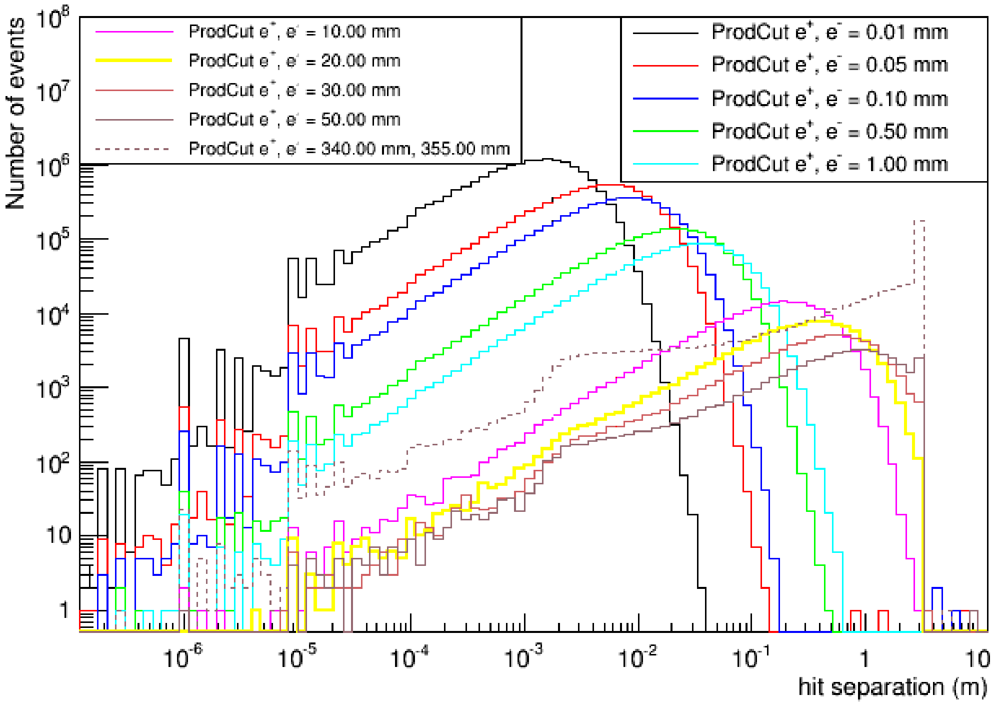

Figure 89: *The distribution of the distance between two hits from the primary muon. Each series has a different cut on electron/positron production, which determines the number of electron tracks that Geant4 must simulate. This in turn determines the number of hits from the primary muon responsible and therefore affects the accuracy of the muon trajectory. This difference in track segment length has a considerable impact on the PoCA calculation in general (Figure 90), but not on the number of EM showers that survive this cut.*

Figure 90 shows a comparison of the distributions in PoCA with respect to the primary muon of first-generation gammas resulting from 2×10^7 muon-induced events, for the usual electron and positron production cuts (340 mm and 355 mm respectively corresponding to ∼100 MeV), as well as 0.5 mm (∼220 keV) and 0.1 mm (∼80 keV). Although the effect in general is large, the number of gammas that survive the cut of 30 cm (indicated by dashed vertical line on Figure 90) is not massively affected. In short, a PoCA cut (30 cm with respect to the muon track, 10 cm with respect to charged hadrons) should perform marginally better in reality than it does when applied to this simulated data (although it still proves very effective).

Figure 91 shows the energy-dependence of the PoCA with respect to the primary muon track. For EM showers with energy greater than ∼ 1.5 GeV, lowering the cut threshold from 30 cm to 10 cm would have a negligible impact on the number of showers being rejected while lowering the risk of erroneously rejecting signal events. This is discussed further in Section 6.3.7.

A similar cut has also been investigated, regarding the distance from the first $\gamma \rightarrow e^+ e^-$ vertex in an EM shower to the primary muon track. This is calculated for each segment of the muon track, searching for the shortest possible distance. This distance for 10^7 of these $\gamma \rightarrow e^+ e^-$ vertices has been compared to their separation at the point of closest approach in Figure 92. From this Figure it is clear that PoCA is the superior cut.

Finally, Figure 93 shows the effect that the smearing process described in Section 5.5 has on the PoCA calculation.

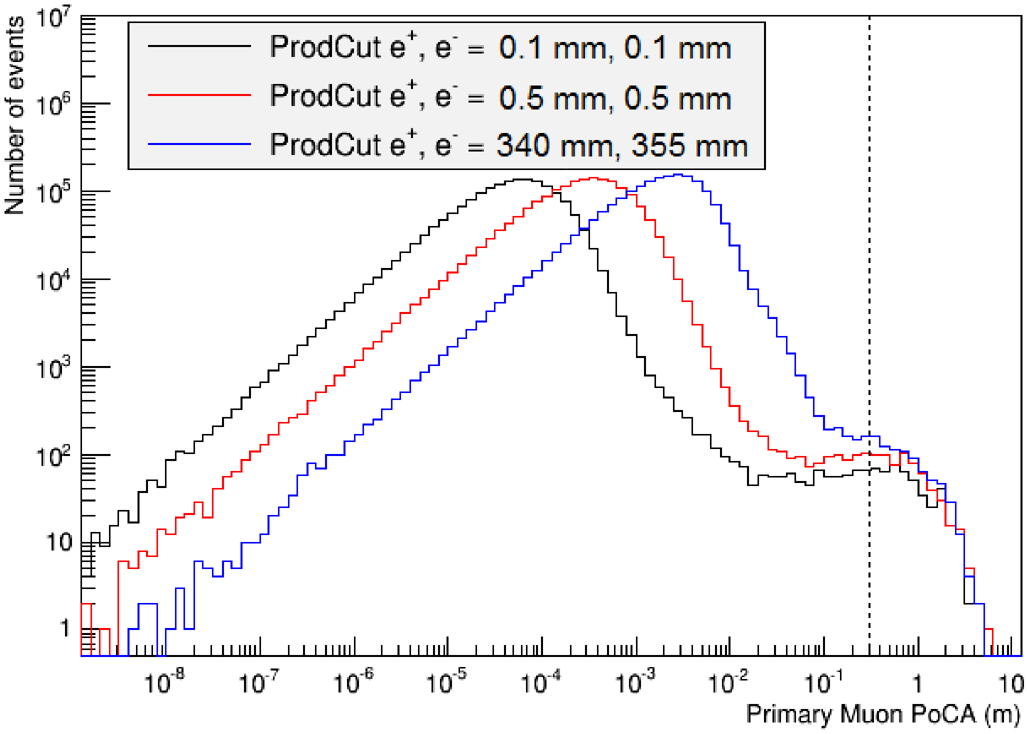

Figure 90: *The distribution of PoCA with respect to the primary muon track of the first-generation gammas resulting from* 2×10^7 *muons, using* 3 *different sets of electron and positron production cuts. One series uses range cuts of* 340 *mm for electrons and* 355 *mm for positrons, which translate to production thresholds of* $\sim$ 100 *MeV each. The second series has the production threshold set at* 0.5 *mm or* $\sim$ 220 *keV and the final series has the production threshold set at* 0.1 *mm or* $\sim$ 80 *keV. This causes more hits to be recorded for the primary muon (since Geant4 is simulating more ionization electrons), which improves the effectiveness of the PoCA cut. The production cuts of the first series* (100 *MeV) have been used for all the results stated in this paper. Since the detector will be dealing with track segments (Figure 89) with a lower limit of a few centimetres, production cuts which produce a similar mean separation for recorded primary hits would be most appropriate. The* 0.1 *mm and* 0.5 *mm cuts represent a better than best-case scenario. The effect of changing the production cuts is large on the whole, but the number of gammas that survive the cut at* 30 *cm (dashed vertical line) is not significantly affected* (832 *in the first series,* 643 *in the second series and* 476 *in the third series). After other cuts have been applied, the difference this causes to the final rate is minor.*

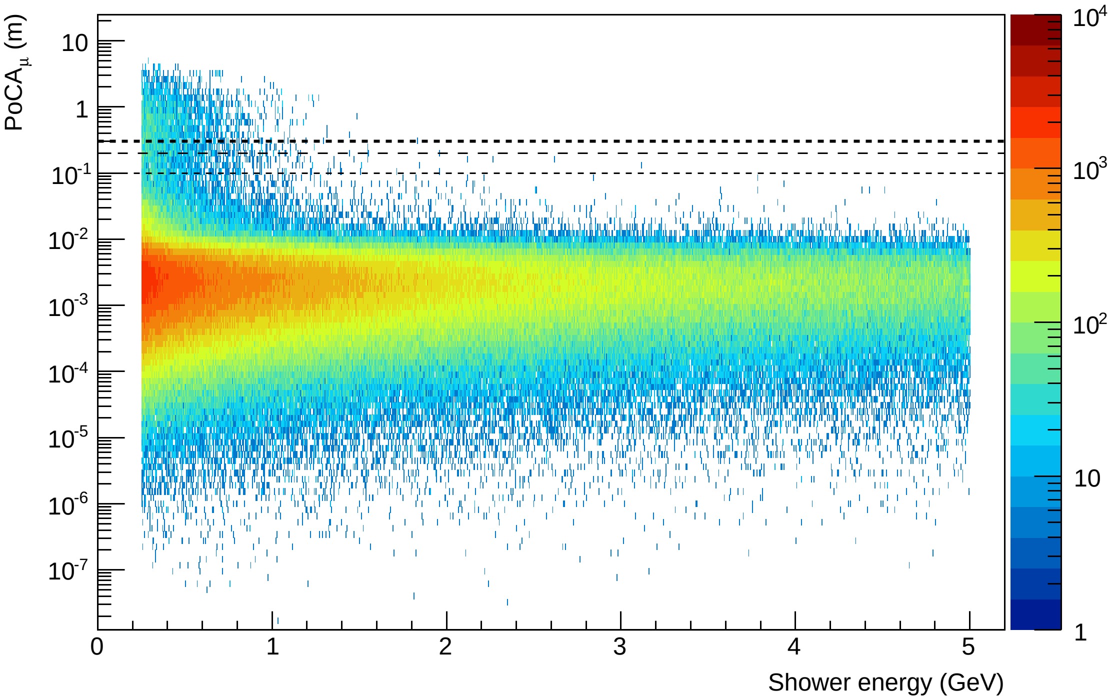

Figure 91: *The energy dependence of the point of closest approach of the first-generation gammas with respect to the primary muon track in events where the primary muon entered the LAr. This is after the application of cuts based on the angle with respect to the beam axis, PoCA with respect to all tracks, and the fiducial volume. The showers appearing below the dashed horizontal lines indicating cut thresholds of* 10 *cm,* 20 *cm and* 30 *cm would be rejected. However, instead of the uniform* $PoCA_\mu > 30$ *cm cut, an energy-dependent cut could be used; with the other cuts applied, almost as many EM showers with energy in excess of* ~ 1.5 *GeV could be rejected by reducing the threshold to* 10 *cm.*

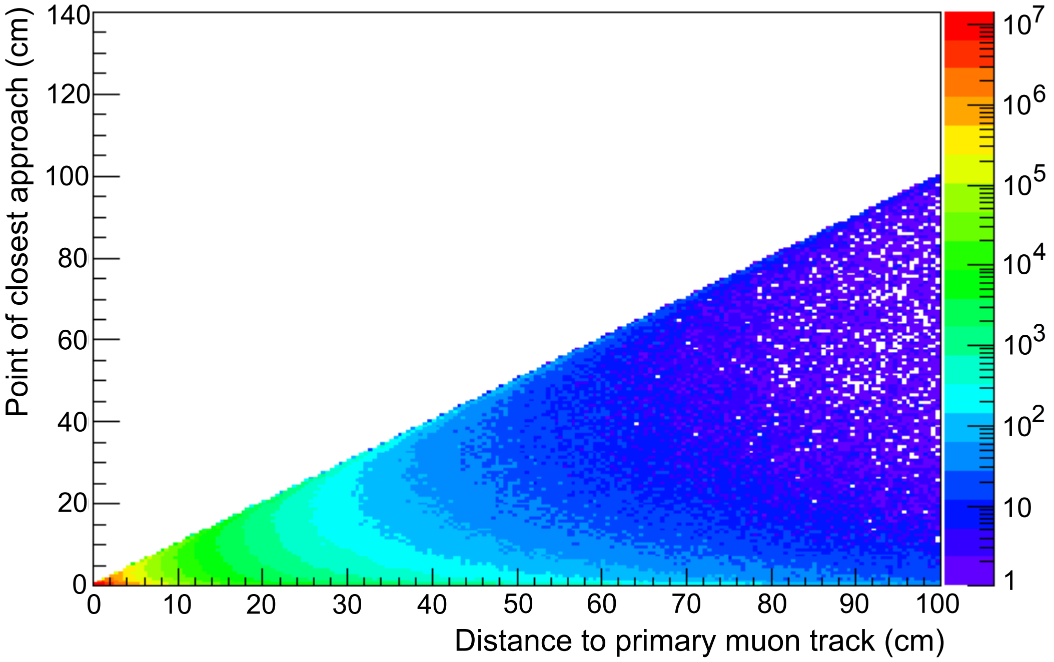

Figure 92: *The shortest distance from the first* $\gamma \rightarrow e^+ e^-$ *vertex at the start of an EM shower to the primary muon track. The PoCA cut is determined to be the superior cut since for a given shortest distance to the track, the PoCA never greater than the shortest distance to the track.*

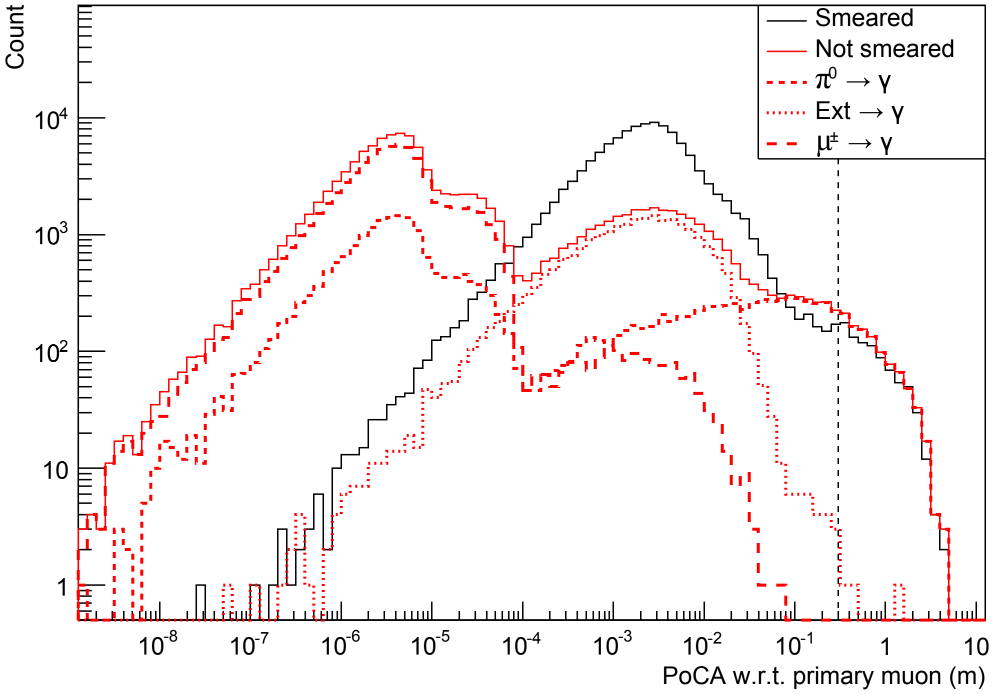

Figure 93: *The effect of position and angular smearing on the PoCA of the first generation gammas with respect to the primary muon track. This is based on* 2×10^7 *muon-induced events out of the main* 2.8×10^8 *events. The distribution before (after) smearing is shown by the solid black (red) line (approximately* 1.2×10^5 *EM showers with no normalization applied). Also shown by dashed lines are specific shower ancestries before smearing is applied. The vertical line indicates the* 30 *cm cut threshold; those EM showers surviving this cut are not significantly affected by smearing despite it having significant effect at smaller PoCA values.*

6.2.3 Beam angle $\theta_{beam}(E)$

This is the angle between the trajectory of the first-generation gammas and the neutrino beam axis. If the gamma is at a sufficiently large angle to the beam, it is assumed that it did not result from a neutrino interaction and can be rejected. This is an energy-dependent cut since it has been shown [308] that, within the relevant energy range (Figure 21) for background showers, lower-energy neutrinos will produce showers at significantly wider angles with respect to the beam than higher energy ones (Figure 94). The function used to determine whether a first-generation gamma is at too wide an angle with respect to the beam to potentially mimic a signal EM shower is as follows:

$$\begin{aligned}\theta_{beam}(E(GeV)) &= 116.523 - 75.8852E + 21.439E^2 \\ &\quad -2.77812E^3 + 0.134062E^4\end{aligned}$$

To calculate this angle the direction cosines $c^{\gamma}_{x,y,z}$ of a first-generation gamma are recorded. With the direction cosines $c^{beam}_{x,y,z}$ of the beam set to $c_x = 0.201078$, $c_y = 0.979575$ and $c_z = 0.104528$, the beam angle is calculated as follows:

$$cos(\theta_{beam}) = \frac{c^{beam} \cdot c^{\gamma}}{|c^{beam}||c^{\gamma}|}. \tag{116}$$

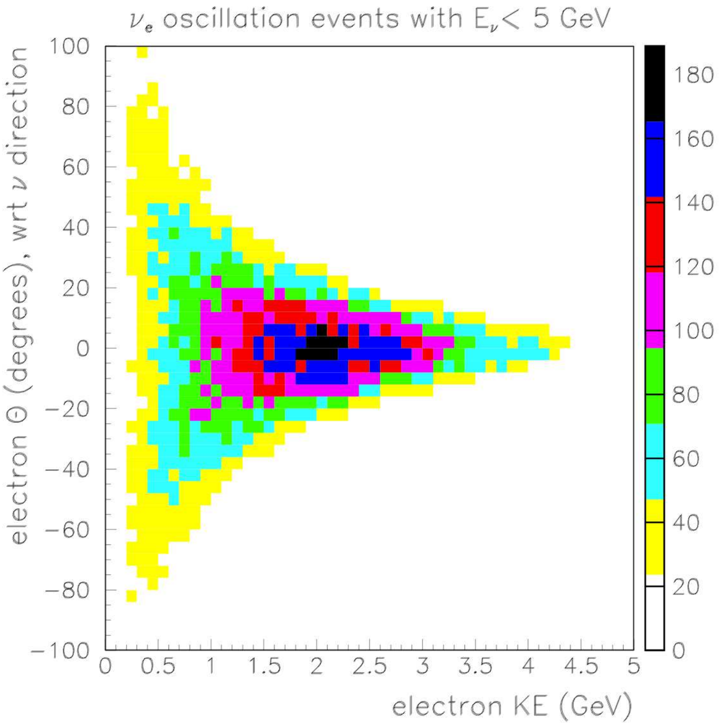

Figure 94: *The energy-dependence of the angle that electrons generated by simulated signal ν_e CC interactions (E_ν > 5 GeV) make with the beam axis [308, 309]. This determines the curve used in the θ_{beam} cut.*

The beam axis is therefore defined such that it produces a 6° slope with respect to the horizon (to allow for the curvature of the Earth), and forms a 7° angle with the 'west' direction (which is necessary since one of the axis of the detector should be oriented along the line drawn from Fermilab to Sanford Underground Research Facility).

6.2.4 'Distance to the nearest LAr volume face' (D)

Showers for which the initial $\gamma \rightarrow e^+e^-$ vertex in the EM shower does not occur deep enough inside the detector are rejected (i.e. a fiducial cut is applied). For each first-generation gamma, the distance D to the nearest active volume face is calculated. This cut aims to reject background EM showers that have started in the surrounding rock. When applying this cut with the detailed dectector geometry (whose total active volume is split up into many cells), it is only calculated with respect to the outward-facing planes of the active volumes within the TPC cells (Figure 127). A cut of D >30 cm is used for the main results, with a range of cut thresholds tested in Section 6.3.7.5.

6.2.5 e/γ separation

EM showers will be possible to identify as background and reject based on whether they start with a single electron track or an e$^+e^-$ pair. A ν_e interaction can generate an electron which produces an invisible gamma, which then produces an electron-positron pair. However, background EM showers will start with just a gamma ('invisible' to the detector), followed by two electron-like tracks rather than one. The detector can distinguish this based on energy deposition measurements, with an energy-dependent failure rate that tails off at ∼10% for showers of energies greater than about 0.5 GeV [310]. Showers that can be verified as starting with two electrons rather than one may be eliminated from the irreducible background. A flat reduction factor of 1/10 is therefore applied to the annual rate in the main results, although this will in fact have some energy dependence (the failure to distinguish worsens at the low end of the energy range - below 0.5 MeV). The effect of having different efficiencies is examined in Section 6.3.7.6. This cut will not be capable of rejecting background showers caused by Compton electrons, which will start with a single electron track, but Compton electrons are not produced in significant amounts in the 0.25-5.00 GeV energy range of the neutrino beam (Figure 75). Also showers that start with $\pi^0 \rightarrow e^+\gamma\,\gamma$ may be suppressed. The photons produced in the decay can be separated by a small angle. The showers that develop from both photons can therefore overlap and possibly appear as having started with one electron, but they may be reconstructed as having started with two photons rather than one electron.

6.2.6 Photon detection

It will take a maximum of ~1.4 ms for the electric field to drift electrons from an ionization track across one of the TPC cells. However, each beam pulse lasts only 10 μs, a period 140 times shorter. Upon excitation of the argon, scintillation light can come from Ar^*+ Ar $\rightarrow\mathrm{Ar}_2^* \rightarrow$ 2Ar $+\gamma$ (after 6 ns) and Ar^++Ar$\rightarrow$ $\mathrm{Ar}_2^+ + e \rightarrow\mathrm{Ar}_2^* \rightarrow$ 2Ar $+\gamma$ (after 1.5 μs) [311]. These photons can be collected by lightguides placed between the wire planes, before being read out by silicon photomultipliers. The photon detection system can supply time information concerning individual events (i.e. the start-time of an event), thus reducing the effective observation time during which background can appear from the maximum drift time (1.4 ms) to the beam spill (10 μs). Thus, a final reduction factor of 1/140 is applied to the background rate once all other cuts have been applied (see also Eq. 113).

6.3 Results for the simple detector geometry and flat surface profile

In this section background estimates are given for the simple detector geometry and the flat surface (Section 5.3.1). The results stated here are from 2.80×10^8 muon-induced events ($E_\mu > 10$ GeV), which represent 0.237 years of statistics.

6.3.1 Background due to primary muons that strike the detector

The number of first-generation gammas that survive each cut (0.25 GeV $< E_\gamma <$ 5.00 GeV, PoCA <30 cm with respect to primary muon track, the angle $\theta_{beam}(E_\gamma)$ with respect to the neutrino beam, PoCA <10 cm with respect to all charged particle tracks, the fiducial cut D <30 cm as well as reductions for e/γ separation and photon detection) is shown in Table 32. The energy distribution of the first-generation gammas according to shower ancestry with only the 0.25 GeV $< E_\gamma <$ 5.00 GeV cut imposed is shown in Figure 95. The energy distribution of the first-generation gammas that survive each successive cut is shown in Figure 96.

Table 32: *The corrected (Section 5.4) annual rate of EM showers due to each type of shower ancestry as successive cuts are applied, for muon-induced events in the simple detector geometry and flat surface profile in which the primary muon strikes the detector's active volume. The overall scaling factor applied to the count obtained from the simulated data (i.e. normalization to annual rate including any necessary corrections) is* 6.36555. *Gaussian errors are shown in the tables unless stated otherwise, and no error is included if it does not exceed* 1% *of the rate. However, if a cut causes the annual rate for a given ancestry to drop to zero or 1×(overall scaling factor), an upper limit at* 90% *confidence level [290] is used, and for any subsequent cuts this upper limit is scaled down by the same amount that those cuts cause the total rate to fall by. The last two columns show the application of scaling factors of 1/10 and 1/140 for $e-\gamma$ separation (Section 6.2.5) and a photon detection system (Eq. 113, Section 6.2.6.*

	E_γ **0.25-5.00 GeV**	**PoCA**$_\mu$	θ_{beam}**(E)**	**PoCA**$_{all}$	**D**	e/γ	γ **detection**
total	1.07×10^7	7.85×10^4	$(3.84\pm0.05)\times10^4$	$(2.04\pm0.04)\times10^4$	$(1.77\pm0.03)\times10^4$	1770±34	12.64±0.24
$\pi^0\rightarrow\gamma$	2.27×10^6	7.80×10^4	$(3.81\pm0.05)\times10^4$	$(2.03\pm0.04)\times10^4$	$(1.77\pm0.04)\times10^4$	1769±34	12.64±0.24
$Ext\rightarrow\gamma$	2.08×10^6	(331±46)	159±32	108±25	0-15.53	0-1.55	0-0.01
$\mu\rightarrow\gamma$	6.34×10^6	0-15.53	0-7.59	0-3.40	0-2.96	0-0.30	0-0.002
$other\rightarrow\gamma$	2.84×10^4	172±33	70±21	0-15.53	0-13.50	0-1.35	0-0.001

Before any cuts are applied, there are 5.06×10^8 EM showers / first-generation gammas per year ($E_\gamma >$ 100 MeV), of which 1.48×10^8 are within the necessary energy range to qualify as potential background candidates (0.25 GeV$< E_\gamma <$ 5.00 GeV), as shown in Table 30. EM showers starting with $\mu\rightarrow e\rightarrow\gamma$ account for 92% of this total, but these are easily rejected since the first electron in that shower connects directly to a muon track. A further 1.3% of showers start with an electron crossing into the detector from outside (hence forth denoted Ext$\rightarrow e\rightarrow\gamma$), which are also dismissed immediately, since only showers which appear to start within the detector need to be considered. Showers with these ancestries have been omitted from all tables and will not be mentioned further.

The majority of the remaining background EM showers have three ancestries (Figure 95). These are showers that start with $\mu\rightarrow\gamma$ (59% of the showers with these three ancestries), $p/n/\pi^\pm\rightarrow\pi^0\rightarrow\gamma$ (21%) and showers starting with an 'external' gamma that has crossed in from outside (hence forth denoted $Ext\rightarrow\gamma$), 19%. The remaining 0.26%

come from various other minor channels (‘$other \rightarrow \gamma$’ in Table 32).

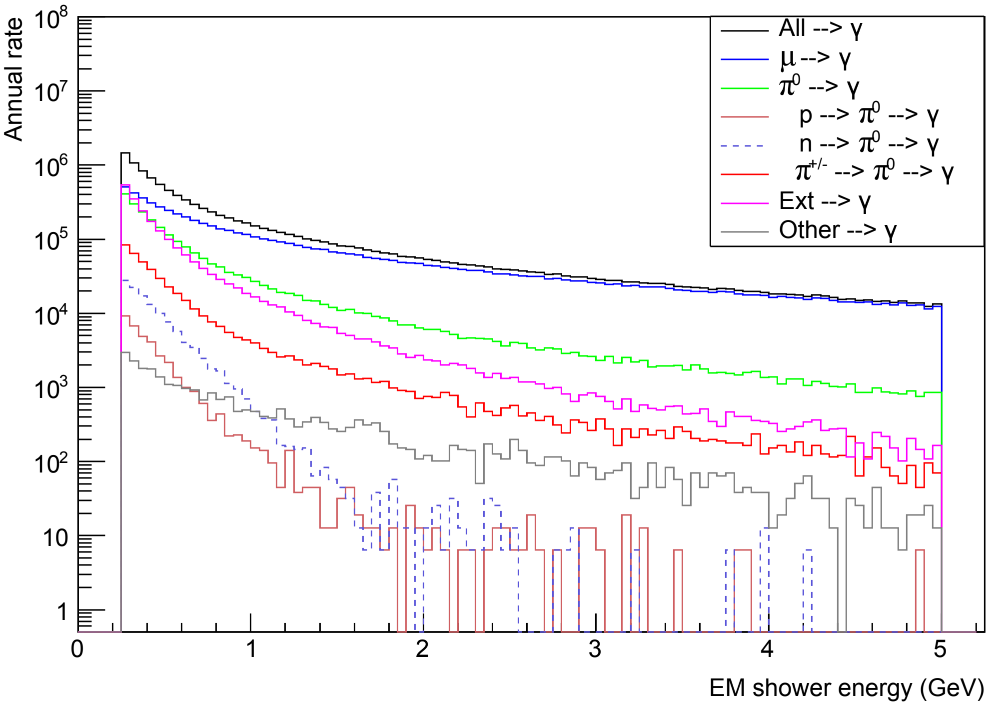

Figure 95: *The energy distribution of first-generation gammas in primary muon-induced events where the primary muon strikes the detector, for the simple detector geometry and flat surface, with only the* $0.25 - 5.00$ *GeV energy requirement imposed. Each significant shower ancestry is shown, namely* $\mu \rightarrow \gamma$, *Ext* $\rightarrow \gamma$ *and* $p/n/\pi^{\pm} \rightarrow \pi^0 \rightarrow \gamma$.

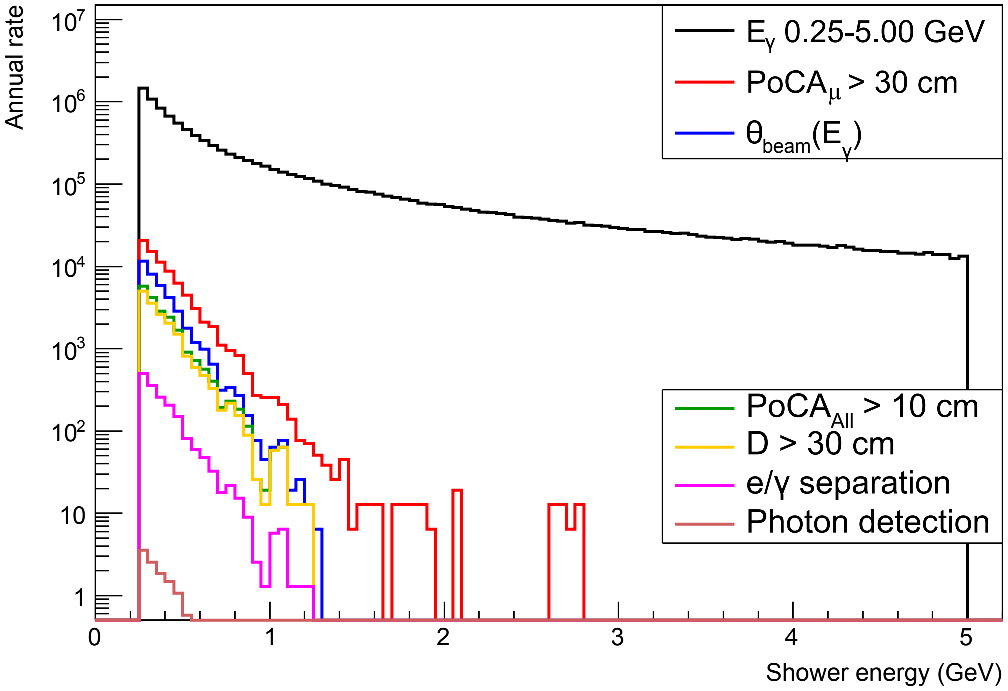

Figure 96: *The energy distribution of first-generation gammas in primary muon-induced events, for the simple detector geometry, where the primary muon strikes the detector, as successive cuts are applied.*

First of all a cut of PoCA >30 cm with respect to the primary muon track is applied. This is a very effective cut, removing 99% of the total background (alternatively a cut of PoCA >10 cm is almost as effective, removing 98.5% of EM showers). This cut elimates 100% of EM showers starting with $\mu \rightarrow \gamma$ and >99.9% of those starting with $Ext \rightarrow \gamma$. Showers starting with $Ext \rightarrow \gamma$ form just 0.42% of the background that survives this cut. From this point on the background is dominated by showers with the ancestry $\pi^0 \rightarrow \gamma$, which now comprise >99% of the remaining total (despite 97% of these showers still having been rejected by this cut). Figure 97 shows the distribution of PoCA with respect to the primary muon track for first-generation gammas of all significant ancestries. Figure 98 shows the position of the first $\gamma \rightarrow e^+e^-$ vertex in each EM shower from these two ancestries ($\pi^0 \rightarrow \gamma$ and $Ext \rightarrow \gamma$).

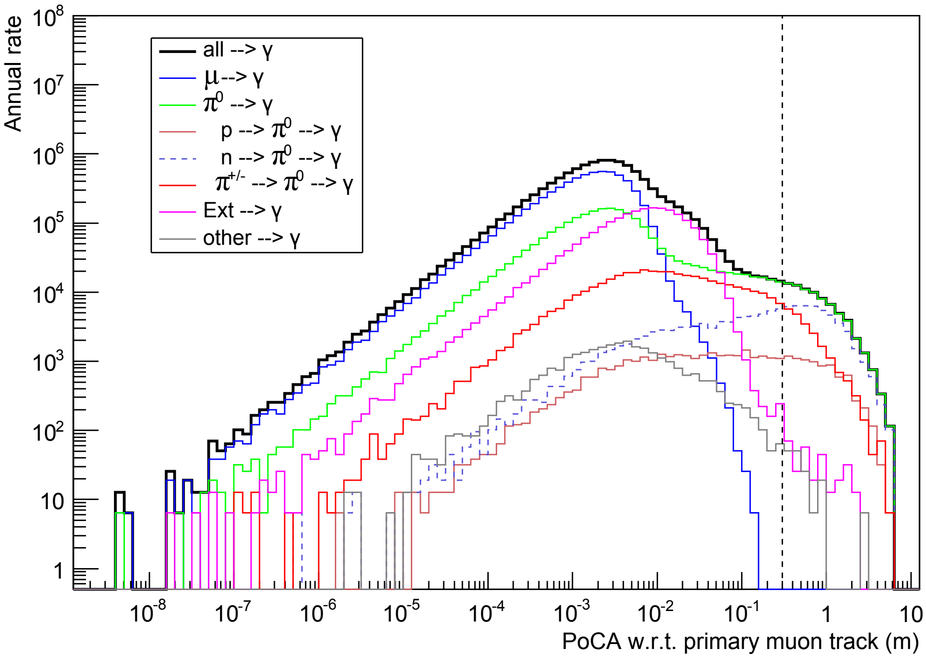

Figure 97: *The distribution of PoCA with respect to the primary muon track for the first-generation gammas in EM showers of important ancestries, for the simple detector geometry, in events where the primary muon strikes the detector. The dashed line indicates the* 30 *cm cut. The cut rejects EM showers to the left of this line as most likely originating from background muons. No other cuts were applied to the gammas shown here but further cuts remove the vast majority of the showers to the right of this line.*

Next is the θ_{beam} cut, which reduces the remaining background by a further 51%, practically independent of the EM shower ancestry. Figure 99 shows a plot of θ_{beam} vs. energy for the first-generation gammas and indicates how many survive the θ_{beam} cut.

A cut of PoCA >10 cm with respect to all other tracks in a given event aside from the primary muon (Figure 100) is then applied, dismissing a further 47% of the showers surviving the θ_{beam} cut. This is slightly more effective at rejecting EM showers that start with $\pi^0 \rightarrow \gamma$ (47% are rejected) than it is at removing EM showers starting with $Ext \rightarrow \gamma$ (32% are rejected).

Finally a cut on $D > 30$ cm (the minimum distance to a wall) removes 13% of the showers surviving this second PoCA cut. This involves all of the few remaining showers that start with $Ext \rightarrow \gamma$ being removed by this cut, as well as 13% of those starting with

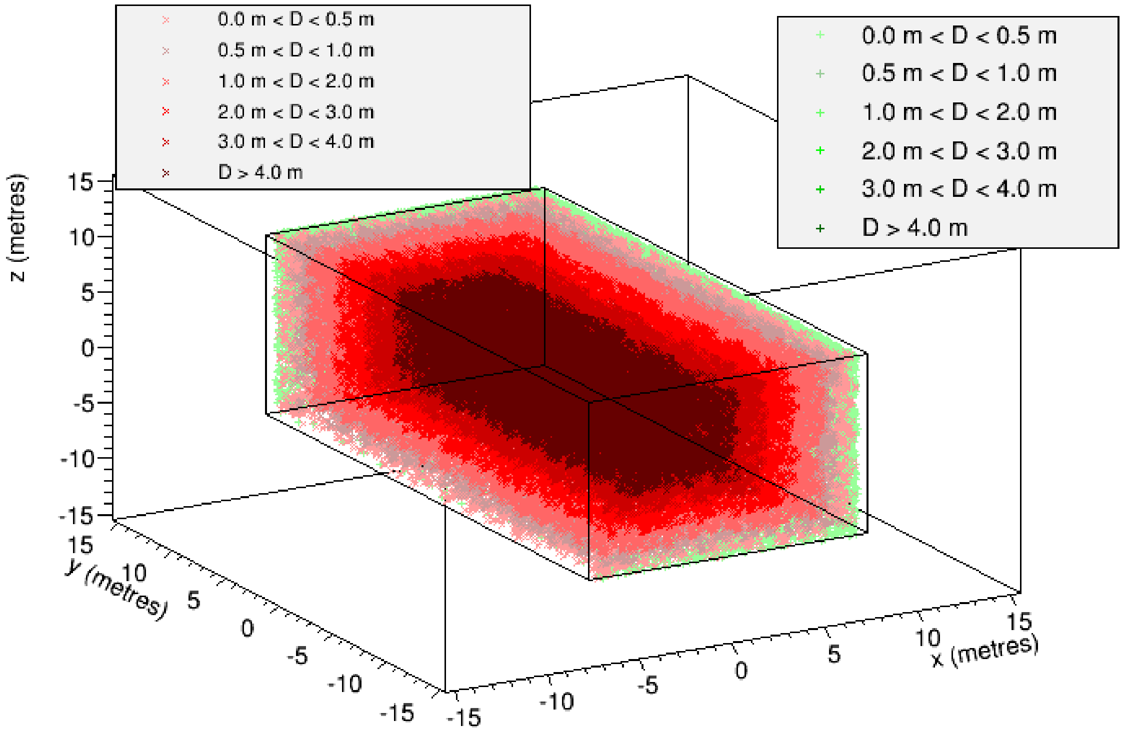

Figure 98: *The positions of the first* $\gamma \to e^+e^-$ *vertex in EM showers whose ancestry is* $Ext \to \gamma$ *(green) and* $\pi^0 \to \gamma$ *(red) due to primary muons that strike the LAr with the simple detector geometry. These showers make up the vast majority of the background once the first PoCA cut eliminates all* $\mu \to \gamma$ *showers. The darkness of the points indicates how far inside the detector each point is.*

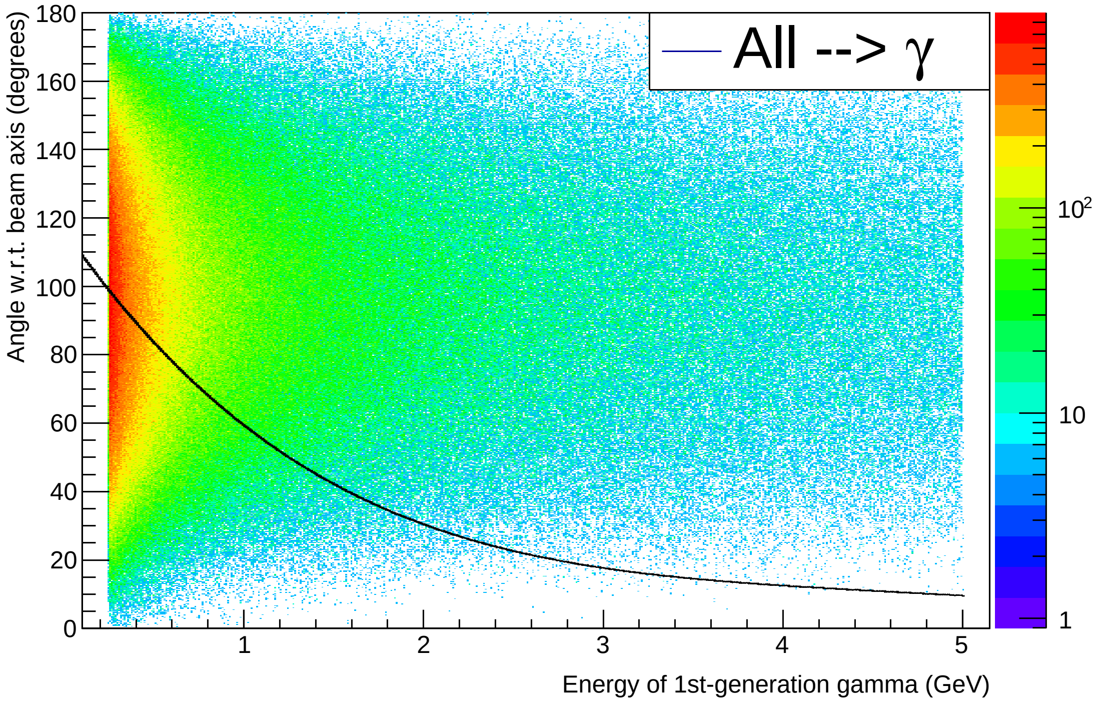

Figure 99: *The energy of the first-generation gammas in EM showers vs. their angle with respect to the beam, for the simple detector geometry, in events where the primary muon strikes the detector. Only those showers below the black curve survive the* θ_{beam} *cut. No other cuts were applied to the gammas shown here.*

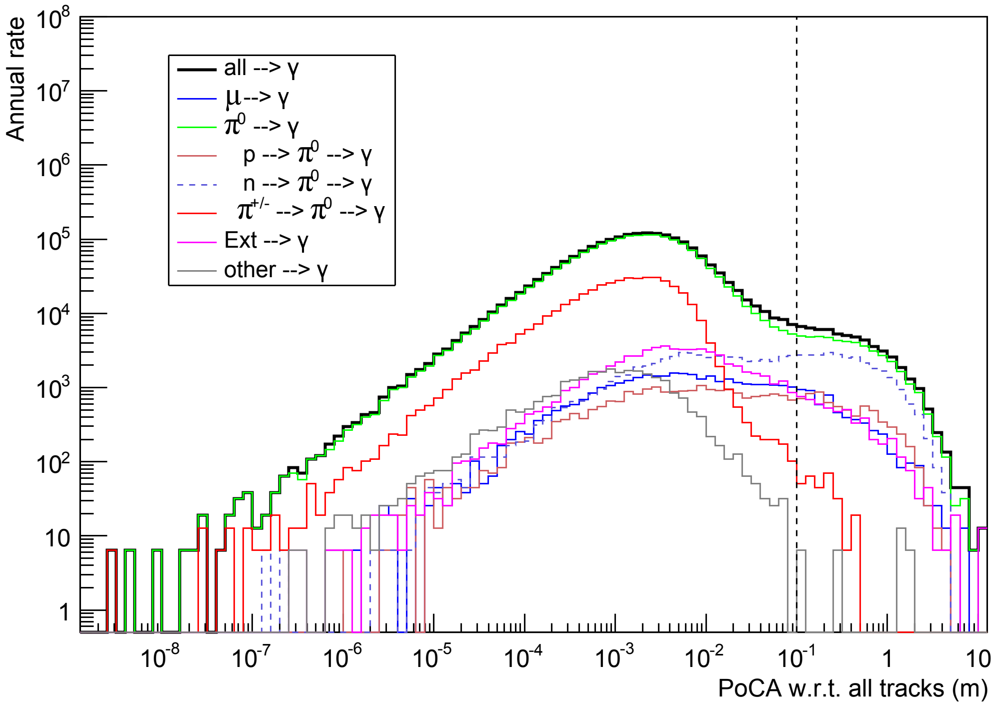

Figure 100: *The distribution of PoCA with respect to all non-primary muon tracks left by charged particles in an event for the first-generation gammas in EM showers of important ancestries, for the simple detector geometry, in events where the primary muon strikes the detector. No other cuts were applied to the gammas shown here. The vertical line at 10 cm indicates the cut treshold.*

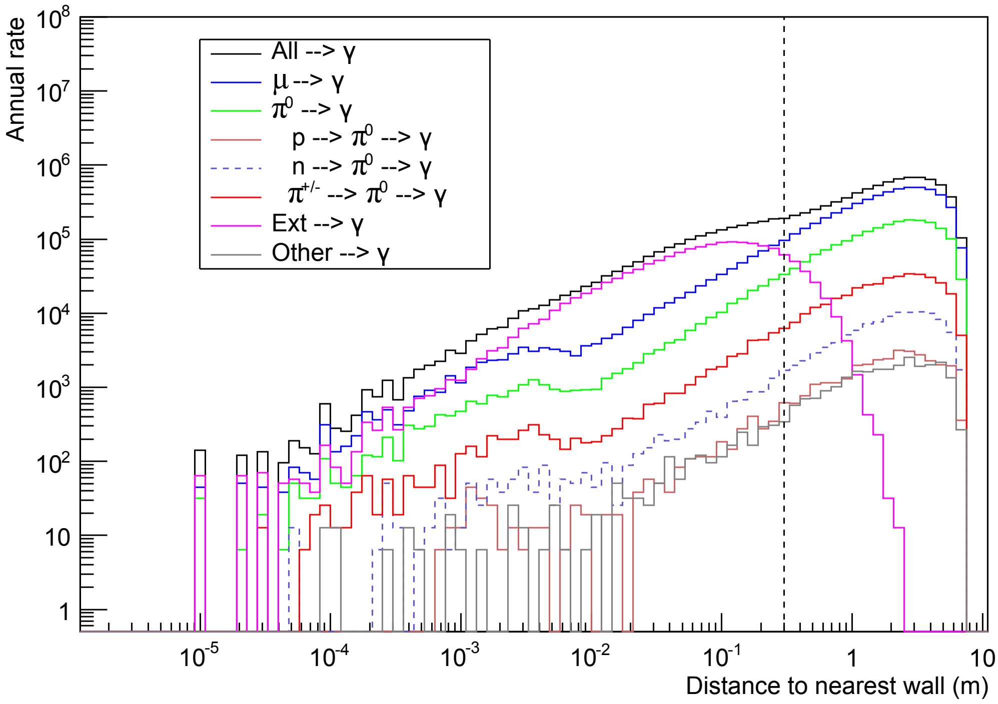

Figure 101: *The distribution of the distance from the nearest wall D to the first $\gamma \rightarrow e^+e^-$ vertex in each EM shower, showing the contribution from important shower ancestries, for the simple detector geometry. The upper limit on this is set by the shortest side of the detector, which measures $30 \times 15 \times 16\ m^3$. The greatest possible distance from a wall is therefore $15\ m\ /\ 2\ =\ 7.5\ m$, which is where these lines cut off. The dashed line at 30 cm indicates the chosen cut value, below which all showers are rejected. This cut efficiently removes gamma-background, where a photon is produced outside of the detector (Ext → γ). No other cuts were applied to the gammas shown here.*

$\pi^0 \to \gamma$. Figure 101 shows the distribution of D for the first $\gamma \to e^+e^-$ vertex of each relevant shower ancestry before any other cuts are applied, making clear that this cut should affect showers starting with $Ext \to \gamma$ significantly more.

After reduction factors are applied for e/γ separation and a photon detection system (which amount to reducing the rate by a factor of $1/10 \times 1/140$), the overall background rate due to primary muons that strike the detector is 12.64±0.24 yr^{-1} (this is 16.53±0.29 yr^{-1} if a cut on PoCA >10 cm instead of 30 cm with respect to the primary muon track is used).

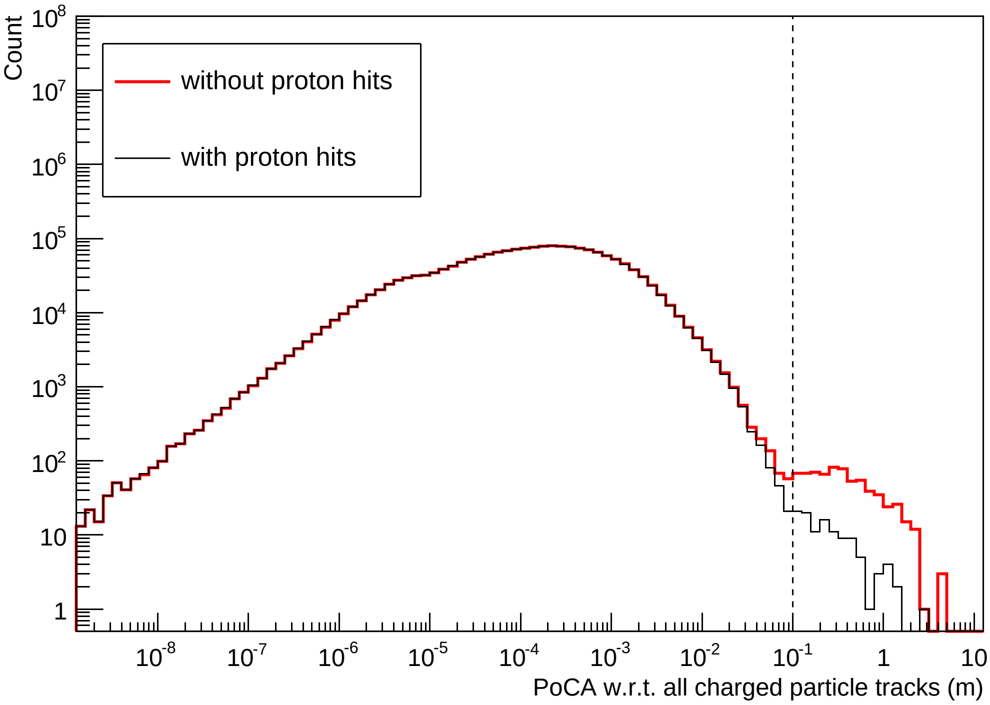

Figure 102: *The distribution of PoCA with respect to all tracks left by charged particles in an event. This cut is applied twice to an additional* 2×10^7 *muon-induced events for which proton hits were recorded. In the first instance (thick red line) hits from protons are not used in the PoCA calculation. The thin black line shows events where the PoCA is calculated with respect to proton tracks as well as tracks from the other charged particles. The number of showers surviving the requirement that PoCA>* 10 *cm (those right of the vertical line) is affected by the availability of proton tracks. The mean PoCA for the distrbution without taking account of protons is* 7.77×10^{-4} *m with* 695 *showers surviving the cut, compared to a mean value of PoCA of* 5.96×10^{-4} *m with* 113 *showers surviving the cut when proton tracks are taken into account. After all other cuts are applied, this difference results in a final background rate that differs by a factor of* 5 *to* 10*. The only results affected by this correction are for the muon-induced background using the simple detector geometry, since it is only for these events that protons tracks were not initially recorded.*

However, results described above have been obtained without recording proton tracks, so these were not available for the second PoCA cut. This reduces the effectiveness of the cut on PoCA with respect to all tracks (Figure 102 compares the effect of inclusion/omission of proton hits on the PoCA cut). Additional simulated data (0.017 years' statistics) with proton hits recorded show that the annual rate after all cuts reduces to

2.84 ± 0.41 yr^{-1}. Results stated in sections 6.4.1, 6.6 for the detailed detector geometry (for which proton hits have been recorded) are in good agreement with this. Proton hits have also been recorded for the other results with the simple detector geometry where primary particles other than muons have been used to generate the events, but have not been recorded for the muon-induced events with the simple geometry and approximate surface profile discussed in Section 6.5.

6.3.2 Background due to primary muons that miss the detector

Events in which the primary muon misses the LAr volume but still has some secondary particles enter it have also been examined. The number of first-generation gammas that survive each cut is shown in Table 33.

Table 33: *The annual rate of EM showers due to each type of shower ancestry as successive cuts are applied, for muon-induced events using the simple detector geometry with the flat surface profile, in which the primary muon misses the detector's active volume. The overall scaling factor applied to the count obtained from the simulated data is* 6.36555 *(Table 28). The cut on PoCA with respect to the primary muon track can not be applied here since the primary muon does not enter the detector, hence the different cut sequence.*

	E_γ 0.25-5.00 GeV	**D**	θ_{beam}**(E)**	**PoCA**$_{all}$	e/γ	γ **detection**
total	$(1.07\pm0.03)\times10^4)$	770 ± 70	222 ± 38	159 ± 32	15.9 ± 3.2	0.11 ± 0.02
$\pi^0 \rightarrow \gamma$	891 ± 75	433 ± 52	178 ± 34	115 ± 27	11.5 ± 2.7	0.08 ± 0.02
$Ext \rightarrow \gamma$	9802 ± 249	337 ± 46	45 ± 17	45 ± 17	4.5 ± 1.7	0.03 ± 0.01
$other \rightarrow \gamma$	0-15.53	0-1.22	0-0.30	0-0.23	0-0.02	0-0.0002

Events in which the primary muon misses the detector but secondary particles still cross inside account for a much smaller fraction of the total events simulated (0.0091%) than those in which the primary muon strikes it. These events contribute 10,694 EM showers annually within the required energy range, 0.1% of the total number of showers surviving the shower energy cut for events in which the primary muon entered the LAr volume. Thus the ratio of muons striking and missing the detector is a factor of ~ 10 smaller than the ratio of the EM shower rates from muons that strike and miss the detector. This can be accounted for by considering that different branches of a single EM shower that starts outside of the LAr can cross inside the LAr and each branch will appear as a new separate shower. Indeed the vast majority of the showers observed (92%) start with $Ext \rightarrow \gamma$, with 8% starting with $\pi^0 \rightarrow \gamma$. Figure 103 shows the positions of the first $\gamma \rightarrow e^+e^-$ vertex in these showers.

The first cut applied is $D > 30$ cm, which removes 93% of the overall background due to this type of event. In terms of specific ancestries, it rejects 97% of showers starting with $Ext \rightarrow \gamma$ and 51% of those starting with $\pi^0 \rightarrow \gamma$. Figure 104 shows the distance of EM showers as a function of distance.

The cut on θ_{beam} removes a further 71% of the overall remaining background. In terms of specific ancestries it removes a further 59% of EM showers starting with $\pi^0 \rightarrow \gamma$ showers and 87% of those starting with $Ext \rightarrow \gamma$ showers. Since there is no favoured azimuth angle for primary muons to approach from (Figure 105), differences in EM shower energy accounts for this cut being more effective at rejecting those starting with $Ext \rightarrow \gamma$ than $\pi^0 \rightarrow \gamma$. Figures 94, 99 show that lower-energy showers are more likely to survive this cut. Figure 106 shows significantly more showers at higher energies with the ancestry $Ext \rightarrow \gamma$ than with $\pi^0 \rightarrow \gamma$ for events in which the primary muon misses the active volume. For comparison, in events in which the primary muon strikes the active volume,

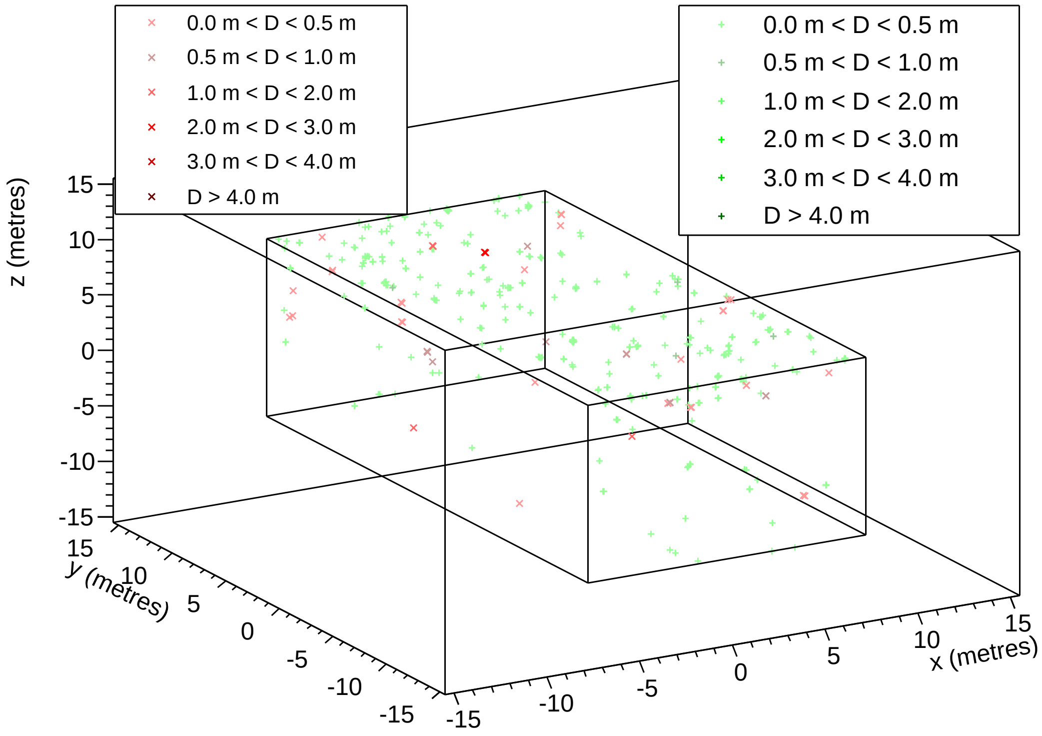

Figure 103: *The position of the first* $\gamma \to e^+e^-$ *vertex in EM showers for events in which primary muons miss the detector. This is comparable to Figure 98 and is colour-coded in the same way. Since the cut on PoCA with respect to to the primary muon cannot be applied here (unlike Figure 98), this represents the background before any cuts are applied. The points are typically just inside the walls and top face of the detector.*

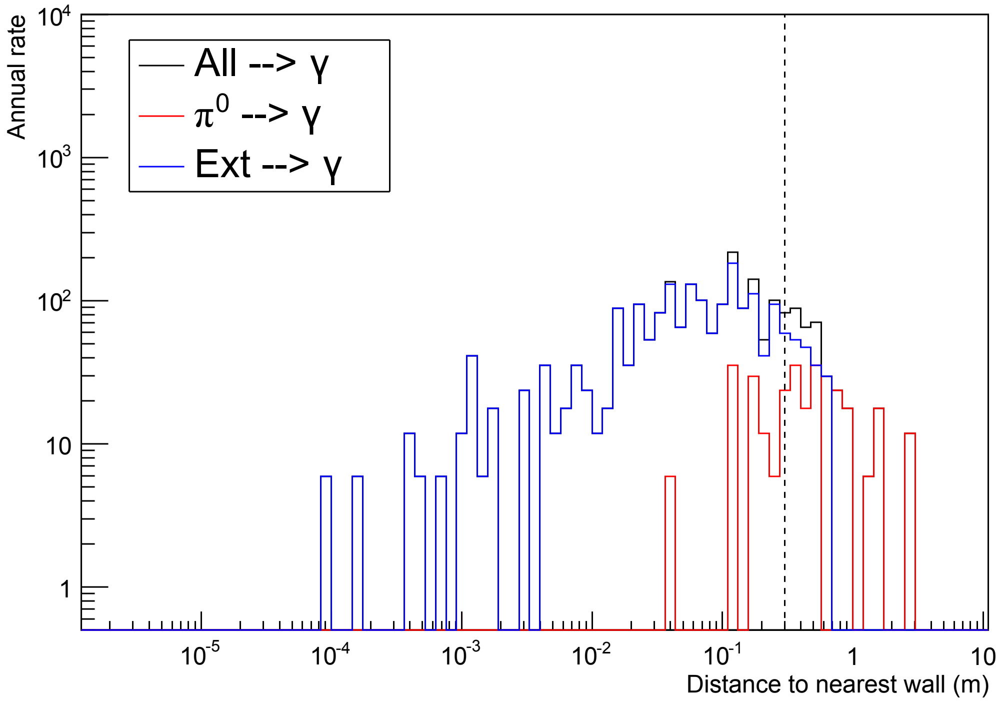

Figure 104: *The distribution of the distances from the nearest wall to the first* $\gamma \to e^+e^-$ *vertex, showing the contribution from each significant shower ancestry, for events in which the primary muon misses the active volume of the simple detector geometry. The dashed line at 30 cm indicates the chosen cut value, below which all showers are identified as background and can be rejected. This may be compared to Figure 101.*

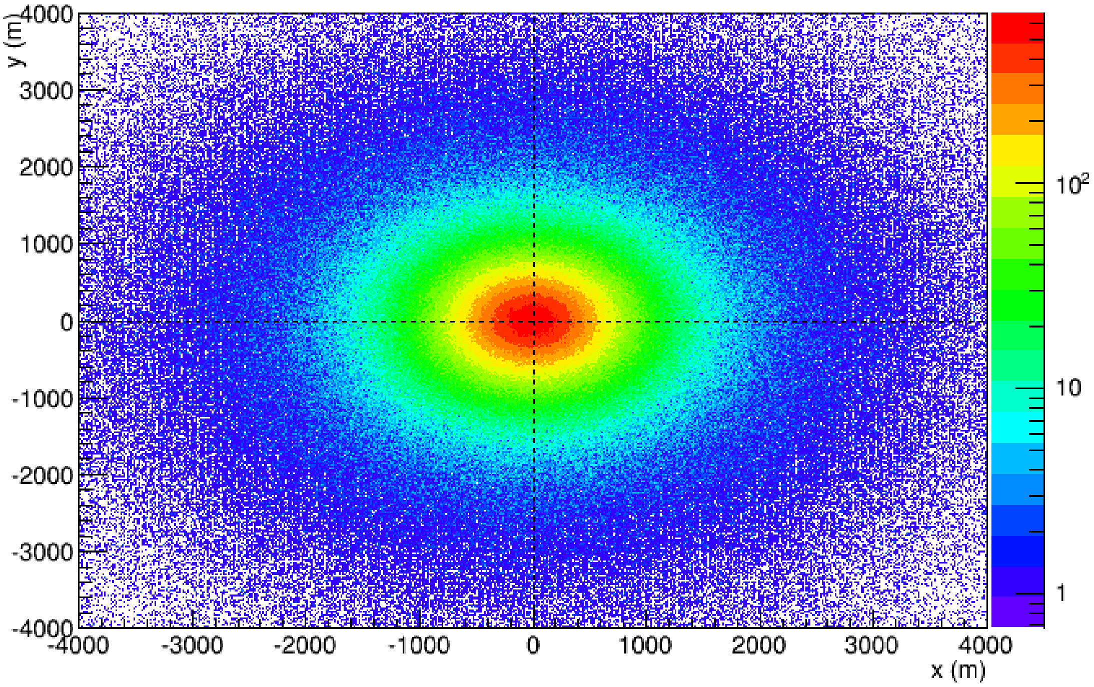

Figure 105: *The initial positions of primary muons used to generate events for the simple detector geometry and flat surface, seen from a bird's eye view. The detector is located at the centre of the image, demonstrating that the flux is symmetric if rotated about the origin.*

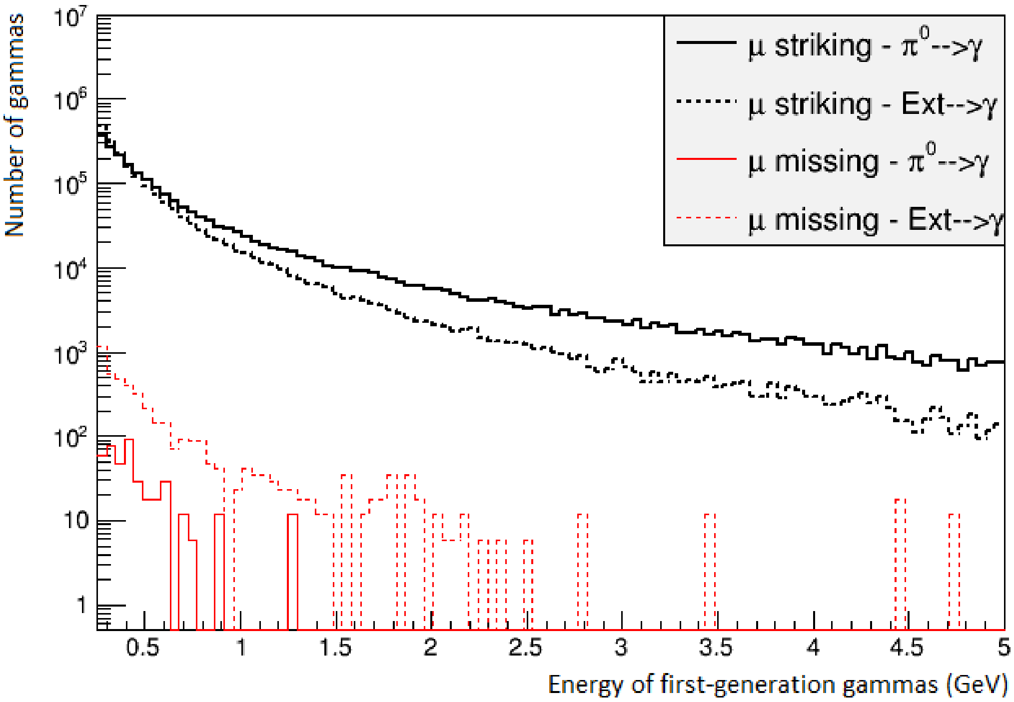

Figure 106: *The energy distribution of the first-generation gamma in showers starting with* $Ext \to \gamma$ *and* $\pi^0 \to \gamma$*, for muon-induced events in which the primary muon either strikes or misses the active volume of the simple detector geometry. This is after application of the cuts prior to the* θ_{beam} *cut (i.e. the energy cut for both types of event, the* $PoCA_\mu$ *cut for events in which the primary muon strikes the detector, and the* D *cut for events in which the primary muon misses the detector).*

the energy spectra for EM showers starting with $\pi^0 \rightarrow \gamma$ and $Ext \rightarrow \gamma$ are more evenly matched, and the θ_{beam} cut is equally efficient at removing showers of both ancestries.

The final cut applied here is a cut on PoCA >10 cm with respect to all tracks left by charged particles, which leaves $Ext \rightarrow \gamma$ showers unaffected (these events happen to feature very few charged tracks at all) but eliminates 36% of the remaining showers that start with $\pi^0 \rightarrow \gamma$.

After correcting for e/γ separation and photon detection, the overall annual background rate due to this type of event is 0.11±0.02 yr^{-1}.

6.3.3 Background due to primary neutrons

These results are based on 1.06×10^7 neutron-induced events, corresponding to 0.220 years of statistics ($E_n > 1$ GeV, sampled from a surface above the detector measuring 38×22 m^2).

The primary neutron leaves no ionization track in the detector to calculate PoCA with respect to, and often does not reach the detector anyway. Instead of a cut on PoCA with respect to a primary track, a cut on the distance to the nearest wall is applied first, meaning that the succession of cuts is the same as is used for the background due to primary muons that miss the detector. The results are shown in Table 34.

Table 34: *The annual rate due to each type of shower ancestry as successive cuts are applied, for neutron-induced events in the simple detector geometry and flat surface profile. The overall scaling factor applied to the count obtained from the simulated data is* 5.19435 *(Table 28).*

	E_γ 0.25-5.00 GeV	**D**	**θ_{beam}(E)**	**PoCA$_{all}$**	e/γ	**γ detection**
total	6.69×10^4	(3.97±0.05)×10^4	(1.39±0.03)×10^4	1725±95	172.5±9.5	1.23±0.07
$\pi^0 \rightarrow \gamma$	(4.85±0.05)×10^4	(3.66±0.04)×10^4	(1.31±0.03)×10^4	1569±90	156.9±9.0	1.12±0.06
$Ext \rightarrow \gamma$	(1.71±0.03)×10^4	2348±110	670±59	156±28	15.6±2.8	0.11±0.02
$other \rightarrow \gamma$	1174±78	888±68	145±27	0-12.67	0-1.27	0-0.009

In this case the background before cuts is 6.69×10^4 yr^{-1} and is dominated by EM showers with the ancestry $p/n/\pi^{\pm} \rightarrow \pi^0 \rightarrow \gamma$ (73% of the total). Showers which start with $Ext \rightarrow \gamma$ account for a further 26% of the total - a significantly higher proportion compared to showers due to primary muons which strike the detector, but also significantly smaller compared to showers from primary muons that miss the LAr.

The cut of $D > 30$ cm is applied first, providing an overall reduction of 40% by removing 25% of showers starting with $\pi^0 \rightarrow \gamma$ and 87% of those starting with $Ext \rightarrow \gamma$.

The θ_{beam} cut eliminates a further 65% of potential background candidates overall, having removed 64% of the remaining $\pi^0 \rightarrow \gamma$ showers and 71% of the remaining $Ext \rightarrow \gamma$ showers.

The PoCA with respect to all tracks cut removes a further 88% of the overall background, dismissing 88% of the remaining showers that start with $\pi^0 \rightarrow \gamma$ as well as 77% of those that start with $Ext \rightarrow \gamma$. Proton hits have been recorded here.

Finally the e/γ separation and photon detection reduce the rate to 1.23±0.07 yr^{-1} overall.

6.3.4 Background due to primary protons

The background due to incoming protons has been estimated based on 10^8 proton-induced events, corresponding to 0.270 years' statistics ($E_p >$100 MeV, sampled from a surface above the detector measuring 50×35 m^2). The results are shown in Table 35.

Table 35: *The annual rate due to each type of shower ancestry as successive cuts are applied, for proton-induced events in the simple detector geometry and flat surface profile. The overall scaling factor applied to the count obtained from the simulated data is* 3.64831 *(Table 28).*

	$\mathbf{E}_\gamma$	**D**	θ_{beam}**(E)**	$\mathbf{PoCA}_{all}$	e/γ	γ **detection**
total	$(1.05\pm0.06)\times10^5$	$(6.51\pm0.05)\times10^4$	$(2.21\pm0.03)\times10^4$	3601 ± 115	360.1 ± 11.5	2.57 ± 0.08
$\pi^0 \rightarrow \gamma$	$(7.81\pm0.05)\times10^4$	$(5.96\pm0.05)\times10^4$	$(2.06\pm0.03)\times10^4$	3335 ± 110	333.5 ± 11.0	2.38 ± 0.08
$Ext \rightarrow \gamma$	$(2.45\pm0.03)\times10^4$	3477 ± 112	1138 ± 64	259 ± 31	25.9 ± 3.1	0.19 ± 0.02
$other \rightarrow \gamma$	2393 ± 93	2028 ± 86	390 ± 38	7.3 ± 5.2	0.73 ± 0.52	0.005 ± 0.004

At ∼1.05×10^5 yr^{-1} before cuts and ∼2.57 yr^{-1} afterwards, the rate of background EM showers in proton-induced events exceeds that from neutron-induced events. This is despite the proton being charged and therefore losing energy more rapidly in the rock surrounding the detector. However, the greater rate due to protons can be accounted for by the proton energy spectrum being harder (Figures 78 and 81).

EM showers that start with $\pi^0 \rightarrow \gamma$ account for 74% of the total, with 23% starting with $Ext \rightarrow \gamma$ and 3% from various other ancestries.

Application of the D cut yields a 38% reduction in the overall background rate, rejecting 24% and 86% of EM showers starting with $\pi^0 \rightarrow \gamma$ and $Ext \rightarrow \gamma$ respectively.

The θ_{beam} cut causes a further 66% reduction in the overall rate, cutting out 66% of showers starting with $\pi^0 \rightarrow \gamma$ and 67% of those starting with $Ext \rightarrow \gamma$.

Next is the cut on PoCA with respect to all tracks, which eliminates 84% of the remaining total background. It dismisses 84% of showers starting with $\pi^0 \rightarrow \gamma$ and 77% of those starting with $Ext \rightarrow \gamma$. Proton hits have been recorded here.

Finally the e/γ separation and photon detection reduce the rate to 2.57 ± 0.08 yr^{-1} overall.

6.3.5 Background due to primary photons

There have been 8×10^7 events simulated using photons with energies in excess of 0.1 GeV, corresponding to 2.317 years' statistics, sampled from a surface above the detector measuring 50×35 m^2. The background due to incoming photons has been found to be negligible. The results are shown in Table 36.

Table 36: *The annual rate as successive cuts are applied, for photon-induced events in the simple detector geometry and flat surface profile. The overall scaling factor applied to the count obtained from the simulated data is* 0.40126 *(Table 28).*

	$\mathbf{E}_\gamma$	**D**	θ_{beam}**(E)**	$\mathbf{PoCA}_{all}$	e/γ	γ **detection**
total	34.5 ± 3.7	34.1 ± 3.7	0 - 0.98	0-0.12	0-0.01	0-0.0001

6.3.6 Summary of total background for simple geometry and flat surface

Table 37 gives a summary of the annual background EM shower rate using the simple detector geometry and a flat surface profile. This is after all cuts have been applied, so these numbers represent the irreducible[40] background that cannot be distinguished from those generated by genuine ν_e interactions. One column shows the annual rate as calculated from the main body of simulated data. Figure 107 shows the energy spectrum

---

[40] "Irreducible" assuming no new cut is introduced or any existing cut is strengthened.

of the EM showers that remain. However, as discussed in Section 6.3.1, the muon-induced rate could be reduced further since proton hits were not recorded in that simulated data. This affects the cut on PoCA with respect to all tracks.

Table 37: *A summary of the annual background EM shower rate using the simple detector geometry and a flat surface profile. The second column indicates the rates calculated from the main body of simulated data. The third column shows the approximate rate had proton hits been recorded for muon-induced events, and if electron / positron production cuts had been set such that they result in shorter and more realistic lengths for muon track segments.*

Primary particle	Annual rate based on large data sets	Annual rate with modified production cuts and recording of proton hits
muons (striking detector)	12.64 ± 0.24	∼1.18 (production cuts)
muons (missing detector)	0.11 ± 0.02	0.11 ± 0.02
protons	2.57 ± 0.08	2.57 ± 0.08
neutrons	1.23 ± 0.07	1.23 ± 0.07
photons	<<1	<<1
total	**16.55 ± 0.26**	**∼5**

A further reduction could be made relating to the choice of Geant4 electron and positron production cuts, as discussed in Section 6.2. By lowering their threshold the cut on PoCA with respect to primary muons could be improved, rejecting further potential background candidates. The corrections discussed here produce rates that are close to those observed in the simulations carried out with the detailed detector geometry, which will be discussed in the coming sections.

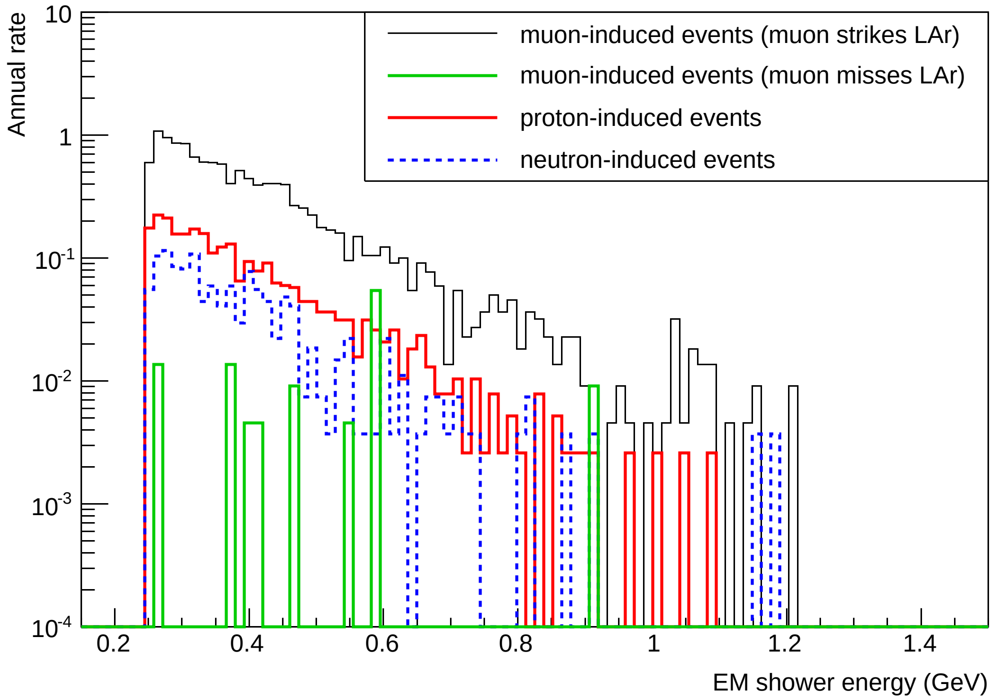

Figure 107: *The distribution of the EM shower energy after all cuts (including scaling factors for e-γ separation and a photon detection system) have been applied, for muon, proton and neutron-induced events with the simple detector geometry and flat surface profile.*

6.3.7 Variation of cut thresholds and rock overburden

Results have so far been stated for a rock overburden spanning 3 m above the detector (Figure 76) and using the following cut thresholds and reduction factor:

$$\begin{gathered} E_\gamma = 0.25 - 5.00 \text{ GeV}, \quad PoCA_\mu > 30 \text{ cm}, \quad PoCA_{all} > 10 \text{ cm}, \quad \theta_{beam}(E_\gamma), \\ D > 30 \text{ cm}, \qquad 90\% \; e/\gamma \text{ separation efficiency.} \end{gathered} \tag{117}$$

However, a range of thresholds have been tested for each of these cuts except for the θ_{beam} cut, its energy-dependence having already been established[41]. The extent of the shielding provided by different rock overburdens has also been investigated.

Table 38 summarises the annual rate of EM showers from the main results discussed in Sections 6.3.1, 6.3.2, 6.3.3, 6.3.4, without the application of any cuts other than the removal of EM showers with the ancestries $Ext \rightarrow e^\pm \rightarrow \gamma$ and $\mu^\pm \rightarrow e^\pm \rightarrow \gamma$.

Table 38: *The annual rate of EM showers due to muon, proton and neutron-generated events used for the main results in Sections 6.3.1, 6.3.2, 6.3.3, 6.3.4 (where a rock overburden of 3 m was used), before the application of any cuts apart from the removal of EM showers with the ancestries* $Ext \rightarrow e^\pm \rightarrow \gamma$ *and* $\mu^\pm \rightarrow e^\pm \rightarrow \gamma$.

Primary particle	$\mu^\pm$ (striking)	$\mu^\pm$ (missing)	p	n
Annual rate	2.55×10^7	$(5.15\pm0.08)\times10^4$	2.35×10^5	1.56×10^5

6.3.7.1 Rock overburden

As discussed in Section 5.4, using primary particles above a higher minimum energy can allow a given fraction of a year to be simulated by fewer events, without missing significant numbers of EM showers. However, for the main results with a 3 m rock overburden, the EM showers that survive all cuts are at the lower end of the allowed energy range (Figure 107). It was speculated that the use of smaller rock overburdens could mean there should be proportionally more EM showers with lower energies[42] but also that primary particles with a higher minimum energy (which are used here to save computation time) could produce fewer low-energy EM showers than there should be. Therefore, to check that using primary particles with minimum energies stated above does not compromise the validity of the results, additional events have been generated for the smallest rock overburden of 1 m (3×10^7 muon-induced events $E_\mu > 1$ GeV, 1×10^6 proton-induced events, $E_p > 0.1$ GeV, 50×35 m^2 injection area and 2.4×10^6 neutron-induced events, $E_n > 0.1$ GeV, 38×22 m^2 injection area) (spectra shown in Figure 78). These events correspond to 0.26%, 0.32% and 0.19% of a year of statistics respectively. The energy spectra of the EM showers before cuts are applied is shown in Figure 108 and the annual rates after cuts are compared in Table 39. This confirms that the EM shower energy spectrum for a 1 m rock overburden is essentially the same regardless of whether primary particles with higher or lower minimum energies are used to generate events.

---

[41] The EM shower energy dependence of this cut has been established by another LBNE working group responsible for simulating ν_e beam signal interactions (Section 6.2.3).

[42] Since a higher proportion of primary particles reaching the detector would have lower energies.

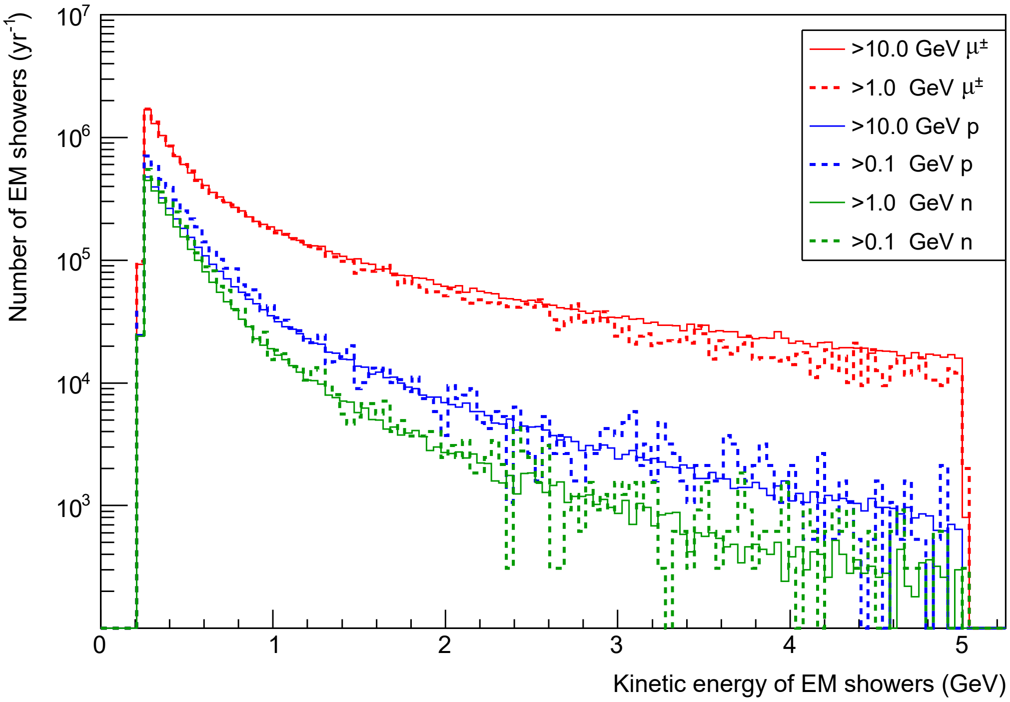

Figure 108: *The energy distributions for EM showers generated by primary particles with the minimum energies that CRY and MUSIC created them with (dashed lines), and also showers generated by primary particles with higher minimum energies (solid lines), for a rock overburden of* 1 *m. There is very little difference regardless of whether primary particles with higher or lower minimum energy are used; only the proton-induced events show a slight disparity below 1 GeV. Table 39 compares the annual rates after standard cuts have been applied.*

Table 39: *A comparison of the annual rates after the application of cuts (standard thresholds used, Eq 117) for events simulated using primary particles with higher and lower minimum energies. For muons this is* $E_\mu > 10$ *GeV vs* > 1 *GeV, for protons,* $E_p > 10$ *GeV vs* > 0.1 *GeV, and for neutrons,* $E_n > 10$ *GeV vs* > 0.1 *GeV. There is no significant difference between the muon-induced annual rates, and for proton and neutron events, the difference is only* ~ 1 *event* yr^{-1} *when their uncertainties are taken into account. Also the annual rates due to the lower minimum energy primaries are based on lower statistics).*

Minimum energy	$\mu^\pm$ (striking)	$\mu^\pm$ (missing)	p	n
Higher	4.80 ± 0.37	0.07 - 0.42	10.98 ± 0.29	8.38 ± 0.35
Lower	3.95 ± 1.19	0 - 1.89	14.77 ± 2.36	11.69 ± 1.61

Further results have been obtained using muons, neutrons and protons to generate events for rock overburdens of 1, 2, 3, 4 and 5 m. Events initiated by muons, protons and neutrons have been simulated, with the statistics and some other information summarised in Table 40. It should be noted that this set of muon-induced events have been simulated with hits by protons being recorded, which was not the case for the main results found in Sections 6.3.1, 6.3.2. The PoCA cut with respect to all tracks except the primary muon is therefore more effective here, as will be discussed further in this section. Since proton hits were already recorded for the proton and neutron-induced events in Sections 6.3.3, 6.3.4, these events are used again here for the 3 m overburden.

Table 40: *A summary of the events simulated using each type of primary particle for each of the* 1, 2, 3, 4 *and* 5 *m rock overburdens.*

	$\mu^{\pm}$ (striking)	$\mu^{\pm}$ (missing)	p	n
Minimum energy	<10.0 GeV	<10.0 GeV	<10.0 GeV	<1.0 GeV
Injection area	N/A	N/A	50×35 m^2	38×22 m^2
Events simulated	5.5×10^7	5.5×10^7	4.0×10^5	2.4×10^6
Years simulated	0.025	0.025	0.050	0.099

Table 41 shows the annual rate of EM showers for the events simulated with each rock overburden, both before and after the application of the cuts (standard cut thresholds summarised in Eq. 117 have been used here). For muon-induced events in which the muon misses the LAr, it was observed that the annual rate prior to cuts being applied falls significantly when increasing the overburden from 1 m to 2 m, but not for each subsequent metre of rock. Additional muon-induced events for some intermediate depths (1.25, 1.50, 1.75, 2.50, 3.50, and 4.50 m) have therefore been simulated (0.90% of a year's statistics for the first four of these overburdens, and 0.45% and 0.38% for the last two) shown in Table 42.

Table 41: *The annual rate of EM showers before (upper table) and after (lower table) the application of the other cuts due to additional muon, proton and neutron-generated events, using rock overburdens ranging between* 1 *m and* 5 *m. For the* 3 *m overburden, the proton and neutron-initiated events are those used in the main results (Sections 6.3.1, 6.3.2, 6.3.3, 6.3.4) but new muon-induced events have been simulated, this time with proton hits being recorded (this was not done for the main results). The difference this makes to the PoCA cut with respect to all tracks except from primary muons can therefore be seen when compared to Table 32. Standard cut thresholds (Eq. 117) have been used, including reductions for e/γ separation and a photon detection system (Sections 6.2.5, 6.2.4). The* 3 *m column here is comparable to Table 38. Upper and lower limits at* 90*% C.L. are used whenever the number of EM showers observed (i.e. prior to the application of a normalization factor) is* 5 *or lower.*

Before cuts	1 m	2 m	3 m	4 m	5 m
$\mu^{\pm}$ (striking)	2.65×10^7	2.55×10^7	2.43×10^7	2.30×10^7	2.20×10^7
$\mu^{\pm}$ (missing)	$(7.23\pm0.08)\times10^5$	$(4.92\pm0.18)\times10^4$	$(4.59\pm0.18)\times10^4$	$(4.90\pm0.18)\times10^4$	$(4.58\pm0.26)\times10^3$
p	5.21×10^6	1.05×10^6	2.35×10^5	$(4.17\pm0.06)\times10^4$	$(8.34\pm0.27)\times10^3$
n	6.00×10^6	9.51×10^5	$(1.56\pm0.02)\times10^5$	$(1.91\pm0.06)\times10^3$	$(3.49\pm0.26)\times10^3$
total	$\mathbf{3.85\times10^7}$	$\mathbf{2.75\times10^7}$	$\mathbf{2.47\times10^7}$	$\mathbf{2.31\times10^7}$	$\mathbf{2.20\times10^7}$

After cuts	1 m	2 m	3 m	4 m	5 m
$\mu^{\pm}$ (striking)	4.09 ± 0.32	4.55 ± 0.33	5.02 ± 0.35	5.14 ± 0.35	3.85 ± 0.31
$\mu^{\pm}$ (missing)	0.07 - 0.43	0.005 - 0.217	0.09 - 0.50	0.05 ± 0.37	0.30 ± 0.12
p	7.76 ± 0.21	3.43 ± 0.14	2.57 ± 0.08	0.49 ± 0.05	0.12 ± 0.03
n	8.05 ± 0.33	2.92 ± 0.20	1.23 ± 0.07	0.30 ± 0.07	0.03 ± 0.02
total	**~ 20**	**~ 11**	**~ 9**	**~ 6**	$\mathbf{4.30 \pm 0.33}$

Figures 109, 110 show the relationship between the rock overburden and the annual rate of EM showers before and after cuts are applied. Since muons penetrate rock so easily, increasing the overburden only slightly reduces the annual rate of EM showers due to muon-induced events where the primary muon strikes the LAr, either before or after the application of cuts.

Table 42: *As in Table 41 but for events due to primary muons that miss the LAr with the LAr volume situated at some additional depths. After the application of the cuts stated in Eq. 117 drops to zero, owing to low statistics, so* 90% *C.L. upper limits are given instead.*

$\mu^{\pm}$ (missing)	1.25 m	1.50 m	1.75 m	2.50 m	3.50 m	4.50 m
Before cuts ($\times 10^4$ yr^{-1})	23.7 ± 0.1	9.04 ± 0.42	6.18 ± 0.35	5.89 ± 0.34	4.95 ± 0.18	4.00 ± 0.43
After cuts yr^{-1})	0 - 0.34	0 - 0.34	0 - 0.34	0 - 0.34	0 - 0.67	0 - 0.80

In events where the primary muon misses the LAr, before the application of cuts the annual background rate is strongly affected as the depth increases between 1 m and 2 m but does not decrease significantly when the overburden becomes greater than 2 m. This is presumably due to muons that approach from wide zenith angles being able to cause fewer EM showers that reach the LAr as the overburden increases towards this point. Once cuts are applied, the overall annual background rate due to cosmic muons missing the LAr has little dependence on the size of the overburden.

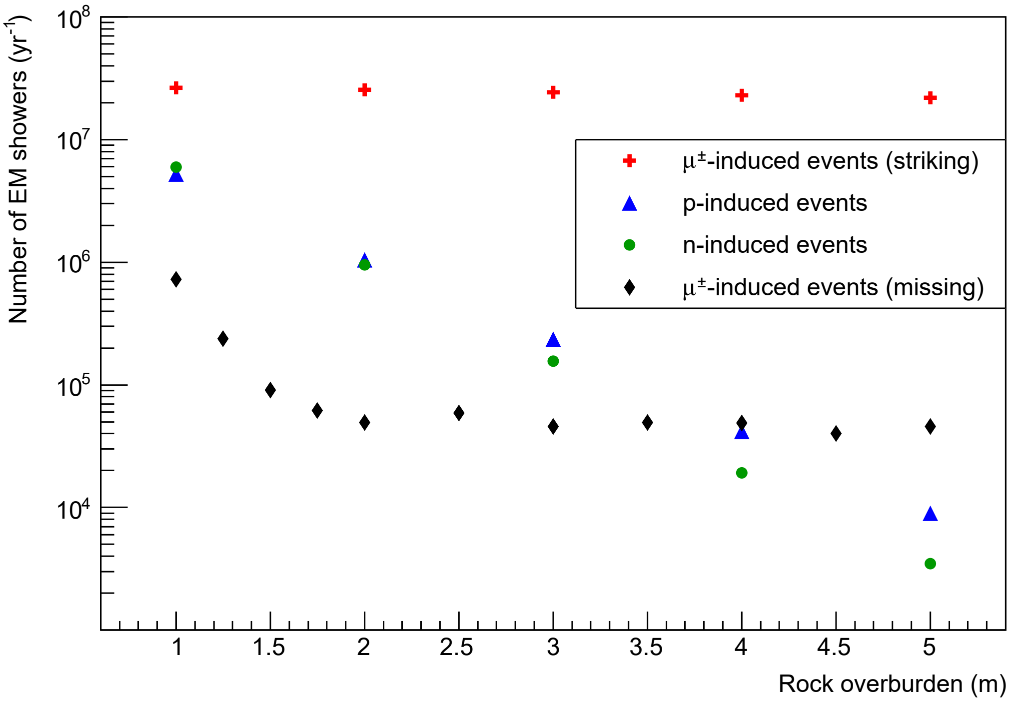

Figure 109: *The effect of rock overburden on the annual rate of background EM showers, before the application of any cuts. Varying the overburden over this range has little effect on the rate of muon-induced events (aside from those in which the muons miss the LAr at overburdens smaller than 2 m) but does significantly affect shielding in events that start with protons and neutrons.*

However, in events initiated by protons and neutrons, the size of the overburden does make a significant difference. In these instances the extra shielding provided by each additional metre of rock above the detector is clear both before and after cuts are applied, with annual EM shower rates matching or exceeding that due to muon-induced events for overburdens of approximately 2 m or less. but becoming far less significant than the muon-induced background with the detector at greater depths.

An overburden of 3 m has been used in the remainder of this section, which from this point only considers the events simulated for the main results found in Sections 6.3.1, 6.3.2, 6.3.3 and 6.3.4 unless otherwise stated. A 3 m overburden is also used in Sections 6.4, 6.6 but also the various geometric components surrounding the LAr volume create a ∼1 m barrier between the LAr and the rock surrounding the detector enclosure. A 3 m overburden was the approximate overburden favoured by the LBNE Collaboration for the surface design since the detector hall was based on the NoVA detector hall, which could accommodate a minimum of 3 m of rock above it [312]. Such an overburden was deemed necessary by the NoVA Collaboration to provide at least 10 radiation lengths to attenuate cosmic ray photons and their EM showers [313].

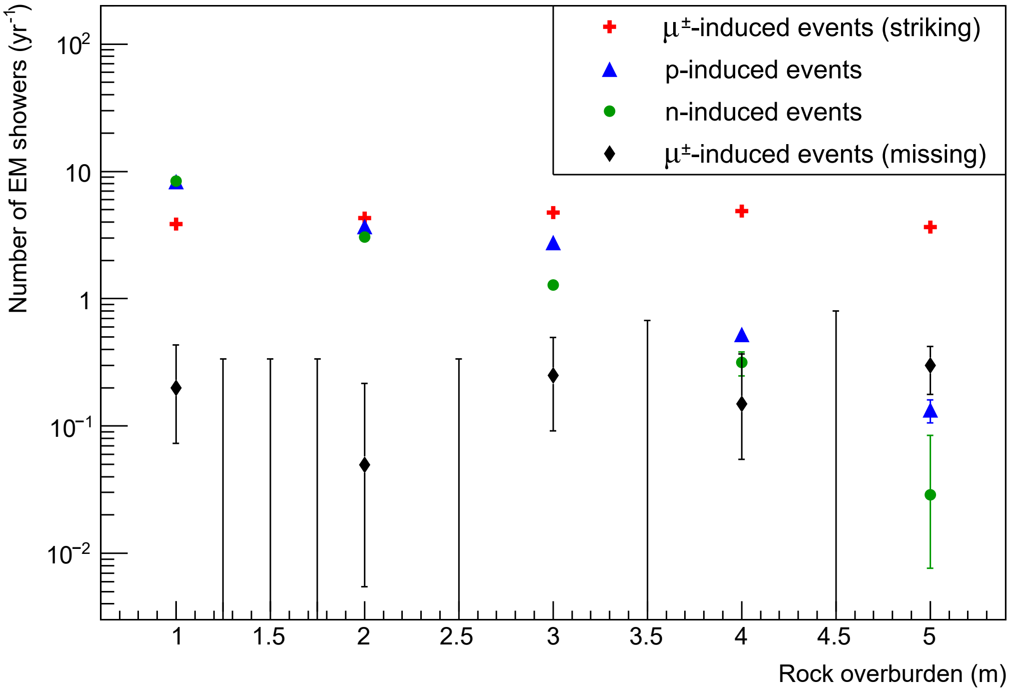

Figure 110: *As in Figure 109 but after the application of standard cuts (Eq. 117). For muon-induced events where the muon misses the LAr, the EM shower count prior to normalization was zero for all non-integer overburdens (owing to lower statistics) and five or less for overburdens except* 5 *m. Upper and lower limits at* 90% *C.L. have therefore been used for the error bars on these points.*

6.3.7.2 Energy range of electromagnetic showers

The EM shower energy cut involves rejecting showers that have energies E_γ outside of the range appropriate for the neutrino beam. These neutrinos will typically have energies between 0.5 GeV and 5.0 GeV (Figure 21) but the neutrino need not impart all of its energy to an electron produced in a CC interaction. To minimise the rejection of signal events, the lower limit on the energy of a background EM shower should be lower than 0.5 GeV. Various lower limits have therefore been tested for the range of energy over which EM showers can qualify as background candidates. For the range $X < E_\gamma < 5$ GeV, lower limits of $X = 0$, 0.125, 0.250, 0.375 and 0.500 GeV have been imposed on EM showers observed in the events used for Sections 6.3.1, 6.3.2, 6.3.3, 6.3.4, with the results shown in Table 43. The relationship between the annual background rate and the choice of X is plotted in Figures 111, 112 before and after the application of any other cuts (standard cut thresholds of Eq. 117 are used for the latter).

Table 43: *The annual rate of EM showers before (upper table) and after (lower table) the application of the other cuts due to muon, proton and neutron-generated events, using various lower limits on EM shower energy. Standard cut thresholds (Eq. 117) have been used for all other cuts.*

Before cuts	0 GeV	0.125 GeV	0.250 GeV	0.375 GeV	0.500 GeV
$\mu^{\pm}$ (striking)	2.42×10^{7}	1.95×10^{7}	1.07×10^{7}	7.66×10^{6}	$6.07\ \times10^{6}$
$\mu^{\pm}$ (missing)	$(5.05\pm0.08)\times10^{4}$	$(3.60\pm0.05)\times10^{4}$	$(1.07\pm0.03)\times10^{4}$	$(5.84\pm0.19\times10^{3}$	$(3.48\pm0.15)\times10^{3}$
p	2.35×10^{5}	1.98×10^{5}	1.05×10^{5}	$(6.32\pm0.05)\times10^{4}$	$(4.06\pm0.04)\times10^{3}$
n	1.56×10^{5}	1.31×10^{5}	6.69×10^{4}	$(3.94\pm0.05)\times10^{4}$	$(2.47\pm0.04)\times10^{3}$
total	$\mathbf{2.60\times10^{7}}$	$\mathbf{2.10\times10^{7}}$	$\mathbf{1.14\times10^{7}}$	$\mathbf{8.21\times10^{6}}$	$\mathbf{6.48\times10^{6}}$

After cuts	0 GeV	0.125 GeV	0.250 GeV	0.375 GeV	0.500 GeV
$\mu^{\pm}$ (striking)	53.8 ± 0.5	40.0 ± 0.4	12.64 ± 0.24	5.54 ± 0.16	2.12 ± 0.10
$\mu^{\pm}$ (missing)	0.88 ± 0.06	0.61 ± 0.05	0.11 ± 0.02	0.08 ± 0.02	0.04 ± 0.02
p	15.41 ± 0.20	10.71 ± 0.17	2.57 ± 0.08	1.11 ± 0.05	0.45 ± 0.03
n	9.59 ± 0.19	6.38 ± 0.15	1.23 ± 0.07	0.55 ± 0.05	0.17 ± 0.03
total	$\mathbf{80 \pm 1}$	$\mathbf{58 \pm 1}$	$\mathbf{16.67 \pm 0.27}$	$\mathbf{7.28 \pm 0.18}$	$\mathbf{2.78 \pm 0.11}$

The energy E_{ν} of a neutrino prior to it undergoing a CC interaction can be related to the energy E_e and scattering angle θ_e of the electron produced via [314]

$$E_{\nu} = \frac{m_n E_e - \frac{1}{2} m_e^2}{m_n - E_e - p_e cos(\theta_e)} \tag{118}$$

where $m_{n,e}$ are electron and neutron masses and p_e is momentum of the electron. Also Figure 94 shows the relationship between the initial energy of $\mathcal{O}(10^4)$ electrons[43] produced in CC interactions by a beam of ν_e (with energy <5 GeV) against their initial angle with respect to the beam. The widest angle observed is approximately 100°, by one or more electrons between 300-400 GeV. According to Eq. 118 an electron produced at 100° by a 0.5 GeV neutrino would have an energy of 0.308 GeV. Based on the ICARUS TPC electromagnetic energy resolution of $\sigma(E) = 0.03 \times \sqrt{E(\text{GeV}}$ (Section 3.2), the uncertainty on a 0.308 GeV electron is ±0.054 GeV. Thus, the lower limit on the energy of such an electron would be 0.252 GeV, so a conservative threshold of 0.25 GeV has been used in Sections 6.3.1, 6.3.2, 6.3.3, 6.3.4. This cut threshold would ensure a negligible loss of signal events, although raising it to 0.308 GeV would still reject very few signal events.

Based on Figure 112, the total annual background rate after cuts with $X = 0.308$ GeV would be approximately 9 yr^{-1} for the results of Sections 6.3.1, 6.3.2, 6.3.3, 6.3.4. Also If the muon-induced events used for the 3 m overburden column in Table 41 were used[44] instead of those in Sections 6.3.1, 6.3.2, the background with $X = 0.308$ GeV would be approximately 5 yr^{-1}.

---

[43] DUNE could observe $\mathcal{O}(10^3)$ ν_e appearance events for an exposure of 150 kT.MW.yr [242].

[44] The difference being that hits from protons have been recorded for these events, meaning the PoCA_{all} cut becomes more effective.

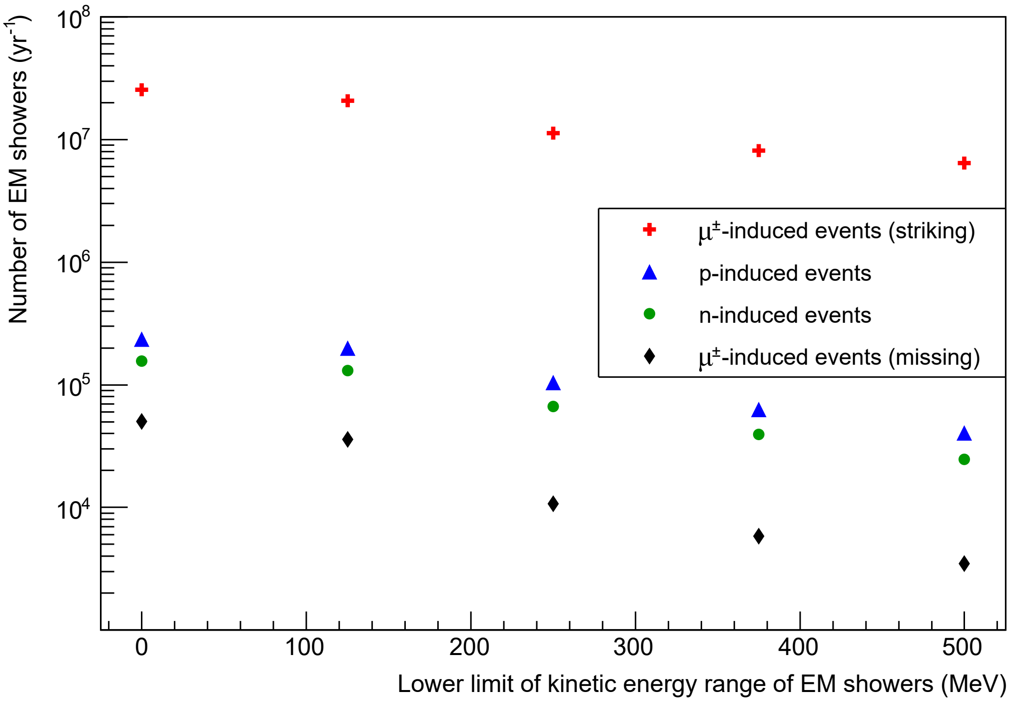

Figure 111: *The relationship between the annual rate of EM showers and the lower limit on the EM shower energy, before the application of any other cuts, for the events used in Sections 6.3.1, 6.3.2, 6.3.3, 6.3.4.*

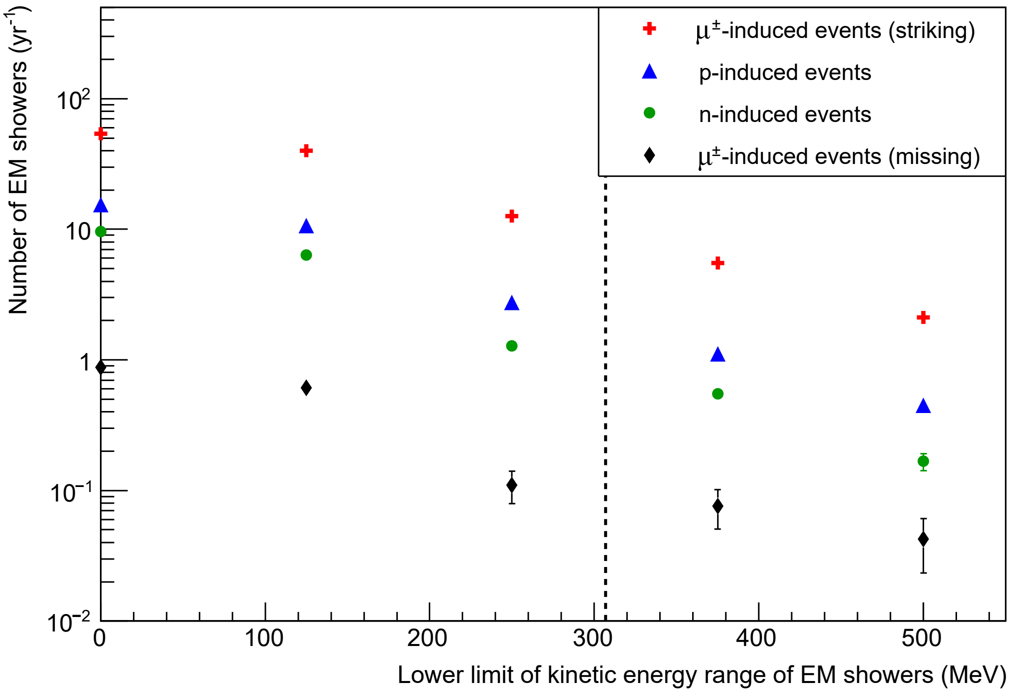

Figure 112: *The relationship between the annual rate of EM showers and the lower limit on the EM shower energy, after the application all other cuts (Eq. 117). The dashed vertical line indicates a slightly less conservative threshold of* 0.308 *GeV discussed in the main text. The error bars on the lowest point in the 'missing muons' series are* 90% *C.L. upper and lower limits (Appendix 8.9) since that annual rate is based on just* 5 *EM showers.*

6.3.7.3 Point of Closest Approach (PoCA) with respect to primary muon track

The Point of Closest Approach (PoCA) cut with respect to the primary muon track involves rejecting any EM shower for which the extrapolated trajectory of the first-generation gamma passes close enough to the primary muon track. Any muon that crosses the detector will have a cylinder defined around it, within which no EM showers from a neutrino CC interaction could be safely counted as signal events. Figure 113 (which is based on 2×10^7 events for which every e^+ and e^- in an event was recorded, Section 6.8) shows that the distance from all the tracks (and $\gamma \rightarrow e^+ e^-$ vertices) in an event to the nearest segment of the primary muon is below 30 cm in 92% of cases. Thus, a reasonable assumption for this cylinder radius is 30 cm. In the main results (Section 6.3.1) the threshold for the minimum PoCA$_\mu$ that a background EM shower can have without being rejected has therefore also been taken as 30 cm; Figure 92 demonstrates that the worst case of the PoCA calculation is the radial distance to the muon track. Thresholds of 10, 20, 30, 40 and 50 cm have also been tested for this cut, with the impact on the annual rate before and after the application of all other cuts (standard thresholds, Eq. 117) shown in Table 44 and Figures 114, 115.

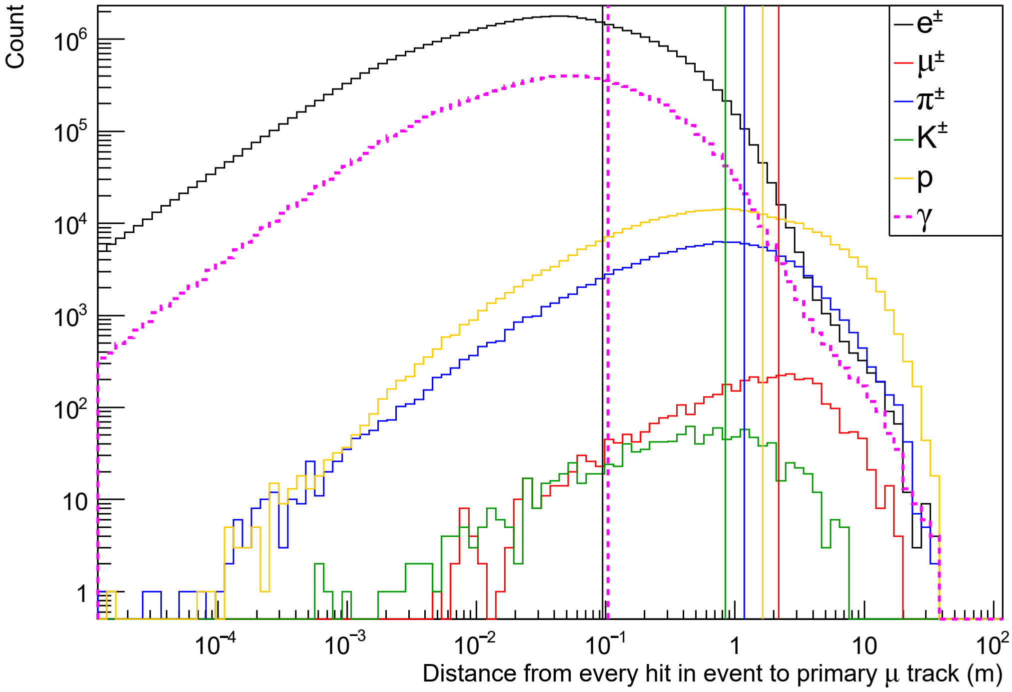

Figure 113: *The distribution of the distance from all hits by charged particles in an event to the nearest segment of the primary muon track. This is based on an additional* 2×10^7 *muon-induced events (*$E_\mu > 10$ *GeV) where all hits from electrons and positrons are recorded, rather than just the first* e^+ *and* e^- *in an EM shower. The mean distance for hits from each type of particle is indicated by the vertical lines and* 92% *of all hits are within* 30 *cm of the primary muon track. Thus, no EM shower starting within a cylinder of radius* ∼30 *cm around the muon track will be possible to safely count as signal, so the cut threshold for PoCA with respect to the muon track in the main results has been taken as* 30 *cm.*

Table 44: *The annual rate of EM showers in events where the primary muon strikes the LAr, using various lower limits on PoCA with respect to the primary muon track, before and after the application of the other cuts. Standard cut thresholds (Eq. 117) have been used for all other cuts. Also the row labelled 'extra events' refers to the extra muon-induced events used for the* 3 *m overburden columns in Table 41; since hits from protons were recorded in these events, the PoCA with respect to all non-primary-muon tracks cut becomes more effective.*

	10 cm	20 cm	30 cm	40 cm	50 cm
Before cuts	4.85×10^5	3.28×10^5	2.48×10^5	1.95×10^5	$1.58\ \times10^5$
After cuts	19.00 ± 0.30	15.09 ± 0.27	12.64 ± 0.24	10.80 ± 0.23	9.28 ± 0.21
After cuts (extra events)	8.43 ± 0.44	6.05 ± 0.37	4.74 ± 0.33	3.73 ± 0.29	3.08 ± 0.27

The choice of cut threshold makes a significant difference to the annual rate both before and after cuts, with each increase of 10 cm bringing significant reductions over the range of thresholds tested. Over this range of cut thresholds, the background rejection varies between 99.4% and 98.1%. When using the most conservative cut threshold of 10 cm, the annual rate after cuts is approximately 19 yr^{-1} (for the main results). This annual background rate is halved if the least conservative threshold of 50 cm is used but this would involve a significant increase in signal event rejection.

To assess the extent that this cut could mistakenly reject signal EM showers from neutrino interactions, the PoCA with respect to 10^7 primary muon tracks is calculated for a hypothetical EM shower generated by a neutrino, with the initial CC electron in the shower travelling parallel to the beam axis. This has calculated for a neutrino causing a shower at a selection of positions within the detector: $x = +15$ m, $y = 0$, 2, 4 and 6 m, and $z = 0$ m.

Table 45: *The percentage of EM showers caused by neutrinos travelling along the beam axis that would have their PoCA with respect to the primary muon track in excess of the various lower limits, and would thus not be mistakenly rejected by this cut.*

$PoCA_\mu$	>5 cm	>10 cm	>20 cm	>30 cm	>40 cm	>50 cm
Survival (%)	99.2	98.6	97.2	95.7	94.3	92.8

The percentage of such neutrino-induced EM showers that would be able to survive a given PoCA_μ cut threshold is plotted in Figure 116 and with a shorter x-axis in Figure 117. Survival rates for a selection of thresholds with the neutrino interaction position set to (15 m, 0 m, 0 m) are shown in Table 45. It should be notes that this is a worst-case scenario since the LAr volume is 30 m long, so even if the ray extrapolated backwards from the electron produced by the CC interaction passed close enough, it would be unnecessary to associate the resulting EM shower with a muon crossing the opposite end of the detector.

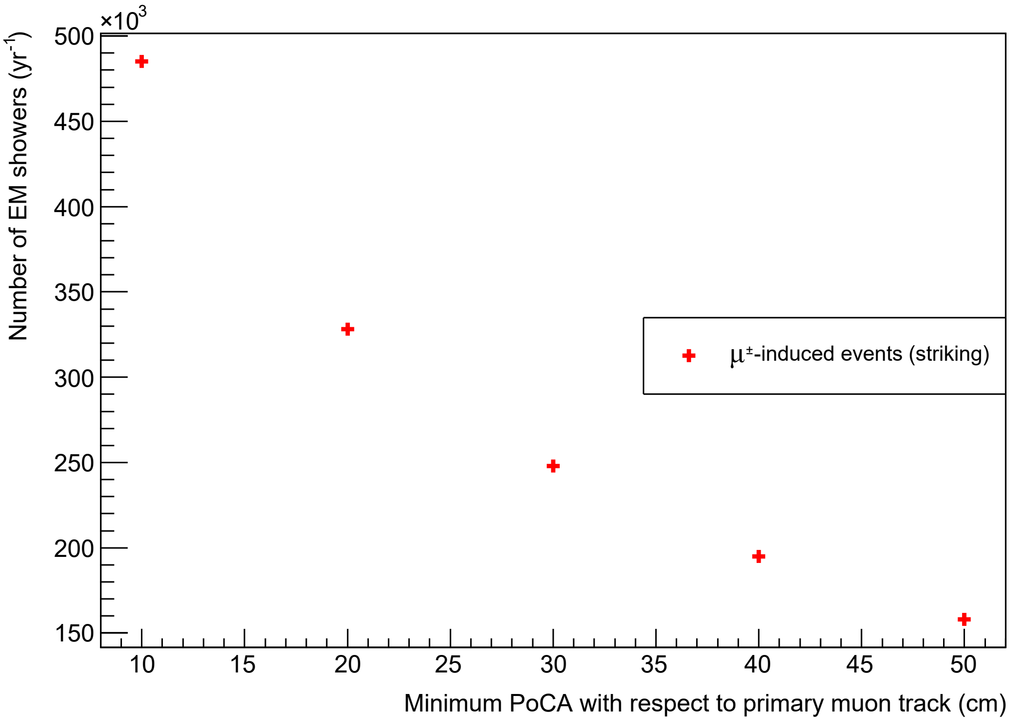

Figure 114: *The relationship between the annual rate of EM showers and the cut threshold of the PoCA of the EM shower with respect to the primary muon track, before the application of any other cuts. The initial background rate without any cuts is* 2.42×10^7 *yr*$^{-1}$ *(Table 38).*

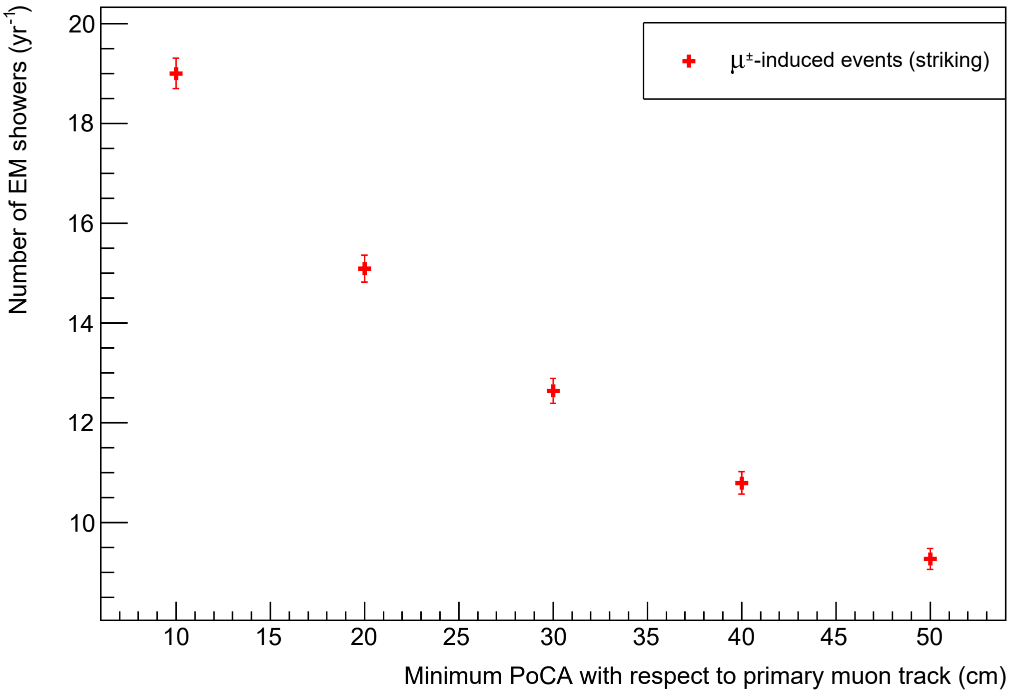

Figure 115: *As in Figure 114 but after the application of all other cuts (standard cut thresholds (Eq. 117) used.*

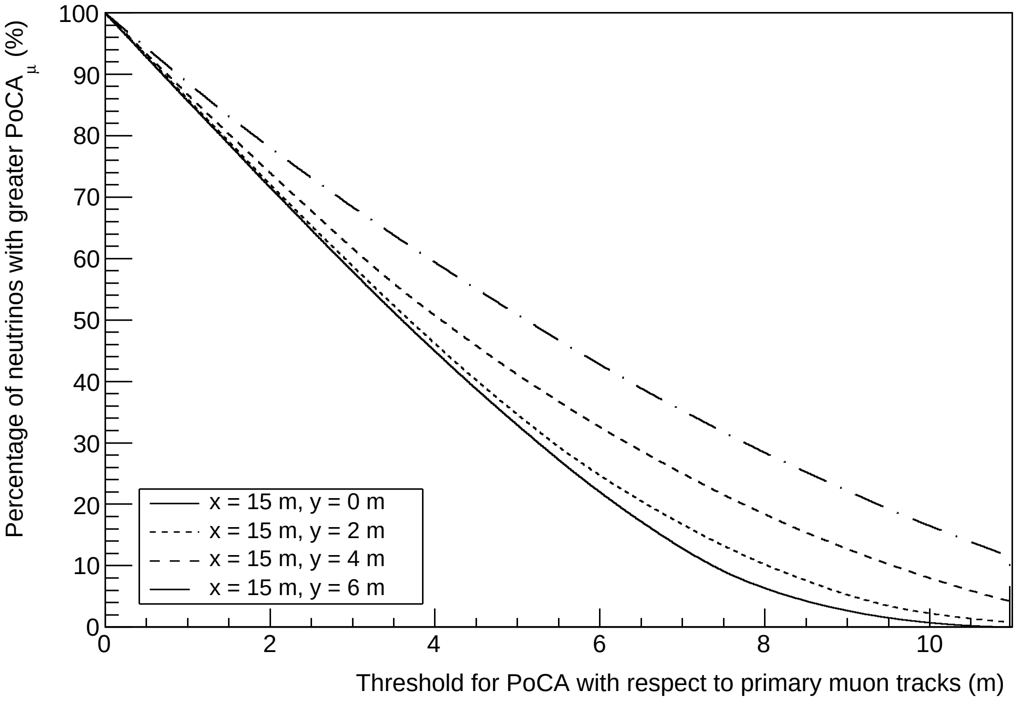

Figure 116: *The percentage of neutrino-induced EM showers that would survive a given threshold for PoCA with respect to the primary muon track. A selection of coordinates have been used for the neutrino interaction vertex (the LAr volume measures* $30 \times 15 \times 16$ *m*^{3}*). The* $y = 0$ *m case represents the most conservative estimate since an electron produced by a neutrino interacting closer to one of the long faces of the detector (which are parallel to the beam axis) will have fewer muon tracks within a set distance from it to calculate PoCA with respect to.*

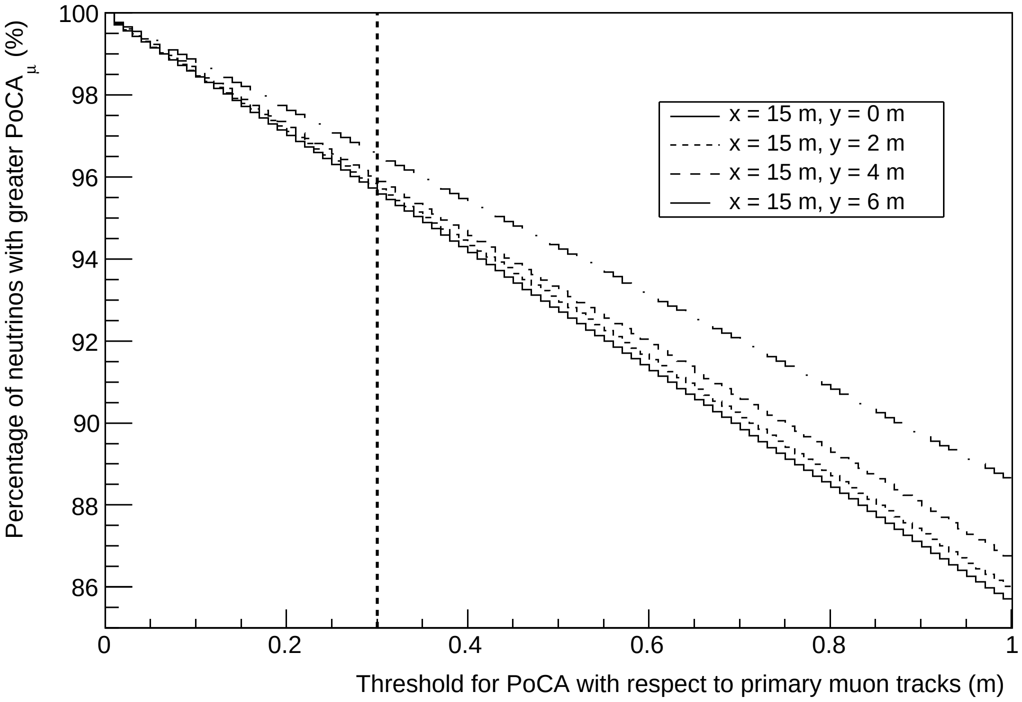

Figure 117: *As in Figure 116 but with shorter x and y-axis ranges.*

Thus, choosing a 30 cm threshold for the PoCA cut with respect to the primary muon track rejects ~99% of the muon-induced background on its own (slightly improvable according to Figure 90)), whilst causing 4.3% of signal events occurring along the central axis of the detector to be rejected.

6.3.7.4 Point of Closest Approach (PoCA) with respect to all non-primary-muon tracks

The cut threshold for the PoCA with respect to all tracks in an event left by charged particles other than the primary muon has been taken as 10 cm in the main results of Sections 6.3.1, 6.3.2, 6.3.3, 6.3.4. Figure 118 shows the distribution of the distance from every $e^{\pm}/\mu^{\pm}/\pi^{\pm}/K^{\pm}/p/\gamma$ hit in an event to the nearest segment of all other charged particle tracks. Over 93% of these hits fall within 10 cm of another track. If a neutrino CC interaction produced an EM shower starting in their vicinity it could not be safely counted as a signal event, so 10 cm has been used for the threshold of this PoCA cut.

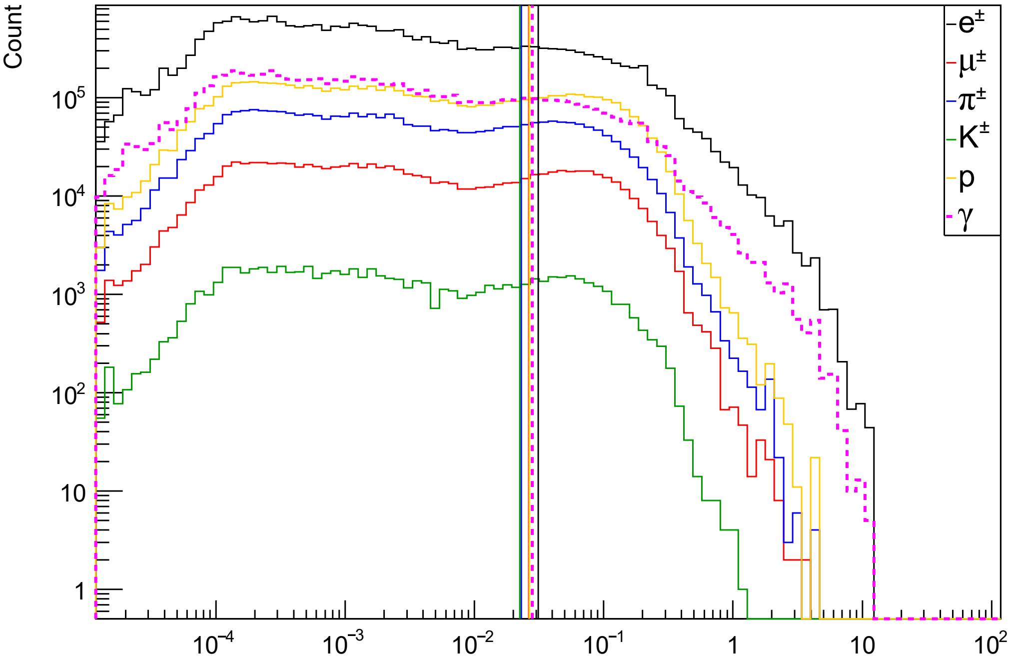

Figure 118: *The distribution of distance from all hits by* $e^{\pm}/\mu^{\pm}/\pi^{\pm}/K^{\pm}/p/\gamma$ *to the nearest segment of all other charged particle tracks except the primary muon track. This is based on an additional* 2×10^7 *muon-induced events (*$E\mu > 10$ *GeV) where all hits from electrons and positrons are recorded, rather than just the first* e^+ *and* e^- *in an EM shower. Over 93% of these hits are within 10 cm of another charged particle. A signal EM shower starting in this region could not be safely identified as such, so a 10 cm cut threshold for PoCA with respect to all tracks except the primary muon track has been used in the main results.*

Various other thresholds for this cut have also been tested. The threshold-dependence of the annual rate of background EM showers before and after all other cuts (standard thresholds, Eq. 117) are shown in Table 46 and in Figures 119, 120. Regarding the amount of signal rejected, the same procedure as was described in Section 6.3.7 for PoCA with respect to the primary muon track has been used again here. Also Table 47 shows the annual rates after all other cuts are applied using additional events generated for a 3 m overburden, in this instance with proton hits being recorded (which affects how this PoCA cut performs). Although the availability of proton tracks do make this cut more effective, the effect of increasing the cut threshold is only small, as is the case with the events upon which Table 46 is based.

Table 46: *The annual rate of EM showers before (upper table) and after (lower table) the application of the other cuts due to muon, proton and neutron-generated events, using various lower limits on PoCA with respect to all charged particle tracks (aside from the primary muon track in events that feature one). Standard cut thresholds (Eq. 117) have been used for all other cuts.*

Before cuts	10 cm	20 cm	30 cm	40 cm	50 cm
$\mu^{\pm}$ (striking)	3.932×10^6	3.893×10^6	3.875×10^6	3.863×10^6	$3.855\ \times10^6$
$\mu^{\pm}$ (missing)	$(8.021\pm0.993)\times10^3$	$(7.954\pm0.988)\times10^3$	$(7.940\pm0.988)\times10^3$	$(7.940\pm0.988)\times10^3$	$(7.940\pm0.988)\times10^3$
p	6.681×10^4	6.306×10^4	6.137×10^4	$(6.042\pm0.05)\times10^4$	$(5.976\pm0.04)\times10^4$
n	$(4.20\pm0.05)\times10^4$	$(3.99\pm0.05)\times10^4$	$(3.91\pm0.05)\times10^4$	$(3.86\pm0.05)\times10^4$	$(3.83\pm0.04)\times10^4$
total	$\mathbf{4.049\times10^6}$	$\mathbf{4.004\times10^6}$	$\mathbf{3.984\times10^6}$	$\mathbf{3.970\times10^6}$	$\mathbf{3.961\times10^6}$

After cuts	10 cm	20 cm	30 cm	40 cm	50 cm
$\mu^{\pm}$ (striking)	12.64 ± 0.24	11.30 ± 0.23	10.53 ± 0.23	9.11± 0.21	7.83 ± 0.19
$\mu^{\pm}$ (missing)	0.11 ± 0.02	0.10 ± 0.02	0.10 ± 0.02	0.10 ± 0.02	0.10 ± 0.02
p	2.57 ± 0.08	2.38 ± 0.08	2.28 ± 0.07	2.20 ± 0.07	2.18 ± 0.07
n	1.23 ± 0.07	1.17 ± 0.07	1.14 ± 0.06	1.13 ± 0.06	1.12 ± 0.06
total	**16.67 ± 0.27**	**15.06 ± 0.26**	**14.16 ± 0.25**	**12.68 ± 0.24**	**11.35 ± 0.22**

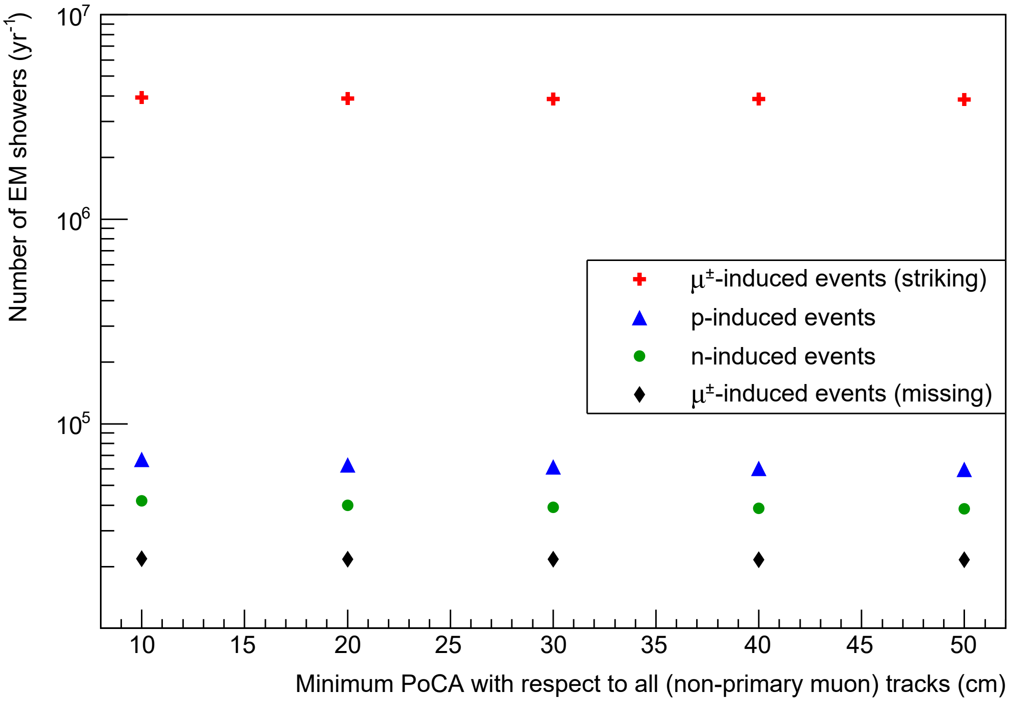

Figure 119: *The relationship between the annual rate of EM showers and the lower limit on PoCA of the EM shower with respect to all tracks other than that due to a primary muon, before the application of any other cuts.*

Table 47: *As in Table 46 but for additional muon-induced events, during which proton hits have been recorded.*

After cuts	10 cm	20 cm	30 cm	40 cm	50 cm
$\mu^{\pm}$ (striking)	5.02 ± 0.35	4.29 ± 0.32	3.95 ± 0.31	3.68 ± 0.30	3.51 ± 0.29
$\mu^{\pm}$ (missing)	0.21 ± 0.10	0.21 ± 0.10	0.21 ± 0.10	0.21 ± 0.10	0.21 ± 0.10

Table 48: *The annual rate of EM showers after the application of the other cuts due to muon, proton and neutron-generated events, for some thresholds lower than 10 cm for the PoCA cut with respect to all charged particle tracks (aside from the primary muon track in events that feature one). Standard cut thresholds (Eq. 117) have been used for all other cuts.*

After cuts	1 cm	2 cm	3 cm	4 cm	5 cm
$\mu^{\pm}$ (striking)	7.55 ± 0.43	6.55 ± 0.40	6.01 ± 0.39	5.87± 0.38	5.70 ± 0.37
$\mu^{\pm}$ (missing)	0.08 - 0.43	0.08 - 0.43	0.08 - 0.43	0.08 - 0.43	0.08 - 0.43
p	3.65 ± 0.09	3.17 ± 0.09	2.97 ± 0.09	2.86 ± 0.08	2.80 ± 0.08
n	1.77 ± 0.08	1.54 ± 0.07	1.42 ± 0.07	1.36 ± 0.07	1.33 ± 0.07
total	**~13**	**~11**	**~11**	**~10**	**~10**

In the main results (Sections 6.3.1, 6.3.2, 6.3.3, 6.3.4), the 10 cm threshold rejects approximately 85% of the background with no other cuts applied. It is clear from Figures 119, 120 that using higher thresholds causes only modest reductions in the annual background rate, whether before or after cuts. Each subsequent increase of 10 cm only slightly decreases the muon-induced background rate (only rejecting a further ~1 EM shower yr^{-1} after cuts if the threshold is increased from 10 cm to 30 cm) and has an even smaller impact on the proton and neutron-induced rates.

The annual rate after cuts for thresholds ranging from 1 to 10 cm is shown in Figure 121 and from 1 to 5 cm in Table 48, where the muon-induced annual rates are based on the same events used for Table 47 (i.e. with proton hits being recorded). The annual rate does rise more significantly as the threshold is decreased from 10 cm to 1 cm.

Figure 122 and Table 49 also show that this cut would reject few EM showers (1.5%) caused by neutrinos propagating along the beam axis with threshold at 10 cm, but this falls steadily as the threshold is increased, dropping below 95% once the threshold is between 30 - 40 cm.

Table 49: *The percentage of EM showers caused by neutrinos travelling along the beam axis that would have their PoCA with respect to all tracks in an event (except the primary muon track) in excess of the various lower limits, and would thus not be mistakenly rejected by this cut. This is calculated based on the events useed in Table 47, for which proton hits were recorded.*

$PoCA_{all}$	>1 cm	>2 cm	>3 cm	>4 cm	>5 cm
Survival (%)	99.9	99.7	99.6	99.4	99.3

$PoCA_{all}$	>10 cm	>20 cm	>30 cm	>40 cm	>50 cm
Survival (%)	98.5	97.0	95.5	94.0	92.5

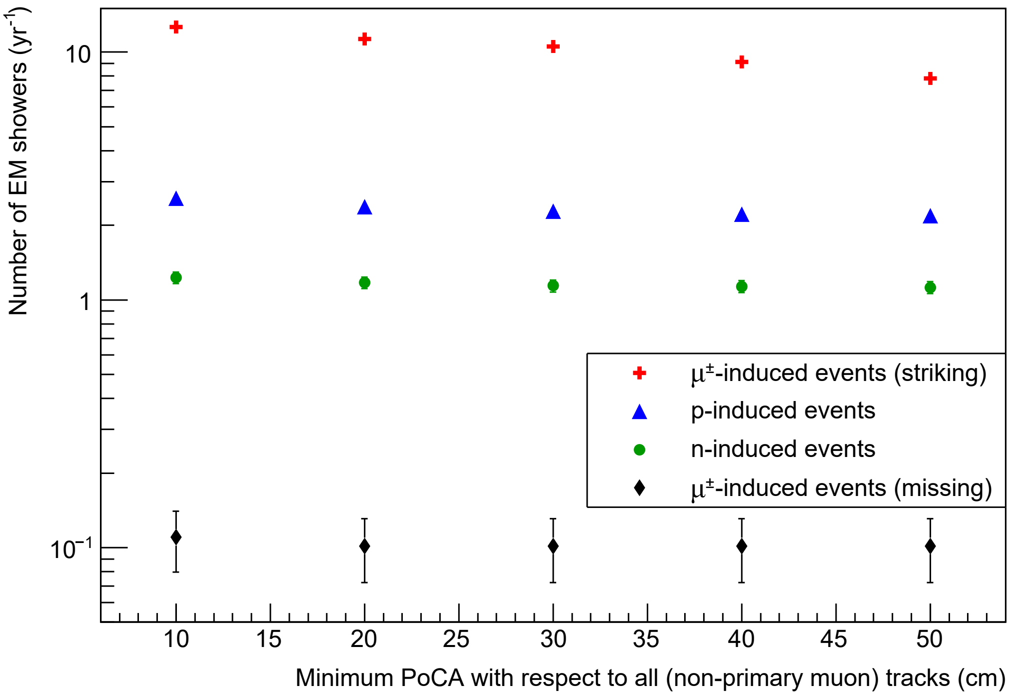

Figure 120: *As in Figure 119 but after the application of all other cuts (standard cut thresholds (Eq. 117) used. This may be compared to Figure 121, for which the lowest threshold plotted is the same as the highest threshold here; the difference is the presence/lack of proton hits for use in the PoCA calculation.*

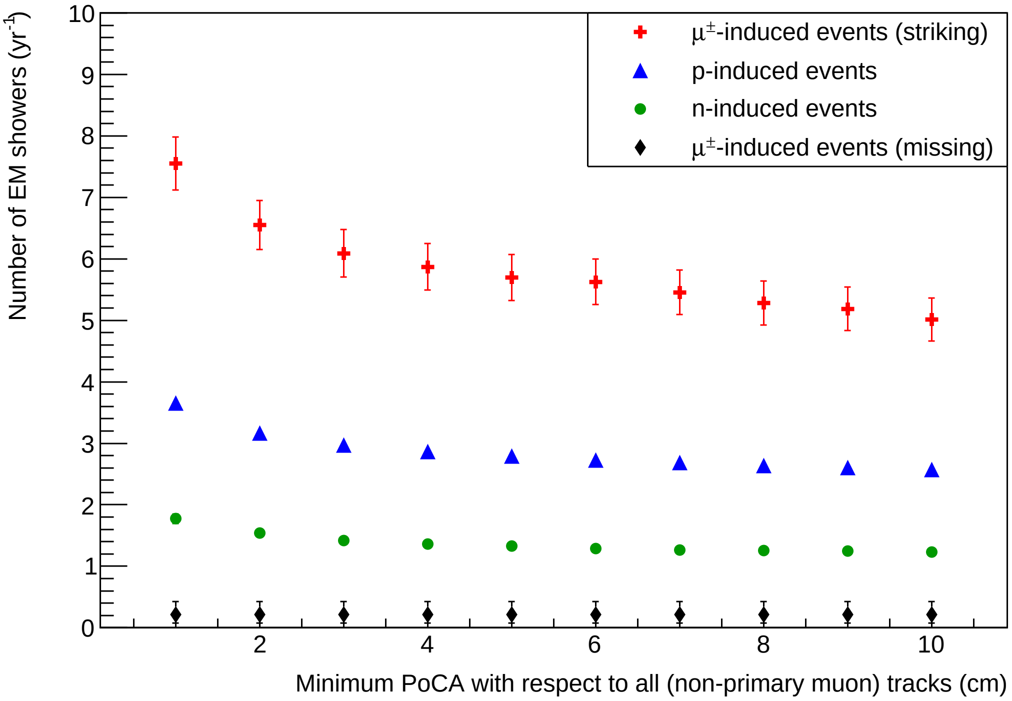

Figure 121: *As in Figure 120 but for cut thresholds under* 10 *cm.*

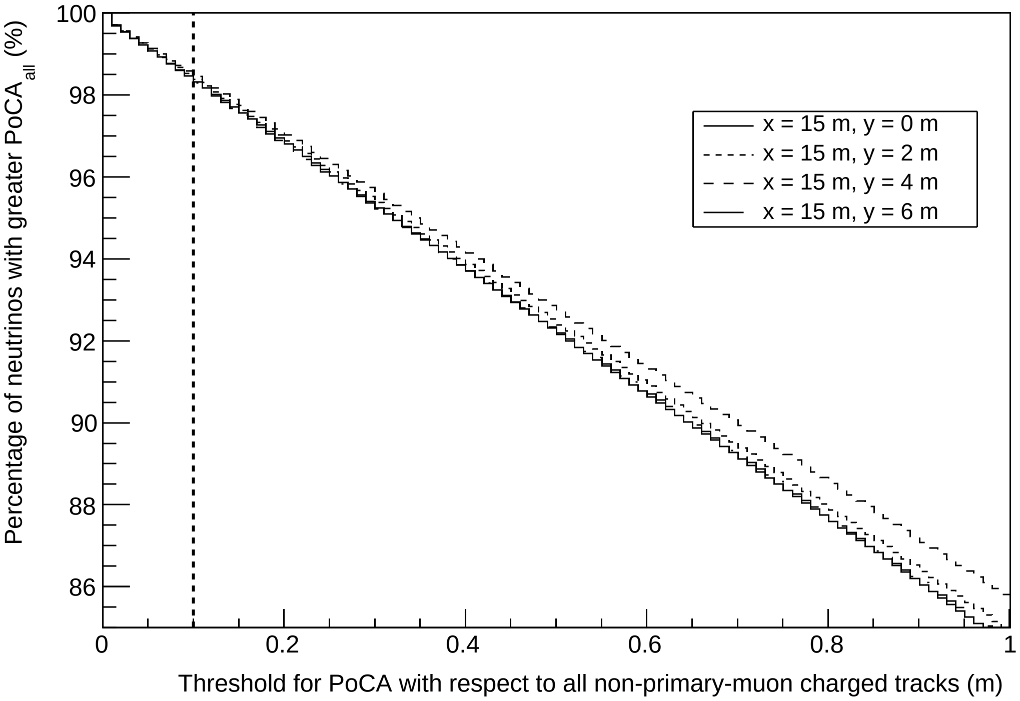

Figure 122: *The percentage of neutrino-induced EM showers travelling along the beam axis that would survive a given threshold for PoCA with respect to all charged particle tracks in an event (except primary muon tracks, where applicable). A selection of coordinates are used for the start of the EM shower, with the x-coordinate always at* 15 *m (i.e. the face of the LAr volume opposite the face that the beam enters through) and the* $z-$*coordinate always at* 0 *m (i.e. half-way up the LAr volume).*

6.3.7.5 Fiducial cut

A fiducial cut has been employed in Sections 6.3.1, 6.3.2, 6.3.3, 6.3.4 to reject background EM showers starting too close to the edges of the LAr volume. Any EM shower that starts no further than some minimum distance D inside the LAr is rejected by this cut. Thresholds for D of 10, 20, 30, 40 and 50 cm have been tested, with the effect on the annual background rate summarised in Table 50 and plotted with and without the application of all other cuts (standard thresholds, Eq. 117) in Figures 123, 124.

The fiducial cut removes large amounts of background when applied alone but the improved background rejection allowed by moving from the most conservative threshold (10 cm) to the least (50 cm) is small. However, Figure 113 shows the distribution of the distance that a first-generation gamma travels before producing the first $\gamma \rightarrow e^+e^-$ vertex in the EM shower; 92% of these vertices occur within 30 cm of the primary muon track, so this is a natural value for the D cut threshold to reject showers that start close to the edge of the LAr volume. Figure 125 demonstrates that a 10 cm threshold means >97% of the target volume is not excluded by this fiducial cut, whereas a 30 cm cut retains >92%.

6.3.7.6 e/γ separation

After the cuts already discussed in this section have been applied, two further reductions are applied to the annual rate. One is for the photon detection system (Section 6.2.6),

Table 50: *The annual rate of EM showers before (upper table) and after (lower table) the application of cuts due to muon, proton and neutron-generated events, using various lower limits on the shortest distance D from the first* $\gamma \rightarrow e^+e^-$ *vertex in an EM shower to an edge of the LAr volume. Standard cut thresholds (Eq. 117) have been used for all other cuts.*

Before cuts	10 cm	20 cm	30 cm	40 cm	50 cm
$\mu^\pm$ (striking)	1.80×10^7	1.61×10^7	1.49×10^7	1.41×10^7	1.34×10^7
$\mu^\pm$ (missing)	$(9.21\pm1.06)\times10^3$	$(4.93\pm0.78)\times10^3$	$(2.83\pm0.59)\times10^3$	$(1.52\pm0.43)\times10^3$	882 ± 329
p	1.81×10^5	1.57×10^5	1.38×10^5	1.23×10^5	1.10×10^5
n	1.19×10^5	1.02×10^5	8.85×10^4	7.76×10^4	6.84×10^4
total	$\mathbf{1.83\times10^7}$	$\mathbf{1.64\times10^7}$	$\mathbf{1.51\times10^7}$	$\mathbf{1.43\times10^7}$	$\mathbf{1.36\times10^7}$

After cuts	10 cm	20 cm	30 cm	40 cm	50 cm
$\mu^\pm$ (striking)	13.22 ± 0.25	12.87 ± 0.25	12.64 ± 0.24	12.35 ± 0.24	12.01 ± 0.24
$\mu^\pm$ (missing)	0.40 ± 0.06	0.19 ± 0.04	0.11 ± 0.02	0.06 ± 0.01	0.06 ± 0.01
p	3.43 ± 0.08	2.93 ± 0.08	2.57 ± 0.08	2.23 ± 0.07	1.94 ± 0.07
n	1.73 ± 0.08	1.43 ± 0.07	1.23 ± 0.07	1.043 ± 0.06	0.92 ± 0.06
total	$\mathbf{18.78 \pm 0.29}$	$\mathbf{17.41 \pm 0.28}$	$\mathbf{16.55 \pm 0.27}$	$\mathbf{15.68 \pm 0.26}$	$\mathbf{14.98 \pm 0.26}$

which shortens the time window during which background events can occur (and therefore reduces the annual background rate) by a factor of 140 (Eq. 113), assumed 100% efficient here. The other reduction is for the e/γ separation discussed in Section 6.2.5. Distinguishing EM showers that start with a lone electron track rather than an electron and a positron emerging from a vertex with an invisible gamma is not 100% efficient; the failure rate has been taken as 10% for the main results in Sections 6.3.1, 6.3.2, 6.3.3, 6.3.4 (i.e. muon, proton and neutron-induced events using the simple detector geometry with the flat surface). The dependence of the annual background EM shower rate on the efficiency of e/γ separation is therefore shown in Figure 126.

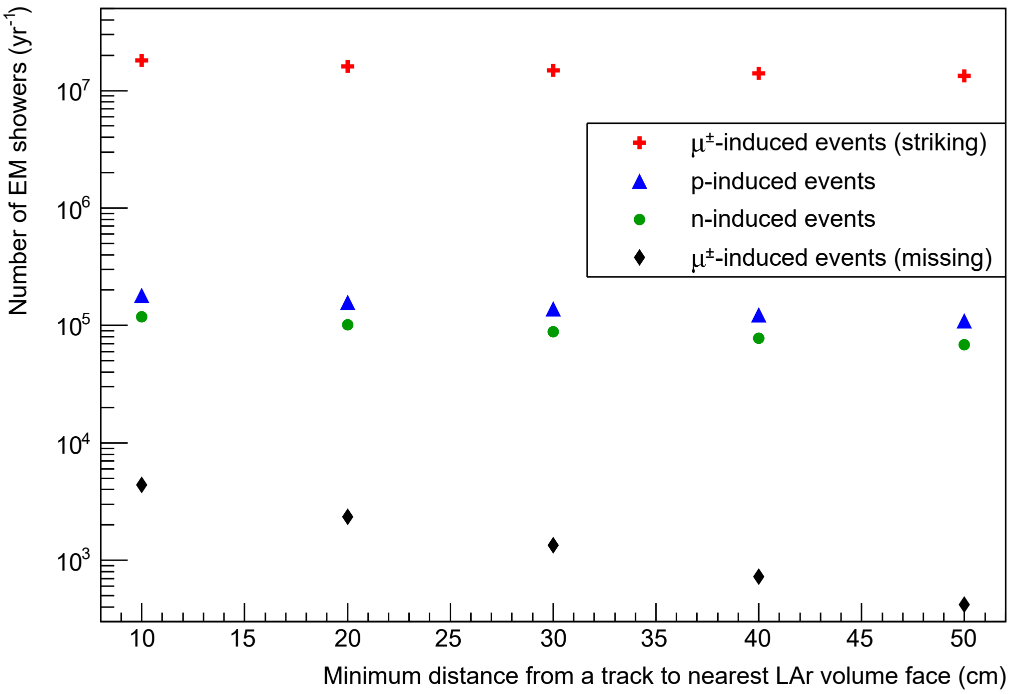

Figure 123: *The relationship between the annual rate of EM showers and the lower limit on the shortest distance D from the first* $\gamma \rightarrow e^+e^-$ *vertex in an EM shower to an edge of the LAr volume, before the application of any other cuts.*

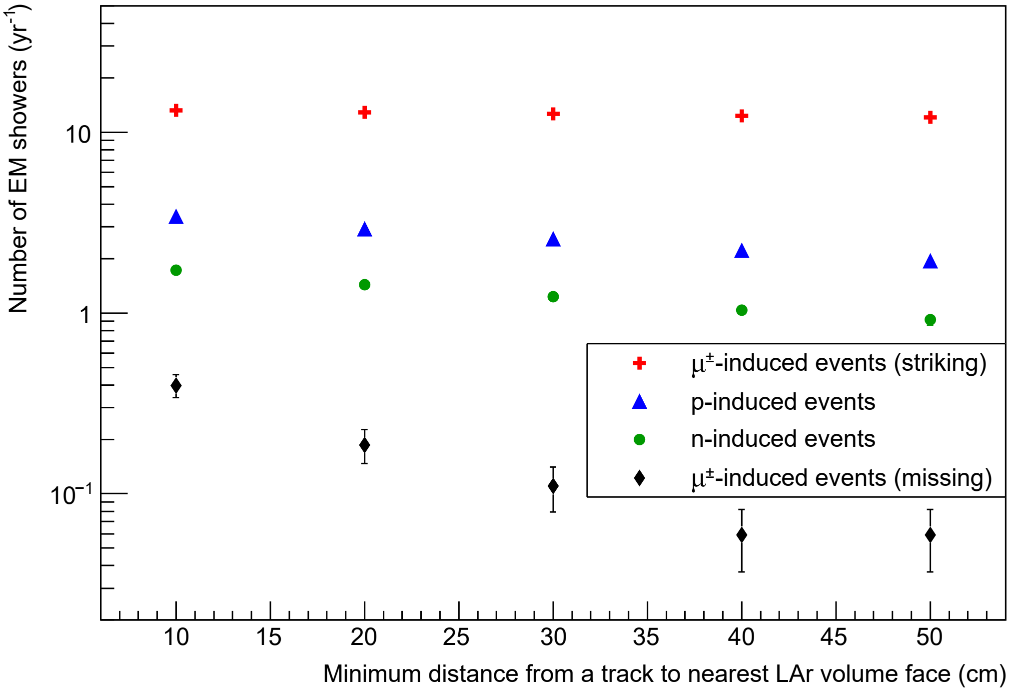

Figure 124: *As in Figure 123 but after the application of all other cuts (standard cut thresholds (Eq. 117) used.*

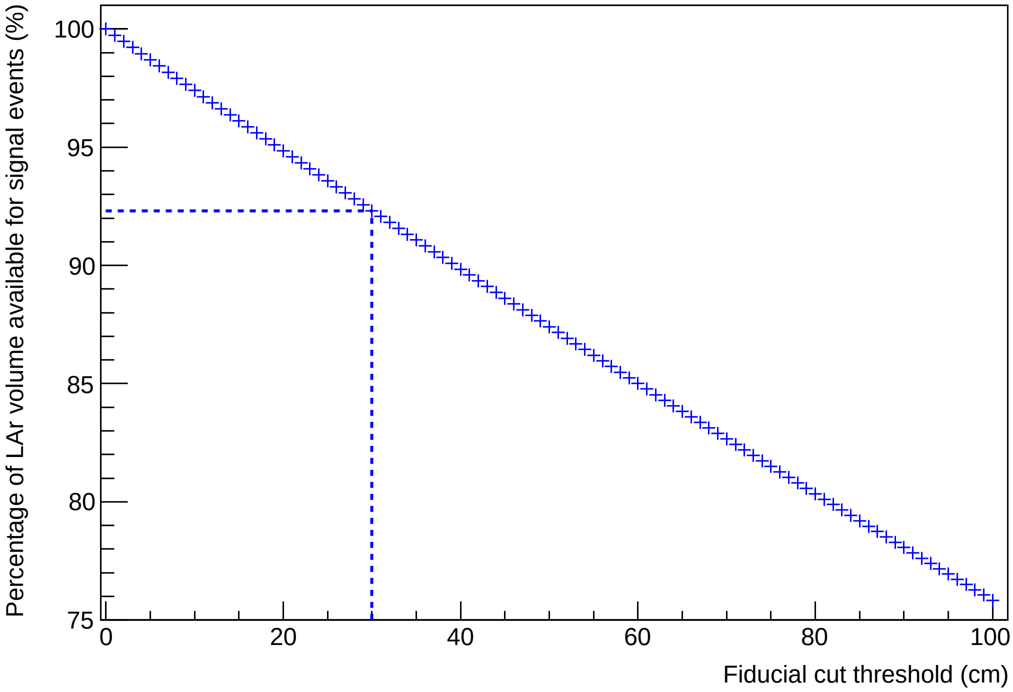

Figure 125: *The percentage of the LAr volume rendered available for signal event detection by a given choice of threshold for the fiducial cut. The vertical and horizontal dashed lines indicate the threshold of* 30 *cm used in the main results (Sections 6.3.1, 6.3.2, 6.3.3, 6.3.4).*

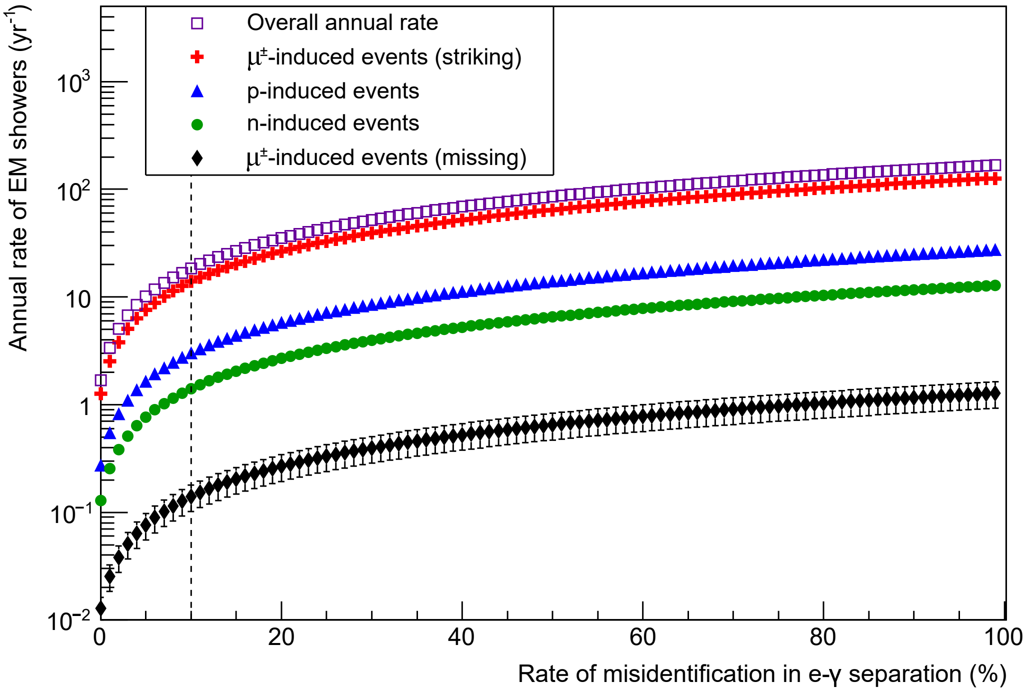

Figure 126: *The dependence of the annual rate of EM showers on the efficiency of the e-γ separation, for the main results of Sections 6.3.1, 6.3.2, 6.3.3, 6.3.4. The cuts that have been applied here are those stated in Eq. 117 and the annual rates have been multiplied by* $1/140$ *because of the photon detection system. The dashed vertical line indicates the* 10% *misidentification rate used throughout the sections stated above.*

6.4 Results for detailed detector geometry and flat surface profile

In this section background estimates are given for simulations using the detailed detector geometry (Section 5.3.2) and the flat surface profile. For the combination of detailed detector geometry and flat surface, there have been 8×10^7 muon-induced events simulated, corresponding to 0.036 years of statistics. It should be noted that, although muons with energies greater than 10 GeV were used both here[45] and for the simple detector geometry, the normalization factors still differ due to having been stored on the surface of differently sized cuboids for the different detectors. The mean time simulated per primary muon event (t_{mean} in Table 28) is 1.78×10^{-5} s (i.e. simulating one million muon-induced events corresponds to 17.8 s of live time) for the muons used for the simple detector geometry and 9.48×10^{-6} s (i.e. 94.8 seconds of live time per million muons injected) for the detailed detector geometry.

6.4.1 Background due to primary muons that strike the detector

Table 51 shows the annual rate from muons that strike the detector below the flat surface. The total number of background EM showers within the required energy range stands at 1.37×10^7 yr^{-1}. This compares with a rate of 1.07×10^7 yr^{-1} overall for the simple detector geometry, but it should be noted that the combined mass of the active volumes is slightly larger for the detailed geometry, with 10.70 kton of LAr available compared to 10.03 kton in the simple detector geometry (Section 5.3). However, even when normalized to a common mass, the detailed detector geometry sees 1.20 times more showers than the simple geometry. The detailed geometry also presents a larger target since its active LAr is split between two cryostats, in TPC cells stacked $9 \times 6 \times 2$ and each measuring $2.52 \times 2.28 \times 7.00$ m^3. The combined area of the top, side and end faces of this arrangement of TPC cells (ignoring the small gaps between them) exposed to the cosmic ray flux is 819.3 m^2, so for two cryostats situated enough apart to act as separate targets for the cosmic ray flux, the total area would be $\sim$ 1638.6 m^2. If the two cryostats were pushed together close enough that that they form an effective $9 \times 12 \times 2$ array the area exposed to the cosmic ray flux would be $\sim$ 1321.1 m^2. Comparing this to the $30 \times 15 \times 16$ m^3 block of LAr used for the simple detector, which has a combined top, side and end faces area of 1170 m^2, the ratio of surface area exposed to cosmic rays is between 1.129 and 1.400, depending on how close together the TPC arrays are. This is compatible with the detailed detector observing 1.20 times as many EM showers as the simple detector geometry even after the minor target mass differences are taken into account.

The total background is comprised of three main ancestries, namely $\mu \rightarrow \gamma$ (48%), $\pi^0 \rightarrow \gamma$ (17%) and $Ext \rightarrow \gamma$ (34%). This compares to contributions of 59%, 21% and 19% respectively for the simple detector geometry. This is due to the detailed detector geometry having its total active LAr volume split into two cryostats and divided into many smaller volumes with gaps left between them. The detailed detector geometry therefore has the possibility of showers starting in gaps deep within the detector enclosure that do not exist for the simple geometry, accounting for the increased contribution from $Ext \rightarrow \gamma$.

---

[45] The muons used for the detailed detector geometry were generated with energies greater than 10 GeV rather than the minimum 1 GeV that the muons used for the simple detector were originally generated at, but only muons over 10 GeV have been used to generate events. This is reflected in the differing amounts of live time that simulating a given number of events with each set of muons would correspond to.

Table 51: *The annual rate due to each type of shower ancestry as successive cuts are applied, for muon-induced events in the detailed detector geometry and flat surface profile in which the primary muon strikes at least one of the detector's active volumes. The overall scaling factor applied to the count obtained from the simulated data is* 38.86366 *(Table 28).*

	$\mathbf{E}_\gamma$	$\mathbf{PoCA}_\mu$	θ_{beam}**(E)**	$\mathbf{PoCA}_{all}$	**D**	e/γ	γ **detection**
total	1.37×10^7	$(6.34\pm0.16)\times10^4$	$(2.95\pm0.11)\times10^4$	3769 ± 383	2720 ± 325	272 ± 32	1.94 ± 0.23
$\pi^0 \rightarrow \gamma$	2.32×10^6	$(5.83\pm0.15)\times10^4$	$(2.72\pm0.10)\times10^4$	3303 ± 358	2565 ± 316	257 ± 32	1.83 ± 0.23
$Ext \rightarrow \gamma$	4.69×10^6	4586 ± 422	1943 ± 275	466 ± 135	155 ± 78	15.5 ± 7.8	0.11 ± 0.06
$\mu \rightarrow \gamma$	6.59×10^6	0-95	0-44	0-5.07	0-3.61	0-0.36	0-0.003
$other \rightarrow \gamma$	$(8.15\pm0.18)\times10^4$	544 ± 145	350 ± 117	0-95	0-68	0-6.8	0-0.048

This is supported by Figures 128, 129, which show the positions of the first-generation gammas that have crossed into an active volume from outside, or which result from a π^0 decaying inside an active volume. These plots demonstrate that a significant number of showers are being generated within the gaps and registering a hit just inside the inward-facing planes of the active volumes. The presence of gaps between the active volumes are frequently used to interpret results in this section.

The choice of detector geometry causes no discernable difference in the efficiency of the cut of PoCA >30 cm with respect to the track left by the primary muon, with >99% of the background being rejected by this cut.

Next the θ_{beam} cut is applied. The θ_{beam} cut fares only slightly better for the detailed detector geometry, which sees 53% of showers rejected compared with 51% in the simple detector geometry; a statistically insignificant difference.

The cut of PoCA >10 cm with respect to all tracks is then applied. It is far more effective with the detailed geometry than the simple geometry, with 87% of the remaining background being rejected with the former compared to just 47% with the latter. This is primarily due to hits from protons being recorded for this set of simulated data whereas this was not done for muon-induced events with the simple geometry.

Finally the 'Distance to nearest wall' cut ($D > 30$ cm) is applied and is seen to be more effective for the detailed geometry, reducing the overall background by a further 28% compared to just 13% with the simple geometry. For the simple geometry there was only one LAr volume, but in this instance there are two, meaning there is more surface area available to apply this cut to (as illustrated in Figure 127). This makes the cut more effective at removing showers starting with $\pi^0 \rightarrow \gamma$ (the main ancestry after the previous cuts have been applied), which are spread evenly throughout the detector; 22% are rejected, compared to 13% with the simple geometry. However, showers with the ancestry $Ext \rightarrow \gamma$ are not evenly spread through the detector but instead occur near the outer faces of the LAr volumes, so having more surface area to apply this cut to does not result in a greater fraction of showers with the ancestry $Ext \rightarrow \gamma$ being rejected. Instead this cut is less effective at removing showers starting with $Ext \rightarrow \gamma$; all of the remaining $Ext \rightarrow \gamma$ showers are rejected by this cut with the simple geometry but only 67% of them are rejected with the detailed geometry. In the detailed detector, muons can interact in gaps between the TPC cells and showers that would have been counted as $\pi^0 \rightarrow \gamma$ instead count as $Ext \rightarrow \gamma$. These $Ext \rightarrow \gamma$ showers deep inside the detector can avoid the fiducial cut. This is demonstrated in Figures 128, 129. For comparison, Figure 98 shows the positions of first-generation gammas from $\pi^0 \rightarrow \gamma$ and $Ext \rightarrow \gamma$ in the simple detector.

After reductions for e/γ separation and photon detection are applied, the overall background rate is 1.94 ± 0.23 yr^{-1}. This compares to the final rate with the simple detector geometry of $\sim$2.84 yr^{-1} if hits from protons are recorded.

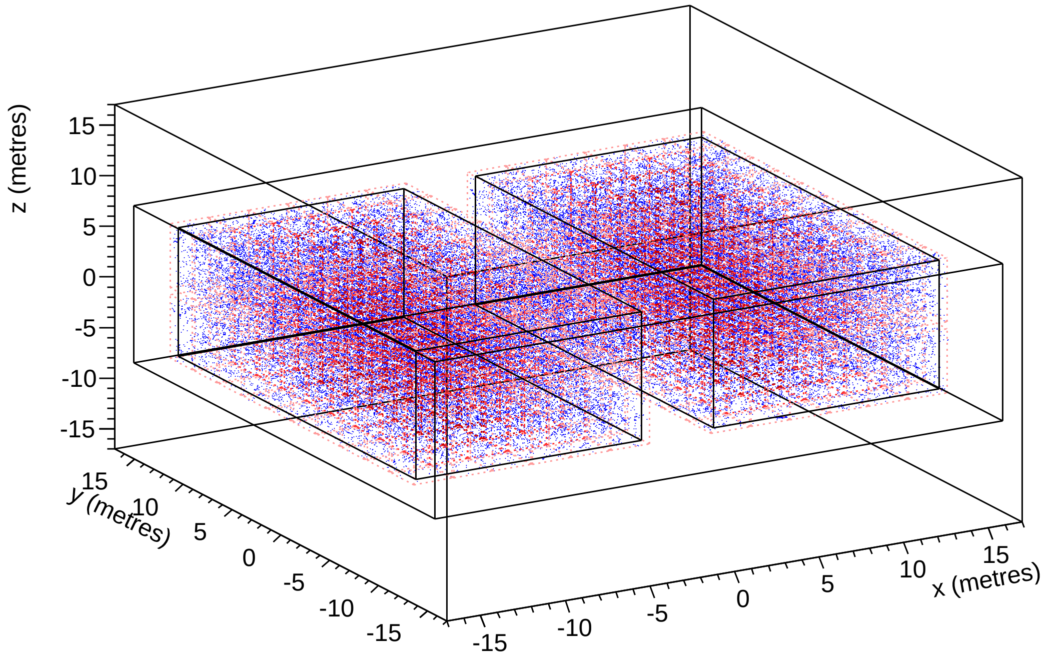

Figure 127: *The positions of 10^5 first-generation gamma upon their conversion to an e^+/e^- pair which result from primary muons that strike an active volume of the detailed detector geometry. The active volumes within each TPC cell are shown in red dashed lines. The black box within the boundary of the TPC cells indicates the fiducial volume (30 cm from the walls). Points from all first-generation gamma ancestries are plotted here, although the vast majority are due to $\mu \to \gamma$, which are efficiently removed by a PoCA cut. Figures 128, 129 only include Ext $\to \gamma$ and $\pi^0 \to \gamma$, which form essentially the whole background once showers with ancestry $\mu \to \gamma$ have been removed.*

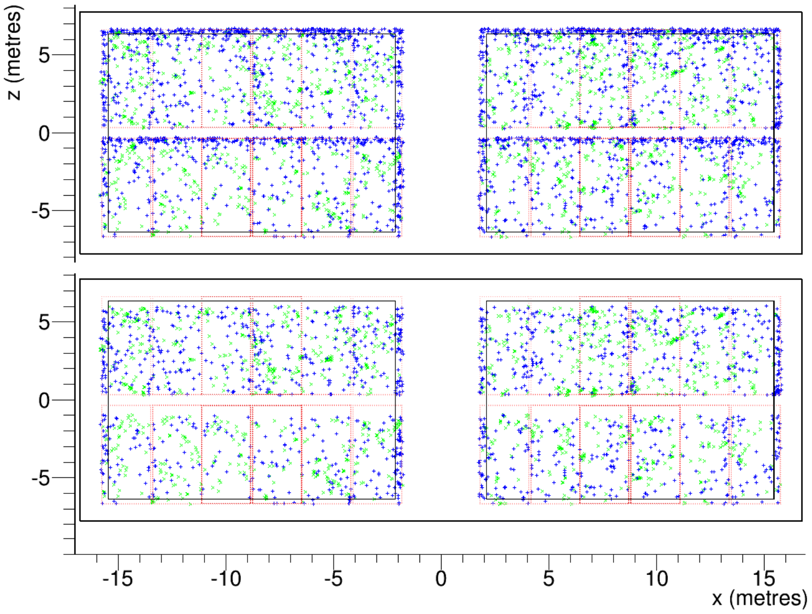

Figure 128: *The positions of some first-generation gammas upon their conversion to an $e^\pm$ pair, in events where primary muons strike an active volume cell in the detailed detector. This view is of the end of the detector (i.e. parallel to the beam direction). Only gammas which have either crossed into an active volume from outside (blue '+' signs), or which are the daughters of π^0 decays (green '×' signs) are plotted. Any points not within the black box inside the red TPC active volumes are eliminated by the fiducial cut. The lower image is the same as the upper image but with the points near the top of each horizontal row of active volumes removed (the relevance of this is explained in Figure 129).*

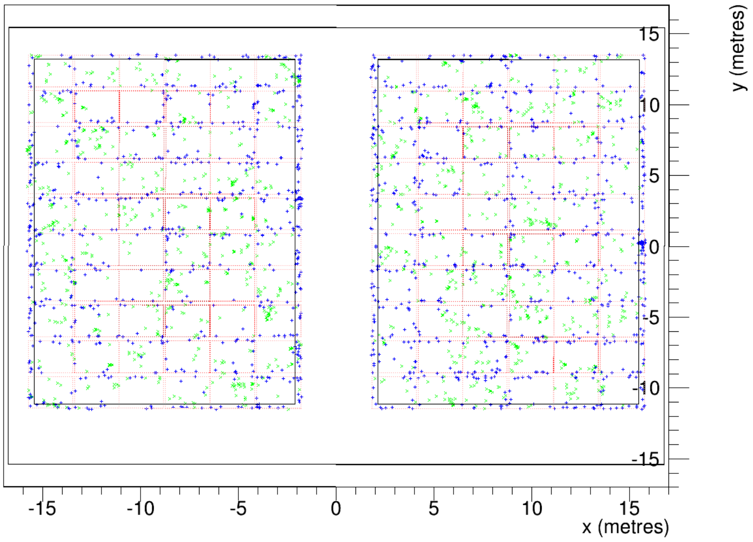

Figure 129: *The same as the lower image in Figure 128 but for a bird's eye view of the detector. With the uppermost gammas removed from each layer of TPC cells (compare upper and lower image in Figure 128 it is clear that a significant amount of the background due to Ext* $\rightarrow \gamma$ *(denoted blue '+' sign) and* $\pi^0 \rightarrow \gamma$ *(green '×' sign) results from muons interacting in the gaps between the active volumes, since the Ext* $\rightarrow \gamma$ *points are typically located just inside an active volume boundary. Showers with the ancestry* $p/n/\pi^{\pm} \rightarrow \pi^0 \rightarrow \gamma$ *often occur deeper into the active volumes, as one would expect.*

6.4.2 Background due to primary muons that miss the detector

Table 52 shows the annual background EM shower rate due to primary muons that never cross into any of the sensitive cells within the LAr volumes. For this type of event, the number of background showers prior to cuts is greater in the detailed detector geometry than with the simple geometry. This is despite the detailed geometry having greater shielding, which only becomes significant for other types of primary particle.

Table 52: *The annual rate due to each type of shower ancestry as successive cuts are applied, for muon-induced events using the detailed detector geometry and flat surface profile in which the primary muon misses the detector's active volumes. The overall scaling factor applied to the count obtained from the simulated data is* 38.86366 *(Table 28).*

	E$_\gamma$	**D**	θ_{beam}**(E)**	**PoCA**$_{all}$	e/γ	γ **detection**
total	$(1.47\pm0.08)\times10^4$	3342±360	1283±223	622±155	4.44±1.11	0.44±0.11
$\pi^0 \rightarrow \gamma$	2720±325	1166±213	428±129	78±55	0.56±0.39	0.06±0.04
Ext $\rightarrow \gamma$	$(1.19\pm0.07)\times10^4$	2138±288	855±182	544±145	3.89±1.04	0.39±0.10
other $\rightarrow \gamma$	4-169	4-169	0-36	0-17.64	0-1.76	0-0.013

The detailed geometry sees an overall rate of 1.47×10^4 yr^{-1}. This compares to an overall rate of 1.07×10^4 yr^{-1} in the simple detector. The simple geometry only having experienced 78% of the total EM showers seen with the detailed geometry is explained by the latter having its total active volume divided into two cryostats and into separate cells with gaps between them. For context, the primary muon misses the the LAr in 0.0091% of muon induced events with the simple detector compared to 0.034% here, although many of those that miss will miss by a relatively long distance since the gap between the cryostats is large.

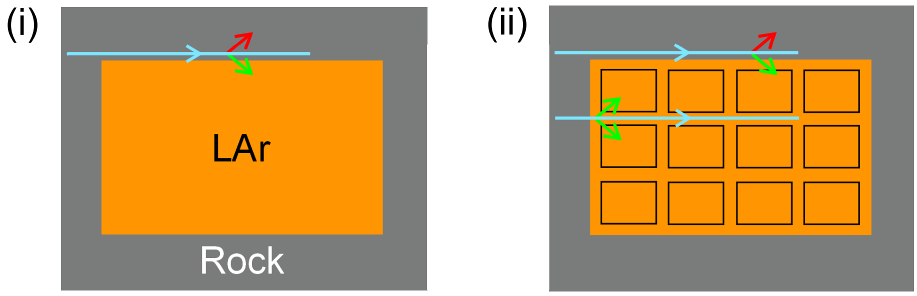

Figure 130: *Diagram (i) shows a primary muon missing the simple detector geometry. The green arrow represents secondary particles entering the LAr, the red represents secondary particles that do not enter. Diagram (ii) shows two primary muons missing the detailed detector geometry. The upper muon misses outside of the boundary of the overall LAr volume, as in diagram (i). The lower muon strikes the overall LAr volume, but still misses the active LAr cells (outlined in black). Secondaries produced by this muon have a shorter distance to travel before they can enter an active LAr region, and are surrounded by these regions (unlike those shown in diagram (i)).*

Regarding specific ancestries, the number of EM showers from the ancestry $Ext \rightarrow \gamma$ observed with the detailed geometry is 1.2 times the number seen with the simple geometry, and again this ancestry accounts for the vast majority of the total showers observed. The difference is even more pronounced for showers starting with $\pi^0 \rightarrow \gamma$, with the detailed geometry recording 3.1 times as many as the simple geometry. Figure 130 helps to interpret this; with the detailed geometry, secondary particles created by a primary muon missing the LAr via gaps between cells are more likely to enter an active LAr region before initiating an EM shower (and thus being counted as $\pi^0 \rightarrow \gamma$ instead of $Ext \rightarrow \gamma$).

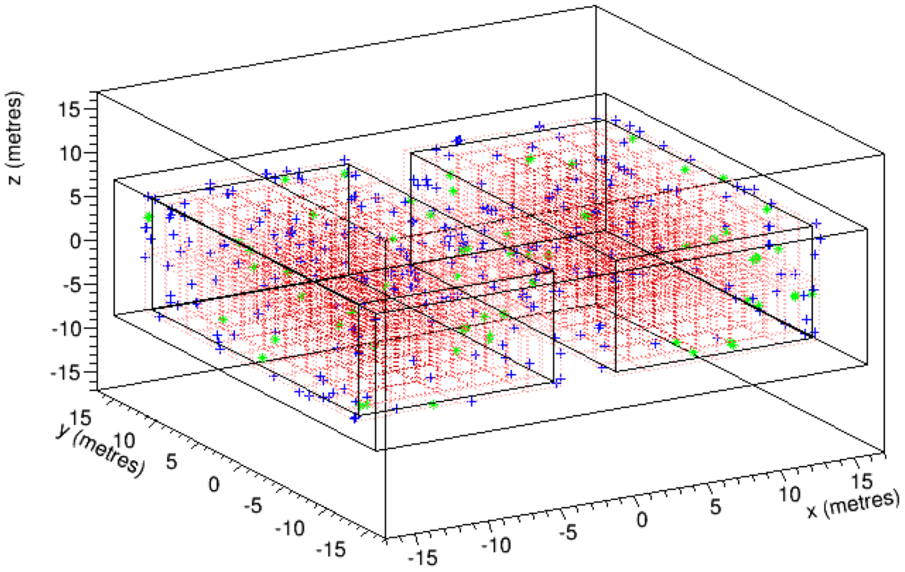

Figure 131: *The position of the first-generation $\gamma \rightarrow e^+e^-$ vertex for EM showers starting with $\pi^0 \rightarrow \gamma$ (green) and $Ext \rightarrow \gamma$ (blue), for events in which the primary muon registers no hit in any active volume. This is for* 0.036 *years of statistics, noting that there are significantly fewer points plotted than the corresponding numbers in Table 52, since the table is normalized to one year (the raw count multiplied by* 38.86366*), and that many points are difficult to distinguish since they often occur close together.*

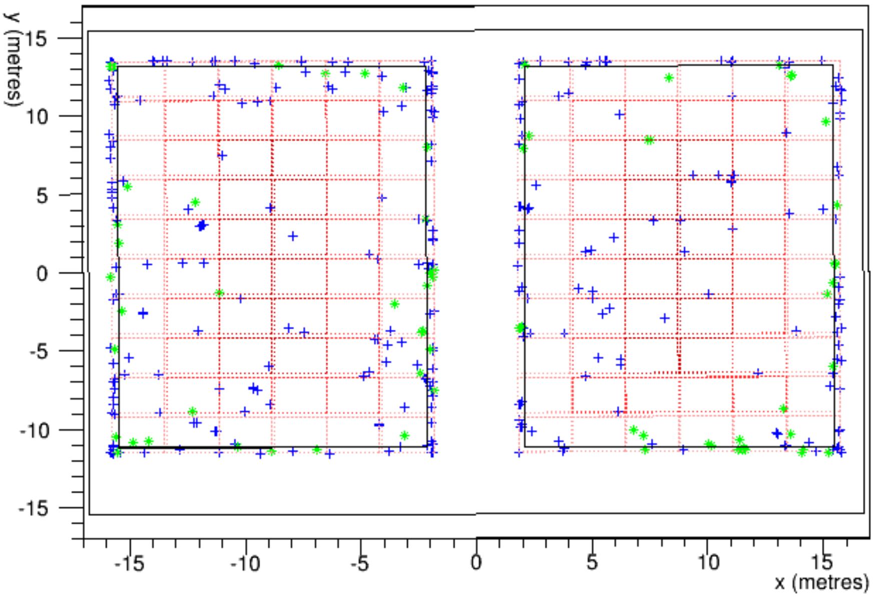

Figure 132: *The same as in Figure 131 but for a bird's eye view of the detector.*

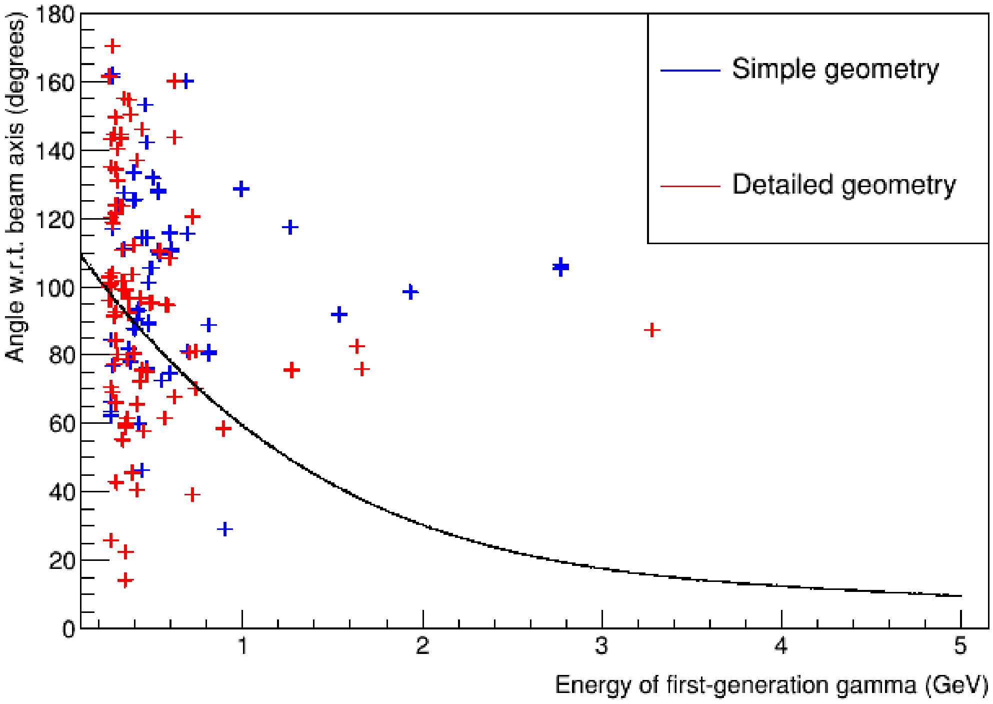

Figure 133: *The angle with respect to the beam axis vs. the energy of the first-generation gammas of EM showers starting with Ext* $\rightarrow \gamma$ *and* $\pi^0 \rightarrow \gamma$ *for events in which the primary muon misses all active volumes, for the simple (blue) and detailed (red) detector geometries, after the D cut has been applied. The mean energy in the simple/detailed geometry is* 0.52 *GeV /* 0.40 *GeV.*

The gaps are narrow, so whilst muons that miss are more likely to have travelled past the outer faces of the LAr, those that do travel through the gaps can create secondaries with a shorter distance to an active region than those that do not; an increased number of EM showers are thus counted as $\pi^0 \to \gamma$. Figures 131, 132 show the positions of the start of EM showers with these two main shower ancestries.

The first cut applied is the fiducial cut ($D > 30$ cm), which becomes less effective overall when using the detailed geometry (where it dismisses 77% of the total) than for the simple geometry (in which 93% were rejected). This is contrary to events in which the primary muon strikes an active volume. In that instance the fiducial cut became more effective after swtiching to the detailed detector geometry, by rejecting more of the showers with ancestry $\pi^0 \to \gamma$ that dominate those events. However, showers with ancestry $Ext \to \gamma$ dominate this type of event, and are able to appear deep inside the detailed geometry where they could not with the simple geometry, thus surviving this cut more often.

The cut on θ_{beam} is also less effective for the detailed detector, with the overall number of showers eliminated by this cut falling from 71% to 62% (similar reductions are observed when considering both of the significant shower ancestries). Figure 133 shows a slightly greater tendency for showers in the detailed detector to form small angles with the beam axis. The long axis of the detector is parallel to the beam axis; since there are two LAr volumes and gaps between the LAr cells[46], there can be more primary muons that miss the detector travelling near-parallel to the beam axis (and therefore more showers also).

The final cut of PoCA >10 cm with respect to all tracks is quite effective for the detailed detector geometry, but note that proton hits for muon-induced events were not recorded for the simple geometry. It yields a 52% reduction in the overall background, eliminating 82% of showers starting with $\pi^0 \to \gamma$ and 37% starting with $Ext \to \gamma$.

After applying the e/γ separation factor and assuming a 100% efficient photon detector, the annual rate of background showers due to primary muons that miss the active volume(s) rises from 0.11 ± 0.02 yr^{-1} with the simple geometry to 0.44 ± 0.11 yr^{-1} with the detailed geometry.

6.4.3 Background due to primary neutrons

For the detailed geometry, 1.1×10^8 neutron-induced events have been simulated, corresponding to 0.653 years of statistics ($E_n > 1$ GeV, sampled from a plane measuring 50×50 m^2 above the detector). Table 53 shows the annual rate as successive cuts are applied. Figure 134 shows the distribution of the energy of the first-generation gamma in each EM shower, as successive cuts are applied.

When moving from the simple to the detailed detector geometry, the overall rate prior to cuts decreases from 6.69×10^4 yr^{-1} to 8405 yr^{-1}. This may be accounted for by the detailed geometry having extra shielding, which is insignificant for incoming muons but not so for the more easily-stopped protons or neutrons. The detailed geometry has an additional 0.5 m of concrete (not including the septum between the cryostats) and 0.8 m of polyurethane surrounding the LAr volumes, as well as 'dead' or non-instrumented regions of LAr surrounding the TPC active volumes.

The choice of detector geometry causes no major difference in the fraction of EM showers coming from each ancestry; showers starting with $\pi^0 \to \gamma$ are 76% of the overall

---

[46] The gaps also run perpendicular to the beam axis, but the detector is shorter along this axis, so a greater increase of showers parallel and antiparallel to the beam axis than showers perpendicular to it is to be expected.

Table 53: *The annual rate due to each type of shower ancestry as successive cuts are applied, for neutron-induced events using the detailed detector geometry and flat surface profile. The overall scaling factor applied to the count obtained from the simulated data is* 1.50706 *(Table 28).*

	$\mathbf{E}_\gamma$	**D**	θ_{beam}**(E)**	**PoCA**$_{all}$	e/γ	γ **detection**
total	8405±113	5697±93	1949±54	225±18	22.5±1.8	0.16±0.01
$\pi^0 \rightarrow \gamma$	6397±98	5050±87	1744±51	194±17	19.4±1.7	0.14±0.01
$Ext \rightarrow \gamma$	1796±52	470±27	169±16	30.1±6.7	3.01±0.67	0.021±0.005
$other \rightarrow \gamma$	209±18	175±16	36.2±7.4	0-3.68	0-0.37	0-0.003

background before cuts here compared with 73% with the simple geometry) and those starting with $Ext \rightarrow \gamma$ are 21% of showers with the detailed geometry vs. 26% with the simple geometry). This minor difference in shower ancestry (attributed to the presence of gaps between TPC active volumes in the detailed detector) is also observed for events in which a primary muon misses all active volumes, but the effect was more pronounced in that instance. The positions of where EM showers with each of the main ancestries start is shown in Figure 135, which may be compared with Figure 127 - there are no EM showers appearing in the lower layer of TPC cells due to this type of primary particle (or from the proton-induced events discussed in the next section).

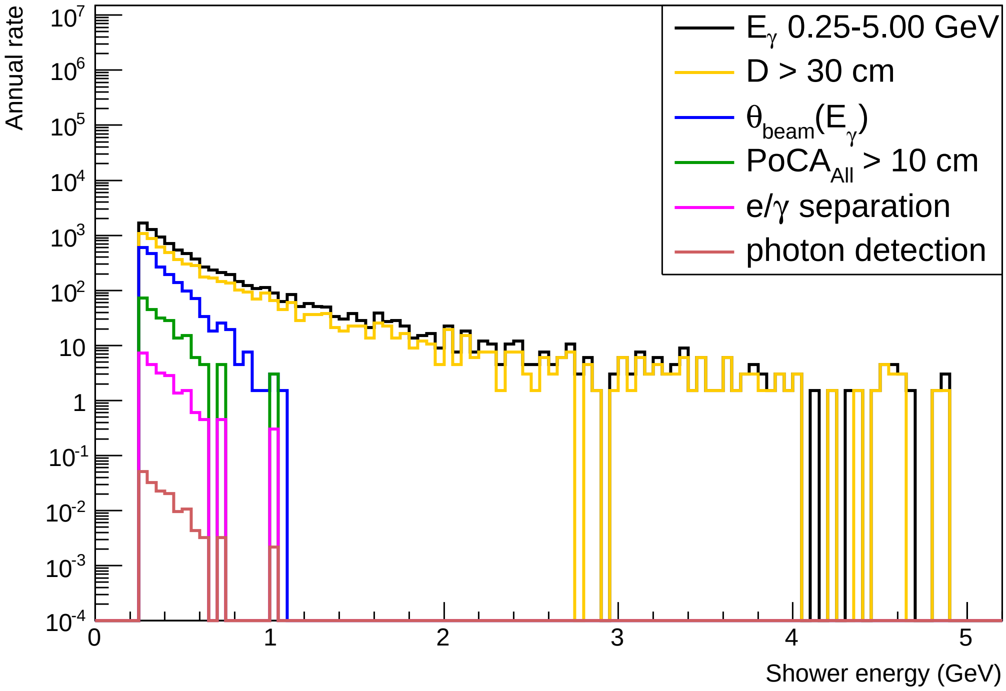

Figure 134: *The energy distribution of first-generation gammas in neutron-induced events for the detailed detector geometry, as successive cuts are applied.*

The fiducial cut ($D > 30$ cm) cut becomes less effective by changing to the detailed geometry. This cut rejects 32% of showers overall for the detailed geometry compared to 41% for the simple geometry. Rejection of showers starting with $\pi^0 \rightarrow \gamma$ shows no significant dependence on the choice of detector geometry but the difference is more pronounced for showers starting with $Ext \to \gamma$. This cut eliminates 74%/86% of EM showers starting with $Ext \to \gamma$ the detailed/simple geometry. Once again these differences may be ascribed to interactions occurring within gaps between active volumes, beyond the region eliminated by this fiducial cut.

The efficiency of the θ_{beam} cut has negligible dependence on the detector geometry for these events, with 65% of EM showers dismissed overall in both cases.

Finally the cut on PoCA >10 cm with respect to all charged tracks has negligible dependence on the detector geometry for these events, once again removing 88% of the remaining total background.

With reductions for e/γ separation and photon detection, the overall background rate is 0.16 ± 0.01 yr^{-1}. This compares to 1.23 ± 0.07 yr^{-1} with the simple geometry. The difference is due to having a greater thickness of material above the detector, which provides increased shielding.

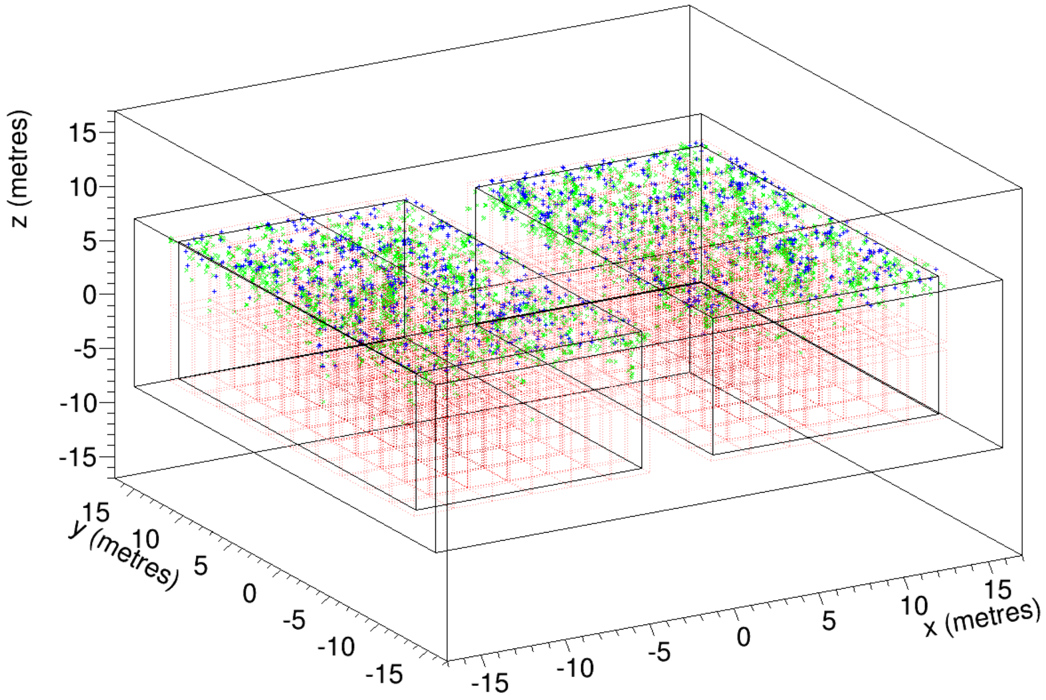

Figure 135: *The positions of the first-generation gamma of showers which start with* $Ext \to \gamma$ *(blue) and* $\pi^0 \to \gamma$ *(green) in neutron-induced events using the detailed detector geometry.*

6.4.4 Background due to primary protons

For the detailed geometry there have been 10^7 proton-induced events simulated, corresponding to 2.482 years of statistics ($E_p > 10$ GeV, sampled from a plane measuring 50×50 m^2 above the detector). Table 54 shows the annual rate as successive cuts are applied. Figure 136 shows the distribution of energy of the first gamma in each EM shower, as successive cuts are applied.

By changing from the simple to the detailed detector geometry, the number of back-

Table 54: *The annual rate due to each type of shower ancestry as successive cuts are applied, for proton-induced events in the detailed detector geometry and flat surface profile. The overall scaling factor applied to the count obtained from the simulated data is* 0.42711 *(Table 28).*

	$\mathbf{E}_{\gamma}$	**D**	θ_{beam}**(E)**	$\mathbf{PoCA}_{all}$	e/γ	γ **detection**
total	1.55×10^4	1.05×10^4	3475±39	319±12	31.9±1.2	0.23±0.01
$\pi^0 \to \gamma$	1.18×10^4	9277±63	3098±36	297±11	29.7±1.1	0.21±0.01
$Ext \to \gamma$	3120±37	858±19	279±11	22±3	2.2±0.3	0.016±0.002
$other \to \gamma$	524±15	424±15	97±6	0-1.04	0-0.10	0-0.001

ground EM showers before cuts falls from 1.05×10^5 yr^{-1} to 1.55×10^4 yr^{-1}. This decrease can be attributed to the detailed detector having greater shielding for the active volumes. The choice of geometry causes no significant difference (2-3%) in the fraction of showers starting with $\pi^0 \to \gamma$ or $Ext \to \gamma$.

The choice of geometry has no significant effect on the efficiency of the $D > 30$ cm cut at rejecting EM showers that start with $\pi^0 \to \gamma$. However, this cut's ability to reject showers starting with $Ext \to \gamma$ is somewhat diminished by changing to the detailed detector geometry (86% → 72%). Once again this can be explained by EM showers starting deep within the detector in gaps between the TPC active volumes, where this cut is not able to reach.

The effectiveness of the θ_{beam} cut's shows negligible dependence on the choice of geometry, removing 67% of the total remaining showers in the detailed detector compared to 66% in the simple detector. The same applies to showers of specific ancestries.

Finally the cut on PoCA >10 cm with respect to all tracks becomes only marginally more effective when changing to the detailed geometry, with this cut removing 90% of the remaining background with the detailed geometry compared to 84% with the simple geometry.

Once reductions for e/γ separation and photon detection are applied, the number of surviving showers drops from 2.57±0.08 yr^{-1} with the simple geometry to 0.23±0.01 yr^{-1} with the detailed geometry.

6.4.5 Summary of total background for detailed geometry and flat surface

A summary of the annual background EM shower rate using the detailed detector geometry and a flat surface profile is shown in Table 55. This is after all cuts have been applied, so these numbers represent the irreducible background that could still be confused with genuine ν_e interactions. A further small reduction could be made relating to the choice of Geant4 electron/positron production cuts and their effect on the cut on PoCA with respect to primary muon tracks, as discussed in Section 6.2.

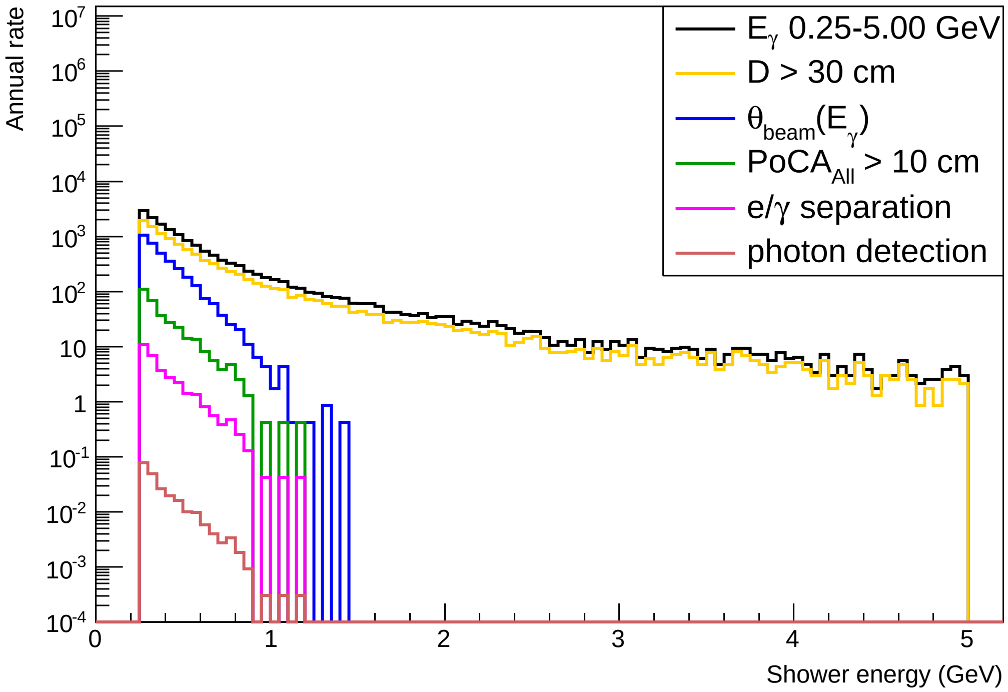

Figure 136: *The energy distribution of first-generation gammas in primary proton-induced events for the detailed detector geometry, as successive cuts are applied.*

Table 55: *A summary of the annual background EM shower rate using the detailed detector geometry and a flat surface profile. Photons have not been simulated because they were shown to give a negligible background for the simple geometry.*

primary particle	annual rate
muons (striking detector)	1.94 ± 0.23
muons (missing detector)	0.44 ± 0.11
protons	0.23 ± 0.01
neutrons	0.16 ± 0.01
total	**2.77 ± 0.26**

6.5 Results for simple detector geometry and approximate surface profile

As a precursor to the results in Section 6.6, a further 8×10^7 muon-induced events ($E_\mu > 10$ GeV) have been simulated using the simple detector geometry corresponding to 0.085 years of live time. For these events a surface profile that roughly approximates the terrain surrounding the once-proposed detector site at 44.344633N and -103.751289W has been used. This is based on the satellite-generated map discussed in Section 5.6, shown from another angle in Figures 137. The detector location used in this simulation corresponds to the same location used for the accurate surface profile in Section 6.6, so the results can be directly compared.

Table 56: *The annual rate due to each type of shower ancestry as successive cuts are applied, for muon-induced events in which the primary muon strikes at least one of the detector's active volumes, in the simple detector geometry with the approximate surface profile. The overall scaling factor applied to the count obtained from the simulated data is* 17.77490 *(Table 28).*

	E_γ 0.25-5.00 GeV	**PoCA_μ**	**θ_{beam}(E)**	**PoCA_{all}**	**D**	e/γ	**γ detection**
total	1.03×10^7	$8.78\pm0.12\times10^4$	$(4.24\pm0.09)\times10^4$	$(2.23\pm0.06)\times10^4$	8781±396	878±40	6.27±0.28
$\pi^0 \rightarrow \gamma$	1.87×10^6	$8.69\pm0.12\times10^4$	$(4.20\pm0.09)\times10^4$	$(2.21\pm0.06)\times10^4$	8692±393	869±39	6.21±0.28
$Ext \rightarrow \gamma$	12.12×10^6	(640±107)	338±77	213±62	89±40	8.89±3.97	0.06±0.03
$\mu \rightarrow \gamma$	6.33×10^6	0-43	0-21	0-11.03	0-4.34	0-0.43	0-0.031
$other \rightarrow \gamma$	2.15×10^4	196±59	9-105	5-55	3-29	0.30-2.90	0.02-0.21

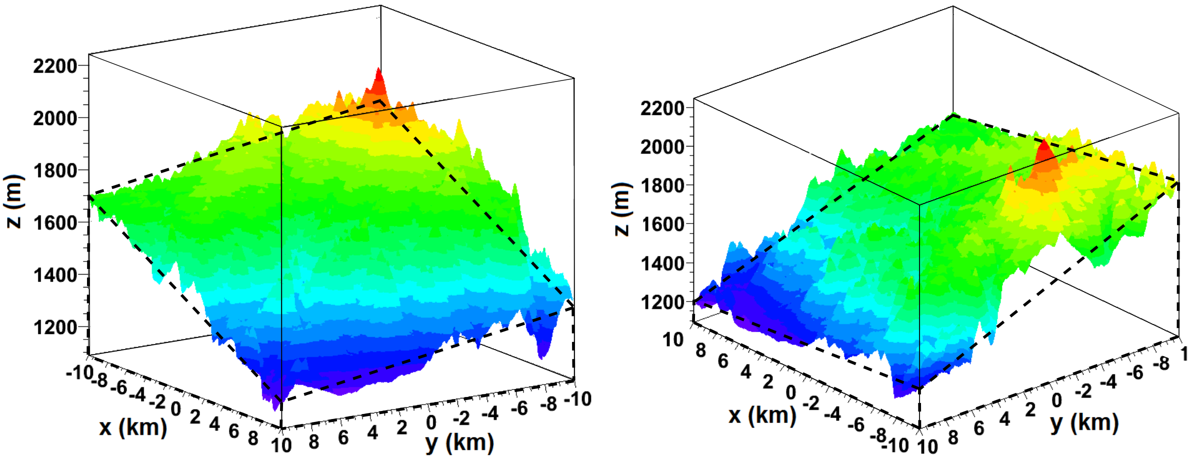

Figure 137: *The surface map of Section 5.6 from two different angles. The dashed lines are guides used to construct a simple approximation to this surface in Geant4 (Figure 138). It should be noted that the x and y axes have units of kilometres whereas the z axis has units of metres, which makes the slope appear far steeper than it is in reality.*

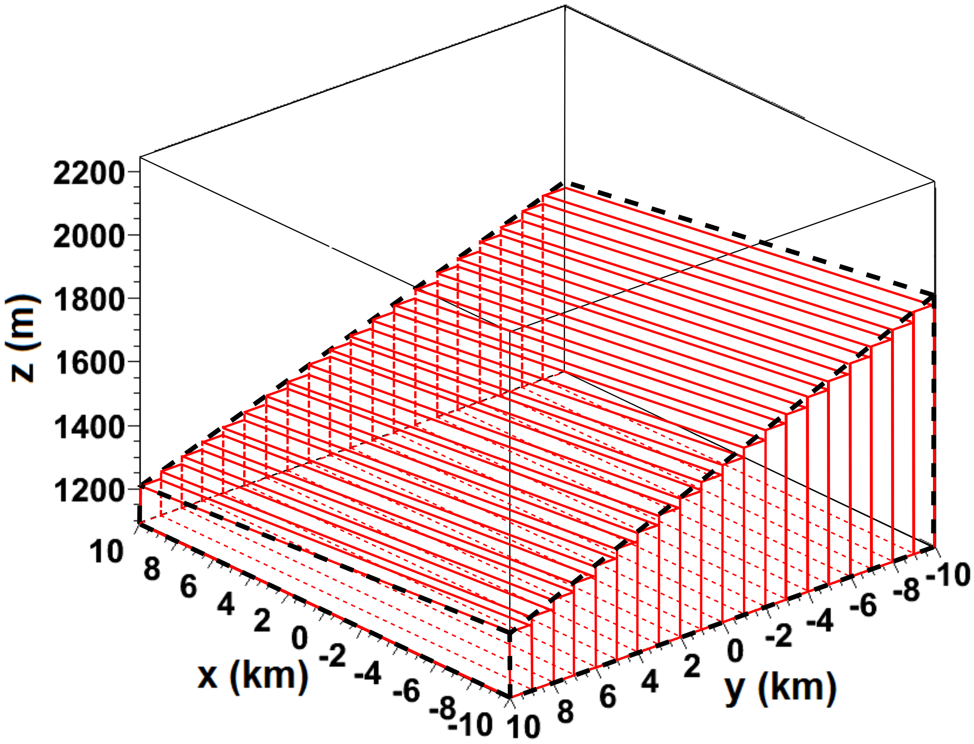

Figure 138: *An illustration of the trapezoids used to construst a rough approximation to the surface profile shown in Figure 137. This is seen from the same angle as the right-hand-side image in Figure 137.*

To approximate the surface a series of (relatively) narrow, sloping trapezoids have been arranged such that they conform to the dashed lines visible in these figures. These trapezoid 'slices' are illustrated in Figure 138. Table 56 shows the annual rate for each significant shower ancestry due to primary muons that strike the LAr volume as successive cuts are applied. Changing from the flat surface profile to this one only has a small effect on the background rate, with the total showers observed here being 96.3% of the number observed with the flat surface (Table 32). Despite this surface pofile being a crude approximation to the actual surface, the reduction to the background it causes turns out to be very close to that caused by the accurate surface profile in Section 6.6. It should be noted that, like the results presented in Section 6.3.1, 6.3.2, these results did not have proton hits available to calculate PoCA with respect to. The annual rate after all cuts is therefore higher than it would otherwise be.

6.6 Results for the detailed detector geometry and accurate surface profile

Here the background is estimated using the detailed detector geometry (Section 5.3.2) and the accurate surface profile discussed in Section 5.6. There have been 2×10^8 muon-induced events simulated, corresponding to 0.1003 years of statistics ($E_\mu > 10$ GeV). No events using proton or neutron primaries have been simulated since the surface is flattened above the detector (Section 5.6) and these primary particles are all injected within this region anyway.

6.6.1 Background due to primary muons which strike an active volume

Replacing the flat surface profile with the accurate one causes the overall rate before cuts to fall from 1.37×10^7 yr^{-1} to 1.32×10^7 yr^{-1} (Table 57), as a result of greater shielding. This 3.65% background reduction caused by the inclusion of the accurate surface profile with the detailed detector geometry is very similar to the 3.7% reduction observed when the approximate surface profile was included for the simple detector geometry (Section 6.5). Figure 139 shows the energy spectra of the first-generation gammas as successive cuts are applied.

Table 57: *The annual rate due to each type of shower ancestry as successive cuts are applied, for muon-induced events using the detailed detector geometry and accurate surface profile in which the primary muon strikes at least one of the detector's active volumes. The overall scaling factor applied to the count obtained from the simulated data is* 13.85514 *(Table 28).*

	$\mathbf{E}_\gamma$	$\mathbf{PoCA}_\mu$	θ_{beam}**(E)**	$\mathbf{PoCA}_{all}$	**D**	e/γ	γ **detection**
total	1.32×10^7	$(6.38\pm0.09)\times10^4$	$(2.87\pm0.06)\times10^4$	3796±229	2854±199	285±20	2.03±0.14
$\pi^0 \rightarrow \gamma$	2.24×10^6	$(5.82\pm0.09)\times10^4$	$(2.62\pm0.06)\times10^4$	3339±215	2743±195	274±20	1.96±0.14
$Ext \rightarrow \gamma$	4.48×10^6	5237±270	2425±183	457±80	111±39	11.1±3.9	0.08±0.03
$\mu \rightarrow \gamma$	6.36×10^6	0-34	0-15.20	0-2.01	0-1.51	0-0.15	0-0.001
$other \rightarrow \gamma$	$(7.87\pm0.10)\times10^4$	333±68	97±37	0-15.20	0-11.43	0-0.11	0-0.002

Changing the surface profile has no statistically significant effect on the efficiency of any of the cuts. The final reductions for e/γ separation and photon detection are then applied. Despite the rate before cuts being slightly lower with the accurate surface profile, after all cuts it sees background rate of 2.03 ± 0.14 yr^{-1} which is in agreement with the 1.94 ± 0.23 yr^{-1} seen with the flat surface.

6.6.2 Background due to primary muons that miss all active volumes

In this type of event there are a total of 1.33×10^4 showers per year at the required energy (Table 58). This is a 10% decrease from the 1.47×10^4 per year observed with the flat surface profile, which can be explained by the accurate surface (i.e. small hills) providing some shielding. This has particular significance for muons approaching from wide zenith angles as these contribute a significant fraction of the EM showers from this category of event (Section 6.3.7.1). The difference in the relative contribution of each ancestry to the total before cuts is negligible when compared to the flat surface profile. Figure 140 shows the energy spectra of the first-generation gammas as successive cuts are applied. The inclusion of the accurate surface profile has no statistically significant impact on the efficiency of the fiducial cut, the θ_{beam} cut or the $PoCA_{all}$ cut, both overall and as far as specific shower ancestries are concerned.

Table 58: *The annual rate due to each type of shower ancestry as successive cuts are applied, for muon-induced events in the detailed detector geometry and accurate surface profile in which the primary muon misses all of the detector's active volumes. The overall scaling factor applied to the count obtained from the simulated data is 13.85514 (Table 28).*

	$\mathbf{E}_\gamma$	**D**	θ_{beam}**(E)**	**PoCA**$_{all}$	e/γ	γ **detection**
total	$(1.33\pm0.04)\times10^4$	2646±191	1067±122	637±94	4.55±0.67	0.46±0.07
$\pi^0 \rightarrow \gamma$	2314±179	790±105	374±72	83±34	0.59±0.24	0.06±0.02
$Ext \rightarrow \gamma$	$(1.09\pm0.04)\times10^4$	1857±160	693±98	554±88	3.96±0.63	0.40±0.06
$other \rightarrow \gamma$	2-60	0-34	0-14	0-8.36	0-0.06	0-0.006

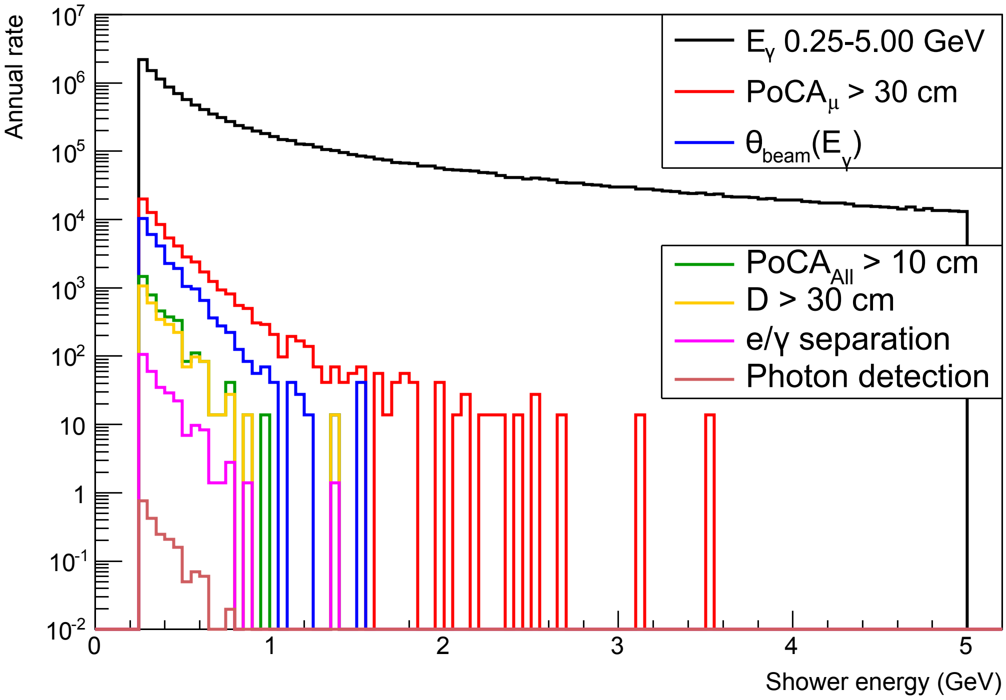

Figure 139: *The energy distribution of first-generation gammas in primary muon-induced events for the detailed detector geometry and accurate surface profile, where the primary muon strikes at least one of the active LAr volumes, as successive cuts are applied.*

After all cuts including the reductions for e/γ separation and photon detection are applied, resulting in a total annual rate of 0.46±0.07 yr^{-1}. This compares to 0.44±0.11 yr^{-1} for the flat surface profile; there is no discernable reduction in the final rate after cuts despite the accurate surface profile producing a slightly lower background rate before cuts being applied (due to its additional shielding).

Table 59 provides a summary of the annual background rate with the detailed detector geometry and accurate surface profile. The inclusion of the accurate surface profile has no significant effect on the background rate after all cuts are applied. Further minor reductions may be applied to this, as discussed in Section 6.7. Figure 141 shows the energy distribution of the showers that remain after all cuts are applied.

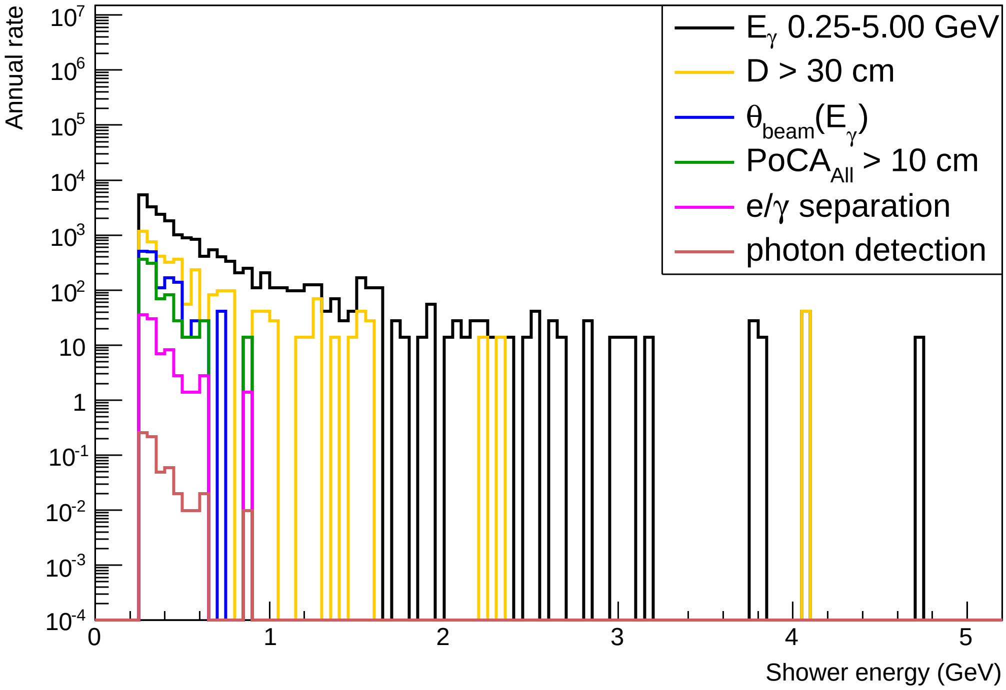

Figure 140: *The energy distribution of first-generation gammas in primary muon-induced events for the detailed detector geometry and accurate surface profile, where the primary muon misses all of the active LAr volumes, as successive cuts are applied.*

Table 59: *A summary of the annual background EM shower rate using the detailed detector geometry and the accurate surface profile. The background rate using the simple detector geometry and flat surface profile is also shown in the final column, where the numbers within brackets on the first and last row are the estimated background rate when proton hits are included in the analysis of muon-generated events.*

primary particle	detailed detector, accurate surface	simple detector, flat surface
muons (striking detector)	2.03 ± 0.24	12.64 ± 0.24 (∼1.18)
muons (missing detector)	0.46 ± 0.07	0.11 ± 0.02
protons	0.23 ± 0.01	2.57 ± 0.08
neutrons	0.16 ± 0.01	1.23 ± 0.07
total	**2.88 ± 0.25**	16.55 ± 0.27 (∼5)

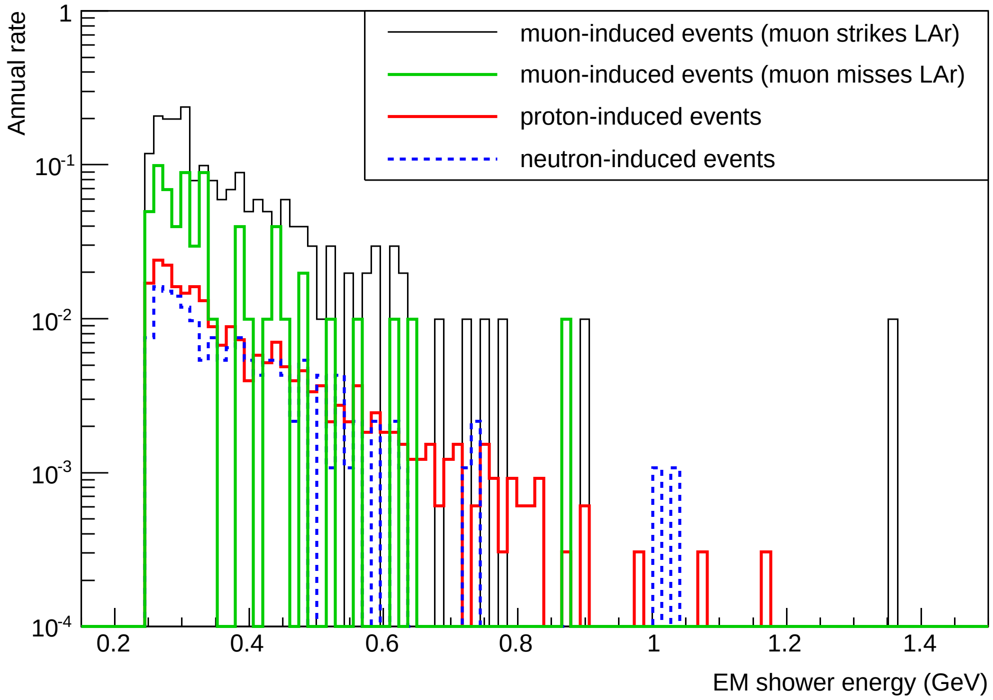

Figure 141: *The distribution of the EM shower energy after all cuts (including scaling factors for e-γ separation and a photon detection system) have been applied, for muon, proton and neutron-induced events with the detailed detector geometry. The muon-induced showers are those generated with the accurate surface profile.*

6.7 Rejecting large events

If there are too many EM showers appearing in a single event then reconstruction will become too difficult and such an event will be ignored. Figure 143 shows the distribution of the number of EM showers in a given event for the detailed detector geometry and accurate surface profile. Note that all of these individual EM showers can be part of a single hadronic shower in an event or a larger single EM shower started outside the target volume, so they look like the individual EM showers.

The final background rate may be reduced further by imposing an upper limit on the number of showers in an event before the event can be rejected. Figure 144 shows how the final background rate due to each type of primary particle varies depending on the threshold chosen. Figure 145 shows how the choice of threshold affects the percentage of the background that survives. For example, dismissing any event in which there are 10 or more showers reduces the muon-induced rate by ∼30% (1.91 $\text{yr}^{-1} \rightarrow \sim$1.27 yr^{-1}), the proton-induced rate by ∼50% (0.23 $\text{yr}^{-1} \rightarrow \sim$0.12 yr^{-1}) and the neutron-induced rate by ∼30% (0.16 $\text{yr}^{-1} \rightarrow \sim$0.11 yr^{-1}) for a combined rate of ∼1.55 yr^{-1}.

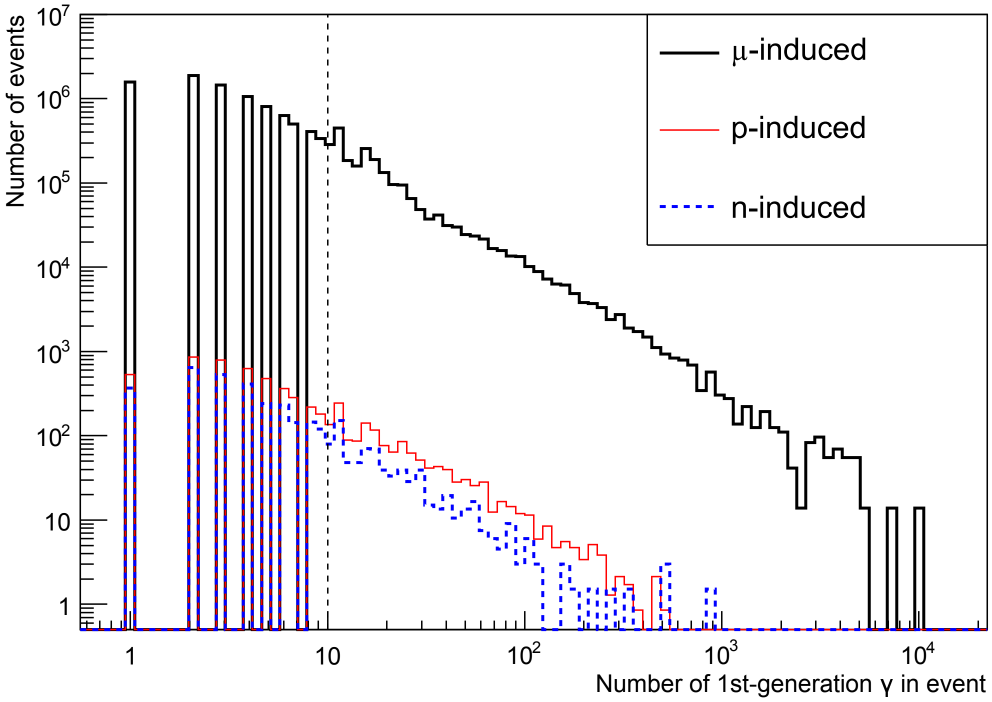

Figure 142: *The distribution of the number of EM showers in a given event, for muon, proton and neutron-induced backrounds, fully normalized and corrected, after all cuts apart from* e/γ *separation and photon detection. The dashed vertical line indicates a possible threshold of* 10 *showers per event.*

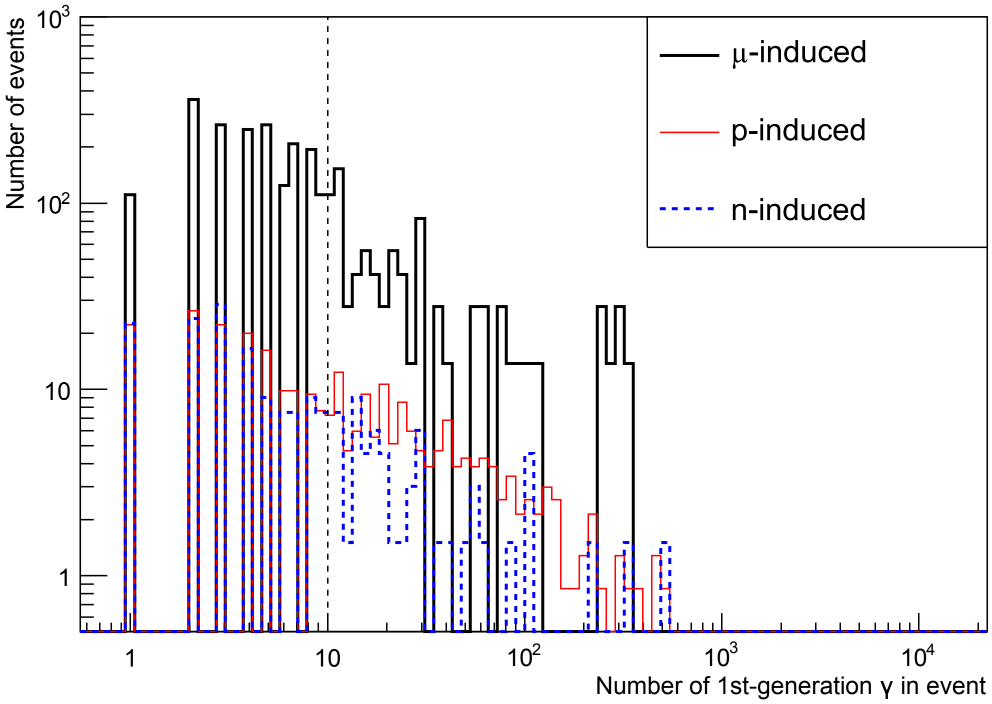

Figure 143: *The distribution of the number of EM showers in a given event, for muon, proton and neutron-induced backrounds, fully normalized and corrected, after all cuts apart from* e/γ *separation and photon detection. The dashed vertical line indicates a possible threshold of* 10 *showers per event.*

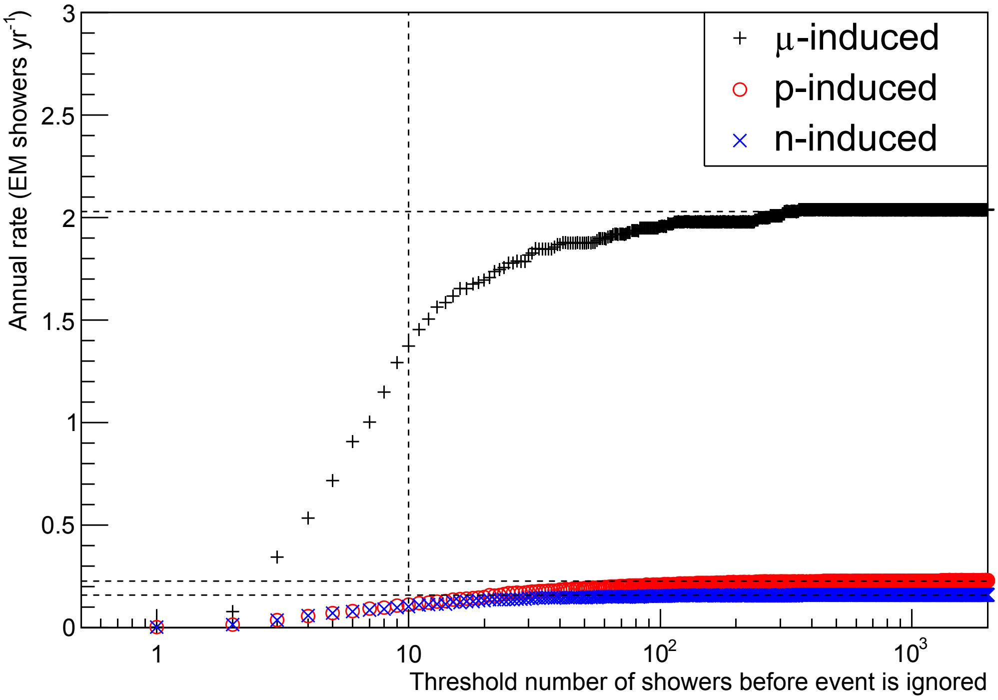

Figure 144: *The dependence of the annual background rate on the choice of upper limit on the number of showers in an event before the event is rejected. A series is shown for muon, proton and neutron- induced events (events where muons miss the detector are not shown). The vertical dashed line indicates a possible choice of threshold (10 showers), above which events are rejected due to reconstruction becoming too difficult. The horizontal dashed lines indicate the annual shower rate without any upper limit imposed.*

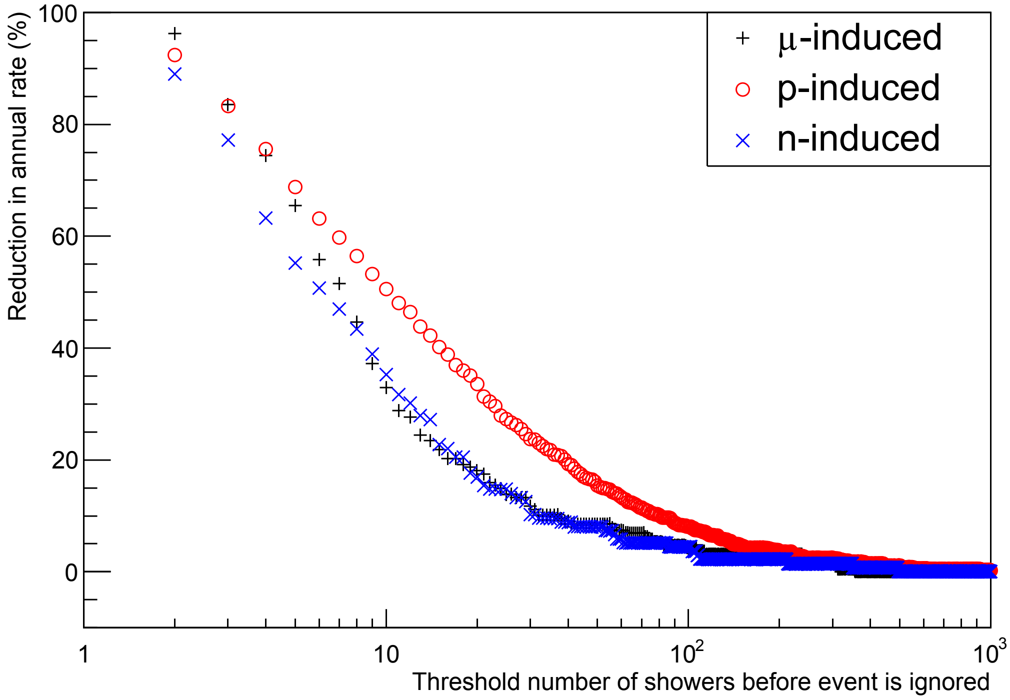

Figure 145: *The reduction (as a percentage) of the final background based on the choice of upper limit on the number of showers in an event before the event is rejected. A series is shown for muon, proton and neutron- induced rates.*

6.8 Detector volume negated by rejecting background

When rejecting a background EM shower, this region of the detector becomes momentarily unavailable to observe signal events with. An additional 2×10^7 muon-induced events (corresponding to 0.017 years of statistics) have been generated with the simple detector geometry, where all hits due to electrons and positrons have been recorded. To estimate the volume of LAr excluded by these showers, three volumes have been defined (illustrated in Figure 146). All showers including those from $\mu \rightarrow e \rightarrow \gamma$ and Ext $\rightarrow e \rightarrow \gamma$ have been considered here.

The first volume (shown on the left pane in Figure 146) involves a cylinder of radius 30 cm around each track segment of the primary muon track. This would contain all showers that would not survive the 30 cm PoCA or 'shortest distance to track' cuts described in Section 6.2.2.

The second volume (shown on the left pane in Figure 146) is a box which has its length along the x, y and z axes determined by the track segments that have the greatest separation along each axis. The coordinates used are taken from all electrons, positrons and first-generation gammas (and the final position of any first-generation gammas) from every shower that appears in a given event. The box is therefore the smallest cuboid that could fully contain all showers in the event and provides a conservative[47] estimate of the detector volume negated by rejecting showers.

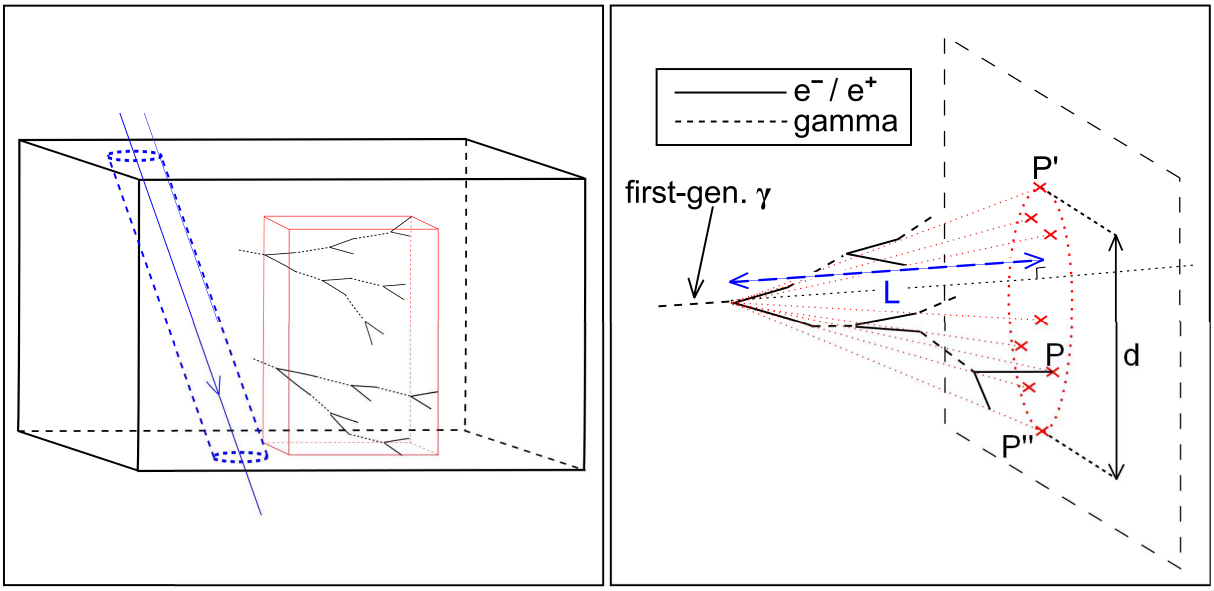

Figure 146: *The left diagram shows a muon-induced event producing two EM showers, where the black box represents the boundary of the detector and the red box is the smallest box that could contain all first-generation gammas in a given event, as well as any electrons and positrons that descend from them. The coordinates used are taken from the end of a track segment rather than the start, hence the first generation gamma on both showers is seen to extend outside of the box. Also shown in this diagram is a cylinder drawn around the muon track. The right diagram shows an example of the cone drawn around an individual shower. The red dotted lines represent the lines drawn through the position of each electron or positron hit (i.e. the end of each solid black line) to the plane oriented perpendicular to the first-generation gamma axis (black dotted line).*

---

[47] A 'conservative' estimate at least when compared to the use of cones around individual showers.

The other volume (shown on the right pane in Figure 146) is a cone that surrounds individual showers. The vertex of the cone is defined as the first $\gamma \rightarrow e^+e^-$ vertex in the shower (i.e. the final position of the first-generation gamma). A ray $\vec{L}$ is then drawn from the cone vertex to the point P, which is the position of the electron or positron hit furthest away from the vertex, in the direction defined by the first-generation gamma trajectory. More rays are then drawn from the vertex, through the positions of all other electron and positron hits. These rays extend until they reach a plane that is oriented perpendicular to $\vec{L}$ and contains point P. One of these rays will intersect this plane at the point P′, which is the furthest intersection point away from point P. This point is used as one point on a circle that defines the base of the cone. The point in the plane P″ that is furthest away from P′ is taken as the point on the circular base of the cone located diametrically opposite to P′. For this cone of height $|\vec{L}|$ and a base of diameter $|\vec{d}|$ (where $\vec{d}$=P″-P′), the volume V is given by

$$V = \frac{\pi}{3}\left(\frac{|\vec{d}|}{2}\right)^2 |\vec{L}|. \tag{119}$$

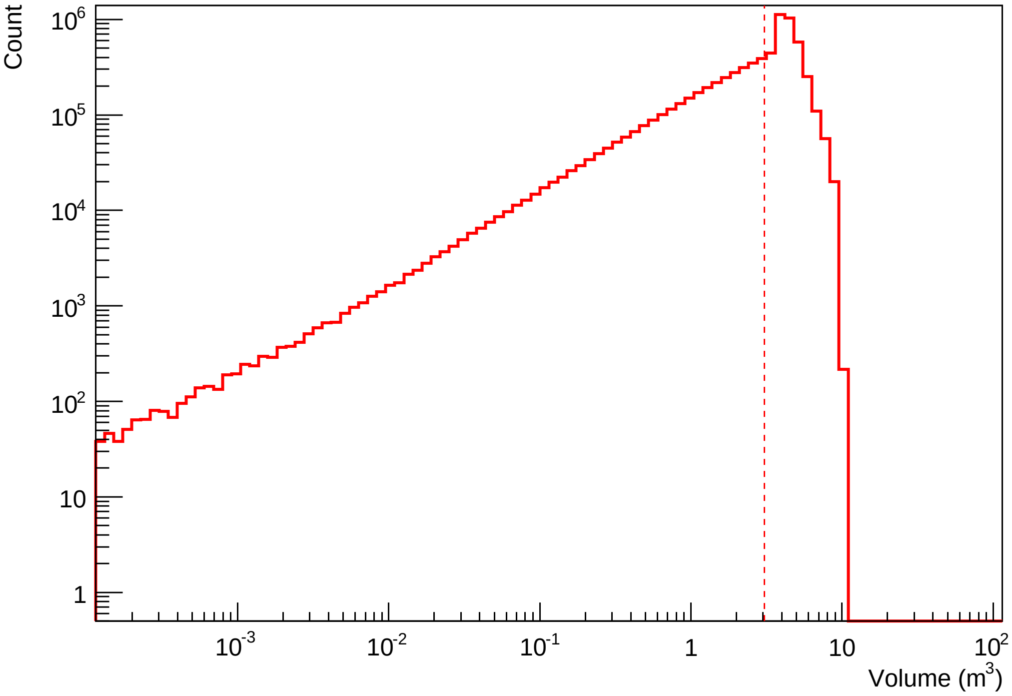

Figure 147: *The distribution of cylindrical volumes of radius* 30 *cm drawn around the primary muon track in* 2×10^7 *muon-induced events (*0.017 *years of statistics) using the simple detector geometry (LAr volume measures* $30 \times 15 \times 16$ *m^3). The dashed vertical line indicates the mean volume of* 3.07 *m^3. It should be noted that this is based on a simple calculation involving only the length of track segments - it does not consider that track lengths of a few cm are from muons that have entered and exited in a corner of the LAr, in which case the actual volume of LAr negated by the muon is smaller than that of the cylinder drawn around the track.*

The distributions of each of these three volumes have been plotted for 2×10^7 events in Figures 147 and 148. The mean volume of the cylinder around the muon track is 3.11 m^3. The mean volume of the box containing all showers in a given event is 34.268 m^3, whereas the mean volume of the cone enclosing individual showers is 0.027 m^3. It can therefore be assumed that individual shower cones generally tend not to overlap.

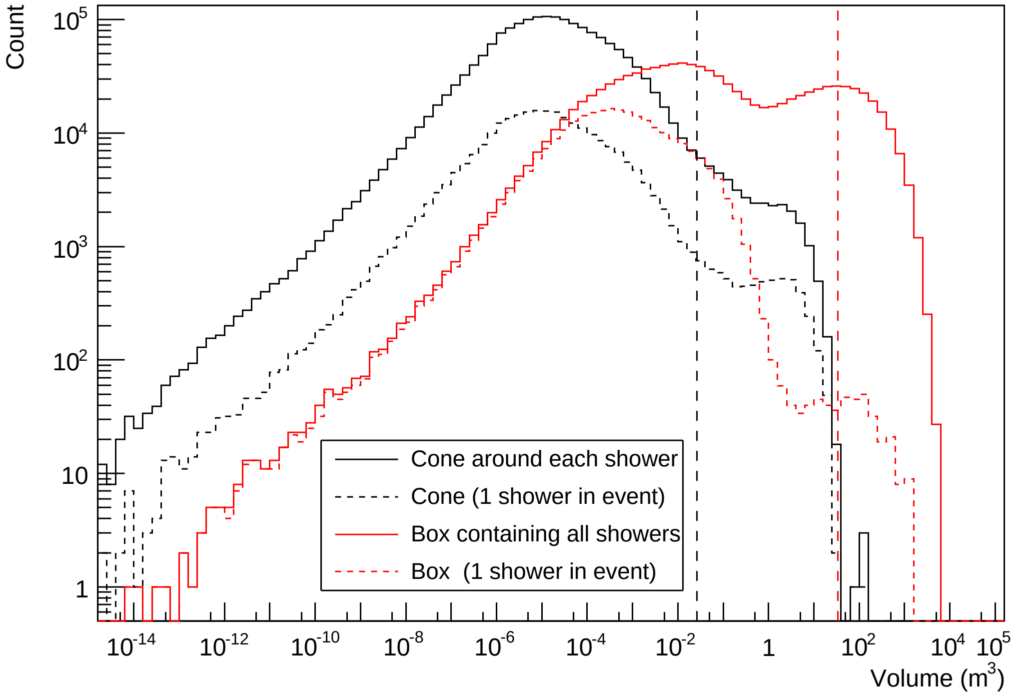

Figure 148: *The volume distribution of the cones enclosing individual EM showers (red) and the boxes containing all EM showers (black) in a given event. The dashed lines represent events in which only one EM shower appeared. The vertical lines indicate the mean value for the two series with solid lines (*0.027 *m^3 for the cones and* 34.268 *m^3 for the boxes). In events with only one EM shower, the mean cone size was The presence of very small volumes here is due to EM showers that start very close to the edge of the LAr; if the e^+ and e^- record a hit before or as they are exiting, this method allows a tiny cone or box to be drawn around them.*

A detector with an active mass of 10 kton of LAr at a density 1392.8 kg m^{-3} corresponds to a volume of 7179.78 m^3, so the average cylinder of radius 30 cm around the primary muon track occupies 0.043% of the active LAr volume. The total volume of the cones surrounding each shower in the average event occupies 4×10^{-4} % of the active LAr volume. The average box enclosing all showers in an event occupies 0.48% of the active LAr volume. When a background EM shower appears, that region of the detector is unavailable for the detection of genuine signal events for the duration of the drift time. Thus it is apparent that rejecting background EM showers still leaves the vast majority of the detector available to capture signal events.

6.9 Background due to $K_L^0 \to \pi^\pm e^\mp \nu_e/\overline{\nu}_e$

A further process capable of mimicking the neutrino signal is $K_L^0 \to \pi^\pm e^\mp \overline{\nu}_e/\nu_e$, since this will appear in the detector as an isolated electron/positron and pion track emerging from the same vertex. The neutrino will carry off a variable fraction of the K_L^0 energy/momentum, meaning that the K_L^0 direction cannot be reconstructed from the two charged particle tracks (unlike what has been done for the first-generation gammas discussed in previous sections). Instead, the electron track rather than the pion track is the subject of the other cuts applied here. Its direction is used for PoCA and θ_{beam} calculations. Since there is only one electron track, the 90% reduction of the final rate based on e/γ separation (i.e. distinguishing EM showers that start with one electron track from those where the first electron is accompanied by a positron) used in previous sections does not apply here. Hits from particles with energies exceeding 100 MeV are recorded, so both or just one of the charged products may have recorded hits. The energy range for potential background of 0.25 GeV - 5.00 GeV still applies .

Tables 60, 61, 62 shows the annual background rate as successive cuts are applied. When the pre-normalized count drops to five or fewer EM showers, upper and lower limits at 90% confidence are given. Upper limits for any subsequent cuts are calculated based on the fraction of EM showers that survive the cut when it has been applied to the first-generation gammas of previous sections that were caused by the same type of primary particle. In the 'total' row, the pre-normalized counts for the previous two rows are combined, then upper and lower limits are applied if necessary, and then the normalization factor is applied.

Table 60: *The annual rate of EM showers with the ancestry $K^0_L \to \pi\, e\, \nu_e$ due to muon-generated events in the detailed detector geometry with the accurate surface profile. The overall scaling factor applied to the count obtained from the simulated data is 13.85514 (Table 28). The initial 222±55 in the first two upper rows corresponds to having observed 16 of each type of event.*

	$\mathbf{E}_\gamma$	$\mathbf{PoCA}_\mu$	θ_{beam} **(E)**	$\mathbf{PoCA}_{all}$	**D**	γ **detection**
$K^0_L \to \pi^+ e^- \overline{\nu}_e$	222±55	2-60	0-34	0-15.3	0-13.3	0-0.094
$K^0_L \to \pi^- e^+ \nu_e$	222±55	15-103	7-82	0-34	0-29	0-0.209
total	443±78	20-119	7-82	0-34	0-29	0-0.209

Table 61: *The annual rate of EM showers with the ancestry $K^0_L \to \pi\, e\, \nu_e$ due to proton-generated events in the detailed detector geometry (the surface profile is irrelevant for this type of primary particle). The overall scaling factor applied to the count obtained from the simulated data is 0.42711 (Table 28).*

	$\mathbf{E}_\gamma$	**D**	θ_{beam} **(E)**	$\mathbf{PoCA}_{all}$	γ **detection**
$K^0_L \to \pi^+ e^- \overline{\nu}_e$	12.0±2.3	7.3±1.8	3.4±1.2	0-1.04	0-0.007
$K^0_L \to \pi^- e^+ \nu_e$	5.6±1.5	0.8-4.3	0.2-2.5	0-1.04	0-0.007
total	17.5±2.7	9.4±1.3	4.3±1.0	0-1.04	0-0.007

Table 62: *The annual rate of EM showers with the ancestry $K^0_L \to \pi\, e\, \nu_e$ due to neutron-generated events in the detailed detector geometry (the surface profile is irrelevant for this type of primary particle). The overall scaling factor applied to the count obtained from the simulated data is 1.50706 (Table 28).*

	$\mathbf{E}_\gamma$	**D**	θ_{beam} **(E)**	$\mathbf{PoCA}_{all}$	γ **detection**
$K^0_L \to \pi^+ e^- \overline{\nu}_e$	0.2-6.6	0.2-6.6	0-3.7	0-0.32	0-0.002
$K^0_L \to \pi^- e^+ \nu_e$	1.7-11.2	0.8-8.9	0-3.7	0-0.32	0-0.002
total	12.2-13.0	1.7-11.2	0-3.7	0-0.32	0-0.002

6.10 Background due to $\pi^0 \rightarrow e^+ e^- \gamma$

A further source of potential background comes from $\pi^0 \rightarrow e^+ e^- \gamma$. These products are formed in ~1.2% of neutral pion decays. The gamma will fall under the wider category of EM showers with the ancestry $\pi^0 \rightarrow \gamma$ and many of those events will already have been rejected by cuts applied to that ancestry. However, the accompanying electrons/positrons can be considered as the start of separate showers themselves with the ancestry $\pi^0 \rightarrow e^\pm$. Since hits were only recorded for particles with energies exceeding 100 MeV, the simulated data gathered presents three possibilities when instances of this decay have occurred; only the electron is recorded, only the positron is recorded, or both are recorded. In reality the detector would observe both particles.

Tables 63, 64, 65 show the annual rate of these showers in muon-, proton- and neutron-induced events as successive cuts are applied and each contains one row for each of the three possibilities. When the pre-normalized count drops to five or fewer background EM showers, upper and lower limits at 90% confidence are given. In the 'total' row, the pre-normalized counts for the previous three rows are combined, then upper and lower limits are applied if necessary, and then the normalization factor is applied.

Table 63: $\pi^0 \rightarrow e^+ e^- \gamma$ *background due to muon-generated events in the detailed detector geometry with the accurate surface profile. The overall scaling factor applied to the count obtained from the simulated data is 13.85514 (Table 28).*

	$\mathbf{E}_\gamma$	$\mathbf{PoCA}_\mu$	θ_{beam} (E)	$\mathbf{PoCA}_{all}$	**D**	γ **detection**
e^- only	1635±151	20-119	7-82	0-34	0-26	0-0.18
e^+ only	1829±159	7-82	0-34	0-4.2	0-3.2	0-0.02
e^- and e^+	8923±352	180±50	20-119	0-34	0-26	0-0.18
total	$(1.24\pm0.04)\times10^4$	263±60	83±34	0-34	0-26	0-0.18

Table 64: $\pi^0 \rightarrow e^+ e^- \gamma$ *background due to proton-generated events in the detailed detector geometry (the surface profile is irrelevant for this type of primary particle). The overall scaling factor applied to the count obtained from the simulated data is 0.42711 (Table 28).*

	$\mathbf{E}_\gamma$	**D**	θ_{beam} (E)	$\mathbf{PoCA}_{all}$	γ **detection**
e^- only	8.5±1.9	3.8±1.3	0.5-3.2	0-1.04	0-0.007
e^+ only	10.7±2.1	7.7±1.8	0.8-4.3	0-1.04	0-0.007
e^- and e^+	42±4	30±4	4.3±1.4	0.05-1.86	0-0.013
total	61±5	41±4	7.7±1.8	0.05-1.86	0-0.013

Table 65: $\pi^0 \rightarrow e^+ e^- \gamma$ *background due to neutron-generated events in the detailed detector geometry (the surface profile is irrelevant for this type of primary particle). The overall scaling factor applied to the count obtained from the simulated data is 1.50706 (Table 28).*

	$\mathbf{E}_\gamma$	**D**	θ_{beam} (E)	$\mathbf{PoCA}_{all}$	γ **detection**
e^- only	2.8-15.1	2.2-13.0	0.8-8.9	0-3.7	0-0.026
e^+ only	0.8-8.9	0.2-6.6	0-3.7	0-1.52	0-0.011
e^- and e^+	27±6	15.1±4.8	0.8-8.9	0-3.7	0-0.026
total	31±7	23±6	2.2-13.0	0-3.7	0-0.026

7 Conclusion

The cosmic muon-induced background to $p \rightarrow K^+ \, \overline{\nu}$ searches for two underground liquid argon detectors has been estimated. Fluxes of muons have been generated and passed to Geant4, which simulates their interactions as they propagate towards and inside the detector. For a detector featuring two LAr volumes with a combined total mass of 16.748 kilotonnes (appropriate for a detector with a 10 kilotonne active/uninstrumented volume of LAr) at a depth of 4850 ft, all background $K^\pm$ resulting from the incoming muons are rejected after applying cuts. Based on 66.681 years of statistics, the rate of background events is determined to be 0-0.038 per year ($< 2.3\times10^{-3}$ kton^{-1} yr^{-1}) at 90% confidence. This is consistent with a similar study [291] based on 100 years of statistics with a different detector at a similar depth, which finds no events surviving cuts and an upper limit of 1.2×10^{-3} kton^{-1} yr^{-1} at 90% confidence. The most important cuts to reject background $K^\pm$ involve dismissing any events in which the primary muon track extends more than 20 cm in the LAr, and events which feature tracks within 10 cm of the LAr edges.

For a second detector featuring two LAr volumes with a combined mass of 52.795 kilotonnes (appropriate for a detector with a 40 kilotonne active/uninstrumented volume of LAr) at a depth of 800 ft, all background $K^\pm$ resulting from the incoming muons are rejected after applying cuts. Based on 1.473 years of statistics, the rate of background events is 0-1.66 per year (< 0.026 kton^{-1} yr^{-1}) at 90% confidence. For this detector, eliminating all background $K^\pm$ required additional cuts on energy deposition in the event whereas the 4850 ft detector did not.

This compares to another study [243] involving 100 kilotonne-years of statistics for a detector with four different rock overburdens, some greater and some smaller than has been used for the 800 ft detector here. For each configuration the study finds an upper limit at 90% C.L. of 2×10^{-3} kton^{-1} yr^{-1}.

In conclusion, assuming 10-20 years of operation and a decay lifetime is in the range of $\sim10^{34}$-10^{35} years, the irreducible cosmic muon-induced background does not pose a problem to the potential detection of proton decay via the channel $p \rightarrow K^+ \, \overline{\nu}$ for the 4850 ft detector. For the 800 ft detector, no $K^\pm$ were found to survive all of the cuts, but the upper limit at 90% C.L. is 1.66 background event per year, which may be problematic. Higher statistics are required for the 800 ft level statistics to make a strong conclusion but as the location of a future detector will be at a deeper site, this is not a priority now.

The cosmic-ray-induced background to ν_e interactions in a 10 kton LBNE detector at the surface has been estimated. Combinations of a simple and detailed detector geometry as well as flat, approximate and accurate surface profiles have been used. Fluxes of cosmic muons, protons, neutrons and photons have been generated and passed to Geant4, which used them to initiate events. The resulting electromagnetic showers, which mimic ν_e interactions, have been counted. A series of cuts have been investigated as a way to identify and dismiss as many of these showers as possible. Before any cuts are applied, the total annual rate of EM showers over 100 MeV observed was $\mathcal{O}(10^8)$ yr^{-1}. The most effective cut is regarding the ‘Point of Closest Approach’ (PoCA) of the EM showers to either the primary muon track or the track of some other charged particle. After all cuts are applied, using the detailed detector geometry and the accurate surface profile, the combined annual rate for the irreducible EM shower background due to all types of primary particle has been estimated as 2.88 ± 0.25 yr^{-1} from EM showers that start with

$\gamma \to e^+ \, e^-$. For EM showers that start with $K_L^0 \to \pi^\pm \, e^\mp \, \nu_e/\overline{\nu}_e$, the upper limits (at 90% C.L.) of the annual rates in muon, proton and neutron-induced events are < 0.21 yr^{-1}, < 0.01 yr^{-1} and < 0.002 yr^{-1} after all cuts are applied (none of these EM showers survive the cuts). For EM showers that start with $\pi^0 \to e^+ \, e^- \, \gamma$ the upper limits (at 90% C.L.) of the annual rates in muon, proton and neutron-induced events are < 0.18 yr^{-1}, < 0.01 yr^{-1} and < 0.03 yr^{-1} after all cuts are applied (again, none of these EM showers survive the cuts).

The surviving background EM showers are all at the low end of the 0.25 - 5.00 GeV energy range of the neutrino beam, with further reductions possible based on the maximum allowed number of EM showers in an event, and with other, more sophisticated cuts. Given an anticipated signal event rate of $\mathcal{O}(100)$ per year, the background rate due to cosmic rays would not preclude the use of a near-surface level detector for studying $\nu_e/\overline{\nu}_e$ appearance (even though a surface-level detector is no longer a priority).

References

[1] J. Butterworth. “The Standard Model: How Far Can It Go and How Can We Tell?”. 2016 (arXiv:1601.02759 [hep-ex]).

[2] UA1 Collaboration. “Experimental Observation of Isolated Large Transverse Energy Electrons With Associated Missing Energy at S=540 GeV”. *Physics Letters B*, 122:103–116, 1983.

[3] UA2 Collaboration. “Observation of Single Isolated Electrons of High Transverse Momentum in Events with Missing Transverse Energy at the CERN $\overline{p}p$ Collider”. *Physics Letters B*, 122:476–485, 1983.

[4] UA2 Collaboration. “Evidence for $\mathrm{Z}^0 \rightarrow e^+e^-$ at the CERN $\overline{p}p$ Collider”. *Physics Letters B*, 129:130–140, 1983.

[5] ATLAS Collaboration. “Observation of a New Particle in the Search for the Standard Model Higgs Boson with the ATLAS Detector at the LHC”. *Physics Letters B*, 716:1–29, 2012 (arXiv:1207.7214 [hep-ex]).

[6] CMS Collaboration. “Observation of a New Boson at a Mass of 125 GeV with the CMS Experiment at the LHC”. *Physics Letters B*, 716 (1):30–61, 2012 (arXiv:1207.7235 [hep-ex]).

[7] TASSO Collaboration. “Evidence for Planar Events in e^+e^- Annihilation at High-energies”. *Physics Letters B*, 86:243, 1979.

[8] D. P. Barber et al. “Discovery of Three Jet Events and a Test of Quantum Chromodynamics at Petra Energies”. *Physical Review Letters*, 43:830, 1979.

[9] PLUTO Collaboration. “Evidence for Gluon Bremsstrahlung in e^+e^- Annihilations at High-energies”. *Physics Letters B*, 86:418, 1979.

[10] JADE Collaboration. “Observation of Planar Three Jet Events in e^+e^- Annihilation and Evidence for Gluon Bremsstrahlung”. *Physics Letters B*, 91:142, 1980.

[11] J. Aubert et al. “Experimental Observation of a Heavy Particle J”. *Physics Letters B*, 33 (23):1404–1406, 1974.

[12] J. Augustin et al. “Discovery of a Narrow Resonance in e^+e^- Annihilation”. *Physics Letters B*, 33 (23):1406–1408, 1974.

[13] S.W. Herb, D. Hom, L. Lederman et al. “Observation of a Dimuon Resonance at 9.5 GeV in 400-GeV Proton-nucleus Collisions”. *Physical Review Letters*, 39 (5):252, 1977.

[14] DZero Collaboration. “Search for High Mass Top Quark Production in $\overline{p}p$ Collisions at $\sqrt{s} = 1.8$ Tev”. *Physical Review Letters*, 74 (13):2422–2426, 1995.

[15] CDF Collaboration. “Observation of Top Quark Production in $\overline{p}p$ Collisions with the Collider Detector at Fermilab”. *Physical Review Letters*, 74 (14):2626–2631, 1995.

[16] C. Quigg. “The Electroweak Theory”. 2002 (arXiv:hep-ph/0204104v1).

[17] D. Hanneke, S. Fogwell Hoogerheide, G. Gabrielse. "Cavity Control of a Single-electron Quantum Cyclotron: Measuring the Electron Magnetic Moment". *Physical Review A*, 83 (5):052122, 2011 (arXiv:1009.4831).

[18] G. Munster, G. Bergner, B. Echtermeyer. "Gauge Theories of the Strong and Electroweak Interactions". *Summer term 2011 Notes*, 2011.

[19] A. Pich. "The Standard Model of Electroweak Interactions". 2005 (arXiv:hep-ph/0502010v1).

[20] S.L. Glashow. "Partial-symmetries of Weak Interactions". *Nuclear Physics*, 22:579, 1961.

[21] S. Weinberg. "A Model of Leptons". *Physical Review Letters*, 19:1264, 1967.

[22] A. Salam. "Elementary Particle Theory", Ed. N. Svartholm. *Almquist and Wiksells, Stockholm*, page 376, 1969.

[23] S.L. Glashow, J. Iliopoulos, L. Maiani. "Weak Interactions with Lepton-hadron Symmetry". *Physical Review D*, 2:1285, 1970.

[24] E.A. Paschos, L. Wolfenstein. "Tests for Neutral Currents in Neutrino Reactions". *Physical Review D*, 7:91, 1973.

[25] I. van Vulpen. "The Standard Model Higgs Boson". *Part of the Lecture Particle Physics II, UvA Particle Physics Master 2013-2014*, 2013.

[26] K.A. Olive et al. (Particle Data Group). "The Standard Model Higgs Boson". *Chinese Physics C*, 38:090001, 2014.

[27] P.J. Mohr, B.N. Taylor, D.B. Newell. "CODATA Recommended Values of the Fundamental Physical Constants:2010". *Review of Modern Physics*, 84:1527, 2012.

[28] P.W. Higgs. "Broken Symmetries and the Masses of Gauge Bosons". *Physical Review Letters*, 13 (16):508–509, 1964.

[29] F. Englert, R. Brout. "Broken Symmetry and the Mass of Gauge Vector Mesons". *Physical Review Letters*, 13 (9):321–323, 1964.

[30] G. S. Guralnik, C. R. Hagen, T. W. B. Kibble. "Global Conservation Laws and Massless Particles". *Physical Review Letters*, 13 (20):585–587, 1964.

[31] C. Maxwell. "The Standard Model". *Lecture Notes for the 2012 RAL School for Experimental High Energy Physics Students*, 2012.

[32] M. Gell-Mann. "A Schematic Model of Baryons and Mesons". *Physics Letters B*, 8:214, 1964.

[33] G. Zweig. "An $SU(3)$ Model for Strong Interaction Symmetry and its Breaking. Versions 1 and 2". *CERN-TH-401, CERN-TH-410*, 1964.

[34] H.D. Politzer. "Reliable Perturbative Results for Strong Interactions?". *Physical Review Letters*, 30:1346, 1973.

[35] D. J. Gross, F. Wilczek. “Ultraviolet Behavior of Nonabelian Gauge Theories”. *Physical Review Letters*, 30:1343, 1973.

[36] R.P. Feynman. “Very High-energy Collisions of Hadrons”. *Physical Review Letters*, 23:1415, 1969.

[37] J. D. Bjorken, E. A. Paschos. “Inelastic Electron Proton and Gamma Proton Scattering, and the Structure of the Nucleon”. *Physical Review*, 185:1975, 1969.

[38] E. D. Bloom et al. “High-energy Inelastic E P Scattering at 6-degrees and 10-degrees”. *Physical Review Letters*, 23:930, 1969.

[39] J. D. Bjorken. “Applications of the Chiral U(6) X (6) Algebra of Current Densities”. *Physical Review*, 148:1467, 1966.

[40] F. Halzen, A. Martin. “Quarks and Leptons: An Introductory Course in Modern Particle Physics”. page 229, 1984.

[41] B. Palash. “An Introductory Course of Particle Physics”. page 43, 1984.

[42] J. Beringer et al. (Particle Data Group). “Review of Particle Physics”. *Physical Review D*, 86:010001, 2012.

[43] M. Kobayashi, T. Maskawa. “CP-violation in the Renormalizable Theory of Weak Interaction”. *Progress of Theoretical Physics*, 49 (2):652–657, 1973.

[44] E.A. Baltz. “Dark Matter Candidates”. *SLAC Summer Institute on Particle Physics (SSI04)*, 2004).

[45] M. Shaposhnikov L. Canetti, M. Drewes. “Matter and Antimatter in the Universe. *New Journal of Physics*, 14:095012, 2012 (arXiv:1204.4186).

[46] M.C. Brak. “The Hierarchy Problem in the Standard Model and Little Higgs Theories.

[47] C. Jarlskog. “CP Violation”. *ISBN: 978-9971-5-0561-5*, page 503, 1989.

[48] J.D. Bjorken. “Standard Model Parameters and the Cosmological Constant”. *Physical Review D*, 64:085008, 2001 (arXiv:hep-ph/0103349).

[49] H. Georgi, S.L. Glashow. “Unity of All Elementary-particle Forces”. *Physical Review Letters*, 32:438, 1974.

[50] A. Zee. “Quantum Field Theory in a Nutshell 2ed., PUP)”, journal = ISBN 0691140340, year = 2010, volume = , pages = ,.

[51] W. Greiner, B. Muller. “Gauge Theory Of Weak Interactions” (Fourth Edition). *ISBN 978-3-540-87842-1*, 2009.

[52] H. Georgi. “Lie Algebras in Particle Physics”. *Perseus Books*, 1999.

[53] W. Garcia. “Supersymmetric SU(5) X U1 Model and Quark Yukawa Couplings”. *Ph.D. thesis (Universidad de Antioquia)*, 2008.

[54] A. Greljo. “Towards Unification: SU(5) and SO(10)”. *Course notes*, 2012.

[55] B. Bajc. “Grand Unifcation and Proton Decay”. *ICTP Summer School 2011*, 2011.

[56] C.P. Burgess. “Introduction to Effective Field Theory”. *Annual Review of Nuclear and Particle Science*, 57:329–362, 2007 (arXiv:hep-th/0701053v2).

[57] I. Dorsner, P. Fileviez Perez. “Distinguishing Between $SU(5)$ and Flipped $SU(5)$”. *Physics Letters B*, 605:391–398, 2005.

[58] P. Nath, P. Fileviez Perez. “Proton Stability in Grand Unified Theories in Strings and in Branes”. *Physics Reports*, 441:191–317, 2007 (arXiv:hep-ph/0601023v3).

[59] M. Claudson, M. B. Wise, L. J. Hall. “Chiral Lagrangian for Deep Mine Physics”. *Nuclear Physics B*, 195:297, 1987.

[60] P. Fileviez Perez. “Fermion Mixings Vs D = 6 Proton Decay”. *Physics Letters B*, 595 (1-4):476–483, 2004.

[61] J. Hisano. “Proton Decay in the Supersymmetric Grand Unified Models”. 2000 (arXiv:hep-ph/0004266).

[62] N. Cabibbo, E. C. Swallow, R. Winston. “Semileptonic Hyperon Decays”. *Annual Review of Nuclear and Particle Science*, 53:39, 2003.

[63] S. Eidelman et al. (Particle Data Group). “Pseudoscalar-meson Decay Constants”. *Physics Letters B*, 592:1, 2004 (http://pdg.lbl.gov).

[64] I. Dorsner, P. Fileviez Perez. “Unification Without Supersymmetry: Neutrino Mass, Proton Decay and Light Leptoquarks”. *Nuclear Physics B*, 723 (1-2):53–76, 2005 (arXiv:hep-ph/0504276v1).

[65] S. Eidelman et al. (Particle Data Group). “Grand Unified Theories”. *Physics Letters B*, 592:1, 2004.

[66] T.M.P. Tait, K.T. Matchev. “Proceedings of the 2011 Theoretical Advanced Study Institute in Elementary Particle Physics: The Dark Secrets of the Terascale”. *TASI 2011, Boulder, Colorado, 6 June-1 July 2011*, 592:35, 2011.

[67] H. Nishino et al. (Super-Kamiokande Collaboration). “Search for Nucleon Decay Into Charged Anti-lepton Plus Meson in Super-Kamiokande I and II”. *Physical Review D*, 85:112001, 2012 (arXiv:1203.4030v2).

[68] K. Abe et al. (Super-Kamiokande Collaboration). “Search for Proton Decay Via $p \to \overline{\nu} K^+$ Using 260 Kiloton-Year Data of Super-Kamiokande”. *Physical Review D*, 90:072005, 2014.

[69] Super Kamiokande Collaboration. “A Search for Nucleon Decay Via $n \to \overline{\nu}\pi^0$ and $p \to \overline{\nu}\pi^+$ in Super Kamiokande”. *Physical Review Letters*, 113:121802, 2014 (arXiv:1305.4391v1).

[70] I. Dorsner, P. Fileviez Perez, R.G. Felipe. “Phenomenological and Cosmological Aspects of a Minimal GUT Scenario”. *Nuclear Physics B*, 747:312, 2006.

[71] H. Georgi, C. Jarlskog. “A New Lepton-quark Mass Relation in a Unified Theory”. *Physics Letters B*, 86:297, 1979.

[72] J.R. Ellis, M.K. Gaillard. "Fermion Masses and Higgs Representations in SU(5)". *Physics Letters B*, 88:315, 1979.

[73] C. Wetterich G. Lazarides, Q. Shafi. "Proton Lifetime and Fermion Masses in An SO(10) Model". *Nuclear Physics B*, 181:287, 1981.

[74] R.N. Mohapatra, G. Senjanovic. "Neutrino Masses and Mixings in Gauge Models with Spontaneous Parity Violation". *Physical Review D*, 23:165, 1981.

[75] Z. Berezhiani. "2/3 Splitting in SUSY GUT: Higgs As Goldstone Boson". 1997 (hep-ph/9703426).

[76] D. Perkins. "Introduction to High Energy Physics". *ISBN 9780521621960*, page 183, 2000.

[77] W. J. Marciano, G. Senjanovic. "Predictions of Supersymmetric Grand Unified Theories". *Physical Review D*, 25:3092, 1982.

[78] D.I. Kazakov. "Lectures Given at the European School On High Energy Physics". *Aug.-Sept. 2000, Caramulo, Portugal*, 2000 (hep-ph/0012288v2).

[79] S.P. Martin. "A Supersymmetry Primer". 2011 (arXiv:hep-ph/9709356v6).

[80] A. Bilal. "Introduction to Supersymmetry". 2001 (arXiv:hep-th/0101055v1).

[81] H. Baer, X. Tata. "8 - The Minimal Supersymmetric Standard Model (weak Scale Supersymmetry From Superfields to Scattering Events)". *ISBN 9780511617270*, 2006 (arXiv:hep-th/0101055v1).

[82] M.E. Gomez. "Yukawa Couplings and Proton Decay in SUSY Models". *European Network on Physics beyond the Standard Model, 1999 JHEP PROCEEDINGS*, 1999.

[83] G.R. Farrar, P. Fayet. "Phenomenology of the Production, Decay, and Detection of New Hadronic States Associated with Supersymmetry". *Physics Letters B*, 76:575, 1978.

[84] G. t' Hooft. "Symmetry Breaking Through Bell-Jackiw Anomalies". *Physical Review Letters*, 37:8, 1976.

[85] S. Wiesenfeldt. "Proton Decay in Supersymmetric Grand Unifed Theories". *Ph.D. Thesis (University of Hamburg*, 2004.

[86] J. Hisano, H. Murayama, T. Yanagida. "Nucleon Decay in the Minimal Supersymmetric SU(5) Grand Unification". *Nuclear Physics B*, 402:46, 1993 (arXiv:hep-ph/9207279).

[87] H. Murayama, A. Pierce. "Not Even Decoupling Can Save Minimal Supersymmetric SU(5)". *Physical Review D*, 65:055009, 2002 (arXiv:hep-ph/9207279).

[88] B. Bajc, P. Fileviez Perez, G. Senjanovic. "Minimal Supersymmetric SU(5) Theory and Proton Decay: Where Do We Stand?". 2002 (arXiv:hep-ph/0210374).

[89] S. Dimopoulos, S. Raby, F. Wilczek. "Proton Decay in Supersymmetric Models". *Physics Letters B*, 112:133, 1982.

[90] K.S. Babu, M.J. Strassler. “A Reexamination of Proton Decay in Supersymmetric Grand Unified Theories”. 1998 (arXiv:hep-ph/9808447v1).

[91] Z.Berezhiani, Z.Tavartkiladze, M.Vysotsky. “d=5 Operators in SUSY GUT: Fermion Masses Versus Proton Decay”. *10th International Seminar on High-Energy Physics (Quarks 98)*, 1998 (arXiv:hep-ph/9809301v2).

[92] K. S. Babu, B. Bajc, Z. Tavartkiladze. “Realistic Fermion Masses and Nucleon Decay Rates in Supersymmetric $SU(5)$ with Vectorlike Matter”. *Physical Review D*, 86:075005, 2012.

[93] M. E. Gomez, J. Rizos, K. Tamvakis. “Suppressing Dimension Five Operators in General $SU(5)$ Models”. *Physical Review D*, 59:015015, 1999 (arXiv:hep-ph/9807289v2).

[94] J. Hisano, D. Kobayashi, T. Kuwahara, N. Nagata. “Decoupling Can Revive Minimal Supersymmetric $SU(5)$”. *Journal of High Energy Physics*, 1307:38, 2013 (arXiv:1304.3651).

[95] C.H. Albright. “SO(10) GUT Models and Their Present Success in Explaining Mass and Mixing Data”. *International Journal of Modern Physics A*, 18:3947, 2003 (arXiv:hep-ph/0212090v1).

[96] J. M. Gipson, R. E. Marshak. “Intermediate Mass Scales in the New SO(10) Grand Unification in the One-loop Approximation”. *Physical Review D*, 31:1705, 1985 (arXiv:hep-ph/0212090v1).

[97] D. Chang, R. N. Mohapatra, J. Gipson, R. E. Marshak, M. K. Parida. “Experimental Tests of New SO(10) Grand Unification”. *Physical Review D*, 31:1718, 1985.

[98] N. G. Deshpande, E. Keith, P. B. Pal. “Implications of LEP Results for SO(10) Grand Unification”. *Physical Review D*, 46:2261, 1993.

[99] N. G. Deshpande, E. Keith, P. B. Pal. “Implications of Results From the CERN e^+e^- Collider LEP for SO(10) Grand Unification with Two Intermediate Stages”. *Physical Review D*, 47:2892, 1993 (hep-ph/9211232).

[100] S. Bertolini, L. Di Luzio, M. Malinsky. “Intermediate Mass Scales in the Non-supersymmetric SO(10) Grand Unification: a Reappraisal”. *Physical Review D*, 80:015013, 2009 (arXiv:0903.4049 [hep-ph]).

[101] N. Craig. “The State of Supersymmetry After Run I of the LHC” Lectures at the Training Week of the GGI Workshop - Beyond the Standard Model After the First Run of the LHC. 2014 (arXiv:1309.0528v2).

[102] K.S. Babu, S. Khan. “A Minimal Non-supersymmetric SO(10) Model: Gauge Coupling Unification, Proton Decay and Fermion Masses”. *Physical Review D*, 92:075018, 2015 (arXiv:1507.06712v1).

[103] A. Maiezza, M. Nemevsek, F. Nesti, G. Senjanovic. “Left-right Symmetry at LHC”. *Physical Review D*, 82:055022, 2010 (arXiv:1005.5160 [hep-ph]).

[104] D. Lee, R. N. Mohapatra, M. K. Parida, M.Rani. “Predictions for Proton Life-time in Minimal Non-supersymmetric SO(10) Models: An Update”. *Physical Review D*, 51:229–235, 1995 (arXiv:hep-ph/9404238v1).

[105] D. Chang, R. N. Mohapatra, M. K. Parida. “Decoupling Parity and SU(2)-r Breaking Scales: a New Approach to Left-right Symmetric Models”. *Physical Review Letters*, 52:1072, 1984.

[106] S. Patra, P. Pritimita. “Post-sphaleron Baryogenesis and $n\overline{N}$ Oscillation in Non-SUSY SO(10) GUT with Gauge Coupling Unification and Proton Decay”. 2014 (arXiv:1405.6836v2).

[107] K. S. Babu, J. C. Pati, F. Wilczek. “Fermion Masses, Neutrino Oscillations, and Proton Decay in the Light of Superkamiokande”. *Nuclear Physics B*, 566:33, 2000 (arXiv:hep-ph/9812538).

[108] J. C. Pati. “Neutrino Masses: Shedding Light On Unification and Our Origin”. *Talk given at the Fujihara Seminar, KEK Laboratory, Tsukuba, Japan, February 23-25, 2004*, 2004 (arXiv:hep-ph/0407220).

[109] J. C. Pati. “A Unified Picture with Neutrino As a Central Feature”. *Proceedings of the XI International Workshop on ”Neutrino Telescopes”, Venice*, 2005 (arXiv:hep-ph/0507307v1).

[110] T. Fukuyama. “SO(10) GUT in Four and Five Dimensions: a Review”. 2012 (arXiv:1212.3407v1).

[111] K.S. Babu, J.C. Pati, F. Wilczek. “Suggested New Modes in Supersymmetric Proton Decay”. *Physics Letters B*, 423:337–347, 1998.

[112] K. S. Babu, R. N. Mohapatra. “Predictive Neutrino Spectrum in Minimal SO(10) Grand Unification”. *Physical Review Letters*, 70:2845, 1993.

[113] K. Matsuda, Y. Koid, T. Fukuyama. “Can the SO(10) Model with Two Higgs Doublets Reproduce the Observed Fermion Masses?”. *Physical Review D*, 64:053015, 2001.

[114] K. Matsuda, Y. Koide, T. Fukuyama, H. Nishiura. “How Far Can the SO(10) Two Higgs Model Describe the Observed Neutrino Masses and Mixings?”. *Physical Review D*, 65:033008, 2002.

[115] T. Fukuyama, N. Okada. “Neutrino Oscillation Data Versus Minimal Supersymmetric SO(10) Model”. *Journal of High Energy Physics*, 0211:011, 2002.

[116] K.S. Babu, J.C. Pati, C. Jogesh. “The Problems of Unification-mismatch and Low Cq: a Solution with Light Vector-like Matter”. *Physics Letters B*, 384:140–150, 1996.

[117] S. M. Barr. “A New Symmetry Breaking Pattern for SO(10) and Proton Decay”. *Physics Letters B*, 112:219, 1982.

[118] J. P. Derendinger, J. E. Kim, D. V. Nanopoulos. “Anti-SU(5)”. *Physics Letters B*, 139:170, 1984.

[119] I. Antoniadis, J. R. Ellis, J. S. Hagelin, D. V. Nanopoulos. "Supersymmetric Flipped SU(5) Revitalized". *Physics Letters B*, 194:231, 1987.

[120] T. Li, D.V. Nanopoulos, J.W. Walker. "Fast Proton Decay". *Physics Letters B*, 693:580–583, 2010.

[121] J. Ellis, D.V. Nanopoulos, J. Walker. "Flipping SU(5) Out of Trouble". *Physics Letters B*, 550:99–107, 2002.

[122] S. Nandi, A. Stern, E. C. G. Sudarshan. "Can Proton Decay Be Rotated Away?". *Physics Letters B*, 113:165, 1982.

[123] I. Dorsner, P. Fileviez Perez. "Could We Rotate Proton Decay Away?". *Physics Letters B*, 606 (2-3):367–370, 2005 (arXiv:hep-ph/0409190v3).

[124] S.M. Barr, I. Dorsner. "Unifying Flipped SU(5) in Five Dimensions". *Physical Review D*, 66:065013, 2002 (arXiv:hep-ph/0205088v2).

[125] C.S. Huang, T. Li, C. Liu, J.P. Shock, Feng Wu, Y.L. Wu. "Embedding Flipped $SU(5)$ Into $SO(10)$". *Journal of High Energy Physics*, 610:35, 2006 (arXiv:hep-ph/0606087).

[126] C. D. Froggatt, H. B. Nielsen. "Hierarchy of Quark Masses, Cabibbo Angles and CP Violation". *Nuclear Physics B*, 147:277, 1979.

[127] K.S. Babu. "TASI Lectures On Flavor Physics". 2009 (arXiv:0910.2948v1).

[128] M. Kakizaki, M. Yamaguchi. "U1 Flavor Symmetry and Proton Decay in Supersymmetric Standard Model". *Journal of High Energy Physics*, 0206:032, 2002 (arXiv:hep-ph/0203192).

[129] Q. Shafia, Z. Tavartkiladzeb. "'Flavor Problem, Proton Decay And Neutrino - Oscillations In SUSY Models With Anomalous U1". *Physics Letters B*, 473 (3-4):272–280, 2000 (arXiv:hep-ph/9911264v2).

[130] S. Kar. "Bulk-brane Models: An Overview and Some Queries (COSGRAV12)". *IOP Publishing -Journal of Physics: Conference Series*, 405:012002, 2012.

[131] L. J. Hall, Y. Nomura. "Complete Theory of Grand Unification in Five Dimensions". *Physical Review D*, 66:075004, 2002.

[132] S. Raby. "Proton Decay". *Plenary Lectures - SUSY'02, DESY, Hamburg, Germany*, 2002.

[133] L.J. Hall, Y. Nomura. "Gauge Unification in Higher Dimensions". *Physical Review D*, 64:055003, 2001.

[134] Y. Nomura. "Strongly Coupled Grand Unification in Higher Dimensions". *Physical Review D*, 65:085036, 2002.

[135] M. L. Alciati, F. Feruglio. "Proton Lifetime From SU(5) Unification in Extra Dimensions". *Journal of High Energy Physics*, 2005:03, 2005.

[136] H. D. Kim, S. Raby. “Unification in 5d SO(10)”. *Journal of High Energy Physics*, 0301:056, 2003 (arXiv:hep-ph/0212348).

[137] W. Buchmuller, L. Covi, D. Emmanuel-Costa, S. Wiesenfeldt. “Flavour Structure and Proton Decay in 6d Orbifold GUTs”. *CERN-PH-TH/2004-043, DESY 03-202*, 2004 (arXiv:hep-ph/0407070v1).

[138] G. Battistoni et al. “The NUSEX Detector”. *Nuclear Instruments and Methods in Physics Research Section A*, 245:277, 1986.

[139] G. Battistoni et al. “Nucleon Stability, Magnetic Monopoles and Atmospheric Neutrinos in the Mont-Blanc Experiment”. *Physics Letters B*, 133:454, 1983.

[140] C. Berger et al. (FREJUS Collaboration). “The Frejus Nucleon Decay Detector”. *Nuclear Instruments and Methods in Physics Research Section A*, 262:463, 1987.

[141] C. Berger et al. (FREJUS Collaboration). “Lifetime limits on (B-L) Violating Nucleon Decay and Dinucleon Decay Modes from the Frejus Experiment”. *Physics Letters B*, 269:227, 1991.

[142] J.E. Bartelt. “Results From The Soudan Prototype Proton Decay Detector”. *Ph.D. Thesis (Minnesota U.)*, 1984.

[143] J.L. Thron. “The Soudan-2 Proton Decay Experiment”. *Nuclear Instruments and Methods in Physics Research Section A*, 283:642, 1989.

[144] M.C. Goodman (Soudan II Collaboration). “Nucleon Decay in Soudan-2”. *26th International Cosmic Ray Conference (ICRC 99), Salt Lake City, UT*, 1999.

[145] R. Becker-Szendy et al. “IMB-3: A Large Water Cherenkov Detector for Nucleon Decay and Neutrino Interactions”. *Nuclear Instruments and Methods in Physics Research Section A*, 324:363, 1993.

[146] R. Becker-Szendy et al. “Search for Proton Decay into $e^+ + \pi^0$ in the IMB-3 Detector”. *Physical Review D*, 42:2974, 1990.

[147] K. S. Hirata et al. (Kamiokande-II Collaboration). “Experimental Study of the Atmospheric Neutrino Flux”. *Physics Letters B*, 205:416, 1988.

[148] Y. Fukuda et al. (Super-Kamiokande Collaboration). “The Super-Kamiokande Detector”. *Nuclear Instrumental Methods A*, 501:418–462, 2003.

[149] K. Abe et al. (The Hyper-Kamiokande Working Group). “A Long Baseline Neutrino Oscillation Experiment Using J-PARC Neutrino Beam and Hyper-Kamiokande”. *18th J-PARC PAC meeting*, 2015 (arXiv:1412.4673v2 [physics.ins-det]).

[150] The LBNE collaboration. “The Long-baseline Neutrino Experiment: Exploring Fundamental Symmetries of the Universe”. 2014 (arXiv:1307.7335).

[151] R.N. Mohapatra et al. “Theory of Neutrinos: a White Paper”. 2005 (arXiv:hep-ph/0510213v2).

[152] B. Pontecorvo. “Mesonium and Antimesonium”. *Soviet Physics JETP*, 6:429, 1957 [Zh. Eksp. Teor. Fiz. 33, 549 (1957)].

[153] B. Pontecorvo. “Inverse Beta Processes and Nonconservation of Lepton Charge”. *Soviet Physics JETP*, 7:172173, 1958 [Zh. Eksp. Teor. Fiz. 34, 247 (1958)].

[154] B. Pontecorvo. “Neutrino Experiments and the Question of Leptonic-charge Conservation”. *Soviet Physics JETP*, 26:984988, 1968.

[155] C. Giunti, C.W. Kim. “Fundamentals of Neutrino Physics and Astrophysics”. *Oxford University Press (ISBN-10: 0198508719)*, 2007.

[156] S. Boyd. “Neutrino Oscillations: Theory and Experiment”. *Course notes, Univeristy of Warwick*, 2015.

[157] C. Giunti. “Theory of Neutrino Oscillations”. 2004 (arXiv:hep-ph/0409230v1).

[158] L. Wolfenstein. “Neutrino Oscillations in Matter”. *Physical Review D*, 17:2369, 1978).

[159] S. P. Mikheyev, A. Y. Smirnov. “Resonance Enhancement Of Oscillations In Matter And Solar Neutrino Spectroscopy”. *Yad. Fiz.*, 42:1441, 1985 (Soviet Journal of Nuclear Physics 42, 913 (1985)]; Nuovo Cimento 9C, 17 (1986)).

[160] Z. Maki, M. Nakagawa, S. Sakata. “Remarks On The Unified Model Of Elementary Particles”. *Prog. Theor. Phys.*, 28:870–880, 1962.

[161] M. Thomson. “Modern Particle Physics”. *Cambridge University Press (ISBN: 9781107034266)*, 2013.

[162] J.W.F. Valle. “Neutrino Physics Overview”. *Journal of Physics: Conference Series*, 53:473, 2006 (arXiv:hep-ph/0608101).

[163] J.L. Hewett et al. “Fundamental Physics at the Intensity Frontier”. *Journal of Physics: Conference Series*, 2012 (ANL-HEP-TR-12-25, SLAC-R-991, FERMILAB-CONF-12-879-PPD, arXiv:1205.2671 [hep-ex]).

[164] C. Luhn. “Trimaximal Tm1 Neutrino Mixing in S4 with Spontaneous CP Violation”. *Nuclear Physics B*, 875:80–100, 2012 (arXiv:1306.2358 [hep-ph]).

[165] M. Raidal. “Relation Between the Neutrino and Quark Mixing Angles and Grand Unification”. *Physical Review Letters*, 93:161801, 2004 (arXiv:hep-ph/0404046 [hep-ph]).

[166] H. Minakata, A. Y. Smirnov. “Neutrino Mixing and Quark-lepton Complementarity”. *Physical Review D*, 70:073009, 2013 (arXiv:hep-ph/0405088 [hep-ph]).

[167] A. Y. Smirnov. “Neutrino Mass, Mixing and Discrete Symmetries”. *Journal of Physics: Conference Series*, 447:012004, 2013 (arXiv:1305.4827 [hep-ph]).

[168] J. Harada. “Non-maximal Theta23, Large Theta13 and Tri-bimaximal Theta12 Via Quark-lepton Complementarity at Next-to-leading Order”. *Europhysics Letters*, 103:21001, 2013 (arXiv:1304.4526 [hep-ph]).

[169] B. Hu. “Trimaximal-cabibbo Neutrino Mixing: a Parametrization in Terms of Deviations From Tribimaximal Mixing”. *Physical Review D*, 87 no. 5:053011, 2013 (arXiv:1212.4079 [hep-ph]).

[170] J. H. Christenson, J. W. Cronin, V. L. Fitch, R. Turlay. “Evidence for the 2π Decay of the K_2^0 Meson System”. *Physical Review Letters*, 13:138, 1964.

[171] H. Minakata, H. Nunokawa. “CP Violation Vs. Matter Effect in Long-baseline Neutrino Oscillation Experiments”. *Physical Review D*, 57:4403–4417, 1998 (arXiv:hep-ph/9705208v2).

[172] C. Jarlskog. “Commutator of the Quark Mass Matrices in the Standard Electroweak Model and a Measure of Maximal CP Nonconservation”. *Physical Review Letters*, 55:1039, 1985.

[173] V. Barger, K. Wisnant, R. J. N. Phillips. “CP Nonconservation in Three-neutrino Oscillations”. *Physical Review Letters*, 45:2084, 1980.

[174] S. Pavkasa. “Proceedings of the Xxth International Conference On High Energy Physics”. *AIP Conference Proceedings No. 68 (AIP, New York, 1981)*, 2:1164, 1981.

[175] H. Nunokawa, S. Parke, J. W. F. Valle. “CP Violation and Neutrino Oscillations”. 2007 (arXiv:0710.0554v2 [hep-ph]).

[176] A. Ibarra, E. Molinaro, S. T. Petcov. “Tev Scale See-saw Mechanisms of Neutrino Mass Generation, the Majorana Nature of the Heavy Singlet Neutrinos and $\beta\beta$-decay”. *Journal of High Energy Physics*, 1009:108, 2010 (arXiv:1007.2378 [hep-ph]).

[177] A. Ibarra, E. Molinar, S. T. Petcov. “Low Energy Signatures of the Tev Scale See-saw Mechanism”. *Physical Review D*, 84:013005, 2011 (arXiv:1103.6217 [hep-ph]).

[178] D. N. Dinh, A. Ibarra, E. Molinar, S. T. Petcov. “The $\mu - e$ Conversion in Nuclei, $\mu \to e\gamma$, $\mu \to 3e$ Decays and Tev Scale See-saw Scenarios of Neutrino Mass Generation”. *Journal of High Energy Physics*, 1208:125, 2012 (arXiv:1205.4671 [hep-ph]).

[179] C. G. Cely, A. Ibarra, E. Molinaro, S. T. Petcov. “Higgs Decays in the Low Scale Type I See-saw Model”. *Physics Letters B*, 718:957, 2013 (arXiv:1208.3654 [hep-ph]).

[180] M. Fukugita, T. Yanagida. “Barygenesis Without Grand Unification”. *Physics Letters B*, 174:45, 1986.

[181] W. Buchmuller, R. D. Peccei, T. Yanagida. “Leptogenesis As the Origin of Matter”. *Annual Review of Nuclear and Particle Science*, 55:311, 2005 (arXiv:[hep-ph/0502169]).

[182] S. Bilenky. “Introduction to the Physics of Massive and Mixed Neutrinos”. *ISBN 978-3-642-14043-3*, 2010.

[183] V. A. Kuzmin, V. A. Rubakov, M. E. Shaposhnikov. “On Anomalous Electroweak Baryon-number Non-conservation in the Early Universe”. *Physics Letters B*, 155:36, 1985 (arXiv:1208.3654 [hep-ph]).

[184] A. Strumia. “Baryogenesis Via Leptogenesis”. 2006 (arXiv:hep-ph/0608347).

[185] S. Pascoli, S.T. Petcov, A. Riotto. “Connecting Low Energy Leptonic CP-violation to Leptogenesis”. *Physical Review D*, 75:083511, 2007 (arXiv:hep-ph/0609125v3).

[186] J. Schechter, J. W. F. Valle. "Neutrino Masses in SU(2) x U(1) Theories". *Physical Review D*, 22:2227, 1980.

[187] J. Schechter, J. W. F. Valle. "Neutrino-oscillation Thought Experiment". *Physical Review D*, 23:1666, 1981.

[188] W. Buchmuller, D. Wyler. "CP Violation, Neutrino Mixing and the Baryon Asymmetry". *Physics Letters B*, 521:291–298, 2001.

[189] S. Pascoli, S.T. Petcov, A. Riotto. "Leptogenesis and Low Energy CP Violation in Neutrino Physics". *Nuclear physics B*, 774:1–52, 2007.

[190] J.N. Bahcall, A.M. Serenelli, S. Basu. "New Solar Opacities, Abundances, Helioseismology, and Neutrino Fluxes". *The Astrophysical Journal*, 621:L85, 2005.

[191] B. T. Cleveland et al. (Homestake). "Measurement of the Solar Electron Neutrino Flux with the Homestake Chlorine Detector". *The Astrophysical Journal*, 496:505–526, 1998.

[192] F. Kaether, W. Hampel, G. Heusser, J. Kiko, T. Kirsten (GALLEX). "Reanalysis of the Gallex Solar Neutrino Flux and Source Experiments". *Physics Letters B*, 685:47–54, 2010 (arXiv:1001.2731).

[193] GNO Collaboration. "Complete Results for Five Years of GNO Solar Neutrino Observations". *Physics Letters B*, 616:174–190, 2005 (arXiv:hep-ex/0504037).

[194] SAGE Collaboration. "Measurement of the Solar Neutrino Capture Rate with Gallium Metal. IIi: Results for the 2002–2007 Data-taking Period". *Physics Letters C*, 80:015807, 2009 (arXiv:0901.2200).

[195] W. C. Haxton, R. G. Hamish Robertson, Aldo M. Serenelli. "Solar Neutrinos: Status and Prospects". 2012 (arXiv:1208.5723v1).

[196] K. S. Hirata et al. (Kamiokande-II Collaboration). "Observation of a Small Atmospheric Muon-neutrino / Electron-neutrino Ratio in Kamiokande". *Physics Letters B*, 280:146, 1992.

[197] Y. Fukuda et al. (Super-Kamiokande Collaboration). "Solar Neutrino Results in Super Kamiokande-III". *Physical Review D*, 83:052010, 2011 (arXiv:1010.0118).

[198] N. Jelley, A. B. McDonald, R.G. Hamish Robertson. "The Sudbury Neutrino Observatory". *Annual Review of Nuclear and Particle Science*, 59:431–465, 2009.

[199] N. Barros, on behalf of the SNO Collaboration. "Final Results From SNO". *Nuclear Physics B (Proceedings Supplement)*, 237-238:107–110, 2013.

[200] J. N. Bahcall. "Solar Models and Solar Neutrinos". 2004 (arXiv:hep-ph/0412068v1).

[201] J.J. Beatty, S. Westerhoff. "The Highest-energy Cosmic Rays". *Annual Review of Nuclear and Particle Science*, 59:319, 2009.

[202] T. Kajita. "Review Atmospheric Neutrinos and Discovery of Neutrino Oscillations". *Proceedings of the Japan Academy, Ser. B*, 86:303, 2010.

[203] T.J. Haines, R.M. Bionta, G. Blewitt, C.B. Bratton, D. Casper, R. Claus et al. "Calculation of Atmospheric Neutrino-induced Backgrounds in a Nucleon-decay Search". *Physical Review Letters*, 57:1986, 1986.

[204] M. Nakahata, K. Arisaka, T. Kajita, M. Koshiba, Y. Oyama, A. Suzuki et al. "Atmospheric Neutrino Background and Pion Nuclear Effect for Kamioka Nucleon Decay Experiment". *Journal of the Physical Society of Japan*, 55:3786–3805, 1986.

[205] T2K Collaboration. "Measurements of Neutrino Oscillation in Appearance and Disappearance Channels by the T2K Experiment with 6.6×10^{20} Protons On Target". *Physical Review D*, 91:072010, 2015 (arXiv:1502.01550v2 [hep-ex]).

[206] MINOS Collaboration. "Combined Analysis of ν_μ Disappearance and $\nu_\mu \rightarrow \nu_e$ Appearance in MINOS Using Accelerator and Atmospheric Neutrinos". *Physical Review Letters*, 112:191801, 2014 (arXiv:1403.0867 [hep-ex]).

[207] A. Himmel (Super Kamiokande Collaboration). "Recent Atmospheric Neutrino Results From Super-Kamiokande". *AIP Conference Proceedings*, 1604:345, 2014 (arXiv:1310.6677 [hep-ex]).

[208] Super Kamiokande Collaboration. "Evidence for the Appearance of Atmospheric Tau Neutrinos in Super Kamiokande". *Physical Review Letters*, 110:181802, 2013 (arXiv:1206.0328).

[209] M. Apollonio et al. "Search for Neutrino Oscillations On a Long Base-line at the Chooz Nuclear Power Station". *The European Physical Journal C*, 27:331–374, 2003 (arXiv:hep-ex/0301017v1).

[210] F.Boehm, J.Busenitz, B.Cook, G.Gratta, H.Henrikson, J.Kornis, D.Lawrence, K.B.Lee, K.McKinney, L.Miller, V.Novikov, A.Piepke, B.Ritchie, D.Tracy, P.Vogel, Y-F.Wang, J.Wolf. "Final Results From the Palo Verde Neutrino Oscillation Experiment". *Physical Review D*, 64:112001, 2001 (arXiv:hep-ex/0107009v1).

[211] KamLAND Collaboration. "First Results From Kamland: Evidence for Reactor Anti-neutrino Disappearance". *Physical Review Letters*, 90:021802, 2003 (arXiv:hep-ex/0212021).

[212] KamLAND Collaboration. "Constraints On Theta13 From a Three-flavor Oscillation Analysis of Reactor Antineutrinos at Kamland". *Physical Review D*, 83:052002, 2003 (arXiv:1009.4771v3 [hep-ex]).

[213] J.I. Crespo-Anadon. "Double Chooz: Latest Results". 2014 (arXiv:1412.3698 [hep-ex]).

[214] The RENO Collaboration. "Observation of Reactor Electron Antineutrino Disappearance in the Reno Experiment". *Physical Review Letters*, 108:191802, 2012 (arXiv:1204.0626v2 [hep-ex]).

[215] On behalf of the RENO Collaboration Seon-Hee Seo. "New Results From Reno and Future Reno-50". *EPS 2015, Vienna, Austria*, 2015.

[216] Bei-Zhen Hu, for the Daya Bay Collaboration. "Recent Results from Daya Bay Reactor Neutrino Experiment". 2015 (arXiv:1505.03641v1 [hep-ex]).

[217] K2K Collaboration. “Detection of Accelerator-produced Neutrinos at a Distance of 250 Km”. *Physics Letters B*, 511:178–184, 2001 (arXiv:hep-ex/0103001v1).

[218] MINOS+ Collaboration. “MINOS+: a Proposal to FNAL to Run MINOS with the Medium Energy Numi Beam”. 2011 (MINOS DocDB-7923).

[219] Alexandre B. Sousa (for the MINOS and MINOS+ Collaborations). “First MINOS+ Data and New Results From MINOS”. 2015 (arXiv:1502.07715v2).

[220] The MINOS Collaboration. “Electron Neutrino and Antineutrino Appearance in the Full Minos Data Sample”. *Physical Review Letters*, 110:171801, 2013 (arXiv:1301.4581v3 [hep-ex]).

[221] The OPERA Collaboration. “Discovery of Tau Neutrino Appearance in the CNGS Neutrino Beam with the OPERA Experiment”. *Physical Review Letters*, 115:121802, 2015 (arXiv:1507.01417v1 [hep-ex]).

[222] D. Ayres et al. (NOvA Collaboration). “The Nova Technical Design Report”. *FERMILAB-DESIGN-2007-01*, 2007 (lss.fnal.gov/archive/design/fermilab-design-2007-01.pdf).

[223] R. Patterson (for the NoVA Collaboration). “First Oscillation Results From NoVA”. *Joint Experimental-Theoretical Seminar, Fermilab*, 2015 (NoVA DocDB-13883).

[224] M. Messier. “Exploring Neutrinos Via Oscillations in the Atmosphere, at Reactors, and at Accelerators”. *Division of Particles and Fields (DPF) 2015, Ann Arbor, MI*, 2015 (NoVA DocDB-13886).

[225] M. B. Avanzini (on behalf of the LAGUNA-LBNO Collaboration). “The LAGUNA-LBNO Project (13th International Conference On Topics in Astroparticle and Underground Physics)”. *Physics Procedia*, 61:524–533, 2015.

[226] The DUNE Collaboration. “LBNF/DUNE Conceptual Design Report - Volume 1: The LBNF and DUNE Projects”. *LBNE DocDB 10687-v8*, June 2015.

[227] The DUNE Collaboration. “Long-baseline Neutrino Facility (LBNF) and Deep Underground Neutrino Experiment (DUNE) Conceptual Design Report 3”. *LBNE DocDB 10689-v27*, August 2015.

[228] The DUNE Collaboration. “Long-baseline Neutrino Facility (LBNF) and Deep Underground Neutrino Experiment (DUNE) Conceptual Design Report Volume 4: The DUNE Detectors at LBNF”. *LBNE DocDB 10690-v12*, August 2015.

[229] K. T. Lesko et al. “Deep Underground Science and Engineering Laboratory - Preliminary Design Report”. 2011 (arXiv:1108.0959).

[230] C. Rubbia. “The Liquid-argon Time Projection Chamber: a New Concept for Neutrino Detectors”. *CERN-EP-INT-77-8*, 1977.

[231] E. Aprile, K. L. Giboni, C. Rubbia. “A Study of Ionization Electrons Drifting Large Distances in Liquid and Solid Argon”. *Nuclear Instruments and Methods in Physics Research A*, 241:62, 1985.

[232] P. Benetti et al. “A 3-ton Liquid Argon Time Projection Chamber”. *Nuclear Instruments and Methods in Physics Research A*, 332:395–412, 1993.

[233] P. Cennini et al. “Performance Of a 3-ton Liquid Argon Time Projection Chamber”. *Nuclear Instruments and Methods in Physics Research A*, 345:230, 1994.

[234] F. Arneodo et al. (ICARUS-Milano Collaboration). “Performance Of a Liquid Argon Time Projection Chamber Exposed To The Wanf Neutrino Beam”. *Physical Review D*, 74:112001, 1993 (arXiv:physics/0609205).

[235] S. Amerio et al. “Design, Construction and Tests of the Icarus T600 Detector”. *Nuclear Instruments and Methods in Physics Research A*, 527:329, 2004.

[236] S. Amoruso et al. (ICARUS Collaboration). “Design, Construction and Tests of the Icarus T600 Detector”. *Nuclear Instruments and Methods in Physics Research A*, 516:68, 2004.

[237] S. Amoruso et al. (ICARUS Collaboration). “Study of Electron Recombination in Liquid Argon with the Icarus TPC”. *Nuclear Instruments and Methods in Physics Research A*, 523:275, 2004.

[238] A. Badertscher, M. Laffranchi, A. Meregaglia, A. Rubbia. “First Operation of a Liquid Argon TPC Embedded in a Magnetic Field”. *New Journal of Physics*, 63:26, 2005 (arXiv:physics/0412080).

[239] A. Badertscher, M. Laffranchi, A. Meregaglia, A. Rubbia. “First Results From a Liquid Argon Time Projection Chamber in a Magnetic Field”. *Nuclear Instruments and Methods in Physics Research A*, 555:294, 2005 (arXiv:physics/0505151).

[240] M. Freund. “Analytic Approximations for Three Neutrino Oscillation Parameters and Probabilities in Matter”. *Physical Review D*, 64:053003, 2001 (arXiv:hep-ph/0103300 [hep-ph]).

[241] W. Marciano, Z. Parsa. “Intense Neutrino Beams and Leptonic CP Violation”. *Nuclear Physics B - Proceedings Supplements*, 221:166–172, 2011 (arXiv:hep-ph/0610258 [hep-ph]).

[242] The DUNE Collaboration. “Long-baseline Neutrino Facility (LBNF) and Deep Underground Neutrino Experiment (DUNE) - Conceptual Design Report Volume 2: The Physics Program for DUNE at LBNF”. *LBNE DocDB 10688-v10*, 2015.

[243] A. Bueno, Z. Dai, Y. Ge, M. Laffranchi, A. Melgarejo et al. “Nucleon Decay Searches with Large Liquid Argon TPC Detectors at Shallow Depths: Atmospheric Neutrinos and Cosmogenic Backgrounds”. *Journal of High Energy Physics*, 0704:41, 2007.

[244] E. Kearns. “Future Experiments for Proton Decay”. *Presentation at ISOUPS (International Symposium: Opportunities in Underground Physics for Snowmass) - cited in "Scientific Opportunities with the Long-Baseline Neutrino Experiment" - LBNE Collaboration (Adams, C. et al.) FERMILAB-CONF-13-300*, 2013.

[245] ALICE Collaboration. “A Very High Momentum Particle Identification Detector”. *The European Physical Journal Plus*, 129:91, 2014 (arXiv:1309.5880 [nucl-ex]).

[246] D. Stefan, A. M. Ankowski. "Nuclear Effects in Proton Decay". *Acta Physica Polonica B*, 40:671–674, 2009 (arXiv:0811.1892 [nucl-th]).

[247] A.M. Ankowski, J.T Sobczyk. "Construction of Spectral Functions for Medium-mass Nuclei". *Physical Review C*, 77:044311, 2008.

[248] O. Buss et al. "Influence of the Nuclear Medium On Inclusive Electron and Neutrino Scattering Off Nuclei". *Physical Review C*, 76:035502, 2007.

[249] O. Benhar et al. "Electron- and Neutrino-nucleus Scattering in the Impulse Approximation Regime". *Physical Review D*, 72:053005, 2005.

[250] A. Heikkinen, N. Stepanov, S. Nikita, J. P. Wellisch. "Bertini Intranuclear Cascade Implementation in Geant4". *Proceedings of CHEP 2003 (The International Conference on Computing in High Energy and Nuclear Physics)*, 2003.

[251] C. Rubbia et al. "Underground Operation of the ICARUS T600 LAr-TPC: First Results". *Journal of Instrumentation*, 6:07011, 2011.

[252] S. Agostinelli et al. (Geant4 Collaboration). "GEANT4: a Simulation Toolkit". *Nuclear Instruments and Methods in Physics Research Section A*, 506:250–303, 2003 (SLAC-PUB-9350, FERMILAB-PUB-03-339).

[253] "Shielding Physics List Description". *http://www.slac.stanford.edu/comp/physics/-geant4/slac_physics_lists/shielding/physlistdoc.html*, 2012.

[254] H. A. Bethe, W. Heitler. "On the Stopping of Fast Particles and on the Creation of Positive Electrons". *Proceedings of the Royal Society (London) A*, 83:146, 1934.

[255] F. Biggs, R. Lighthill. *Preprint Sandia Laboratory, SAND 87-0070*, 83:146, 1990.

[256] T.A. Carlson. "Photoelectron and Auger Spectroscopy". *Springer (ISBN 978-1-4757-0118-0)*, page 337, 1976.

[257] M. Gavrila, S. Sauter. "Relativistic K-Shell Photoeffect". *Physical Review*, 113:514, 1959.

[258] P.V. Degtyarenko, M.V. Kossov, J.P. Wellisch. "Chiral Invariant Phase Space Event Generator I. Nucleon-antinucleon Annihilation at Rest". *European Physical Journal A*, 8:217–222, 2000.

[259] P.V. Degtyarenko, M.V. Kossov, J.P. Wellisch. "Chiral Invariant Phase Space Event Generator - II. Nuclear Pion Capture at Rest and Photonuclear Reactions Below the Delta(3,3) Resonance". *European Physical Journal A*, 9:411–420, 2001.

[260] P.V. Degtyarenko, M.V. Kossov, J.P. Wellisch. "Chiral Invariant Phase Space Event Generator - III. Modeling of Real and Virtual Photon Interactions with Nuclei Below Pion Production Threshold". *European Physical Journal A*, 9:421–424, 2001.

[261] G.Folger, J.P. Wellisch. "String Parton Models in Geant4". *CHEP03, La Jolla, California*, 2003 (arXiv:nucl-th/0306007v1).

[262] K.K. Gudima, S.G. Mashnik, V.D. Toneev. "Cascade-Exciton Model of Nuclear-Reactions". *Nuclear Physics A*, 401:329, 1983.

[263] Xavier Roque. “Moller Scattering: A Neglected Application of Early Quantum Electrodynamics”. *Archive for History of Exact Sciences 16*, 44:197–264, 1983.

[264] H. J. Bhabha. “The Scattering of Positrons by Electrons with Exchange on Dirac’s Theory of the Positron”. *Proceedings of the Royal Society A*, 154:195, 1936.

[265] M.J. Berger, S.M. Seltzer. “Bremsstrahlung and Photoneutrons from Thick Tungsten and Tantalum Targets”. *Physical Review C*, 2:621, 1970.

[266] S. Goudsmit, J.L. Saunderson. “Multiple Scattering of Electron”. *Physical Review*, 57:24, 1940.

[267] W. Heitler. “Quantum Theory of Radiation Monographs on Physics”. *Clarendon Press, Oxford (ISBN 10: 0198512120)*, 1954.

[268] H. Bertini. “Low-Energy Intranuclear Cascade Calculation”. *Physical Review*, 131:1801, 1963.

[269] B. Andersson, G. Gustafson, P. Hong. “The Fritiof Model for Very-High-Energy Hadronic Collisions”. *Zeitschrift fur Physik C Particles and Fields*, 57:485–494, 1993.

[270] S. Eidelman et al. “Review of Particle Physics”. *Physics Letters B*, 592:2, 2004.

[271] R.J. Glauber. “High Energy Physics and Nuclear Structure”. *Plenum Press, NY*, 1970.

[272] H. C. Fesefeldt. “A Study of Proportional Counter Readout in Uranium Calorimeters”. *Nuclear Instruments and Methods in Physucs Research Section A*, 267:367, 1988.

[273] K. Amako et al. “Geant4 Physics Reference Manual”. *http://geant4.web.cern.ch/geant4/UserDocumentation/UsersGuides/PhysicsReferenceManual/fo/PhysicsReferenceManual.pdf*, 2015.

[274] S.A. Bass et al. “Microscopic Models for Ultrarelativistic Heavy Ion Collisions”. *Progress in Particle and Nuclear Physics*, 41:225, 1998.

[275] B. T. Jordan. “Geochemistry Tectonic Setting of the Yates Unit of the Poorman Formation DUSEL Bedrock) and Other Northern Black Hills Amphibolites”. *Geological Society of America Abstracts with Programs*, 41:271, 2009.

[276] The LBNE Collaboration. “LBNE FD Parameters Spreadsheet”. *LBNE DocDB 3383*, Jan 2014.

[277] K. Nakamura et al. (Particle Data Group. “Review of Particle Physics - cosmic rays”. *Journal of Physics G: Nuclear and Particle Physics*, 37:075021, 2010.

[278] T. K. Gaisser. “Cosmic Rays and Particle Physics”. *Cambridge University Press (ISBN 0521339316)*, 1990.

[279] M. Garcia-Munoz J.A. Simpson. “Cosmic Ray Lifetime in the Galaxy - Experimental Results and Models”. *Space Science Reviews*, 46:205–224, 1988.

[280] L. O'C Drury M. A. Malkov. "Nonlinear Theory of Diffusive Acceleration of Particles by Shock Waves". *Reports on Progress in Physics*, 64:421–489, 2001.

[281] N.V. Mokhov D.E. Groom and S.I. Striganov. "Muon Stopping-power and Range Tables". *Atomic Data and Nuclear Data Tables*, 78:183, 2001 (arXiv:hep-ph/9803488v3.

[282] M. Spurio S. Cecchini. "Atmospheric Muons: Experimental Aspects. 2012 (arXiv:1208.1171v1 [astro-ph.EP]).

[283] K.A. Olive et al. (Particle Data Group. "Review of Particle Physics - cosmic rays". *Chinese Physics C*, 38:090001, 2014.

[284] P. Antonioli, C. Ghetti, E.V. Korolkova, V.A. Kudryavtsev, G. Sartorelli. "A Three-dimensional Code for Muon Propagation Through the Rock: MUSIC". *Astroparticle Physics*, 7:357, 1997.

[285] V. A. Kudryavtsev. "Muon Simulation Codes MUSIC and MUSUN for Underground Physics". *Computer Physics Communications*, 180:339, 2009.

[286] The LVD Collaboration. "Muon 'depth-intensity' Relation Measured by the Lvd Underground Experiment and Cosmic-ray Muon Spectrum at Sea Level". *Physical Review D*, 58:092005, 1998.

[287] K.A. Olive et al. (Particle Data Group). "$K^\pm$ / $\pi^\pm$ / $\mu^\pm$ particle listings". *Chinese Physics C*, 38:090001, 2014.

[288] T. Suzuki, D. F. Measday, J.P. Roalsvig. "Total Nuclear Capture Rates for Negative Muons". *Physical Review C*, 35:2212, 1987.

[289] M. Sorel. "Expected Performance of An Ideal Liquid Argon Neutrino Detector with Enhanced Sensitivity to Scintillation Light". *Journal of Instrumentation*, 9:10002, 2014 (arXiv:1405.0848 [physics.ins-det]).

[290] G. J. Feldman, R. D. Cousins. "A Unified Approach to the Classical Statistical Analysis of Small Signals". *Physical Review D*, 57:3873–3889, 1998.

[291] J. Klinger, V.A. Kudryavtsev, M. Richardson, N.J.C. Spooner. "Muon-induced Background to Proton Decay in the $p \to K^+\overline{\nu}$ Decay Channel with Large Underground Liquid Argon TPC Detectors". *Physics Letters B*, 746:44–47, 2015 (arXiv:1504.06520).

[292] N.S. Bowden. "Review Report: Mini-Review of Operation of the LBNE Far Detector at the Surface". *LBNE DocDB 6493*, 2012.

[293] S. Agostinelli, J. Allison, K. Amako et al. "Geant4 - a Simulation Toolkit". *Nuclear Instruments and Methods in Physics Research Section A: Accelerators, Spectrometers, Detectors and Associated Equipment*, 2003.

[294] S. Agostinelli, J. Allison, K. Amako et al. "Geant4 Developments and Applications". *IEEE Transactions on Nuclear Science*, 53:270, 2006.

[295] B. Baller. "LAr-FD Parameters Spreadsheet". *LBNE DocDB 3383-v39*, 2013.

[296] M. Aglietta et al. (The LVD Collaboration). “Muon 'Depth-intensity' Relation Measured by the LVD Underground Experiment and Cosmic-ray Muon Spectrum at Sea Level”. *Physical Review D*, 58:092005, 1998.

[297] C. Hagmann, D Lange, D Wright. “Cosmic-ray Shower Generator (CRY) for Monte Carlo Transport Codes”. *Technical Manual, 5 pages. Lawrence Livermore National Laboratory, Livermore, CA.http://nuclear.llnl.gov/simulation/cry.pdf*, 2008.

[298] C. Hagmann, D Lange, D Wright. “Monte Carlo Simulation of Proton-induced Cosmic-ray Cascades in the Atmosphere”. *Lawrence Livermore National Laboratory, UCRL-TR*, 2007.

[299] L.S. Waters et al. “The MCNPX Monte Carlo radiation transport code”. *AIP Conf. Proc.*, 896:81–90, 2007.

[300] G. Brooke and A. Wolfendale. “Momentum Spectrum of Cosmic Ray Protons Near Sea Level in Momentum Range 0.6-150 GeV/c”. *Proceedings of the Physical Society*, 83:848, 1964.

[301] H. Kornmayer et al. “High-Energy Cosmic-Ray Neutrons at Sea-Level”. *Journal of Physica G - Nuclear and Particle Physics*, 21:439, 1995.

[302] J.F. Ziegler. “Terrestrial Cosmic Ray Intensities”. *IBM Journal of Research and Development*, 42:117–140, 1998.

[303] T. Blackwell, V.A. Kudryavtsev, M. Richardson. “Cosmic-ray Spectra from CRY”. *LBNE DocDB 7517-v3*, 2013.

[304] J. N. Capdevielle G. Shatz T. Thouw D. Heck, J. Knapp. “CORSIKA: A Monte Carlo Code to Simulate Extensive Air Showers”. *Wissenschaftliche Berichte FZKA*, 1998.

[305] M. Bishai, The LBNE Collaboration. “The Long-Baseline Neutrino Experiment, Exploring Fundamental Symmetries of the Universe”. *LBNE DocDB 8087*, 2014.

[306] D. Cherdack, Colorado State University. “The LBNE Fast MC”. *LBNE DocDB 7806*, 2013.

[307] J. K. de Jong. “Atmospheric Muon Simulation for LBNE”. *LBNE DocDB 3144*, 2012.

[308] D. Mei C. Zhang, D. Barker. “USD Cosmogenics Backgrounds Simulation Overview”. *LBNE DocDB 6621-v1*, 2012.

[309] J. Strait. “Muon-induced Background for Beam Neutrinos at the Surface”. *LBNE DocDB 6232-v2*, 2012.

[310] D. Coelho, M. Szydagis, R. Svoboda. “Improving Electron / Gamma Separation”. *LBNE DocDB 8458*, 2014.

[311] A. Hitachi et. al. “Effect of Ionization Density on the Time Dependence of Luminescence from Liquid Argon and Xenon”. *Physical Review B*, 27:5279, 1983.

[312] The LBNE Collaboration. “Long-Baseline Neutrino Experiment (LBNE) Project Conceptual Design Report Volume 6: Conventional Facilities at the Far Site”. *LBNE DocDB 5017*, October 2012.

[313] D.S. Ayres et al. “NoVA Technical Design Report”. October 2007.

[314] J.A. Thomas and P.L. Vahle. “Neutrino Oscillations: Present Status and Future Plans”. *ISBN: 978-981-277-197-1*, Ch.5:93, 2008.

[315] H.F. Jones. “Groups, Representations and Physics”. *CRC Press (ISBN 9781420050295)*, 1998.

[316] S. Haywood. “Symmetries and Conservation Laws”. *Course notes (Lecture 3) (Rutherford Appleton Laboratory)*, 2016.

[317] C. Quigg. “Gauge Theories of the Strong, Weak and Electromagnetic Interactions”. *ISBN: 9780691135489*, 1983.

[318] W. Greiner, B. Muller. “Quantum Mechanics - Symmetries, 2nd Ed.”. *ISBN 0-387-58080-8*, 1994.

[319] W.-M. Yao et al. (Particle Data Group). “Pseudoscalar-meson Decay Constants”. *Journal of Physics G*, 33:1, 2006.

[320] Z. Tavartkiladze. “Proton Stability In Supersymmetric SU(5)”. *Physical Review D*, 76:055012, 2007 (arXiv:hep-ph/0610394 v1).

[321] P. Nath, A. H. Chamseddine, R. Arnowitt. “Nucleon Decay In Supergravity Unified Theories”. *Physical Review D*, 32:2348, 1985 (arXiv:hep-ph/9708469v1).

[322] K. Nakamura et al. (Particle Data Group). “Statistics”. *Journal of Physics G*, 37:075021, 2010 and 2011 partial update for the 2012 edition (pdg.lbl.gov).

[323] E.L. Crow and R.S. Gardnek. “Confidence Intervals for the Expectation of a Poisson Variable”. *Biometrika*, 46:441–453, 1959).

8 Appendix

8.1 Generators of SU(2)

The generators of the $SU(2)$ group (the 2 × 2 Pauli Matrices) τ_i:

$$\tau_1 = \begin{pmatrix} 0 & 1 \\ 1 & 0 \end{pmatrix}, \quad \tau_2 = \begin{pmatrix} 0 & -i \\ i & 0 \end{pmatrix}, \quad \tau_3 = \begin{pmatrix} 1 & 0 \\ 0 & -1 \end{pmatrix}.$$

8.2 Generators of SU(3)

The generators of the $SU(3)$ group (the 3 × 3 Gell-Mann Zweig matrices) λ_i:

$$\lambda^1 = \begin{pmatrix} 0 & 1 & 0 \\ 1 & 0 & 0 \\ 0 & 0 & 0 \end{pmatrix}, \quad \lambda^2 = \begin{pmatrix} 0 & -i & 0 \\ i & 0 & 0 \\ 0 & 0 & 0 \end{pmatrix}, \quad \lambda^3 = \begin{pmatrix} 1 & 0 & 0 \\ 0 & -1 & 0 \\ 0 & 0 & 0 \end{pmatrix}, \quad \lambda^4 = \begin{pmatrix} 0 & 0 & 1 \\ 0 & 0 & 0 \\ 1 & 0 & 0 \end{pmatrix},$$

$$\lambda^5 = \begin{pmatrix} 0 & 0 & -i \\ 0 & 0 & 0 \\ i & 0 & 0 \end{pmatrix}, \quad \lambda^6 = \begin{pmatrix} 0 & 0 & 0 \\ 0 & 0 & 1 \\ 0 & 1 & 0 \end{pmatrix}, \quad \lambda^7 = \begin{pmatrix} 0 & 0 & 0 \\ 0 & 0 & -i \\ 0 & i & 0 \end{pmatrix}, \quad \lambda^8 = \frac{1}{\sqrt{3}} \begin{pmatrix} 1 & 0 & 0 \\ 0 & 1 & 0 \\ 0 & 0 & -2 \end{pmatrix}.$$

8.3 SU(5) representations and their Standard Model decompositions

In the construction of the $SU(5)$ GUT discussed in Section 2.2.2, the various SM fields are organised into mutliplets non-arbitrarily, in a manner informed by sets of numbers enclosed by parentheses. To clarify their meaning, one may first start by considering the left-handed ν_e and e. They are grouped together in one doublet where they are distinguished by the third component of their weak isospin, T_3.

In quantum mechanics a state vector ψ is a unit vector in a complex Hilbert space. The simplest Hilbert space for the ν_{eL} and e_L is for each to span a copy of the complex numbers $\mathbb{C}$. If $\psi = \alpha\nu_{eL} + \beta e_L$ then the Hilbert space for ψ is the direct sum[48]:

$$\mathbb{C} \oplus \mathbb{C} \cong \mathbb{C}^2 \qquad \text{with the basis vectors} \qquad \nu_{eL} = \begin{pmatrix} 1 \\ 0 \end{pmatrix} \in \mathbb{C}^2, \qquad e_L = \begin{pmatrix} 0 \\ 1 \end{pmatrix} \in \mathbb{C}^2.$$

This also applies to each generation of quark doublet, but for each quark there are also three colour states available, so the three states can each span a copy of $\mathbb{C} \oplus \mathbb{C} \oplus \mathbb{C} \cong \mathbb{C}^3$:

$$\begin{pmatrix} u_{r,g,b} \\ d_{r,g,b} \end{pmatrix}_L \rightarrow \; u_r, u_g, u_b \in \mathbb{C}^3, \quad d_r, d_g, d_b \in \mathbb{C}^3, \quad u_L = \begin{pmatrix} 1 \\ 0 \end{pmatrix} \in \mathbb{C}^2, \quad d_L = \begin{pmatrix} 0 \\ 1 \end{pmatrix} \in \mathbb{C}^2$$

---

[48] In general, if a system's state can lie in Hilbert space V or Hilbert space W, the total Hilbert space is $V \oplus W$.

Since these quarks can be one of two weak isospin states and a given colour[49], then two-flavour, three-colour state vectors span the vector space

$$\mathbb{C}^3 \oplus \mathbb{C}^3 \cong \mathbb{C}^2 \otimes \mathbb{C}^3.$$

Also the right-handed quarks and leptons are $SU(2)$ singlets, so instead their Hilbert space is $\mathbb{C} \otimes \mathbb{C}^3$. However, they differ by their hypercharge; this is used to label $\mathbb{C}$, e.g. $\mathrm{Y}(\nu_{eL}) = \mathrm{Y}(e_L) = \text{-}1$, so ν_{eL} and e_L each span a copy of $\mathbb{C}_Y = \mathbb{C}_{-1}$. Table 66 summarises the various Hilbert spaces appropriate for the first generation of SM fermions, and presents them in a more compact notation involving parentheses in the third column.

Table 66: *A summary of the appropriate Hilbert spaces for the SM fermions, with the third column a more compact of what appears in the second column. The third number in the parentheses is $Y/2$ rather than Y, in keeping with the convention used in many texts describing the $SU(5)$ GUT.*

	$SU(3)_C \times SU(2)_L \times U(1)_Y$	Notation
$\begin{pmatrix} u_r u_g u_b \\ d_r d_g d_b \end{pmatrix}_L$	$\mathbb{C}^3 \otimes \mathbb{C}^2 \otimes \mathbb{C}_{\frac{1}{3}}$	(3, 2, $\frac{1}{6}$)
$(u_r u_g u_b)_R$	$\mathbb{C}^3 \otimes \mathbb{C} \otimes \mathbb{C}_{\frac{4}{3}}$	(3, 1, $\frac{2}{3}$)
$(d_r d_g d_b)_R$	$\mathbb{C}^3 \otimes \mathbb{C} \otimes \mathbb{C}_{\frac{-2}{3}}$	(3, 1, -$\frac{1}{3}$)
$\begin{pmatrix} \nu_e \\ e \end{pmatrix}_L$	$\mathbb{C} \otimes \mathbb{C}^2 \otimes \mathbb{C}_{-1}$	(1, 2, -$\frac{1}{2}$)
ν_{eR}	$\mathbb{C} \otimes \mathbb{C} \otimes \mathbb{C}_0$	(1, 1, 0)
e_R	$\mathbb{C} \otimes \mathbb{C} \otimes \mathbb{C}_{-2}$	(1, 1, -1)

Section 2.2.2 contains discussion of the 'irreducible representations' of the SM. In group theory [315], a group G (with elements $g \in G$) can have a 'representation' in some vector space, which in this context is a set of square, invertible matrices $D(g)$ that translate the operations of the various group elements into operators in the vector space, and obey $D(g_1)D(g_2) = D(g_1 g_2)$. Other representations can be found by a similarity transformation, i.e. $D' = SDS^{-1}$. If a representation matrix can be transferred into a block-diagonal form by such a similarity transformation then it is said to be 'reducible'. All of the SM representations that live in the spaces denoted in Table 2 are irreducible; the 2-D and 3-D representations of $SU(2)$ and $SU(3)$ involved here are the matrices in Appendices 8.1, 8.2, which cannot be broken down further into block diagonal form by similarity transformations.

Given group representations r_1 and r_2 of dimensions n_1 and n_2 one can define another representation of dimension $n_1 + n_2$ which is the direct sum of $r_1 \oplus r_2$; that is, a block diagonal matrix

$$r_1 \oplus r_2 = \begin{pmatrix} r_1 & \mathbf{0} \\ \mathbf{0} & r_2 \end{pmatrix}.$$

In general any unitary representation r can be written as the direct sum $r = r_1 \oplus r_2 \oplus ... r_m$ where the $r_{i=1,2...,m}$ are irreducible. This means, for example, that a 5-D representation

---

[49] In general, to combine two systems, i.e. if a system consists of one part confined to Hilbert space V and another part with a Hilbert space W, then the direct product $V \otimes W$ is the Hilbert space of the combined system.

of the $SU(5)$ group can be built from the direct sum of 2-D and 3-D irreducible representations involving $SU(2)$ and $SU(3)$. Conversely it is said that such a representation can be 'decomposed' into a direct sum of these lower-dimensional irreducible representations.

Given the vector space options for the SM fields stated in Table 66, the underlying space in which a 5-D representation composed of irreducible representations of the SM can act could be constructed from the direct sum of 3-D and 2-D spaces $(\mathbb{C}^3 \otimes \mathbb{C}) \oplus (\mathbb{C} \otimes \mathbb{C}^2)$. The possibilities for the $(\mathbb{C}^3 \otimes \mathbb{C})$ part of this direct sum are restated more compactly in the third columnd rows 2 and 3 of Table 66 (the actual choice is explained in Appendix 8.4). Also the only option for the $(\mathbb{C} \otimes \mathbb{C}^2)$ part is in row 4.

A representation is termed a 'fundamental' representation when the corresponding basis is the orthogonal unit column vectors; the N-dimensional generators of $SU(N)$ are therefore fundamental representations (e.g. for weak interactions the $SU(2)$ generators act on doublets $(1,0)^T$, $(0,1)^T$). However, there is often ambiguity in terminology among physics texts [316]. For example, the 5-D column vectors $(1,0,0,0,0)^T$, $(0,1,0,0,0)^T$ etc. are sometimes referred to as the $SU(5)$ fundamental representation. For brevity this is done throughout Section 2.2.2 when discussing the **5** multiplet, and for the remainder of these appendices.

Also, as discussed in Appendix 8.4, other irreducible representations able to accommodate more fields than the **5** can be constructed out of the fundamental representation. Table 67 shows the SM decompositions for some relevant $SU(5)$ representations.

Table 67: *The decomposition of the irreducible representations of* $SU(5)$ *into Standard Model gauge quantum numbers.*

Dim	$(SU(3), SU(2), \frac{1}{2}Y)$
5	$(3,1,-\frac{1}{3}) \oplus (1,2,\frac{1}{2})$
10	$(3,2,\frac{1}{6}) \oplus (3^*,1,-\frac{2}{3}) \oplus (1,1,1)$
15	$(6,1,-\frac{2}{3}) \oplus (3,2,\frac{1}{4}) \oplus (1,3,1)$
24/24*	$(8,1,0) \oplus (3,2,-\frac{5}{6}) \oplus (3^*,2,\frac{5}{6}) \oplus (1,3,0) \oplus (1,1,0)$
45	$(8,2,\frac{1}{2}) \oplus (6^*,1,-\frac{1}{3}) \oplus (3,3,-\frac{1}{3}) \oplus (3^*,2,-\frac{7}{6}) \oplus (3,1,-\frac{1}{3}) \oplus (3^*,1,\frac{4}{3}) \oplus (1,2,\frac{1}{2})$
50	$(8,2,\frac{1}{2}) \oplus (6,1,\frac{4}{3}) \oplus (6^*,3,-\frac{1}{3}) \oplus (3^*,2,-\frac{7}{6}) \oplus (3,1,-\frac{1}{3}) \oplus (1,1,-2)$

8.4 Construction of SU(5) representations

The SM may be further embedded into the $SU(5)$ framework through the use of Young's diagrams [51] [317] [318]. These are diagrams built out of boxes $\square$ that denote the fundamental representation of some symmetry group, in this case $SU(5)$. Further irreducible representations of different dimension (i.e. containing different numbers of fields, by which they are named; **5**, **10**, **15** etc.) can be determined using these box diagrams.

To construct a Young diagram to find irreducible representations of $SU(N)$, one arranges rows of boxes $\square$ from left to right, in no more than N rows. Each row may not contain more boxes than the row above it. The first box in each row is placed underneath the left-most box in the row above it. The number of additional boxes a row has compared to the one below it can be represented numerically, for example:

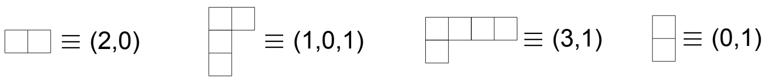

Figure 149: *Young's diagrams examples.*

The number of dimensions D that a Young diagram has (i.e. the number of fields it can accommodate) can be calculated from

$$D = \prod_i \frac{N + d_i}{h_i}, \qquad h_i = 1 + (\textit{number of } \Box \textit{ below } i^{th} \textit{ in same column}) \tag{120}$$

$$+ (\textit{number of } \Box \textit{ to right of } i^{th} \textit{ in same row}) \tag{121}$$

where i indicates the box in question, d_i is found by adding $+1(-1)$ for every step rightwards (downwards) this i^{th} box is from the upper-left box. For example, in the case of $SU(N = 5)$, the (2,0) and (0,1) in Figure149 have dimensions

$$D_{(2,0)} = \frac{N + d_1}{h_1} \times \frac{N + d_2}{h_2} = \frac{5+0}{2} \times \frac{5+1}{1} = 15, \qquad D_{(0,1)} = \frac{5+0}{2} \times \frac{5-1}{1} = 10.$$

In this scheme a horizontal row diagram can be recognised as a symmetric tensor and a vertical column an antisymmetric tensor. Thus, the representations **15** and **10** are symmetric and antisymmetric $SU(5)$ representations respectively. In $SU(5)$ models the **10** is used to accommodate ten of the fifteen SM fields, with the other five fields placed in the fundamental representation **5**.

Higher-dimensional representations can be found by taking product of the fundamental representation $\Box$ with other diagrams. Any such product can be decomposed into irreducible representations by forming every allowed combination of every box participating in the product. This may be demonstrated in the following two examples:

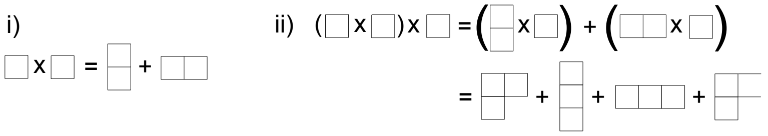

Figure 150: *Young's diagrams examples.*

Thus in terms of dimensions, Figure 150 *i*) reads $\mathbf{5} \times \mathbf{5} = \mathbf{10} + \mathbf{15}$ and Figure 150 *ii*) reads $\mathbf{5} \times \mathbf{5} \times \mathbf{5} = \mathbf{40} + \overline{\mathbf{10}} + \mathbf{35} + \mathbf{40}$, where each can be verified via Eq. 120.

Similarly the $SU(5)$ representations can be decomposed in terms of SM irreducible representations and are referred to in compact notation of parentheses containing their SM gauge quantum numbers [52] (Table 67). The full $SU(3) \times SU(2) \times U(1)$ fifteen-dimensional representation for the right-handed fermions is as follows:

$$(3, 1, \tfrac{2}{3}) \oplus (3, 1, -\tfrac{1}{3}) \oplus (1, 1, -1) \oplus (\overline{3}, 2, -\tfrac{1}{6}) \oplus (1, 2, \tfrac{1}{2}), \tag{122}$$

The aim is to configure **5** such that it transforms as a five-dimensional subset of the full $SU(3) \times SU(2) \times U(1)$ representation, with $SU(2) \times U(1)$ symmetry. The only five-dimensional combinations of the constituents of Eq. 122 are:

$$(3, 1, \tfrac{2}{3}) \oplus (1, 2, \tfrac{1}{2}), \qquad (3, 1, -\tfrac{1}{3}) \oplus (1, 2, \tfrac{1}{2}).$$

The only valid choice of these two possibilities is the second one, since the $U(1)$ hypercharge generator $\frac{1}{2}Y$ (Section 2.2.2) must be traceless ($\frac{2}{3}+\frac{2}{3}+\frac{2}{3}+\frac{1}{2}+\frac{1}{2}=3$ compared to $-\frac{1}{3}-\frac{1}{3}-\frac{1}{3}+\frac{1}{2}+\frac{1}{2}=0$). Thus, the SM decomposition of the $SU(5)$ fundamental representation is

$$\mathbf{5} = (3,1,-\tfrac{1}{3}) \oplus (1,2,\tfrac{1}{2}).$$

From Figure 150, the asymmetric part of the tensor product $\mathbf{5}\times\mathbf{5}$ is the $\mathbf{10}$. The SM decomposition of $\mathbf{10}$ can then be found by the asymmetric tensor product of the decomposition of $\mathbf{5}$:

$$[(3,1,-\tfrac{1}{3}) \oplus (1,2,\tfrac{1}{2}) \otimes (3,1,-\tfrac{1}{3}) \oplus (1,2,\tfrac{1}{2})]_{AS} = (\overline{3},1,-\tfrac{1}{3}) \oplus (1,1,1) \oplus (3,2,\tfrac{1}{6})$$

The specific choice of fermion fields assigned to $\mathbf{5}$ (or rather, $\overline{\mathbf{5}}$) with the remaining ten fields placed in $\mathbf{10}$, as discussed in Section 2.2.2.

8.5 Generators of SU(5)

The generators of the $SU(5)$ group $t^{13,\dots,24}$ which relate to the twelve non-Standard Model gauge bosons $X^i_\mu, Y^i_\mu, \overline{X}^i_\mu, \overline{Y}^i_\mu$ in $SU(5)$ theories:

$$t^{13} = \begin{pmatrix}1&0\\0&0\\0&0\end{pmatrix}, \quad t^{14} = \begin{pmatrix}-i&0\\0&0\\0&0\end{pmatrix}, \quad t^{15} = \begin{pmatrix}0&1\\0&0\\0&0\end{pmatrix}, \quad t^{16} = \begin{pmatrix}0&-i\\0&0\\0&0\end{pmatrix}, \quad t^{17} = \begin{pmatrix}0&0\\1&0\\0&0\end{pmatrix},$$

$$t^{18} = \begin{pmatrix}0&0\\-i&0\\0&0\end{pmatrix}, \quad t^{19} = \begin{pmatrix}0&0\\0&1\\0&0\end{pmatrix}, \quad t^{20} = \begin{pmatrix}0&0\\0&-i\\0&0\end{pmatrix}, \quad t^{21} = \begin{pmatrix}0&0\\0&0\\1&0\end{pmatrix}, \quad t^{22} = \begin{pmatrix}0&0\\0&0\\-i&0\end{pmatrix},$$

$$t^{23} = \begin{pmatrix}0&0\\0&0\\0&1\end{pmatrix}, \quad t^{24} = \begin{pmatrix}0&0\\0&0\\0&-i\end{pmatrix}.$$

The first twelve generators of $SU(5)$ are already stated in Section 2.2.2.

8.6 SU(5) gauge boson matrix

The $SU(5)$ gauge bosons are arranged in the adjoint representation **24** (Table 67) according to Eq. 28. This has been constructed as follows [53]:

$$\frac{1}{\sqrt{2}}T^{\alpha}V_{\mu}^{\alpha} = \begin{pmatrix} g_{11} & g_{12} & g_{13} & \overline{X}^{r} & \overline{Y}^{r} \\ g_{21} & g_{22} & g_{23} & \overline{X}^{g} & \overline{Y}^{g} \\ g_{31} & g_{32} & g_{33} & \overline{X}^{b} & \overline{Y}^{b} \\ X^{r} & X^{g} & X^{b} & \frac{W^3}{\sqrt{2}} & W^{+} \\ Y^{r} & Y^{g} & Y^{b} & W^{-} & -\frac{W^3}{\sqrt{2}} \end{pmatrix} + \frac{B}{\sqrt{30}}\begin{pmatrix} -2 & 0 & 0 & 0 & 0 \\ 0 & -2 & 0 & 0 & 0 \\ 0 & 0 & -2 & 0 & 0 \\ 0 & 0 & 0 & 3 & 0 \\ 0 & 0 & 0 & 0 & 3 \end{pmatrix}$$

$$= \begin{pmatrix} g_{11}-\frac{2B}{\sqrt{30}} & g_{12} & g_{13} & \overline{X}^{r} & \overline{Y}^{r} \\ g_{21} & g_{22}-\frac{2B}{\sqrt{30}} & g_{23} & \overline{X}^{g} & \overline{Y}^{g} \\ g_{31} & g_{32} & g_{33}-\frac{2B}{\sqrt{30}} & \overline{X}^{b} & \overline{Y}^{b} \\ X^{r} & X^{g} & X^{b} & \frac{W^3}{\sqrt{2}}+\frac{3B}{\sqrt{30}} & W^{+} \\ Y^{r} & Y^{g} & Y^{b} & W^{-} & -\frac{W^3}{\sqrt{2}}+\frac{3B}{\sqrt{30}} \end{pmatrix}$$

8.7 SUSY SU(5) proton decay rate calculation

The decay rate in the channel $p \to K^{+}\overline{\nu}$ is calculated as follows: [58]

$$\Gamma_{p\to K^{+}\overline{\nu}} = \frac{\beta_p^2 m_p}{32\pi M_T f_\pi^2}\left(1-\frac{m_K^2}{m_p^2}\right)^2 |\mathcal{A}_{K\nu}|^2 A_L^2 (A_S^L)^2 \left|1+\frac{m_p(D+F)}{m_B}\right|^2$$

where β_p is a three-quark strong interaction matrix element between the vacuum $|0\rangle$ and the proton $|p\rangle$ and defined by

$$\langle 0|\epsilon_{abc}\epsilon_{\alpha\beta}u_{aL}^{\alpha}d_{bL}^{\beta}u_{L}^{\gamma}|p\rangle = \beta u_L^{\gamma}$$

M_T is the Higgs triplet mass, m_B is the average baryon mass, f_π is the pion decay constant [319], A_S^L is a factor for renormalization from the GUT scale to the electroweak scale [320], A_L takes into account renormalization from the electroweak scale M_Z to the proton decay scale of 1 GeV [61], and D, F are parameters of the chiral Lagrangian (the 'chiral Lagrangian' technique [59] is used to translate operators at quark level to those at hadron level):

$$M_T \approx 10^{16}\,GeV \qquad m_B = 1150\,MeV \qquad A_S^L = 2.03 \qquad A_L = 1.43$$
$$D+F = 1.2670, \qquad f_\pi = 130\,MeV.$$

Also the factor $\mathcal{A}_{K\nu}$ is defined as

$$\mathcal{A}_{K\nu} = sin(2\beta M_W^2)^{-1}\alpha_2^2 P_2 m_c m_i^d V_{i1}^{\dagger} V_{21} V_{22}\left[I(\tilde{c};\tilde{d}_i;\tilde{W}) + I(\tilde{c};\tilde{e}_i;\tilde{W})\right]$$

where V is the CKM matrix, P_i are generational phases

$$P_i = e^{i\gamma_i}, \qquad \Sigma_i\gamma_i = 0, \qquad i = 1,2,3,$$

α_2 is weak coupling at the GUT scale, m_c and m_i^d are the masses of charm and down-type quarks, $I(\tilde{c};\tilde{d}_i;\tilde{W}), I(\tilde{c};\tilde{e}_i;\tilde{W})$ are dressing loop functions [321], and

$$tan(\beta) = \frac{v_2}{v_1} \qquad\qquad (v_i \equiv \langle H_i \rangle)$$

with $\langle H_i \rangle$ the vacuum expectation value of the neutral component of the Higgs doublet.

8.8 Flipped SU(5) representations

In Flipped $SU(5)$ GUTs the arrangement of the first generation of fermions into the $SU(5) \times U(1)$ group representations is different to how they are arranged in conventional $SU(5)$ (Section 2.2.2). In Flipped $SU(5)$ they are arranged as follows:

$$\bar{\mathbf{5}} = \begin{pmatrix} u_1^c \\ u_2^c \\ u_3^c \\ e^- \\ -\nu_e \end{pmatrix}_L , \qquad \mathbf{10} = \begin{pmatrix} 0 & d_3^c & -d_2^c & -u^1 & -d^1 \\ -d_3^c & 0 & d_1^c & -u^2 & -d^2 \\ d_2^c & -d_1^c & 0 & -u^3 & -d^3 \\ u^1 & u^2 & u^3 & 0 & \nu^c \\ d^1 & d^2 & d^3 & -\nu^c & 0 \end{pmatrix}_L , \qquad \mathbf{1} = e^+. \qquad (123)$$

8.9 The Feldman-Cousins "Unified Approach" to the counstruction of classical confidence intervals

The results found in Sections 4, 6 sometimes involve the discussion of very low event rates. Instead of taking a count n to have an uncertainty of $\pm\sqrt{n}$ as is done with large counts, for low counts it is more appropriate that their uncertainties expressed in terms of confidence levels. In such instances, a Particle Data Group-endorsed [322] prescription for determining upper and lower limits is described by G.J. Feldman and R.D. Cousins in the 1998 paper "A Unified Approach to the Classical Statistical Analysis of Small Signals" [290].

Feldman and Cousins take a classical/frequentist approach rather than Bayesian. One may consider an experiment seeking the true value μ_t of some unknown parameter μ, by measuring some observable quantity x. In the Bayesian view one calculates the probability $\mathcal{P}$ of μ_t being somewhere in the range μ_1 and μ_2, having obtained a measurement x_0, by assuming some probability density function (PDF) $P(\mu_t|x_0)$. The probability is then calculated by integrating the PDF between two limits of μ_t:

$$\mathcal{P} = \int_{\mu_1}^{\mu_2} P(\mu_t|x_0)\, d\mu_t.$$

Whilst this procedure has the strength of being able to incorporate such information as the results of previous experiments, a non-subjective method has been sought. Instead of the "Bayesian intervals" discussed above, Feldman and Cousins present confidence intervals which have a different interpretation and have some advantages that will be discussed later in this appendix.

The Feldman-Cousins approach instead considers general PDFs $P(x|\mu)$ rather than $P(x_0|\mu_t)$ and deals with a varying confidence intervals $[\mu_1, \mu_2]$ in an ensemble of identical experiments with a fixed μ. These $[\mu_1, \mu_2]$ are members of a set of confidence intervals that obey:

$$P(\mu \in [\mu_1, \mu_2]) = \alpha$$

where μ_1, μ_2 are functions of the observable quantity x. This equation holds for every allowed μ and thus, for a fraction α of this ensemble of experiments, the intervals contain the true value μ_t. For example, if $\alpha = 0.9$ and the experiment was repeated 100 times, the true value of the parameter μ would fall within the interval $[\mu_1, \mu_2]$ 90 times.

This method uses Neyman's Construction, which involves a graph of the parameter μ plotted against the measured quanity x. For each allowed value of μ one plots a horizontal confidence interval in x spanning an interval $[x_1, x_2]$ according to the appropriate $P(x|\mu)$, i.e.:

$$P(x \in [x_1, x_2]|\mu) = \alpha.$$

This is repeated for many values of μ to form a confidence belt (such as the generic one illustrated in Figure 151), at which point the construction is complete. Then a measurement of x can be made and a vertical line is drawn on the plot at this measured value. This vertical line may intersect many of the horizontal lines plotted for each possible value of μ; the subsection of this vertical line over which it intersects the horizontal acceptance intervals gives the confidence interval in μ. For example, the confidence belt in Figure 151, a measurement of $x \approx 3.27$ determines that μ spans approximately 1.30-3.25 at this "coverage" α. If $P(\mu \in [\mu_1, \mu_2]) < \alpha$ for any value of μ then for that value of μ the intervals are said to "under-cover", or "over-cover" if $P(\mu \in [\mu_1, \mu_2]) > \alpha$. The latter case means being more conservative than the stated confidence level α.

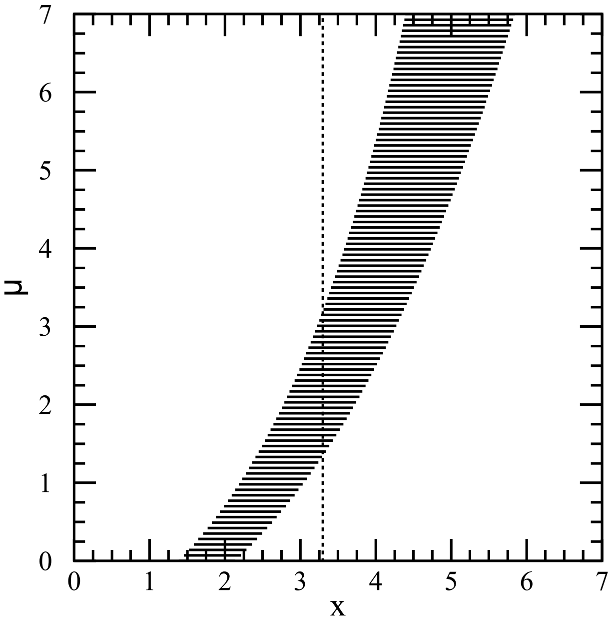

Figure 151: *A generic confidence belt to illustrate the procedure for constructing confidence intervals for the parameter μ based on having measured some quantity x.*

The horizontal confidence intervals are determined based on some PDF $P(x|\mu)$. Phenomena such as proton decay or neutrino interaction are Poisson processes, i.e. one seeks to count such events, which are anticipated to occur at some average rate but still randomly and discretely. The observable quantity x is the total event count n (signal and background), and given some known number of background events b then

$$P(n|\mu) = (\mu + b)^n \frac{e^{-(\mu+b)}}{n!}.$$

Due to the discreteness of n in such Poisson processes, the confidence intervals slightly and unavoidably over-cover.

Part of the motivation for Feldman and Cousins was the under-coverage caused by physicists "flip-flopping" in how they report their results. This refers to the decision between quoting upper limits to upper and lower limits once their data reached, for example, a 3 σ threshold, which results in some under-coverage. For example, a physicist dealing with a Poisson process with background $b = 3$ may make a choice between Figure 152 (i) or (ii) (which show standard confidence belts constructed according to Crow and Gardner [323]). Another problem arises if, say, they have measured $n = 0$ with an expected background $b = 3$; in these figures the vertical line drawn at this n would intercept none of the confidence belt.

To tackle these problems, Feldman and Cousins proposed using a certain ordering principle when deciding which values of n to place in the horizontal acceptance interval for a given μ. For each n one calculates a ratio R of two likelihoods; the likelihood of measuring n given a mean signal μ, and the likelihood of measuring n given the physically-allowed best-fit mean of μ:

$$R = \frac{P(n|\mu)}{P(n|\mu_{best})}$$

where μ_{best} is the value of μ that maximises $P(n|\mu)$. Values of n are added to the horizontal acceptance interval of the appropriate value of μ in order of descending R until the correct coverage has been reached[50]. Figure 153 shows their confidence belt for a Poisson process with a signal mean of $\mu = 0.5$ and a background of $b = 3.0$. At small n the confidence interval transitions smoothly between upper limits only and upper and lower limits (meaning no need to "flip-flop"), and there are no empty intervals even when $n = 0$.

Feldman and Cousins provide reference tables (for $\alpha = 68.27\%, 90.0\%, 95.0\%$ and 99.0%) that state upper and lower limits for a Poisson signal mean, for common observed numbers of events n and backgrounds b. Upper and lower limits are stated at 90% confidence level in this thesis are generally applied to counts that have dropped to 1 or 0 (unless otherwise stated). The relevant table is therefore the one reproduced in Figure 154, and in these background estimation studies, b has been taken as 0. Any normalization factors used to convert a raw count to an annual rate is also applied to the upper and lower limits read from this table.

---

[50] Reached or exceeded; the discrete nature of the variable n causes the summed probabilty to exceed α, i.e. to slightly 'overcover' or be marginally more conservative than the intended α.

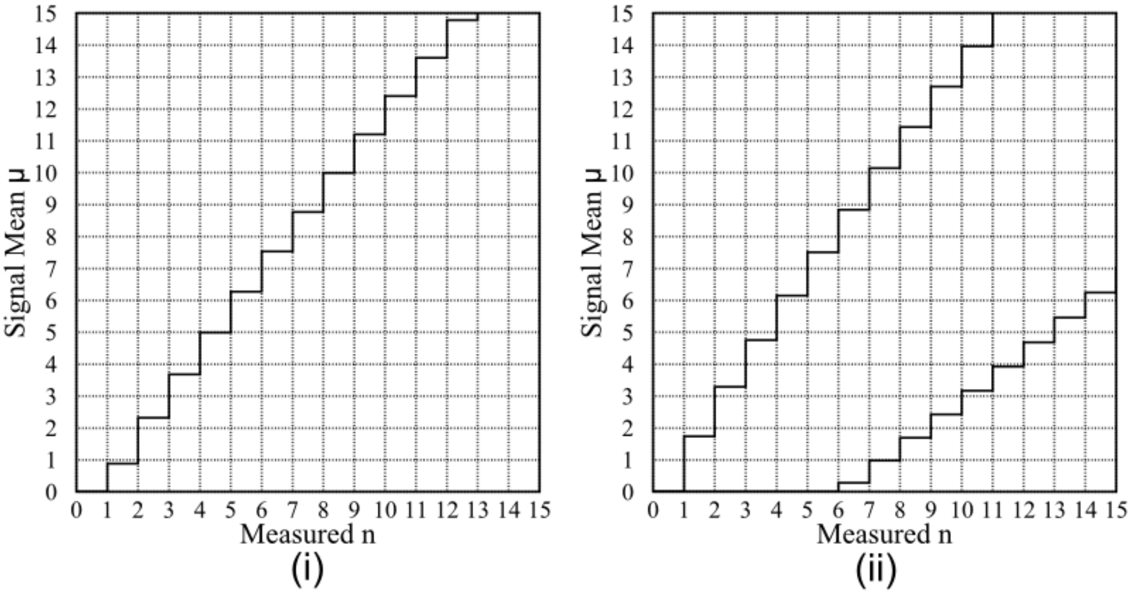

Figure 152: *From [290]: (i) Standard confidence belt for* 90% *C.L. upper limits, for unknown Poisson signal mean* μ *in the presence of Poisson background with known mean* $b = 3.0$*. The second line in the belt is at* $n = +\infty$*. (ii) Standard confidence belt for* 90% *C.L. central confidence intervals, for unknown Poisson signal mean* μ *in the presence of Poisson background with known mean* $b = 3.0$*.*

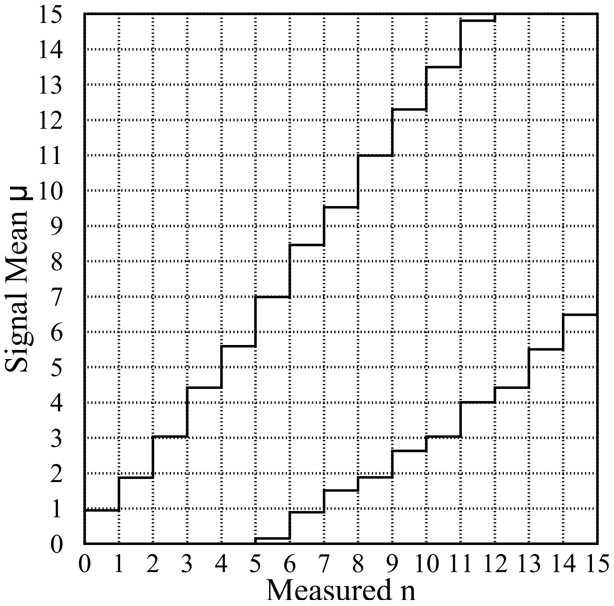

Figure 153: *From [290]: Confidence belt based on the ordering principle proposed by Feldman and Cousins, for* 90% *C.L. confidence intervals for unknown Poisson signal mean* μ *in the presence of Poisson background with known mean* $b = 3.0$*.*

$n_0 \backslash b$	0.0	0.5	1.0	1.5	2.0	2.5	3.0	3.5	4.0	5.0
0	0.00, 2.44	0.00, 1.94	0.00, 1.61	0.00, 1.33	0.00, 1.26	0.00, 1.18	0.00, 1.08	0.00, 1.06	0.00, 1.01	0.00, 0.98
1	0.11, 4.36	0.00, 3.86	0.00, 3.36	0.00, 2.91	0.00, 2.53	0.00, 2.19	0.00, 1.88	0.00, 1.59	0.00, 1.39	0.00, 1.22
2	0.53, 5.91	0.03, 5.41	0.00, 4.91	0.00, 4.41	0.00, 3.91	0.00, 3.45	0.00, 3.04	0.00, 2.67	0.00, 2.33	0.00, 1.73
3	1.10, 7.42	0.60, 6.92	0.10, 6.42	0.00, 5.92	0.00, 5.42	0.00, 4.92	0.00, 4.42	0.00, 3.95	0.00, 3.53	0.00, 2.78
4	1.47, 8.60	1.17, 8.10	0.74, 7.60	0.24, 7.10	0.00, 6.60	0.00, 6.10	0.00, 5.60	0.00, 5.10	0.00, 4.60	0.00, 3.60
5	1.84, 9.99	1.53, 9.49	1.25, 8.99	0.93, 8.49	0.43, 7.99	0.00, 7.49	0.00, 6.99	0.00, 6.49	0.00, 5.99	0.00, 4.99
6	2.21,11.47	1.90,10.97	1.61,10.47	1.33, 9.97	1.08, 9.47	0.65, 8.97	0.15, 8.47	0.00, 7.97	0.00, 7.47	0.00, 6.47
7	3.56,12.53	3.06,12.03	2.56,11.53	2.09,11.03	1.59,10.53	1.18,10.03	0.89, 9.53	0.39, 9.03	0.00, 8.53	0.00, 7.53
8	3.96,13.99	3.46,13.49	2.96,12.99	2.51,12.49	2.14,11.99	1.81,11.49	1.51,10.99	1.06,10.49	0.66, 9.99	0.00, 8.99
9	4.36,15.30	3.86,14.80	3.36,14.30	2.91,13.80	2.53,13.30	2.19,12.80	1.88,12.30	1.59,11.80	1.33,11.30	0.43,10.30
10	5.50,16.50	5.00,16.00	4.50,15.50	4.00,15.00	3.50,14.50	3.04,14.00	2.63,13.50	2.27,13.00	1.94,12.50	1.19,11.50
11	5.91,17.81	5.41,17.31	4.91,16.81	4.41,16.31	3.91,15.81	3.45,15.31	3.04,14.81	2.67,14.31	2.33,13.81	1.73,12.81
12	7.01,19.00	6.51,18.50	6.01,18.00	5.51,17.50	5.01,17.00	4.51,16.50	4.01,16.00	3.54,15.50	3.12,15.00	2.38,14.00
13	7.42,20.05	6.92,19.55	6.42,19.05	5.92,18.55	5.42,18.05	4.92,17.55	4.42,17.05	3.95,16.55	3.53,16.05	2.78,15.05
14	8.50,21.50	8.00,21.00	7.50,20.50	7.00,20.00	6.50,19.50	6.00,19.00	5.50,18.50	5.00,18.00	4.50,17.50	3.59,16.50
15	9.48,22.52	8.98,22.02	8.48,21.52	7.98,21.02	7.48,20.52	6.98,20.02	6.48,19.52	5.98,19.02	5.48,18.52	4.48,17.52
16	9.99,23.99	9.49,23.49	8.99,22.99	8.49,22.49	7.99,21.99	7.49,21.49	6.99,20.99	6.49,20.49	5.99,19.99	4.99,18.99
17	11.04,25.02	10.54,24.52	10.04,24.02	9.54,23.52	9.04,23.02	8.54,22.52	8.04,22.02	7.54,21.52	7.04,21.02	6.04,20.02
18	11.47,26.16	10.97,25.66	10.47,25.16	9.97,24.66	9.47,24.16	8.97,23.66	8.47,23.16	7.97,22.66	7.47,22.16	6.47,21.16
19	12.51,27.51	12.01,27.01	11.51,26.51	11.01,26.01	10.51,25.51	10.01,25.01	9.51,24.51	9.01,24.01	8.51,23.51	7.51,22.51
20	13.55,28.52	13.05,28.02	12.55,27.52	12.05,27.02	11.55,26.52	11.05,26.02	10.55,25.52	10.05,25.02	9.55,24.52	8.55,23.52

Figure 154: *From [290]: 90% C.L. intervals for the Poisson signal mean* μ*, for total events observed* n_0*, for known mean background* b *ranging from* 0 *to* 5*. The intervals enclosed within the red box are the relevant ones for results stated in thesis.*